

# AJNR

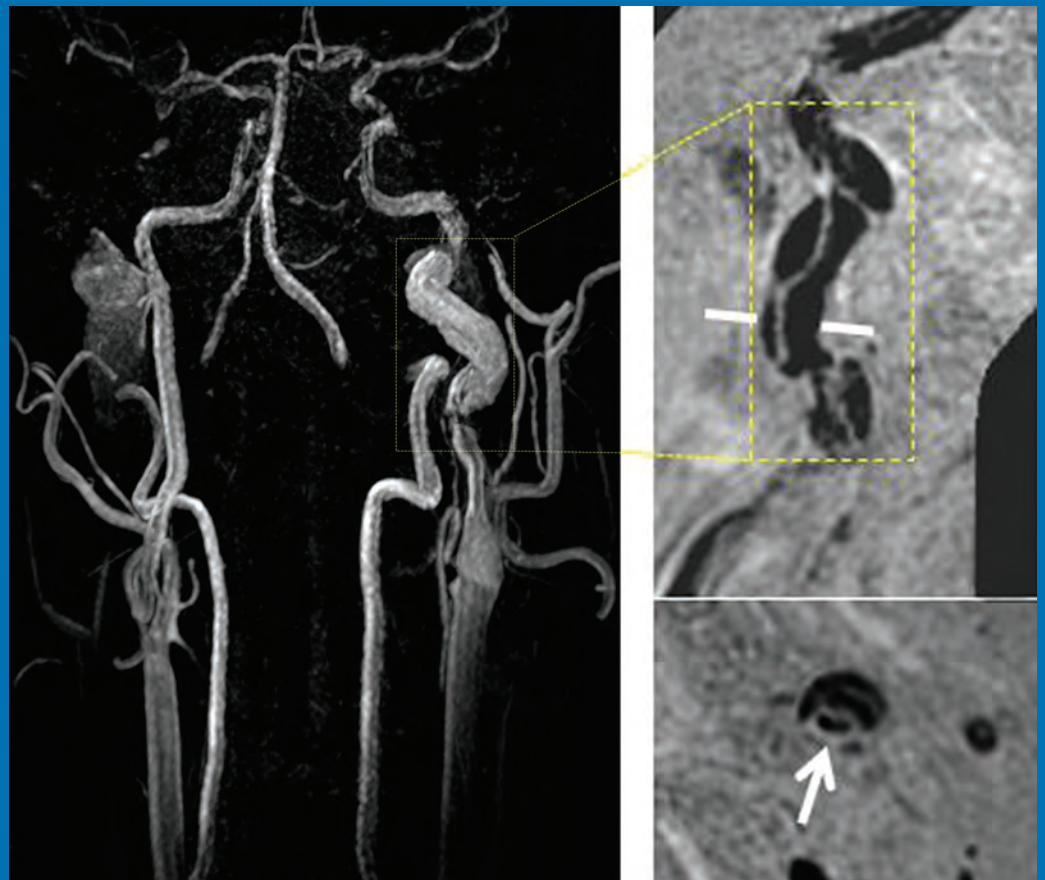
## AMERICAN JOURNAL OF NEURORADIOLOGY

SEPTEMBER 2015  
VOLUME 36  
NUMBER 9  
WWW.AJNR.ORG

THE JOURNAL OF DIAGNOSTIC AND  
INTERVENTIONAL NEURORADIOLOGY

Iterative reconstruction of temporal bone CT  
Aqueductal stroke volume and NPH  
Repeatability of CBV in glioblastoma

Official Journal ASNR • ASFNR • ASHNR • ASPNR • ASSR



# Engineered

by MicroVention®



## HYDROGEL ADVANCED COILS

The clinical benefits of **hydrogel** NOW engineered with the softness of bare platinum on the **V-Trak® Advanced Coil System**.

### INDICATIONS FOR USE:

The HydroCoil® Embolic System (HES) is intended for the endovascular embolization of intracranial aneurysms and other neurovascular abnormalities such as arteriovenous malformations and arteriovenous fistulae. The HES is also intended for vascular occlusion of blood vessels within the neurovascular system to permanently obstruct blood flow to an aneurysm or other vascular malformation and for arterial and venous embolizations in the peripheral vasculature. The device should only be used by physicians who have undergone pre-clinical training in all aspects of HES procedures as prescribed by MicroVention.

MICROVENTION, V-Trak, HydroCoil, HydroFrame, HydroFill and HydroSoft are registered trademarks of MicroVention, Inc. Scientific and clinical data related to this document are on file at MicroVention, Inc. Refer to Instructions for Use, contraindications and warnings for additional information. Federal (USA) law restricts this device for sale by or on the order of a physician. © 2015 MicroVention, Inc. 6/15



# Frame, Fill, Finish



**HydroFrame<sup>®</sup>**  
HydroCoil<sup>®</sup> Embolic System



**HydroFill<sup>®</sup>**  
HydroCoil<sup>®</sup> Embolic System



**HydroSoft<sup>®</sup>**  
HydroCoil<sup>®</sup> Embolic System

- CLINICALLY STUDIED HYDROGEL
- EFFECTIVE<sup>1,2,3</sup>
- ESTABLISHED SAFETY PROFILE<sup>4</sup>
- SOFTER DESIGN<sup>5</sup>

For more information or a product demonstration,  
contact your local MicroVention representative:



**MicroVention, Inc.**

**Worldwide Headquarters**

1311 Valencia Avenue  
Tustin, CA 92780 USA

MicroVention UK Limited

MicroVention Europe, S.A.R.L.

MicroVention Deutschland GmbH

**microvention.com**

PH +1.714.247.8000

PH +44 (0) 191 258 6777

PH +33 (1) 39 21 77 46

PH +49 211 210 798-0

References

1. Speirs, Burke, Lee, and Ala. The next generation HydroCoil: initial clinical experience with the HydroFill embolic coil. J NeuroIntervent Surg, 2013.
2. Brinjikiji et al. Abstract 112. Presented at: International Stroke Conference 2015, Nashville, Tennessee, February 11-13, 2015.
3. Lee, Seo, Less, Cho, Kang and Han. Mid-term outcome of intracranial aneurysms treated with HydroSoft coils compared to historical controls treated with bare platinum coils: a single-center experience. Acta Neurochir, 156:1687-1694, 2014.
4. Laymond et al. Patients prone to recurrence after endovascular treatment: periprocedural results of the PRET randomized trial on large and recurrent aneurysms, AJNR AM J Neuroradiol, 2014.
5. Data on file at MicroVention, Inc.



# COILING OPTIMIZED



**NOW AVAILABLE**

**BARRICADE COMPLEX  
FINISHING COIL**

- ◆ Extremely soft profile of The Barricade Finishing coil now in a complex shape
- ◆ Excellent microcatheter stability for confident coil placement
- ◆ Available in a size range of 1mm-5mm

## BARRICADE™ COIL SYSTEM



MADE IN AMERICA

The Barricade Coil System is intended for the endovascular embolization of intracranial aneurysms and other neurovascular abnormalities such as arteriovenous malformations and arteriovenous fistulae. The System is also intended for vascular occlusion of blood vessels within the neurovascular system to permanently obstruct blood flow to an aneurysm or other vascular malformation and for arterial and venous embolizations in the peripheral vasculature. Refer to the instructions for use for complete product information.

18 TECHNOLOGY DRIVE #169, IRVINE CA 92618

p: 949.788.1443 | f: 949.788.1444

[WWW.BLOCKADEMEDICAL.COM](http://WWW.BLOCKADEMEDICAL.COM)

MKTG-031 Rev. A



**BLOCKADE**  
M E D I C A L

# AJNR

## AMERICAN JOURNAL OF NEURORADIOLOGY

SEPTEMBER 2015  
VOLUME 36  
NUMBER 9  
WWW.AJNR.ORG

Publication Preview at [www.ajnr.org](http://www.ajnr.org) features articles released in advance of print. Visit [www.ajnrblog.org](http://www.ajnrblog.org) to comment on AJNR content and chat with colleagues and AJNR's News Digest at <http://ajnrdigest.org> to read the stories behind the latest research in neuroimaging.

### 1579 PERSPECTIVES

*S.G. Imbesi*

### REVIEW ARTICLE



1580

Reversible Cerebral Vasoconstriction Syndrome, Part 2: Diagnostic Work-Up, Imaging Evaluation, and Differential Diagnosis *T.R. Miller, et al.*

ADULT BRAIN

### LEVEL 1 EBM EXPEDITED PUBLICATION



1589

The Benefits of High Relaxivity for Brain Tumor Imaging: Results of a Multicenter Intraindividual Crossover Comparison of Gadobenate Dimeglumine with Gadoterate Meglumine (The BENEFIT Study)

*M. Vaneckova, et al.*

ADULT BRAIN

### PATIENT SAFETY



1599

Temporal Bone CT: Improved Image Quality and Potential for Decreased Radiation Dose Using an Ultra-High-Resolution Scan Mode with an Iterative Reconstruction Algorithm *S. Leng, et al.*

HEAD & NECK  
PEDIATRICS

### FUNCTIONAL VIGNETTE

1604

Memory Part 3: The Role of the Fornix and Clinical Cases

*F.D. Raslau, et al.*

ADULT BRAIN  
PEDIATRICS

### GENERAL CONTENTS



1609

Early Quantification of Hematoma Hounsfield Units on Noncontrast CT in Acute Intraventricular Hemorrhage Predicts Ventricular Clearance after Intraventricular Thrombolysis *J. Kornbluth, et al.*

ADULT BRAIN  
PEDIATRICS

1616

Neuroradiologic Diagnosis of Minor Leak prior to Major SAH: Diagnosis by T1-FLAIR Mismatch *S. Oda, et al.*

ADULT BRAIN  
INTERVENTIONAL



1623

Aqueductal Stroke Volume: Comparisons with Intracranial Pressure Scores in Idiopathic Normal Pressure Hydrocephalus *G. Ringstad, et al.*

ADULT BRAIN

1631

*Commentary*  
Intracranial Pressure versus Phase-Contrast MR Imaging for Normal Pressure Hydrocephalus *W.G. Bradley*

1633

*Reply* *G. Ringstad, et al.*



1635

Cerebral Microbleeds, CSF p-Tau, and Cognitive Decline: Significance of Anatomic Distribution *G.C. Chiang, et al.*

ADULT BRAIN



1642

Cerebral Microbleeds in Patients with Dementia with Lewy Bodies and Parkinson Disease Dementia *S.W. Kim, et al.*

ADULT BRAIN



1648

Effects of Type 2 Diabetes on Brain Structure and Cognitive Function: African American–Diabetes Heart Study MIND *C.T. Whitlow, et al.*

ADULT BRAIN



1654

Repeatability of Standardized and Normalized Relative CBV in Patients with Newly Diagnosed Glioblastoma *M.A. Prah, et al.*

ADULT BRAIN

# 66%

of Patients in MR CLEAN  
Were Treated with a  
Trevor<sup>®</sup> Stent Retriever

stryker<sup>®</sup>  
Neurovascular

Trevor<sup>®</sup>  
PROVUE RETRIEVER

## MR CLEAN<sup>1</sup>

First clinical evidence for intra-arterial  
treatment with stent retrievers

- **Largest** of the randomized AIS trials<sup>2</sup>, with over 500 patients enrolled
- The Trevor Retriever was the **#1** device used in the **MR CLEAN** Trial

<sup>1</sup> O.A. Berkhemer et al. A Randomized Trial for Intra-arterial Treatment for Acute Ischemic Stroke. *N Eng J Med* December 2014.

<sup>2</sup> MR CLEAN is the largest AIS Trial in which stent retrievers were used.  
<http://www.mrclean-trial.org/>

-  1662 **Correlation of Asymmetry Indices Measured by Arterial Spin-Labeling MR Imaging and SPECT in Patients with Crossed Cerebellar Diaschisis** *K.M. Kang, et al.* **ADULT BRAIN**
- 1669 **Visualization of the Medial and Lateral Geniculate Nucleus on Phase Difference Enhanced Imaging** *M. Kitajima, et al.* **ADULT BRAIN**
- 1675 **Cortical Activation Through Passive-Motion Functional MRI** *A.F. Choudhri, et al.* **FUNCTIONAL PEDIATRICS**
-  1682 **Complications in Stent-Assisted Endovascular Therapy of Ruptured Intracranial Aneurysms and Relevance to Antiplatelet Administration: A Systematic Review** *C.-W. Ryu, et al.* **INTERVENTIONAL**
- 1689 **HydroCoils Are Associated with Lower Angiographic Recurrence Rates Than Are Bare Platinum Coils in Treatment of “Difficult-to-Treat” Aneurysms: A Post Hoc Subgroup Analysis of the HELPS Trial** *W. Brinjikji, et al.* **INTERVENTIONAL**
-  1695 **Wall Mechanical Properties and Hemodynamics of Unruptured Intracranial Aneurysms** *J.R. Cebal, et al.* **INTERVENTIONAL**
- 1704 **Computerized Angiographic Occlusion Rating for Ruptured Clipped Aneurysms is Superior to Subjective Occlusion Rating** *A.R. Al-Schameri, et al.* **INTERVENTIONAL**
-  1710 **RNA-Sequencing Analysis of Messenger RNA/MicroRNA in a Rabbit Aneurysm Model Identifies Pathways and Genes of Interest** *M. Holcomb, et al.* **INTERVENTIONAL**
-  1716 **Evolution of Flow-Diverter Endothelialization and Thrombus Organization in Giant Fusiform Aneurysms after Flow Diversion: A Histopathologic Study** *I. Szikora, et al.* **INTERVENTIONAL**
-  1721 **Intrasaccular Flow Disruption in Acutely Ruptured Aneurysms: A Multicenter Retrospective Review of the Use of the WEB** *T. Liebig, et al.* **INTERVENTIONAL**
- 1728 **Long-Term Follow-Up Results following Elective Treatment of Unruptured Intracranial Aneurysms with the Pipeline Embolization Device** *A.H.Y. Chiu, et al.* **INTERVENTIONAL**
-  1735 **pCONus Device for the Endovascular Treatment of Wide-Neck Middle Cerebral Artery Aneurysms** *B. Gory, et al.* **INTERVENTIONAL**
-  1741 **Artery of the Superior Orbital Fissure: An Undescribed Branch from the Pterygopalatine Segment of the Maxillary Artery to the Orbital Apex Connecting with the Anteromedial Branch of the Inferolateral Trunk** *H. Kiyosue, et al.* **INTERVENTIONAL HEAD & NECK**
- 1748 **C-Arm Flat Detector CT Parenchymal Blood Volume Thresholds for Identification of Infarcted Parenchyma in the Neurointerventional Suite** *M. Kamran, et al.* **INTERVENTIONAL**
- 1756 **Histologic Analysis of Retrieved Clots in Acute Ischemic Stroke: Correlation with Stroke Etiology and Gradient-Echo MRI** *S.K. Kim, et al.* **INTERVENTIONAL**
- 1763 **The Preventive Effect of Endovascular Treatment for Recurrent Hemorrhage in Patients with Spinal Cord Arteriovenous Malformations** *Y. Niimi, et al.* **INTERVENTIONAL SPINE**
-  1769 **Characterization of Craniocervical Artery Dissection by Simultaneous MR Noncontrast Angiography and Intraplaque Hemorrhage Imaging at 3T** *Q. Li, et al.* **EXTRACRANIAL VASCULAR HEAD & NECK INTERVENTIONAL**
-  1776 **Accuracy of Preoperative Imaging in Detecting Nodal Extracapsular Spread in Oral Cavity Squamous Cell Carcinoma** *A.H. Aiken, et al.* **HEAD & NECK**
- 1782 **Increased Prevalence of Developmental Venous Anomalies in Children with Intracranial Neoplasms** *B.V. Jones, et al.* **PEDIATRICS**
-  1786 **Choroid Plexus Neoplasms: Toward a Distinction between Carcinoma and Papilloma Using Arterial Spin-Labeling** *V. Dangouloff-Ros, et al.* **PEDIATRICS ADULT BRAIN**
- 1791 **35 YEARS AGO IN AJNR**



From cervical to sacral  
**we've got you covered.**

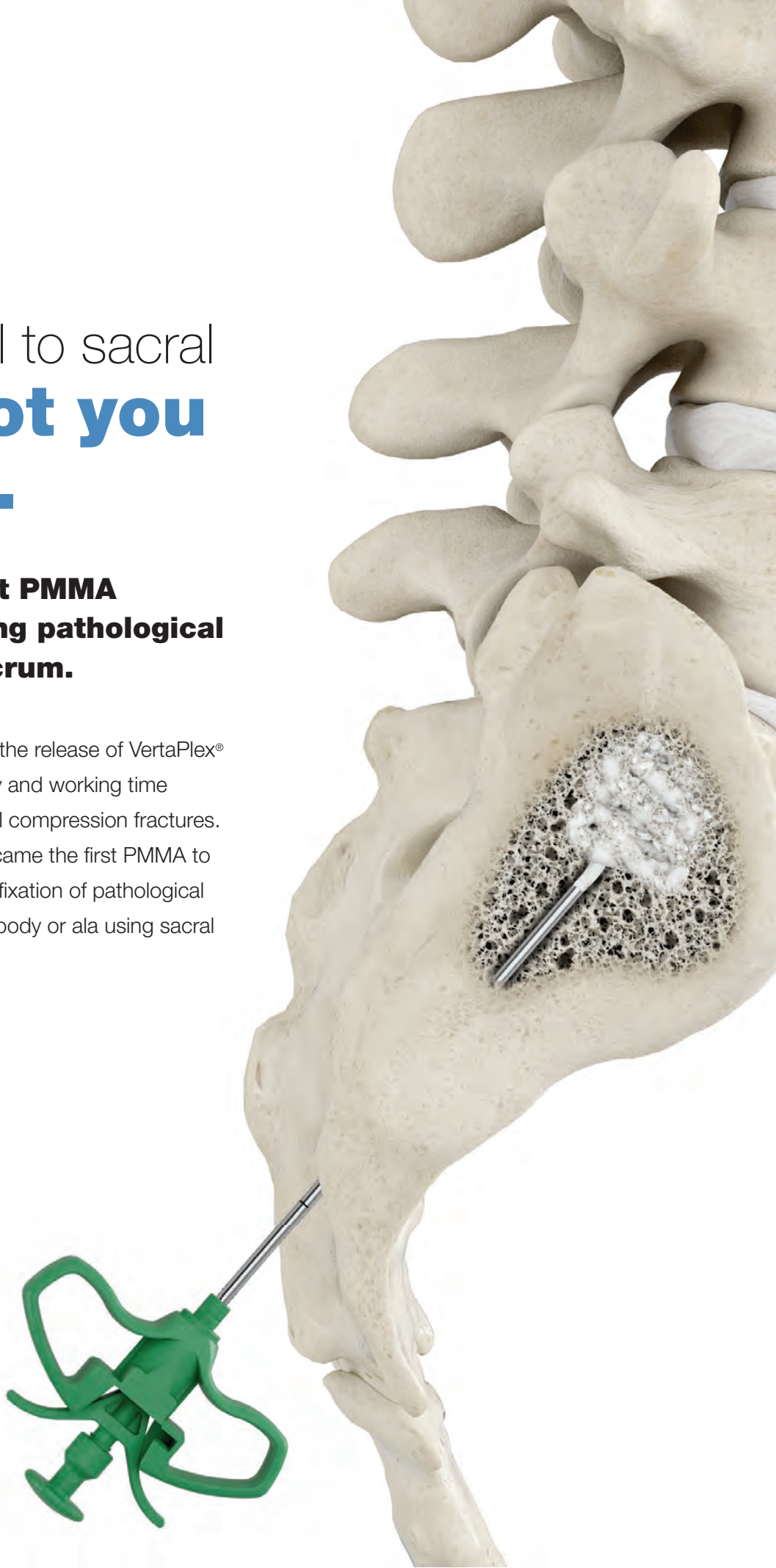
**Introducing the first PMMA indicated for treating pathological fractures of the sacrum.**

Stryker set the bar in 2008 with the release of VertaPlex® HV, addressing specific viscosity and working time preferences for treating vertebral compression fractures. Now in 2015, VertaPlex® HV became the first PMMA to receive 510(k) clearance for the fixation of pathological fractures of the sacral vertebral body or ala using sacral vertebroplasty or sacroplasty.

**[strykerIVS.com](http://strykerIVS.com)**

Products referenced with TM designation are trademarks of Stryker. Products referenced with ® designation are registered trademarks of Stryker.

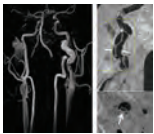
The information presented in this overview is intended to demonstrate the breadth of Stryker product offerings. Always refer to the package insert, product label and/or user instructions before using any Stryker product. Products may not be available in all markets. Product availability is subject to the regulatory or medical practices that govern individual markets. Please contact your Stryker representative if you have questions about the availability of Stryker products in your area.



## ONLINE FEATURES

### LETTERS

- E60** **Is Radiofrequency Ablation an Alternative to Thyroidectomy?**  
*S. Tez, et al.*
- E61** **Reply** *J.H. Baek*
- E62** **Sentinel Headache: A Warning Sign Preceding Every Fourth Aneurysmal Subarachnoid Hemorrhage** *H. Joswig, et al.*
- E64** **Reply** *S. Oda, et al.*



Simultaneous noncontrast angiography and intraplaque hemorrhage (SNAP) MR imaging of carotid pseudoaneurysm and intimal flaps.



Indicates Editor's Choices selection



Indicates Fellows' Journal Club selection



Indicates open access to non-subscribers at [www.ajnr.org](http://www.ajnr.org)



Indicates article with supplemental on-line table



Indicates article with supplemental on-line photo



Indicates article with supplemental on-line video



Evidence-Based Medicine Level 1



Evidence-Based Medicine Level 2



THE FOUNDATION OF THE ASNR



## THE FOUNDATION OF THE ASNR SYMPOSIUM 2016: EMERGENCY NEURORADIOLOGY MAY 21-22

## ASNR 54<sup>TH</sup> ANNUAL MEETING MAY 23-26



**Howard A. Rowley, MD, ASNR 2016 Program Chair/President-Elect**  
Programming developed in cooperation with ...

**American Society of Functional Neuroradiology (ASFNR)**  
Christopher G. Filippi, MD

**American Society of Head and Neck Radiology (ASHNR)**  
Lindell R. Gentry, MD

**American Society of Pediatric Neuroradiology (ASPNR)**  
Erin Simon Schwartz, MD

**American Society of Spine Radiology (ASSR)**  
Gregory J. Lawler, MD

**Society of NeuroInterventional Surgery (SNIS)**  
Charles J. Prestigiacomo, MD

**American Society of Neuroradiology (ASNR) Health Policy Committee**  
Robert M. Barr, MD, FACR

**Computer Science and Informatics (CSI) Committee**  
John L. Go, MD

**Research Scientists Committee**  
Dikoma C. Shungu, PhD

**ABSTRACT DEADLINE:**  
**Friday, December 11, 2015**

Please visit [www.asnr.org/2016](http://www.asnr.org/2016)  
for more information

**ASNR 54<sup>TH</sup> ANNUAL MEETING**  
c/o American Society of Neuroradiology  
800 Enterprise Drive, Suite 205  
Oak Brook, Illinois 60523-4216  
Phone: 630-574-0220  
Fax: 630 574-0661  
[www.asnr.org/2016](http://www.asnr.org/2016)

SCAN NOW  
TO VISIT  
OUR WEBSITE



**SAVE THE DATE... MAY 21-26, 2016**  
**WASHINGTON MARRIOTT WARDMAN PARK • WASHINGTON DC**

### Official Journal:

American Society of Neuroradiology  
 American Society of Functional Neuroradiology  
 American Society of Head and Neck Radiology  
 American Society of Pediatric Neuroradiology  
 American Society of Spine Radiology

### EDITOR-IN-CHIEF

**Jeffrey S. Ross, MD**

Staff Neuroradiologist, Barrow Neurological Institute, St. Joseph's Hospital, Phoenix, Arizona

### SENIOR EDITORS

**Harry J. Cloft, MD, PhD**

Professor of Radiology and Neurosurgery, Department of Radiology, Mayo Clinic College of Medicine, Rochester, Minnesota

**Thierry A.G.M. Huisman, MD**

Professor of Radiology, Pediatrics, Neurology, and Neurosurgery, Chairman, Department of Imaging and Imaging Science, Johns Hopkins Bayview, Director, Pediatric Radiology and Pediatric Neuroradiology, Johns Hopkins Hospital, Baltimore, Maryland

**C.D. Phillips, MD, FACR**

Professor of Radiology, Weill Cornell Medical College, Director of Head and Neck Imaging, New York-Presbyterian Hospital, New York, New York

**Pamela W. Schaefer, MD**

Clinical Director of MRI and Associate Director of Neuroradiology, Massachusetts General Hospital, Boston, Massachusetts, Associate Professor, Radiology, Harvard Medical School, Cambridge, Massachusetts

**Charles M. Strother, MD**

Professor of Radiology, Emeritus, University of Wisconsin, Madison, Wisconsin

**Jody Tanabe, MD**

Professor of Radiology and Psychiatry, Chief of Neuroradiology, University of Colorado, Denver, Colorado

### EDITORIAL BOARD

Ashley H. Aiken, Atlanta, Georgia  
 A. James Barkovich, San Francisco, California  
 Walter S. Bartynski, Charleston, South Carolina  
 Barton F. Branstetter IV, Pittsburgh, Pennsylvania  
 Jonathan L. Brisman, Lake Success, New York  
 Julie Bykowski, San Diego, California  
 Donald W. Chakeres, Columbus, Ohio  
 Asim F. Choudhri, Memphis, Tennessee  
 Alessandro Cianfoni, Lugano, Switzerland  
 Colin Derdeyn, St. Louis, Missouri  
 Rahul S. Desikan, San Diego, California  
 Richard du Mesnil de Rochemont, Frankfurt, Germany  
 Clifford J. Eskey, Hanover, New Hampshire  
 Massimo Filippi, Milan, Italy  
 David Fiorella, Cleveland, Ohio  
 Allan J. Fox, Toronto, Ontario, Canada  
 Christine M. Glastonbury, San Francisco, California  
 John L. Go, Los Angeles, California  
 Wan-Yuo Guo, Taipei, Taiwan  
 Rakesh K. Gupta, Lucknow, India  
 Lotfi Hacin-Bey, Sacramento, California  
 David B. Hackney, Boston, Massachusetts  
 Christopher P. Hess, San Francisco, California  
 Andrei Holodny, New York, New York  
 Benjamin Huang, Chapel Hill, North Carolina  
 George J. Hunter, Boston, Massachusetts  
 Mahesh V. Jayaraman, Providence, Rhode Island  
 Valerie Jewells, Chapel Hill, North Carolina  
 Timothy J. Kaufmann, Rochester, Minnesota  
 Kenneth F. Layton, Dallas, Texas  
 Ting-Yim Lee, London, Ontario, Canada  
 Michael M. Lell, Erlangen, Germany  
 Michael Lev, Boston, Massachusetts  
 Karl-Olof Lovblad, Geneva, Switzerland  
 Franklin A. Marden, Chicago, Illinois  
 M. Gisele Matheus, Charleston, South Carolina  
 Joseph C. McGowan, Merion Station, Pennsylvania  
 Kevin R. Moore, Salt Lake City, Utah  
 Christopher J. Moran, St. Louis, Missouri  
 Takahisa Mori, Kamakura City, Japan  
 Suresh Mukherji, Ann Arbor, Michigan  
 Amanda Murphy, Toronto, Ontario, Canada  
 Alexander J. Nemeth, Chicago, Illinois  
 Laurent Pierot, Reims, France  
 Jay J. Pillai, Baltimore, Maryland  
 Whitney B. Pope, Los Angeles, California  
 M. Judith Donovan Post, Miami, Florida  
 Tina Young Poussaint, Boston, Massachusetts  
 Joana Ramalho, Lisbon, Portugal

Otto Rapalino, Boston, Massachusetts  
 Àlex Rovira-Cañellas, Barcelona, Spain  
 Paul M. Ruggieri, Cleveland, Ohio  
 Zoran Rumboldt, Rijeka, Croatia  
 Amit M. Saindane, Atlanta, Georgia  
 Erin Simon Schwartz, Philadelphia, Pennsylvania  
 Aseem Sharma, St. Louis, Missouri  
 J. Keith Smith, Chapel Hill, North Carolina  
 Maria Vittoria Spampinato, Charleston, South Carolina  
 Gordon K. Sze, New Haven, Connecticut  
 Krishnamoorthy Thamburaj, Hershey, Pennsylvania  
 Kent R. Thielen, Rochester, Minnesota  
 Cheng Hong Toh, Taipei, Taiwan  
 Thomas A. Tomsick, Cincinnati, Ohio  
 Aquilla S. Turk, Charleston, South Carolina  
 Willem Jan van Rooij, Tilburg, Netherlands  
 Arastoo Vossough, Philadelphia, Pennsylvania  
 Elysa Widjaja, Toronto, Ontario, Canada  
 Max Wintermark, Charlottesville, Virginia  
 Ronald L. Wolf, Philadelphia, Pennsylvania  
 Kei Yamada, Kyoto, Japan

### EDITORIAL FELLOW

Hillary R. Kelly, Boston, Massachusetts

### SPECIAL CONSULTANTS TO THE EDITOR

#### AJNR Blog Editor

Neil Lall, Denver, Colorado

#### Case of the Month Editor

Nicholas Stence, Aurora, Colorado

#### Case of the Week Editors

Juan Pablo Cruz, Santiago, Chile

Sapna Rawal, Toronto, Ontario, Canada

#### Classic Case Editor

Sandy Cheng-Yu Chen, Taipei, Taiwan

#### Clinical Correlation Editor

Christine M. Glastonbury, San Francisco, California

#### Facebook Editor

Peter Yi Shen, Sacramento, California

#### Health Care and Socioeconomics Editor

Pina C. Sanelli, New York, New York

#### Physics Editor

Greg Zaharchuk, Stanford, California

#### Podcast Editor

Yvonne Lui, New York, New York

#### Twitter Editor

Ryan Fitzgerald, Little Rock, Arkansas

### YOUNG PROFESSIONALS ADVISORY COMMITTEE

Asim K. Bag, Birmingham, Alabama

Anna E. Nidecker, Sacramento, California

Peter Yi Shen, Sacramento, California

Founding Editor

Juan M. Taveras

Editors Emeriti

Mauricio Castillo, Robert I. Grossman,

Michael S. Huckman, Robert M. Quencer

Managing Editor

Karen Halm

Electronic Publications Manager

Jason Gantenberg

Executive Director, ASNR

James B. Gantenberg

Director of Communications, ASNR

Angelo Artemakis

AJNR (Am J Neuroradiol ISSN 0195-6108) is a journal published monthly, owned and published by the American Society of Neuroradiology (ASNR), 800 Enterprise Drive, Suite 205, Oak Brook, IL 60523. Annual dues for the ASNR include \$170.00 for journal subscription. The journal is printed by Cadmus Journal Services, 5457 Twin Knolls Road, Suite 200, Columbia, MD 21045; Periodicals postage paid at Oak Brook, IL and additional mailing offices. Printed in the U.S.A. POSTMASTER: Please send address changes to American Journal of Neuroradiology, P.O. Box 3000, Denville, NJ 07834, U.S.A. Subscription rates: nonmember \$380 (\$450 foreign) print and online, \$305 online only; institutions \$440 (\$510 foreign) print and basic online, \$875 (\$940 foreign) print and extended online, \$365 online only (basic), extended online \$790; single copies are \$35 each (\$40 foreign). Indexed by PubMed/Medline, BIOSIS Previews, Current Contents (Clinical Medicine and Life Sciences), EMBASE, Google Scholar, HighWire Press, Q-Sensei, RefSeek, Science Citation Index, and SCI Expanded. Copyright © American Society of Neuroradiology.



CALL FOR  
APPLICATIONS

# ARRS/ASNR Scholarship in Neuroradiology

Applications are being accepted in any area of research related to neuroradiology. Applications should describe the unique nature of the research effort independent of existing research efforts, and should have well-defined goals for the funding period of the grant.

The two-year scholarship will provide \$150,000 (\$75,000 per year); it requires a minimum fifty percent time commitment.

## Eligibility

- Applicant must be a member of both ARRS and ASNR at the time of application and for the duration of the award.
- Applicant must hold a full-time faculty position in a department of radiology, radiation oncology, or nuclear medicine within a North American educational institution at the time of application.
- Applicant must be within 5 years of initial faculty appointment with an academic rank of instructor or assistant professor (or equivalent).
- Applicant must have completed advanced training and be certified by the American Board of Radiology (ABR) or on track for certification.
- Applicant must have completed neuroradiology training in an accredited ACGME neuroradiology fellowship program.

The deadline for receipt of applications is **November 23, 2015**.

Log onto [www.arrs.org/RoentgenFund/Scholarships/ARRS\\_ASNR.aspx](http://www.arrs.org/RoentgenFund/Scholarships/ARRS_ASNR.aspx) or [foundation.asnr.org](http://foundation.asnr.org) for more information.

This scholarship is funded by The Roentgen Fund® in conjunction with The Foundation of the American Society of Neuroradiology. To support this and other important scholarships with a generous tax-deductible contribution, visit [roentgenfund.arrs.org](http://roentgenfund.arrs.org).

Application  
Deadline:  
**November  
23**

**ARRS**  
Your Medical Imaging Society  
CONNECT • LEARN • ADVANCE

[www.arrs.org](http://www.arrs.org)

THE FOUNDATION OF THE ASNR





This wide-angle close-up photograph of a Hawksbill turtle was taken while scuba diving in the Tuamotu Archipelago of Tahiti at approximately 60 foot depth using an underwater 8-megapixel housed digital camera with a 15 mm lens and a master strobe mounted separately on the camera arm at a distance of 2.5 feet from the subject. Steven G. Imbesi, Professor of Radiology and Neurosurgery, University of California, San Diego Medical Center, San Diego, California

# Reversible Cerebral Vasoconstriction Syndrome, Part 2: Diagnostic Work-Up, Imaging Evaluation, and Differential Diagnosis

T.R. Miller, R. Shivashankar, M. Mossa-Basha, and D. Gandhi



## ABSTRACT

**SUMMARY:** The diagnostic evaluation of a patient with reversible cerebral vasoconstriction syndrome integrates clinical, laboratory, and radiologic findings. Imaging plays an important role by confirming the presence of cerebral vasoconstriction; monitoring potential complications such as ischemic stroke; and suggesting alternative diagnoses, including CNS vasculitis and aneurysmal subarachnoid hemorrhage. Noninvasive vascular imaging, including transcranial Doppler sonography and MR angiography, has played an increasingly important role in this regard, though conventional angiography remains the criterion standard for the evaluation of cerebral artery vasoconstriction. Newer imaging techniques, including high-resolution vessel wall imaging, may help in the future to better discriminate reversible cerebral vasoconstriction syndrome from primary angiitis of the CNS, an important clinical distinction.

**ABBREVIATIONS:** PACNS = primary angiitis of the CNS; RCVS = reversible cerebral vasoconstriction syndrome; TCD = transcranial Doppler sonography; VWI = vessel wall imaging

Reversible cerebral vasoconstriction syndrome (RCVS) is a clinical and radiologic syndrome characterized by the hyperacute onset of severe headache and reversible segmental vasoconstriction of the cerebral arterial vasculature.<sup>1-5</sup> In the first part of this review, we discussed the historical background, possible pathogenesis, and clinical features of RCVS. In this second part, we will explore the diagnostic work-up of suspected cases of RCVS, with an emphasis on the role of imaging in the diagnosis of the entity and monitoring potential complications. This includes high-resolution MR vessel wall imaging (VWI), a new technique that may help differentiate RCVS from alternative diagnoses by characterizing pathologic changes in the wall of affected cerebral arteries. Finally, we will discuss how to integrate both clinical and radiographic features in suspected cases of RCVS to formulate a tailored differential diagnosis. Special emphasis will be placed on differentiating RCVS from aneurysmal subarachnoid hemorrhage and primary angiitis of the CNS (PACNS).

## Diagnostic Work-Up and Imaging Evaluation

Appropriate care of patients suspected of having RCVS begins with a prompt diagnostic work-up to exclude alternative diagnoses, such as aneurysmal subarachnoid hemorrhage and PACNS.<sup>6</sup> This includes obtaining a complete medical history, with particular attention paid to any common RCVS triggers that may be present; detailed physical examination; CSF analysis; and non-contrast head CT to evaluate for intracranial hemorrhage.<sup>2,7-9</sup> CSF analysis is an important element in the diagnostic work-up of RCVS, which is reflected in its inclusion in the diagnostic criteria of the syndrome. In most cases of RCVS, findings of CSF analysis will be unremarkable, with red and white blood cell counts and protein levels either within normal limits or only mildly elevated.<sup>2,7,9-13</sup> Finally, findings of other laboratory tests, including serum analysis for markers of inflammation such as erythrocyte sedimentation rate and C-reactive protein, are also usually within normal limits in patients with RCVS.<sup>2,9,14</sup>

The role of neuroimaging in patients with RCVS includes demonstration of cerebral vasoconstriction, evaluation of alternative diagnoses, and monitoring potential complications such as intracranial hemorrhage, vasogenic edema, and ischemic stroke.<sup>4,7,9</sup> Although conventional angiography has been the criterion standard for evaluation of cerebral vasoconstriction in suspected cases of RCVS, noninvasive imaging modalities such as transcranial Doppler sonography (TCD), CT angiography, and MR angiography are being used with increasing frequency (Table 1).<sup>4,5,9,12,15</sup> When present, cerebral vasoconstriction involves

From the Department of Diagnostic Radiology (T.R.M., R.S., D.G.), Section of Neuroradiology, University of Maryland Medical Center, Baltimore, Maryland; and Department of Diagnostic Radiology (M.M.-B.), Section of Neuroradiology, University of Washington, Seattle, Washington.

Please address correspondence to Dheeraj Gandhi, MD, University of Maryland Medical Center, Department of Diagnostic Radiology, Room N2W78, 22 South Greene St, Baltimore, MD 21201; e-mail: Dgandhi@umm.edu

Indicates open access to non-subscribers at www.ajnr.org

<http://dx.doi.org/10.3174/ajnr.A4215>

**Table 1: Role of imaging modalities in the management of RCVS**

Role of Imaging Modalities
Transcranial Doppler sonography
Diagnosis of vasoconstriction
Monitoring of vasoconstriction
Noncontrast CT, CT angiography
Detection of cerebral vasoconstriction
Evaluation for complications such as SAH
Provide plausible alternative diagnoses such as cerebral aneurysm
MR imaging, MR angiography
Detection of cerebral vasoconstriction
Evaluation for complications such as ischemic stroke
Provide plausible alternative diagnoses such as cortical vein thrombosis
Vessel wall imaging
Catheter angiography
Detection of cerebral vasoconstriction, criterion standard
Demonstration of reversibility of vasoconstriction following intra-arterial vasodilator therapy
Possible treatment with vasodilator or balloon angioplasty

multiple vascular territories and results in a beaded appearance of medium-to-large cerebral arteries with multifocal areas of narrowing interspersed with normal-caliber segments.<sup>1,4,7,12,14</sup> The severity and distribution of vasoconstriction can fluctuate among examinations, with some areas improving and others worsening.<sup>1,2,9,16,17</sup> Although the above angiographic findings are highly suggestive of RCVS in the appropriate clinical setting, they remain nonspecific and can be encountered with various other types of CNS vasculopathies and vasculitis.<sup>2,14,18-20</sup>

The initial angiographic evaluation findings in suspected cases of RCVS may be unremarkable in the 4–5 days following patient presentation.<sup>1,2,4,5,21</sup> In fact, cerebral vasoconstriction may not be visualized in up to one-third of patients with RCVS during the first week following symptom onset.<sup>22</sup> As suggested by Ducros and Bousser,<sup>2</sup> this finding may be due to segmental vasoconstriction in RCVS beginning in small, peripheral arterioles before subsequently proceeding centripetally to involve medium and large cerebral arteries, which are more readily visualized.<sup>23</sup> If cerebral vasoconstriction is not demonstrated on initial vascular imaging and other diagnoses have been excluded, the patient should be managed as if he or she has possible or probable RCVS.<sup>1</sup>

The following sections further explore the various imaging techniques available for evaluation of suspected cases of RCVS, followed by a more detailed discussion of alternative diagnoses.

### Transcranial Doppler Sonography

TCD has been used to monitor the evolution of vasoconstriction in patients with RCVS by measuring mean and peak blood flow velocities in proximal cerebral arteries around the circle of Willis.<sup>9,21,24</sup> A prospective study of 67 patients found that 69% of patients with RCVS had elevated middle cerebral and internal carotid artery velocities, with means of 163 and 148 cm/s, respectively.<sup>12</sup> Peak mean cerebral flow velocities were typically present just >3 weeks following symptom onset (22 days). Serial TCD examinations may be more sensitive for detecting RCVS-related elevations in cerebral arterial flow than single examinations because TCD findings may be unremarkable early in the course of the syndrome.<sup>2</sup> Normalization of TCD parameters is typically

seen by 12 weeks, paralleling the delay in resolution of cerebral vasoconstriction seen with other vascular imaging modalities such as CT and MR angiography.<sup>24,25</sup>

However, alterations in TCD parameters do not appear to be as profound as those seen in patients with aneurysmal subarachnoid hemorrhage.<sup>5,24</sup> Only 13% of patients with RCVS in 1 series fulfilled the TCD diagnostic criteria for mild vasospasm.<sup>24</sup> TCD may play a role in monitoring potential complications of RCVS. Chen et al<sup>24</sup> noted that transcranial color Doppler sonography indicators of cerebral vasoconstriction, including elevated mean flow velocities in the MCA (>120 cm/s) and an elevated Lindergaard Index (>3), were associated with an increased risk of developing posterior reversible encephalopathy syndrome.

### Noncontrast CT and CT Angiography

Noncontrast head CT should be the initial examination performed for patients presenting with symptoms suggestive of RCVS, particularly thunderclap headache. Noncontrast CT is an effective way to screen patients for the presence of intracranial hemorrhage, including subarachnoid and intraparenchymal hemorrhage, as well as ischemic stroke. Subarachnoid hemorrhage associated with RCVS is often small in amount and confined to cerebral sulci near the vertex. It may be a subtle finding on noncontrast CT.<sup>10</sup> If subarachnoid hemorrhage is present, the distribution of blood, cisternal versus sulcal, can help direct further diagnostic evaluations. Finally, noncontrast CT may demonstrate multifocal infarcts of varying ages, which can suggest the alternative diagnosis of CNS vasculitis.

CT angiography can be used to demonstrate segmental vasoconstriction suggestive of RCVS.<sup>8</sup> It can also serve to evaluate other potential etiologies of patient symptoms and findings, including cerebral aneurysm, pituitary hemorrhage, arterial dissection, and, occasionally, arterial narrowing and irregularity suggestive of CNS vasculitis. Dual-energy CTA may aid in the diagnosis of cerebral vasoconstriction in suspected cases of RCVS and the evaluation of potential alternative diagnoses such as cerebral aneurysm, by improved bone removal at the skull base.<sup>8</sup> However, one important drawback of this technique is the increased radiation exposure to the patient.<sup>8</sup> Finally, CT venography can also be performed with CTA with a slightly delayed scan following contrast administration, potentially allowing the diagnosis of cortical vein and/or dural sinus thrombosis.

### Brain MR Imaging and MR Angiography

Brain MR imaging is often performed in suspected cases of RCVS, and findings can appear normal or demonstrate evidence of complications of the syndrome, such as watershed infarcts or posterior reversible encephalopathy syndrome.<sup>10,12,14,16</sup> For example, T2 FLAIR-weighted imaging can be used to evaluate for subarachnoid hemorrhage and cerebral edema, while diffusion-weighted imaging is helpful in evaluating for watershed infarcts. Susceptibility-weighted imaging can help evaluate the presence of intracranial hemorrhage. Ischemic infarctions in RCVS are typically watershed in location and bilateral, presumably reflecting impaired cerebral blood flow secondary to severe cerebral vasoconstriction.<sup>2,7</sup> In addition, MR imaging can also evaluate potential alternative diagnoses, including PACNS, dural sinus thrombosis,

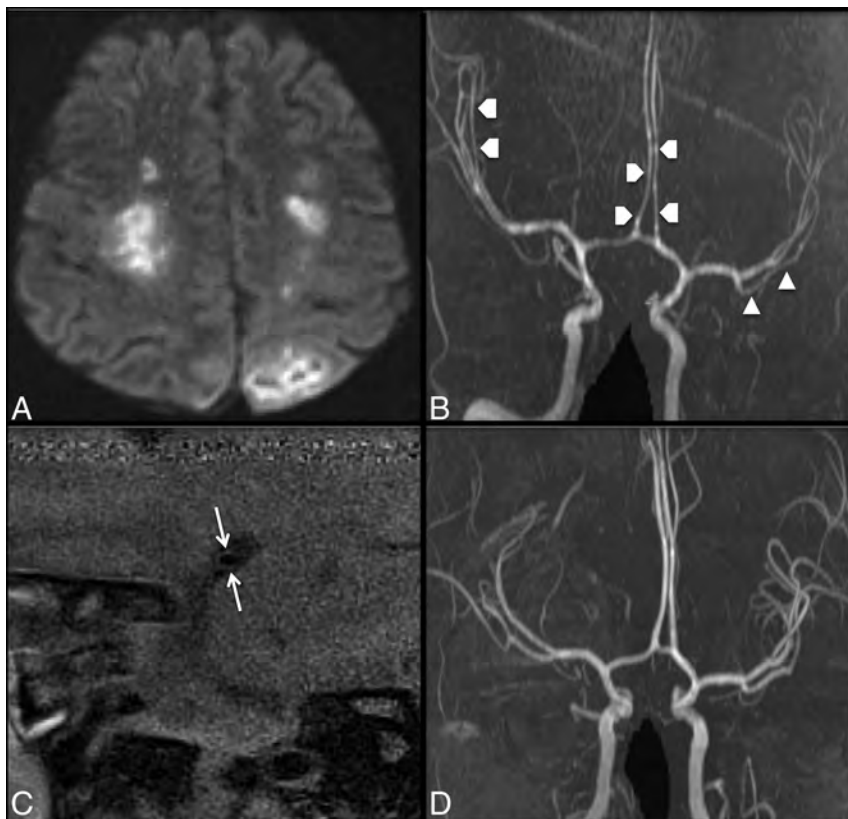


**FIG 1.** A 55-year-old woman who presented with severe headache and developed left-sided weakness. DWI (A) shows multifocal infarcts involving the centrum semiovale and left posterior parietal lobe. On coronal 3D reformatted TOF MRA (B), there is diffuse narrowing of the bilateral middle and anterior cerebral arteries (white arrowheads). Parasagittal postcontrast T1 high-resolution VWI of the M1 arterial segment of the left MCA (C) shows mild wall thickening and minimal enhancement (similar findings were noted in the right M1 arterial segment, not shown). The patient was diagnosed with RCVS, with subsequent resolution of cerebral vasoconstriction (D).

pituitary apoplexy, cortical vein thrombosis, and arterial dissection.

Hyperintense vessels along cerebral sulci on T2 FLAIR imaging have been noted in patients with RCVS (22%) and correlate with more severe vasoconstriction as measured by TCD.<sup>16,26-28</sup> In one study, the presence of hyperintense vessels was associated with a higher risk incidence of ischemic stroke and posterior reversible encephalopathy syndrome.<sup>26</sup> Hyperintense vessels on T2 FLAIR imaging have previously been described in association with other conditions involving severe cerebral artery stenosis or occlusion, including acute large-vessel ischemic stroke and Moyamoya disease. The hyperintense vessels are thought to represent slow flow in either distal cortical arteries or leptomeningeal anastomotic collaterals.<sup>22,27,28</sup> However, hyperintense vessels on T2 FLAIR imaging must be differentiated from subarachnoid hemorrhage, which may also be present in patients with RCVS. SWI may be helpful in this regard by identifying the latter.<sup>16,22</sup>

MR angiography is an effective way of diagnosing and monitoring the evolution of RCVS-related vasoconstriction, allowing patients to avoid exposure to ionizing radiation and the small risk of complications associated with conventional angiography.<sup>12,29</sup> Chen et al<sup>29</sup> followed a group of patients with RCVS with serial MRA and showed that the severity of segmental cerebral vasocon-

striction peaked in these patients around day 16 following symptom onset and significantly improved in most patients by 1 month. However, the evolution of cerebral vasoconstriction was not uniform, with some cerebral arteries improving on serial scans and others worsening.<sup>29</sup> They also found that combined segmental vasoconstriction scores in the M1 and P2 arterial segments were most closely associated with the complications of ischemic stroke and posterior reversible encephalopathy syndrome.<sup>29</sup> One limitation of MRA is the evaluation of small, distal cerebral arteries, which are better evaluated on conventional angiography, given its superior spatial resolution.<sup>29</sup>

### Vessel Wall Imaging

High-resolution MR VWI is a relatively new technique that is being increasingly used in the evaluation of cerebrovascular disease, including CNS vasculitis, RCVS, cerebral aneurysms, Moyamoya disease and syndrome, arterial dissection, and intracranial atherosclerosis.<sup>20,30-34</sup> This method can use high-resolution 2D or 3D imaging, frequently with pre- and postcontrast T1 or proton-attenuation sequences.<sup>20,32,35-38</sup> In addition, high-resolution T2-weighted imaging can be used for multicontrast

imaging.<sup>33,39-41</sup> In contradistinction to conventional angiographic imaging techniques that primarily evaluate the blood vessel lumen, such as conventional angiography, this approach provides information regarding the blood vessel wall itself, which is typically only 1–2 mm thick in proximal intracranial vessels.<sup>42</sup>

VWI has been described as black-blood imaging because it results in low signal in the vessel lumen, thereby aiding in the visualization of the blood vessel wall. VWI can be technically challenging to perform however, due to the small caliber and tortuous course of the intracranial arteries, necessitating high spatial resolution and thus high-field-strength magnets. Specific blood vessel wall abnormalities that can be detected by using VWI include vessel wall thickening, which can be further characterized as smooth versus irregular or concentric versus eccentric; and vessel wall enhancement and signal characteristics.<sup>20,30,31,43</sup>

There has been considerable recent interest in using VWI to help differentiate RCVS from CNS vasculitis, which can overlap in clinical and conventional imaging features.<sup>20,30</sup> Mandell et al<sup>30</sup> used VWI to evaluate a small group of patients presenting with multifocal narrowing of large intracranial arteries, suspicious for vasculitis or RCVS. They found that while patients ultimately diagnosed with both RCVS and CNS vasculitis demonstrated arterial wall thickening, wall enhancement was present only in cases of CNS vasculitis. The authors hypothesized that this finding was

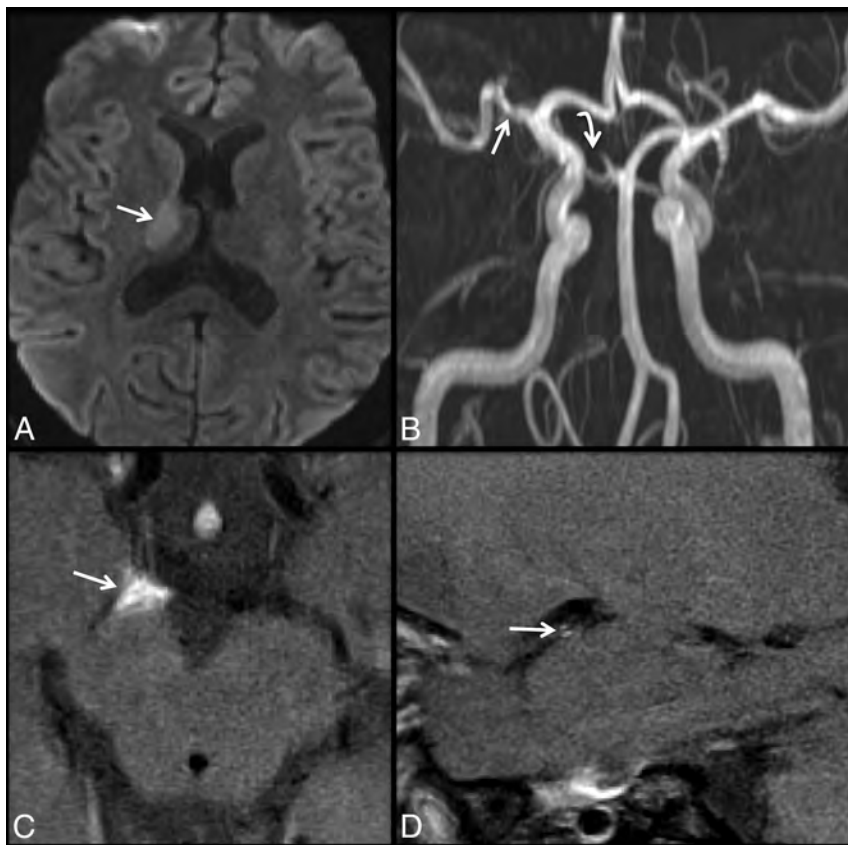


**FIG 2.** A 35-year-old man with a history of Behçet vasculitis who presented with left-sided weakness. DWI (A) demonstrates an acute infarct involving the right thalamus and posterior limb of the internal capsule (*white arrow*). Coronal 3D reformat of TOF MRA (B) reveals irregularity and narrowing of the M1 arterial segment of the right MCA (*white arrow*) and occlusion or high-grade stenosis of the P1 arterial segment of the right PCA (*curved white arrow*). On axial T1 postcontrast high-resolution VWI (C), there is prominent enhancement and enlargement of the right posterior cerebral artery (*white arrow*). Sagittal T1 postcontrast VWI (D) demonstrates typical tram-track, circumferential enhancement of the right M1 MCA (*white arrow*), consistent with vasculitic inflammation.

consistent with pathology results of patients with RCVS who have undergone biopsy—namely, vasoconstriction without an underlying inflammatory vessel wall infiltrate.<sup>30</sup>

A more recent article by Obusez et al<sup>20</sup> compared VWI findings in a larger group of patients diagnosed with RCVS and CNS vasculitis ( $n = 13$  in each group). They found that 12 of 13 patients diagnosed with CNS vasculitis demonstrated multifocal, short-segment vessel wall thickening, with 9 having concentric and 3 having eccentric wall enhancement (Fig 1). In contradistinction, of the 13 patients diagnosed with RCVS, 10 demonstrated diffuse uniform wall thickening, of which only 4 had associated mild wall enhancement. A minority in each group underwent follow-up VWI, which demonstrated earlier resolution of imaging findings in patients with diagnosed RCVS. These results suggest that VWI may be a useful tool in differentiating RCVS and CNS vasculitis, though further investigation is needed (Fig 2).

### Perfusion Imaging

Perfusion imaging is being increasingly used in the evaluation and monitoring of cerebrovascular diseases such as RCVS and can be performed by using CT or MR imaging techniques.<sup>44</sup> CT perfu-

sion is performed by repeatedly imaging through the brain during the administration of an iodine contrast bolus. The resulting patient radiation exposure is a potential drawback of this method, particularly in those patients requiring multiple scans. MR perfusion techniques include T1 dynamic contrast-enhanced and dynamic susceptibility contrast MR imaging, the latter performed by rapid, repeat echo-planar imaging of the brain during the passage of a gadolinium contrast bolus, with resulting loss of intra-arterial signal secondary to susceptibility effects from the paramagnetic contrast.<sup>44</sup> Alternatively, arterial spin-labeling perfusion is a completely noninvasive MR imaging technique that does not require the administration of gadolinium contrast but instead uses an electromagnetic spin inversion to tag water molecules, which then serve as a freely diffusible flow tracer.<sup>45</sup>

On the basis of our own clinical experience and a few isolated case reports, perfusion imaging in RCVS may show multifocal areas of hypoperfusion that often include cerebral watershed zones corresponding to the involved vascular territories (Fig 3).<sup>46,47</sup> These areas of perfusion abnormality may worsen acutely and, in some instances, progress to watershed infarction as previously discussed.<sup>47</sup> Changes in cerebral perfusion may correspond to the evolution of

arterial vasoconstriction, and this information could potentially be used to track treatment response (eg, vasodilator therapy) and provide physiologic information regarding the effects of individual stenoses.<sup>46</sup> However, given the relative paucity of published data, further research into the potential role of perfusion imaging in the evaluation and monitoring of RCVS is needed.

### Catheter Angiography

Conventional angiography remains the imaging criterion standard for the evaluation of cerebral vasculature and may detect cerebral vasoconstriction in patients whose initial noninvasive vascular imaging findings appear unremarkable.<sup>12</sup> This is particularly true in the evaluation of small, distal cortical vessels, which are suboptimally evaluated by CTA or MRA secondary to their inferior spatial resolution. Ducros and Boussier<sup>2</sup> found that noninvasive imaging with MRA and CTA demonstrated sensitivity for detecting RCVS-vasoconstriction of 80% compared with conventional angiography. In our experience, conventional angiography has been proved an invaluable tool when clinical diagnosis is equivocal and noninvasive imaging findings are normal. For example, it may help evaluate patients with sus-

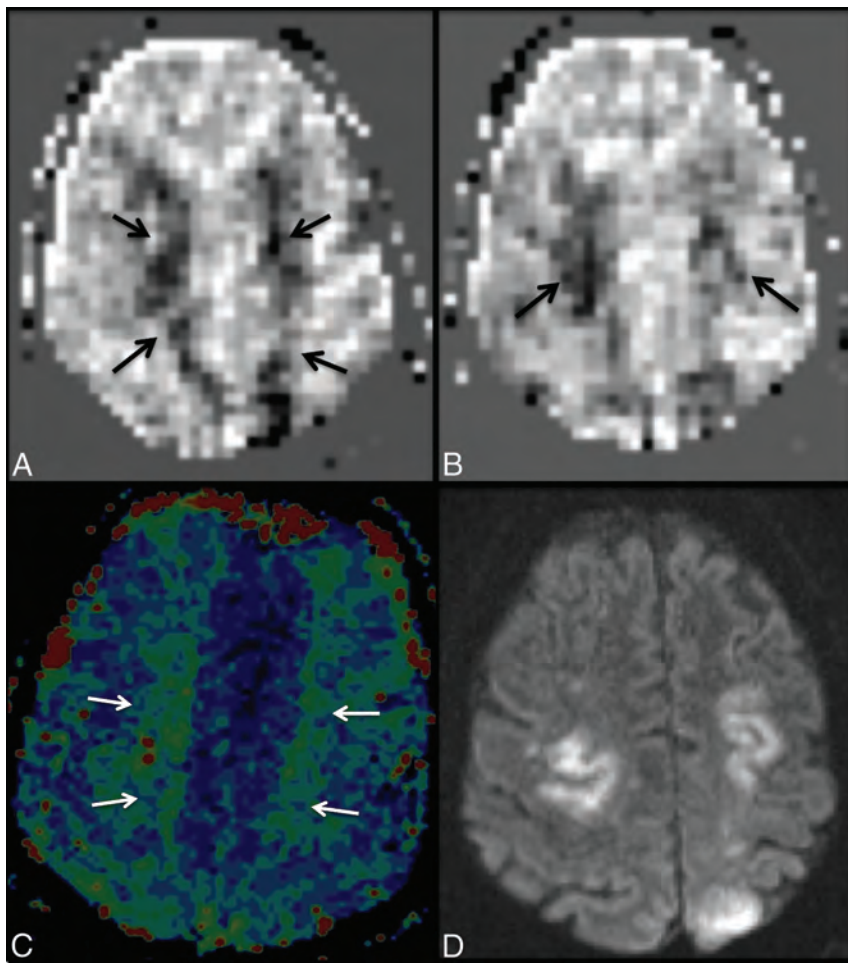


**FIG 3.** A 55-year-old woman (the same patient as in Fig 1) with RCVS complicated by ischemic infarcts. Axial CBF pulsed arterial spin-labeling maps (A and B) show multiple regions of diminished perfusion involving anterior cerebral artery/MCA watershed territories (black arrows), with T2\* DSC perfusion time-to-peak maps (C) demonstrating delayed time-to-peak in these same regions (white arrows). These areas of perfusion abnormality correspond, in part, to regions of restriction diffusion/ischemic infarct on DWI (D).

pected RCVS who either present in a somewhat atypical fashion (eg, more insidious-onset headache, no obvious risk factors) or demonstrate a plausible alternative diagnosis (eg, cerebral aneurysm arising from the circle of Willis). In these instances, better visualization of the character and distribution of cerebral artery irregularity and the morphology of any cerebral aneurysms present can be helpful.

Additionally, DSA may provide complementary information to aid the diagnosis, including reversibility of vasoconstriction following intra-arterial administration of a vasodilator.<sup>48-52</sup> Because diagnostic confirmation of RCVS is usually retrospective following spontaneous resolution of clinical and angiographic findings in 1-3 months, there is often a substantial delay in confirming the diagnosis. Consequently, demonstration of reversibility following intra-arterial vasodilator administration can be clinically useful in the early recognition of RCVS, as opposed to the partial or incomplete improvement often seen with other vasospastic disorders.<sup>52</sup> At this time, the potential risks of such a diagnostic challenge remain uncertain and perhaps may be unnecessary if the clinical and radiologic findings are otherwise supportive of a diagnosis of RCVS.

Although conventional angiography is generally a safe procedure when performed by experienced operators, a suggestion has been made that there may be an increased risk of transient ischemic attack in patients with RCVS. Ducros et al<sup>12</sup> reported a 9% incidence of new transient neurologic deficits within 1 hour following conventional angiography in 67 patients. However, Katz et al,<sup>53</sup> in their retrospective study, failed to demonstrate a similar increased risk of clinical deterioration in patients with RCVS undergoing conventional angiography. In our experience, both published and unpublished, we have found no increase in complication rates following cerebral angiography for RCVS.<sup>10</sup>

### Differential Diagnosis

As previously discussed, presenting symptoms, sequelae, and radiographic features of RCVS can significantly overlap other frequently encountered medical conditions involving the CNS (Table 2).<sup>1,2,7,15,21,23</sup> Furthermore, treatment of some of these alternative diagnoses, including aneurysmal subarachnoid hemorrhage and PACNS, varies considerably from that of RCVS, making an accurate diagnosis critical to ensuring appropriate patient care.<sup>13,19</sup> The following section will highlight important clinical and radiologic findings that can help differentiate some of these entities from RCVS.

**Cerebral Aneurysm Rupture with Subarachnoid Hemorrhage.** Differentiating RCVS from aneurysmal subarachnoid hemorrhage can be challenging due to the overlap in patient symptomatology and radiographic features.<sup>54</sup> In particular, the scenario of thunderclap headache, sulcal subarachnoid hemorrhage, and a remote cerebral aneurysm at or near the circle of Willis can be particularly difficult.<sup>55</sup> As previously discussed, the relapsing-remitting thunderclap headache typical of RCVS would be highly unusual for patients with aneurysmal subarachnoid hemorrhage.<sup>1,2,11,12,21,29</sup> Although aneurysmal subarachnoid hemorrhage is overall the most common cause of nonprimary thunderclap headache, RCVS is the most probable diagnosis in patients who experience episodic thunderclap headaches for 1-2 weeks.<sup>55</sup>

Furthermore, patients with aneurysmal subarachnoid hemorrhage often demonstrate acute, progressive neurologic decline following presentation due to complications such as increased intracranial pressure and communicating hydrocephalus, which, again, would be atypical for RCVS. A retrospective analysis of patients with RCVS ( $n = 38$ ), aneurysmal subarachnoid hemor-

rhage ( $n = 515$ ), and cryptogenic subarachnoid hemorrhage ( $n = 93$ ) by Muehlschlegel et al<sup>56</sup> found that among other factors, younger patient age, less severe neurologic symptoms, and better clinical grade (ie, lower Hunt and Hess scale score) were predictive of RCVS as opposed to aneurysmal subarachnoid hemorrhage. However, one clinical scenario that could more closely mimic RCVS would be a patient experiencing a small sentinel hemorrhage from a cerebral aneurysm, which could produce a similar clinical course with waxing and waning symptoms.<sup>55</sup>

Imaging can also help differentiate RCVS from aneurysmal (or perimesencephalic) subarachnoid hemorrhage. First, many patients with RCVS will have unremarkable findings on a noncontrast head CT examination, without evidence of intracranial hemorrhage or infarct.<sup>2</sup> In cases of RCVS complicated by intracranial hemorrhage, the pattern has focal subarachnoid hemorrhage most often confined to superficial cerebral sulci, which is in contradistinction to aneurysmal subarachnoid hemorrhage, in which blood is most often centered at the basal cisterns/circle of Willis.<sup>2,5,10,15,16</sup> This pattern of subarachnoid hemorrhage may also help differentiate RCVS from nonaneurysmal subarachnoid hemorrhage on angiography, which typically predominate in the perimesencephalic region.<sup>16</sup>

In patients who present with thunderclap headache and localized, sulcal subarachnoid hemorrhage, the presence of a cerebral aneurysm arising more proximally near the circle of Willis can pose a diagnostic challenge.<sup>15</sup> In these instances, evaluating the patient's clinical course and symptomatology may help differentiate the 2 diagnoses. VWI may be useful in these instances by evaluating the aneurysm for wall enhancement, which would suggest inflammation and possible recent rupture. However, the validity of this technique remains uncertain.

Differentiating RCVS cerebral vasoconstriction from arterial vasospasm associated with aneurysmal subarachnoid hemorrhage can also be difficult. On the basis of their clinical experience

and review of the literature, Ansari et al<sup>10</sup> suggested several diagnostic criteria to help differentiate these 2 entities, focusing on the severity, distribution, and time of onset of cerebral artery narrowing and the relation of these findings to a potential culprit aneurysm (Table 3). Unfortunately, none of these diagnostic criteria, either alone or in combination, are entirely specific for RCVS vasoconstriction or arterial vasospasm. For example, although RCVS vasoconstriction is often noted to involve distal cerebral arteries, more proximal vessel involvement occurs. In addition, the delay in the appearance of RCVS vasoconstriction may mimic the typical time course of arterial vasospasm. Conversely, hyperacute vasospasm may occasionally be associated with aneurysmal subarachnoid hemorrhage.<sup>15</sup> Consequently, considering the patient's overall clinical picture and radiographic features may be the most effective way of differentiating these 2 entities.

**Primary Angiitis of the CNS.** Although differentiating severe RCVS and PACNS can be challenging because the 2 entities overlap in clinical and radiographic features, the distinction is critical because treatment significantly differs.<sup>2,7,13</sup> Patients with PACNS often experience a fulminant course with a poor prognosis if immunosuppressive therapy with steroids and cytotoxic agents is not initiated early, while these medications are not beneficial in patients with RCVS and may be harmful.<sup>1,2,13,14</sup> Fortunately, a correct diagnosis can be made in most patients by considering multiple factors, including the onset and severity of patient symptoms, patient demographics, CSF and imaging findings, and specific disease sequelae.

The headache associated with PACNS is often slowly progressive with an insidious onset, differing markedly from the typical thunderclap headache of RCVS in both time course and peak severity.<sup>1,2,7,13,16,18,19,57</sup> Patient demographics in these disease entities also demonstrate significant differences. RCVS is typically encountered in young-to-middle-aged women, as opposed to PACNS, which is most often seen in older men.<sup>14,18,19</sup> Analysis of CSF is also helpful because patients with PACNS, in contradistinction to RCVS, typically demonstrate elevations of CSF protein levels and white blood cell count, with values often  $>100$  mg/dL and 5–10 cells/mm, respectively.<sup>1,2,7,10,16,18</sup> Finally, the early clinical course of the patient can help distinguish these 2 entities. RCVS generally follows a benign, self-limited course with supportive care, while clinical deterioration would be expected in PACNS without prompt immunosuppressive therapy.<sup>2,18</sup>

Nonvascular imaging findings can also help differentiate PACNS and RCVS. Most patients with PACNS will demonstrate evidence of multifocal infarcts of varying ages on presentation (90%), compared with initial MR imaging findings in patients with RCVS, which are often unremarkable.<sup>2,18</sup> This finding is

**Table 2: Potential alternative diagnoses**

Aneurysmal SAH
Primary angiitis of the CNS
Migraine
Cortical vein thrombosis
Pituitary apoplexy
Amyloid angiopathy
Hypertensive hemorrhage
PRES
Giant cell arteritis
Arterial dissection
Spontaneous intracranial hypotension
Meningitis

**Note:**—PRES indicates posterior reversible encephalopathy syndrome.

**Table 3: Proposed criteria for differentiating RCVS vasoconstriction from SAH vasospasm<sup>10</sup>**

RCVS Vasoconstriction	Vasospasm-Aneurysmal SAH
No evidence of ruptured aneurysm or vascular malformation	Plausible target lesion identified
Diffuse and disproportionate extent of cerebral vasoconstriction relative to amount of SAH	Severity of vasospasm correlates with amount of hemorrhage and is most pronounced in the vicinity of the lesion
Beaded appearance of alternating areas of segmental vasoconstriction preferentially involving distal 2nd- and 3rd-order cerebral branches	Smooth, long segmental narrowing for proximal arteries at circle of Willis
Development of vasoconstriction in first 4–5 days after symptom onset, or persistence past 3 weeks	Development of vasospasm peaking between 4 and 14 days after hemorrhage

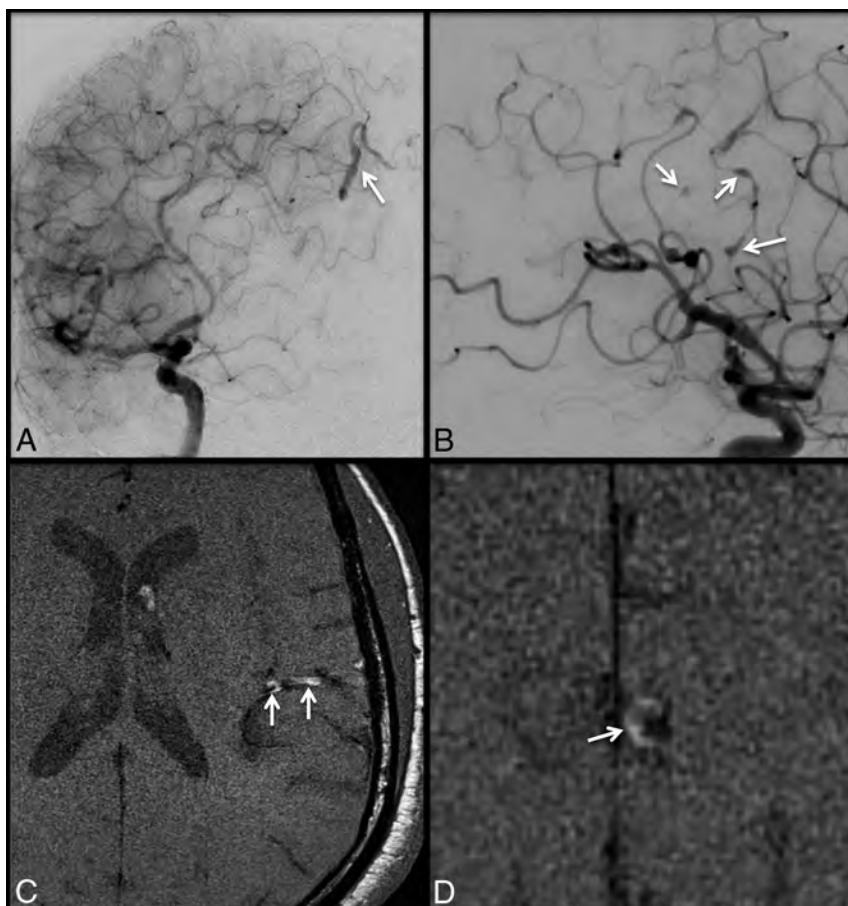


**FIG 4.** A 59-year-old man with a history of seizures, who was subsequently found to have multifocal infarcts in several vascular territories (not shown). Subsequent catheter angiograms (A and B) demonstrate marked irregularity of branches of the distal right anterior cerebral artery (white arrow, A) and left MCA (white arrows, B), with multifocal areas of narrowing and saccular and fusiform dilatation. On axial T1 precontrast high-resolution VWI (C), there is intrinsic T1 mural hyperintensity in involved MCA (white arrows) and anterior cerebral artery branches. On axial T1 postcontrast high-resolution VWI (D), there are accompanying areas of eccentric vessel wall enhancement (white arrow, D).

consistent with the later timeframe during which ischemic stroke typically occurs in the course of RCVS, as previously discussed.<sup>12</sup> Hemorrhagic complications, including cortical subarachnoid hemorrhage and concomitant posterior reversible encephalopathy syndrome, which are well-established features of RCVS, are extremely unusual in cases of PACNS.<sup>1,14,18</sup>

Imaging of the cerebral vasculature can also assist in the diagnostic work-up. Although PACNS can produce a pattern of multifocal narrowing and irregularity of mid-to-distal cerebral arteries that is indistinguishable from RCVS, most cases will appear unremarkable on angiographic imaging.<sup>2,18–20</sup> This appearance is true even for the criterion standard of conventional angiography, which has a reported sensitivity of only 20%–64% for detecting CNS vasculitis.<sup>7,10,29</sup> Alternatively, cerebral vasoconstriction is often apparent in cases of RCVS at presentation or shortly thereafter. Some authors have argued that certain angiographic features are more characteristic of PACNS, including eccentric luminal narrowing and abrupt vessel occlusions (Fig 4).<sup>2,7,10</sup> However, the specificity of these findings for PACNS remains uncertain. Finally, improvement in cerebral artery narrowing following in-

tra-arterial vasodilator therapy has also been proposed as a feature distinguishing RCVS from PACNS.<sup>52</sup>

**Cortical Vein Thrombosis.** Cortical vein thrombosis is another potential cause of both thunderclap headache and convexity subarachnoid hemorrhage and should be considered in the differential diagnosis with RCVS in the appropriate clinical setting. Postpartum women are one specific subgroup of patients who are at increased risk for both disease entities.<sup>1</sup> MR imaging, including susceptibility sequences and MRV, can provide high specificity for the diagnosis of cortical vein thrombosis. MR imaging can demonstrate characteristic susceptibility artifacts associated with a superficial cortical vein consistent with thrombus. Both RCVS and cortical vein thrombosis can lead to ischemic stroke, often a week or more after the onset of symptoms. As is the case with primary angiitis of the CNS, distinguishing RCVS from cortical vein thrombosis is critical because treatment of the latter often entails anticoagulation, which carries significant risks and has not been shown to be beneficial in RCVS.

**Migraine Headache and Stroke.** The association between migraine headache and RCVS can make differentiating these 2 entities challenging.<sup>1,5,16</sup> Both entities can present with thunderclap headache, associated photo- and phonophobia, and nausea and vomiting.<sup>7</sup>

Furthermore, migrainous headaches have rarely even been associated with ischemic stroke. However, most patients with a history of migraine who present with RCVS describe the quality and severity of the pain as being different from that in their typical migraine.<sup>7,15</sup> Ischemic stroke in patients with migraine tends to be limited to a single vascular territory, as opposed to RCVS, in which multiterritory involvement is common.<sup>7</sup>

**Amyloid Angiography.** Although both amyloid angiopathy and RCVS can result in lobar intraparenchymal hematoma and cortical subarachnoid hemorrhage, amyloid angiography is encountered in older individuals and typically does not present with a thunderclap or acute-onset headache.<sup>1,58</sup> Kumar et al<sup>58</sup> retrospectively evaluated a group of patients with atraumatic convexity subarachnoid hemorrhage and found 2 distinct patterns of clinical presentation. In patients younger than 60 years of age, presentation with abrupt, severe headache was common, and most of these individuals were presumptively diagnosed with RCVS. In contradistinction, patients older than 60 years of age most commonly presented with transitory neurologic deficits and had evi-

dence of leukoaraiosis and microhemorrhages on MR imaging. Most of these patients were diagnosed with cerebral amyloid angiopathy.

## CONCLUSIONS

Imaging plays a critical role in the diagnosis and management of RCVS. Noninvasive techniques such as MR angiography are being increasingly used in clinical practice, though cerebral angiography remains the criterion standard for the detection of cerebral vasoconstriction. Clinical and imaging features of RCVS can overlap other disorders of the central nervous system considerably, particularly primary angiitis of the CNS. However, newer imaging techniques, particularly vessel wall imaging, may offer increased specificity for the diagnosis.

## REFERENCES

1. Ducros A. **L37: reversible cerebral vasoconstriction syndrome—distinction from CNS vasculitis.** *Presse Med* 2013;42(4 pt 2):602–04
2. Ducros A, Boussier MG. **Reversible cerebral vasoconstriction syndrome.** *Pract Neurol* 2009;9:256–67
3. Gupta S, Zivadinov R, Ramasamy D, et al. **Reversible cerebral vasoconstriction syndrome (RCVS) in antiphospholipid antibody syndrome (APLA): the role of centrally acting vasodilators—case series and review of literature.** *Clin Rheumatol* 2014;33:1829–33
4. Marder CP, Donohue MM, Weinstein JR, et al. **Multimodal imaging of reversible cerebral vasoconstriction syndrome: a series of 6 cases.** *AJNR Am J Neuroradiol* 2012;33:1403–10
5. Sheikh HU, Mathew PG. **Reversible cerebral vasoconstriction syndrome: updates and new perspectives.** *Curr Pain Headache Rep* 2014;18:414
6. Stary JM, Wang BH, Moon SJ, et al. **Dramatic intracerebral hemorrhagic presentations of reversible cerebral vasoconstriction syndrome: three cases and a literature review.** *Case Rep Neurol Med* 2014;2014:782028
7. Calabrese LH, Dodick DW, Schwedt TJ, et al. **Narrative review: reversible cerebral vasoconstriction syndromes.** *Ann Intern Med* 2007;146:34–44
8. Lin CH, Chen YY, Chiu LA, et al. **Dual energy computed tomography angiography for the rapid diagnosis of reversible cerebral vasoconstriction syndromes: report of a case.** *Acta Neurol Taiwan* 2013;22:36–42
9. Singhal AB, Bernstein RA. **Postpartum angiopathy and other cerebral vasoconstriction syndromes.** *Neurocrit Care* 2005;3:91–97
10. Ansari SA, Rath TJ, Gandhi D. **Reversible cerebral vasoconstriction syndromes presenting with subarachnoid hemorrhage: a case series.** *J Neurointerv Surg* 2011;3:272–78
11. Bain J, Segal D, Amin R, et al. **Call-Fleming syndrome: headache in a 16-year-old girl.** *Pediatr Neurol* 2013;49:130–33.e1
12. Ducros A, Boukobza M, Porcher R, et al. **The clinical and radiological spectrum of reversible cerebral vasoconstriction syndrome: a prospective series of 67 patients.** *Brain* 2007;130(pt 12):3091–101
13. Hajj-Ali RA, Furlan A, Abou-Chebel A, et al. **Benign angiopathy of the central nervous system: cohort of 16 patients with clinical course and long-term followup.** *Arthritis Rheum* 2002;47:662–69
14. Hammad TA, Hajj-Ali RA. **Primary angiitis of the central nervous system and reversible cerebral vasoconstriction syndrome.** *Curr Atheroscler Rep* 2013;15:346
15. Edlow BL, Kasner SE, Hurst RW, et al. **Reversible cerebral vasoconstriction syndrome associated with subarachnoid hemorrhage.** *Neurocrit Care* 2007;7:203–10
16. Singhal AB, Hajj-Ali RA, Topcuoglu MA, et al. **Reversible cerebral vasoconstriction syndromes: analysis of 139 cases.** *Arch Neurol* 2011;68:1005–12
17. Ducros A. **Reversible cerebral vasoconstriction syndrome.** *Lancet Neurol* 2012;11:906–17
18. Hajj-Ali RA, Singhal AB, Benseler S, et al. **Primary angiitis of the CNS.** *Lancet Neurol* 2011;10:561–72
19. Koopman K, Uyttenboogaart M, Luijckx GJ, et al. **Pitfalls in the diagnosis of reversible cerebral vasoconstriction syndrome and primary angiitis of the central nervous system.** *Eur J Neurol* 2007;14:1085–87
20. Obusez EC, Hui F, Hajj-Ali RA, et al. **High-resolution MRI vessel wall imaging: spatial and temporal patterns of reversible cerebral vasoconstriction syndrome and central nervous system vasculitis.** *AJNR Am J Neuroradiol* 2014;35:1527–32
21. Grooters GS, Sluzewski M, Tijssen CC. **How often is thunderclap headache caused by the reversible cerebral vasoconstriction syndrome?** *Headache* 2014;54:732–35
22. Chen SP, Wang SJ. **Hyperintense vessels: an early MRI marker of reversible cerebral vasoconstriction syndrome?** *Cephalalgia* 2014;34:1038–39
23. Calic Z, Choong H, Schlaphoff G, et al. **Reversible cerebral vasoconstriction syndrome following indomethacin.** *Cephalalgia* 2014;34:1181–86
24. Chen SP, Fuh JL, Chang FC, et al. **Transcranial color Doppler study for reversible cerebral vasoconstriction syndromes.** *Ann Neurol* 2008;63:751–57
25. Koopman K, Teune LK, ter Laan M, et al. **An often unrecognized cause of thunderclap headache: reversible cerebral vasoconstriction syndrome.** *J Headache Pain* 2008;9:389–91
26. Chen SP, Fuh JL, Lirng JF, et al. **Hyperintense vessels on FLAIR imaging in reversible cerebral vasoconstriction syndrome.** *Cephalalgia* 2012;32:271–78
27. Iancu-Gontard D, Oppenheim C, Touze E, et al. **Evaluation of hyperintense vessels on FLAIR MRI for the diagnosis of multiple intracerebral arterial stenoses.** *Stroke* 2003;34:1886–91
28. Kameda T, Namekawa M, Shimazaki H, et al. **Unique combination of hyperintense vessel sign on initial FLAIR and delayed vasoconstriction on MRA in reversible cerebral vasoconstriction syndrome: a case report.** *Cephalalgia* 2014;34:1093–96
29. Chen SP, Fuh JL, Wang SJ, et al. **Magnetic resonance angiography in reversible cerebral vasoconstriction syndromes.** *Ann Neurol* 2010;67:648–56
30. Mandell DM, Matouk CC, Farb RI, et al. **Vessel wall MRI to differentiate between reversible cerebral vasoconstriction syndrome and central nervous system vasculitis: preliminary results.** *Stroke* 2012;43:860–62
31. Küker W, Gaertner S, Nagele T, et al. **Vessel wall contrast enhancement: a diagnostic sign of cerebral vasculitis.** *Cerebrovasc Dis* 2008;26:23–29
32. Swartz RH, Bhuta SS, Farb RI, et al. **Intracranial arterial wall imaging using high-resolution 3-Tesla contrast-enhanced MRI.** *Neurology* 2009;72:627–34
33. Ryoo S, Cha J, Kim SJ, et al. **High-resolution magnetic resonance wall imaging findings of Moyamoya disease.** *Stroke* 2014;45:2457–60
34. Kim YJ, Lee DH, Kwon JY, et al. **High resolution MRI difference between Moyamoya disease and intracranial atherosclerosis.** *Eur J Neurol* 2013;20:1311–18
35. Qiao Y, Steinman DA, Qin Q, et al. **Intracranial arterial wall imaging using three-dimensional high isotropic resolution black blood MRI at 3.0 Tesla.** *J Magn Reson Imaging* 2011;34:22–30
36. Natori T, Sasaki M, Miyoshi M, et al. **Evaluating middle cerebral artery atherosclerotic lesions in acute ischemic stroke using magnetic resonance T1-weighted 3-dimensional vessel wall imaging.** *J Stroke Cerebrovasc Dis* 2014;23:706–11
37. van der Kolk AG, Zwanenburg JJ, Brundel M, et al. **Intracranial vessel wall imaging at 7.0-T MRI.** *Stroke* 2011;42:2478–84
38. Qiao Y, Zeiler SR, Mirbagheri S, et al. **Intracranial plaque enhancement in patients with cerebrovascular events on high-spatial-resolution MR images.** *Radiology* 2014;271:534–42
39. Degnan AJ, Gallagher G, Teng Z, et al. **MR angiography and imaging**

- for the evaluation of middle cerebral artery atherosclerotic disease. *AJNR Am J Neuroradiol* 2012;33:1427–35
40. Xu WH, Li ML, Gao S, et al. **In vivo high-resolution MR imaging of symptomatic and asymptomatic middle cerebral artery atherosclerotic stenosis.** *Atherosclerosis* 2010;212:507–11
  41. Niizuma K, Shimizu H, Takada S, et al. **Middle cerebral artery plaque imaging using 3-Tesla high-resolution MRI.** *J Clin Neurosci* 2008;15:1137–41
  42. Kamath S. **Observations on the length and diameter of vessels forming the circle of Willis.** *J Anat* 1981;133(pt 3):419–23
  43. Xu WH, Li ML, Gao S, et al. **Middle cerebral artery intraplaque hemorrhage: prevalence and clinical relevance.** *Ann Neurol* 2012;71:195–98
  44. Hochberg AR, Young GS. **Cerebral perfusion imaging.** *Semin Neurol* 2012;32:454–65
  45. Telischak NA, Detre JA, Zaharchuk G. **Arterial spin labeling MRI: clinical applications in the brain.** *J Magn Reson Imaging* 2014 Sep 19. [Epub ahead of print]
  46. Komatsu T, Kimura T, Yagishita A, et al. **A case of reversible cerebral vasoconstriction syndrome presenting with recurrent neurological deficits: evaluation using noninvasive arterial spin labeling MRI.** *Clin Neurol Neurosurg* 2014;126:96–98
  47. Rosenbloom MH, Singhal AB. **CT angiography and diffusion-perfusion MR imaging in a patient with ipsilateral reversible cerebral vasoconstriction after carotid endarterectomy.** *AJNR Am J Neuroradiol* 2007;28:920–22
  48. Ioannidis I, Nasis N, Agjianniotaki A, et al. **Reversible cerebral vasoconstriction syndrome: treatment with multiple sessions of intra-arterial nimodipine and angioplasty.** *Interv Neuroradiol* 2012;18:297–302
  49. French KF, Hoesch RE, Allred J, et al. **Repetitive use of intra-arterial verapamil in the treatment of reversible cerebral vasoconstriction syndrome.** *J Clin Neurosci* 2012;19:174–76
  50. Farid H, Tatum JK, Wong C, et al. **Reversible cerebral vasoconstriction syndrome: treatment with combined intra-arterial verapamil infusion and intracranial angioplasty.** *AJNR Am J Neuroradiol* 2011;32:E184–87
  51. Elstner M, Linn J, Muller-Schunk S, et al. **Reversible cerebral vasoconstriction syndrome: a complicated clinical course treated with intra-arterial application of nimodipine.** *Cephalalgia* 2009;29:677–82
  52. Linn J, Fesl G, Ottomeyer C, et al. **Intra-arterial application of nimodipine in reversible cerebral vasoconstriction syndrome: a diagnostic tool in select cases?** *Cephalalgia* 2011;31:1074–81
  53. Katz BS, Fugate JE, Ameriso SF, et al. **Clinical worsening in reversible cerebral vasoconstriction syndrome.** *JAMA Neurol* 2014;71:68–73
  54. Nickle C, Muro K, Getch CC, et al. **Severe reversible cerebral vasoconstriction syndrome mimicking aneurysmal rupture and vasospasm.** *Neurocrit Care* 2007;7:81–85
  55. Chen SP, Fuh JL, Wang SJ. **Reversible cerebral vasoconstriction syndrome: current and future perspectives.** *Expert Rev Neurother* 2011;11:1265–76
  56. Muehlschlegel S, Kursun O, Topcuoglu MA, et al. **Differentiating reversible cerebral vasoconstriction syndrome with subarachnoid hemorrhage from other causes of subarachnoid hemorrhage.** *JAMA Neurol* 2013;70:1254–60
  57. Nouh A, Ruland S, Schneck MJ, et al. **Reversible cerebral vasoconstriction syndrome with multivessel cervical artery dissections and a double aortic arch.** *J Stroke Cerebrovasc Dis* 2014;23:e141–43
  58. Kumar S, Goddeau RP Jr, Selim MH, et al. **Atraumatic convexal subarachnoid hemorrhage: clinical presentation, imaging patterns, and etiologies.** *Neurology* 2010;74:893–99

# The Benefits of High Relaxivity for Brain Tumor Imaging: Results of a Multicenter Intraindividual Crossover Comparison of Gadobenate Dimeglumine with Gadoterate Meglumine (The BENEFIT Study)

M. Vaneckova, M. Herman, M.P. Smith, M. Mechl, K.R. Maravilla, J. Weichet, M.V. Spampinato, J. Žižka, F.J. Wippold II, J.J. Baima, R. Babbel, E. Bültmann, R.Y. Huang, J.-H. Buhk, A. Bonafé, C. Colosimo, S. Lui, M.A. Kirchin, N. Shen, G. Pirovano, and A. Spinazzi



## ABSTRACT

**BACKGROUND AND PURPOSE:** Gadobenate dimeglumine (MultiHance) has higher r1 relaxivity than gadoterate meglumine (Dotarem) which may permit the use of lower doses for MR imaging applications. Our aim was to compare 0.1- and 0.05-mmol/kg body weight gadobenate with 0.1-mmol/kg body weight gadoterate for MR imaging assessment of brain tumors.

**MATERIALS AND METHODS:** We performed crossover, intraindividual comparison of 0.1-mmol/kg gadobenate with 0.1-mmol/kg gadoterate (Arm 1) and 0.05-mmol/kg gadobenate with 0.1-mmol/kg gadoterate (Arm 2). Adult patients with suspected or known brain tumors were randomized to Arm 1 (70 patients) or Arm 2 (107 patients) and underwent 2 identical examinations at 1.5T. The agents were injected in randomized-sequence order, and the 2 examinations were separated by 2–14 days. MR imaging scanners, imaging sequences (T1-weighted spin-echo and T1-weighted high-resolution gradient-echo), and acquisition timing were identical for the 2 examinations. Three blinded readers evaluated images for diagnostic information (degree of definition of lesion extent, lesion border delineation, visualization of lesion internal morphology, contrast enhancement) and quantitatively for percentage lesion enhancement and lesion-to-background ratio. Safety assessments were performed.

**RESULTS:** In Arm 1, a highly significant superiority ( $P < .002$ ) of 0.1-mmol/kg gadobenate was demonstrated by all readers for all end points. In Arm 2, no significant differences ( $P > .1$ ) were observed for any reader and any end point, with the exception of percentage enhancement for reader 2 ( $P < .05$ ) in favor of 0.05-mmol/kg gadobenate. Study agent-related adverse events were reported by 2/169 (1.2%) patients after gadobenate and by 5/175 (2.9%) patients after gadoterate.

**CONCLUSIONS:** Significantly superior morphologic information and contrast enhancement are demonstrated on brain MR imaging with 0.1-mmol/kg gadobenate compared with 0.1-mmol/kg gadoterate. No meaningful differences were recorded between 0.05-mmol/kg gadobenate and 0.1-mmol/kg gadoterate.

**ABBREVIATIONS:** GBCA = gadolinium-based contrast agent; LBR = lesion-to-background ratio; SI = signal intensity; TIGRE = T1-weighted high resolution gradient-echo; TISE = T1-weighted spin-echo

A series of large-scale, multicenter, intraindividual, crossover studies have shown that gadobenate dimeglumine (Multi-

Hance; Bracco Diagnostics, Princeton, New Jersey) is superior to gadopentetate dimeglumine (Magnevist; Bayer HealthCare, Wayne, New Jersey),<sup>1,2</sup> gadodiamide (Omniscan; GE Healthcare, Princeton, New Jersey),<sup>3</sup> and gadobutrol (Gadavist; Bayer HealthCare)<sup>4</sup> for enhanced MR imaging of central nervous system tumors when administered at an equivalent approved dose of 0.1 mmol/kg body weight. The superior imaging performance (ie, significantly greater lesion enhancement and diagnostic informa-

Received May 20, 2015; accepted after revision June 8.

From the Charles University in Prague (M.V.), First Faculty of Medicine and General University Hospital, Prague, Czech Republic; University Hospital Olomouc (M.H.), Olomouc, Czech Republic; Beth Israel Deaconess Medical Center (M.P.S.), Boston, Massachusetts; Faculty of Medicine (M.M.), University Hospital Brno, Masaryk University, Brno, Czech Republic; MR Research Laboratory (K.R.M.), University of Washington, Seattle, Washington; Na Homolce Hospital (J.W.), Prague, Czech Republic; Department of Radiology and Radiological Science (M.V.S.), Medical University of South Carolina, Charleston, South Carolina; University Faculty of Medicine in Hradec Králové (J.Ž.), University Hospital Hradec Králové and Charles University in Prague, Prague, Czech Republic; Mallinckrodt Institute of Radiology (F.J.W.), Washington University School of Medicine, St. Louis, Missouri; Clinical Radiologists, S.C. (J.J.B.), Springfield, Illinois; Good Samaritan Regional Medical Center (R.B.), Corvallis, Oregon; Institute of Diagnostic and Interventional Neuroradiology (E.B.), Hannover, Germany; Harvard Medical School (R.Y.H.), Brigham and Women's Hospital, Boston, Massachusetts; University Medical Center Hamburg Eppendorf (J.-H.B.), Hamburg, Germany; Hôpital Gui de Chauliac (A.B.), Montpellier, France; Policlinico "Agostino Gemelli" (C.C.), Rome, Italy; West China Hospital of Sichuan

University (S.L.), Chengdu, Sichuan, China; Global Medical & Regulatory Affairs (M.A.K.), Bracco Imaging S.p.A., Milan, Italy; and Global Medical & Regulatory Affairs (N.S., G.P., A.S.), Bracco Diagnostics, Monroe, New Jersey.

Please address correspondence to Manuela Vaneckova, MD, Charles University in Prague, First Faculty of Medicine and General University Hospital, Kateřinská 30, CZ-12808 Prague 2, Czech Republic; e-mail: man.van@post.cz

Indicates open access to non-subscribers at [www.ajnr.org](http://www.ajnr.org)

EBM Evidence-Based Medicine Level 1.

<http://dx.doi.org/10.3174/ajnr.A4468>

tion) can be ascribed to the higher r1 relaxivity of gadobenate in vivo,<sup>5</sup> which translates into greater signal-intensity (SI) enhancement on T1-weighted images. An early study in 23 patients suggested that 0.1-mmol/kg gadobenate may provide superior contrast enhancement compared with 0.1-mmol/kg gadoterate meglumine (Dotarem; Guerbet, Aulnay-sous-Bois, France), another gadolinium-based contrast agent (GBCA) with lower r1 relaxivity.<sup>6</sup> However, the sample size was too small to draw firm conclusions. Another more recent study has demonstrated superiority in the quality of visualization of brain lesions for a three-quarter (0.075-mmol/kg) dose of gadobenate over a full 0.1-mmol/kg dose of gadoterate in patients undergoing cranial MR imaging.<sup>7</sup> These results suggest that better or similar SI enhancement and similar imaging performance may be achieved with a reduced gadobenate dose.

The purpose of this multicenter, multinational study in 177 patients referred for morphologic brain MR imaging was first to confirm previous findings<sup>6</sup> in demonstrating imaging superiority for 0.1-mmol/kg gadobenate over 0.1-mmol/kg gadoterate in a properly sized and powered clinical study; and second, to ascertain whether half-dose (0.05-mmol/kg) gadobenate provides similar diagnostic information to full-dose (0.1-mmol/kg) gadoterate when these agents are administered in 2 otherwise identical MR imaging examinations at 1.5T using a rigorous, double-blind, randomized, intraindividual, crossover study design.

## MATERIALS AND METHODS

The study was compliant with the Health Insurance Portability and Accountability Act, was conducted according to Good Clinical Practice standards, and was registered at [www.clinicaltrials.gov](http://www.clinicaltrials.gov) (NCT02070380). Ethics committee approval was obtained from all investigating centers, and all patients signed an approved informed consent form before enrollment.

### Patients

One hundred seventy-seven patients referred for contrast-enhanced MR imaging for known or suspected brain tumors were prospectively enrolled in a consecutive manner at 14 participating centers between February 2014 and February 2015 and underwent at least 1 contrast-enhanced MR imaging examination. Two centers enrolled 30 patients each, while a further 8 centers enrolled between 7 and 26 patients. The remaining 4 centers enrolled between 1 and 4 patients. Patients were ineligible if they received any investigational drug within 30 days before study agent administration. Subjects were also excluded if they were to receive any treatment between the 2 examinations that could affect lesion visualization (eg, radiation therapy, steroids, or chemotherapy). Patients were also ineligible if they were pregnant or nursing or had impaired renal function, congestive heart failure, claustrophobia, history of reaction to prior gadolinium contrast agent administration, a cardiac pacemaker, or other contraindications to MR imaging.

The 177 enrolled patients were prospectively randomized to 1 of 2 study arms by means of a central computer-generated randomization code list that was provided to each site before patient enrollment for the assignment of a study arm and an investigational product. To maintain the study blind, a drug-dispensing

person was selected at each site for the duration of the study. The drug-dispensing person was responsible for dispensing the 2 investigational products to the appropriate personnel, according to the randomization list. Arm 1 saw 70 patients (29 men, 41 women; mean age,  $55.3 \pm 15.2$  years; range, 19–86 years) randomized to receive equivalent 0.1-mmol/kg doses of gadobenate and gadoterate in 2 otherwise identical examinations, while in Arm 2, 107 patients (55 men, 52 women; mean age,  $58.3 \pm 13.1$  years; range, 26–86 years) received randomized doses of 0.05-mmol/kg gadobenate and 0.1-mmol/kg gadoterate. Gadobenate was administered first to 31 and 53 patients (Arms 1 and 2, respectively), while gadoterate was administered first to 39 and 54 patients, respectively.

### MR Imaging

MR imaging was performed on 1.5T systems from several vendors (Avanto/Aera,  $n = 67$ ; Siemens, Erlangen, Germany; Achieva/Intera,  $n = 66$ ; Philips Healthcare, Best, the Netherlands; HDxt/Excite,  $n = 44$ ; GE Healthcare, Milwaukee, Wisconsin) by using a multichannel head coil. Despite the benefits of 3T systems, particularly for advanced imaging techniques, 1.5T systems were used in this study because they are still more commonly used throughout the United States, Europe, and other areas worldwide.

A rigorously controlled imaging protocol comprising T1-weighted spin-echo (T1SE), T2-weighted fast spin-echo, and T2-weighted FLAIR acquisitions before contrast injection and T1SE and 3D T1-weighted high-resolution gradient-echo (T1GRE) acquisitions after injection ensured protocol uniformity across sites and within individual patients. Sequence parameters varied within predefined ranges necessitated by the use of different imaging systems. However, the same MR imaging scanner, imaging planes, section prescriptions, and sequence parameters were used for both examinations in each patient. Scan parameters were as follows: for the T1SE sequence: TR = 400–707 ms, TE = 8–15 ms, excitations = 1–2, section thickness = 4–5 mm, FOV =  $22 \times 17$ – $24 \times 24$  cm; for the T1GRE sequence: TR = 6–2200 ms, TE = 2–5 ms, flip angle =  $8^\circ$ – $30^\circ$ , excitations = 0.8–1, section thickness = 1–3 mm, FOV =  $23 \times 18$ – $29 \times 29$  cm. Parallel imaging was not used for any patient. Axial scans were all acquired along the inferior callosal plane to ensure image comparability between scans within patient comparisons and across patients.

IV contrast agent administration to patients in Arm 1 was performed identically for both examinations at 0.1 mmol/kg of body weight (0.2 mL/kg for both agents) by using either manual bolus injection ( $n = 57$ ) or a power injector ( $n = 13$ ). Contrast administration to patients in Arm 2 was performed at 0.1 mmol/kg for gadoterate but at 0.05 mmol/kg (0.1 mL/kg) for gadobenate, again by manual bolus injection ( $n = 83$ ) or a power injector ( $n = 24$ ). All injections were followed by a saline flush of up to 30 mL. To maintain the study blind, an independent drug-dispensing person administered each agent in the order determined by the randomization list.

Postcontrast image acquisition began at a prespecified time between 3 and 10 minutes after injection but could vary within this range depending on the site-specific protocol. However, the timing and order of postcontrast sequences were mandated to be identical for both examinations within each patient. The interval

between MR imaging examinations was >48 hours to avoid carryover effects but <14 days to minimize the chance of disease progression.

### **Image Evaluation**

All images were evaluated by 3 independent neuroradiologists (A.B., C.C., S.L.; 34, 35, and 7 years of neuroradiology experience, respectively) who were unaffiliated with the study centers and blinded to the contrast agent used, patient clinical and radiologic information, and interpretations by on-site investigators. Each reader evaluated all patient images independently on a multimonitor workstation (AquariusNET Server, Version 4.4.1.4; Tera-Recon, San Mateo, California) in terms of qualitative and quantitative end points.

Qualitative and quantitative assessment of images from each patient in each study arm was performed with images presented in global matched-pairs fashion. For each randomized patient number, all images from examination 1 were displayed simultaneously with the images from examination 2. Each reader could perform all routine interactive image manipulation functions (ie, window/level, zoom, pan) on both image sets. If the postinjection images from either examination were considered technically inadequate by any of the 3 readers (eg, if artifacts compromised interpretability), no further assessment was performed for that patient by that reader. Once the readers' assessments were recorded and signed on an electronic case report form, the data base for that reading was automatically locked.

### **Qualitative Assessment**

Technically adequate images were evaluated qualitatively for diagnostic information and scored in terms of overall diagnostic preference and quality of the following: 1) lesion border delineation, 2) definition of extent of disease, 3) visualization of lesion internal morphology, and 4) lesion contrast enhancement compared with surrounding normal tissue. All assessments were performed by using 3-point scales from -1 (examination 1 better) through 0 (examinations equal) to +1 (examination 2 better). For the various end points, superiority for 1 examination was recorded if it allowed better separation of  $\geq 1$  lesion from surrounding tissue, structures, or edema; better definition of lesion extent; clearer depiction of intralesion features; better contrast between lesions and surrounding normal tissue; or the ability to identify  $\geq 1$  lesion seen only on that examination.

### **Quantitative Assessment**

Quantitative evaluation was also performed by each reader, independently, by using a simultaneous matched-pairs approach. SI measurements were made by using ROIs positioned on up to 3 enhancing lesions per patient identified on postcontrast images from both examinations and on areas of normal brain parenchyma in the same section. To ensure that ROIs of equal size (placed to include the largest possible area) were positioned at identical coordinates on all corresponding image sets, each ROI placed on the selected postinjection image from one examination appeared simultaneously on the corresponding image from the other examination. Minor adjustments to the ROI position were permitted to allow for slight differences in patient alignment, al-

ways taking care to avoid the inclusion of vessels. When multiple lesions were present, ROIs were placed on up to 3 of the largest, most conspicuous lesions. SI values determined on a pixel-by-pixel basis were used to calculate the percentage enhancement ( $E\%$ ) of lesions and the postcontrast-precontrast lesion-to-background ratio (LBR) on T1SE sequences by using the equations below:

$$E\% = \frac{\text{SI of lesion (postcontrast)} - \text{SI of lesion (precontrast)}}{\text{SI of lesion (precontrast)}} \times 100,$$

$$\text{LBR} = \frac{\text{SI of lesion}}{\text{SI of brain}}$$

### **Safety Assessments**

Monitoring for adverse events was performed from the time the patient signed the informed consent form until 24 hours after administration of the first study agent and then from the moment the second study agent was administered until 24 hours after administration of the second agent. Events were classified as serious according to the definitions of the US Food and Drug Administration in the Code of Federal Regulation Title 21, Volume 5 Revised, as of April 1, 2014 (<http://www.accessdata.fda.gov/scripts/cdrh/cfdocs/cfcfr/cfrsearch.cfm?fr=312.32>). Decisions on event severity and its relationship to the study agent (has reasonable possibility or not) were made by the investigating radiologist.

### **Statistical Analysis**

Power determination was based on the primary efficacy assumption that gadobenate is superior to gadoterate according to reader preference. Sample sizes were determined (nQuery Advisor, Version 7.0; Statistical Solutions, Cork, Ireland) on the basis of the results of a previous study that had a similar crossover design.<sup>3</sup> For the full-dose gadobenate arm (Arm 1) assuming an "equal" response in 50% of cases, a ratio of preference for either agent of 4:1, and an effect size of 0.18, evaluation of 61 subjects was considered necessary to demonstrate the difference in preference with 85% of power at an  $\alpha$  level of .05. Considering a drop-out rate of 15%, enrollment of approximately 72 subjects was needed. For the half-dose gadobenate arm (Arm 2), again assuming an "equal" response in 50% of cases but with a ratio of preference for either agent of 3:1 and an effect size of 0.125, evaluation of 88 subjects was considered necessary for 85% of power at an  $\alpha$  level of .05. If one assumed a drop-out rate of 15%, enrollment of approximately 104 subjects was needed.

Differences in demographic characteristics between the 2 administration orders within each study arm were tested by using the  $t$  test for continuous variables or the Fisher exact test for categorical variables.

Analysis of blinded-reader evaluations was performed by using the statistical software package SAS, Version 9.2 (SAS Institute, Cary, North Carolina). The distribution of reader preferences in diagnostic information end points was tested statistically by using the Wilcoxon signed rank test. Interreader agreement for diagnostic findings was presented as percentage agreement for the 3 readers and assessed by using generalized  $\kappa$  statistics. Agreement

**Table 1: Final lesion diagnoses**

Lesion Diagnosis	Arm 1: 0.1-mmol/kg Gadobenate vs 0.1-mmol/kg Gadoterate (n = 63)	Arm 2: 0.05-mmol/kg Gadobenate vs 0.1-mmol/kg Gadoterate (n = 96)
Anaplastic astrocytoma	1	1
Pilocytic astrocytoma	–	2
Low-grade astrocytoma	3	1
Oligoastrocytoma	1	3
High-grade glioma	1	1
Glioblastoma multiforme	10	18
Oligodendroglioma	2	–
Malignant lymphoma	1	3
Metastatic tumors, total	26	47
Lung	13	23
Breast	6	4
Melanoma	4	2
Ovarian	–	2
Kidney	1	3
Other	1	7
Unknown	1	6
Tumor (unknown origin)	–	3
Ependymoma	2	–
Meningioma	11	7
Schwannoma	2	1
Hemangioblastoma	1	5
Cystic craniopharyngioma	1	1
Acute disseminate encephalomyelitis	1	–
Neurofibromatosis	–	1
Capillary telangiectasia	–	1
Subdural hematoma	–	1

was classified as excellent ( $\kappa > 0.8$ ), good ( $\kappa = 0.61-0.8$ ), moderate ( $\kappa = 0.41-0.6$ ), fair ( $\kappa = 0.21-0.4$ ), or poor ( $\kappa \leq 0.2$ ).

Differences between gadobenate and gadoterate in terms of quantitative parameters were analyzed by using a mixed-effects model. The change from predose was the response variable, and factors included in the model were patient, sequence, study agent, and predose score; “patient” nested within “sequence” was the random effect. “Study period” was also included to test for potential carryover effects. The Fisher exact test was used to compare the incidence of adverse events for the 2 agents. All statistical tests were conducted at a significance level of  $P < .05$ .

## RESULTS

### Patients

All 177 enrolled patients who underwent at least 1 contrast-enhanced MR imaging examination were included in the overall safety population. Seven patients randomized to Arm 1 and 11 patients randomized to Arm 2 were excluded from efficacy evaluations because of protocol violations. These 18 patients included 10 who prematurely discontinued after the first examination (withdrawal of consent [ $n = 5$ ], surgical intervention [ $n = 2$ ], change of hospital [ $n = 1$ ], steroid therapy initiated and CT performed [ $n = 1$ ], and stroke detected on examination 1 [ $n = 1$ ]) and 8 who were excluded after undergoing both examinations (began chemotherapy after examination 1 [ $n = 1$ ], stroke [ $n = 2$ ], differences of  $>2$  minutes between injection and postdose acquisition start times [ $n = 2$ ], steroid therapy initiated shortly before examination 1 [ $n = 1$ ], contrast extravasation [ $n = 1$ ], and higher contrast dose (42%) administered for examination 2 [ $n = 1$ ]). The final efficacy populations therefore comprised 63 patients in Arm 1 (23 men, 40 women; mean age,  $56.2 \pm 14.9$  years; range, 19–86 years) and 96 in Arm 2 (49 men, 47 women; mean age,

$58.2 \pm 13.4$  years; range, 26–86 years). There were no meaningful between-sequence differences in either study arm for sex ( $P = 1.0$ ,  $P = .841$ ; Arms 1 and 2, respectively), age ( $P = .634$ ,  $P = .038$ ), age group (18–64 years,  $\geq 65$  years;  $P = .274$ ,  $P = .283$ ), weight ( $P = .467$ ,  $P = .212$ ), height ( $P = .281$ ;  $P = .333$ ), or race ( $P = 1.0$ ;  $P = .496$ ) distribution. The diagnoses of the 159 patients evaluated are presented in Table 1. Intra-axial lesions represented approximately 71% of all patient diagnoses in Arm 1 and 79% of patient diagnoses in Arm 2.

### Qualitative Image Assessment

Tables 2 and 3 present the results of the 3 blinded readers for global diagnostic preference, lesion-border delineation, disease extent, internal morphology, and qualitative assessment of contrast enhancement for patients in Arms 1 and 2, respectively. Highly significant ( $P \leq .0023$ ) superiority for gadobenate over gadoterate was noted by all readers for all qualitative assessments in patients receiving

0.1-mmol/kg doses of both agents (Table 2). Conversely, no significant differences were noted by any reader for any qualitative parameter among patients receiving 0.05-mmol/kg gadobenate and 0.1-mmol/kg gadoterate (Table 3). Agreement among the 3 blinded readers was high for all assessments in Arm 2, ranging from 63.4% of patients for global diagnostic preference to 84.9% of patients for visualization of internal lesion morphology. Slightly lower levels of agreement were noted for assessments in Arm 1. Examples of comparative enhancement between gadobenate and gadoterate are shown in Figs 1 and 2.

### Quantitative Evaluation

Readers 1, 2, and 3 recorded lesion SI measurements relative to normal brain parenchyma for 63, 66, and 54 lesions (Arm 1) and 84, 89, and 78 lesions (Arm 2), respectively, on T1SE images and for 60, 61, and 51 lesions (Arm 1) and 82, 85, and 75 lesions (Arm 2), respectively, on T1GRE images. No lesions below 5 mm were measured by any of the readers. Analysis of quantitative SI data revealed no carryover effects across readers for any assessment ( $P > .05$ ). The mean percentage signal enhancement of lesions on T1SE images was significantly ( $P \leq .0006$ ) higher for gadobenate compared with gadoterate for all 3 readers in patients given 0.1-mmol/kg doses of both agents (Arm 1), while no meaningful differences were noted between 0.05-mmol/kg gadobenate and 0.1-mmol/kg gadoterate (Arm 2) (Fig 3A).

Similar results were obtained for determinations of LBR (Fig 3B); all 3 readers reported significantly ( $P < .0001$ ) higher values for LBR with 0.1-mmol/kg gadobenate compared with 0.1-mmol/kg gadoterate, while no differences were noted between 0.05-mmol/kg gadobenate and 0.1-mmol/kg gadoterate. LBR findings on T1GRE images were similar: all 3 readers noted sig-

**Table 2: Qualitative assessment of patients with brain tumors: intraindividual comparison of 0.1-mmol/kg gadobenate and 0.1-mmol/kg gadoterate<sup>a</sup>**

Diagnostic Information End Point	Reader	Gadobenate		Gadoterate Preferred	Significance (P Value) <sup>b</sup>	3-Reader Agreement κ Value (% Agreement)
		Preferred	No Difference			
Global diagnostic preference	1	31 (49.2%)	31 (49.2%)	1 (1.6%)	<.0001	0.273 (50.8%)
	2	51 (82.3%)	9 (14.5%)	2 (3.2%)	<.0001	
	3	43 (69.4%)	17 (27.4%)	2 (3.2%)	<.0001	
Lesion-border delineation	1	29 (46.0%)	33 (52.4%)	1 (1.6%)	<.0001	0.271 (44.3%)
	2	34 (54.8%)	27 (43.5%)	1 (1.6%)	<.0001	
	3	25 (40.3%)	35 (56.5%)	2 (3.2%)	<.0001	
Definition of disease extent	1	15 (23.8%)	48 (76.2%)	0	<.0001	0.286 (57.4%)
	2	18 (29.0%)	43 (69.4%)	1 (1.6%)	<.0001	
	3	15 (24.2%)	45 (72.6%)	2 (3.2%)	.0023	
Visualization of lesion internal morphology	1	10 (15.9%)	53 (84.2%)	0	.002	0.215 (54.1%)
	2	14 (22.6%)	48 (77.4%)	0	.0001	
	3	23 (37.1%)	38 (61.3%)	1 (1.6%)	<.0001	
Lesion contrast enhancement	1	31 (49.2%)	31 (49.2%)	1 (1.6%)	<.0001	0.249 (49.2%)
	2	51 (82.3%)	9 (14.5%)	2 (3.2%)	<.0001	
	3	43 (69.4%)	17 (27.4%)	2 (3.2%)	<.0001	

<sup>a</sup> Comparisons based on the number of patients with both postdose T1SE images assessed and technically adequate: *n* = 63 for reader 1, *n* = 62 for readers 2 and 3. Numbers in parentheses, except where noted, represent proportions of patients.

<sup>b</sup> Wilcoxon signed rank test.

**Table 3: Qualitative assessment of patients with brain tumors: intraindividual comparison of 0.05-mmol/kg gadobenate and 0.1-mmol/kg gadoterate<sup>a</sup>**

Diagnostic Information End Point	Reader	Gadobenate		Gadoterate Preferred	Significance (P Value) <sup>b</sup>	3-Reader Agreement κ Value (% Agreement)
		Preferred	No Difference			
Global diagnostic preference	1	14 (14.6%)	75 (78.1%)	7 (7.3%)	.13	0.505 (63.4%)
	2	18 (19.2%)	56 (59.6%)	20 (21.3%)	.75	
	3	15 (15.8%)	63 (66.3%)	17 (17.9%)	.73	
Lesion-border delineation	1	11 (11.4%)	76 (79.2%)	9 (9.4%)	.824	0.493 (71.0%)
	2	12 (12.8%)	66 (70.2%)	16 (17.0%)	.46	
	3	8 (8.4%)	77 (81.1%)	10 (10.5%)	.815	
Definition of disease extent	1	6 (6.3%)	84 (87.5%)	6 (6.3%)	1.00	0.443 (79.6%)
	2	5 (5.3%)	83 (88.3%)	6 (6.4%)	1.00	
	3	7 (7.4%)	80 (84.2%)	8 (8.4%)	1.00	
Visualization of lesion internal morphology	1	4 (4.2%)	88 (91.7%)	4 (4.2%)	1.00	0.459 (84.9%)
	2	3 (3.2%)	87 (92.6%)	4 (4.3%)	1.00	
	3	5 (5.3%)	82 (86.3%)	8 (8.4%)	.581	
Lesion contrast enhancement	1	10 (10.4%)	77 (80.2%)	9 (9.4%)	1.00	0.531 (66.7%)
	2	18 (19.2%)	56 (59.6%)	20 (21.3%)	.75	
	3	14 (14.7%)	64 (67.4%)	17 (17.9%)	.598	

<sup>a</sup> Comparisons based on the number of patients with both postdose T1SE images assessed and technically adequate: *n* = 96 for reader 1, *n* = 94 for reader 2, and *n* = 95 for reader 3. Numbers in parentheses, except where noted, represent proportions of patients.

<sup>b</sup> Wilcoxon signed rank test.

nificantly ( $P < .0001$ , all 3 readers) higher postcontrast LBR values for 0.1-mmol/kg gadobenate compared with 0.1-mmol/kg gadoterate (reader 1:  $1.67 \pm 0.46$  versus  $1.41 \pm 0.29$ ; reader 2:  $1.62 \pm 0.5$  versus  $1.33 \pm 0.35$ ; reader 3:  $1.69 \pm 0.46$  versus  $1.4 \pm 0.32$ ), whereas no reader noted significant differences between 0.05-mmol/kg gadobenate and 0.1-mmol/kg gadoterate (reader 1:  $1.4 \pm 0.32$  versus  $1.41 \pm 0.31$ ,  $P = .76$ ; reader 2:  $1.35 \pm 0.29$  versus  $1.33 \pm 0.31$ ,  $P = .229$ ; reader 3:  $1.42 \pm 0.29$  versus  $1.4 \pm 0.29$ ,  $P = .471$ ).

### Safety

In Arm 1, no patients (0/65; 0%) reported any adverse events that were considered related to 0.1-mmol/kg gadobenate, whereas 1 patient (1/70; 1.4%) reported 1 nonserious event (headache of moderate intensity) that was considered related to 0.1-mmol/kg gadoterate. In Arm 2, two patients (2/104; 1.9%) reported 1 adverse event each (dizziness of mild intensity, nausea of moderate intensity) that was considered related to 0.05-mmol/kg gadobenate, whereas 4 patients (4/105; 3.8%) reported 5 adverse

events (injection site swelling, injection site pruritus, dysgeusia, headache, pruritus; all of mild intensity) that were considered related to 0.1-mmol/kg gadoterate. There were no significant differences in the incidence of adverse events in either arm (Arm 1:  $P = 1.0000$ ; Arm 2:  $P = .6829$ ). No serious adverse events were reported.

### DISCUSSION

A recent independent determination of GBCA relaxivity values in human whole blood has shown that whereas most contrast agents approved for CNS imaging have  $r_1$  relaxivity values between 3.9 and 4.6  $L \times \text{mmol}^{-1} \times \text{seconds}^{-1}$  at 1.5T, that of gadobenate is higher at 6.2  $L \times \text{mmol}^{-1} \times \text{seconds}^{-1}$ .<sup>5</sup> That differences in  $r_1$  relaxivity reflect differences in diagnostic efficacy is borne out by evidence from numerous large-scale intraindividual crossover studies.<sup>1-4,8-11</sup> These studies have shown that differences in SI enhancement and imaging performance reflect differences in  $r_1$  relaxivity and that the magnitude of the differences in SI enhancement

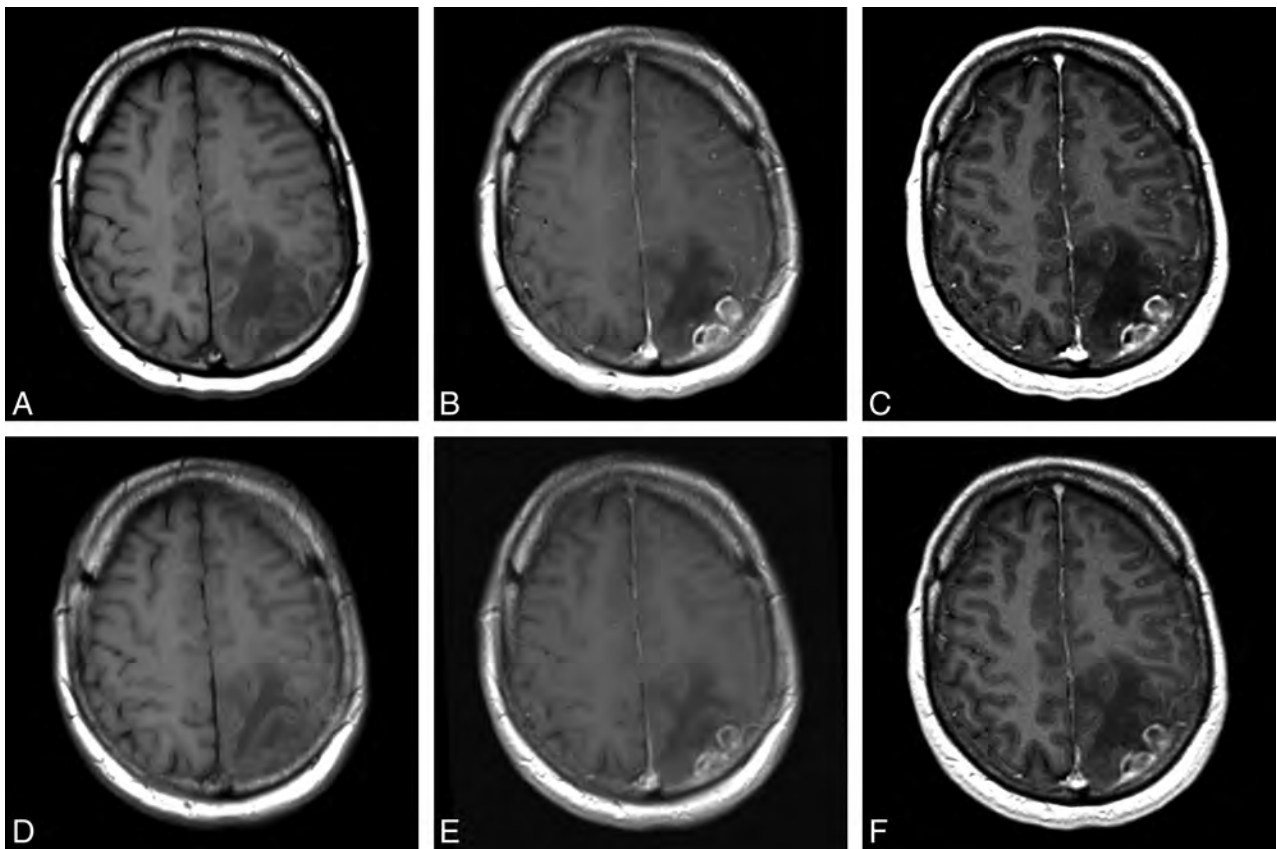


**FIG 1.** A 53-year-old man with left parietal glioblastoma. Images acquired before (unenhanced T1SE, A) and after (T1SE, B; T1GRE, C) administration of 0.1-mmol/kg gadobenate. Images acquired before (unenhanced T1SE, D) and after (T1SE, E; T1GRE, F) administration of 0.1-mmol/kg gadoterate. Aggressive-appearing mass with inhomogeneous enhancement shows greater lesion enhancement on images obtained with gadobenate. All blinded readers scored gadobenate images significantly higher for global preference, internal morphology, and contrast enhancement.

reflects the magnitude of the difference in  $r_1$  relaxivity.<sup>12</sup> Thus, large-scale, well-controlled, prospective clinical studies have found minimal differences between GBCAs with similar  $r_1$  relaxivity (eg, gadopentetate dimeglumine versus gadoteridol<sup>8</sup>:  $r_1$ ,  $\sim 4.2$  versus  $4.4 \text{ L} \times \text{mmol}^{-1} \times \text{seconds}^{-1}$  or gadoteridol versus gadobutrol<sup>9,10</sup>:  $r_1$ ,  $4.4$  versus  $4.6 \text{ L} \times \text{mmol}^{-1} \times \text{seconds}^{-1}$ ), slightly improved imaging performance for GBCAs with minimally higher  $r_1$  relaxivity values (eg, gadobutrol versus gadoterate<sup>11</sup>), and substantially improved SI enhancement and imaging performance for GBCAs with markedly higher  $r_1$  relaxivity (ie, gadobenate versus gadopentetate,<sup>1,2</sup> gadobenate versus gadodiamide,<sup>3</sup> gadobenate versus gadobutrol<sup>4</sup>).

Our results fully support these previous findings in confirming significantly superior imaging performance for gadobenate over gadoterate for both qualitative and quantitative enhancement when these agents are administered at equivalent approved doses of 0.1 mmol/kg body weight. In terms of diagnostic preference, readers 1, 2, and 3 preferred gadobenate in 31 (49.2%), 51 (82.3%), and 43 (69.4%) patients, respectively, compared with just 1, 2, and 2 patients for gadoterate ( $P < .0001$ , all readers), while highly significant ( $P \leq .0023$ ) superiority was noted by all readers for all other qualitative parameters.

The importance of  $r_1$  relaxivity is highlighted by the quantitative results of this study compared with those of other studies. Thus, Anzalone et al<sup>11</sup> noted differences in percentage lesion enhancement and LBR of  $\sim 9.9\%$  (97.962 versus 89.164) and  $\sim 3.6\%$

(1.596 versus 1.541), respectively, for gadobutrol versus gadoterate, which reflect a difference in  $r_1$  relaxivity of  $\sim 18\%$  based on values determined by Shen et al.<sup>5</sup> In a comparison of gadobenate and gadobutrol, Siedl et al<sup>4</sup> reported differences in percentage lesion enhancement and LBR of 21.8%–24.7% and 21.4%–25.0%, respectively, which reflect a greater difference in  $r_1$  relaxivity of  $\sim 35\%$ . In this study, we determined larger differences in percentage lesion enhancement and LBR of 27.6%–31.7% and 29.2%–38.1%, respectively, for equivalent doses of gadobenate and gadoterate, which reflect the still greater difference in  $r_1$  relaxivity of  $\sim 59\%$ . Notably, in the study by Anzalone et al,<sup>11</sup> the slightly greater  $r_1$  relaxivity of gadobutrol compared with gadoterate led to improved imaging performance for gadobutrol for some, though not all, qualitative end points, and not all blinded readers demonstrated significant preference for gadobutrol.

Whereas the findings for Arm 1 might be considered unsurprising on the basis of previous findings,<sup>1-4,6,13-16</sup> those for Arm 2 might also have been anticipated on the basis of these same findings and those of Khouri Chalouhi et al,<sup>7</sup> who demonstrated a markedly better signal-to-noise ratio for a three-quarter dose of gadobenate compared with a full dose of gadoterate in 31 patients who underwent cranial MR imaging examinations with both agents. In our study, all 3 blinded, expert neuroradiologists expressed no preference for either half-dose gadobenate or full-dose gadoterate in most cases. In the few cases in which a reader ex-

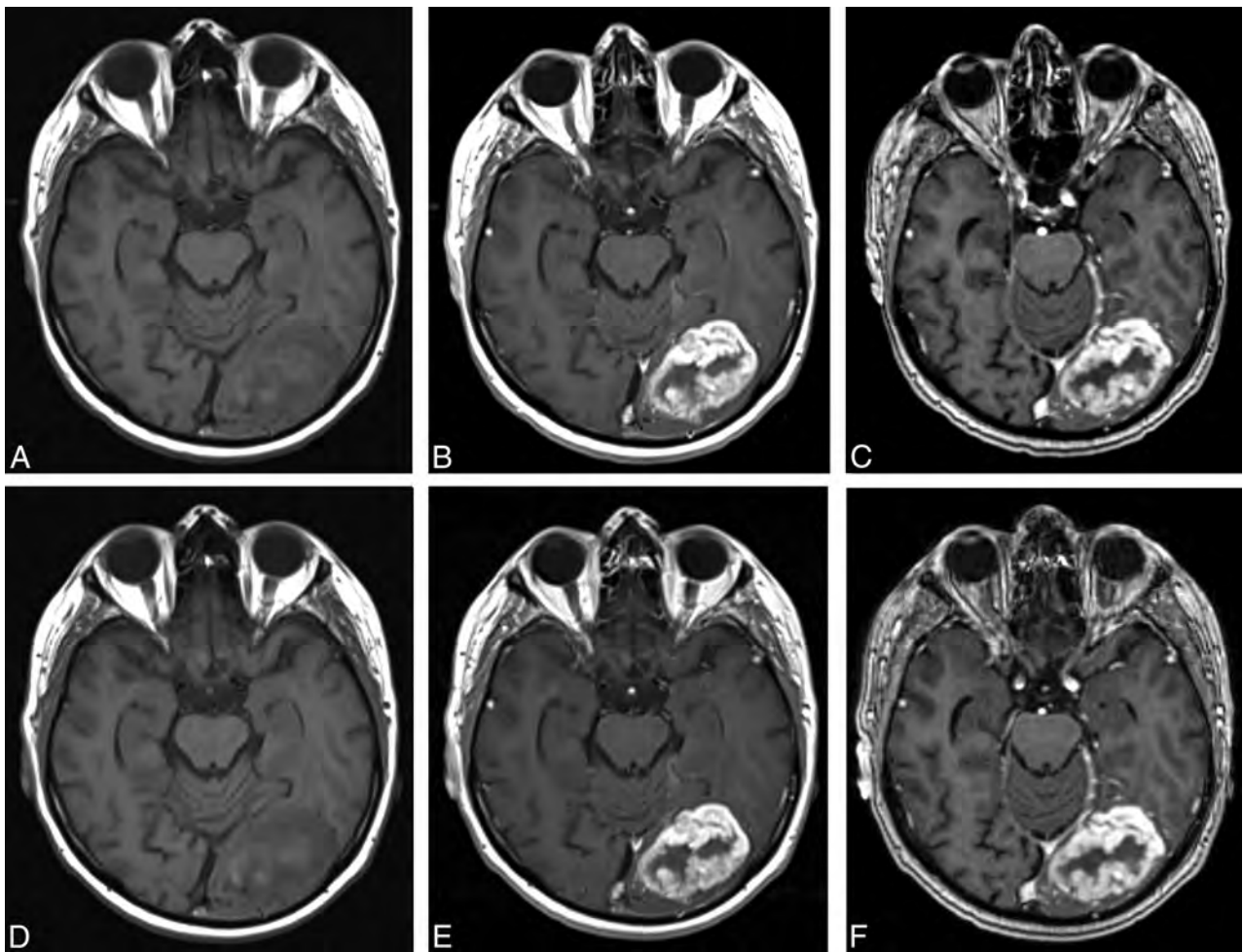


**FIG 2.** A 77-year-old man with a left occipital anaplastic astrocytoma. Images acquired before (unenhanced T1SE, *A*) and after (T1SE, *B*; TIGRE, *C*) administration of 0.05-mmol/kg gadobenate. Images acquired before (unenhanced T1SE, *D*) and after (T1SE, *E*; TIGRE, *F*) administration of 0.1-mmol/kg gadoterate. A single irregular ring-enhancing mass is clearly seen in both examinations; similar appearances and lesion definition and size are seen in both. All blinded readers gave similar scores for global preference, border delineation, internal morphology, and contrast enhancement, indicating equivalence for 0.05-mmol/kg gadobenate versus 0.1-mmol/kg gadoterate.

pressed preference, the number preferring 0.1-mmol/kg gadoterate was approximately equal to the number preferring 0.05-mmol/kg gadobenate. Similar findings were noted for quantitative enhancement measurements: no significant differences between 0.1-mmol/kg gadoterate and 0.05-mmol/kg gadobenate were noted either for mean percentage signal enhancement (apart from reader 2 who noted higher percentage enhancement with half-dose gadobenate) or for pre- to postdose changes in LBR. The interreader agreement for assessment of images was good in all cases (complete agreement for 63.4%–84.9% of patients among qualitative end points). Although the interreader agreement for lesion characterization was considered only moderate ( $\kappa = 0.44$ – $0.53$ ), agreement was determined across 3 blinded readers rather than 2 as has been the case in some studies<sup>17</sup>; clearly, complete agreement among 3 readers is less likely than complete agreement between 2. That the  $\kappa$  values and reader agreement in Arm 2 were higher than those in Arm 1 is due to the skewed distribution of preferences in Arm 1 with readers preferring gadobenate in many more patients than gadoterate. Skewed preferences of this type are known to lower  $\kappa$  values.<sup>18</sup>

In terms of clinical impact, the possibility of obtaining similar diagnostic information with a half-dose of gadobenate is potentially highly beneficial, not only in patients at risk of delayed adverse reactions such as nephrogenic systemic fibrosis and in light of recent concerns over intracranial gadolinium (Gd)<sup>3+</sup> deposition<sup>19–24</sup> but also in patients who require multiple GBCA doses during either a short-term period (eg, patients undergoing intraoperative MR imaging) or an extended period (eg, patients requiring regular postoperative follow-up examinations). Although not evaluated in this study, half-dose gadobenate may also be of value in patients who require long-term routine evaluation of disease evolution (eg, patients with multiple sclerosis). In this latter case, a clear understanding of the differences between GBCAs in terms of relaxivity and enhancement potential is fundamental to avoid misinterpretation of imaging findings (ie, to avoid interpretations of disease progression or therapy response, which, in reality, may be due solely to the different enhancement potential of various agents at equivalent doses).

In regard to the risk of delayed adverse reactions, whereas gadoterate has a macrocyclic structure and is widely considered a safe



Disclosures: Manuela Vaneckova—UNRELATED: Other: Dr Vaneckova received speaker honoraria and consultant fees from Biogen Idec, Novartis, Merck Serono, and Teva, as well as support for research activities from Biogen Idec. Miroslav Herman—RELATED: Grant: Bracco Diagnostics.\* Comments: funding support for a clinical trial study. Martin P. Smith—RELATED: Grant: Bracco Diagnostics.\* Comments: research grant for recruitment and enrollment of subjects for a study; UNRELATED: Consultancy: Bayer HealthCare, Comments: consultant for contrast agent, strategic, and technical development; Grants/Grants Pending: Bayer HealthCare,\* Comments: research grant for recruitment and enrollment of subjects for a study. Kenneth R. Maravilla—RELATED: Grant: Bracco,\* Comments: clinical trial grant (payment to the University of Washington); UNRELATED: Consultancy: Guerbet; Grants/Grants Pending: Bayer HealthCare,\* Guerbet,\* Comments: clinical trial grants for contrast media evaluation; Payment for Lectures (including service on Speakers Bureaus): ABC Medical Education; Payment for Development of Educational Presentations: ABC Medical Education. Maria Vittoria Spampinato—RELATED: Grant: Bracco,\* Comments: I was a coinvestigator in the clinical trial discussed in this article. Jan Žižka—RELATED: Other: Bracco.\* Comments: clinical trial: payments for performing MRI examinations in subjects undergoing the clinical trial MH-148. Franz J. Wipplod II—RELATED: Grant: Phase IV, double-blind, multicenter, randomized, 2-arm crossover study to compare 0.1 mmol/kg of MultiHance with 0.1 mmol/kg of Dotarem in MR Imaging of the brain (BENEFIT); Principal Investigator, 2014 to present; institution received support for performing patient recruitment and scans.\* Raymond Y. Huang—RELATED: Other: The cost of conducting the clinical trial at the Dana Farber Cancer Institute/Brigham and Women's Hospital site included MRI, research coordinator fee, and pharmacy costs; the members of the institutional review board were paid by the sponsor (Bracco). Jan-Hendrik Buhk—UNRELATED: Consultancy: Codman Neurovascular (Advisory Board) Germany, Austria, and Switzerland. Miles A. Kirchin—OTHER RELATIONSHIPS: Miles A. Kirchin is an employee of Bracco Imaging S.p.A. Alain Bonafé—RELATED: Fees for Participation in Review Activities such as Data Monitoring Boards, Statistical Analysis, Endpoint Committees, and the Like: Bracco. Cesare Colosimo—UNRELATED: Consultancy: Bayer Pharma, Bracco Diagnostics. Gianpaolo Pirovano—OTHER RELATIONSHIPS: employee of Bracco Diagnostics. Ningyan Shen—OTHER RELATIONSHIPS: employee of Bracco Diagnostics. Alberto Spinazzi—OTHER RELATIONSHIPS: Alberto Spinazzi, MD, is an employee of Bracco Diagnostics, the company that sponsored the clinical trial that is the subject of this publication. Su Lui—RELATED: Support for Travel to Meetings for the Study or Other Purposes: Bracco Diagnostics, Comments: As one of the blind readers, the company covered my traveling fee from China to Italy to join the study; Fees for Participation in Review Activities such as Data Monitoring Boards, Statistical Analysis, Endpoint Committees, and the Like: Bracco Diagnostics, Comments: Bracco Diagnostics paid me for reading the images for the MH-148 study. \*Money paid to the institution.

## REFERENCES

1. Maravilla KR, Maldjian JA, Schmalfuss IM, et al. **Contrast enhancement of central nervous system lesions: multicenter intraindividual crossover comparative study of two MR contrast agents.** *Radiology* 2006;240:389–400 CrossRef Medline
2. Rumboldt Z, Rowley HA, Steinberg F, et al. **Multicenter, double-blind, randomized, intra-individual crossover comparison of gadobenate dimeglumine and gadopentetate dimeglumine in MRI of brain tumors at 3 Tesla.** *J Magn Reson Imaging* 2009;29:760–67 CrossRef Medline
3. Rowley HA, Scialfa G, Gao PY, et al. **Contrast-enhanced MR imaging of brain lesions: a large-scale intraindividual crossover comparison of gadobenate dimeglumine versus gadodiamide.** *AJNR Am J Neuroradiol* 2008;29:1684–91 CrossRef Medline
4. Seidl Z, Vymazal J, Mechl M, et al. **Does higher gadolinium concentration play a role in the morphologic assessment of brain tumors? Results of a multicenter intraindividual crossover comparison of gadobutrol versus gadobenate dimeglumine (the MERIT Study).** *AJNR Am J Neuroradiol* 2012;33:1050–58 CrossRef Medline
5. Shen Y, Goerner FL, Snyder C, et al. **T1 relaxivities of gadolinium-based magnetic resonance contrast agents in human whole blood at 1.5, 3, and 7 T.** *Invest Radiol* 2015;50:330–38 CrossRef Medline
6. Colosimo C, Knopp MV, Barreau X, et al. **A comparison of Gd-BOPTA and Gd-DOTA for contrast-enhanced MRI of intracranial tumours.** *Neuroradiology* 2004;46:655–65 CrossRef Medline
7. Khouri Chalouhi K, Papini GD, Bandirali M, et al. **Less is better? Intraindividual and interindividual comparison between 0.075 mmol/kg of gadobenate dimeglumine and 0.1 mmol/kg of gadoterate meglumine for cranial MRI.** *Eur J Radiol* 2014;83:1245–49 CrossRef Medline
8. Greco A, Parker JR, Ratcliffe CG, et al. **Phase III, randomized, double-blind, cross-over comparison of gadoteridol and gadopentetate dimeglumine in magnetic resonance imaging of patients with intracranial lesions.** *Australas Radiol* 2001;45:457–63 CrossRef Medline
9. Maravilla KR, Smith MP, Vymazal J, et al. **Are there differences between macrocyclic gadolinium contrast agents for brain tumor imaging? Results of a multicenter intraindividual crossover comparison of gadobutrol with gadoteridol (the TRUTH study).** *AJNR Am J Neuroradiol* 2015;36:14–23 CrossRef Medline
10. Gutierrez JE, Rosenberg M, Seemann J, et al. **Safety and efficacy of gadobutrol for contrast-enhanced magnetic resonance imaging of the central nervous system: results from a multicenter, double-blind, randomized, comparator study.** *Magn Reson Insights* 2015;8:1–10 CrossRef Medline
11. Anzalone N, Scarabino T, Venturi C, et al. **Cerebral neoplastic enhancing lesions: multicenter, randomized, crossover intraindividual comparison between gadobutrol (1.0M) and gadoterate meglumine (0.5M) at 0.1 mmol Gd/kg body weight in a clinical setting.** *Eur J Radiol* 2013;82:139–45 CrossRef Medline
12. Kanal E, Maravilla K, Rowley HA. **Gadolinium contrast agents for CNS imaging: current concepts and clinical evidence.** *AJNR Am J Neuroradiol* 2014;35:2215–26 CrossRef Medline
13. Colosimo C, Ruscalleda J, Korves M, et al. **Detection of intracranial metastases: a multicenter, inpatient comparison of gadobenate dimeglumine-enhanced MRI with routinely used contrast agents at equal dosage.** *Invest Radiol* 2001;36:72–81 CrossRef Medline
14. Knopp MV, Runge VM, Essig M, et al. **Primary and secondary brain tumors at MR imaging: bicentric intraindividual crossover comparison of gadobenate dimeglumine and gadopentetate dimeglumine.** *Radiology* 2004;230:55–64 CrossRef Medline
15. Essig M, Tartaro A, Tartaglione T, et al. **Enhancing lesions of the brain: intraindividual crossover comparison of contrast enhancement after gadobenate dimeglumine versus established gadolinium comparators.** *Acad Radiol* 2006;13:744–51 CrossRef Medline
16. Kuhn MJ, Picozzi P, Maldjian JA, et al. **Evaluation of intraaxial enhancing brain tumors on magnetic resonance imaging: intraindividual crossover comparison of gadobenate dimeglumine and gadopentetate dimeglumine for visualization and assessment, and implications for surgical intervention.** *J Neurosurg* 2007;106:557–66 CrossRef Medline
17. Koenig M, Schulte-Altendorneburg G, Piontek M, et al. **Intra-individual, randomised comparison of the MRI contrast agents gadobutrol versus gadoteridol in patients with primary and secondary brain tumours, evaluated in a blinded read.** *Eur Radiol* 2013;23:3287–95 CrossRef Medline
18. Feinstein AR, Cicchetti DV. **High agreement but low kappa, I: the problems of two paradoxes.** *J Clin Epidemiol* 1990;43:543–49 CrossRef Medline
19. Kanda T, Ishii K, Kawaguchi H, et al. **High signal intensity in the dentate nucleus and globus pallidus on unenhanced T1-weighted MR images: relationship with increasing cumulative dose of a gadolinium-based contrast material.** *Radiology* 2014;270:834–41 CrossRef Medline
20. Errante Y, Cirimele V, Mallio CA, et al. **Progressive increase of T1 signal intensity of the dentate nucleus on unenhanced magnetic resonance images is associated with cumulative doses of intravenously administered gadodiamide in patients with normal renal function, suggesting dechelation.** *Invest Radiol* 2014;49:685–90 CrossRef Medline
21. Kanda T, Osawa M, Oba H, et al. **High signal intensity in dentate nucleus on unenhanced T1-weighted MR images: association with linear versus macrocyclic gadolinium chelate administration.** *Radiology* 2015;275:803–09 CrossRef Medline
22. McDonald RJ, McDonald JS, Kallmes DF, et al. **Intracranial gadolin-**

- ium deposition after contrast-enhanced MR imaging. *Radiology* 2015;275:772–82 CrossRef Medline
23. Quattrocchi CC, Mallio CA, Errante Y, et al. **Gadodiamide and dentate nucleus T1 hyperintensity in patients with meningioma evaluated by multiple follow-up contrast-enhanced magnetic resonance examinations with no systemic interval therapy.** *Invest Radiol* 2015; 50:470–72 CrossRef Medline
  24. Radbruch A, Weberling LD, Kieslich PJ, et al. **Gadolinium retention in the dentate nucleus and globus pallidus is dependent on the class of contrast agent.** *Radiology* 2015;275:783–91 CrossRef Medline
  25. Idée JM, Port M, Robic C, et al. **Role of thermodynamic and kinetic parameters in gadolinium chelate stability.** *J Magn Reson Imaging* 2009;30:1249–58 CrossRef Medline
  26. Heverhagen JT, Krombach GA, Gizewski E. **Application of extracellular gadolinium-based MRI contrast agents and the risk of nephrogenic systemic fibrosis.** *Rofo* 2014;186:661–69 CrossRef Medline
  27. Soulez G, Bloomgarden DC, Rofsky NM, et al. **Nephrogenic systemic fibrosis in patients with stages 3 to 5 chronic kidney disease undergoing MRI with the injection of gadobenate dimeglumine or gadoteridol: findings from prospective cohort studies.** *AJR Am J Roentgenol*. In press
  28. Nandwana SB, Moreno CC, Osipow MT, et al. **Gadobenate dimeglumine administration and nephrogenic systemic fibrosis: is there a real risk in patients with impaired renal function?** *Radiology* 2015 Apr 15. [Epub ahead of print] CrossRef Medline
  29. American College of Radiology (ACR) Manual on Contrast Media. Version 9. 2013. <http://www.acr.org/quality-safety/resources/~media/37D84428BF1D4E1B9A3A2918DA9E27A3.pdf/>. Accessed June 19, 2015
  30. The Royal Australian and New Zealand College of Radiologists. **Guideline on the Use of Gadolinium-Containing MRI Contrast Agents in Patients with Renal Impairment.** <https://www.nephrology.edu.au/members/documents/GuidelinesontheUseofGadolinium-containingMRIContrastAgents10thSeptember.pdf>. Accessed June 19, 2015
  31. Kirchin MA, Lorusso V, Pirovano G. **Compensatory biliary and urinary excretion of gadobenate ion after administration of gadobenate dimeglumine (MultiHance®) in cases of impaired hepatic or renal function: a mechanism that may aid in the prevention of nephrogenic systemic fibrosis?** *Br J Radiol* 2015;88: 20140526 CrossRef Medline
  32. Noebauer-Huhmann IM, Szomolanyi P, Kronnerwetter C, et al. **Brain tumours at 7T MRI compared to 3T—contrast effect after high and full standard contrast agent dose: initial results.** *Eur Radiol* 2015;25:106–12 CrossRef Medline
  33. Sandstede JJ, Beer M, Lipke C, et al. **Time course of contrast enhancement patterns after Gd-BOPTA in correlation to myocardial infarction and viability: a feasibility study.** *J Magn Reson Imaging* 2001;14:789–94 CrossRef Medline
  34. Achenbach M, Figiel JH, Burbelko M, et al. **Prospective comparison of image quality and diagnostic accuracy of 0.5 molar gadobenate dimeglumine and 1.0 molar gadobutrol in contrast-enhanced runoff magnetic resonance angiography of the lower extremities.** *J Magn Reson Imaging* 2010;32:1166–71 CrossRef Medline
  35. Morana G, Grazioli L, Kirchin MA, et al. **Solid hypervascular liver lesions: accurate identification of true benign lesions on enhanced dynamic and hepatobiliary phase magnetic resonance imaging after gadobenate dimeglumine administration.** *Invest Radiol* 2011;46: 225–39 CrossRef Medline
  36. Schneider G, Probst T, Kirchin MA, et al. **Low-dose gadobenate dimeglumine-enhanced MRI of the kidney for the differential diagnosis of localized renal lesions.** *Radiol Med* 2015 Jun 19. [Epub ahead of print] CrossRef Medline

# Temporal Bone CT: Improved Image Quality and Potential for Decreased Radiation Dose Using an Ultra-High-Resolution Scan Mode with an Iterative Reconstruction Algorithm

S. Leng, F.E. Diehn, J.I. Lane, K.K. Koeller, R.J. Witte, R.E. Carter, and C.H. McCollough



## ABSTRACT

**BACKGROUND AND PURPOSE:** Radiation dose in temporal bone CT imaging can be high due to the requirement of high spatial resolution. In this study, we assessed whether CT imaging of the temporal bone by using an ultra-high-resolution scan mode combined with iterative reconstruction provides higher spatial resolution and lower image noise than a z-axis ultra-high-resolution mode.

**MATERIALS AND METHODS:** Patients with baseline temporal bone CT scans acquired by using a z-axis ultra-high-resolution protocol and a follow-up scan by using the ultra-high-resolution–iterative reconstruction technique were identified. Images of left and right temporal bones were reconstructed in the axial, coronal, and Poschl planes. Three neuroradiologists assessed the spatial resolution of the following structures: round and oval windows, incudomalleolar and incudostapedial joints, basal turn spiral lamina, and scutum. The paired z-axis ultra-high-resolution and ultra-high-resolution–iterative reconstruction images were displayed side by side in random order, with readers blinded to the imaging protocol. Image noise was compared in ROIs over the posterior fossa.

**RESULTS:** We identified 8 patients, yielding 16 sets of temporal bone images (left and right). Three sets were excluded because the patient underwent surgery between the 2 examinations. Spatial resolution was comparable (Poschl) or slightly better (axial and coronal planes) with ultra-high-resolution–iterative reconstruction than with z-axis ultra-high-resolution. A paired *t* test indicated that noise was significantly lower with ultra-high-resolution–iterative reconstruction than with z-axis ultra-high-resolution ( $P < .001$ ), with a mean noise reduction of 37% (range, 18%–49%).

**CONCLUSIONS:** The ultra-high-resolution–iterative reconstruction scan mode has similar or slightly better resolution relative to the z-axis ultra-high-resolution mode for CT of the temporal bone but significantly ( $P < .01$ ) lower image noise, which may enable the dose to be reduced by approximately 50%.

**ABBREVIATIONS:** IR = iterative reconstruction; UHR = ultra-high-resolution; zUHR = z-axis ultra-high-resolution

Since the introduction of multidetector techniques, CT has become a major diagnostic technique for temporal bone imaging because its high spatial resolution is well-suited to the task of visualizing the fine anatomic structures of the middle and inner ear.<sup>1–5</sup> To improve spatial resolution, different approaches have been introduced. One of these is the use of an attenuating comb filter to reduce the detector aperture in both fan and cone angle directions, which is referred to as the z-axis ultra-high-resolution

(zUHR) technique.<sup>6</sup> This technique, in combination with a flying focal spot technique, provides nominal image thickness thinner than the detector cell size at the isocenter.<sup>6,7</sup>

Due to the requirement for high spatial resolution, the radiation dose in temporal CT can be high, especially with the zUHR technique because its dose efficiency is reduced as photons passing through the patient are blocked from the detector by the comb filters in both fan and cone angle directions.<sup>8</sup> A recent focus of CT imaging has been to reduce patient exposure to ionizing radiation, following the as low as reasonably achievable principle.<sup>9–13</sup> However, the consequent reduction in photons can adversely affect image quality and present a great challenge when imaging small, anatomically complex structures embedded in attenuating bone, such as those of the middle and inner ear. Iterative reconstruction (IR) is a promising reconstruction technique that is superior to standard filtered back-projection reconstructions and theoretically can be

Received November 3, 2014; accepted after revision February 16, 2015.

From the Departments of Radiology (S.L., F.E.D., J.I.L., K.K.K., R.J.W., C.H.M.) and Health Sciences Research, Division of Biomedical Statistics and Informatics (R.E.C.), Mayo Clinic, Rochester, Minnesota.

Paper previously presented at: Annual Meeting of the Radiological Society of North American, December 1–6, 2013; Chicago, Illinois.

Please address correspondence to Shuai Leng, PhD, Department of Radiology, Mayo Clinic, 200 First St SW, Rochester, MN 55905; e-mail: leng.shuai@mayo.edu

<http://dx.doi.org/10.3174/ajnr.A4338>

used to improve resolution at standard radiation doses or to maintain current resolution by using a reduced radiation dose.<sup>14-17</sup>

Recently, a new technique combining a deconvolution technique and an IR algorithm, referred to as ultra-high-resolution (UHR)-IR, has been introduced to improve dose efficiency of the zUHR mode. Phantom studies demonstrated that this technique improved dose efficiency by removing the comb filter along the cone (z) direction.<sup>8</sup> In this study, we retrospectively reviewed temporal bone CT examinations in patients who had baseline studies by using the standard zUHR technique and follow-up examinations by using UHR-IR to determine whether UHR-IR provided improved resolution and lower noise than zUHR in the clinical setting, which could enable reductions in dose.

## MATERIALS AND METHODS

### Patient Enrollment and CT Scans

This retrospective study was approved by our institutional review board and was Health Insurance Portability and Accountability Act-compliant. Patients with temporal bone CT scans acquired by using a zUHR protocol who underwent a follow-up scan by using the UHR-IR technique were identified by searching the electronic medical records. Patients who had not provided authorization for research were excluded from this study. Temporal bones in which inner ear surgery was performed between the 2 examinations were also excluded.

Baseline scans were acquired on a 64-section CT scanner (Sensation 64; Siemens, Forchheim, Germany) by using the zUHR mode (12 × 0.3 mm collimation), with a tube potential of 120 kV, 400 effective mAs, 1-second rotation time, and 0.8 helical pitch. The automatic exposure control was off, and the volume CT dose index was 88 mGy. Images were reconstructed by using a standard filtered back-projection algorithm with a special kernel designed for the UHR mode (U70). Images were reconstructed with 0.4-mm section thickness at 0.3-mm increments. Both the z-axis and in-plane flying focal spot were used for data acquisition.<sup>6,7</sup>

The follow-up UHR-IR scans were conducted on a 128-section CT scanner (Somatom Definition Flash; Siemens) by using the UHR scan mode (16 × 0.6 mm collimation), with a tube potential of 120 kV, 375 effective mAs, 1-second rotation time, and 0.8 helical pitch. The automatic exposure control was off, and the volume CT dose index was 82 mGy. Images were reconstructed by using an IR algorithm (sinogram-affirmed iterative reconstruction, SAFIRE; Siemens) with a special kernel designed for the UHR mode (V80). The strength of the IR algorithm was set at 3 on a scale of 1 (least noise reduction) to 5 (most noise reduction). The thinnest available image section thickness (0.5 mm) was used, with an increment of 0.3 mm.

For both original and follow-up examinations, images of the left and right temporal bones were reconstructed in the axial, coronal, and Poschl planes, as per our routine clinical protocol.

### Assessment of Spatial Resolution

Image quality was independently assessed by 3 fellowship-trained neuroradiologists experienced in temporal bone image interpretation, with a focus on differences in image sharpness (spatial resolution) between the 2 techniques. All images were reviewed

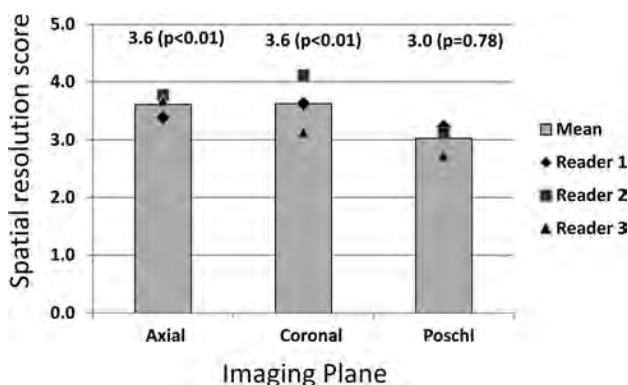


**FIG 1.** Spatial resolution scores for images in the axial, coronal, and Poschl planes, averaged across individual structures in each imaging plane. The scale assessed UHR-IR images relative to zUHR images: 1 = inferior resolution with degraded visualization, 2 = slightly inferior resolution without affecting visualization, 3 = equivalent, 4 = slightly superior resolution without affecting visualization, 5 = superior resolution with improved visualization. The means are shown as lined bars, with the value above each bar. Statistical significance was determined with the Wilcoxon signed rank test.

on a calibrated monitor used for clinical diagnosis located inside a darkened room, with ambient light <10 lux. Baseline and follow-up images of the same patient and same side of the head in the 3 planes were displayed side by side in a randomized order, with the readers blinded to reconstruction parameters. The 3 neuroradiologist reviewers assessed the spatial resolution on each of the axial, coronal, and Poschl planes, focusing on the following structures: round window, incudomalleal joint, and basal turn spiral lamina (axial plane); oval window and scutum (coronal plane); and the basal turn spiral lamina and incudostapedial joint (Poschl plane). Readers compared the spatial resolution of the displayed image on the left with that displayed on the right, and another investigator (not a reader) determined post hoc which image was zUHR and which was UHR-IR to apply the following grading scale to the UHR-IR images (relative to the zUHR images) for each structure: 1 = inferior resolution with degraded visualization, 2 = slightly inferior resolution without affecting visualization, 3 = equivalent, 4 = slightly superior resolution without affecting visualization, 5 = superior resolution with improved visualization.

### Image Noise Measurement

Image noise was measured as the SD of CT numbers inside a circular ROI placed on the axial images. The ROI size was approximately 0.4 cm<sup>2</sup> and was placed over the posterior fossa area, with locations matched as closely as possible between those of the zUHR and UHR-IR scans.

### Statistical Analysis

The Wilcoxon signed rank test was performed to compare the scores of image resolution between UHR-IR and zUHR for the aforementioned individual structures (round window, incudomalleal joint, oval window, incudostapedial joint, spiral lamina in the basal turn, and scutum) and reconstruction planes (axial, coronal, and Poschl). For the comparison of spatial resolution in reconstruction planes, the averaged score of structures in the plane was used. A 2-tailed paired *t* test was used to compare image

### Spatial resolution scores and P values

	Round Window	Incudomalleolar Joint	Basal Turn Spiral Lamina	Oval Window Scutum	Incudostapedial Joint
Mean score	4.05	4.05	2.69	3.71	3.53
P value	<.001	<.001	.0083	.0011	.0037

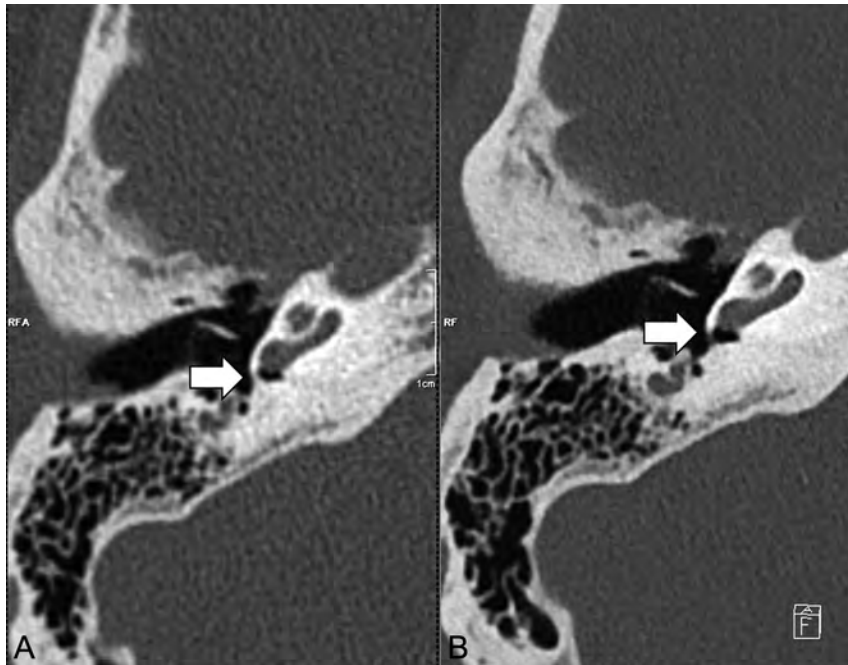


**FIG 2.** Comparison of spatial resolution of the round window. Representative axial CT images of the round window of the same patient scanned with the zUHR technique (A) and UHR-IR technique (B). The UHR-IR technique produced superior spatial resolution and lower image noise.

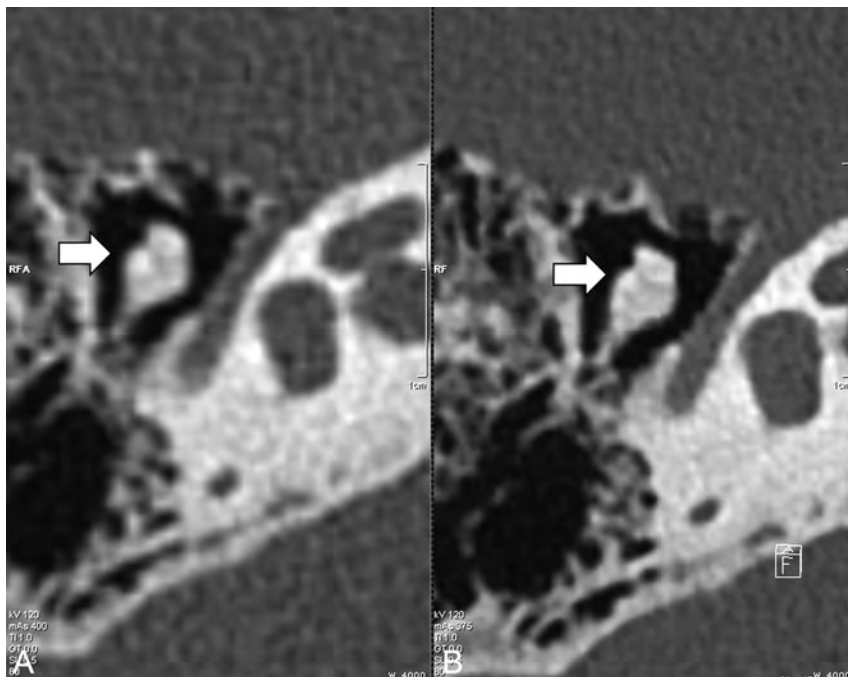


**FIG 3.** Comparison of the spatial resolution of the incudomalleolar joint. Representative axial images of the incudomalleolar joint of the same patient scanned with the zUHR technique (A) and UHR-IR technique (B). The UHR-IR technique produced superior spatial resolution and lower image noise.

noise between the 2 techniques. With both tests,  $P < .01$  was considered a statistically significant difference. The difference in image noise between the 2 techniques was calculated, and dose reduction was estimated on the basis of the relationship between image noise and radiation dose (ie, radiation dose is inversely proportional to the square of image noise in CT).

## RESULTS

### Study Sample

We identified 8 patients (2 male and 6 female; age ranges, 16–75 years of age) who had initial examinations with the zUHR technique and underwent a follow-up scan by using the new UHR-IR technique. Images from the left and right side of each patient provided 16 sets of temporal bone CT images. Three of these datasets were excluded because the patient had inner ear surgery between the 2 examinations; this change left 13 sets of images included in the final data analysis. The median time interval between examinations was 12 months (range, 1–34 months). For the initial examinations, the principal indications were the following: hearing loss ( $n = 4$ ; 2 conductive and 2 sensorineural), inflammatory disease ( $n = 2$ ), trauma ( $n = 1$ ), and skeletal dysplasia ( $n = 1$ ). For the follow-up examinations, the indications were the following: postoperative evaluation ( $n = 3$ ; 1 internal auditory canal decompression, 1 cochlear implant, and 1 ossicular reconstruction), follow-up or ruling out inflammatory disease ( $n = 3$ ), further evaluation of bilateral fractures ( $n = 1$ ), and follow-up of a presumed mastoid hemangioma ( $n = 1$ ).

### Spatial Resolution

Spatial resolution scores showed that the 3 readers found the UHR-IR images to be of significantly higher quality ( $P < .01$ , Wilcoxon signed rank test) than the zUHR images in the axial and coronal planes but not in the Poschl plane (Fig 1). Spatial resolution scores of individual structures showed that readers found the UHR-IR images to be of significantly higher quality ( $P < .01$ , Wilcoxon signed rank test) for the round window, incudomalleolar joint, oval window and scutum (Table). UHR images had

higher quality than zUHR images for the incudostapedial joint, but the difference was not statistically significant (Table). For the basal turn spiral lamina, UHR images had a lower quality than zUHR images (Table). The superior sharpness produced by the UHR-IR technique can be seen in representative images at the round window and incudomalleolar joint (Figs 2 and 3).

#### Noise and Potential Dose Reduction

In all cases, images obtained with UHR-IR had lower noise than those obtained with zUHR (all,  $P < .01$ ; paired  $t$  test; Fig 4). In representative images (Fig 5), the UHR-IR and zUHR techniques produced similar sharpness, but the UHR-IR images had much

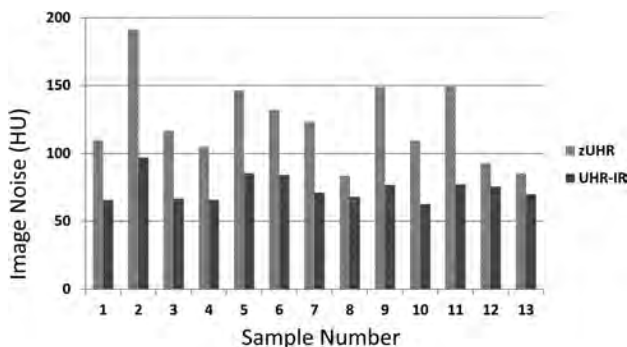


**FIG 4.** Lower image noise in images acquired with UHR-IR. Image noise was measured at the posterior fossa in axial images from each of the 13 datasets by using the zUHR and UHR-IR techniques.



**FIG 5.** Spatial resolution and image noise in images from a representative patient. Axial (A and B) and coronal (C and D) CT images of the same patient scanned with the zUHR technique (A and C) and UHR-IR technique (B and D). Substantial noise reduction was achieved by using the UHR-IR technique.

lower image noise in both the axial and coronal planes. The mean noise reduction by using UHR-IR, relative to zUHR, was 37% (range, 18%–49%). This translated to a dose reduction potential of 61% (range, 33%–74%).

#### DISCUSSION

Reduction in the ionizing radiation dose has been a major focus of technology development in diagnostic CT in recent years.<sup>9–11,14,18</sup> Temporal bone CT requires a high radiation dose relative to other diagnostic CT examinations; for example, temporal bone CT by using the standard technique at our institution (zUHR) results in a volume CT dose index of 88 mGy, compared with 38–69 mGy for a routine head CT examination. Given that radiation reduction can adversely affect image quality, techniques that allow dose reduction without sacrificing image resolution would be exceedingly useful in this area of CT imaging.

In this study, radiation dose reduction was achieved by using 2 techniques: 1) the deconvolution technique, and 2) iterative reconstruction. The deconvolution technique allows removal of the comb filter along the z-direction compared with zUHR, which substantially improves the dose efficiency by increasing the number of photons detected by the detector. Most important, the spatial resolution was preserved, which was substantially better than that in other scanners without the comb filter techniques.<sup>6</sup> Iterative reconstruction has the potential to reduce image noise and radiation dose compared with standard filtered back-projection reconstruction algorithms in many studies,<sup>14–17</sup> including in the

temporal bone.<sup>13</sup> The amount of dose reduction highly depends on the specific vendor, scanner platform and imaging task. Dose reduction in this study was a combination of these 2 techniques, similar to that demonstrated in the previous phantom studies by comparing filtered back-projection–zUHR, IR-zUHR, and IR-UHR.<sup>8</sup>

It is important to maintain the spatial resolution while reducing image noise and radiation dose, especially in temporal bone CT, in which high spatial resolution is critical. In this study, we found that the UHR-IR scan mode by using a z-deconvolution technique produced resolutions similar to or slightly better than those produced by the zUHR mode, but with significantly (37%) lower image noise. This reduced image noise could potentially allow UHR-IR to be used to reduce the dose by >50% on the basis of the relationship between image noise and radiation dose in CT. This study was performed by using the IR-UHR technique on the second-generation dual-source scanner (Flash) and compared to the same patients' prior examinations on older scanners. By comparing scans from the same patients, we avoided the potential compounding fac-

tor caused by patient-to-patient variation. The IR-UHR technique has also been implemented on the third-generation dual-source scanner, and dose reduction was reported by comparing scans of different patients randomly assigned to the first-, second-, and third-generation dual-source scanners.<sup>19</sup> Given the improved source and detector technologies, more dose reduction may be achievable by using the third-generation dual-source scanner.

There are several limitations to this study. The first is the small patient cohort, due to the limited number of patients scanned with both zUHR and UHR-IR. However, image noise was lower with UHR-IR for each individual case, and the paired *t* test showed this difference to be statistically different. Another limitation is that the retrospective methodology did not permit standardization of the time interval between examinations. The third limitation of this study is that the zUHR examinations were performed on a different scanner platform from that of the UHR-IR examinations. This was because prior examinations were only available on a different scanner platform and because the new scanner was only recently available. The amount of dose reduction could be potentially less if the zUHR examinations were performed on the same new scanner platform.

## CONCLUSIONS

This study demonstrated that UHR-IR reduces image noise by >30% while providing similar or better spatial resolution than the existing zUHR technique. This may enable a substantial reduction in radiation dose without a corresponding loss of resolution. This is a considerable achievement for temporal bone CT, which currently requires one of the highest doses in clinical CT imaging. These preliminary findings need to be corroborated with further studies performed with a reduced radiation dose.

## ACKNOWLEDGMENTS

The authors thank Thomas Vrieze, Mike Bruesewitz, Sally Reinhart, and Christine Tipka for helping collect patient data and Kristina Nunez and Naomi Ruff for their assistance in manuscript preparation.

Disclosures: Cynthia H. McCollough—UNRELATED: Grants/Grants Pending: Siemens.\* Comments: Dr McCollough reports grants from Siemens, outside the submitted work. \*Money paid to the institution.

## REFERENCES

1. Lane JI, Lindell EP, Witte RJ, et al. **Middle and inner ear: improved depiction with multiplanar reconstruction of volumetric CT data.** *Radiographics* 2006;26:115–24
2. Lane JI, Witte RJ. *Temporal Bone: An Imaging Atlas.* Berlin: Springer-Verlag; 2009
3. Purcell DD, Fischbein NJ, Patel A, et al. **Two temporal bone computed tomography measurements increase recognition of malformations and predict sensorineural hearing loss.** *Laryngoscope* 2006;116:1439–46
4. Swartz JD, Loevner LA. *Imaging of the Temporal Bone.* New York: Thieme Medical; 2008
5. Noble JH, Dawant BM, Warren FM, et al. **Automatic identification and 3D rendering of temporal bone anatomy.** *Otol Neurotol* 2009;30:436–42
6. Flohr T, Stierstorfer K, Süß C, et al. **Novel ultrahigh resolution data acquisition and image reconstruction for multi-detector row CT.** *Med Phys* 2007;34:1712
7. Flohr TG, Stierstorfer K, Ulzheimer S, et al. **Image reconstruction and image quality evaluation for a 64-slice CT scanner with z-flying focal spot.** *Med Phys* 2005;32:2536–47
8. McCollough CH, Leng S, Sunnegardh J, et al. **Spatial resolution improvement and dose reduction potential for inner ear CT imaging using a z-axis deconvolution technique.** *Med Phys* 2013;40:061904
9. McCollough C, Chen G, Kalender WA, et al. **Achieving routine submSv CT scanning: report from the summit on management of radiation dose in CT.** *Radiology* 2012;264:567–80
10. McCollough CH, Primak AN, Braun N, et al. **Strategies for reducing radiation dose in CT (PMC 2743386).** *Radiol Clin North Am* 2009;47:27–40
11. Yu L, Liu X, Leng S, et al. **Radiation dose reduction in CT: techniques and future perspective.** *Imaging Med* 2009;1:65–84
12. Nauer C, Rieke A, Zubler C, et al. **Low-dose temporal bone CT in infants and young children: effective dose and image quality.** *AJNR Am J Neuroradiol* 2011;32:1375–80
13. Niu Y, Mehta D, Zhang Z, et al. **Radiation dose reduction in temporal bone CT with iterative reconstruction technique.** *AJNR Am J Neuroradiol* 2012;33:1020–26
14. Thibault JB, Sauer KD, Bouman CA, et al. **A three-dimensional statistical approach to improved image quality for multislice helical CT.** *Med Phys* 2007;34:4526–44
15. Winklehner A, Karlo C, Puipe G, et al. **Raw data-based iterative reconstruction in body CTA: evaluation of radiation dose saving potential.** *Eur Radiol* 2011;21:2521–26
16. Singh S, Kalra MK, Hsieh J, et al. **Abdominal CT: comparison of adaptive statistical iterative and filtered back projection reconstruction techniques.** *Radiology* 2010;257:373–83
17. Silva AC, Lawder HJ, Hara A, et al. **Innovations in CT dose reduction strategy: application of the adaptive statistical iterative reconstruction algorithm.** *AJR Am J Roentgenol* 2010;194:191–99
18. National Council on Radiation Protection and Measurements. **Ionizing radiation exposure of the population of the United States.** Bethesda: National Council on Radiation Protection and Measurements; 2009: Report 160
19. Meyer M, Haubenreisser H, Raupach R, et al. **Initial results of a new generation dual source CT system using only an in-plane comb filter for ultra-high resolution temporal bone imaging.** *Eur Radiol* 2015;25:178–85

## Memory Part 3: The Role of the Fornix and Clinical Cases

F.D. Raslau, J.C. Augustinack, A.P. Klein,  J.L. Ulmer, V.P. Mathews, and  L.P. Mark

The fornix is the major white matter outflow tract from the hippocampus, and pathology involving the fornix would be expected to affect memory. Pathologic processes that affect the hippocampal formation and parahippocampal gyrus, including the entorhinal cortex, correlate with specific types of memory deficits,<sup>1-10</sup> but the clinical consequences of lesions of the fornix have not been emphasized as often. A familiarity with the anatomy and imaging of the fornix helps to anticipate the clinical impact of pathology and treatment that involves this strategic structure.

The fornix, named for its archlike configuration (Figs 1 and 2), is formed from the fimbria, which is the fringelike medial continuation of the alveus that sits on the superior surface of the hippocampus just below the ependymal lining on the floor of the temporal horn of the lateral ventricles (Fig 3). The posterior portion of the fornix, the crus, also forms the posterior medial margin of the lateral ventricles (Fig 4). The crura are joined across the midline by the psalterium (lyre or Harp of David), also called the hippocampal commissure or commissure of the fornix.<sup>11</sup> The body of the fornix is situated at the dome of the fornical archlike configuration and is connected to the inner surface of the corpus callosum via the septum pellucidum (Fig 5A). This portion of the fornix is situated at the upper margin of the velum interpositum, which is traversed by the internal cerebral veins, and is above the third ventricle but below the body of the lateral ventricles. The foramen of Monro forms the anterior border of the velum interpositum, which is open at its posterior aspect at the position of the pineal gland (Fig 5B).

The white matter fibers of the columns of the fornix have a more superoinferior orientation, forming the anterior portion of the fornical arch, and are also joined to the posterior margin of the genu of the corpus callosum via the septum pellucidum (Fig 6). At

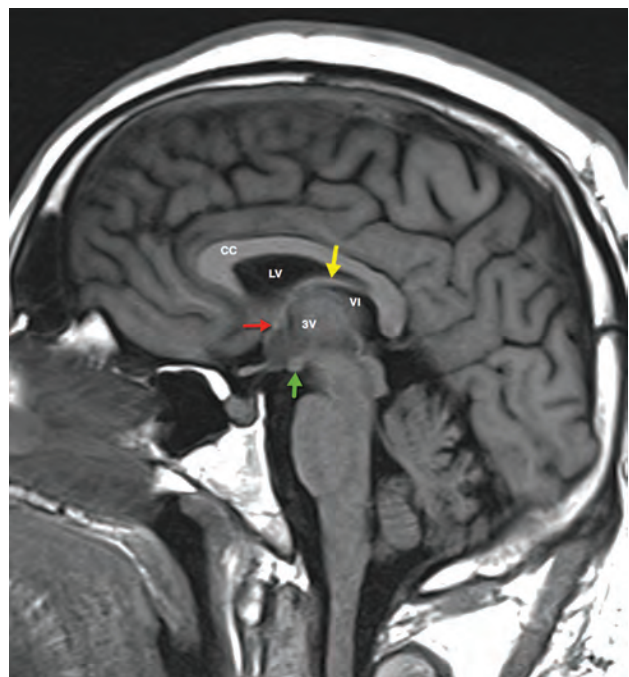


**FIG 1.** Sagittal T1-weighted image showing the archlike configuration of the fornix (yellow arrow) at the upper margin of the velum interpositum (VI), which is situated between the lateral (LV) and third (3V) ventricles. The fornix is attached to the septum pellucidum, which in turn is attached to the inner curving surface of the corpus callosum (CC). The fornix bifurcates at the level of the anterior commissure (red arrow), with the postcommissural fibers projecting to the mammillary bodies (green arrow).

the level of the anterior commissure, the columns of the fornix split, with most of the fibers coursing posterior to the anterior commissure to form the postcommissural fibers that project to the mammillary bodies, while the minority of precommissural fibers run anterior to the anterior commissure to project to the medial prefrontal cortex, nucleus accumbens, and septal nuclei, which are located deep to the medial aspect of the frontal lobes inferior to the rostrum of the corpus callosum. The fornix also sends smaller fibers to the anterior thalamus.

Clinical and experimental data suggest a functional distribution of the fornical fibers.<sup>12-16</sup> The left fornix primarily carries verbal memory information, while the right carries visuospatial

From the Department of Radiology (F.D.R.), University of Kentucky, Lexington, Kentucky; Department of Radiology (J.C.A.), Harvard Medical School, Boston, Massachusetts; Athinoula A. Martinos Center for Biomedical Imaging (J.C.A.), Massachusetts General Hospital and Harvard Medical School, Boston, Massachusetts; and Department of Radiology (A.P.K., J.L.U., V.P.M., L.P.M.), Medical College of Wisconsin, Milwaukee, Wisconsin.

Please address correspondence to Leighton P. Mark, MD, Froedtert Hospital, Department of Radiology, Neuroradiology Section, 9200 West Wisconsin Ave, Milwaukee, WI 53226; e-mail: lmark@mcw.edu

<http://dx.doi.org/10.3174/ajnr.A4371>

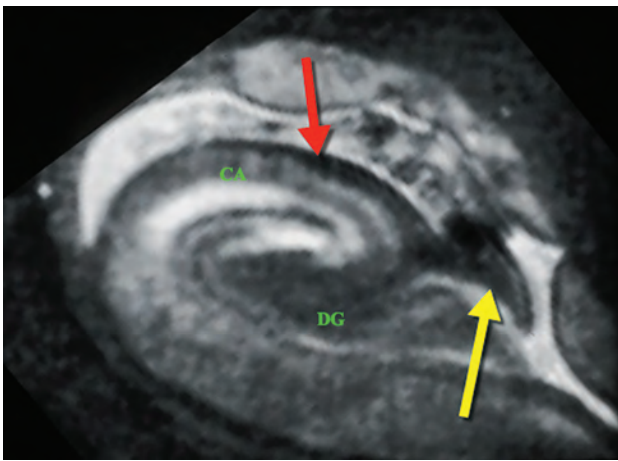


**FIG 2.** High-resolution coronal T2-weighted image of the right hippocampal formation showing the dark signal of the white matter fibers of the alveus (red arrow) positioned on top of Ammon's horn (CA) of the hippocampus and below the CSF of the temporal horn of the lateral ventricle, which also contains the choroid plexus (not labeled). The dentate gyrus (DG) is shown. The alveus thickens at its medial margin to form the fimbria (yellow arrow).

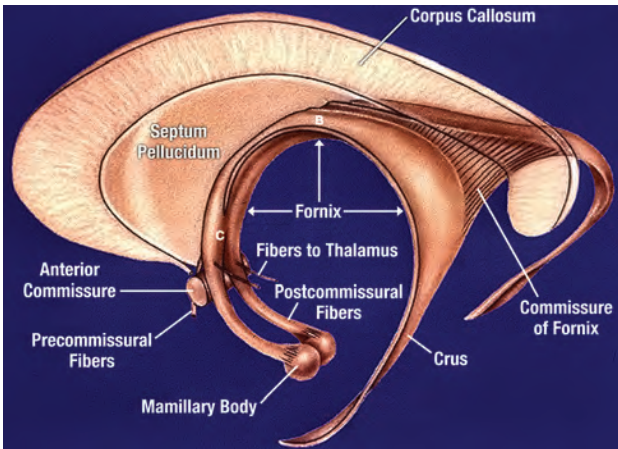


**FIG 3.** Schematic overview of the fornix from the side. The fimbria forms the crus of the fornix, which is joined to the opposite fornix across the midline by the commissure of the fornix (hippocampal commissure, psalterium). The body of the fornix (B) at the top of the fornical arch is connected to the inferior surface of the body of the corpus callosum by the septum pellucidum. The column of the fornix (C) has a more superoinferior orientation and is connected to the posterior margin of the genu of the corpus callosum by the septum pellucidum. The columns of the fornix are split at the level of the anterior commissure with most the fibers (postcommissural fibers) projecting to the mammillary bodies. Published with permission from the estate of David L. Daniels.

memory information (Fig 7). In addition, the medial fornix carries fibers from the caudal hippocampus, which processes exteroceptive signals and integrates object recognition within a spatial context (ie, scene learning). The lateral aspect of the fornix is presumed to carry projections from the more rostral hippocampus, which processes interoceptive signals for emotional and motivational learning and memory (Fig 8).

Knowledge of this anatomy helps to anticipate clinical deficits and surgical risks. Figure 9 shows the imaging of a 23-year-old woman who presented with progressive headaches over a 2-month period. An unusual lesion was noted within the anterior

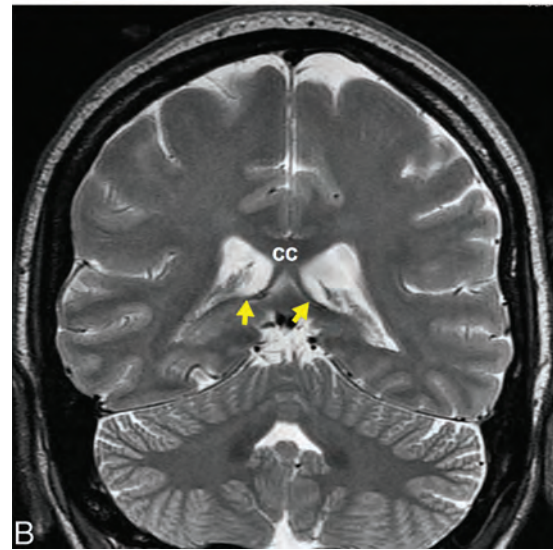
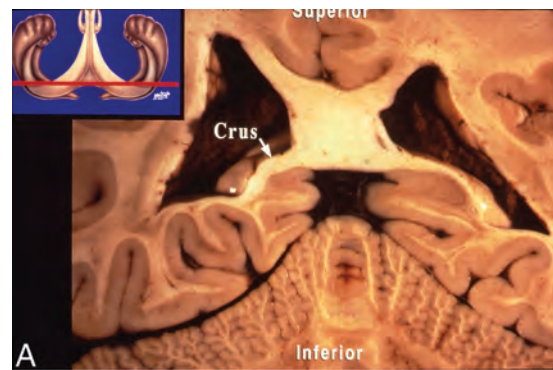


**FIG 4.** A, Coronal anatomic specimen with a schematic reference image. The white matter fibers of the crus of the fornix can be seen forming the inferior medial margin of the posterior aspect of the body of the lateral ventricles at the level of the splenium of the corpus callosum. B, Coronal T2-weighted image shows the dark signal of the crura of the fornices (yellow arrows) forming the inferior medial margin of the posterior lateral ventricles at the level of the posterior aspect of the body of the corpus callosum (CC).

right lateral ventricle, causing some obstruction of the foramen of Monro. More important, the mass impinged on and displaced the columns of the fornices, right more than left. The neurosurgeons were advised about the close proximity of the fornices to the medial margin of the tumor and the risk of memory impairment. The patient underwent an endoscopic subtotal resection, in which the lesion was discovered to be a glioneuronal neoplasm, which was tightly adherent to the fornical columns. On postoperative day 1, the patient experienced new memory deficits with no recall of the surgery or reason for the surgery. Neuropsychological testing months later showed moderately impaired delayed recall of both verbal and visuospatial materials.

Figure 10A shows an axial gradient-echo image of a 60-year-old patient who presented with headaches and memory problems. A large collection of blood was noted in the cistern of the velum interpositum, with superior lateral displacement and compression of the body of the fornices. Cerebral angiography did not reveal any cause for the hemorrhage, and the patient was then monitored with serial MR imaging. Figure 10B shows atrophy of the mammillary bodies, left greater than right, 5 months later. The hematoma had significantly diminished in size with time, but

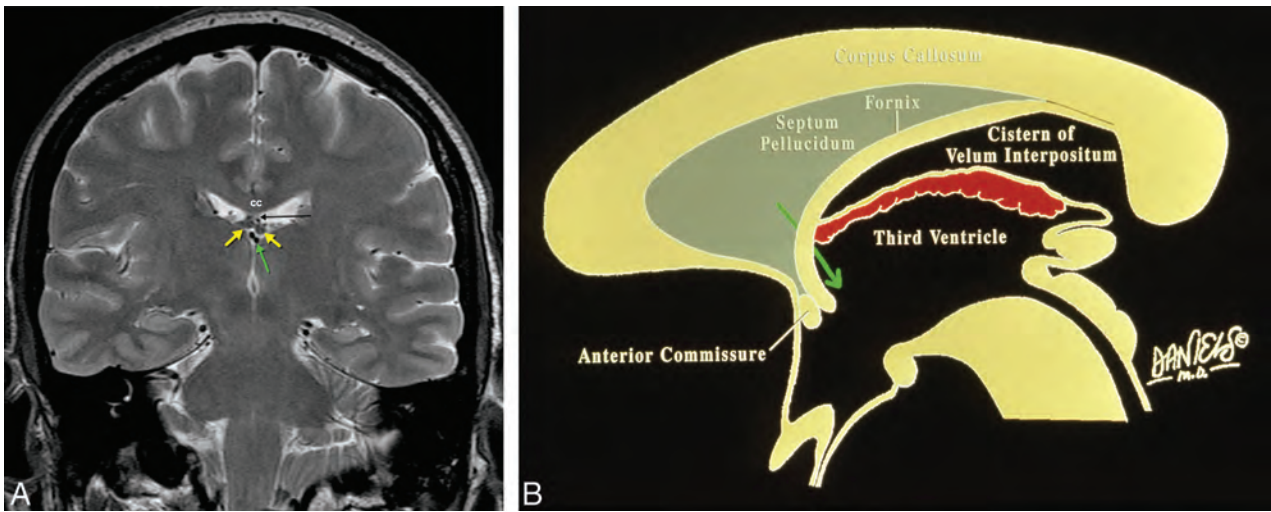


**FIG 5.** A, Coronal T2-weighted image shows the body of the fornices (yellow arrows) attached to the inferior margin of the body of the corpus callosum (CC) via the septum pellucidum (black arrow). The body of the fornices are at the upper aspect of the velum interpositum, which is traversed by the internal cerebral veins (green arrow), situated above the third ventricle but inferomedial to the body of the lateral ventricles. B, Sagittal schematic shows the position of the fornix relative to the velum interpositum. The foramen of Monro (green arrow) forms the anterior border of the velum interpositum, while the posterior border opens between the splenium of the corpus callosum above and the pineal gland below into the quadrigeminal plate cistern. The choroid plexus (red) is indicated at the roof of the third ventricle below but not within the velum interpositum. Published with permission from the estate of David L. Daniels.

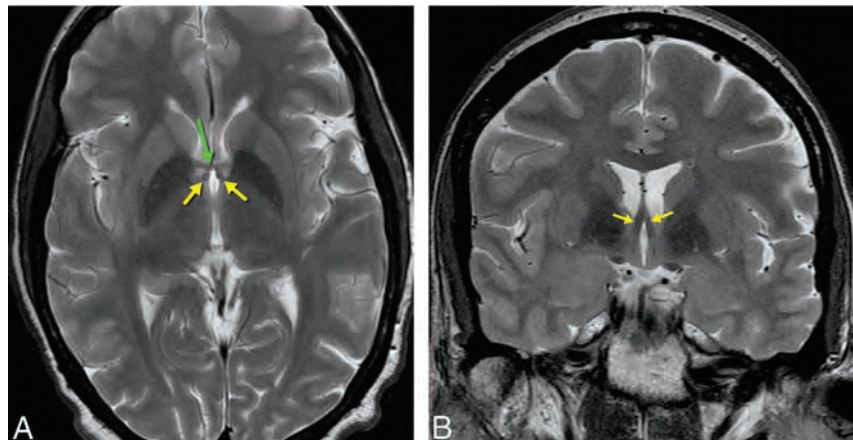


**FIG 6.** A, Axial T2-weighted image shows the postcommissural fibers of the fornix (yellow arrows) coursing posterior to the anterior commissure (green arrow). B, Coronal T2-weighted image shows the superoinferior orientation of the columns of the fornix (yellow arrows).

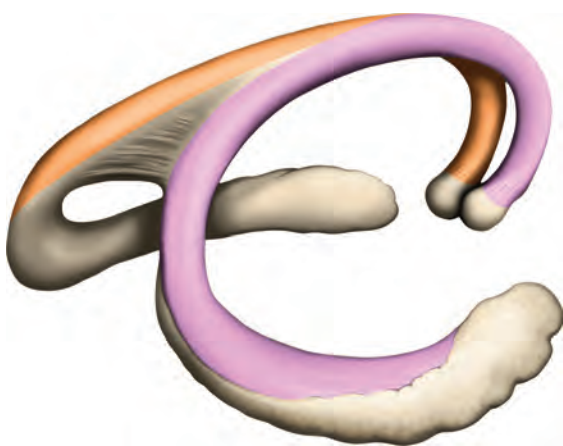


**FIG 7.** Drawing showing verbal memory information carried primarily by the left fornix (orange), while the visuospatial memory information is primarily transmitted by the right fornix (light purple).

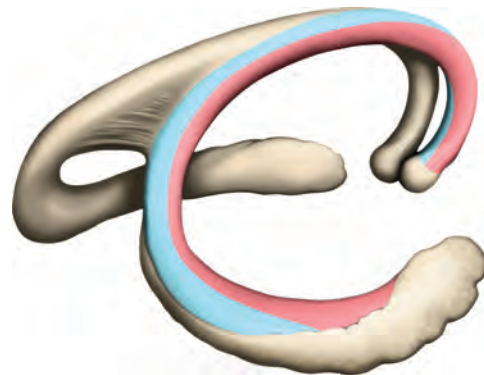


**FIG 8.** Drawing shows the medial aspect of the fornix (light blue) carrying fibers from the posterior hippocampus for processing of exteroceptive information for scene learning. The more lateral fibers (light red), meanwhile, carry fibers from the more rostral portions of the hippocampus for processing of interoceptive signals for emotional and motivational memory and learning.

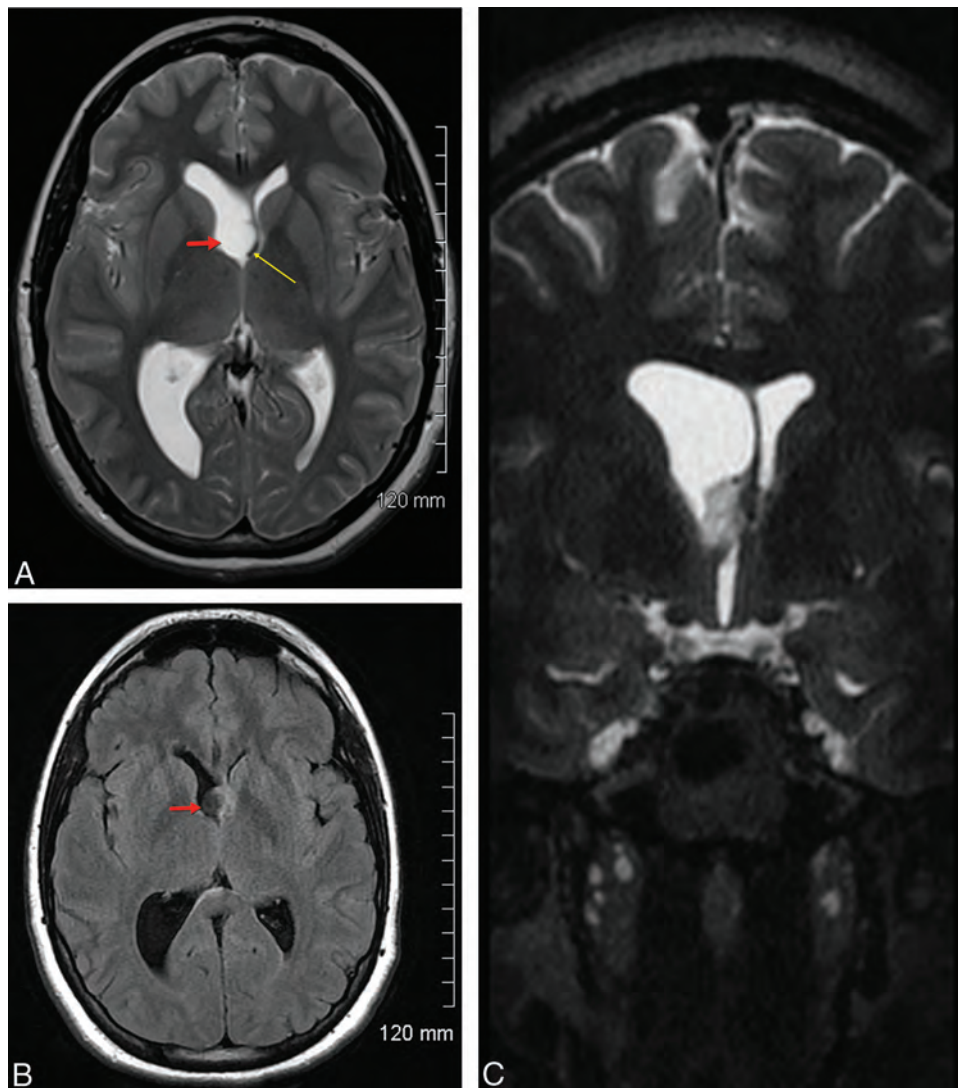


**FIG 9.** A, T2-weighted axial image shows a glioneuronal tumor (*red arrow*) within the right lateral ventricle near the foramen of Monro displacing and distorting the septum pellucidum and columns of the fornices (*yellow arrow*). B, The intraventricular glioneuronal tumor (*red arrow*) is better visualized on the axial FLAIR image. C, Postoperative coronal T2-weighted image shows the intraventricular neoplasm still distorting the columns of the fornix and septum pellucidum.

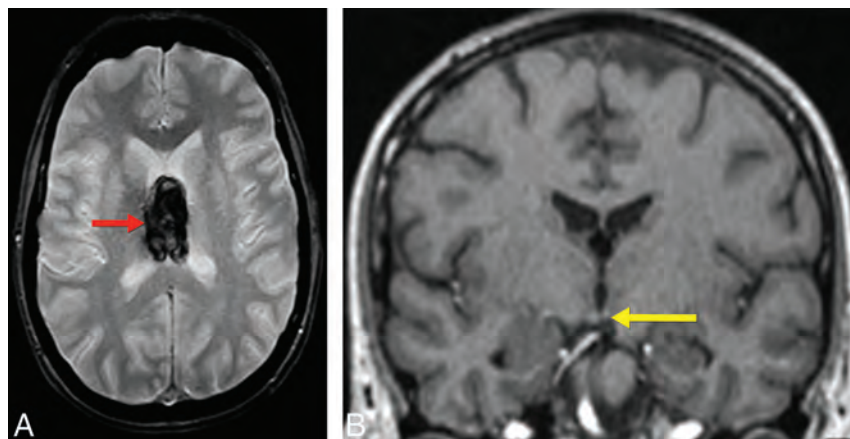


**FIG 10.** A, Gradient recalled-echo image shows hemorrhage (*red arrow*) in the cistern of the velum interpositum involving the bodies of the fornices. B, Coronal T1-weighted image 5 months later without treatment shows atrophy of the mammillary bodies, worse on the left (*yellow arrow*).

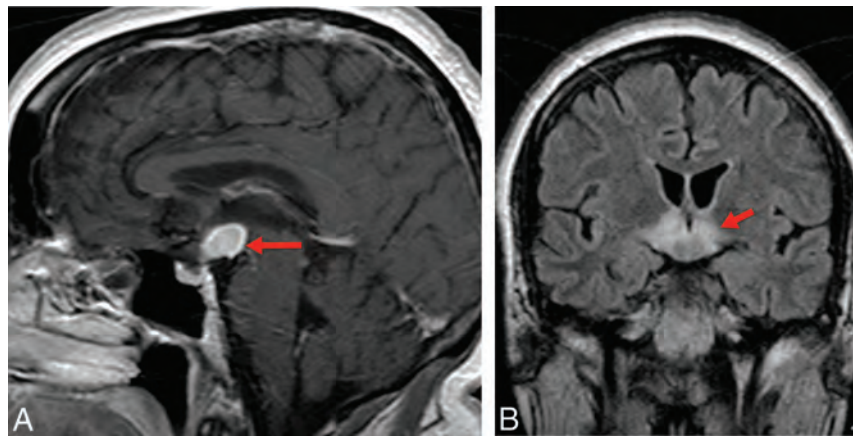


**FIG 11.** A, Sagittal T1 postcontrast image shows an enhancing mass involving the floor of the hypothalamus and mammillary body with extension into the third ventricle. B, Coronal FLAIR image shows extensive abnormal signal involving the hypothalamus on either side of the midline. Pathology (not shown) showed this to be Langerhans cell histiocytosis.

neuropsychological testing showed that the patient had residual memory impairment, verbal more than visuospatial. This is expected given the lateralization of the verbal memory fibers to the left fornix and its greater involvement by the hematoma as reflected in the smaller left mammillary body. Figure 11 shows the initial imaging of a 56-year-old woman who presented with new onset of memory loss. She would often repeat the same question during the appointment with her doctor, not remembering that her question had already been answered. The infiltrating enhancing lesion of her mammillary bodies, including much of the remainder of the hypothalamus demonstrated on the MR imaging examination, proved to be Langerhans cell histiocytosis.

The effort of investigations in the basic neurosciences will continue to expand and deepen our knowledge of the processes that constitute the experience that is memory, and our everyday clinical effort to understand the functional anatomy of the extended hippocampal network that subserves memory is useful to predict the dysfunctional implications of strategically located lesions and enhance the role of the neuroradiologist in diagnosis and guiding treatment.

## ACKNOWLEDGMENTS

In memory of David L. Daniels, MD, whose medical artwork continues to inspire us.

Disclosures: Vincent P. Mathews—UNRELATED: Payment for Lectures (including service on Speakers Bureaus); Eli Lilly, Comments: speakers bureau for Amyvid in 2013.

## REFERENCES

1. Augustinack JC, Huber KE, Postelnicu GM, et al. Entorhinal verrucae geometry is coincident and correlates with Alzheimer's lesions: a combined neuropathology and high-resolution ex vivo MRI analysis. *Acta Neuropathol* 2012;123:85–96
2. Augustinack JC, Schneider A, Mandelkow EM, et al. Specific tau phosphorylation sites correlate with severity of neuronal cytopathology in Alzheimer's disease. *Acta Neuropathol* 2002;103:26–35
3. Augustinack JC, van der Kouwe AJ, Salat DH, et al. H.M.'s contributions to neuroscience: a review and autopsy studies. *Hippocampus* 2014;24:1267–86
4. Bannerman DM, Rawlins JN, McHugh SB, et al. Regional dissociations within the hippocampus: memory and anxiety. *Neurosci Biobehav Rev* 2004;28:273–83
5. Block RI, O'Leary DS, Ehrhardt JC, et al. Effects of frequent marijuana use on brain tissue volume and composition. *Neuroreport* 2000;11:491–96
6. Block RI, O'Leary DS, Hichwa RD, et al. Effects of frequent marijuana use on memory-related regional cerebral blood flow. *Pharmacol Biochem Behav* 2002;72:237–50
7. Dickerson BC, Feczko E, Augustinack JC, et al. Differential effects of aging and Alzheimer's disease on medial temporal lobe cortical thickness and surface area. *Neurobiol Aging* 2009;30:432–40
8. Moser MB, Moser EI. Functional differentiation in the hippocampus. *Hippocampus* 1998;8:608–19
9. Van Hoesen GW, Augustinack JC, Dierking J, et al. The parahippocampal gyrus in Alzheimer's disease: clinical and preclinical neuroanatomical correlates. *Ann N Y Acad Sci* 2000;911:254–74
10. Van Hoesen, G, Augustinack J, Redman S, Ventromedial temporal lobe pathology in dementia, brain trauma, and schizophrenia. *Ann N Y Acad Sci* 1999;877: 575–94
11. Gloor P, Salanova V, Olivier A, et al., The human dorsal hippocampal commissure: an anatomically identifiable and functional pathway. *Brain* 1993;116(pt 5):1249–73
12. Cameron AS, Archibald YM. Verbal memory deficit after left fornix removal: a case report. *Int J Neurosci* 1981;12:201
13. Hodges JR, Carpenter K. Anterograde amnesia with fornix damage following removal of IIIrd ventricle colloid cyst. *J Neurol Neurosurg Psychiatry* 1991;54:633–38
14. McMackin D, Cockburn J, Anslow P, et al. Correlation of fornix damage with memory impairment in six cases of colloid cyst removal. *Acta Neurochir (Wien)* 1996;135:12–18
15. Saunders RC, Aggleton JP. Origin and topography of fibers contributing to the fornix in macaque monkeys. *Hippocampus* 2007;17:396–411
16. Tucker DM, Roeltgen DP, Tully R, et al. Memory dysfunction following unilateral transection of the fornix: a hippocampal disconnection syndrome. *Cortex* 1988;24:465–472

# Early Quantification of Hematoma Hounsfield Units on Noncontrast CT in Acute Intraventricular Hemorrhage Predicts Ventricular Clearance after Intraventricular Thrombolysis

J. Kornbluth, S. Nekoovaght-Tak, N. Ullman, J.R. Carhuapoma, D.F. Hanley, and W. Ziai



## ABSTRACT

**BACKGROUND AND PURPOSE:** Thrombolytic efficacy of intraventricular rtPA for acute intraventricular hemorrhage may depend on hematoma composition. We assessed whether hematoma Hounsfield unit quantification informs intraventricular hemorrhage clearance after intraventricular rtPA.

**MATERIALS AND METHODS:** Serial NCCT was performed on 52 patients who received intraventricular rtPA as part of the Clot Lysis Evaluation of Accelerated Resolution of Intraventricular Hemorrhage trial and 12 controls with intraventricular hemorrhage, but no rtPA treatment. A blinded investigator calculated Hounsfield unit values for intraventricular hemorrhage volumes on admission (t0), days 3–4 (t1), and days 6–9 (t2). Controls were matched uniquely to 12 rtPA-treated patients for comparison.

**RESULTS:** Median intraventricular hemorrhage volume on admission for patients treated with intraventricular rtPA was 31.9 mL (interquartile range, 34.1 mL), and it decreased to 4.9 mL (interquartile range, 14.5 mL) (t2). Mean ( $\pm$ standard error of the mean) Hounsfield unit for intraventricular hemorrhage was 52.1 (0.59) at t0 and decreased significantly to 50.1 (0.63) (t1), and to 45.1 (0.71) (t2). Total intraventricular hemorrhage Hounsfield unit count was significantly correlated with intraventricular hemorrhage volume at all time points (t0:  $P = .002$ ; t1:  $P < .001$ ; t2:  $P < .001$ ). On serologic and CSF analysis at t0, only higher CSF protein was positively correlated with intraventricular hemorrhage Hounsfield units ( $P = .03$ ). In 24 matched patients treated with rtPA and controls, total intraventricular hemorrhage Hounsfield units were significantly lower in patients treated with rtPA at t2 ( $P = .02$ ). Higher Hounsfield unit quantification of fourth ventricle hematomas independently predicted slower clearance of this ventricle (95% CI, 0.02–0.14;  $P = .02$ ), along with higher intraventricular hemorrhage volume (95% CI, 0.02–0.41;  $P = .03$ ) and lower CSF protein levels (95% CI,  $-0.003$  to  $-0.002$ ;  $P < .001$ ).

**CONCLUSIONS:** Intraventricular hemorrhage Hounsfield unit counts decrease significantly in the acute phase and to a greater extent with intraventricular rtPA treatment. Intraventricular hemorrhage Hounsfield units are correlated significantly with CSF protein and not with serum erythrocyte or platelet concentrations. Hounsfield unit counts may reflect intraventricular hemorrhage clot composition and rtPA sensitivity.

**ABBREVIATIONS:** CLEAR = Clot Lysis Evaluation of Accelerated Resolution of Intraventricular Hemorrhage; EVD = external ventricular drain; HU = Hounsfield unit; ICH = intracerebral hemorrhage; IQR = interquartile range; IVH = intraventricular hemorrhage; SEM = standard error of the mean; t0 = admission; t1 = days 3–4; t2 = days 6–9

Intraventricular hemorrhage (IVH) occurs in approximately 45% of patients following spontaneous intracerebral hemorrhage (ICH) and is an independent predictor of morbidity and mortality.

Previous studies demonstrated that administration of intraventricular rtPA in acute is safe and accelerates clot resolution in experimental models and humans.<sup>4,5</sup> Evaluation of clot lysis is determined most commonly by serial CT imaging, in which it is assumed that high-attenuation blood represents the actual contour of the solid clot. Less is known about factors that impact the CT attenuation coefficient (in Hounsfield units [HUs]) of intraventricular blood and whether CT attenuation is indicative of clot composition or the success of intraventricular thrombolysis in acute IVH. An analysis of

Received November 19, 2014; accepted after revision January 15, 2015.

From the Department of Neurology (J.K.), Division of Neurocritical Care, Tufts University School of Medicine, Boston, Massachusetts; and Department of Neurology (J.K., J.R.C., W.Z.), Division of Neurocritical Care, and Department of Neurology (S.N.-T., N.U., J.R.C., D.F.H., W.Z.), Division of Brain Injuries Outcomes, Johns Hopkins University School of Medicine, Baltimore, Maryland.

The CLEAR study was funded by the US Food and Drug Administration, division of Orphan Products Development, and the National Institutes of Health (clinicaltrials.gov identifier: NCT00650858). D.F.H. is funded by CLEAR III SU01-NS062851-03, and Minimally Invasive Surgery and rtPA for Intracerebral Hemorrhage Evacuation II SR01-NS046309-07.

Paper previously presented at: Annual Conference of the German Society of Neurocritical Care and Emergency Medicine, January 23–26, 2013; Mannheim, Germany.

Please address correspondence to Wendy Ziai, MD, MPH, Johns Hopkins University School of Medicine, Division of Neurocritical Care, Phipps-455, 600 N Wolfe St, Baltimore, MD 21287; e-mail: wziai@jhmi.edu

Indicates open access to non-subscribers at [www.ajnr.org](http://www.ajnr.org)

Evidence-Based Medicine Level 2.

<http://dx.doi.org/10.3174/ajnr.A4393>

factors that impact intraventricular clot lysis rates in patients with large IVH causing obstructive hydrocephalus, who were treated with intraventricular rtPA, found that higher baseline serum plasminogen and lower platelet counts were independently associated with an increase in clot lysis during the first few days.<sup>6</sup> This finding suggests that intraventricular thrombus composition may impact IVH clot removal.

In acute ischemic stroke, thrombus composition in large arteries can be evaluated on the basis of HUs detected by thin-section NCCT.<sup>7</sup> HU counts may aid in predicting recanalization (and resistance to thrombolytics) with intravascular rtPA.<sup>7,8</sup> We sought to assess the change in the CT attenuation coefficient of IVH in patients treated with intraventricular rtPA (versus an external ventricular drain [EVD] alone) and to determine radioattenuation characteristics of intraventricular clot based on HU measurements that may predict the efficacy of thrombolysis.

## MATERIALS AND METHODS

### Study Design

This was a post hoc analysis of patients chosen from a hospital ICH registry and from a multicenter trial involving 52 randomized adult patients with obstructive hydrocephalus secondary to IVH and spontaneous ICH volume of <30 mL requiring urgent EVD. Twelve cases (11 enrolled in the trial plus 1 from the ICH registry), all treated with intraventricular rtPA, were each matched to 1 unique patient from the ICH registry, all of whom received an EVD within 2 days of IVH onset, but no rtPA (controls).

All except 1 case came from the dose-finding study of The Clot Lysis Evaluation Accelerated Resolution of Intraventricular Hemorrhage trial (CLEAR IVH) ( $n = 52$ ). Patients were either randomized 1:1 ( $n = 16$ ) to receive intraventricular rtPA at doses of 0.3 or 1.0 mg q12 hours (CLEAR A) or 1.0 mg q12 hours or q8 hours ( $n = 36$ ) (CLEAR B). The nonenrolled case received intraventricular rtPA, 1 mg every 12 hours, and was managed in accordance with the study protocol.

Patients and controls were matched according to total IVH volume, ICH volume, and ICH location. IVH and ICH volumes were matched within 10 mL on the basis of computerized volumetric analysis of the diagnostic CT. Patients receiving placebos from the CLEAR IVH trials could not be used due to lack of electronic CT data for this cohort. This study was approved by the institutional review board of each participating site.

### Patient Selection

Inclusion criteria for the trial required that an EVD had been inserted, a CT scan obtained at least 6 hours later showed no significant new occurrence or increase in size of any hematoma, and the first dose of rtPA could be given within 48 hours of diagnostic head CT. Patients treated with rtPA had an EVD inserted within 24 hours of diagnostic CT in 45 patients and on day 2 in 7. Control patients had an EVD inserted within 24 hours of diagnostic CT in 10 patients and within 48 hours in 2. Exclusion criteria for study patients included the following: traumatic brain injury, posterior fossa parenchymal hemorrhage, parenchymal hemorrhage volume of >30 mL, suspected intracerebral aneurysm or arteriovenous malformation (excluded by appropriate diagnostic

studies), any severe complicating illness, active internal bleeding, current use of heparin (but not antiplatelet agents), coagulopathy with prothrombin time or partial thromboplastin time outside the normal range, platelet count of <75 IU/mm<sup>3</sup>, pregnancy, and age younger than 18 years. Controls and 1 patient treated with tPA were not enrolled in the study due to the following: inability to enroll within the allowed time window ( $n = 3$ ), baseline ICH volume of >30 mL ( $n = 2$ ), consent declined ( $n = 1$ ), and presentation while the study was not enrolling patients ( $n = 7$ ). Only patients who underwent at least 2 more CT scans after their admission CT (t0) with at least 1 during days 2–4 (t1) and days 5–9 (t2) after admission were included.

### Patient Management

EVDs were placed by the neurosurgical staff in patients with symptomatic hydrocephalus and a Glasgow Coma Scale score of <8. Initial catheters were placed contralateral to side of greatest IVH volume in 47/65 patients (72%) (37 patients treated with rtPA, 10 controls) and ipsilateral, in 15 patients (23%). Three patients had simultaneous bilateral EVDs (5%).

rtPA was delivered after attempting aspiration of at least 4 mL of CSF. Isovolumetric injection of rtPA was followed by a 2-mL flush of nonbacteriostatic normal saline. After each injection, the EVD was closed for 1 hour to allow time for rtPA-clot interaction and was reopened only if necessary to control medically refractory intracranial pressure elevation. After the clamping period, the EVD was reopened to drain CSF at the gradient set by the treating physician. The first injection of rtPA occurred no sooner than 12 hours but no later than 48 hours after the diagnostic CT and at least 6 hours after EVD placement. rtPA injections continued at the specified interval until clearance of hyperattenuated blood from the third and fourth ventricles was observed on daily head CT or for a maximum of 12 doses in the CLEAR A and B studies. In patients and controls, EVDs were kept open, with a drainage gradient specified by the treating physician (0–20 mm Hg) until it was determined appropriate to wean.

### Radiologic Assessment

Neuroimaging was performed on fourth-generation CT scanners at each participating study site. CT scans chosen for analysis were the following: admission day 1 CT (t0), days 2–4 CT (t1), and days 5–9 CT (t2). CT scans for each interval were chosen as close as possible in time for each case-control pair. Most CT scans consisted of 4- to 5-mm-thick sections through both the skull base and cerebrum. In 10 patients, 19 CT scans consisted of 10–15 sections of 3-mm thickness for the skull base and 10–12 sections of 6-mm thickness for the cerebrum. A single blinded researcher (S.N.-T.) manually mapped out ROIs around the intraventricular and parenchymal hematomas and around the contour of each ventricle on continuous images from representative CT scans by using an open-source DICOM viewer software program for MAC (OsiriX Imaging Software, Version 4.1; <http://www.osirix-viewer.com>) (Fig 1). A semiautomated threshold-based approach with a range of 40–80 HU was used to initially identify regions and then was manually adjusted to obtain the best delineation of blood clot and avoid artifacts introduced by higher attenuation CSF. The software adjusts for changes in section thickness and thereby corrects for different CT techniques across centers.

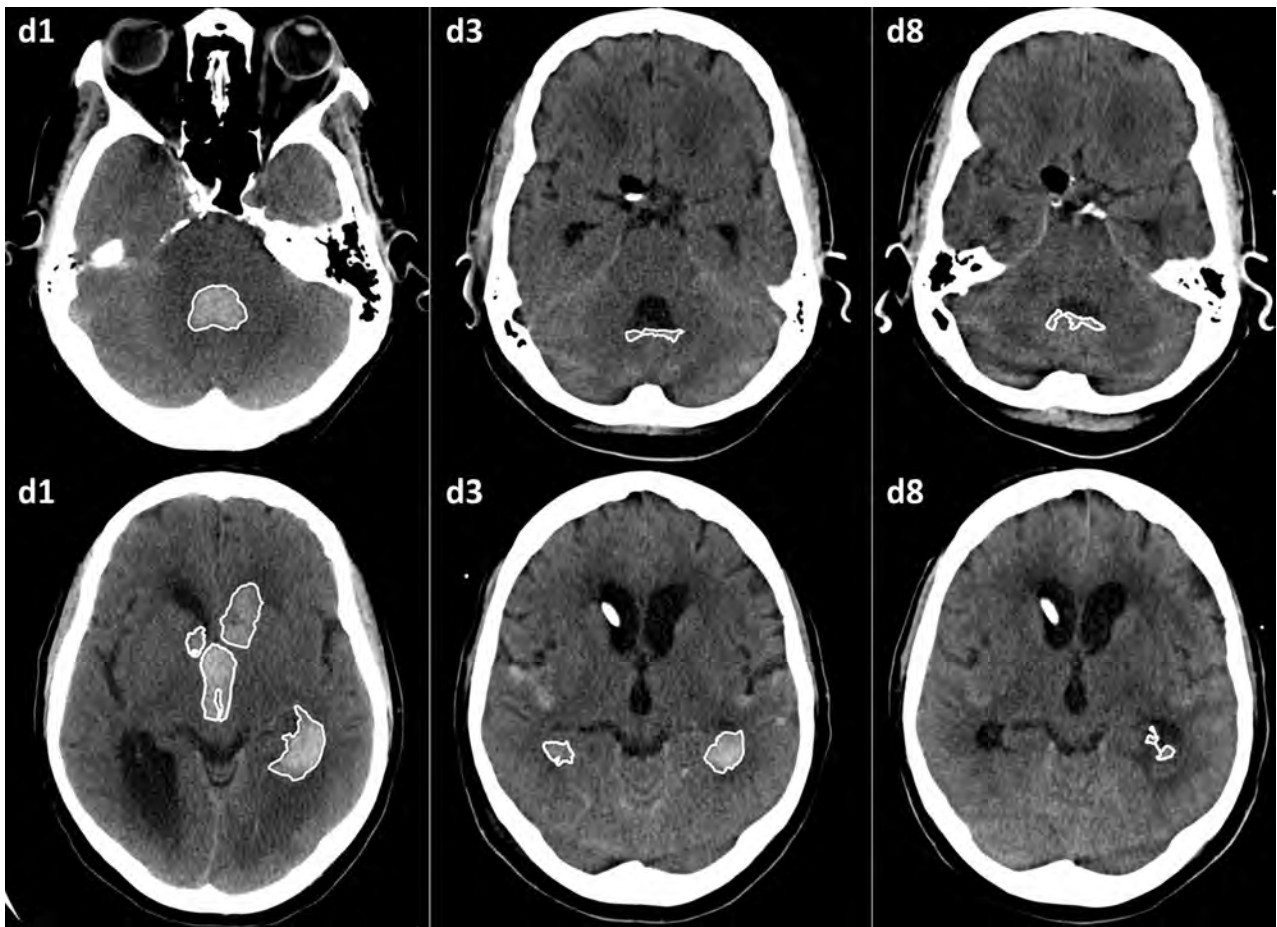


**FIG 1.** ROI mapping of IVH in a typical patient on days 1, 3, and 8.

The volumes and mean HU counts of the IVH and ICH clots and of the ventricular fluid not containing acute blood were calculated with this semiautomatic procedure. The HU values were obtained for each ROI by averaging all voxels within the ROI. IVH ROIs were analyzed as total IVH values and by component ventricle location (right and left lateral, third and fourth ventricles).

#### Data Analysis

We collected demographic and baseline characteristics, including the following serologic and CSF data at initial presentation or at EVD insertion: hematocrit, platelet count, prothrombin time, partial thromboplastin time, plasma fibrinogen level, CSF red blood cell and white blood cell counts, CSF protein level, and CSF glucose level. For univariate analysis, we correlated mean HU counts from all patients in the trial ( $N = 52$ ) with IVH and ICH volumes, serologic and CSF data at initial presentation, sex, number of and total rtPA doses, side of the EVD relative to predominant IVH volume, and ventricle component across time points by using Spearman correlation tests and Student  $t$  tests as appropriate. In 24 matched patients, demographic variables, baseline characteristics, IVH and ICH volumes, HUs, and serologic and CSF data were compared between patients treated with rtPA and controls by using the Student  $t$  test and  $\chi^2$  or the Fisher exact test as appropriate. The Wilcoxon signed rank test was used to compare variables with non-normal distributions. Data are presented as mean  $\pm$  standard error of the mean (SEM) or median (interquar-

tile range [IQR]) unless otherwise indicated. Statistical analysis was performed with STATA 11.0 (StataCorp, College Station, Texas). A value of  $P < .05$  was significant.

## RESULTS

### Patients Treated with rtPA

Patient demographics and radiographic findings for patients in the trial are outlined in Table 1. IVH volume decreased significantly at both t1 and t2 relative to t0 in patients treated with rtPA ( $N = 52$ ) ( $P < .001$  for both). Progression of HU counts with time (Fig 2) showed that total ventricular HU counts decreased significantly from  $52.14 \pm 0.59$  (t0) to  $50.11 \pm 0.63$  (t1) ( $P = .002$ ) to  $45.05 \pm 0.71$  (t2) ( $P < .001$ ; t2 versus t0). The decrease in HU counts was significant for all ventricular compartments when analyzed individually. IVH volume was significantly correlated with HU counts at all time points: t0 (Spearman  $\rho = 0.41$ ,  $P = .002$ ); t1 ( $\rho = 0.70$ ,  $P < .001$ ); and t2 ( $\rho = 0.64$ ,  $P < .001$ ).

Time from EVD placement to resolution of casted third or fourth ventricle clot occurred at a median of 2.7 days (range, 0.29–8.46 days) and 2.2 days (range, 0.23–5.78 days), respectively, and was positively correlated with third or fourth ventricle HU counts at t0, respectively (third ventricle:  $\rho = 0.30$ ,  $P = .04$ ; fourth ventricle:  $\rho = 0.37$ ,  $P = .02$ ); higher HU correlated with longer time to clot resolution. The third ventricle failed to clear in 3 patients from t0 to t2. Factors at t0 independently associated with slower clearance of the

**Table 1: Clinical and radiologic characteristics of patients treated with rtPA (N = 52)**

	rtPA-Treated (N = 52)	P Value (Where Appropriate)
<b>Clinical characteristics</b>		
Age (yr) (mean ± SEM)	55.6 ± 1.4	
Male/female	34:18	
Admission GCS (median) (IQR)	8.5 (9.0)	
<b>Radiographic characteristics</b>		
ICH location (%)		
Basal ganglia	8 (15.4)	
Caudate	2 (3.8)	
Thalamus	25 (48.1)	
Lobar	6 (11.5)	
Primary IVH	11 (21.2)	
Admission Graeb score <sup>21</sup> (median) (IQR)	7 (3)	
Total IVH volume (cm <sup>3</sup> ) (median) (IQR)		
t0	31.94 (34.1)	
t1	12.84 (26.23)	.001 (t1 vs t0) <sup>a</sup>
t2	4.86 (14.49)	.001 (t2 vs t0) <sup>a</sup>
Total IVH HU counts (mean ± SEM)		
t0	52.14 ± 0.59	
t1	50.11 ± 0.63	.002 (t1 vs t0) <sup>a</sup>
t2	45.05 ± 0.71	.001 (t2 vs t0) <sup>a</sup>
Total CSF HU counts (mean ± SEM)		
t0	12.37 ± 0.37	
t1	11.77 ± 0.37	.18 (t1 vs t0)
t2	11.30 ± 0.33	.01 (t2 vs t0) <sup>a</sup>
Hematoma (ICH) volume (cm <sup>3</sup> ) (median) (IQR)		
t0	7.0 (10.11)	
t1	5.35 (9.39)	.001 (t1 vs t0) <sup>a</sup>
t2	5.04 (8.06)	.001 (t2 vs t0) <sup>a</sup>
Hematoma (ICH) HU counts (mean ± SEM)		
t0	55.06 ± 0.82	
t1	54.78 ± 0.86	.74 (t1 vs t0)
t2	48.42 ± 0.84	.001 (t2 vs t0) <sup>a</sup>
Change in IVH volume (cm <sup>3</sup> ) (median) (IQR)		
Days 2–4 (t1–t0)	–15.36 (18.13)	.001 <sup>a</sup>
Days 5–9 (t2–t0)	–17.72 (21.84)	.001 <sup>a</sup>
Change in ICH volume (cm <sup>3</sup> ) (median) (IQR)		
Days 2–4 (t1–t0)	–1.59 (3.22)	.001 <sup>a</sup>
Days 5–9 (t2–t0)	–1.66 (3.8)	.001 <sup>a</sup>
Change in IVH HU counts (mean ± SEM)		
Days 2–4 (t1–t0)	–2.03 ± 0.62	.002 <sup>a</sup>
Days 5–9 (t2–t0)	–6.89 ± 0.74	.001 <sup>a</sup>
Change in ICH HU counts (mean ± SEM)		
Days 2–4 (t1–t0)	–0.28 ± 0.86	.74
Days 5–9 (t2–t0)	–6.65 ± 1.12	.001 <sup>a</sup>

**Note:**—GCS indicates Glasgow Coma Scale.

<sup>a</sup>Significant.

fourth ventricle were higher fourth ventricle HU counts (95% CI, 0.02–0.14;  $P = .02$ ), larger fourth ventricle IVH volume (95% CI, 0.02–0.41;  $P = .03$ ), and lower CSF protein levels (95% CI, –0.003 to –0.002;  $P < .001$ ). Factors at t0 independently associated with slower clearance of the third ventricle were larger third ventricle IVH volume (95% CI, 0.04–0.57;  $P = .03$ ) and lower CSF protein levels (95% CI, –0.004 to –0.001;  $P = .007$ ), but not third ventricle HU counts ( $P = .35$ ). Lower initial HU counts were significantly correlated with greater change in IVH volume from admission to t1 ( $\rho = -0.28$ ,  $P = .048$ ), but not at t2 ( $P = .11$ ). After adjustment for admission IVH volume, however, initial HU counts were not significantly associated with the change in IVH volume. The decrease in mean IVH HU counts for all ventricles with time did not correlate with the number of doses of IVR rtPA at t1 ( $\rho = 0.12$ ,  $P = .43$ ) or t2 ( $\rho = -0.23$ ,  $P = .11$ ). There was no correlation between the side of

EVD placement and the ipsilateral decrease in HU over the duration of the investigation ( $P = .60$ ).

### Matched Pairs

Patients and controls ( $n = 24$ ) were well-matched in baseline ICH and IVH volume (Table 2). t1 and t2 CT scans were performed at a mean of  $3.2 \pm 0.88$  days and  $6.2 \pm 1.4$  days after admission, which was not different between groups ( $P = .59$  [t1],  $P = .10$  [t2]). IVH volume decreased significantly faster at both t1 and t2 relative to t0 in patients treated with rtPA compared with controls. The mean IVH HU count in the rtPA group was 52.71 (1.18) at t0 and decreased significantly to 49.01 (0.98) at t1, and to 45.05 (1.24) at t2. IVH HU counts in controls were not significantly different from those in patients treated with rtPA at t0 and t1 but were significantly higher at t2 (49.48 [1.33],  $P = .02$ ) (Fig 3).

### Correlation with Serologic and CSF Data

There was no significant correlation between admission CT total IVH HU count and the admission values of serum platelet count, prothrombin time, partial thromboplastin time, fibrinogen level, hemoglobin level, and hematocrit level or white blood cell count. Admission ICH HU count showed a trend correlation with serum hematocrit ( $\rho = 0.26$ ,  $P = .06$ ). Higher CSF protein (median, 112 g/dL; range, 2.11–986 g/dL) was significantly positively correlated with IVH HU ( $\rho = 0.42$ ,  $P = .03$ ). CSF glucose levels and white blood cell counts were not correlated with IVH HU counts. There was a weakly positive correlation between CSF red blood cell count and IVH HU ( $\rho =$

0.34,  $P = .07$ ). There were no positive correlations between patient serologic markers and HU change from t0 to t2.

HU levels of CSF not containing high-attenuation blood (ie, CSF with HU < 40) decreased nonsignificantly from t0 to t2. No measured CSF components were correlated with these low-attenuation CSF HU counts.

### Clinical Outcomes

Adjudicated safety events in the dose-finding studies of the CLEAR IVH trials on which this study is based totaled 3/52 (5.8%) symptomatic hemorrhages at any time up to 72 hours after the last dose of rtPA, 1 (2.0%) case of bacterial ventriculitis, and 8 (17%) deaths at 30 days. One patient required a ventriculoperitoneal shunt (2%).

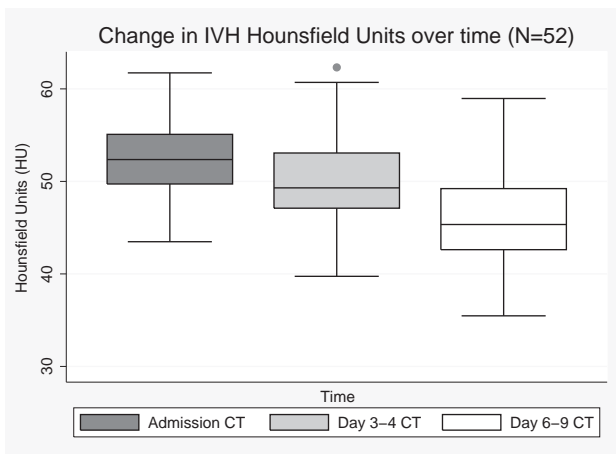


**FIG 2.** Change in total IVH HU counts with time in patients treated with rtPA.

## DISCUSSION

We found that intraventricular clot HU counts decreased during the first week after IVH, both in controls and patients treated with rtPA, though with significantly greater change in the treated group. CSF has a HU number of 0–24 (depending on protein content), and the range for whole blood is linearly related to hematocrit level.<sup>9,10</sup> Compared with unclotted whole blood (HU count of 56 with hematocrit level of 45%), when whole blood coagulates in vitro, the clot retracts and HU count rises to, for example, 75 with hematocrit level elevation to 80%.<sup>11</sup> It is believed that the high-attenuation intraventricular cast seen on CT after spontaneous IVH is solid clot, which has been confirmed by postmortem examination in a dog model.<sup>12</sup> The HU values observed on admission CT scans in this study were similar to those in unclotted whole blood. Despite “retraction” of parenchymal clots, ICH HU counts decreased during the observation period as did IVH HU counts. This finding likely indicates that most retraction had already occurred within the first few hours of bleeding and that other factors (ie, fibrinolytic activity and possibly absorption) were occurring at the t1 and t2 CT times. Lower attenuation of ventricular clots with time likely reflects both suspension of the clot in CSF and fibrinolysis causing solid clot to become liquid whole blood at least at the surface, which forms a low-hematocrit, low-attenuation blood-CSF mixture. In vitro, fibrinolysis of a solid clot decreases attenuation by 15–20 HU, blurring the margin between solid and liquid blood.<sup>13</sup> In CSF where HU counts changed relatively little during the period of observation, red blood cells likely fall away from the solid clot and are removed by the steady flow of CSF, which keeps attenuation values low and maintains a clear interface between clot and CSF. The greater decrease in HU counts in patients treated with rtPA compared with controls in Fig 3 likely reflects a combination of increased lytic activity and perhaps improved CSF flow, especially at t2 when most patients treated with rtPA had opened the lower ventricular system.

Two factors were significantly correlated with higher admission ventricular clot HU counts: higher IVH volume and higher expelled CSF protein. ICH volume was not significantly correlated with ICH HU except at t2. The absolute changes in ICH and IVH HU counts from t0 to t2 in the whole rtPA-treated group

were similar, but with much smaller change in ICH volume. This result might mean that decreased attenuation of IVH associated with clot dissolution is not influenced by rtPA. However, in the matched-pair data, changes in IVH volume and IVH HU counts were significantly greater in the patients treated with rtPA versus controls, whereas the decrease in ICH HU counts was not significantly different at T2 between groups and decreased by less than HU in the ventricles. These observations suggest that fibrinolytic activity is associated with HU counts. Whether intraventricular rtPA may influence fibrinolytic activity of parenchymal hematomas is not clear from this analysis.

Higher CSF protein was significantly correlated with total ventricular clot HUs; this finding is not surprising given its positive influence on CSF attenuation. Earlier reports with first-generation CT scanners described a linear relationship between CSF protein and the CT attenuation coefficient, though with only a small variation in HUs across the spectrum from normal to pathologic values, consistent with our data.<sup>10</sup> Therefore we adjusted for both IVH volume and CSF protein to assess whether HU counts predict time to clearance of the third and fourth ventricles on CT, a commonly used end point of intraventricular fibrinolysis that determines the end of dosing. We found that higher HU quantification of the fourth, but not the third, ventricle hematoma was significantly associated with slower clearance of this ventricle in the setting of intraventricular rtPA administration after adjusting for compartmental IVH volume and CSF protein.

Intraventricular clots contain varying amounts of fibrin, platelets, and red blood cells. Clots with more red blood cells would be expected to have a higher concentration of hemoglobin and therefore HU counts compared with those with more fibrin and platelets. Prior models of intra-arterial clot have shown that more radioattenuated clots may contain proportionately more red blood cells than platelets and may be more amenable to thrombolysis with rtPA.<sup>14</sup> We previously found that a lower serum platelet count was associated with faster clearance of ventricular clot.<sup>6</sup> These results appear to be inconsistent with those in this study, which found no relationship between admission IVH HU counts and serum hematocrit or platelet count and only a weak positive correlation with CSF red blood cell count, findings suggesting that radioattenuation characteristics of intravascular and intraventricular clots reflect different properties. HU counts of ventricular clots may also reflect attenuation of the fibrin mesh network. Dissolution of thrombus depends on diffusion and permeation of thrombolytic into the clot, which may be impaired by a tighter clot structure associated with a higher attenuation coefficient, independent of clot size or CSF protein.

Faster clearance of the lower ventricular system (both third and fourth ventricles) was independently associated with higher CSF protein at t0, suggesting that higher protein levels may be associated with greater CSF fibrinolytic activity. Approximately 80% of CSF protein is serum-derived, and 20% is produced intrathecally.<sup>15</sup> However, bleeding into the ventricles contributes significantly to initial CSF protein levels, raising the possibility that fibrinolytic enzymes such as serum plasminogen are contributing to this effect. Higher CSF protein levels may also be the result of greater clot dissolution and not a causative factor.

This study was limited in several ways. The sample size was

**Table 2: Clinical and radiologic data for matched pairs**

	rtPA-Treated (N = 12)	Control (N = 12)	P Value
<b>Clinical characteristics</b>			
Age (yr) (mean ± SEM)	52.8 ± 2.0	57.5 ± 1.9	.21
Sex, male/female	11:1	7:5	.06
Admission GCS (median) (IQR)	8.5 (6)	5.5 (4.5)	.06
<b>Radiographic characteristics</b>			
ICH location			
Basal ganglia	2	3	.57
Caudate	3	1	
Thalamus	7	8	
Admission Graeb score (median) (IQR)	8 (1.5)	8 (4)	.19
Total IVH volume (cm <sup>3</sup> ) (mean ± SEM) <sup>12</sup>			
t0	26.0 ± 2.51	26.34 ± 3.24	.87
t1	13.56 ± 2.70	25.20 ± 3.73	.005 <sup>a</sup>
t2	6.26 ± 1.36	18.63 ± 2.83	.002 <sup>a</sup>
Total ventricular volume (cm <sup>3</sup> ) (mean ± SEM)			
t0	69.13 ± 5.85	84.11 ± 8.40	.18
t1	34.78 ± 4.96	56.57 ± 5.70	.01 <sup>a</sup>
t2	24.80 ± 2.67	57.57 ± 10.32	.01 <sup>a</sup>
Hematoma (ICH) volume (cm <sup>3</sup> ) (mean ± SEM)			
t0	12.93 ± 3.59	14.29 ± 3.23	.39
t1	14.21 ± 3.93	14.92 ± 2.97	.74
t2	11.17 ± 3.64	13.76 ± 3.19	.29
IVH HU counts (mean ± SEM)			
t0	52.71 ± 1.18	52.05 ± 0.96	.70
t1	49.01 ± 0.98	50.42 ± 1.55	.35
t2	45.05 ± 1.24	49.48 ± 1.33	.02
ICH HU counts (mean ± SEM)			
t0	56.24 ± 1.84	54.12 ± 1.17	.25
t1	55.79 ± 1.08	52.80 ± 1.08	.04 <sup>a</sup>
t2	52.06 ± 1.28	52.56 ± 1.10	.77
<b>Radiologic outcomes</b>			
Change in IVH volume (cm <sup>3</sup> ) (median) (IQR)			
Days 2–4 (t1–t0)	–10.88 (12.84)	–1.24 (2.78)	.002 <sup>a</sup>
Days 5–9 (t2–t0)	–18.65 (14.88)	–6.85 (6.36)	.002 <sup>a</sup>
Change in ICH volume (cm <sup>3</sup> ) (median) (IQR)			
Days 2–4 (t1–t0)	0.24 (1.91)	–.06 (2.99)	.88
Days 5–9 (t2–t0)	–1.98 (3.25)	–1.15 (2.33)	.27
Change in IVH HU counts (mean ± SEM)			
Days 2–4 (t1–t0)	–3.70 ± 1.44	–1.63 ± 1.50	.07
Days 5–9 (t2–t0)	–7.66 ± 1.87	–2.58 ± 1.23	.02 <sup>a</sup>
Change in ICH HU counts (mean ± SEM)			
Days 2–4 (t1–t0)	–0.59 ± 1.55	–1.31 ± 1.51	.63
Days 5–9 (t2–t0)	–4.18 ± 2.23	–1.55 ± 1.39	.25

**Note:**—GCS indicates Glasgow Coma Scale.

<sup>a</sup> Significant.

relatively small, but all patients were treated with the same protocolized approach to imaging and clinical management. We tried to minimize bias with the matched case-control design for comparison of EVD-only versus patients treated with rtPA. Cases and controls were carefully matched on IVH and ICH volumes and ICH location to minimize differences between groups. This matching resulted in a limited pool of patients. Determining the exact margin of the clot-CSF interface is a potential source of error, though an HU threshold of 40 was applied similarly by using a semiautomated approach and all CT scans were evaluated and mapped by a single blinded researcher. Associations between HU quantification and change in IVH volumes reflect the most accurate assessment methods available but may have been affected by disparities in sampling, patient age, and time of EVD placement. Numerous factors have been shown to influence clearance rates of intraventricular blood after rtPA administration,

including the location of the external ventricular drain,<sup>16</sup> bilateral-versus-single EVD,<sup>17</sup> the location of intraventricular blood, dose of thrombolytic,<sup>18</sup> and serum and CSF components. Our investigation examined the radiographic characteristics that complement these data.

Finally, it remains to be determined whether changing intraventricular clot volume and characteristics translates into positive outcomes. Several meta-analyses (on observational studies and small randomized trials) all suggested that intraventricular rtPA may be an effective strategy for reducing mortality and improving functional outcome, with the potential for decreasing permanent shunt rates without significant increase in complications.<sup>19–21</sup> Adverse events in this study were lower than the reported rates and support data showing that intraventricular fibrinolysis does not significantly increase the risk of rehemorrhage or infection.<sup>21</sup> The soon-to-be-completed Phase III multinational, randomized controlled trial (Clot Lysis Evaluation of Accelerated Resolution of Intraventricular Hemorrhage [CLEAR-III]) of 500 patients with primary or secondary spontaneous IVH randomized to intraventricular fibrinolysis with rtPA or placebo should provide the highest quality evidence on the benefits and complications of this treatment.<sup>22</sup>

## CONCLUSIONS

Attenuation of intraventricular hemorrhage is significantly associated with CSF protein levels and may reflect properties of IVH clot structure yet to be defined. A significantly greater reduction in IVH attenuation during the acute

phase occurs with intraventricular rtPA administration compared with EVD alone. HU measurement on NCCT may be useful in predicting the effectiveness of intraventricular rtPA, especially in the fourth ventricle.

**Disclosures:** Joshua Kornbluth—UNRELATED: Grants/Grants Pending: Pfizer.\* **Comments:** grant support for an unrelated project. Daniel F. Hanley—RELATED: National Institutes of Health/National Institute of Neurological Disorders and Stroke.\* **Comments:** CLEAR III and Minimally Invasive Surgery and rtPA for Intracerebral Hemorrhage Evacuation II and III clinical trials; Provision of Writing Assistance, Medicines, Equipment, or Administrative Support: Genentech.\* **Comments:** supply rtPA drug for clinical trials CLEAR and Minimally Invasive Surgery and rtPA for Intracerebral Hemorrhage Evacuation; UNRELATED: Consultancy: BrainScope; Expert Testimony: expert witness on brain hemorrhage; Payment for Lectures (including service on Speakers Bureaus): honoraria from various universities. Natalie Ullman—RELATED: Grant: The CLEAR study was funded by the US Food and Drug Administration, division of Orphan Products Development, and National Institutes of Health (clinicaltrials.gov identifier: NCT00650858)\*; additional funding by CLEAR III 5U01-NS062851-03, and Minimally Invasive Surgery and rtPA for Intracerebral Hemorrhage

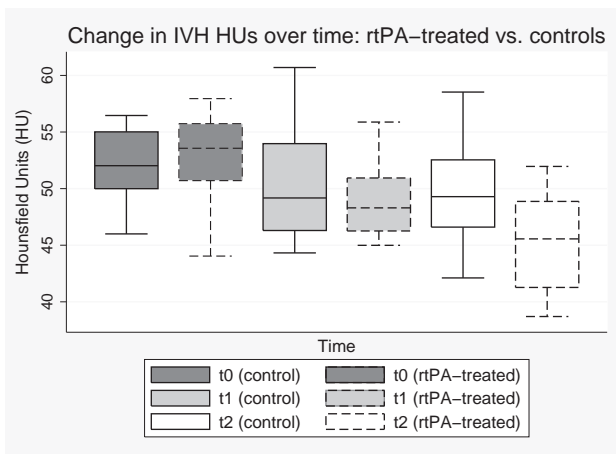


**FIG 3.** Change in IVH HU with time in patients treated with rtPA versus controls ( $n = 24$ ).

Evacuation II 5R01-NS046309-07.\* Wendy Ziai—RELATED: Grant: National Institutes of Health/National Institute of Neurological Disorders and Stroke 5U01.\* Comments: receive funding as a site investigator for this study. \*Money paid to the institution.

## REFERENCES

1. Diringner MN, Edwards DF, Zazulia AR. **Hydrocephalus: a previously unrecognized predictor of poor outcome from supratentorial intracerebral hemorrhage.** *Stroke* 1998;29:1352–57 CrossRef Medline
2. Tuhirim S, Dambrosia JM, Price TR, et al. **Prediction of intracerebral hemorrhage survival.** *Ann Neurol* 1988;24:258–63 CrossRef Medline
3. Steiner T, Diringner MN, Schneider D, et al. **Dynamics of intraventricular hemorrhage in patients with spontaneous intracerebral hemorrhage: risk factors, clinical impact, and effect of hemostatic therapy with recombinant activated factor VII.** *Neurosurgery* 2006;59:767–73; discussion 773–74 CrossRef Medline
4. Naff N, Williams M, Keyl PM, et al. **Low-dose recombinant tissue-type plasminogen activator enhances clot resolution in brain hemorrhage: the intraventricular hemorrhage thrombolysis trial.** *Stroke* 2011;42:3009–16 CrossRef Medline
5. Naff NJ, Williams MA, Rigamonti D, et al. **Blood clot resolution in human cerebrospinal fluid: evidence of first-order kinetics.** *Neurosurgery* 2001;49:614–19; discussion 619–21 CrossRef Medline
6. Ziai WC, Muschelli J, Thompson CB, et al. **Factors affecting clot lysis rates in patients with spontaneous intraventricular hemorrhage.** *Stroke* 2012;43:1234–39 CrossRef Medline
7. Puig J, Pedraza S, Demchuk A, et al. **Quantification of thrombus Hounsfield units on noncontrast CT predicts stroke subtype and early recanalization after intravenous recombinant tissue plasminogen activator.** *AJNR Am J Neuroradiol* 2012;33:90–96 CrossRef Medline
8. Kirchhof K, Welzel T, Mecke C, et al. **Differentiation of white, mixed, and red thrombi: value of CT in estimation of the prognosis of thrombolysis phantom study.** *Radiology* 2003;228:126–30 CrossRef Medline
9. New PF, Aronow S. **Attenuation measurements of whole blood and blood fractions in computed tomography.** *Radiology* 1976;121:635–40 CrossRef Medline
10. Norman D, Price D, Boyd D, et al. **Quantitative aspects of computed tomography of the blood and cerebrospinal fluid.** *Radiology* 1977;123:335–38 CrossRef Medline
11. Scott WR, New PF, Davis KR, et al. **Computerized axial tomography of intracerebral and intraventricular hemorrhage.** *Radiology* 1974;112:73–80 CrossRef Medline
12. Pang D, Scialbasi RJ, Horton JA. **Lysis of intraventricular blood clot with urokinase in a canine model, part 3: effects of intraventricular urokinase on clot lysis and posthemorrhagic hydrocephalus.** *Neurosurgery* 1986;19:553–72 CrossRef Medline
13. Bergström M, Ericson K, Levander B, et al. **Variation with time of the attenuation values of intracranial hematomas.** *J Comput Assist Tomogr* 1977;1:57–63 CrossRef Medline
14. Kim EY, Heo JH, Lee SK, et al. **Prediction of thrombolytic efficacy in acute ischemic stroke using thin-section noncontrast CT.** *Neurology* 2006;67:1846–48 CrossRef Medline
15. Watson MA, Scott MG. **Clinical utility of biochemical analysis of cerebrospinal fluid.** *Clin Chem* 1995;41:343–60 Medline
16. Jaffe J, Melnychuk E, Muschelli J, et al. **Ventricular catheter location and the clearance of intraventricular hemorrhage.** *Neurosurgery* 2012;70:1258–63; discussion 1263–64 CrossRef Medline
17. Hinson HE, Melnychuk E, Muschelli J, et al. **Drainage efficiency with dual versus single catheters in severe intraventricular hemorrhage.** *Neurocrit Care* 2012;16:399–405 CrossRef Medline
18. Webb AJ, Ullman NL, Mann S, et al. **Resolution of intraventricular hemorrhage varies by ventricular region and dose of intraventricular thrombolytic: the Clot Lysis: Evaluating Accelerated Resolution of IVH (CLEAR IVH) program.** *Stroke* 2012;43:1666–68 CrossRef Medline
19. Staykov D, Bardutzky J, Huttner HB, et al. **Intraventricular fibrinolysis for intracerebral hemorrhage with severe ventricular involvement.** *Neurocrit Care* 2011;15:194–209 CrossRef Medline
20. Gaberel T, Magheru C, Parienti JJ, et al. **Intraventricular fibrinolysis versus external ventricular drainage alone in intraventricular hemorrhage: a meta-analysis.** *Stroke* 2011;42:2776–81 CrossRef Medline
21. Khan NR, Tsigoulis G, Lee SL, et al. **Fibrinolysis for intraventricular hemorrhage: an updated meta-analysis and systematic review of the literature.** *Stroke* 2014;45:2662–69 CrossRef Medline
22. Ziai WC, Tuhirim S, Lane K, et al; CLEAR III Investigators. **A multicenter, randomized, double-blinded, placebo-controlled phase III study of Clot Lysis Evaluation of Accelerated Resolution of Intraventricular Hemorrhage (CLEAR III).** *Int J Stroke* 2014;9:536–42 CrossRef Medline
23. Graeb DA, Robertson WD, Lapointe JS, et al. **Computed tomographic diagnosis of intraventricular hemorrhage: etiology and prognosis.** *Radiology* 1982;143:91–96 CrossRef Medline

# Neuroradiologic Diagnosis of Minor Leak prior to Major SAH: Diagnosis by T1-FLAIR Mismatch

S. Oda, M. Shimoda, A. Hirayama, M. Imai, F. Komatsu, H. Shigematsu, J. Nishiyama, and M. Matsumae

## ABSTRACT

**BACKGROUND AND PURPOSE:** In major SAH, the only method to diagnose a preceding minor leak is to ascertain the presence of a warning headache by interview; however, poor clinical condition and recall bias can cause inaccuracy. We devised a neuroradiologic method to diagnose previous minor leak in patients with SAH and attempted to determine whether warning (sentinel) headaches were associated with minor leaks before major SAH.

**MATERIALS AND METHODS:** We retrospectively evaluated 127 patients who were admitted with SAH within 48 hours of ictus. Previous minor leak before major SAH was defined as T1WI-detected clearly bright hyperintense subarachnoid blood accompanied by SAH blood on FLAIR images that was distributed over a larger area than bright hyperintense subarachnoid blood on T1WI (T1-FLAIR mismatch).

**RESULTS:** The incidence of warning headache before SAH was 11.0% (14 of 127 patients, determined by interview). The incidence of T1-FLAIR mismatch (neuroradiologic diagnosis of minor leak before major SAH) was 33.9% (43 of 127 patients). Of the 14 patients with warning headache, 13 had a minor leak diagnosed by T1-FLAIR mismatch at the time of admission. Variables identified by multivariate analysis as significantly associated with minor leak diagnosed by T1-FLAIR mismatch included 80 years of age or older, rebleeding after admission, intracerebral hemorrhage on CT, and mRS scores of 3–6.

**CONCLUSIONS:** We conclude that warning headaches diagnosed by interview are not a product of recall bias but are the result of actual leaks from aneurysms.

**ABBREVIATIONS:** BHSB = bright hyperintense subarachnoid blood; ICH = intracerebral hemorrhage

A severe, sudden headache, known as a warning or sentinel headache, sometimes presents during the days or weeks before aneurysmal SAH.<sup>1,2</sup> These warning headaches have been interpreted as reflecting a minor or warning leak that arises from the first small bleed from an aneurysm before a major SAH.<sup>3,4</sup> However, in patients who have had major SAH, the presence of a warning headache can only be determined by interview and relies on recall, and there are no established neuroradiologic diagnostic procedures to prove the existence of a previous minor leak. Accurate diagnosis of previous warning headaches by interview is difficult because of the inability to obtain complete information from patients in poor clinical

conditions. One report states that warning headaches are innocuous and unrelated to SAH because an alternative explanation of warning headache is recall bias.<sup>5</sup>

In the subacute phase of SAH (>3–4 days after onset), T1WI depicts subarachnoid blood as high-signal-intensity areas. FLAIR images depict subarachnoid blood as high-signal-intensity areas from the acute-to-subacute phase of SAH. In patients with SAH with T1-detected clearly bright hyperintense subarachnoid blood (BHSB), we proposed a “T1-FLAIR mismatch” to define patients who had experienced a prior minor leak: BHSB on T1WI obtained at admission was considered subacute and FLAIR hyperintense blood that was more extensive than this was considered acute (with the T1 clearly BHSB component defined as the subacute minor leak). Using this diagnostic procedure, we investigated the association between warning headaches and what was considered a minor leak on MR imaging (ie, the first SAH, due to a ruptured aneurysm that occurred before major SAH). Furthermore, we studied the clinical features of patients with SAH with a neuroradiologically diagnosed minor leak before major SAH.

Received December 11, 2014; accepted after revision February 9, 2015.

From the Department of Neurosurgery (S.O., M.S., A.H., M.I., F.K., H.S., J.N.), Tokai University Hachioji Hospital, Tokyo, Japan; and Department of Neurosurgery (M.M.), Tokai University School of Medicine, Kanagawa, Japan.

Please address correspondence to Masami Shimoda, MD, Department of Neurosurgery, Tokai University Hachioji Hospital, 1838 Ishikawa-machi, Hachioji, Tokyo 192-0032, Japan; e-mail: mashimoda-nsu@umin.ac.jp

<http://dx.doi.org/10.3174/ajnr.A4325>

## MATERIALS AND METHODS

### Patient Population

Subjects were selected from the 210 patients in the nontraumatic aneurysmal acute-phase SAH data base at our hospital between September 2002 and May 2014. Of these patients, 12 receiving conservative therapy instead of surgery because of the absence of brain stem reflexes and 12 with SAH due to ruptured dissecting aneurysms were excluded from this study. The remaining 186 patients underwent acute-stage aneurysmal surgery by craniotomy or an interventional procedure within 72 hours of SAH onset. From these 186 patients, we identified 127 who were admitted within 48 hours of SAH onset and underwent adequate MR imaging, including DWI, FLAIR imaging, T1WI, and CT, on admission. These 127 patients with SAH had stable vital signs reflecting adequate respiration and circulation and underwent serial MR imaging and CT after admission. All MR imaging studies were preceded by the procurement of informed consent by the patient and/or their relative. Initial MR imaging on admission was performed before conventional angiographic, surgical, or endovascular procedures in all cases.

Clinical and imaging records were evaluated retrospectively. Study approval was obtained from the Institutional Review Board for Clinical Research at our university.

### Imaging Protocol

For patients with aneurysmal SAH, we routinely performed serial MR imaging on admission, within 2–7 days after surgery, and before patients were discharged. Serial MR imaging was performed for the evaluation of primary brain damage, surgical complications, and ischemic lesions due to vasospasm. At all time points, serial MR imaging included axial conventional T1WI, FLAIR, DWI, and MRA and was performed by using a 1.5T superconducting magnet (Signa Excite or HDx; GE Healthcare, Milwaukee, Wisconsin) with a quadrature head coil. Pulse sequences were as follows: FLAIR (TR/TE, 8000/120 ms; TI, 2000 ms; section thickness/section gap, 7.0/1.0 mm; FOV, 24 × 24 cm; NEX, 1; matrix, 256 × 224), T1WI (TR/TE, 2000/24 ms; TI, 750 ms; section thickness/section gap, 7.0/1.0 mm; FOV, 24 × 24 cm; NEX, 2; matrix, 256 × 192), and 3D time-of-flight MRA (TR/TE, 27/6.8 ms; flip angle, 16°; bandwidth, 14.7 Hz; FOV, 18 × 18 cm; slab thickness, 70 mm; section thickness, 1.2 mm; matrix 256 × 192; NEX, 1). MR imaging was completed within 13–15 minutes. Contrast material such as gadolinium was not used in this study. In the evaluation of FLAIR images, we carefully distinguished the disease or pathologic condition accompanied by hyperintensity in the subarachnoid space on FLAIR images from artifacts such as CSF pulsation or metallic artifacts, infectious meningitis, and leptomeningeal metastasis or anastomosis. For the subjects in this study, we did not perform highly concentrated oxygen inhalation before or at the time of the MR imaging.

Plain CT scans were obtained in all patients in whom SAH was diagnosed by MR imaging on admission. The CT section thickness was 4 mm. 3D CTA was performed in all patients to identify ruptured aneurysms and estimate major-vessel early vasospasm.

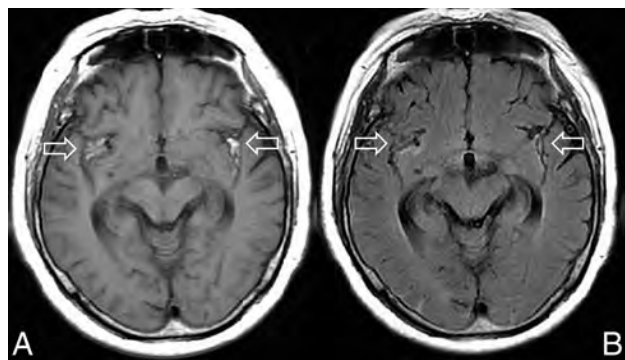


**FIG 1.** A 77-year-old woman with a ruptured right middle cerebral artery aneurysm who was admitted 5 days after onset. T1WI on admission shows BHSB in the bilateral Sylvian fissure (A, arrows) that matches the blood distribution on the FLAIR image (B, arrows). These findings are typical of subacute SAH with T1-FLAIR-matched SAH that was not associated with rebleeding. Reprinted with permission from Shimoda M. Neuroimaging for headache. *Journal of Clinical and Experimental Medicine (IGAKU NO AYUMI)* 2012;243:1086–94; Ishiyaku Publishers, Inc.

### Definition of Variables

The clinical grade of each patient was determined on admission according to the World Federation of Neurological Surgeons grading system.<sup>6</sup> The severity of SAH was classified by using CT findings according to the Fisher scale.<sup>7</sup> Warning headache was defined as a sudden and unusually severe headache of at least 1 hour followed by a symptom-free interval or marked improvement of symptoms before admission due to major SAH. The presence of a warning headache was diagnosed by a thorough interview of patients and their relatives or accompanying persons.

Among patients with T1WI-detected clearly BHSB on admission MR imaging, if the distribution of SAH on T1 (T1 BHSB component) almost entirely matched the distribution of SAH on FLAIR (FLAIR hyperintense component), patients were diagnosed with subacute SAH not associated with rebleeding and were thus excluded from the study (Fig 1). In the remaining patients with T1WI-detected BHSB, if the subarachnoid blood on FLAIR images was distributed over a larger area than the BHSB on T1WI (T1-FLAIR mismatch), this finding was taken as an indication of new, acute SAH. T1WI-detected BHSB in these patients represents subacute SAH due to a previous minor leak (Fig 2). If FLAIR-detected SAH had no T1-detected BHSB on admission MR imaging, SAH was considered acute.

Diagnosis of intracerebral hemorrhage (ICH) was defined as a blood collection with a diameter of >1 cm detected by CT. Large intra-Sylvian hematoma was based on the presence of clots of >5 mL. Rebleeding after admission was defined as a definite increase in the volume of blood visible on CT accompanied by sudden exacerbation of consciousness compared with baseline MR imaging or CT on admission. Delayed ischemic neurologic deficits were defined as the appearance of a focal neurologic abnormality following recovery from the immediate postoperative state. CT and MR imaging findings were interpreted by at least 2 senior stroke neurosurgeons (M.S. and S.O.), with 32 and 27 years of experience, respectively. In the case of disagreement between raters, diagnosis was obtained by consensus.

Outcome was assessed at 3 months by using the mRS.<sup>8</sup> Pa-

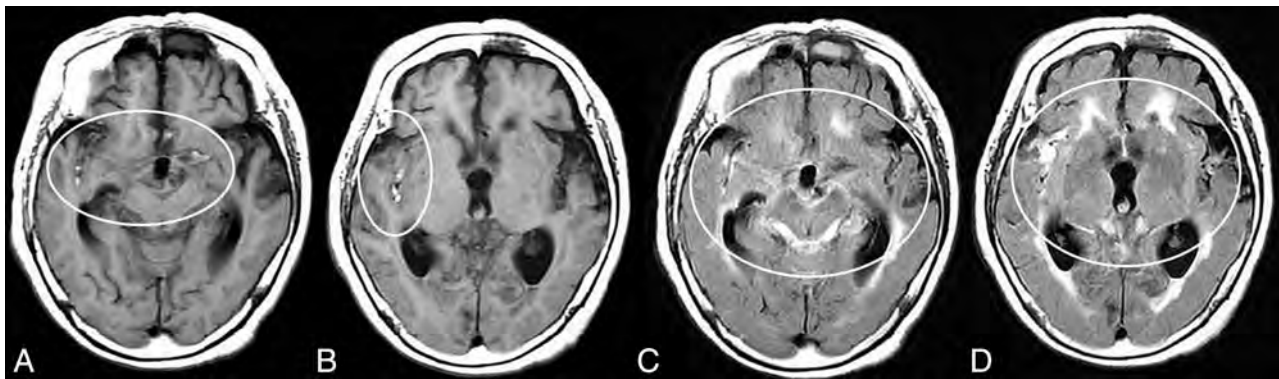


**FIG 2.** Typical neuroradiologic findings in a patient with minor leak before major SAH attack. Images are from an 80-year-old woman with a ruptured right middle cerebral artery aneurysm. T1WI on admission shows clearly iso- to mildly hyperintense blood obscuring the right Sylvian fissure, in addition to the more conspicuous bright T1 foci (A and B, circles). These findings indicate subacute subarachnoid blood due to a minor leak that occurred before the major attack. FLAIR images on admission show the SAH in the acute phase in the quadrigeminal cistern and left Sylvian fissure (C and D, circles), in addition to the BHSB on T1WI. We defined this as T1-FLAIR mismatch and used it as a neuroradiologic diagnosis of minor leak that occurred before major SAH.

**Table 1: Clinical features, neurologic status, and CT features on admission<sup>a</sup>**

	Total	T1-FLAIR Mismatch		P Value
		Positive	Negative	
No. of patients	127	43 (33.9)	84 (66.1)	
Warning sign				
Positive	14	13 (30.2)	1 (1.2)	<.001
Negative	54	2 (4.7)	52 (61.9)	
Unknown	59	28 (65.1)	31 (36.9)	
Mean age (yr)	61.5 ± 14.2	66.5 ± 13.2	58.9 ± 14.0	.004
Age range (yr)	21–89	40–85	21–89	
Elderly patients				
Older than 80 years	12	10 (23.3)	2 (2.4)	<.001
Female sex	89	32 (74.4)	57 (67.9)	.541
Rebleeding after admission	28	19 (44.2)	9 (1.7)	<.001
WFNS grade on admission				
Grades I–II	97	28 (65.1)	69 (82.1)	.028
Grades IV–V	28	13 (30.2)	15 (17.9)	.120
Fisher group				
Group 3	85	30 (69.8)	55 (65.5)	.550
Intracerebral hemorrhage	25	19 (44.2)	6 (7.1)	<.001
Acute hydrocephalus	61	26 (60.5)	35 (41.7)	.060
Aneurysm site				
Anterior communicating artery	41	9 (20.9)	32 (38.1)	
Anterior cerebral artery	8	4 (9.3)	4 (4.8)	
Internal carotid artery	38	12 (27.9)	26 (31.0)	
Middle cerebral artery	31	17 (39.5)	14 (16.7)	
Posterior circulation	8	0	8 (9.5)	.051
Aneurysm size				
>5 mm	75	31 (72.1)	44 (52.4)	.037
>10 mm	8	3 (7.0)	5 (6.0)	1.000

**Note:**—WFNS indicates World Federation of Neurological Surgeons.

<sup>a</sup> Values are No. (%) unless otherwise stated. The “No. of patients” row shows the percentage of the total number of patients, whereas all other percentages in the “Positive” and “Negative” columns are the percentages of patients with positive and negative findings, respectively.

tients were stratified into favorable outcome (mRS score of 0–2) and unfavorable outcome (mRS score of 3–6). Postoperative management was administered according to previously reported protocols.<sup>9</sup>

### Statistical Analysis

The significance of clinical factors potentially associated with minor leak before major attack diagnosed by T1-FLAIR mismatch on admission was determined by the Fisher exact test for categoric

variables and an independent sample 2-tailed Student *t* test for continuous variables. Clinical factors with a significance level of *P* < .05 were subjected to multivariate logistic regression analysis with the occurrence of minor leak diagnosed by T1-FLAIR mismatch on admission as the dependent variable. Statistical analyses were performed by using commercially available software (SPSS, Version 22.0 for Windows; IBM, Armonk, New York).

## RESULTS

### Warning Headache and T1-FLAIR Mismatch

The incidence of warning headache determined by interview was 11.0% (14/127 patients). Fifty-four patients (42.5%) reported no history of warning headache before admission, and the presence or absence of warning headache was unknown in the remaining 59 patients (Table 1). Among the 14 patients who had a warning headache before the major attack, 12 were younger than 80 years of age.

Adverse events, such as neurologic deterioration or rebleeding from the aneurysm during or immediately after MR imaging did not occur in any patient.

According to neuroradiologic diagnosis by using T1-FLAIR mismatch, the overall incidence of minor leak before major SAH was 33.9% (43/127 patients) (Table 1). Of the 14 patients with a history of warning headache before admission, 13 had previous minor leak diagnosed by T1-FLAIR mismatch on admission. In the remaining patient, the diagnosis of minor leak by T1-FLAIR mismatch was not possible because major SAH developed within 48 hours of the warning headache (minor leak) onset. In the 113 patients without a history of warning headache before admission,

30 (23.6%) had T1-FLAIR mismatch on admission and therefore had a potential minor leak before admission diagnosed by T1-FLAIR mismatch.

### Pre- and Postoperative Clinical Factors and T1-FLAIR Mismatch

Tables 1 and 2 summarize the pre- and postoperative clinical factors that were significantly different between patients with and without T1-FLAIR mismatch on admission. Two patients had a major vessel vasospasm detected by 3D CTA or conventional digital subtraction angiography on admission. Both patients had a minor leak diagnosed by T1-FLAIR mismatch. In 35 of the 43 patients with T1-FLAIR mismatch on admission (81.4%), MRA findings were indistinct due to subacute subarachnoid blood caused by the minor leak, particularly in the vessel around the ruptured aneurysm. In the 8 patients with minor leak before admission and without obfuscation of the visibility on MRA, subarachnoid clots on T1WI were small.

In all patients with T1-FLAIR mismatch and ICH, the high-intensity signal on T1WI was present in the cistern around the ruptured aneurysm, and ICH was depicted as a high-intensity signal on FLAIR images (Fig 3).

Ten of the 12 elderly patients with SAH (80 years of age or older) had a minor leak diagnosed by T1-FLAIR mismatch. In 9 of

these 10 elderly patients with T1-FLAIR mismatch, the presence or absence of a warning headache could not be determined by interview due to poor clinical condition.

Multivariate stepwise logistic regression analysis revealed that 80 years of age or older, the presence of rebleeding after admission, ICH on CT, and mRS scores of 3–6 were significantly associated with the diagnosis of minor leak by T1-FLAIR mismatch on admission (Table 3).

## DISCUSSION

### Incidence of Minor Leak in Previous Reports

According to Jakobsson et al,<sup>1</sup> the reported incidence of warning signs in patients with SAH ranges from 13.5% to 60%. They emphasized that the true incidence of warning signs is difficult to establish because it is difficult or impossible to obtain complete information from patients in poor clinical condition or who die before reaching a hospital.<sup>1</sup> In addition to headaches, a previous study noted several nonspecific symptoms as warning signs,<sup>10</sup> the incidences of which greatly differed.<sup>1</sup> Thus, the diagnosis of a minor leak by interview has poor accuracy, and it is difficult to grasp the clinical significance of an interview-diagnosed minor leak.

Our results revealed that 13 of 14 patients with a history of warning headache before admission had a minor leak before the major attack, as indicated by neuroradiologic images on admission. Therefore, we propose that warning headaches diagnosed by interview are not a product of recall bias but are the result of actual leaks from aneurysms (ie, a first SAH). In the future, neuroradiologic diagnosis could be used to investigate the clinical significance of minor leaks that cannot be diagnosed by interview.

### Neuroradiologic Diagnosis of Minor Leak before Major Attack

The T1 relaxation time of acute subarachnoid blood is relatively shorter

**Table 2: Surgery and subsequent events<sup>a</sup>**

	Total	T1-FLAIR Mismatch		P Value
		Positive	Negative	
No. of patients	127	43 (33.9)	84 (66.1)	
Aneurysm operation				
Craniotomy	105	36 (83.7)	69 (82.1)	1.000
Coiling	22	7 (16.3)	15 (17.9)	
Delayed angiographic vasospasm	35	19 (44.2)	16 (19.0)	.003
DIND	22	16 (37.2)	6 (7.1)	<.001
Infarction due to delayed vasospasm on DWI	30	17 (39.5)	13 (15.5)	.003
Chronic hydrocephalus <sup>b</sup>	54	23 (62.2)	31 (37.8)	.029
mRS score at 3 months				
>3–6	41	28 (65.1)	13 (15.5)	<.001

**Note:**—DIND indicates delayed ischemic neurologic deficits.

<sup>a</sup> The “No. of patients” row shows the percentage of the total number of patients, whereas all other percentages in the “Positive” and “Negative” columns are the percentages of patients with positive and negative findings, respectively.

<sup>b</sup> The incidence of chronic hydrocephalus was calculated for the surviving patients.

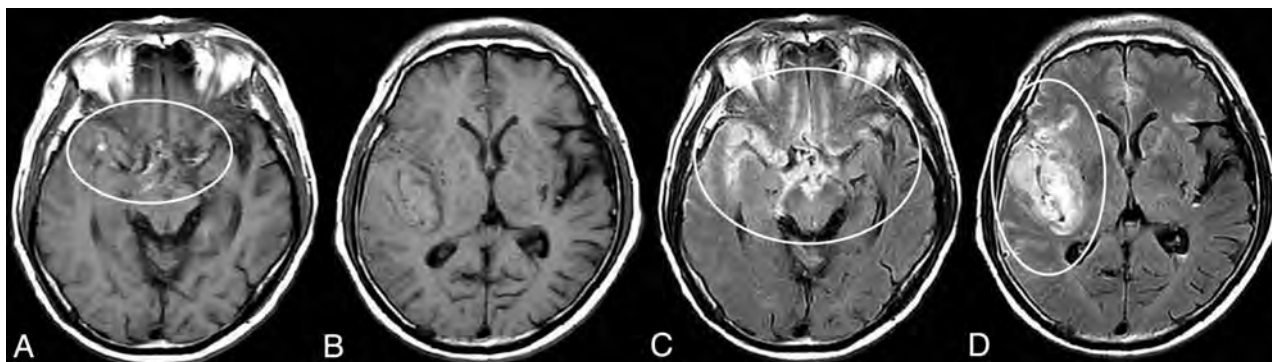


**FIG 3.** Typical neuroradiologic findings in a case with minor leak before a major SAH attack with intra-Sylvian hematoma. Images are from a 66-year-old woman with a ruptured right middle cerebral artery aneurysm. T1WI shows iso- to mildly hyperintense blood obscuring the right Sylvian fissure and suprasellar cistern, in addition to the more conspicuous bright T1 foci including the neighboring area of the ruptured aneurysm. An intra-Sylvian hematoma is depicted as an iso-intense signal (A circle, B). FLAIR images show the intra-Sylvian hematoma and SAH (right Sylvian fissure, suprasellar and right ambient cistern) as a high-intensity signal, which indicates acute blood (C and D, circles).

**Table 3: Results of multivariate logistic regression analysis for the presence of a minor leak before admission diagnosed by T1-FLAIR mismatch**

	Odds Ratio	95% CI	P Value
Preoperative clinical factors			
Age older than 80 years	8.475	1.639–43.478	.011
Rebleeding	5.291	2.028–13.889	.001
Associated neuroradiologic findings on admission			
Intracerebral hemorrhage on CT	7.197	2.457–20.833	<.001
Postoperative factors			
mRS score 3–6	6.690	2.548–17.564	<.001

than that of normal CSF.<sup>11,12</sup> However, T1WI is not useful for the diagnosis of SAH in the acute phase because the degree of T1 shortening replaces normally black CSF space with isointensity. Beyond 4 days after SAH onset, conversion of oxyhemoglobin to methemoglobin increases gradually.<sup>13,14</sup> Methemoglobin is a paramagnetic substance that causes substantial T1 shortening. Therefore, methemoglobin accumulation causes T1 shortening in the subacute and chronic phases,<sup>15</sup> and T1WI is useful for SAH diagnosis in these phases.

Recently, several authors have reported that FLAIR and T2\*-weighted imaging sequences are the most sensitive and useful for detecting SAH in the acute and subacute phases.<sup>16–18</sup> However, FLAIR and T2\*-weighted imaging sequences are not useful for the diagnosis of the onset stage of the subarachnoid blood and cannot differentiate subarachnoid blood in the subacute and acute phases. As mentioned above, because subarachnoid blood is depicted clearly as BHSB on T1WI around 3 to 4 days after SAH onset, any BHSB that is detected by T1WI on admission is blood that is in the subacute phase (ie, occurred before admission). If there is a mismatch between the distribution of subarachnoid blood on T1WI and on FLAIR images, the blood depicted on FLAIR images but not T1WI is the more recent, new acute hemorrhage. This hemorrhage is the second hemorrhage (major attack) that resulted in hospitalization. Therefore, the BHSB detected by T1WI is in the subacute phase and must have occurred before admission. In this study, we interpreted this bleeding as having arisen from a minor leak.

While it is reasonable to label blood as subacute if it is hyperintense on T1WI, acute blood can also show increased T1 signal.<sup>13,19</sup> Mitchell et al<sup>19</sup> reported a sensitivity of 50% for T1 hyperintensity in the acute stage of SAH. However, their study was of a small sample ( $n = 20$ ) and therefore included some patients in the subacute phase. In these studies, a strict evaluation of the timing of MR imaging relative to the onset of SAH is necessary. The acute phase of SAH is usually defined as within 72 hours of onset. In our study, we excluded patients with SAH who were admitted 48–72 hours after onset because this time window represents a period of oxyhemoglobin-to-methemoglobin conversion. We investigated MR imaging findings only in patients admitted within 48 hours of major SAH.

Subarachnoid blood can be very heterogeneous, and not all subacute blood will be T1 hyperintense. Many factors can affect these characteristics, including subarachnoid blood aging more slowly than cerebral hematomas (due to higher oxygen tension in

CSF) and likely different proportions of CSF and subarachnoid blood compounding the picture. From previous studies with small sample sizes, the sensitivity of T1 hyperintensity in the subacute stage of SAH ranged from 33% to 36%.<sup>19,20</sup> Bradley<sup>21</sup> reported that it was difficult to diagnose T1 hyperintensity in the subacute stage of SAH if there was an extremely small hemorrhage because the red blood cells are likely to have been resorbed by the time significant methemoglobin formation would have occurred. That a diagnosis of minor leak by T1-FLAIR mismatch and the evaluation of the exact staging of subarachnoid blood by the MR imaging has limitations is unavoidable.

Methemoglobin has high signal intensity on time-of-flight MRA and obscures signals from vessels and aneurysms.<sup>22,23</sup> Obfuscation of the visibility of a ruptured aneurysm on MRA becomes a simple neuroradiologic indicator of the presence of subarachnoid blood in the subacute phase due to a minor leak. Grandin et al<sup>23</sup> reported that phase-contrast MRA could easily overcome these problems of obfuscation in the MRA. However, to limit the duration of the examination, we did not perform phase-contrast MRA.

#### **Minor Leaks in Elderly Patients with SAH**

From our results and those of a previous report,<sup>24</sup> the incidence of a warning headache before a major attack was low in elderly patients with SAH. However, the frequency of potential minor leak according to T1-FLAIR mismatch was high in elderly patients with SAH. The causes of this result are unknown. We speculate that the age-associated enlargement of the subarachnoid space due to cortical atrophy may be 1 reason for the high incidence of potential minor leaks without warning headache in elderly patients. In other words, because an increase in intracranial pressure may not occur even in the presence of an aneurysmal rupture, symptoms due to minor leak would be milder in elderly patients than in younger patients with SAH. Therefore, it could be relatively rare that elderly patients with SAH go to the hospital at the time of the first attack due to minor leak, and they are often only brought to the hospital for a major SAH attack.

#### **Minor Leaks and ICH due to a Ruptured Aneurysm**

Several pathologic studies have reported that ICH due to a ruptured aneurysm occurs by indirect or direct rupture of an aneurysm in the brain.<sup>25–27</sup> ICH due to indirect rupture in the brain is caused by obstruction of the subarachnoid space due to the presence of blood, fibrin, and fibrous arachnoidal adhesions after previous bleeding.<sup>27</sup> By contrast, ICH due to direct rupture into the brain occurs due to the adhesion of the aneurysm sac to the pia mater.<sup>25,26</sup> One report also suggested that the adhesion of the aneurysm sac to the pia mater may be facilitated by previous bleeding.<sup>25</sup> This possibility indicates that the likelihood of ICH due to aneurysm rupture is increased by the presence of a previous hemorrhage, such as a minor leak. Indeed, in our study, in all patients diagnosed with a minor leak and ICH on admission, the high-signal-intensity lesion on T1WI corresponded to subarachnoid blood in the neighboring area of the ruptured aneurysm. On the other hand, ICH was depicted as a high-signal-intensity lesion on

FLAIR images and DWI on admission and did not show high signal intensity on T1WI. These findings suggest that the ICH present on admission was a new, acute lesion.

### Minor Leaks and Rebleeding

Previous reports have indicated that a warning headache is a risk factor for rebleeding, because a fragile aneurysm that ruptured at the time of the minor leak is prone to rebleeding.<sup>28,29</sup> Additionally, existing literature indicates that the rate of rebleeding is higher in patients with ICH than in patients without ICH.<sup>29,30</sup> Our results and previous reports suggest that a minor leak is related closely to ICH and rebleeding. Therefore, in patients who experienced a minor leak before the major SAH, emergency surgery should be performed as soon as possible because these patients have a high probability of both rebleeding and ICH.<sup>28,29</sup>

### Minor Leak and Prognosis

Unexpectedly, several previous studies have reported that the presence of a warning leak had no impact on outcome.<sup>24,31</sup> In these studies, the true outcome of patients with SAH with a minor leak was difficult to establish because of the difficulty of obtaining complete information on the presence or absence of a warning headache by interview. Jakobsson et al<sup>1</sup> emphasized that outcomes were particularly unfavorable in patients with a short interval ( $\leq 3$  days) from interview-diagnosed warning headache to SAH. Although our neuroradiologic diagnostic procedure for a minor leak cannot be used to identify patients who had  $< 2$  days between minor leak and major SAH, our results, combined with those of Jakobsson et al,<sup>1</sup> emphasize that the prognosis of patients with SAH with a minor leak before a major attack is unfavorable.

### Limitations

In patients with an extremely small amount of subacute blood, the sensitivity of the diagnosis of T1 hyperintensity may decrease. In addition, this neuroradiologic diagnostic procedure cannot be used to diagnose minor leaks in patients admitted  $> 48$  hours after major SAH attack. Similarly, this procedure cannot be used to diagnose minor leaks in patients who had major SAH within 48 hours of minor leak onset. It is difficult to distinguish between patients with preceding headache due to the occurrence of dissection without SAH<sup>32</sup> and patients with minor leak (SAH) due to ruptured dissecting aneurysms. Therefore, we excluded patients with dissecting cerebral aneurysms from this study.

### CONCLUSIONS

In this study, we have proposed a method to define patients who had a prior minor leak: T1-detected BHSB on admission MR imaging was considered subacute, and FLAIR hyperintense blood that was more extensive than this was deemed the acute component. The T1 hyperintense component was defined as a subacute minor leak. We found that almost all patients with warning headache diagnosed by interview had a minor leak according to our

definition. We conclude that warning headaches are not a product of recall bias but are the result of actual leaks.

### REFERENCES

1. Jakobsson KE, Saveland H, Hillman J, et al. **Warning leak and management outcome in aneurysmal subarachnoid hemorrhage.** *J Neurosurg* 1996;85:995–99
2. Linn FH, Wijdicks EF, van der Graaf Y, et al. **Prospective study of sentinel headache in aneurysmal subarachnoid haemorrhage.** *Lancet* 1994;344:590–93
3. Gillingham FJ. **The management of ruptured intracranial aneurysms.** *Scott Med J* 1967;12:377–83
4. Drake CG. **Progress in cerebrovascular disease: management of cerebral aneurysm.** *Stroke* 1981;12:273–83
5. Linn FH, Rinkel GJ, Algra A, et al. **The notion of “warning leaks” in subarachnoid haemorrhage: are such patients in fact admitted with a rebleed?** *J Neurol Neurosurg Psychiatry* 2000;68:332–36
6. Drake CG. **Report of World Federation of Neurological Surgeons Committee on a Universal Subarachnoid Hemorrhage Grading Scale.** *J Neurosurg* 1988;68:985–86
7. Fisher CM, Kistler JP, Davis JM. **Relation of cerebral vasospasm to subarachnoid hemorrhage visualized by computerized tomographic scanning.** *Neurosurgery* 1980;6:1–9
8. Shinohara Y, Minematsu K, Amano T, et al. **Modified Rankin scale with expanded guidance scheme and interview questionnaire: interrater agreement and reproducibility of assessment.** *Cerebrovasc Dis* 2006;21:271–78
9. Shimoda M, Hoshikawa K, Shiramizu H, et al. **Early infarction detected by diffusion-weighted imaging in patients with subarachnoid hemorrhage.** *Acta Neurochir (Wien)* 2010;152:1197–205
10. Hauerberg J, Andersen BB, Eskesen V, et al. **Importance of the recognition of a warning leak as a sign of a ruptured intracranial aneurysm.** *Acta Neurol Scand* 1991;83:61–64
11. Spickler E, Lufkin R, Teresi L, et al. **MR imaging of acute subarachnoid hemorrhage.** *Comput Med Imaging Graph* 1990;14:67–77
12. Ogawa T, Inugami A, Shimosegawa E, et al. **Subarachnoid hemorrhage: evaluation with MR imaging.** *Radiology* 1993;186:345–51
13. Bradley WG Jr, Schmidt PG. **Effect of methemoglobin formation on the MR appearance of subarachnoid hemorrhage.** *Radiology* 1985;156:99–103
14. Wahlgren NG, Lindquist C. **Haem derivatives in the cerebrospinal fluid after intracranial haemorrhage.** *Eur Neurol* 1987;26:216–21
15. Ogawa T, Inugami A, Fujita H, et al. **MR diagnosis of subacute and chronic subarachnoid hemorrhage: comparison with CT.** *AJR Am J Roentgenol* 1995;165:1257–62
16. Shimoda M, Hoshikawa K, Shiramizu H, et al. **Problems with diagnosis by fluid-attenuated inversion recovery magnetic resonance imaging in patients with acute aneurysmal subarachnoid hemorrhage.** *Neurol Med Chir (Tokyo)* 2010;50:530–37
17. Noguchi K, Seto H, Kamisaki Y, et al. **Comparison of fluid-attenuated inversion-recovery MR imaging with CT in a simulated model of acute subarachnoid hemorrhage.** *AJNR Am J Neuroradiol* 2000;21:923–27
18. Imaizumi T, Chiba M, Honma T, et al. **Detection of hemosiderin deposition by T2\*-weighted MRI after subarachnoid hemorrhage.** *Stroke* 2003;34:1693–98
19. Mitchell P, Wilkinson ID, Hoggard N, et al. **Detection of subarachnoid haemorrhage with magnetic resonance imaging.** *J Neurol Neurosurg Psychiatry* 2001;70:205–11
20. Noguchi K, Ogawa T, Seto H, et al. **Subacute and chronic subarachnoid hemorrhage: diagnosis with fluid-attenuated inversion-recovery MR imaging.** *Radiology* 1997;203:257–62
21. Bradley WG Jr. **MR appearance of hemorrhage in the brain.** *Radiology* 1993;189:15–26
22. Ida M, Kurisu Y, Yamashita M. **MR angiography of ruptured aneurysms in acute subarachnoid hemorrhage.** *AJNR Am J Neuroradiol* 1997;18:1025–32

23. Grandin CB, Cosnard G, Hammer F, et al. **Vasospasm after subarachnoid hemorrhage: diagnosis with MR angiography.** *AJNR Am J Neuroradiol* 2000;21:1611–17
24. Okawara SH. **Warning signs prior to rupture of an intracranial aneurysm.** *J Neurosurg* 1973;38:575–80
25. Tomlinson BE. **Brain changes in ruptured intracranial aneurysm.** *J Clin Pathol* 1959;12:391–99
26. Crompton MR. **Intracerebral haematoma complicating ruptured cerebral berry aneurysm.** *J Neurol Neurosurg Psychiatry* 1962;25:378–86
27. Robertson EG. **Cerebral lesions due to intracranial aneurysms.** *Brain* 1949;72:150–85
28. Beck J, Raabe A, Szelenyi A, et al. **Sentinel headache and the risk of rebleeding after aneurysmal subarachnoid hemorrhage.** *Stroke* 2006;37:2733–37
29. Güresir E, Beck J, Vatter H, et al. **Subarachnoid hemorrhage and intracerebral hematoma: incidence, prognostic factors, and outcome.** *Neurosurgery* 2008;63:1088–93; discussion 1093–94
30. Naidech AM, Janjua N, Kreiter KT, et al. **Predictors and impact of aneurysm rebleeding after subarachnoid hemorrhage.** *Arch Neurol* 2005;62:410–16
31. Juvela S. **Minor leak before rupture of an intracranial aneurysm and subarachnoid hemorrhage of unknown etiology.** *Neurosurgery* 1992;30:7–11
32. Mizutani T. **Natural course of intracranial arterial dissections.** *J Neurosurg* 2011;114:1037–44

# Aqueductal Stroke Volume: Comparisons with Intracranial Pressure Scores in Idiopathic Normal Pressure Hydrocephalus

G. Ringstad, K.E. Emblem, O. Geier, N. Alperin, and P.K. Eide



## ABSTRACT

**BACKGROUND AND PURPOSE:** Aqueductal stroke volume from phase-contrast MR imaging has been proposed for predicting shunt response in normal pressure hydrocephalus. However, this biomarker has remained controversial in use and has a lack of validation with invasive intracranial monitoring. We studied how aqueductal stroke volume compares with intracranial pressure scores in the presurgical work-up and clinical score, ventricular volume, and aqueduct area and assessed the patient's response to shunting.

**MATERIALS AND METHODS:** Phase-contrast MR imaging was performed in 21 patients with probable idiopathic normal pressure hydrocephalus. Patients were selected for shunting on the basis of pathologically increased intracranial pressure pulsatility. Patients with shunts were offered a second MR imaging after 12 months. Ventricular volume and transverse aqueductal area were calculated, as well as clinical symptom score.

**RESULTS:** No correlations between aqueductal stroke volume and preoperative scores of mean intracranial pressure or mean wave amplitudes were observed. Preoperative aqueductal stroke volume was not different between patients with shunts and conservatively treated patients ( $P = .69$ ) but was correlated with ventricular volume ( $R = 0.60, P = .004$ ) and aqueductal area ( $R = 0.58, P = .006$ ) but not with the severity or duration of clinical symptoms. After shunting, aqueductal stroke volume ( $P = .006$ ) and ventricular volume ( $P = .002$ ) were reduced. A clinical improvement was seen in 16 of 17 patients who had shunts (94%).

**CONCLUSIONS:** Aqueductal stroke volume does not reflect intracranial pressure pulsatility or symptom score, but rather aqueduct area and ventricular volume. The results do not support the use of aqueductal stroke volume for selecting patients for shunting.

**ABBREVIATIONS:** ASV = aqueductal stroke volume; ICP = intracranial pressure; iNPH = idiopathic normal pressure hydrocephalus; MWA = mean ICP wave amplitude; PCMR = phase-contrast MR imaging

Idiopathic normal pressure hydrocephalus (iNPH) is characterized by dementia, incontinence, and gait disturbance<sup>1</sup> and can be treated by ventriculoperitoneal shunt surgery. However, the disease can be difficult to separate from other neurodegenerative disorders such as Alzheimer and Parkinson diseases.<sup>2</sup> Selection criteria for surgical shunting have been heterogeneous, and the

clinical response to this treatment has, accordingly, been reported to range from 29% to 90%.<sup>3-5</sup> Previous investigators have, therefore, sought to establish noninvasive parameters from MR imaging studies. After Bradley et al<sup>6</sup> first reported an increased CSF flow void in the aqueduct associated with a favorable shunt response, studies using phase-contrast MR imaging (PCMR) have demonstrated aqueductal flow parameters, and in particular the aqueductal stroke volume (ASV), to be useful in the diagnosis and selection of patients for shunt surgery<sup>7-13</sup> and in the follow-up of patients with shunts.<sup>14</sup> However, other studies do not reproduce the beneficial utility of measuring aqueductal flow<sup>15-18</sup>; therefore, the use of ASV in iNPH remains disputed. Accordingly, comparisons with invasive intracranial measurements are warranted.

Continuous monitoring of intracranial pressure (ICP) and single cardiac-induced ICP waves in patients with iNPH has revealed elevated mean ICP wave amplitudes (MWAs) in those responding to shunts, compared with those not responding.<sup>19,20</sup> Hence, in this hospital, diagnostic preoperative monitoring of MWA is used routinely and predicts a beneficial shunt response in

Received December 15, 2014; accepted after revision February 11, 2015.

From the Department of Radiology and Nuclear Medicine (G.R.) and Intervention Centre (K.E.E., O.G.), Oslo University Hospital-Rikshospitalet, Oslo, Norway; Department of Radiology (N.A.), University of Miami Miller School of Medicine, Miami, Florida; Department of Neurosurgery (P.K.E.), Oslo University Hospital, Oslo, Norway; and Faculty of Medicine (P.K.E.), University of Oslo, Oslo, Norway.

Paper previously presented in part at: Annual Meeting of the Radiological Society of North America, December 1-6, 2013; Chicago, Illinois (No. SSM14-05, RSNA ID: 13021973).

Please address correspondence to Geir Ringstad, MD, Department of Radiology and Nuclear Medicine, Oslo University Hospital-Rikshospitalet, Postboks 4950 Nydalen, 0424 Oslo, Norway; e-mail address: gringsta@ous-hf.no

Indicates open access to non-subscribers at www.ajnr.org

<http://dx.doi.org/10.3174/ajnr.A4340>

9 of 10 patients with iNPH.<sup>19</sup> Elevated MWA is indicative of reduced intracranial compliance (ie, reduced pressure-volume reserve capacity),<sup>21,22</sup> which may be a pathophysiologic mechanism behind iNPH.<sup>19,23-25</sup> Increased ASV in iNPH has been attributed to reduced intracranial compliance.<sup>26</sup> If ASV should express reduced intracranial compliance and thereby predict shunt response, a positive correlation between ASV and MWA seems reasonable.

The purpose of this study was therefore to compare ASV from phase-contrast MR imaging with preoperative ICP scores, clinical normal pressure hydrocephalus scores, and MR imaging–derived ventricular volume and aqueductal area in patients with iNPH before and after shunting.

## MATERIALS AND METHODS

### Patient Inclusion and Study Design

The study was approved by the institutional review board of Oslo University Hospital. Inclusion was by written and oral informed consent.

Of 28 consecutive patients with iNPH undergoing assessment for probable iNPH within the department of neurosurgery, 7 patients were excluded because of motion artifacts at PCMR and/or termination of the examination before completion of the PCMR sequence. Accordingly, 21 patients with iNPH (10 women, 11 men; range, 56–84 years) with successful PCMR were included in this prospective observational study. The assessment included clinical examination with determination of iNPH symptom severity, PCMR, and overnight ICP monitoring. The patients with iNPH who underwent shunt surgery were invited to a second PCMR after 12 months.

### Clinical Management

The assessment of patients with iNPH for shunt surgery followed the clinical routine at the department of neurosurgery. Clinical grading of the severity of symptoms was performed by using the normal pressure hydrocephalus grading scale of this department,<sup>19</sup> which assesses the combined severity of gait disturbance, urinary incontinence, and dementia. Each component is graded from 1 to 5, with a possible total score of 3 (worst) to 15 (best). According to the institutional routine, the decision for shunt surgery is based on a combination of clinical assessment, radiologic assessment, and the results of continuous ICP monitoring.<sup>19</sup>

The shunt response was defined as an increase by at least 2 points on the normal pressure hydrocephalus grading scale, and the clinical score was assessed at regular intervals, 3, 6, and 12 months (including imaging after 12 months) following shunting.

### MR Image Acquisition

The techniques for CSF velocity imaging with MR imaging have previously been described in detail.<sup>27</sup>

MR imaging was performed on a 3T Achieva system (Philips Healthcare, Best, the Netherlands). The MR imaging parameters for aqueductal flow were TR = 24 ms and TE = 16 ms, voxel size =  $0.60 \times 0.80 \times 4.00$  mm<sup>3</sup>, velocity encoding = 10 cm/s, and 30–40 phases with retrospective peripheral cardiac gating. The scan was obtained in a section perpendicular to the aqueduct (Fig 1C).

The MR imaging protocol also included 3D T1-weighted ultrafast gradient echo, acquisition matrix =  $256 \times 256 \times 192$  with voxel size  $1.0/1.0/1.0$  mm<sup>3</sup>, flip angle = 7, TR/TE = 8.6/2.3 ms, which was used for segmentation of the supratentorial ventricles for the volumetric analysis.

### MR Image Postprocessing

All examinations were postprocessed by using Q-flow software (Philips Healthcare). The aqueduct was manually defined in all the phase images with an ROI in each section (Fig 1D) by a neuroradiologist with 7 years of experience who was blinded to clinical data. Care was taken not to include nonmoving tissue elements in the imaging plane to avoid background noise in the MR imaging signal.

ASV was estimated after correction for potential aliasing by sinusoid curve fitting and was defined as the mean of systolic and diastolic volumetric CSF flow during 1 cardiac cycle minus net flow (Fig 1B).

Calculation of supratentorial ventricular volume (referred to as “ventricular volume”) was performed by a 3D medical image segmentation software ITK-SNAP 2.4 ([www.itksnap.org](http://www.itksnap.org)),<sup>28</sup> which provides semiautomatic segmentation by using active contour methods. For the segmentation, the region competition method by Zhu and Yuille<sup>29</sup> was used. The segmentation result was controlled visually and, if necessary, corrected manually (in ITK-SNAP).

### ICP Monitoring

All patients underwent continuous overnight ICP monitoring. As previously described in detail,<sup>19</sup> an ICP sensor was placed in the brain parenchyma through a small burr-hole in the skull with the patient under local anesthesia. Overnight monitoring was done in the patient ward by using a computerized system (Sensometrics Technology; dPCOM AS, Oslo, Norway) for automatic identification of individual cardiac-induced single ICP waves. The amplitude of the ICP wave was identified as the pressure difference between the systolic maximum and diastolic minimum pressures (Fig 1A). The mean ICP wave amplitude is determined as the average of all single ICP waves during consecutive 6-second time intervals, while the mean ICP is the average of absolute ICP relative to a zero pressure level. For the patients in this study, the MWA and mean ICP values were determined for the 6-second time windows from 11 PM to 7 AM (ie, 4 800 6-second time windows). During this recording period, both the average of MWA and mean ICP were determined, as well as the percentage of MWA of  $\geq 5$  mm Hg and the percentage of mean ICP of  $\geq 15$  mm Hg, during the recording period.

According to the institutional routine, primarily the MWA is used for selection to shunting. Threshold levels of MWA representing an indication for shunting are MWA, on average, of  $\geq 4$  mm Hg and/or the percentage of MWA of  $\geq 5$  mm Hg in  $\geq 10\%$  of recording time.

### Statistical Analysis

Under the assumption of normal distribution, correlations were determined by the Pearson correlation coefficient, and pre- and postsurgical values of ASV and ventricular volume were compared by using a paired-samples *t* test. Comparison of ASV be-

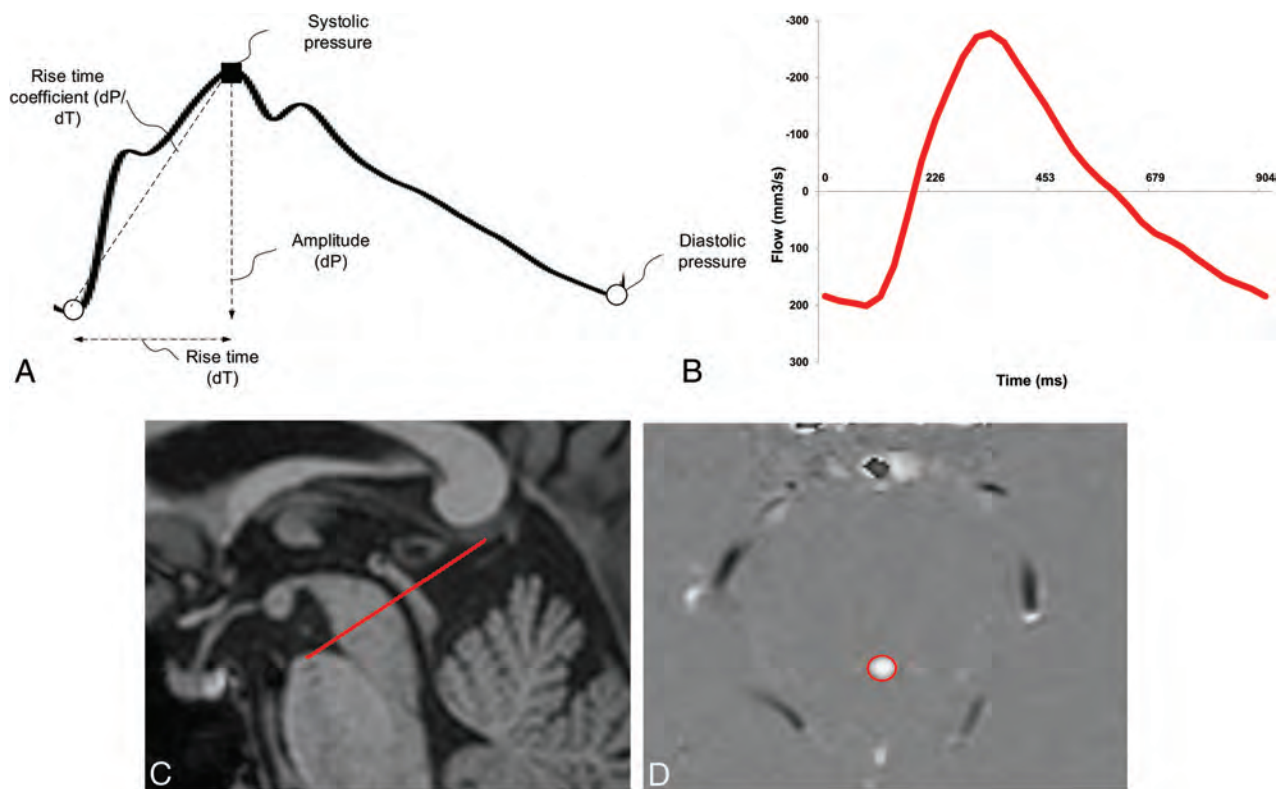


**FIG 1.** The study compared aqueductal flow–based pulsatility, expressed by ASV, with pressure-based intracranial pulsatility, expressed by MWA. *A*, Single cardiac-induced ICP wave, the MWA, is determined as the average of amplitudes from single ICP waves during consecutive 6-second time intervals. *B*, ASV is defined as the mean of systolic and diastolic volumetric CSF flow in the aqueduct during 1 cardiac cycle (area under/over the flow curve) minus net aqueductal flow. *C*, The aqueductal flow curve is based on section orientation (*red line*) perpendicular to the aqueduct. *D*, PCMR with manually drawn ROI (*red circle*) defines the aqueduct.

**Table 1: Patient data**

	Idiopathic Normal Pressure Hydrocephalus		
	Total Population Median (Range)	Shunt Group Median (Range)	Conservative Group Median (Range)
No.	21	17	4
Age (yr)	74 (56–84)	74 (56–84)	74 (60–79)
Sex (female/male)	10:11	8:9	2:2
Preoperative clinical state			
NPH score <sup>19</sup>	10 (4–13)	10 (4–13)	11 (9–13)
Duration of symptoms (yr)	2 (0.5–10)	2 (1.0–10.0)	0.8 (0.5–10.0)
Postoperative clinical state 12 mo after surgery			
NPH score	12 (8–15)	12 (8–15)	8

**Note:**—NPH indicates normal pressure hydrocephalus.

tween patients with shunts (shunt group) and conservatively treated patients (conservative group) was performed with an independent samples *t* test. The significance level was set to .05. Statistical analysis was performed by using SPSS Statistics, Version 20 (IBM, Armonk, New York).

## RESULTS

### Patients

Table 1 presents patient data.

Among the 17/21 (81%) patients selected for shunting, 16/17 patients with shunts (94%) improved clinically (shunt responders), while 1 (6%) had no clinical improvement (shunt nonresponder). Among the 12 patients with PCMR after shunting, 11 patients (92%) were responders.

### MR Imaging Data and ICP Scores

Table 2 presents the PCMR-derived ASV and the ventricular volume and aqueduct area before/after shunting and the preoperative ICP scores of the 21 patients with iNPH.

As further illustrated in Fig 2, ASV before surgery did not differ between patients found eligible (shunt group) or noneligible (conservative group) for shunting ( $P = .69$ ).

In the shunt group, ASV was reduced from a median of 111  $\mu\text{L}$  before to a median of 68  $\mu\text{L}$  after surgery ( $P = .01$ , Fig 2A), while the ventricular volume was a median of 137 mL before and a median of 105 mL after surgery ( $P = .001$ , Fig 2B). There was no significant change in the aqueductal area after shunting ( $P = .94$ ).

There was a positive correlation between ASV and ventricular

**Table 2: MRI-derived measures and ICP scores**

	Idiopathic Normal Pressure Hydrocephalus		
	Total Population (n = 21) Median (Range)	Shunt Group (n = 17) Median (Range)	Conservative Group (n = 4) Median (Range)
MRI measures			
Aqueduct stroke volume ( $\mu\text{L}$ )			
Before shunt	111 (26–417)	109 (26–417)	130 (36–163)
After shunt		68 (17–201)	–
Ventricular volume (ml)			
Before shunt	138 (41–266)	137 (41–266)	143 (105–152)
After shunt		105 (34–230)	–
Aqueductal area ( $\text{mm}^2$ )			
Before shunt	14 (9–38)	14 (9–38)	13 (9–36)
After shunt		12 (9–58)	–
ICP scores			
Mean ICP (mm Hg)			
Average	6.1 (–1.8–11.9)	6.1 (–1.8–11.9)	5.8 (3.0–8.8)
Percentage $\geq 15$ mm Hg	0 (0–2)	0 (0–2)	0 (0–0)
Mean ICP wave amplitude (MWA, mm Hg)			
Average	4.5 (3.1–7.9)	4.7 (3.5–7.9)	3.4 (3.1–5.2)
Percentage $\geq 5$ mm Hg	26 (1–100)	27 (2–100)	3 (1–58)

volume before surgery ( $R = 0.60, P = .004$ ; Fig 3A) and after shunting ( $R = 0.73, P = .007$ ; Fig 3B). Moreover, there was also a positive correlation between ASV and aqueduct area before surgery ( $R = 0.58, P = .006$ ). We did not find any significant correlation either between ASV and preoperative normal pressure hydrocephalus scores ( $R = 0.29, P = .21$ ) or between ASV and the duration of iNPH symptoms ( $R = 0.26, P = .26$ ).

While the mean ICP was comparable between the shunt and conservative groups, MWA was elevated in the surgery group (Table 2). There were no correlations between ASV and mean ICP (Fig 4A), or ASV and MWA (Fig 4B). In addition, no correlations between ASV and the percentage of mean ICP of  $\geq 15$  mm Hg or between ASV and the percentage of MWA of  $\geq 5$  mm Hg were observed.

## DISCUSSION

The main observation of this study was that CSF flow-based pulsatility expressed by ASV did not compare with intracranial pressure pulsatility expressed by MWA. On the other hand, ASV correlated with ventricular volume and aqueduct area.

Even though PCMR-based aqueductal flow has previously been extensively investigated and advocated by some as a tool for selection of patients for shunt surgery in iNPH, comparisons with invasive intracranial measurements have been very limited. To our knowledge, there is 1 previous study that compared PCMR-derived ASV with ICP monitoring.<sup>30</sup> This study reported an association between ASV and a temporal subpeak of the ICP wave, but the result was based on a small cohort of 7 patients and the clinical significance of the findings has been disputed.<sup>31</sup>

In our study, a high proportion of the patients in the iNPH cohort had signs of reduced intracranial compliance by increased MWA after overnight ICP monitoring (17/21). MWA of  $\geq 4$  mm Hg or the percentage of MWA of  $\geq 5$  mm Hg in  $\geq 10\%$  of recording time or both were previously reported to predict shunt response in iNPH<sup>19</sup> and have been considered as indicative of impaired intracranial compliance.<sup>21</sup> Using the MWA for selection for shunt treatment gave an excellent shunt

response in 16 of 17 (94%) patients in this study. A positive shunt response can be considered a marker of “true” iNPH, and the high response rate suggests that our study cohort was representative of iNPH and contained few patients with diseases that clinically might present similarly, with similar ASV values.<sup>32</sup> We reproduced previous findings of ASV being elevated in patients with iNPH compared with healthy controls<sup>33</sup> and in contrast to elderly patients in general, in whom ASV has been reported to be reduced.<sup>34</sup> However, ASV varied over a wide range in patients found both eligible and noneligible for surgical shunting on the basis of MWA, and ASV values overlapped between the groups. Accordingly, our results question the clinical utility of the ASV parameter, both with respect to its ability to diagnose iNPH and its predictive value for a clinically favorable shunt response.

There may be several reasons why ASV does not compare with MWA. First, as for all PCMR measurements, ASV is obtained from a time window of just a few minutes, while MWA represents a mean value from an 8-hour time window with registration of several thousand single waves, where frequent physiologic pressure fluctuations during the recording period are typically observed.<sup>19,35</sup> For ASV to be a valid marker of intracranial pulsatility, one would have to assume that the limited time window, from which it is obtained, demonstrates values that are representative of the underlying condition. To our knowledge, no previous observations support such an assumption being valid.

Several factors might influence aqueductal flow. It has previously been suggested that the systolic, inward expansion of the brain against enlarged ventricles is a fundamental cause of increased ASV, before irreversible atrophy occurs.<sup>26</sup> Other contributions might be from the difference in CSF pressure between the third and fourth ventricles, the heart rate, and the aqueductal geometry and mainly at which level flow in the aqueduct is assessed.<sup>36</sup> In this study, a strong association between aqueductal area and ASV was found; however, this does not necessarily imply causality. As pointed out by Chiang et al,<sup>33</sup> it seems reasonable that the aqueduct can adapt to increased flow, similar to the ad-

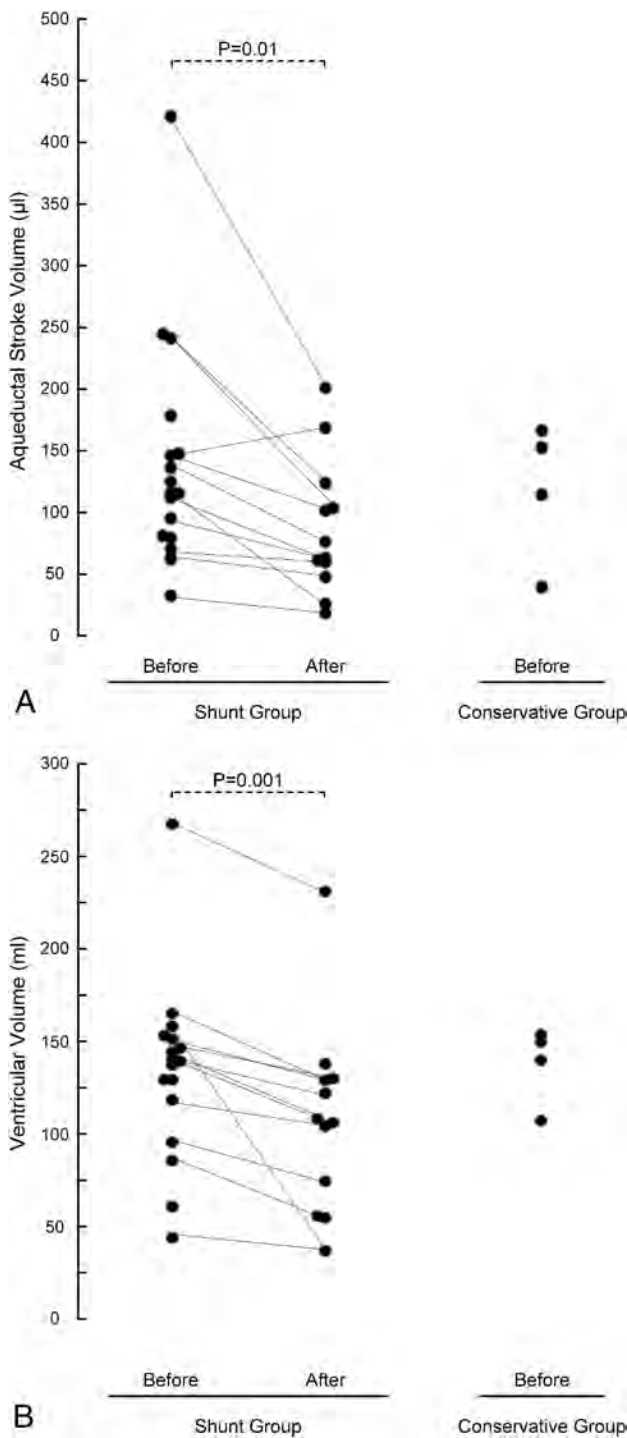


**FIG 2.** ASV (A) and ventricular volume (B) are presented for patients with shunts and iNPH before ( $n = 17$ ) and after ( $n = 12$ ) shunting (surgery group) and for conservatively managed patients with iNPH (conservative group,  $n = 4$ ) before management. Significance levels are presented in the plots.

aptation of the blood vessel lumen area to maintain a wall shear stress within a normal range.<sup>37</sup>

ASV and ventricular volume declined after shunting; this change is consistent with that in previous studies,<sup>14,38</sup> while aqueductal area did not change. While ASV did not reflect the clinical severity of iNPH preshunting and did not compare with any pressure parameters, reduced ASV after shunting might therefore

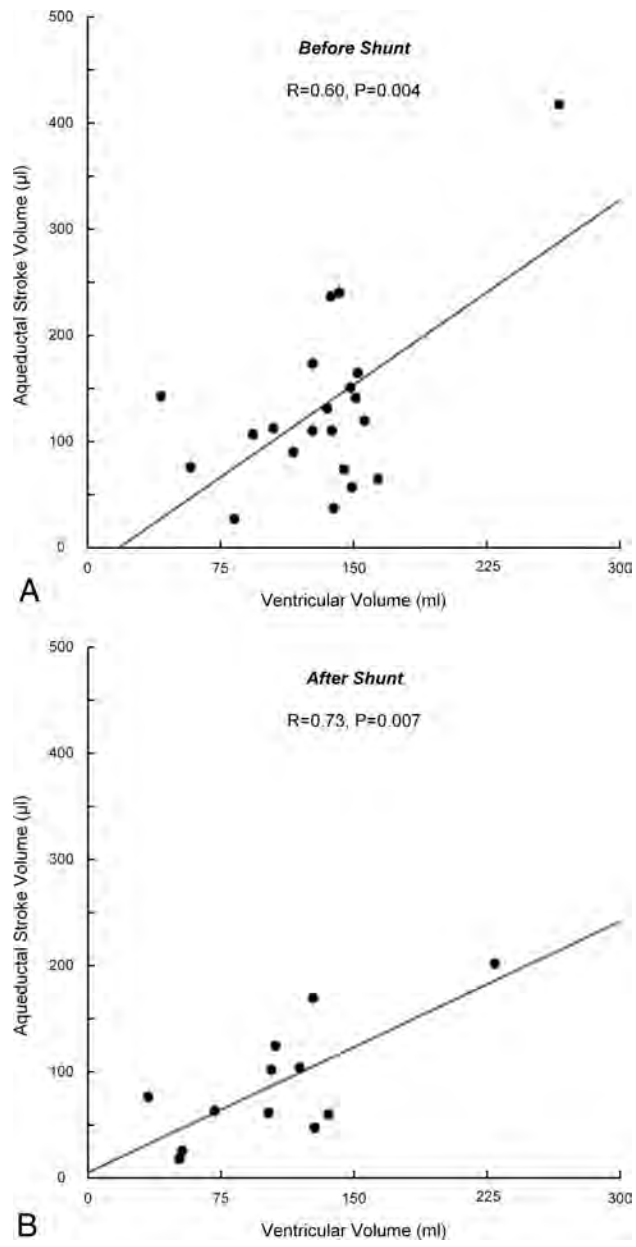


**FIG 3.** For patients with iNPH, the correlations between ASV and ventricular volume before ( $n = 21$ ) (A) and after ( $n = 12$ ) (B) shunt surgery are presented. The Pearson correlation coefficients and significance levels are presented in the plots.

be primarily influenced by reduced ventricular size, rather than reflecting a clinical response, contrary to what has been suggested previously.<sup>14</sup> ASV also correlated positively with ventricular volume before shunting; this correlation confirms previous observations<sup>33</sup> but is contradictory to a more recent study by Chaarani et al.<sup>36</sup> In our study, the statistical significance of this positive correlation was dependent on 1 patient with extreme values, both ASV and ventricular volume.

The lack of correlation between ASV and symptom severity could theoretically be due to a decline in ASV as a sign of long-standing progressive cerebral ischemic changes and atrophy, making the iNPH irreversible, which was postulated by Scollato et al,<sup>39</sup> who followed patients with unshunted iNPH and found a decline in ASV after typically 18–20 months of symptom dura-

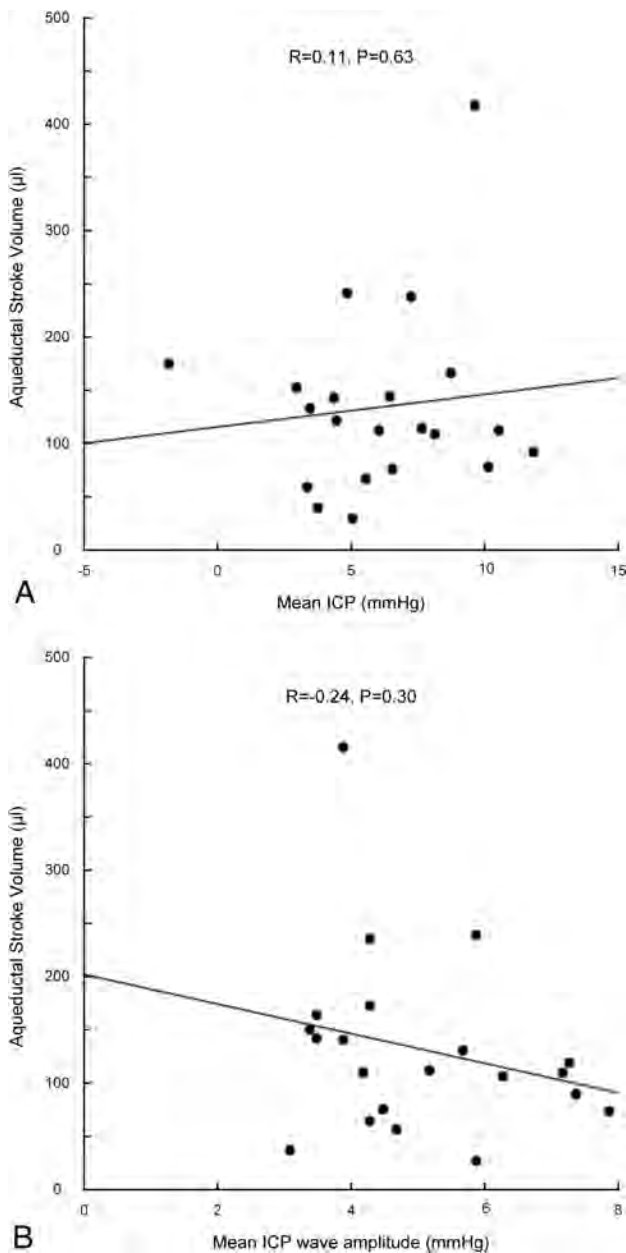


**FIG 4.** For patients with iNPH ( $n = 21$ ), the correlations between ASV and mean ICP (A) and ASV and MWA (B) before shunt surgery are presented. The Pearson correlation coefficients and significance levels are presented in the plots.

tion. We found no such tendency toward ASV being in the lower range among patients with long-standing symptoms; however, the median of symptom duration in our cohort was 2 years, and hence the number of patients with a longer disease history was limited.

While MWA was increased in shunt responders in the present study, as previously reported,<sup>19</sup> no such relationship between the occurrence of so-called B waves and shunt response has been shown.<sup>19,40</sup> In this context, the MWA is computed from the single cardiac-induced ICP waves, while B waves are short-lasting (< 1 minute) increases in static ICP (mean ICP). It has previously been reported that occurrences of B waves and single ICP waves (expressed by the MWA) do not correlate.<sup>41</sup>

### Limitations

Some limitations with this study should be noted. The patients were too few to determine the accuracy of ASV as a diagnostic test in iNPH, especially due to the small number of patients in subgroups such as the conservatively managed group ( $n = 4$ ) and the nonresponsive group with shunts ( $n = 1$ ). A lack of correlations between tested variables may have been a reflection of few study subjects. Finally, the statistical correlations that were demonstrated in the study do not necessarily imply causality between the variables.

The reported accuracy of PCMR volumetric flow measurements in pulsatile flow is within 2.8%,<sup>42</sup> and calculation of aequeductal stroke volume is less sensitive to inaccuracies from manual selection of ROIs than is the calculation of flow velocity.<sup>27,33</sup> However, measurements of aequeductal flow can be influenced by flow aliasing, which is characterized by its apparent high velocity in the opposite direction to the average velocity in the defined area of interest. This was corrected for with the same algorithm applied to all patients, as described in the “Materials and Methods” section.

Another limitation might be the PCMR resolution with a pixel size of  $0.60 \times 0.80 \text{ mm}^2$  in the transverse plane, which is lower than that in the previous study of Bradley et al,<sup>9</sup> supporting ASV as a shunt predictor. The inability to find the utility of ASV in our study could therefore have been influenced by inferior image resolution. However, other studies demonstrating a beneficial use of ASV in iNPH have used a pixel size comparable<sup>8,10,11,13</sup> or inferior<sup>12</sup> to that applied in our study. While reducing the pixel size would reduce the number of pixels from nonmoving tissue elements being included in the ROI defining the aequeduct, the use of larger pixels improves the signal-to-noise ratio and even more by use of a 3T magnetic field strength, as in our study, compared with 1.5T.

A reference ROI can be placed in the adjacent cerebral peduncle to rule out partial volume effect and mass brain movement during aequeductal flow measurement with PCMR. Such a correction was not applied in this study. Contribution from mass brain movement to the ASV value has been reported to be small though<sup>7</sup> and should not be expected to influence the results of the current measurements substantially.

### CONCLUSIONS

In this cohort of patients with iNPH, ASV was not associated with invasively measured ICP scores or symptom severity of iNPH but was correlated with ventricular volume and aequeduct area. The results do not support the use of ASV as a non-invasive tool to diagnose reduced intracranial compliance in patients with iNPH who are candidates for shunting. The composition of the study cohort, with a small fraction of nonresponders to shunting and few conservatively treated patients, did not allow a more direct assessment of ASV as a marker for shunt responsiveness in iNPH.

Disclosures: Kyrre E. Emblem—RELATED: Grant: South-Eastern Norway Regional Health Authority Grant 2013069\*; UNRELATED: Patents (planned, pending or issued): NordicNeuroLabs AS.\* Oliver Geier—UNRELATED: Patents (planned, pending or issued): Siemens Germany, Comments: Patent attorney was paid by Siemens. Noam Alperin—UNRELATED: Stock/Stock Options: Aplerin Nonin-

vative Diagnostics. Per Kristian Eide—RELATED: Stock/Stock Options: dPCom AS, Oslo, Norway, Comments: financial interest (shares) in the software company (dPCom AS, Oslo) manufacturing the software (Sensometrics software) used for analysis of the ICP recordings. \*Money paid to the institution.

## REFERENCES

1. Adams RD, Fisher CM, Hakim S, et al. **Symptomatic occult hydrocephalus with "normal" cerebrospinal-fluid pressure: a treatable syndrome.** *N Engl J Med* 1965;273:117–26
2. Relkin N, Marmarou A, Klinge P, et al. **Diagnosing idiopathic normal-pressure hydrocephalus.** *Neurosurgery* 2005;57:S4–16; discussion ii–v
3. Krauss JK, Droste DW, Vach W, et al. **Cerebrospinal fluid shunting in idiopathic normal-pressure hydrocephalus of the elderly: effect of periventricular and deep white matter lesions.** *Neurosurgery* 1996;39:292–99; discussion 299–300
4. Vanneste JA. **Three decades of normal pressure hydrocephalus: are we wiser now?** *J Neurol Neurosurg Psychiatry* 1994;57:1021–25
5. Hebb AO, Cusimano MD. **Idiopathic normal pressure hydrocephalus: a systematic review of diagnosis and outcome.** *Neurosurgery* 2001;49:1166–84; discussion 1184–86
6. Bradley WG Jr, Whitemore AR, Kortman KE, et al. **Marked cerebrospinal fluid void: indicator of successful shunt in patients with suspected normal-pressure hydrocephalus.** *Radiology* 1991;178:459–66
7. Al-Zain FT, Rademacher G, Meier U, et al. **The role of cerebrospinal fluid flow study using phase contrast MR imaging in diagnosing idiopathic normal pressure hydrocephalus.** *Acta Neurochir Suppl* 2008;102:119–23
8. Kim DS, Choi JU, Huh R, et al. **Quantitative assessment of cerebrospinal fluid hydrodynamics using a phase-contrast cine MR image in hydrocephalus.** *Childs Nerv Syst* 1999;15:461–67
9. Bradley WG Jr, Scalzo D, Queral J, et al. **Normal-pressure hydrocephalus: evaluation with cerebrospinal fluid flow measurements at MR imaging.** *Radiology* 1996;198:523–29
10. Sharma AK, Gaikwad S, Gupta V, et al. **Measurement of peak CSF flow velocity at cerebral aqueduct, before and after lumbar CSF drainage, by use of phase-contrast MRI: utility in the management of idiopathic normal pressure hydrocephalus.** *Clin Neurol Neurosurg* 2008;110:363–68
11. Luetmer PH, Huston J, Friedman JA, et al. **Measurement of cerebrospinal fluid flow at the cerebral aqueduct by use of phase-contrast magnetic resonance imaging: technique validation and utility in diagnosing idiopathic normal pressure hydrocephalus.** *Neurosurgery* 2002;50:534–43; discussion 543–44
12. Abbey P, Singh P, Khandelwal N, et al. **Shunt surgery effects on cerebrospinal fluid flow across the aqueduct of Sylvius in patients with communicating hydrocephalus.** *J Clin Neurosci* 2009;16:514–18
13. El Sankari S, Fichten A, Gondry-Jouet C, et al. **Correlation between tap test and CSF aqueductal stroke volume in idiopathic normal pressure hydrocephalus.** *Acta Neurochir Suppl* 2012;113:43–46
14. Scollato A, Gallina P, Gautam B, et al. **Changes in aqueductal CSF stroke volume in shunted patients with idiopathic normal-pressure hydrocephalus.** *AJNR Am J Neuroradiol* 2009;30:1580–86
15. Delwel EJ, de Jong DA, Avezaat CJ. **The prognostic value of clinical characteristics and parameters of cerebrospinal fluid hydrodynamics in shunting for idiopathic normal pressure hydrocephalus.** *Acta Neurochir (Wien)* 2005;147:1037–42; discussion 1042–43
16. Bateman GA, Loiselle AM. **Can MR measurement of intracranial hydrodynamics and compliance differentiate which patient with idiopathic normal pressure hydrocephalus will improve following shunt insertion?** *Acta Neurochir (Wien)* 2007;149:455–62; discussion 462
17. Kahlon B, Annertz M, Stahlberg F, et al. **Is aqueductal stroke volume, measured with cine phase-contrast magnetic resonance imaging scans useful in predicting outcome of shunt surgery in suspected normal pressure hydrocephalus?** *Neurosurgery* 2007;60:124–29; discussion 129–30
18. Dixon GR, Friedman JA, Luetmer PH, et al. **Use of cerebrospinal fluid flow rates measured by phase-contrast MR to predict outcome of ventriculoperitoneal shunting for idiopathic normal-pressure hydrocephalus.** *Mayo Clin Proceed* 2002;77:509–14
19. Eide PK, Sorteberg W. **Diagnostic intracranial pressure monitoring and surgical management in idiopathic normal pressure hydrocephalus: a 6-year review of 214 patients.** *Neurosurgery* 2010;66:80–91
20. Eide PK. **Intracranial pressure parameters in idiopathic normal pressure hydrocephalus patients treated with ventriculo-peritoneal shunts.** *Acta Neurochir (Wien)* 2006;148:21–29; discussion 29
21. Eide PK, Sorteberg W. **Association among intracranial compliance, intracranial pulse pressure amplitude and intracranial pressure in patients with intracranial bleeds.** *Neurol Res* 2007;29:798–802
22. González-Darder JM, Barcia-Salorio JL. **Pulse amplitude and volume-pressure relationships in experimental hydrocephalus.** *Acta Neurochir (Wien)* 1989;97:166–70
23. Black PM, Ojemann RG, Tzouras A. **CSF shunts for dementia, incontinence, and gait disturbance.** *Clin Neurosurg* 1985;32:632–51
24. Bateman GA. **Vascular compliance in normal pressure hydrocephalus.** *AJNR Am J Neuroradiol* 2000;21:1574–85
25. Graff-Radford NR, Godersky JC, Jones MP. **Variables predicting surgical outcome in symptomatic hydrocephalus in the elderly.** *Neurology* 1989;39:1601–04
26. Greitz D. **Radiological assessment of hydrocephalus: new theories and implications for therapy.** *Neurosurg Rev* 2004;27:145–65; discussion 166–67
27. Nitz WR, Bradley WG Jr, Watanabe AS, et al. **Flow dynamics of cerebrospinal fluid: assessment with phase-contrast velocity MR imaging performed with retrospective cardiac gating.** *Radiology* 1992;183:395–405
28. Yushkevich PA, Piven J, Hazlett HC, et al. **User-guided 3D active contour segmentation of anatomical structures: significantly improved efficiency and reliability.** *Neuroimage* 2006;31:1116–28
29. Zhu SC, Yuille AY. **Region competition: unifying snakes, region growing, and Bayes/MDL for multiband image segmentation.** *IEEE Trans Pattern Anal Mach Intell* 1996;18:884–900
30. Hamilton R, Baldwin K, Fuller J, et al. **Intracranial pressure pulse waveform correlates with aqueductal cerebrospinal fluid stroke volume.** *J Appl Physiol* 2012;113:1560–66
31. Tain RW, Alperin N. **Intracranial pressure dynamics are not linked to aqueductal cerebrospinal fluid stroke volume.** *J Appl Physiol* 2013;114:1645
32. Bateman GA, Levi CR, Schofield P, et al. **The pathophysiology of the aqueduct stroke volume in normal pressure hydrocephalus: can comorbidity with other forms of dementia be excluded?** *Neuroradiology* 2005;47:741–48
33. Chiang WW, Takoudis CG, Lee SH, et al. **Relationship between ventricular morphology and aqueductal cerebrospinal fluid flow in healthy and communicating hydrocephalus.** *Invest Radiol* 2009;44:192–99
34. Stoquart-ElSankari S, Baledent O, Gondry-Jouet C, et al. **Aging effects on cerebral blood and cerebrospinal fluid flows.** *J Cereb Blood Flow Metab* 2007;27:1563–72
35. Wagshul ME, Eide PK, Madsen JR. **The pulsating brain: a review of experimental and clinical studies of intracranial pulsatility.** *Fluids Barriers CNS* 2011;8:5
36. Chaarani B, Capel C, Zmudka J, et al. **Estimation of the lateral ventricles volumes from a 2D image and its relationship with cerebrospinal fluid flow.** *Biomed Res Int* 2013;2013:215989
37. Reneman RS, Arts T, Hoeks AP. **Wall shear stress: an important determinant of endothelial cell function and structure—in the arterial system in vivo. Discrepancies with theory.** *J Vasc Res* 2006;43:251–69
38. Singer OC, Melber J, Hattingen E, et al. **MR volumetric changes after diagnostic CSF removal in normal pressure hydrocephalus.** *J Neurol* 2012;259:2440–46
39. Scollato A, Tenenbaum R, Bahl G, et al. **Changes in aqueductal CSF**

- stroke volume and progression of symptoms in patients with unshunted idiopathic normal pressure hydrocephalus. *AJNR Am J Neuroradiol* 2008;29:192–97
40. Stephensen H, Andersson N, Eklund A, et al. **Objective B wave analysis in 55 patients with non-communicating and communicating hydrocephalus.** *J Neurol Neurosurg Psychiatry* 2005;76:965–70
41. Eide PK, Sorteberg W. **Simultaneous measurements of intracranial pressure parameters in the epidural space and in brain parenchyma in patients with hydrocephalus.** *J Neurosurg* 2010;113:1317–25
42. Frayne R, Steinman DA, Ethier CR, et al. **Accuracy of MR phase contrast velocity measurements for unsteady flow.** *J Magn Reson Imaging* 1995;5:428–31

## Intracranial Pressure versus Phase-Contrast MR Imaging for Normal Pressure Hydrocephalus

The article by Ringstad et al,<sup>1</sup> in this issue of the *American Journal of Neuroradiology* suggests that invasive intracranial pressure monitoring is a better way to select patients for shunting for normal pressure hydrocephalus (NPH) than phase-contrast MR imaging. The authors advocated placing an intracranial pressure (ICP) monitor through a burr-hole into the brain parenchyma and measuring the mean amplitude of the ICP waves (MWA) for 8 hours while the patient is sleeping. Phase-contrast MR imaging (PCMR), on the other hand, is performed noninvasively in a few minutes to determine the aqueductal CSF stroke volume (ASV).<sup>2</sup> This technique, when properly performed, allows the determination of the ASV, which is the average of the cranio-caudal and caudocranial CSF flow volumes during systole and diastole, respectively.<sup>3</sup>

The basis of the elevated MWA is decreased intracranial compliance (ie, a stiffer brain, which is 1 feature of NPH). The basis of an elevated ASV is a combination of enlarged ventricles and no atrophy. Because NPH eventually leads to atrophy, the ASV decreases and the patient is less likely to respond to ventriculoperitoneal shunting.

The authors divided 21 patients with clinical NPH into 2 groups: “shunt” ( $n = 17$ ) and “conservative” ( $n = 4$ ) based on MWA elevation. Sixteen of the 17 patients with shunts responded favorably during a year of follow-up, improving their NPH scores from 10 to 12 (zero being the worst and 15 being the best), while the 4 conservative patients without shunts worsened from 11 to 8 (Table 1). The authors used their finding that the ASV was higher in the unshunted conservative group (Table 2) to denigrate the value of PCMR. An alternate explanation of these data might be that MWA elevation was not useful in distinguishing the patients who should have been shunted from those who would not have benefited from a shunt (ie, their conservative group). On the basis of the elevated ASV, in fact, the patients in the conservative group with NPH symptoms might have benefited from a shunt rather than having their conditions deteriorate across time. As pointed out by the authors, with only 4 patients in the conservative group, this comparison is hardly statistically significant.

Our group has been using the finding of hyperdynamic CSF flow through the aqueduct as a predictor of shunt-responsive

NPH for >30 years. In the early days of MR imaging (1983–1984), we used a marked aqueductal CSF flow void on conventional proton-attenuation weighted images without flow compensation to select patients for shunting. We found the association of hyperdynamic CSF flow and shunt responsiveness significant ( $P < .003$ ).<sup>4</sup>

With the subsequent ubiquitous use of flow compensation and fast spin-echo (with the rephasing effects of the multiple 180° radiofrequency pulses), the CSF flow void sign became less sensitive (though it still remains highly specific). This result led us in the early 1990s to use PCMR to determine the volume of CSF flowing up or down over the cardiac cycle (ie, the ASV).<sup>2</sup> In the mid-1990s, we evaluated 19 patients with symptoms of NPH who were subsequently shunted.<sup>3</sup> All 13 patients with an ASV of >42 uL on that particular MR imaging system responded to shunting, while only half of the 6 patients with an ASV of <42 uL responded (ie, the ASV as we measured it had a 100% positive predictive value). While we initially thought that all the patients with ASVs of <42 uL had atrophy, Scollato et al<sup>5</sup> pointed out that some of these patients may, in fact, have been very early in their disease because their ASV 6 months later was increased.

Ringstad et al<sup>1</sup> pointed out that some investigators have been unsuccessful in using the ASV to discriminate those patients who will respond from those who will not respond to shunting for NPH. Unfortunately, not everyone uses the same technique. Our technique<sup>2,3</sup> uses a  $512 \times 512$  matrix over a 16-cm FOV, yielding pixels 0.312 mm on a side. Larger pixels (like the  $0.6 \times 0.8$  mm used in the present study) are more susceptible to partial volume averaging of stationary tissue in the surrounding midbrain. This susceptibility may explain why Ringstad et al<sup>1</sup> used a velocity-encoding factor (VENC) of only 10 cm/s, whereas we find that we need a VENC of 10, 20, and 30 cm/s to maximize accuracy (lower VENC) and avoid aliasing (higher VENC). While the authors fit the data to a sinusoidal curve to remove aliasing when present, this fitting requires manual processing, while our technique using 3 VENCs can be processed with routine flow-analysis software (eg, ReportCARD; GE Healthcare, Milwaukee, Wisconsin; or NOVA; VasSol, River Forest, Illinois).

Some investigators have been critical of the specific value of

42- $\mu$ L ASV as a discriminator; however, this measurement is unfortunately machine- and software-dependent. To diagnose hyperdynamic CSF flow, one needs to first determine the normal ASV in the elderly population. Thus, when we start using a new MR imaging system for this determination, we always perform the measurement on 10–20 elderly patients without enlarged ventricles. We then look for a volumetric flow rate of twice the normal rate to diagnose hyperdynamic CSF flow. We have found that this correlates with shunt-responsive NPH in appropriately symptomatic patients.

In regard to using patients without enlarged ventricles to determine the normal ASV, patients who eventually develop NPH often have had enlarged ventricles for many years before symptom onset.<sup>6</sup> We call this “pre-NPH,”<sup>6</sup> while Kato et al<sup>7</sup> labeled it “asymptomatic ventricular enlargement with features of idiopathic NPH on MR imaging.”

In our institution, our neurologists and neurosurgeons use PCMR and a high-volume tap test to determine which patients should be shunted for symptomatic NPH. However, screening techniques vary around the world. Some sites go beyond the outpatient tap test and use external lumbar drainage, which is a 3-day in-patient procedure in which 10 mL of CSF is removed every hour via a lumbar catheter with gait reassessment at the end.<sup>8</sup> In Sweden, the saline infusion technique is often used to determine increased resistance to inflow.<sup>9</sup> In Japan, a midcoronal MR imaging scan is used to look for the disproportionately enlarged subarachnoid space hydrocephalus (DESH) pattern, which includes an Evans ratio of  $>0.3$ , enlarged Sylvian cisterns, and a tight superior convexity subarachnoid space.<sup>10</sup> In fact, Ishikawa et al<sup>11</sup> have reported that the tap test adds nothing to the selection of patients with NPH for shunting if a DESH pattern is present. Since learning of the DESH pattern 4 years ago, we have added coronal imaging to our rule out NPH protocol. Unfortunately, we have had less success with the DESH sign than the Japanese investigators, with DESH correlating with neither ASV nor shunt response.

In summary, the diagnosis of shunt-responsive NPH seems to vary by region and specialty. As demonstrated by Ringstad et al,<sup>1</sup> neurosurgeons seem to be comfortable with placing an ICP monitor in the brain to measure compliance. If you are a radiologist, PCMR to measure the ASV may be the preferred technique. While these tests are measuring different properties of shunt-responsive NPH, I suspect, given the choice, that most patients would prefer the less invasive evaluation.

## REFERENCES

1. Ringstad G, Emblem KE, Geier O, et al. **Aqueductal stroke volume: comparisons with intracranial pressure scores in idiopathic normal pressure hydrocephalus.** *AJNR Am J Neuroradiol* 2015 May 14. [Epub ahead of print] CrossRef Medline
2. Nitz WR, Bradley WG Jr, Watanabe AS, et al. **Flow dynamics of cerebrospinal fluid: assessment with phase-contrast velocity MR imaging performed with retrospective cardiac gating.** *Radiology* 1992; 183:395–405 CrossRef Medline
3. Bradley WG Jr, Scalzo D, Queralt J, et al. **Normal-pressure hydrocephalus: evaluation with cerebrospinal fluid flow measurements at MR imaging.** *Radiology* 1996;198:523–29 CrossRef Medline
4. Bradley WG Jr, Whittemore AR, Kortman KE, et al. **Marked cerebrospinal fluid void: indicator of successful shunt in patients with suspected normal-pressure hydrocephalus.** *Radiology* 1991;178: 459–66 CrossRef Medline
5. Scollato A, Tenenbaum R, Bahl G, et al. **Changes in aqueductal CSF stroke volume and progression of symptoms in patients with unshunted idiopathic normal pressure hydrocephalus.** *AJNR Am J Neuroradiol* 2008;29:192–97 CrossRef Medline
6. Bradley WG Jr, Bahl G, Alksne JF. **Idiopathic normal pressure hydrocephalus may be a “two hit” disease: benign external hydrocephalus in infancy followed by deep white matter ischemia in late adulthood.** *J Magn Reson Imaging* 2006;24:747–55 CrossRef Medline
7. Kato T, Iseki C, Takahashi Y, et al. **iNPH (idiopathic normal pressure hydrocephalus) and AVIM (asymptomatic ventriculomegaly with features of iNPH on MRI)** [in Japanese]. *Rinsho Shinkeigaku* 2010;50:963–65 CrossRef Medline
8. Marmarou A, Young HF, Aygok GA, et al. **Diagnosis and management of idiopathic normal-pressure hydrocephalus: a prospective study in 151 patients.** *J Neurosurg* 2005;102:987–97 CrossRef Medline
9. Qvarlander S, Malm J, Eklund A. **CSF dynamic analysis of a predictive pulsatility-based infusion test for normal pressure hydrocephalus.** *Med Biol Eng Comput* 2014;52:75–85 CrossRef Medline
10. Hashimoto M, Ishikawa M, Mori E, et al; Study of INPH on Neurological Improvement (SINPHONI). **Diagnosis of idiopathic normal pressure hydrocephalus is supported by MRI-based scheme: a prospective cohort study.** *Cerebrospinal Fluid Res* 2010;7:18 CrossRef Medline
11. Ishikawa M, Hashimoto M, Mori E, et al. **The value of the cerebrospinal fluid tap test for predicting shunt effectiveness in idiopathic normal pressure hydrocephalus.** *Fluids Barriers CNS* 2012;9:1 CrossRef Medline

W.G. Bradley Jr

Department of Radiology  
University of California San Diego Health System  
San Diego, California

<http://dx.doi.org/10.3174/ajnr.A4507>

## REPLY:

We thank Dr Bradley for the Commentary<sup>1</sup> on our article<sup>2</sup> entitled “Aqueductal Stroke Volume: Comparisons with Intracranial Pressure Scores in Idiopathic Normal Pressure Hydrocephalus.”

The purpose behind using aqueductal stroke volume (ASV) as a predictor of shunt response in normal pressure hydrocephalus (NPH) should be providing additional value to already measurable sizes such as ventricular volume and thereby differentiating NPH from other types of dementia not expected to benefit from shunt surgery. Bradley<sup>3</sup> and Greitz<sup>4</sup> have proposed that the pathophysiology behind the increased ASV in NPH is due to compression of the ventricles by the increased inward expansion of the arterial pulse pressure. Indeed, increased intracranial pressure pulsatility is a strong indicator of reduced intracranial compliance,<sup>5</sup> which is thought to be a main underlying mechanism of NPH.<sup>6</sup> However, the physiologic explanation for a possible link between the magnitude of ASV and NPH has been called into question.<sup>7</sup> Our comparisons of ASV with intracranial pressure (ICP) and ICP amplitudes should, therefore, be highly relevant.

A noninvasive tool for selecting patients with NPH for surgery would certainly be preferable, provided that the method is not inferior to invasive methods in terms of overall patient outcome. The use of ASV for this purpose was proposed by Bradley et al,<sup>8</sup> when a beneficial shunt response was seen in 12/12 shunt responders with ASV above 42  $\mu\text{L}$ . ASV was also measured in 24 additional patients who were not shunted, but the range and distribution of these measurements above/below the 42  $\mu\text{L}$  threshold were not reported in the article. While some studies have supported the use of aqueductal flow rate for the diagnosis of NPH<sup>9,10</sup> and related flow rate to a possible shunt response,<sup>11,12</sup> few other studies have reproduced the beneficial utility of ASV in identifying patients likely to respond to surgical shunting,<sup>13,14</sup> and the diagnostic sensitivity and specificity of the method have never been assessed, to our knowledge. In contradistinction, several studies have not been able to demonstrate any association between a clinical improvement after shunting and increased ASV<sup>15-17</sup> or flow rate.<sup>18</sup> ASV has, however, been found to be elevated in several forms of dementia<sup>19</sup> and was strongly correlated with ventricular morphology.<sup>20</sup>

Our study incorporated a previously validated methodology for predicting shunt response by invasive ICP monitoring as well as measurements of ASV by phase-contrast MR imaging to allow direct comparison between 2 proposed predictors of shunt response. The shunt response rate in the study was 94%, indicating “true” NPH. The results indicate that ASV is related to ventricular size and aqueductal area, rather than reflecting the underlying pathophysiology of reduced intracranial compliance and increased pulsatile ICP or symptom severity. These results suggest that the ASV parameter should be used with care, even though ASV is measured noninvasively. In particular, the inability of a test to identify patients who should not undergo surgical shunting is problematic. The current treatment of NPH is brain surgery (shunt surgery), with a risk of severe complications such as cerebral bleeds and infection.<sup>21-25</sup> Deadly outcome of shunting may be anticipated in approximately 1/100 patients, whereas less serious problems related to shunting are

observed in as many as one-third of shunted patients. In a previous report of shunting of 130 patients, a threshold of ICP wave amplitudes of  $>4$  mm Hg on average and  $>5$  mm Hg in  $>10\%$  of recording time had a positive predictive value of 0.93 and negative predictive value of 0.91.<sup>22</sup> Thus, among patients with NPH with an ICP wave amplitude above the threshold, shunt response was seen in 9/10 patients, while it was seen in 1/10 patients with an ICP wave amplitude below the threshold.

We do not share Dr Bradley’s view that all studies opposing the use of ASV have failed to demonstrate its beneficial use due to technical flaws. Although the image resolution of our method of  $0.6 \times 0.8$  mm<sup>2</sup> has allowed partial volume averaging at the outer border of the aqueduct, the large aqueductal lumen area associated with hydrocephalus (in our study, the median area was 14 mm<sup>2</sup>) should contain a sufficient number of voxels to derive reliable measurements. It is therefore unlikely that the pixel size used in this study has resulted in large errors that are on the order of the ASV magnitude. Moreover, the effect of any residual flow aliasing was further minimized by a standard aliasing postprocessing correction approach.

Which phase-contrast MR imaging (PCMR) is optimal is a matter of debate. In the now almost 20-year-old study from 1996,<sup>8</sup> still referred to as the main promoter study for the use of ASV in NPH,<sup>1</sup> the loss of a signal-to-noise ratio from high image resolution had to be (partially) compensated for by reducing the bandwidth and by using a half-Fourier algorithm. Still, the signal-to-noise ratio appeared to be substantial, and readers with special interest in the field are encouraged to retrospectively assess the original PCMR images presented in the article. Additionally, the compensations for loss of the signal-to-noise ratio resulted in a scan time of 14 minutes. From our experience, impairments due to motion artifacts may be a challenge when a 14-minute scan time is applied in patients with cognitive decline. In comparison with our study, the examinations may also have been affected by a lower magnetic field strength (1.5T versus 3T) and an inferior temporal resolution (18 frames per cardiac cycle versus 30–40).

Obviously, the ASV threshold level of 42  $\mu\text{L}$  established from the 1996 study has been abandoned.<sup>1</sup> It is now stated in the Commentary<sup>1</sup> to our article that ASV can be measured on any MR imaging scanner in “10–20 elderly patients without enlarged ventricles,” and by doubling this calibration value, one would identify shunt-responsive NPH. In our opinion, this approach seems somewhat arbitrary, and we await the scientific basis for this general recommendation.

Finally, we agree with Dr Bradley that methods for selecting patients with NPH to undergo surgical shunting vary by region and specialty. However, ASV measurements have never gained widespread acceptance. Because of the noninvasive nature of this tool, its use would certainly have been embraced by many if the evidence for its utility was convincing. It would have been most welcome and convenient to the neurologic community if the complex pathophysiology deciding the shunt response in NPH could be described by 1 single CSF flow parameter obtained from a few-minutes-long time interval. Our study, unfortunately, suggests this is not the case.

## REFERENCES

1. Bradley WG. Intracranial pressure versus phase-contrast MRI for normal pressure hydrocephalus. *AJNR Am J Neuroradiol*. In press
2. Ringstad G, Emblem KE, Geier O, et al. Aqueductal stroke volume: comparisons with intracranial pressure scores in idiopathic nor-

- mal pressure hydrocephalus. *AJNR Am J Neuroradiol* 2015 May 14. [Epub ahead of print] CrossRef Medline
3. Bradley WG Jr. **MR prediction of shunt response in NPH: CSF morphology versus physiology.** *AJNR Am J Neuroradiol* 1998;19:1285–86 Medline
  4. Greitz D. **Radiological assessment of hydrocephalus: new theories and implications for therapy.** *Neurosurg Rev* 2004;27:145–65; discussion 166–67 CrossRef Medline
  5. Botta S, Poulidakos D, Kurtcuoglu V. **Phantom model of physiologic intracranial pressure and cerebrospinal fluid dynamics.** *IEEE Trans Biomed Eng* 2012;59:1532–38 CrossRef Medline
  6. Wagshul ME, Eide PK, Madsen JR. **The pulsating brain: a review of experimental and clinical studies of intracranial pulsatility.** *Fluids Barriers CNS* 2011;8:5 CrossRef Medline
  7. Tain RW, Alperin N. **Intracranial pressure dynamics are not linked to aqueductal cerebrospinal fluid stroke volume.** *J Appl Physiol* (1985) 2013;114:1645 CrossRef Medline
  8. Bradley WG Jr, Scalzo D, Queralto J, et al. **Normal-pressure hydrocephalus: evaluation with cerebrospinal fluid flow measurements at MR imaging.** *Radiology* 1996;198:523–29 CrossRef Medline
  9. Al-Zain FT, Rademacher G, Meier U, et al. **The role of cerebrospinal fluid flow study using phase contrast MR imaging in diagnosing idiopathic normal pressure hydrocephalus.** *Acta Neurochir Suppl* 2008;102:119–23 CrossRef Medline
  10. Luetmer PH, Huston J, Friedman JA, et al. **Measurement of cerebrospinal fluid flow at the cerebral aqueduct by use of phase-contrast magnetic resonance imaging: technique validation and utility in diagnosing idiopathic normal pressure hydrocephalus.** *Neurosurgery* 2002;50:534–43; discussion 543–44 Medline
  11. Sharma AK, Gaikwad S, Gupta V, et al. **Measurement of peak CSF flow velocity at cerebral aqueduct, before and after lumbar CSF drainage, by use of phase-contrast MRI: utility in the management of idiopathic normal pressure hydrocephalus.** *Clin Neurol Neurosurg* 2008;110:363–68 CrossRef Medline
  12. El Sankari S, Fichten A, Gondry-Jouet C, et al. **Correlation between tap test and CSF aqueductal stroke volume in idiopathic normal pressure hydrocephalus.** *Acta Neurochir Suppl* 2012;113:43–46 CrossRef Medline
  13. Abbey P, Singh P, Khandelwal N, et al. **Shunt surgery effects on cerebrospinal fluid flow across the aqueduct of Sylvius in patients with communicating hydrocephalus.** *J Clin Neurosci* 2009;16:514–18 CrossRef Medline
  14. Scollato A, Gallina P, Gautam B, et al. **Changes in aqueductal CSF stroke volume in shunted patients with idiopathic normal-pressure hydrocephalus.** *AJNR Am J Neuroradiol* 2009;30:1580–86 CrossRef Medline
  15. Algin O, Hakyemez B, Parlak M. **The efficiency of PC-MRI in diagnosis of normal pressure hydrocephalus and prediction of shunt response.** *Acad Radiol* 2010;17:181–87 CrossRef Medline
  16. Kahlon B, Annertz M, Ståhlberg F, et al. **Is aqueductal stroke volume, measured with cine phase-contrast magnetic resonance imaging scans useful in predicting outcome of shunt surgery in suspected normal pressure hydrocephalus?** *Neurosurgery* 2007;60:124–29; discussion 129–30 Medline
  17. Bateman GA, Loiseau AM. **Can MR measurement of intracranial hydrodynamics and compliance differentiate which patient with idiopathic normal pressure hydrocephalus will improve following shunt insertion?** *Acta Neurochir* 2007;149:455–62; discussion 462 CrossRef Medline
  18. Dixon GR, Friedman JA, Luetmer PH, et al. **Use of cerebrospinal fluid flow rates measured by phase-contrast MR to predict outcome of ventriculoperitoneal shunting for idiopathic normal-pressure hydrocephalus.** *Mayo Clinic Proc* 2002;77:509–14 CrossRef Medline
  19. Bateman GA, Levi CR, Schofield P, et al. **The pathophysiology of the aqueduct stroke volume in normal pressure hydrocephalus: can comorbidity with other forms of dementia be excluded?** *Neuroradiology* 2005;47:741–48 CrossRef Medline
  20. Chiang WW, Takoudis CG, Lee SH, et al. **Relationship between ventricular morphology and aqueductal cerebrospinal fluid flow in healthy and communicating hydrocephalus.** *Invest Radiol* 2009;44:192–99 CrossRef Medline
  21. Hebb AO, Cusimano MD. **Idiopathic normal pressure hydrocephalus: a systematic review of diagnosis and outcome.** *Neurosurgery* 2001;49:1166–84; discussion 1184–86 Medline
  22. Eide PK, Sorteberg W. **Diagnostic intracranial pressure monitoring and surgical management in idiopathic normal pressure hydrocephalus: a 6-year review of 214 patients.** *Neurosurgery* 2010;66:80–91 CrossRef Medline
  23. Stranjalis G, Kalamatianos T, Koutsarnakis C, et al. **Twelve-year hospital outcomes in patients with idiopathic hydrocephalus.** *Acta Neurochir Suppl* 2012;113:115–17 CrossRef Medline
  24. Hommelstad J, Madsø A, Eide PK. **Significant reduction of shunt infection rate in children below 1 year of age after implementation of a perioperative protocol.** *Acta Neurochir (Wien)* 2013;155:523–31 CrossRef Medline
  25. Tisell M, Hellström P, Ahl-Börjesson G, et al. **Long-term outcome in 109 adult patients operated on for hydrocephalus.** *Br J Neurosurg* 2006;20:214–21 CrossRef Medline

**G. Ringstad**

Department of Radiology

**K.E. Emblem**

The Intervention Centre

**O. Geier**

The Intervention Centre

Oslo University Hospital–Rikshospitalet

Oslo, Norway

**N. Alperin**

University of Miami Miller School of Medicine

Miami, Florida

**P.K. Eide**

Department of Neurosurgery

Oslo University Hospital–Rikshospitalet

Oslo, Norway

# Cerebral Microbleeds, CSF p-Tau, and Cognitive Decline: Significance of Anatomic Distribution

G.C. Chiang, J.C. Cruz Hernandez, K. Kantarci, C.R. Jack Jr, and M.W. Weiner; for the Alzheimer's Disease Neuroimaging Initiative



## ABSTRACT

**BACKGROUND AND PURPOSE:** Cerebral microbleeds are associated with aging, hypertension, and Alzheimer disease. Microbleeds in a lobar distribution are believed to reflect underlying amyloid angiopathy, whereas microbleeds in the deep gray matter and infratentorial brain are commonly seen with hypertension. However, it is unknown how microbleeds in either distribution are related to Alzheimer pathogenesis. The purpose of this analysis was to test whether lobar and deep gray/infratentorial microbleeds demonstrate differential associations with CSF amyloid- $\beta$  and phosphorylated tau 181 protein levels and longitudinal cognitive decline.

**MATERIALS AND METHODS:** A total of 626 subjects (151 cognitively normal, 389 with mild cognitive impairment, and 86 with Alzheimer disease) from the Alzheimer's Disease Neuroimaging Initiative who had undergone 3T MR imaging and lumbar puncture were included in the analysis. The number and location of microbleeds were assessed visually. Associations between lobar or deep gray/infratentorial microbleeds with CSF amyloid- $\beta$  levels, abnormal CSF phosphorylated tau 181 protein levels, and longitudinal cognitive decline were assessed by using ordinary least-squares, logistic, and mixed-effects regression models while adjusting for covariates.

**RESULTS:** Having  $\geq 3$  lobar microbleeds was associated with lower levels of CSF amyloid- $\beta$  ( $P = .001$ ). After adjusting for CSF amyloid- $\beta$  level, lobar microbleeds were independently associated with a higher likelihood of having an abnormal CSF phosphorylated tau 181 protein level ( $P = .004$ ). Lobar microbleeds were associated with accelerated longitudinal cognitive decline ( $P = .007$ ). Deep gray/infratentorial microbleeds revealed no significant associations.

**CONCLUSIONS:** The distribution of microbleeds revealed different associations with amyloid- $\beta$  and phosphorylated tau 181 protein levels and cognition. Lobar and deep gray/infratentorial microbleeds should be considered separately with regard to Alzheimer disease pathogenesis.

**ABBREVIATIONS:** A $\beta$  = amyloid- $\beta$ ; AD = Alzheimer disease; ADAS = Alzheimer Disease Assessment Scale; ADNI = Alzheimer's Disease Neuroimaging Initiative; APOE = apolipoprotein E; p-tau = phosphorylated tau 181 protein

Cerebral microbleeds, typically associated with aging, hypertension, and Alzheimer disease (AD), are common findings on gradient recalled-echo and susceptibility-weighted MR imaging sequences. In a population-based study in which a gradient recalled-echo sequence at 1.5T was used, approximately 36% of

the people  $>80$  years old were found to have microbleeds, compared with only 7% of the people who were 45–50 years old.<sup>1</sup> In a systematic review of studies that used echo-planar and gradient recalled-echo sequences at 0.5–3T, hypertensive individuals were reported to be 4 times more likely than those in the general population to have microbleeds,<sup>2</sup> particularly in association with other signs of small-vessel disease, such as white matter hyperintensities and lacunar infarcts.<sup>3,4</sup> In a review of multiple studies that used gradient recalled-echo and SWI sequences at 1.5T and 3T, people with mild cognitive impairment and Alzheimer disease were reported to have microbleeds at a prevalence of 20%–43% and 18%–32%, respectively, compared with 0%–19% in cogni-

Received January 9, 2015; accepted after revision February 22.

From the Department of Radiology (G.C.C.), Division of Neuroradiology, Weill Cornell Medical College, New York-Presbyterian Hospital, New York, New York; Department of Biomedical Engineering (J.C.C.H.), Cornell University, Ithaca, New York; Department of Radiology (K.K., C.R.J.), Mayo Clinic, Rochester, Minnesota; and Department of Radiology and Biomedical Imaging (M.W.W.), University of California, San Francisco, California.

This work was supported in part by National Institutes of Health National Center for Advancing Translational Sciences/Clinical and Translational Science Center grant ULI TR000457-06.

Paper previously presented at: Annual Meeting of the American Society of Neuroradiology, May 20–23, 2013; San Diego, California.

Please address correspondence to Gloria C. Chiang, MD, Department of Radiology, Division of Neuroradiology, Weill Cornell Medical College, New York-Presbyterian

Hospital, 525 East 68th St, Starr Pavilion, Box 141, New York, NY 10065; e-mail: gcc9004@med.cornell.edu

Indicates open access to non-subscribers at [www.ajnr.org](http://www.ajnr.org)

Evidence-Based Medicine Level 2.

<http://dx.doi.org/10.3174/ajnr.A4351>

tively normal individuals.<sup>5</sup> In the setting of AD, microbleeds are associated with global brain amyloidosis, seen with increased uptake on positron-emission tomography scans by using [<sup>18</sup>F]florbetapir<sup>6</sup> and decreased levels of CSF amyloid- $\beta$  (A $\beta$ ).<sup>5</sup>

The anatomic distribution of microbleeds is believed to reflect their underlying pathology. Microbleeds located in the deep gray matter and infratentorial brain are typically seen in hypertensive individuals<sup>2,7</sup> and correspond to foci of hemosiderin leakage from small abnormal blood vessels.<sup>8</sup> Conversely, microbleeds in the setting of aging and AD are typically lobar, at the corticosubcortical junction,<sup>2,7</sup> and correspond to amyloid- $\beta$  deposition along vessel walls,<sup>9</sup> also known as amyloid angiopathy. However, it remains unclear whether microbleeds, either from hypertension or amyloid angiopathy, relate to tau pathology or cognitive changes that lead to Alzheimer pathogenesis<sup>10</sup> independent of global brain amyloidosis.

The purpose of our analysis was to determine whether the distribution of microbleeds, either lobar or deep gray/infratentorial, has differential associations with downstream events in Alzheimer pathogenesis. Specifically, by using data from the multicenter Alzheimer's Disease Neuroimaging Initiative (ADNI) ([adni.loni.usc.edu](http://adni.loni.usc.edu)),<sup>11</sup> we tested the hypotheses that lobar microbleeds 1) are associated with brain amyloidosis, reflected by lower CSF amyloid- $\beta$  levels, 2) predict the presence of tau pathology after overall brain amyloidosis is adjusted for, and 3) predict greater longitudinal cognitive decline.

## MATERIALS AND METHODS

### Subjects

The subjects of these analyses were 626 ADNI participants who had undergone 3T MR imaging and lumbar puncture for CSF analysis (151 cognitively normal, 389 with mild cognitive impairment, and 86 with AD). The ADNI is a longitudinal multicenter observational cohort study designed to identify imaging and biochemical biomarkers for the diagnosis and monitoring of AD.<sup>12</sup> The study was approved by the institutional review board of each of the participating institutions. Informed written consent was obtained from each participant at each site. Each of the subjects who enrolled in the ADNI-2 or ADNI-Grand Opportunity underwent a T2\* gradient recalled-echo sequence, which was used to enumerate the microbleeds in the brain. Subjects were between the ages of 55 and 90 years and showed no clinical or structural evidence of a significant neurologic or psychiatric disease and no systemic medical illness or laboratory abnormalities that would interfere with follow-up. To reduce confounding by comorbid vascular disease, a subject was enrolled in the ADNI only if he or she had a low modified Hachinski score of  $\leq 4$ .<sup>13</sup> Cognitive function was assessed by using the Alzheimer Disease Assessment Scale (ADAS),<sup>14</sup> which is the most widely used measure for clinical trials.

### MR Image Acquisition

Each subject underwent a standardized 3T MR imaging protocol, which included T2\* gradient recalled-echo and T1-weighted 3D MPRAGE sequences (<http://adni.loni.usc.edu/methods/documents/mri-protocols/>). This standardized protocol was distributed digitally to all ADNI-certified scanners and included the following

parameters for the gradient recalled-echo sequence: TE, 20 ms; TR, 650 ms; flip angle, 20°; section thickness, 4 mm; section gap, 0 mm. Before any subject was scanned using this protocol, an ADNI phantom was used to assess linear and nonlinear spatial distortion, signal-to-noise ratio, and image contrast, which were reviewed by a single quality-control center to ensure harmonization among the sites.<sup>15</sup>

Microbleeds were quantified visually by a board-certified neuroradiologist with subspecialty certification (G.C.C.). Microbleeds were defined as hypointense lesions within the brain parenchyma that measured  $< 10$  mm on the gradient recalled-echo sequence. Only microbleeds that were considered definite were included in the analysis.

Microbleeds were classified visually by location as 1) deep gray matter/infratentorial, if they involved the basal ganglia, thalami, brain stem, or cerebellum, or 2) lobar, if they involved other regions of the brain parenchyma.

### CSF Biomarkers

Each subject included in this analysis underwent lumbar puncture to obtain CSF samples for quantifying levels of CSF amyloid- $\beta$  and phosphorylated tau 181 protein (p-tau).<sup>16</sup> Briefly, each lumbar puncture was performed with a 20- or 24-gauge spinal needle at the baseline visit after an overnight fast. The CSF samples were transferred into polypropylene transfer tubes, frozen on dry ice within 1 hour after collection, and shipped on dry ice overnight to a single designated laboratory. After thawing for 1 hour at room temperature and gentle mixing, 0.5-mL aliquots were prepared from these samples. The aliquots were then stored in bar-coded labeled polypropylene vials at  $-80^{\circ}\text{C}$  and measured by using the xMAP Luminex platform (Luminex, Austin, Texas) with INNO-BIA AlzBio3 (Innogenetics, Ghent, Belgium) immunoassay kit-based reagents. Monoclonal antibodies specific for A $\beta$  and p-tau, which have been found to be useful in predicting AD, were used as reagents.<sup>17</sup> Total CSF tau level was not included in this analysis, because it was not available for some of the participants. In addition, p-tau has a higher specificity and negative predictive value for ruling out the presence of AD with 90% probability.<sup>18</sup>

### Apolipoprotein E Genotyping

Each participant underwent *apolipoprotein E* (APOE) genotyping at the baseline visit. Approximately 6 mL of blood was obtained from each participant in an ethylenediamine tetraacetic acid tube, gently mixed by inversion, and shipped at ambient temperature to a single designated laboratory within 24 hours of collection for genotyping analysis.

### Statistical Analysis

All statistical analyses were programmed in STATA version 13 (StataCorp, College Station, Texas). Comparisons of baseline variables among the groups were performed by using the Wilcoxon rank sum, Fisher exact, Kruskal Wallis, or  $\chi^2$  test, depending on the number of groups and type and distribution of the variables.

To test the hypothesis that lobar microbleeds are associated with overall brain amyloidosis, we used ordinary least-squares regression with age, sex, years of education, history of hyperten-

**Table 1: Baseline group characteristics**

Characteristic	Microbleeds Absent	P Value <sup>a</sup>	Microbleeds Present			P Value <sup>b</sup>
			Lobar Microbleeds Only	Mixed Lobar and Deep Gray/Infratentorial Microbleeds	Deep Gray/Infratentorial Microbleeds Only	
No. of subjects	407		163	29	27	
Mean age (SD), y	72 (7.6)	<.001 <sup>c</sup>	74 (7.0)	77 (6.4)	77 (9.0)	.06
Sex, male/female	218:189	.15	100:63	17:12	14:13	.64
Mean education (SD), y	16 (2.6)	.24	16 (2.9)	16 (2.9)	16 (2.3)	.78
% with HTN	47	.28	46	72	67	.009 <sup>d</sup>
% with APOE4	43	.15	53	52	26	.03 <sup>d</sup>
% with APOE2 allele	7	>.99	6	7	19	.06
% with NL	26	.14	20	10	33	.10
% with MCI	61	.80	61	79	56	.33
% with AD	12	.18	18	10	11	.41

**Note:**—HTN indicates hypertension; MCI, mild cognitive impairment; NL, normal cognitive function; SD, standard deviation.

<sup>a</sup> P values compare baseline variables between those without microbleeds and those with microbleeds (combining the 3 groups with different types of microbleeds).

<sup>b</sup> P values compare baseline variables among the 3 groups with microbleeds.

<sup>c</sup> Significance according to the Wilcoxon rank sum test.

<sup>d</sup> Significance according to the  $\chi^2$  test.

sion, APOE2 and APOE4 status, and diagnostic group (normal cognitive function, mild cognitive impairment, or AD) as covariates. CSF A $\beta$  values were log transformed for normality and included as the outcome variable. Lobar microbleeds were dichotomized as 0 or 1 (indicating presence or absence, respectively) and used as the predictor. The number of lobar microbleeds was then categorized as an ordinal variable of 0, 1, 2, 3, or >3 to determine whether increasing numbers of lobar microbleeds were associated with greater brain amyloidosis, reflected by decreased CSF A $\beta$  levels. The regressions were then repeated by using deep gray/infratentorial microbleeds, categorized as dichotomous or ordinal variables, to differentiate between microbleeds that may have been associated with hypertension and those associated with amyloid angiopathy.

To determine whether lobar microbleeds are associated with tau pathology, we used logistic regression, adjusting for age, sex, years of education, history of hypertension, APOE2 and APOE4 status, and diagnostic group. CSF A $\beta$  level was also included as a covariate, dichotomized as normal or abnormal on the basis of the previously published cutoff of 192 pg/mL,<sup>19</sup> to determine the effect of microbleeds independent of global brain amyloidosis. We then dichotomized abnormal CSF p-tau levels by using a cutoff of 23 pg/mL,<sup>19</sup> which was used as the outcome variable. Lobar versus deep gray/infratentorial microbleeds were again included as the predictor, either as a dichotomous or ordinal variable. The sensitivity, specificity, positive predictive value, and negative predictive value of lobar microbleeds in predicting an abnormal CSF p-tau level were also calculated post hoc.

To determine whether lobar microbleeds are associated with a longitudinal change in cognition, we used the following linear mixed-effects model:  $ADAS_{ij} = (B_0 + \beta_0) + \beta_1 MCH_i + (\beta_2 + \beta_3 MCH_i) t_{ij} + \text{covariates} + \varepsilon_{ij}$ . ADAS<sub>ij</sub> represents the ADAS score of subject *i* at time point *j*, MCH<sub>*i*</sub> represents the presence or absence of lobar microbleeds in each subject, and *t*<sub>*ij*</sub> represents the time interval between ADAS tests. *B*<sub>0</sub> and  $\beta_0$  are the coefficients for the random and fixed variations in baseline ADAS scores, respectively. The coefficient  $\beta_1$  represents the fixed effect of having lobar microbleeds at baseline. Finally,  $\beta_2 + \beta_3$  are the coefficients for time-dependent changes in ADAS scores, irrespective of respec-

tive, of the presence of microbleeds. The error term  $\varepsilon_{ij}$  represents random noise.

## RESULTS

Subject characteristics are presented in Table 1. Of the 626 subjects, 407 (65%) had no microbleeds, whereas 219 (35%) had at least one microbleed. Of the 219 subjects with microbleeds, 192 (88%) had at least one lobar microbleed, and 27 (12%) had only deep gray/infratentorial microbleeds. As expected, the subjects with microbleeds were older ( $P < .001$ ).<sup>1</sup> Those with lobar microbleeds, either alone or in combination with deep gray/infratentorial microbleeds, were more likely to be APOE4 carriers ( $P = .03$ ), which has also been described previously.<sup>1</sup> Finally, those with mixed lobar and infratentorial or only infratentorial microbleeds were more likely to have a history of hypertension ( $P = .009$ ).

### **Having $\geq 3$ Lobar Microbleeds Was Associated with Abnormal Levels of CSF A $\beta$ , Whereas Having Deep Gray/Infratentorial Microbleeds Was Not**

After adjusting for covariates, having at least one lobar microbleed was associated with greater brain amyloidosis, reflected by a lower CSF A $\beta$  level, though this association did not reach statistical significance (coefficient =  $-0.04$ ;  $P = .08$ ). However, accounting for increasing numbers of microbleeds, having 3 (coefficient =  $-0.30$ ;  $P = .001$ ) or >3 (coefficient =  $-0.18$ ;  $P = .001$ ) lobar microbleeds was also associated with lower levels of CSF A $\beta$  (Table 2). Deep gray/infratentorial microbleeds were not associated with CSF A $\beta$  levels ( $P = .64$ ), and increasing numbers of deep gray/infratentorial microbleeds also were not associated with CSF A $\beta$  levels ( $P = .29-.97$ ).

### **Lobar Microbleeds Are Associated with a Higher Likelihood of Having an Abnormal CSF p-Tau Level, Independent of the CSF A $\beta$ Level; Deep Gray/Infratentorial Microbleeds Are Not Associated with Abnormal CSF p-Tau Levels**

Using logistic regression after adjusting for the CSF A $\beta$  level, having at least one lobar microbleed was associated with more than

**Table 2: Regression model demonstrating association between lobar microbleeds and CSF amyloid- $\beta$  level (log transformed)**

CSF A $\beta$ (Log Transformed)	Coefficient (95% CI)	P Value
No. of lobar microbleeds		
1	-0.005 (-0.057 to 0.047)	.85
2	-0.030 (-0.12 to 0.056)	.49
3	-0.30 (-0.48 to -0.12)	.001
>3	-0.18 (-0.29 to -0.068)	.002
Age	-0.007 (-0.0098 to -0.0041)	<.001
Male sex	-0.013 (-0.055 to -0.030)	.57
Years of education	0.003 (-0.0046 to 0.011)	.40
APOE4	-0.23 (-0.28 to -0.19)	<.001
APOE2	0.059 (-0.022 to 0.14)	.15
MCI	-0.078 (-0.13 to -0.028)	.002
AD	-0.26 (-0.33 to -0.19)	<.001
History of hypertension	-0.011 (-0.052 to 0.031)	.61

Note:—MCI indicates mild cognitive impairment.

**Table 3: Regression model demonstrating association between lobar microbleeds and likelihood of an abnormal CSF p-tau level**

Abnormal CSF p-Tau Level	Odds Ratio (95% CI)	P Value
No. of lobar microbleeds		
1	2.82 (1.52–5.24)	.001
2	1.24 (0.51–3.01)	.64
3	0.37 (0.081–1.73)	.21
>3	3.22 (0.40–25.9)	.27
Abnormal CSF A $\beta$ level	3.40 (2.16–5.34)	<.001
Age	1.01 (0.99–1.04)	.32
Male sex	0.93 (0.61–1.42)	.74
Years of education	0.98 (0.90–1.06)	.56
APOE4	2.33 (1.42–3.84)	.001
APOE2	1.02 (0.52–2.02)	.95
MCI	1.05 (0.67–1.67)	.83
AD	3.5 (1.15–10.7)	.03
History of hypertension	0.98 (0.65–1.48)	.92

Note:—MCI indicates mild cognitive impairment.

double the odds of having an abnormal CSF p-tau level ( $P = .004$ ). The sensitivity and specificity of detecting an abnormal CSF p-tau level with the presence of at least one lobar microbleed were 35% and 82%, respectively. The positive and negative predictive values of at least one lobar microbleed for an abnormal CSF p-tau level were 86% and 29%, respectively.

Having deep gray/infratentorial microbleeds was not associated with abnormal CSF p-tau levels ( $P = .97$ ). Unlike with CSF A $\beta$  levels, no dose-response relationship was seen; having one lobar microbleed was most associated with an abnormal CSF p-tau level, with an odds ratio of 2.8 ( $P = .001$ ) (Table 3).

### Lobar Microbleeds Are Associated with Accelerated Longitudinal Cognitive Decline

Using a linear mixed-effects model and adjusting for covariates, including CSF A $\beta$  level and diagnostic group, having at least one lobar microbleed was significantly associated with an accelerated longitudinal change in ADAS score ( $P = .007$ ) of 1.4 points per year compared with 0.8 points per year for those without lobar microbleeds. Furthermore, having >3 lobar microbleeds was significantly associated with an increase of 2.3 points per year ( $P < .001$ ) (Table 4). Deep gray/infratentorial microbleeds were not associated with change in ADAS scores ( $P = .31$ ).

**Table 4: Mixed-effects regression model demonstrating an association between lobar microbleeds and longitudinal change in ADAS**

No. of Lobar Microbleeds	Annual Change in ADAS (95% CI)	P Value
0	0.78 (0.52 to 1.03)	<.001
1	1.35 (0.92 to 1.78)	.025
2	0.36 (-0.61 to 1.32)	.41
3	0.50 (-2.07 to 3.07)	.83
>3	2.34 (1.51 to 3.18)	<.001

## DISCUSSION

The following are the major findings of our analysis: 1) having  $\geq 3$  lobar microbleeds is associated with global brain amyloidosis, whereas having deep gray/infratentorial microbleeds is not; 2) lobar microbleeds, unlike deep gray/infratentorial microbleeds, are associated with elevated CSF p-tau levels but with no dose-response relationship; and 3) lobar microbleeds, unlike deep gray/infratentorial microbleeds, are associated with accelerated longitudinal cognitive decline. Overall, the results of our analysis suggest a differential association of lobar versus deep gray/infratentorial microbleeds with Alzheimer pathogenesis, which reveals the importance of lobar microbleeds in prognostication, independent of CSF A $\beta$  levels.

The first major finding, that lobar microbleeds are associated with greater overall brain amyloidosis, is concordant with the results of previous studies that showed lower CSF A $\beta$  levels<sup>3,20,21</sup> and higher uptake on PET amyloid scans<sup>5,6</sup> in people with microbleeds. Previous studies have also suggested that lobar microbleeds are more suggestive of underlying amyloid angiopathy,<sup>2,7,9</sup> which is seen concomitantly in 78%–98% of postmortem examinations of the brains of people with Alzheimer disease.<sup>22</sup> The finding that only higher numbers of lobar microbleeds were found to be associated with abnormal CSF A $\beta$  levels suggests that severe amyloid angiopathy is related more to overall brain amyloidosis and may contribute to the disease process. On the other hand, deep gray/infratentorial microbleeds, which are associated more typically with hypertension, were not associated with CSF A $\beta$  levels. Previous work also demonstrated that deep gray, not lobar, microbleeds are associated with small-vessel disease.<sup>23</sup> Therefore, hypertension may produce deep gray/infratentorial microbleeds and small-vessel changes but is likely involved in Alzheimer pathogenesis from a nonamyloid pathway, such as decreased cognitive reserve.

The second major finding is that having at least one lobar microbleed, unlike having deep gray/infratentorial microbleeds, was associated with greater odds of having an abnormal CSF p-tau level, after adjusting for CSF A $\beta$  levels. Furthermore, in post hoc analyses, we found that the presence of at least one lobar microbleed had a high positive predictive value for an abnormal CSF p-tau level. However, the absence of lobar microbleeds had a low negative predictive value for excluding the presence of an abnormal CSF p-tau level. A recent study in a memory clinic population found a similar association between microbleeds and CSF total tau, but not CSF p-tau, levels in individuals without dementia.<sup>21</sup> The fact that they did not find an association between microbleeds and p-tau levels may reflect technical differences in the assay or the fact that p-tau is more specific for neurodegeneration in

cohorts with more comorbid vascular disease. Nonetheless, both of our studies revealed an association between microbleeds and elevated levels of forms of CSF tau. One hypothesis is that microbleeds might reflect damaged microvasculature, resulting in decreased blood flow to neurons, ischemia, neuronal degeneration, and increased tau pathology. In postmortem studies, p-tau seems to have increased aggregation around arteries and arterioles with A $\beta$  in the vessel walls.<sup>24</sup> Alternatively, microbleeds might induce enough inflammation, without duration, to cause an elevated CSF p-tau level. In an animal model, microhemorrhages were seen to trigger inflammation and activated microglia, macrophages, and lymphocytes<sup>9,25</sup> rather than cell death or ischemia. This inflammation may be sufficient to produce neuronal release of tau into the extracellular space. This inflammation may also contribute to further Alzheimer pathogenesis. Finally, the presence of lobar microbleeds, reflecting amyloid angiopathy, may suggest that a patient is farther along in the Alzheimer disease cascade.<sup>10</sup> In this case, lobar microbleeds, in addition to an abnormal CSF A $\beta$  level, may signal more severe underlying disease.

The third major finding is that having at least one lobar microbleed is associated with accelerated longitudinal cognitive decline. Results discussed in the literature evaluating the association between microbleeds and cognitive decline have been variable, depending on the cohort studied (community-based populations,<sup>26-29</sup> people with a history of stroke or suspected stroke,<sup>30-33</sup> or subjects in a memory clinic who had mild cognitive impairment/AD<sup>3,34-38</sup>) and whether cognition was being evaluated on a cross-sectional<sup>26,30-32,34,35</sup> or longitudinal<sup>27,33,36-39</sup> basis. Most of these studies demonstrated an association between microbleeds and either global or executive impairment<sup>3,26,28,30-32</sup> cross-sectionally, as well as increased progression of memory impairment,<sup>38</sup> greater longitudinal changes in Mini-Mental State Examination scores,<sup>36</sup> higher likelihood of mild cognitive impairment converting to AD,<sup>27</sup> and increased risk of developing incident dementia.<sup>39</sup> One study also found cognitive improvement after stroke if no microbleeds were present,<sup>33</sup> which suggests a detrimental role of microbleeds on cognitive recovery. However, none of these studies adjusted for concomitant Alzheimer pathology, which may have driven the longitudinal changes in cognition. In our study, the association between lobar microbleeds and accelerated cognitive decline persisted after adjusting for CSF A $\beta$  levels, which suggests that microbleeds alone, perhaps reflecting underlying amyloid angiopathy, lead to cognitive impairment. This finding mirrors that of a postmortem study that found that moderate-to-severe amyloid angiopathy is associated with perceptual speed and episodic memory, even after adjusting for concomitant AD pathology.<sup>40</sup> We also found that having  $\geq 3$  lobar microbleeds was more associated with decreasing cognition, similar to the results of previous studies that found greater cognitive decline with  $\geq 2$ <sup>39</sup> or  $\geq 5$ <sup>28</sup> lobar microbleeds. The finding that deep/infratentorial microbleeds were not associated with cognitive decline is concordant with results of a previous study<sup>32</sup> but differs from those of another study that found mixed, not strictly lobar, microbleeds were associated with cognitive decline.<sup>39</sup> Again, the differential effect on cognitive decline secondary to microbleed location may hint at differing etiologies of microbleeds.

Our study has several limitations. First, the ADNI is not a community sample. The cohort consisted of more white people, people who were more highly educated, and people who had fewer comorbidities than a community population at this age.<sup>11</sup> Furthermore, subjects were excluded from the ADNI if they had significant comorbid vascular disease, reflected by a modified Hachinski score of  $>4$ .<sup>13</sup> Therefore, although we did not find a significant effect on hypertension-related deep gray/infratentorial microbleeds on tau pathology and cognition, a significant association may be found in people with more significant vascular disease. As a result, generalization of these findings should be approached with caution, and further validation in prospective population-based cohorts, particularly those with concomitant vascular disease, is required.

## CONCLUSIONS

The distribution of microbleeds provides clinically significant information, not only in suggesting differences in underlying etiology (ie, amyloid angiopathy versus hypertension) but also in demonstrating different associations with downstream events in Alzheimer pathogenesis (ie, tau and cognitive decline). Those who perform neuroimaging evaluations of older individuals who are being assessed for cognitive decline should consider microbleed distribution in their reports.

## ACKNOWLEDGMENTS

Data used in the preparation of this article were obtained from the Alzheimer's Disease Neuroimaging Initiative database (adni.loni.usc.edu). As such, the investigators within the ADNI contributed to the design and implementation of the ADNI and/or provided data but did not participate in the analysis or writing of this report. A complete listing of ADNI investigators can be found at [http://adni.loni.usc.edu/wp-content/uploads/how\\_to\\_apply/ADNI\\_Acknowledgement\\_List.pdf](http://adni.loni.usc.edu/wp-content/uploads/how_to_apply/ADNI_Acknowledgement_List.pdf).

The ADNI was launched in 2003 by the National Institute on Aging, the National Institute of Biomedical Imaging and Bioengineering, the Food and Drug Administration, private pharmaceutical companies, and nonprofit organizations as a \$60-million 5-year public-private partnership. The primary goal of the ADNI has been to test whether serial MR imaging, positron-emission tomography, other biologic markers, and clinical and neuropsychological assessment can be combined to measure the progression of mild cognitive impairment and early Alzheimer disease. Determination of sensitive and specific markers of very early AD progression is intended to aid researchers and clinicians to develop new treatments and monitor their effectiveness and to lessen the time and cost of clinical trials.

The principal investigator of this initiative is Michael W. Weiner, MD, VA Medical Center and University of California, San Francisco. The ADNI is the result of efforts of many coinvestigators from a broad range of academic institutions and private corporations, and subjects have been recruited from  $>50$  sites across the United States and Canada. The initial goal of the ADNI was to recruit 800 subjects, but the ADNI was followed by ADNI-Grand Opportunity and ADNI-2. To date, these 3 protocols have recruited  $>1500$  adults to participate in the research, consisting of cognitively normal older individuals, people with early or late

mild cognitive impairment, and people with early AD. The follow-up duration of each group is specified in the protocols for ADNI-1, ADNI-2, and ADNI-Grand Opportunity. Subjects originally recruited for ADNI-1 and ADNI-Grand Opportunity had the option to be followed in ADNI-2. For up-to-date information, please see [www.adni-info.org](http://www.adni-info.org).

Data collection and sharing for this project were funded by the Alzheimer's Disease Neuroimaging Initiative (National Institutes of Health grant U01 AG024904) and Department of Defense ADNI (Department of Defense award W81XWH-12-2-0012). The ADNI is funded by the National Institute on Aging and the National Institute of Biomedical Imaging and Bioengineering and through generous contributions from the following: Alzheimer's Association; Alzheimer's Drug Discovery Foundation; Araclon Biotech; BioClinica; Biogen Idec; Bristol-Myers Squibb; Eisai; Elan Pharmaceuticals; Eli Lilly; EuroImmun; F. Hoffmann-La Roche and its affiliated company Genentech; Fujirebio; GE Healthcare; IXICO; Janssen Alzheimer Immunotherapy Research & Development; Johnson & Johnson Pharmaceutical Research & Development; Medpace; Merck & Co; Meso Scale Diagnostics; NeuroRx Research; Neurotrack Technologies; Novartis Pharmaceuticals Corporation; Pfizer; Piramal Imaging; Servier; Synarc; and Takeda Pharmaceutical Company. The Canadian Institutes of Health Research is providing funds to support ADNI clinical sites in Canada. Private sector contributions are facilitated by the Foundation for the National Institutes of Health ([www.fnih.org](http://www.fnih.org)). The grantee organization is the Northern California Institute for Research and Education, and the study is coordinated by the Alzheimer's Disease Cooperative Study at the University of California, San Diego. ADNI data are disseminated by the Laboratory for Neuro Imaging at the University of Southern California.

Disclosures: Gloria C. Chiang—*RELATED: Grant:* National Center for Advancing Translational Sciences/Clinical and Translational Science Center. Kejal Kantarci—*RELATED: Grant:* National Institutes of Health,\* *Comments:* R01AG040042, P50 AG44170/Project 2, and Minnesota Partnership for Biotechnology and Medical Genomics (PO0359020); *OTHER:* serves on the data safety monitoring board for Pfizer, Janssen Alzheimer Immunotherapy, and Takeda Global Research & Development Center and receives research support from the National Institutes of Health (grant R01AG040042 [principal investigator], Mayo Clinic Alzheimer's Disease Research Center/Project one grant P50 AG16574/P1 [principal investigator], grant P50 AG44170/Project 2 [principal investigator], and grant R01 AG11378 [coinvestigator]). Clifford Jack—*RELATED: Grant:* National Institutes of Health (AG11378 and AG041851)\*; *UNRELATED: Consultancy:* Eli Lilly; *OTHER:* provides consulting services for Siemens Healthcare and receives research funding from the National Institutes of Health (grants R01-AG011378, R01-AG041851, R01-AG037551, U01-HL096917, U01-AG032438, and U01-AG024904) and the Alexander Family Alzheimer's Disease Research Professorship of the Mayo Foundation. Michael Wiener—*RELATED: Grant:* National Institutes of Health/National Institute on Aging/National Institute of Mental Health,\* Department of Defense,\* Alzheimer's Association,\* Alzheimer's Drug Discovery Foundation,\* Merck,\* Avid,\* and the Veterans Administration\*; *Consulting Fee or Honorarium:* Synarc, Pfizer, Janssen, KJ Associates, Easton Associates, Harvard University, University of California, Los Angeles, Alzheimer's Drug Discovery Foundation, Neurotrope Bioscience, Avid Radiopharmaceuticals, Clearview Healthcare Partners, Perceptive Informatics, Smartfish AS, Decision Resources, Araclon, Merck, Defined Health, and Genentech; *Support for Travel to Meetings for the Study or Other Purposes:* Pfizer, Paul Sabatier University, MCI Group France, Travel eDreams, Neuroscience School of Advanced Studies, Danone Trading, BV, CTAD Ant Congress, Kenes International, ADRC, University of California, Los Angeles, University of California, San Diego, Sanofi-Aventis Groupe, University Center Hospital, Toulouse, Araclon, AC Immune, Nutricia, Eli Lilly, New York Academy of Sciences, National Brain Research Center, India for Johns Hopkins Medicine, Consortium for Multiple Sclerosis Centers, Northwestern University, Fidelity Biosciences Research Initiative, and University of Pennsylvania. He served on the Editorial Boards for Alzheimer's & Dementia and MRI. He received honoraria from Pfizer, Tohoku University,

and Danone Trading, BV; *OTHER:* has been on scientific advisory boards for Pfizer and BOLT International; has been a consultant for Pfizer, Janssen, KJ Associates, Easton Associates, Harvard University, inThought, INC Research, University of California, Los Angeles, Alzheimer's Drug Discovery Foundation, and Sanofi-Aventis Groupe; has received funding for travel from Pfizer, Alzheimer's disease PD meeting, Paul Sabatier University, Novartis, Tohoku University, MCI Group, France, Travel eDreams, Neuroscience School of Advanced Studies, Danone Trading, BV, and CTAD ANT Congress; serves as an associate editor of *Alzheimer's & Dementia*; has received honoraria from Pfizer, Tohoku University, and Danone Trading, BV; has research support from Merck, Avid, Department of Defense, and Veterans Administration; and has stock options in Synarc and Elan. \*Money paid to the institution.

## REFERENCES

- Poels MM, Vernooij MW, Ikram MA, et al. **Prevalence and risk factors of cerebral microbleeds: an update of the Rotterdam Scan Study.** *Stroke* 2010;41:S103–06 CrossRef Medline
- Cordonnier C, Al-Shahi Salman R, Wardlaw J. **Spontaneous brain microbleeds: systematic review, subgroup analyses and standards for study design and reporting.** *Brain* 2007;130:1988–2003 CrossRef Medline
- Goos JD, Kester MI, Barkhof F, et al. **Patients with Alzheimer disease with multiple microbleeds: relation with cerebrospinal fluid biomarkers and cognition.** *Stroke* 2009;40:3455–60 CrossRef Medline
- Wardlaw JM, Lewis SC, Keir SL, et al. **Cerebral microbleeds are associated with lacunar stroke defined clinically and radiologically, independently of white matter lesions.** *Stroke* 2006;37:2633–36 CrossRef Medline
- Yates PA, Villemagne VL, Ellis KA, et al. **Cerebral microbleeds: a review of clinical, genetic, and neuroimaging associations.** *Front Neurol* 2014;4:205 CrossRef Medline
- Kantarci K, Gunter JL, Tosakulwong N, et al; Alzheimer's Disease Neuroimaging Initiative. **Focal hemosiderin deposits and  $\beta$ -amyloid load in the ADNI cohort.** *Alzheimers Dement* 2013;9:S116–23 CrossRef Medline
- Park JH, Seo SW, Kim C, et al. **Pathogenesis of cerebral microbleeds: in vivo imaging of amyloid and subcortical ischemic small vessel disease in 226 individuals with cognitive impairment.** *Ann Neurol* 2013;73:584–93 CrossRef Medline
- Fazekas F, Kleinert R, Roob G, et al. **Histopathologic analysis of foci of signal loss on gradient-echo T2\*-weighted MR images in patients with spontaneous intracerebral hemorrhage: evidence of microangiopathy-related microbleeds.** *AJNR Am J Neuroradiol* 1999;20:637–42 Medline
- Schrag M, McAuley G, Pomakian J, et al. **Correlation of hypointensities in susceptibility-weighted images to tissue histology in dementia patients with cerebral amyloid angiopathy: a postmortem MRI study.** *Acta Neuropathol* 2010;119:291–302 CrossRef Medline
- Jack CR Jr, Knopman DS, Jagust WJ, et al. **Tracking pathophysiological processes in Alzheimer's disease: an updated hypothetical model of dynamic biomarkers.** *Lancet Neurol* 2013;12:207–16 CrossRef Medline
- Petersen RC, Aisen PS, Beckett LA, et al. **Alzheimer's Disease Neuroimaging Initiative (ADNI): clinical characterization.** *Neurology* 2010;74:201–09 CrossRef Medline
- Mueller SG, Weiner MW, Thal LJ, et al. **Ways toward an early diagnosis in Alzheimer's disease: the Alzheimer's Disease Neuroimaging Initiative (ADNI).** *Alzheimers Dement* 2005;1:55–66 CrossRef Medline
- Rosen WG, Terry RD, Fuld PA, et al. **Pathological verification of ischemic score in differentiation of dementias.** *Ann Neurol* 1980;7:486–88 CrossRef Medline
- Rosen WG, Mohs RC, Davis KL. **A new rating scale for Alzheimer's disease.** *Am J Psychiatry* 1984;141:1356–64 CrossRef Medline
- Gunter JL, Bernstein MA, Borowski BJ, et al. **Measurement of MRI scanner performance with the ADNI phantom.** *Med Phys* 2009;36:2193–205 CrossRef Medline
- Shaw LM. **PENN biomarker core of the Alzheimer's Disease Neuroimaging Initiative.** *Neurosignals* 2008;16:19–23 CrossRef Medline
- Hansson O, Zetterberg H, Buchhave P, et al. **Association between**

- CSF biomarkers and incipient Alzheimer's disease in patients with mild cognitive impairment: a follow-up study. *Lancet Neurol* 2006; 5:228–34 CrossRef Medline
18. Mitchell A, Brindle N. CSF phosphorylated tau—does it constitute an accurate biological test for Alzheimer's disease? *Int J Geriatr Psychiatry* 2003;18:407–11 CrossRef Medline
  19. Shaw LM, Vanderstichele H, Knapik-Czajka M, et al. Cerebrospinal fluid biomarker signature in Alzheimer's disease neuroimaging initiative subjects. *Ann Neurol* 2009;65:403–13 CrossRef Medline
  20. Yates PA, Sirisriro R, Villemagne VL, et al; AIBL Research Group. Cerebral microhemorrhage and brain  $\beta$ -amyloid in aging and Alzheimer disease. *Neurology* 2011;77:48–54 CrossRef Medline
  21. Kester MI, Goos JD, Teunissen CE, et al. Associations between cerebral small-vessel disease and Alzheimer disease pathology as measured by cerebrospinal fluid biomarkers. *JAMA Neurol* 2014;71:855–62 CrossRef Medline
  22. Kalaria RN, Ballard C. Overlap between pathology of Alzheimer disease and vascular dementia. *Alzheimer Dis Assoc Disord* 1999;13:S115–23 CrossRef Medline
  23. Vernooij MW, van der Lugt A, Ikram MA. Prevalence and risk factors of cerebral microbleeds: the Rotterdam Scan Study. *Neurology* 2008;70:1208–14 CrossRef Medline
  24. Williams S, Chalmers K, Wilcock GK, et al. Relationship of neurofibrillary pathology to cerebral amyloid angiopathy in Alzheimer's disease. *Neuropathol Appl Neurobiol* 2005;31:414–21 CrossRef Medline
  25. Rosidi NL, Zhou J, Pattanaik S, et al. Cortical microhemorrhages cause local inflammation but do not trigger widespread dendrite degeneration. *PLoS One* 2011;6:e26612 CrossRef Medline
  26. Takashima Y, Mori T, Hashimoto M, et al. Clinical correlating factors and cognitive function in community-dwelling healthy subjects with cerebral microbleeds. *J Stroke Cerebrovasc* 2011;20:105–10 CrossRef Medline
  27. Kirsch W, McAuley G, Holshouser B, et al. Serial susceptibility weighted MRI measures brain iron and microbleeds in dementia. *J Alzheimers Dis* 2009;17:599–609 CrossRef Medline
  28. Poels MM, Ikram MA, van der Lugt A, et al. Cerebral microbleeds are associated with worse cognitive function: the Rotterdam Scan Study. *Neurology* 2012;78:326–33 CrossRef Medline
  29. Qiu C, Cotch MF, Sigurdsson S, et al. Cerebral microbleeds, retinopathy, and dementia: the AGES-Reykjavik Study. *Neurology* 2010;75:2221–28 CrossRef Medline
  30. Werring DJ, Frazer DW, Coward LJ, et al. Cognitive dysfunction in patients with cerebral microbleeds on T2\*-weighted gradient-echo MRI. *Brain* 2004;127:2265–75 CrossRef Medline
  31. Patel B, Lawrence AJ, Chung AW, et al. Cerebral microbleeds and cognition in patients with symptomatic small vessel disease. *Stroke* 2013;44:356–61 CrossRef Medline
  32. Gregoire SM, Scheffler G, Jäger HR, et al. Strictly lobar microbleeds are associated with executive impairment in patients with ischemic stroke or transient ischemic attack. *Stroke* 2013;44:1267–72 CrossRef Medline
  33. Tang WK, Chen YK, Lu JY, et al. Absence of cerebral microbleeds predicts reversion of vascular "cognitive impairment no dementia" in stroke. *Int J Stroke* 2011;6:498–505 CrossRef Medline
  34. Pettersen JA, Sathiyamoorthy G, Gao FQ, et al. Microbleed topography, leukoaraiosis, and cognition in probable Alzheimer disease from the Sunnybrook dementia study. *Arch Neurol* 2008;65:790–95 CrossRef Medline
  35. Nakata Y, Shiga K, Yoshikawa K, et al. Subclinical brain hemorrhages in Alzheimer's disease: evaluation by magnetic resonance T2\*-weighted images. *Ann N Y Acad Sci* 2002;977:169–72 CrossRef Medline
  36. van der Vlies AE, Goos JD, Barkhof F, et al. Microbleeds do not affect rate of cognitive decline in Alzheimer disease. *Neurology* 2012;79:763–69 CrossRef Medline
  37. Haller S, Bartsch A, Nguyen D, et al. Cerebral microhemorrhage and iron deposition in mild cognitive impairment: susceptibility-weighted MR imaging assessment. *Radiology* 2010;257:764–73 CrossRef Medline
  38. Ayaz M, Boikov AS, Haacke EM, et al. Imaging cerebral microbleeds using susceptibility weighted imaging: one step toward detecting vascular dementia. *J Magn Reson Imaging* 2010;31:142–48 CrossRef Medline
  39. Miwa K, Tanaka M, Okazaki S, et al. Multiple or mixed cerebral microbleeds and dementia in patients with vascular risk factors. *Neurology* 2014;83:646–53 CrossRef Medline
  40. Arvanitakis Z, Leurgans SE, Wang Z, et al. Cerebral amyloid angiopathy pathology and cognitive domains in older persons. *Ann Neurol* 2011;69:320–27 CrossRef Medline

# Cerebral Microbleeds in Patients with Dementia with Lewy Bodies and Parkinson Disease Dementia

S.W. Kim, S.J. Chung, Y.-S. Oh, J.H. Yoon, M.K. Sunwoo, J.Y. Hong, J.-S. Kim, and P.H. Lee



## ABSTRACT

**BACKGROUND AND PURPOSE:** The burden of amyloid  $\beta$  is greater in patients with dementia with Lewy bodies than in those with Parkinson disease dementia, and an increased amyloid  $\beta$  load is closely related to a higher incidence of cerebral microbleeds. Here, we investigated the prevalence and topography of cerebral microbleeds in patients with dementia with Lewy bodies and those with Parkinson disease dementia to examine whether cerebral microbleeds are more prevalent in patients with dementia with Lewy bodies than in those with Parkinson disease dementia.

**MATERIALS AND METHODS:** The study population consisted of 42 patients with dementia with Lewy bodies, 88 patients with Parkinson disease dementia, and 35 controls who underwent brain MR imaging with gradient recalled-echo. Cerebral microbleeds were classified as deep, lobar, or infratentorial.

**RESULTS:** The frequency of cerebral microbleeds was significantly greater in patients with dementia with Lewy bodies (45.2%) than in those with Parkinson disease dementia (26.1%) or in healthy controls (17.1%;  $P = .017$ ). Lobar cerebral microbleeds were observed more frequently in the dementia with Lewy bodies group (40.5%) than in the Parkinson disease dementia (17%;  $P = .004$ ) or healthy control (8.6%;  $P = .001$ ) group, whereas the frequencies of deep and infratentorial cerebral microbleeds did not differ among the 3 groups. Logistic regression analyses revealed that, compared with the healthy control group, the dementia with Lewy bodies group was significantly associated with the presence of lobar cerebral microbleeds after adjusting for age, sex, nonlobar cerebral microbleeds, white matter hyperintensities, and other vascular risk factors (odds ratio, 4.39 [95% CI, 1.27–15.25]). However, compared with the healthy control group, the Parkinson disease dementia group was not significantly associated with lobar cerebral microbleeds.

**CONCLUSIONS:** This study showed that patients with dementia with Lewy bodies had a greater burden of cerebral microbleeds and exhibited a lobar predominance of cerebral microbleeds than did patients with Parkinson disease dementia.

**ABBREVIATIONS:**  $A\beta$  = amyloid  $\beta$ ; CMB = cerebral microbleed; DLB = dementia with Lewy bodies; PDD = Parkinson disease dementia; WMH = white matter hyperintensity

Both dementia with Lewy bodies (DLB) and Parkinson disease dementia (PDD) are clinically characterized by parkinsonism and dementia but are distinctive in terms of the temporal relationship between the onset of dementia and parkinsonism.<sup>1,2</sup> In terms of neuropathology, diffuse cortical Lewy bodies constitute the main substrate of dementia in both diseases.<sup>3</sup> However, the

burden of amyloid  $\beta$  ( $A\beta$ ) is greater in patients with DLB than in those with PDD. A recent neuropathologic study revealed that patients with DLB had greater plaque density than those with PDD.<sup>4</sup> In some patients with DLB, the density of  $A\beta$  deposits in the temporal lobe was comparable with that in patients with Alzheimer disease.<sup>5</sup> A neuroimaging study that used <sup>11</sup>C-Pittsburgh compound-B positron-emission tomography also revealed a greater  $A\beta$  burden in patients with DLB than in patients with PDD.<sup>6</sup> Thus, concomitant amyloid pathology in patients with

Received September 10, 2014; accepted after revision February 25, 2015.

From the Department of Neurology (S.W.K., S.J.C., P.H.L.), Yonsei University College of Medicine, Seoul, South Korea; Department of Neurology (Y.-S.O., J.-S.K.), Catholic University College of Medicine, Seoul, South Korea; Department of Neurology (J.H.Y.), Ajou University College of Medicine, Suwon, South Korea; Department of Neurology (M.K.S.), Bundang Jesaeng General Hospital, Seongnam, South Korea; Department of Neurology (J.Y.H.), Yonsei University Wonju College of Medicine, Wonju, South Korea; Severance Biomedical Science Institute (P.H.L.), Seoul, South Korea.

This research was supported by a grant of the Korea Health Technology R&D Project through the Korea Health Industry Development Institute (KHIDI), funded by the Ministry of Health & Welfare, Republic of Korea (grant H14C0093).

Please address correspondence to P.H. Lee, MD, PhD, Department of Neurology, Yonsei University College of Medicine, 250 Seongsanno, Seodaemun-gu, Seoul 120-752, South Korea; e-mail: phisland@chol.net

Indicates open access to non-subscribers at [www.ajnr.org](http://www.ajnr.org)

Indicates article with supplemental on-line table.

<http://dx.doi.org/10.3174/ajnr.A4337>

DLB is considered to contribute to the early development of dementia in addition to diffuse cortical Lewy body pathology.

Cerebral microbleeds (CMBs) are small, rounded, homogeneous, hypointense lesions on T2\*-weighted gradient recalled-echo imaging<sup>7</sup> and are correlated histologically with hemosiderin deposits from the breakdown products of blood that leaks from small vessels.<sup>8</sup> Ample evidence suggests that an increased A $\beta$  load is closely related to a higher prevalence of CMBs because the accumulation of A $\beta$  within vessel walls triggers the vasculopathy of cerebral amyloid angiopathy in patients with Alzheimer disease.<sup>9</sup> In a study of Alzheimer disease pathology, Schrag et al<sup>10</sup> found that CMBs observed in MR imaging were correlated pathologically to microhemorrhages in areas in which A $\beta$  had been deposited in adjacent vessel walls. Using <sup>11</sup>C-Pittsburgh compound-B positron-emission tomography, Yates et al<sup>11</sup> also reported that positive <sup>11</sup>C-Pittsburgh compound-B positron-emission tomography scan results predicted the occurrence of lobar CMBs in healthy controls. In this study, we tested the hypothesis that a difference in A $\beta$  load between patients with DLB and those with PDD would be associated with variations in the burden and distribution pattern of CMBs in such patients. Therefore, this study was performed to explore the prevalence and topography of CMBs in patients with DLB and those with PDD.

## MATERIALS AND METHODS

### Subjects

Patient data were collected retrospectively from 3 tertiary referral hospitals (Severance Hospital and Saint Mary's Hospital [Seoul, South Korea] and Ajou University Hospital [Suwon, South Korea]). Medical and imaging data of 67 patients with DLB (43 from Severance Hospital, 13 from Ajou University Hospital, and 11 from Saint Mary's Hospital) and 132 patients with PDD (51 from Severance Hospital, 31 from Ajou University Hospital, and 50 from Saint Mary's Hospital) were reviewed. Of these patients, 42 with DLB and 88 with PDD who underwent brain MR imaging with T2\*-weighted gradient recalled-echo were included in the study to analyze patterns of CMBs.

DLB was diagnosed according to the revised consensus criteria for DLB,<sup>12</sup> and PDD was diagnosed on the basis of Movement Disorder Society consensus criteria for dementia associated with Parkinson disease.<sup>1</sup> Of 42 patients with DLB, 39 underwent <sup>18</sup>F-fluoropropylcarbomethoxyiodophenyl-nortropane positron emission tomography scans, and all of them revealed decreased dopamine transporter uptake in the posterior putamen. In addition, the other 3 patients underwent cardiac <sup>123</sup>I-metaiodobenzylguanidine scintigraphy, which in each of them revealed decreased uptake in the delayed image. Basic demographic data, including sex, age, and history of hypertension, diabetes mellitus, and/or cerebrovascular accident, were analyzed. A history of hypertension was defined as previous physician-diagnosed hypertension with or without prescription of antihypertensive agents, and a history of diabetes was defined on the basis of self-report or the use of hypoglycemic agents. A history of cerebrovascular accident was defined as a transient ischemic attack or stroke diagnosed by a physician. Serum levels of cholesterol measured during the diagnostic work-up were also recorded. Cognitive function was evaluated by using the Korean Mini-Mental State Examina-

tion. Parkinsonian motor symptoms were assessed by using the Unified Parkinson's Disease Rating Scale Part III. Exclusion criteria included the presence of other neurodegenerative diseases that may account for dementia. Patients with a history of using drugs that cause parkinsonism (antipsychotics, gastrointestinal prokinetic drugs, antiepileptic drugs, or L-type calcium channel blockers) were excluded, and possible medical comorbidities were excluded by using laboratory tests. Patients with any history of head trauma were also excluded. Healthy age- and sex-matched elderly volunteers were included as controls for the imaging analyses. They were recruited by advertisements about the project or were healthy relatives of patients with movement disorders or dementia ( $n = 35$ ; mean age, 73.3 years). The healthy controls did not have active neurologic disorders or cognitive complaints, and they exhibited normal performance on neuropsychological tests (minimum score of 27 on the Korean Mini-Mental State Examination). The University of Yonsei Institutional Review Board approved the research, which adhered to the tenets of the Declaration of Helsinki.

### MR Imaging Protocol

Brain MR imaging scans were obtained by using a 3T system (Intera Achieva [Philips Healthcare, Best, the Netherlands] or Magnetom Trio [Siemens, Erlangen, Germany]). Conventional 2D T2\*-weighted gradient recalled-echo imaging in the axial plane was obtained for the detection of CMBs with the following parameters: matrix, 100–256  $\times$  100–256; section thickness, 5 mm; repetition time, 500–1000 ms; echo time, 15–25 ms; and flip angle, 18°–25°. Axial FLAIR images were also obtained to evaluate white matter hyperintensities by using the following parameters: matrix, 256–352  $\times$  192–256; section thickness, 5 mm; echo time, 85–138 ms; repetition time, 9600–11,000 ms; TI, 2200–2800 ms; and flip angle, 90°.

### MR Imaging Assessment

CMBs were defined as a small, rounded, homogeneous, hypointense lesions on T2\*-weighted gradient recalled-echo imaging; these lesions had to be distinct from other findings that mimic CMBs, and more than half of each lesion had to be surrounded by brain parenchyma.<sup>7</sup> Other potential mimics include vessel flow voids, calcifications, and iron depositions. According to anatomic location, CMBs were classified as deep (lesions in caudate, thalamus, putamen, globus pallidus, corpus callosum, internal capsule, and external capsule), lobar (lesions in the frontal, parietal, temporal, occipital lobe, and periventricular area), or infratentorial (lesions in brain stem and cerebellum).<sup>13</sup> The presence of CMBs in each location was assessed. White matter hyperintensities (WMHs) were defined as ill-defined hyperintense lesions on FLAIR images. WMHs were graded according to the rating scale suggested by Wahlund et al,<sup>14</sup> which uses a 4-point scale: 0 (no lesion), 1 (focal lesion), 2 (beginning confluence), and 3 (diffuse involvement). Scoring was performed in 5 regions (frontal, parieto-occipital, temporal, infratentorial, and basal ganglia) in the right and left hemispheres; the sum of scores ranged from 0 to 30. Brain MR imaging was reviewed independently by 2 raters, both of whom had a great deal of experience in the assessment of CMBs and the calculation of WMH scores (S.W.K. and S.J.C.). The 2

**Table 1: Demographic characteristics of the patients with DLB or PDD and healthy controls<sup>a</sup>**

Characteristic	Controls (n = 35)	Patients with DLB (n = 42)	Patients with PDD (n = 88)	P	P <sub>1</sub> <sup>b</sup>	P <sub>2</sub> <sup>c</sup>	P <sub>3</sub> <sup>d</sup>
Sociodemographics							
Age, y	73.3 ± 2.4	75.1 ± 6.1	73.7 ± 7	.117			
Sex, male	10 (28.6)	18 (42.9)	32 (36.4)	.431			
Risk factors							
Hypertension	17 (48.6)	25 (59.5)	41 (46.6)	.376			
Diabetes mellitus	7 (20)	16 (38.1)	18 (20.5)	.071			
Cigarette smoking	2 (5.7)	4 (9.5)	12 (13.8)	.196			
Total cholesterol, mg/dl	174.0 ± 29.1	160.7 ± 30.3	175.6 ± 38.3	.083			
Cerebrovascular disease							
Cortical infarction	0 (0)	3 (7.1)	4 (4.5)	.295			
Lacunar infarction	7 (20)	14 (33.3)	17 (19.3)	.184			
WMH score	1.7 ± 2.1	5 ± 3.7	3.4 ± 3.6	.001	<.0001	.082	.121
K-MMSE score	28.4 ± 1.1	19.1 ± 5.1	20.3 ± 4.5	<.0001	<.0001	<.0001	.483
UPDRS-III score		29.2 ± 13.7	28.8 ± 15.1	.935			

**Note:**—K-MMSE indicates Korean Mini-Mental State Examination; UPDRS-III, Unified Parkinson's Disease Rating Scale Part III.

<sup>a</sup> Values are expressed as number (%) of subjects or mean ± SD.

<sup>b</sup> Healthy controls vs patients with DLB.

<sup>c</sup> Healthy controls vs patients with PDD.

<sup>d</sup> Patients with DLB vs those with PDD.

raters were blind to the clinical data. Interrater reliabilities for the presence in CMBs in deep, lobar, and infratentorial areas were excellent ( $\kappa = 0.86, 0.93,$  and  $0.91,$  respectively), and interrater reliability for the total WMH scores was good (correlation coefficients =  $0.74$ ). The presence and topography of chronic infarcts was also assessed on the basis of radiologic reports.

### Statistical Analysis

Statistical analyses were performed by using SPSS software (version 18.0; IBM, Armonk, New York). Baseline demographic characteristics of the 3 groups were compared by ANOVA and  $\chi^2$  tests for continuous and categorical variables. Post hoc comparisons with Bonferroni correction were performed to detect significant differences between each pair of groups. The  $\chi^2$  or Fisher exact test was used to compare the number of patients with CMBs between groups. Logistic regression analyses were performed to assess the contributions of factors to the presence of lobar CMBs. Covariates considered significant at a  $P$  value of  $<.3$  in the univariate model were included in multivariate analysis, and a  $P$  value of  $<.05$  was considered statistically significant.

### RESULTS

Of the 67 patients with DLB and 132 patients with PDD, 42 and 88, respectively, were enrolled in the present study. There were no significant differences in age, sex, vascular risk factors, severity of Parkinsonian motor symptoms, or general cognition between the subjects who were and were not enrolled in the study (On-line Table). The demographic characteristics of the subjects enrolled in the study are presented in Table 1. The groups did not differ significantly in age or sex. The frequencies of hypertension, diabetes mellitus, and smoking and the level of total cholesterol did not differ among the groups. The frequencies of both cortical and lacunar infarcts did not differ significantly among the groups. WMH scores were significantly higher in patients with DLB (5) than in healthy controls (1.7;  $P < .0001$ ) but were not significantly different from those in the PDD group (3.4;  $P < .121$ ). Korean Mini-Mental State Examination scores were significantly lower in the DLB (19.1) and PDD (20.3) patient groups than in the healthy

**Table 2: Prevalence and distribution of cerebral microbleeds in patients with DLB or PDD and controls<sup>a</sup>**

Cerebral Microbleed Characteristic	Healthy Controls (n = 35)	Patients with DLB (n = 42)	Patients with PDD (n = 88)	P <sup>b</sup>	P <sub>1</sub> <sup>c,d</sup>	P <sub>2</sub> <sup>c,e</sup>	P <sub>3</sub> <sup>c,f</sup>
Overall	6 (17.1)	19 (45.2)	23 (26.1)	.017	.009	.289	.029
Deep	2 (5.7)	8 (19.1)	11 (12.5)	.216	.1	.346	.323
Lobar	3 (8.6)	17 (40.5)	15 (17)	.001	.001	.230	.004
Infratentorial	1 (2.9)	5 (11.9)	7 (8)	.341	.212	.438	.523

<sup>a</sup> Values are expressed as number (%) of subjects.

<sup>b</sup> From the  $\chi^2$  or Fisher exact test.

<sup>c</sup> Bonferroni-corrected  $P$  values of the post hoc pair-wise comparison tests.

<sup>d</sup> Healthy controls versus patients with DLB.

<sup>e</sup> Healthy controls versus patients with PDD.

<sup>f</sup> Patients with DLB versus those with PDD.

controls (28.4;  $P < .0001$ ) but did not differ between the DLB and PDD groups.

Table 2 shows the results of CMB analysis among the groups. The frequency of CMBs was significantly greater in patients with DLB (45.2%) than in those with PDD (26.1%) and healthy controls (17.1%;  $P = .017$ ; Figure). According to post hoc analysis, the frequency of CMBs in the DLB group was significantly higher than in the PDD ( $P = .029$ ) and healthy control ( $P = .009$ ) groups, whereas the frequency of CMBs in the PDD group did not differ significantly from that in the healthy control group. The analysis of CMBs according to location revealed that the frequencies of deep and infratentorial CMBs did not differ among the healthy control (5.7% and 2.9%, respectively), PDD (12.5% and 8%, respectively), and DLB (19.1% and 11.9%, respectively) groups, whereas lobar CMBs were observed more frequently in patients with DLB (40.5%;  $P = .001$ ) than in those with PDD (17%) and in healthy controls (8.6%). On post hoc analysis, the frequency of lobar CMBs was higher in the DLB group than in the PDD ( $P = .004$ ) and healthy control ( $P = .001$ ) groups, whereas the frequency of lobar CMBs in the PDD group did not differ significantly from that in the healthy control group.

Of the 17 patients with DLB and lobar CMBs, the CMBs were observed in the frontal areas in 5 patients (29.4%), the parietal areas in 7 (41.2%), the temporal areas in 7 (41.2%), and the occipital areas in 6 (35.3%). Of the 15 patients with PDD with lobar

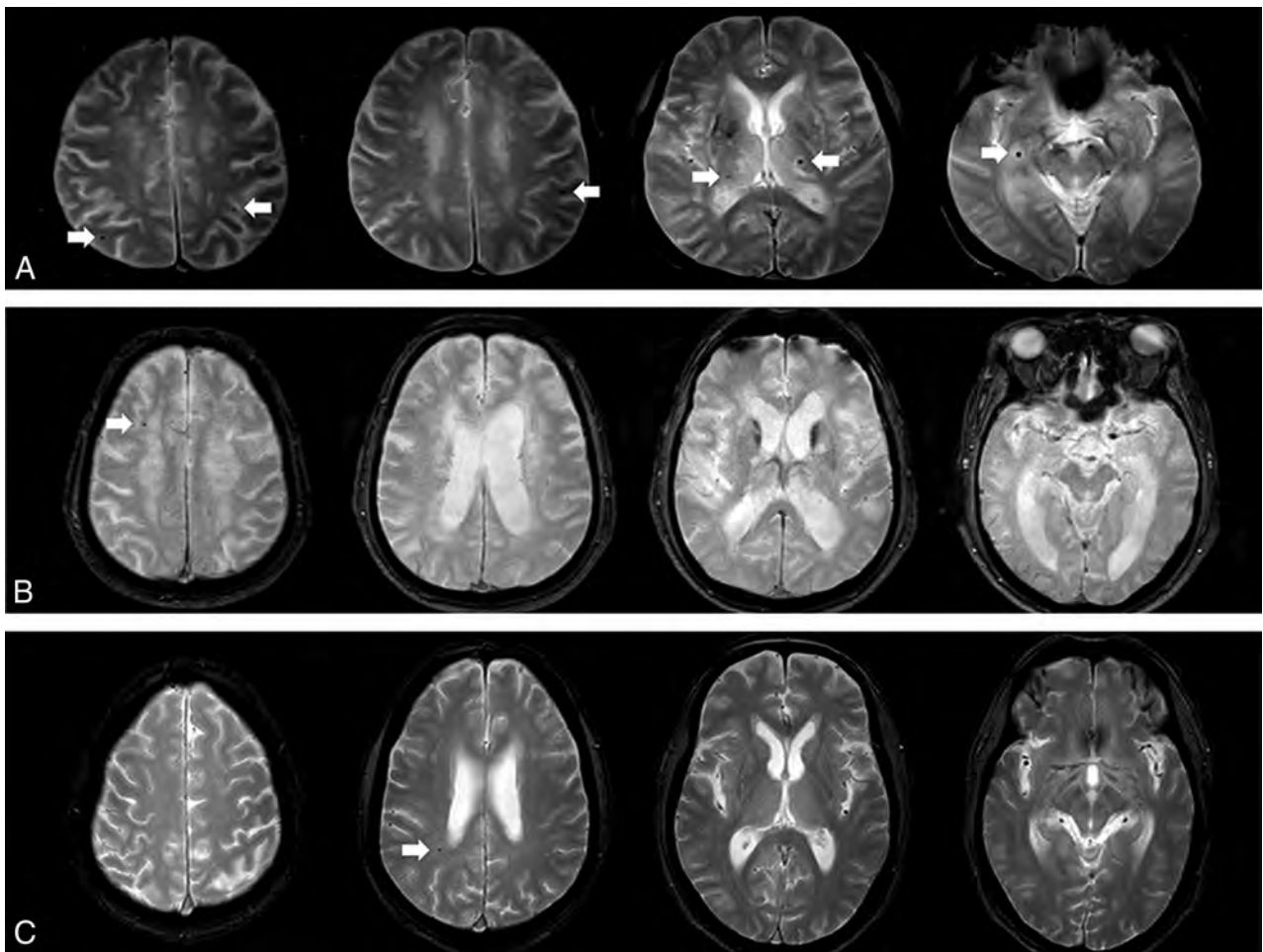


**FIGURE.** Examples of cerebral microbleeds observed in axial MR imaging obtained with conventional 2D T2\*-weighted gradient recalled-echo. A, MR imaging from a patient with DLB showing multiple CMBs (white arrows) in the bilateral thalamus, bilateral parietal lobe, and right temporal lobe. Also shown are MR images from a patient with PDD, showing a right periventricular CMB (B; white arrow), and from a healthy control, showing a right periventricular CMB (C; white arrow).

CMBs, CMBs were observed in the frontal areas in 4 patients (26.7%), the parietal areas in 7 (46.7%), the temporal areas in 5 (33.3%), and the occipital areas in 2 (13.3%). The topography of lobar CMBs did not differ significantly between the patients with DLB and those with PDD.

Logistic regression analyses were performed to investigate the independent determinants of lobar CMBs. When the analyses were unadjusted, DLB and WMHs were significantly associated with the presence of lobar CMBs relative to the healthy control group. After adjusting for age, sex, hypertension, diabetes mellitus, nonlobar CMBs, and WMHs, DLB was found to be significantly and independently associated with the presence of lobar CMBs relative to the control group (odds ratio, 4.39 [95% confidence interval, 1.27–15.25];  $P = .02$ ). However, PDD was not significantly associated with lobar CMBs relative to the healthy control group (Table 3).

## DISCUSSION

This study showed that patients with DLB had a greater burden of CMBs with lobar predominance than did patients with PDD. In addition, DLB, but not PDD, was independently associated with the presence of lobar CMBs. These data suggest that apart from

**Table 3: Multivariate analysis of determinants for lobar CMBs**

Variable	Univariate		Multivariate <sup>a</sup>	
	OR (95% CI)	P	OR (95% CI)	P
Group				
Controls	Reference		Reference	
Patients with DLB	5.5 (1.66–18.2)	.005	4.39 (1.27–15.25)	.02
Patients with PDD	1.63 (0.5–5.28)	.417	1.41 (0.42–4.73)	.577
Hypertension	1.79 (0.85–3.78)	.124	1.85 (0.52–6.6)	.342
Diabetes mellitus	1.91 (0.74–4.98)	.184	1.31 (0.35–4.89)	.688
Smoking	0.24 (0.3–1.93)	.317		
CVA	1.33 (0.33–5.41)	.687		
Cholesterol	0.99 (0.98–1.01)	.53		
Nonlobar CMBs	2.23 (0.84–6.27)	.097	0.97 (0.11–8.82)	.975
WMH	1.31 (1.12–1.53)	.001	1.44 (1.14–1.81)	.002

**Note:**—CVA indicates cerebrovascular accident.

<sup>a</sup> On multivariate analysis, data were adjusted for age and sex.

Lewy bodies, the pathologic correlates responsible for DLB may be attributable to more frequent lobar CMBs in patients with DLB than in those with PDD.

In terms of the patterns of CMB distribution, hypertensive vasculopathy usually affects small perforating arterioles in the deep gray matter, thus resulting in CMBs in the basal ganglia, thalamus, and brain stem.<sup>8</sup> In the present study, patients with

DLB did not differ from those with PDD with respect to the CMBs located in deep or infratentorial structures, which suggests that the burden of hypertensive vasculopathy may be similar in patients with these conditions. In contrast to hypertensive vasculopathy, cerebral amyloid angiopathy usually involves leptomeningeal and cortical arterial vessels, which leads to a lobar distribution of CMBs.<sup>15</sup> In the present study, patients with DLB exhibited a higher frequency of lobar CMBs than did healthy controls or those with PDD. Additional analysis of the topography of lobar CMBs revealed that the distribution of lobar CMBs did not differ significantly between patients with DLB and those with PDD. However, although statistical significance was not attained, lobar CMBs tended to be more frequent in the occipital areas of patients with DLB than in those with PDD. Similarly, CMBs in patients with Alzheimer disease and those with cerebral amyloid angiopathy exhibit occipital predominance.<sup>16,17</sup> These findings suggest that there may be an association between DLB and cerebrovascular amyloid deposition.

The high prevalence and lobar predominance of CMBs in patients with DLB are consistent with the results of a previous neuropathologic study,<sup>18</sup> in which cerebral mini-bleeds (bleeding lesions found mainly around small vessels, evident on microscopic examination but not visible macroscopically) were observed more frequently in patients with Alzheimer disease and those with DLB than in those with frontotemporal dementia and controls. Furthermore, mini-bleeds were frequently observed in the cerebral cortex and subcortical white matter of patients with DLB, and amyloid deposition in the vessels of brains with DLB was also greater than that in controls.<sup>18</sup> Other pathologic studies also indirectly supported the relationship between DLB and CMBs. High cortical amyloid burdens and/or plaque densities were evident in patients with DLB, and these features are closely associated with CMBs.<sup>11</sup> Ballard et al<sup>4</sup> reported that patients with DLB had greater plaque density than those with PDD, and Deramecourt et al<sup>19</sup> reported that patients with DLB had a considerable A $\beta$  burden, comparable to that in patients with Alzheimer disease. Thus, concomitant Alzheimer disease pathology, frequently accompanied by cerebral amyloid angiopathy, may lead to an increased likelihood of CMBs in patients with DLB. On the other hand, the relationship between CMBs and PDD has not been studied in detail. Although the results of pathologic studies of cortical A $\beta$  plaque load or cerebral amyloid angiopathy pathology in patients with PDD have been inconsistent, the A $\beta$  burden is regarded as less severe in patients with PDD than in those with DLB.<sup>4</sup> Imaging studies that used <sup>11</sup>C-Pittsburgh compound-B positron-emission tomography, which can detect cerebral amyloid angiopathy and diffuse plaque and neuritic plaque, showed a low amyloid burden in patients with PDD, which was comparable to those in Parkinson's disease and in healthy controls.<sup>20</sup> Burack et al<sup>21</sup> performed a neuropathologic examination of 3 patients with PDD who underwent <sup>11</sup>C-Pittsburgh compound-B positron-emission tomography within 15 months of death, and cerebral amyloid angiopathy was absent in 2 and only mild in the third.

Another factor that may explain the higher prevalence of CMBs in patients with DLB relative to those with PDD may be differences in characteristics of the amyloid plaque. Both neu-

ritic dense-core plaques and diffuse plaques are found in patients with DLB, whereas diffuse plaques are more prevalent in those with PDD.<sup>2,21,22</sup> According to pathologic studies, compared with the diffuse plaques that are usually less harmful, dense-core plaques are known to be associated with vessel walls and to enclose vessels.<sup>23</sup> Furthermore, a neuropathologic study in patients with Alzheimer disease and patients with Down syndrome revealed a close relationship between senile plaque and hemosiderin deposits, suggesting that dense-core plaques may be sites of microhemorrhage.<sup>24</sup> Thus, the high proportion of dense-core plaques in patients with DLB may have contributed to the higher prevalence of CMBs in the DLB group in the present study.

The limitations of this study need to be addressed. Its retrospective design is one of the main limitations, and it is possible that selection biases affected the choice of study population. Second, we used conventional 2D T2\*-weighted gradient recalled-echo, which is less sensitive than accelerated 3D T2\*-weighted gradient recalled-echo for detecting CMBs.<sup>25</sup> Moreover, susceptibility-weighted imaging, which is more sensitive for detecting CMBs than conventional T2\*-weighted gradient recalled-echo,<sup>26</sup> has become possible. Thus, conventional 2D T2\*-weighted gradient recalled-echo may have caused us to underestimate the number of CMBs. Third, the MR imaging platforms and sequence parameters used in this study were not uniform. However, the rates of CMBs in patients with DLB and in those with PDD were similar across the 3 participating hospitals (47.4%, 45.5%, and 41.7% in the DLB group and 26.5%, 28.1%, and 22.7% in the PDD group at Severance Hospital, Saint Mary's Hospital, and Ajou University Hospital, respectively). Finally, other measures of A $\beta$  load (CSF A $\beta$  and positron-emission tomography) and *Apolipoprotein E* status were not available because of the retrospective study design.

## CONCLUSIONS

The present study showed that the burden and topography of CMBs differed between patients with DLB and those with PDD. Patients with DLB had a greater burden of CMBs than did patients with PDD, and they exhibited a lobar predominance of CMBs. Furthermore, DLB, but not PDD, was significantly associated with the presence of lobar CMBs.

## REFERENCES

1. Emre M, Aarsland D, Brown R, et al. **Clinical diagnostic criteria for dementia associated with Parkinson's disease.** *Mov Disord* 2007;22:1689–707; quiz 1837 Medline
2. McKeith IG, Galasko D, Kosaka K, et al. **Consensus guidelines for the clinical and pathologic diagnosis of dementia with Lewy bodies (DLB): report of the consortium on DLB international workshop.** *Neurology* 1996;47:1113–24 CrossRef Medline
3. Tsuboi Y, Dickson DW. **Dementia with Lewy bodies and Parkinson's disease with dementia: are they different?** *Parkinsonism Relat Disord* 2005;11:S47–51 CrossRef Medline
4. Ballard C, Ziabreva I, Perry R, et al. **Differences in neuropathologic characteristics across the Lewy body dementia spectrum.** *Neurology* 2006;67:1931–34 CrossRef Medline
5. Armstrong RA, Cairns NJ, Lantos PL. **Beta-amyloid deposition in the temporal lobe of patients with dementia with Lewy bodies:**

- comparison with non-demented cases and Alzheimer's disease. *Dement Geriatr Cogn Disord* 2000;11:187–92 CrossRef Medline
6. Edison P, Rowe CC, Rinne JO, et al. **Amyloid load in Parkinson's disease dementia and Lewy body dementia measured with [<sup>11</sup>C]PIB positron emission tomography.** *J Neurol Neurosurg Psychiatry* 2008;79:1331–38 CrossRef Medline
  7. Greenberg SM, Vernooij MW, Cordonnier C, et al; Microbleed Study Group. **Cerebral microbleeds: a guide to detection and interpretation.** *Lancet Neurol* 2009;8:165–74 CrossRef Medline
  8. Fazekas F, Kleinert R, Roob G, et al. **Histopathologic analysis of foci of signal loss on gradient-echo T2\*-weighted MR images in patients with spontaneous intracerebral hemorrhage: evidence of microangiopathy-related microbleeds.** *AJNR Am J Neuroradiol* 1999;20:637–42 Medline
  9. Goos JD, Teunissen CE, Veerhuis R, et al. **Microbleeds relate to altered amyloid-[beta] metabolism in Alzheimer's disease.** *Neurobiol Aging* 2012;33:1011.e1-9 CrossRef Medline
  10. Schrag M, McAuley G, Pomakian J, et al. **Correlation of hypointensities in susceptibility-weighted images to tissue histology in dementia patients with cerebral amyloid angiopathy: a postmortem MRI study.** *Acta Neuropathol* 2010;119:291–302 CrossRef Medline
  11. Yates PA, Sirisriro R, Villemagne VL, et al. **Cerebral microhemorrhage and brain-amyloid in aging and Alzheimer disease.** *Neurology* 2011;77:48–54 CrossRef Medline
  12. McKeith IG, Dickson DW, Lowe J, et al; Consortium on DLB. **Diagnosis and management of dementia with Lewy bodies: third report of the DLB Consortium.** *Neurology* 2005;65:1863–72 CrossRef Medline
  13. Vernooij MW, van der Lugt A, Ikram MA, et al. **Prevalence and risk factors of cerebral microbleeds: the Rotterdam Scan Study.** *Neurology* 2008;70:1208–14 CrossRef Medline
  14. Wahlund LO, Barkhof F, Fazekas F, et al. **A new rating scale for age-related white matter changes applicable to MRI and CT.** *Stroke* 2001;32:1318–22 CrossRef Medline
  15. Knudsen KA, Rosand J, Karluk D, et al. **Clinical diagnosis of cerebral amyloid angiopathy: validation of the Boston criteria.** *Neurology* 2001;56:537–39 CrossRef Medline
  16. Pettersen JA, Sathiyamoorthy G, Gao FQ, et al. **Microbleed topography, leukoaraiosis, and cognition in probable Alzheimer disease from the Sunnybrook dementia study.** *Arch Neurol* 2008;65:790–95 CrossRef Medline
  17. Rosand J, Muzikansky A, Kumar A, et al. **Spatial clustering of hemorrhages in probable cerebral amyloid angiopathy.** *Ann Neurol* 2005;58:459–62 CrossRef Medline
  18. De Reuck J, Deramecourt V, Cordonnier C, et al. **Prevalence of small cerebral bleeds in patients with a neurodegenerative dementia: a neuropathological study.** *J Neurol Sci* 2011;300:63–66 CrossRef Medline
  19. Deramecourt V, Bombois S, Maurage CA, et al. **Biochemical staging of synucleinopathy and amyloid deposition in dementia with Lewy bodies.** *J Neuropathol Exp Neurol* 2006;65:278–88 CrossRef Medline
  20. Gomperts SN, Rentz DM, Moran E, et al. **Imaging amyloid deposition in Lewy body diseases.** *Neurology* 2008;71:903–10 CrossRef Medline
  21. Burack MA, Hartlein J, Flores HP, et al. **In vivo amyloid imaging in autopsy-confirmed Parkinson disease with dementia.** *Neurology* 2010;74:77–84 CrossRef Medline
  22. Harding AJ, Halliday GM. **Cortical Lewy body pathology in the diagnosis of dementia.** *Acta Neuropathol* 2001;102:355–63 Medline
  23. Kumar-Singh S. **Cerebral amyloid angiopathy: pathogenetic mechanisms and link to dense amyloid plaques.** *Genes Brain Behav* 2008;7(suppl 1):67–82 CrossRef Medline
  24. Cullen KM, Kócsi Z, Stone J. **Microvascular pathology in the aging human brain: evidence that senile plaques are sites of microhaemorrhages.** *Neurobiol Aging* 2006;27:1786–96 CrossRef Medline
  25. Vernooij MW, Ikram MA, Wielopolski PA, et al. **Cerebral microbleeds: accelerated 3D T2\*-weighted GRE MR imaging versus conventional 2D T2\*-weighted GRE MR imaging for detection.** *Radiology* 2008;248:272–77 CrossRef Medline
  26. Nandigam RN, Viswanathan A, Delgado P, et al. **MR imaging detection of cerebral microbleeds: effect of susceptibility-weighted imaging, section thickness, and field strength.** *AJNR Am J Neuroradiol* 2009;30:338–43 CrossRef Medline

# Effects of Type 2 Diabetes on Brain Structure and Cognitive Function: African American–Diabetes Heart Study MIND

C.T. Whitlow, K.M. Sink, J. Divers, S.C. Smith, J. Xu, N.D. Palmer, C.E. Hugenschmidt, J.D. Williamson, D.W. Bowden, B.I. Freedman, and J.A. Maldjian



## ABSTRACT

**BACKGROUND AND PURPOSE:** Rates of type 2 diabetes are higher among African Americans compared with individuals of European ancestry. The purpose of this investigation was to determine the relationship between MR imaging measures of brain structure (volume of GM, WM, WM lesions) and cognitive function in a population of African Americans with type 2 diabetes. These MR imaging measures of brain structure are affected by type 2 diabetes–associated macrovascular and microvascular disease and may be associated with performance on tasks of cognitive function in the understudied African American population.

**MATERIALS AND METHODS:** African Americans with type 2 diabetes enrolled in the African American–Diabetes Heart Study MIND study ( $n = 263$ ) were evaluated across a broad range of cognitive domains and imaged with brain MR imaging. Associations between cognitive parameters and MR imaging measures of whole-brain GM, WM, and WM lesion volumes were assessed by using adjusted multivariate models.

**RESULTS:** Lower GM volume was associated with poorer performance on measures of general cognitive function, working memory, and executive function. Higher WM lesion volume was associated with poorer performance on a smaller subset of cognitive domains compared with GM volume but included aspects of working memory and executive function. There were no statistically significant associations with WM volume.

**CONCLUSIONS:** Markers of cortical atrophy and WM lesion volume are associated with cognitive function in African Americans with type 2 diabetes. These associations are described in an African American cohort with disease control similar to that of individuals of European ancestry, rather than underserved African Americans with poor access to health care. Interventions to reduce cortical atrophy and WM disease may improve cognitive outcomes in this understudied population.

**ABBREVIATIONS:** T2D = type 2 diabetes; HbA1c = hemoglobin A1c; MMSE = Mini-Mental State Examination; MoCA = Montreal Cognitive Assessment; DSC = Digit Symbol Coding Task; VFA = verbal fluency for animals

The number of individuals with type 2 diabetes (T2D) is increasing throughout the world, and the prevalence of this disease is projected to rise during the next several decades. Estimates

indicate that diabetes will affect 366 million people in 2030, compared with 171 million in 2000.<sup>1</sup> T2D results in microvascular and macrovascular disease that produces end-organ damage leading to high morbidity and mortality.<sup>2</sup> Microvascular damage within the brain is associated with cerebral atrophy and other changes thought to underlie T2D-associated cognitive impairment.<sup>3–6</sup> Furthermore, evidence is growing that the central nervous system effects of T2D may accelerate the rate of cognitive decline among the elderly and increase the risk of developing dementia and Alzheimer disease.<sup>7–9</sup>

Rates of T2D are higher among African Americans compared with individuals of European ancestry.<sup>10</sup> As such, the prevalence of T2D-associated central nervous system and cognitive sequelae among African Americans may also be higher. Few studies, however, have characterized the association between brain structure and cognitive function in a large comprehensively phenotyped

Received October 6, 2014; accepted after revision February 7, 2015.

From the Department of Radiology, Section of Neuroradiology (C.T.W., J.A.M.); Advanced Neuroscience Imaging Research Laboratory (C.T.W., J.A.M.); Department of Biomedical Engineering (C.T.W., J.A.M.); Department of Internal Medicine, Section on Gerontology and Geriatric Medicine (K.M.S., C.E.H., J.D.W.); Division of Public Health Sciences, Department of Biostatistical Sciences (J.D.); Department of Biochemistry (S.C.S., J.X., N.D.P., D.W.B.); Center for Diabetes Research, Center for Genomics and Personalized Medicine Research (N.D.P., D.W.B., B.I.F.); Department of Internal Medicine, Section on Nephrology (B.I.F.), Wake Forest School of Medicine, Winston-Salem, North Carolina.

This work was supported by R01 NS075107 (J.D., J.A.M., B.I.F.), NS058700 (D.W.B.), and DK071891 (B.I.F.).

Please address correspondence to Christopher T. Whitlow, MD, PhD, MHA, Advanced Neuroscience Imaging Research Laboratory, Department of Radiology, Neuroradiology, Translational Science Institute, Wake Forest University Health Sciences, Winston-Salem, NC 27157-1088; e-mail: cwhitlow@wakehealth.edu

Indicates open access to non-subscribers at [www.ajnr.org](http://www.ajnr.org)

Indicates article with supplemental on-line table.

<http://dx.doi.org/10.3174/ajnr.A4321>

cohort of African Americans with T2D, particularly those with relatively well-controlled vascular disease risk factors (hypertension and hyperlipidemia) and access to adequate health care.<sup>11</sup> The purpose of this investigation was to determine the relationship between MR imaging measures of brain structure and cognitive function in an African American population with T2D enrolled in the African American–Diabetes Heart Study MIND. We hypothesized that lower brain volume and a higher burden of WM disease would be associated with poorer performance on tests spanning a variety of cognitive domains.

## MATERIALS AND METHODS

### Participants

The Wake Forest University Health Sciences institutional review board approved this study, and all participants provided written informed consent. A cohort of 263 unrelated African Americans with T2D were recruited for this investigation as part of the African American–Diabetes Heart Study MIND, funded by the National Institutes of Health. The objectives of the African American–Diabetes Heart Study MIND are to improve our understanding of the risk factors for impaired cognitive function and abnormalities of cerebral architecture in the understudied African American population with T2D.

Participants included in this study were diagnosed with T2D in the absence of diabetic ketoacidosis with the onset of clinical disease after 30 years of age on the basis of the following: 1) active medical treatment (insulin and/or oral hypoglycemic agents), 2) nonfasting blood sugar of  $\geq 200$  mg/dL, 3) fasting blood sugar of  $\geq 126$  mg/dL, or 4) hemoglobin A1c (HbA1c) of  $\geq 6.5\%$ . Fasting measures of glucose, HbA1c, low-density lipoprotein cholesterol, high-density lipoprotein cholesterol, triglycerides, thyroid stimulating hormone, and vitamin B<sub>12</sub> were acquired. Medical and educational histories, vital signs, and active medications were also recorded.

### Cognitive Testing

The cognitive battery was organized to evaluate a broad range of cognitive domains known to be associated with brain microvascular disease, which can be present in the setting of T2D.<sup>12,13</sup> A single investigator (K.M.S.) was responsible for quality control and training, certification, and assessment of study staff responsible for conducting cognitive tests. General cognitive function was assessed with the modified Mini-Mental State Examination (MMSE) and Montreal Cognitive Assessment (MoCA).<sup>14–16</sup> We included the MoCA in addition to the modified MMSE due to its added measures of executive function and increased sensitivity for detecting early cognitive impairment. The Rey Auditory Verbal Learning Test is a word list recall task that evaluates verbal learning and memory<sup>17</sup> and has been reported to correlate strongly with executive function.<sup>18</sup> The Digit Symbol Coding Task (DSC) is a subtest of the Wechsler Adult Intelligence Scale (3rd ed) that is used to assess visual motor speed, sustained attention, and working memory,<sup>19</sup> which have been associated with future cognitive decline.<sup>20,21</sup> Additional aspects of executive function were evaluated with the verbal fluency for animals (VFA) task and the Stroop test.<sup>22–26</sup> Depression and anxiety represent possible confounding variables that may affect the relationship between cognitive func-

tion and brain structure. Depression and anxiety were evaluated with the Center for Epidemiologic Studies Depression scale<sup>27</sup> and the Anxiety Brief Symptom Inventory,<sup>28</sup> respectively.

### Brain MR Imaging

**MR Imaging Acquisition.** Scanning for the initial 73 subjects was performed on a 1.5T Excite HD scanner (GE Healthcare, Milwaukee, Wisconsin) with twin-speed gradients by using a neurovascular head coil (GE Healthcare). High-resolution T1 anatomic images were obtained by using a 3D volumetric inversion recovery echo-spoiled gradient-echo sequence (TR = 7.36 ms, TE = 2.02 ms, TI = 600 ms, flip angle = 20°, 124 sections, FOV = 24 cm, matrix size = 256 × 256, 1.5-mm section thickness). FLAIR images were acquired in the axial plane (TR = 8002 ms, TE = 101.29 ms, TI = 2000 ms, flip angle = 90°, FOV = 24 cm, matrix size = 256 × 256, 3-mm section thickness). Because of a change in MR imaging equipment at the Wake Forest University Health Sciences Center for Biomolecular Imaging, scanning of the subsequent 190 participants was performed on a 3T Magnetom Skyra MR imaging scanner (Siemens, Erlangen, Germany) by using a high-resolution 20-channel head/neck coil (Siemens). T1-weighted anatomic images were obtained by using a 3D volumetric MPRAGE sequence (TR = 2300 ms, TE = 2.99 ms, TI = 900 ms, flip angle = 9°, 192 sections, voxel dimension = 0.97 × 0.97 × 1 mm). FLAIR images were acquired by using a 3D sampling perfection with application-optimized contrasts by using a different flip angle evolution (Siemens) inversion recovery sequence (TR = 6000 ms, TE = 283 ms, TI = 2200 ms, flip angle = 120°, 160 sections, voxel dimensions = 1.1 × 1.1 × 1 mm).

**Image Segmentation.** Structural T1 images were segmented into GM, WM, and CSF and normalized to Montreal Neurological Imaging space by using the Diffeomorphic Anatomical Registration Through Exponentiated Lie Algebra high-dimensional warping (<http://www.neurometrika.org/node/34>) and the SPM8 software (<http://www.fil.ion.ucl.ac.uk/spm/software/spm8>)<sup>29</sup> new-segment procedure, as implemented in the VBM8 toolbox (<http://dbm.neuro.uni-jena.de/vbm.html>). Total GM and WM volume and intracranial volume (comprising GM + WM + CSF) were determined from the VBM8 automated segmentation procedure, which outputs a text file with values for native space total GM, WM, and CSF volumes. Whole-brain volumes (GM and WM) are reported milliliters. GM and WM volumes adjusted for intracranial volume were used in the linear regression models.

**White Matter Lesion Segmentation.** White matter lesion segmentation was performed by using the Lesion Segmentation Toolbox ([http://www.academia.edu/2729347/LST\\_A\\_Lesion\\_Segmentation\\_Tool\\_For\\_SPM](http://www.academia.edu/2729347/LST_A_Lesion_Segmentation_Tool_For_SPM))<sup>30</sup> for SPM8 at a threshold (k) of 0.25.<sup>31</sup> Normalization to Montreal Neurological Imaging space was accomplished by coregistration with the structural T1 and applying the normalization parameters computed in the VBM8 segmentation procedure. The white matter lesion was determined by summing the binary lesion maps and multiplying by the voxel volume; it was reported in milliliters.

**Table 1: Demographic and laboratory results in African American–Diabetes Heart Study MIND participants (N = 263)**

Variable	Mean	SD
Age (yr)	60.4	9.6
Duration of diabetes (yr)	14.3	8.9
Age of diabetes diagnosis (yr)	46.0	11.0
Body mass index (kg/m <sup>2</sup> )	34.1	7.9
Glucose (mg/dL)	147.5	60.3
HbA1c (%)	8.2	2.1
LDL cholesterol (mg/dL)	109.1	37.7
HDL cholesterol (mg/dL)	47.2	11.9
Triglycerides (mg/dL)	115.7	72.3
Systolic blood pressure (mm Hg)	131.2	18.6
Diastolic blood pressure (mm Hg)	75.4	10.8
Thyroid stimulating hormone (μIU/mL)	2.0	1.6
Vitamin B <sub>12</sub> (pg/mL)	690.0	417.3

Note.—LDL indicates low-density lipoprotein; HDL, high-density lipoprotein.

### Statistical Analyses

**Interscanner Variability.** Fifteen study participants underwent scanning by using both 1.5T and 3T MR imaging to account for between-scanner variation. Both datasets for each participant were processed by using identical methods. Adjustments were made to account for any systematic differences in volumetric measures between scanners.<sup>32,33</sup> Linear regression was used to estimate calibration equations between the 1.5T and 3T measurements. These equations were used to determine the corresponding 3T MR imaging value from an MR imaging scan performed on a 1.5T scanner. *R*<sup>2</sup> values obtained from the calibration equations also provide an estimate of the reliability of 1.5T measurements as predictors of the 3T MR imaging values.

Linear models were fitted to test for associations between measures of cognitive performance (independent variables) and brain MR imaging measures (dependent variables). GM and WM volumes were adjusted for intracranial volume (comprising GM + WM + CSF). The Box-Cox method<sup>33</sup> was applied to identify the appropriate transformation best approximating the distributional assumptions of conditional normality and the homogeneity of variance of the residuals. This method suggested taking the natural logarithm of WM lesion volume and the squared value of the intracranial volume–adjusted WM and GM volumes. Models were run unadjusted and successively adjusted for age, sex, body mass index, T2D severity (HbA1c), and level of education (1 = less than high school, 2–5 = number of years in high school, 5 = graduate, 6–9 number of years in college [9 = graduate], 10 = postgraduate degree). Adjusted results refer to the model testing for the association between MR imaging variables and cognitive function after adjustment for all 5 covariates. An  $\alpha$  level of  $\leq .05$  was used for all statistical tests.

### RESULTS

Tables 1 and 2 present demographic and laboratory characteristics of the cohort, and Table 3 contains results of brain MR imaging and cognitive function measurements. The reliability coefficient between MR imaging measures obtained on the 1.5T and 3T scanners ranged between 98% for the intracranial volume and 92% for the GM volume. Unadjusted and adjusted analyses were performed to determine the relationships between continuous measures of cerebral anatomy and cognitive function (On-line

**Table 2: Group characteristics in African American–Diabetes Heart Study MIND (N = 263)**

Variable	No. (% of Total Cohort)
Female	165 (62.7%)
Hypertension	87 (33.1%)
Insulin use	108 (41.1%)
Lipid medication	93 (54.7%)
Smoking	
Never	117 (44.7%)
Former	91 (34.7%)
Current	54 (20.6%)
Education	
Less than a high school diploma	27 (10.3%)
High school diploma	76 (28.9%)
Some college or a college diploma	115 (43.7%)
Graduate education	45 (17.1%)

**Table 3: MRI and cognitive function measures in African American–Diabetes Heart Study MIND**

Variable	Mean	SD	No.
MRI results			
GM volume, unadjusted (mL)	732.2	57.7	263
GM/ICV (%) <sup>a</sup>	43.3	2.8	263
WM volume, unadjusted (mL)	629.6	46.7	263
WM/ICV (%) <sup>a</sup>	37.3	2.3	263
WM lesion volume (mL)	7.9	14.7	263
Cognitive function measures			
3MSE (score, 0–100)	84.6	9.0	256
MoCA (score, 0–30)	19.9	3.9	261
RAVLT (score, 0–75)	38.0	9.0	263
DSC (score, 0–133)	48.1	15.9	262
VFA	15.7	4.6	262
Stroop errors	3.4	6.3	258
Stroop interference (seconds; trial 3 to trial 2)	31.6	16.1	256
CESD	8.0	5.3	262
BSI-Anxiety	4.9	4.5	262

Note.—ICV indicates intracranial volume; 3 MSE, modified MMSE; RAVLT, Rey Auditory Verbal Learning Test; CESD, Center for Epidemiologic Studies Depression Scale; BSI-Anxiety, Brief Symptom Inventory.

<sup>a</sup> Whole-brain measures adjusted for total ICV.

Table). Results of the fully adjusted models, including the effects of age, sex, body mass index, HbA1c, and level of education, follow. No significant relationships were detected between glycemic control assessed by HbA1c with WM lesion volume, GM volume, or WM volume ( $P = .51$ ,  $P = .36$ , and  $P = .35$ , respectively; data not shown). There were also no statistically significant associations between MR imaging measures and the depression and anxiety evaluations ( $P > .05$ ).

As shown in the On-line Table, the modified MMSE had a positive association with GM volume ( $P = .0023$ ) but no statistically significant association with WM volume ( $P = .18$ ) or WM lesion volume ( $P = .15$ ). The MoCA had a positive association with GM volume ( $P = .022$ ), but no significant association with WM volume ( $P = .43$ ) or WM lesion volume ( $P = .82$ ). DSC had a positive association with GM volume ( $P = .015$ ) and a negative association with WM lesion volume ( $P = 6.7 \times 10^{-4}$ ), but no significant association with WM volume ( $P = .12$ ). Stroop interference had a negative association with GM volume ( $P = .035$ ) and a positive association with WM lesion volume ( $P = 4.6 \times 10^{-3}$ ), but no significant association with WM volume ( $P = .26$ ). The Rey Auditory Verbal Learning Test, VFA, and Stroop errors were not significantly associated with any of the brain MR imag-

ing measures ( $P > .05$ ). Measures of effect size are provided in the last columns of the On-line Table for lower GM and WM and higher WM lesion volume associated with cognitive test performance. The subcolumns labeled “Absolute” and “%” report the absolute and percentage differences from the mean cognitive score computed for each 1 SD change in MR imaging measure. For example, 1 SD lower GM volume corresponds to lower modified MMSE (“Absolute,” “%”:  $-10.7$ ,  $-12.6\%$ ), MoCA ( $-1.2$ ,  $-6.2\%$ ), and DSC ( $-2.7$ ,  $-5.5\%$ ) scores and a higher Stroop interference (2.1, 6.8%) score compared with group mean scores reported in Table 3. A 1-SD higher WM lesion volume corresponds to lower DSC (“Absolute,” “%”:  $-3.3$ ,  $-6.9\%$ ) and higher Stroop interference (2.9, 9.0%) scores compared with group mean scores reported in Table 3.

## DISCUSSION

The African American-Diabetes Heart Study MIND was designed to improve our understanding of T2D-associated risk factors for impaired cognitive function and abnormalities of cerebral architecture in the understudied African American population with levels of disease control similar to those of individuals of European ancestry. In general, lower whole-brain GM volume and higher WM lesion volume were associated with poorer cognitive performance in this cohort. Measures of GM atrophy, as characterized by lower GM volume, were associated with the greatest number of cognitive domains evaluated, including a variety of general measures of cognitive function, working memory, and executive function. WM lesion volume was associated with a smaller subset of cognitive domains compared with GM volume, including aspects of working memory and executive function. In contrast to measures of GM atrophy and WM lesion volume, there were no statistically significant associations between any measures of cognitive function and WM volume. Furthermore, a few measures of cognitive function demonstrated no associations with measures of cerebral anatomy. Specifically, there were no statistically significant associations with verbal fluency, as measured with VFA, and any of the brain MR imaging measures.

As opposed to prior studies of brain anatomy and cognition in African Americans with T2D, participants in the African American-Diabetes Heart Study MIND had relatively good access to health care.<sup>34,35</sup> This is reflected by high rates of statin use and mean blood pressures, universal treatment for hypertension, and HbA1c and lipid profiles reflecting a level of control seen in studies comprising subjects with European ancestry. As such, the results of this study may not be generalizable to African Americans with T2D that is poorly monitored and/or controlled. T2D is known to be associated with structural changes in the brain, similar to those reported in our study, including cerebral atrophy and WM lesions that correlate with the presence of microvascular and macrovascular ischemic disease.<sup>36-41</sup> Other cross-sectional studies of T2D have reported associations among brain atrophy, WM lesion burden, and diminished cognitive function. In 1 study, MR imaging variables were used in a stepwise regression model that demonstrated the strongest relationship between GM atrophy and cognitive function, with WM volume and WM lesion volume demonstrating relatively smaller effects on the model.<sup>6</sup>

These findings may have relevance in the context of our data in

which GM volume was associated with the greatest number of cognitive domains evaluated and WM lesion volume was associated with a smaller subset of cognitive functions. Such findings regarding brain anatomy and cognitive function are important because it is thought that T2D-associated changes in the brain may underlie the increased risk of developing dementia among this population, including a reported 50%–100% increased risk of developing Alzheimer disease.<sup>42-44</sup> Very likely many factors link MR imaging measures of cerebral anatomy and cognitive function. However, adjustment for age, sex, body mass index, T2D severity (HbA1c), and level of education did not affect these relationships in this study. These findings suggest that the impact of diabetes on brain volume, WM lesion load, and cognitive function that we report was not directed through these pathways.

Our results provide an extensive characterization of brain structure and cognitive function focused solely on the understudied African American population with T2D and well-controlled cardiovascular disease risk factors. Strengths include the relatively large sample size of African Americans with diabetes and the breadth of cognitive functions evaluated, which included a variety of domains previously shown to be affected by T2D. This study also used quantitative structural MR imaging measures that have been applied in numerous studies of T2D. However, this study adds to the previous literature by using fully quantitative measures of WM lesion volume previously validated in this cohort,<sup>31</sup> rather than qualitative and semiquantitative measures of WM lesion load.

The limitations of this study include the lack of a nondiabetic control group, cross-sectional design, and lack of covariates that could be related to potential mechanisms, such as medication use and inflammatory markers. This study also focused on whole-brain MR imaging measures rather than evaluating individual brain ROIs such as the hippocampus and frontal lobes, which may more specifically underlie performance in the cognitive domains evaluated. Such investigations of specific ROIs will be conducted in the future once data collection for the entire African American-Diabetes Heart Study MIND cohort is completed.

## CONCLUSIONS

Results from the African American-Diabetes Heart Study MIND cohort reveal that cognitive function is associated with markers of cortical atrophy and WM lesion volume, independent of diabetes severity in African Americans with T2D. These associations between brain structure and cognitive function are described in a cohort of African Americans with disease control similar to that of individuals of European ancestry, rather than underserved African Americans with poor access to health care. Taken together, our data suggest that interventions to reduce cortical atrophy and white matter disease may have the potential to improve cognitive outcomes in this understudied population.

## ACKNOWLEDGMENTS

The authors thank the African American-Diabetes Heart Study MIND participants and study staff for their valuable contributions.

Disclosures: Christopher T. Whitlow—*RELATED: Grant:* National Institutes of Health,\* National Institute of Neurological Disorders and Stroke,\* *Comments:* R01 NS075107. Kaycee M. Sink—*RELATED: Grant:* National Institutes of Health (National Institute of Neurological Disorders and Stroke)\*; *UNRELATED: Grants/Grants Pending:* Navidea Pharmaceuticals,\* Alzheimer's Association,\* *Comments:* 1) Navidea Pharmaceuticals, site Principal Investigator for a clinical trial involving an amyloid imaging agent, 2) Alzheimer's Association, study clinician on an investigator-initiated grant, 3) all other grant funding is federal or not relevant to this work. Jasmin Divers—*RELATED: Grant:* National Institutes of Health.\* Christina E. Hugenschmidt—*RELATED: Grant:* National Institute of Diabetes and Digestive and Kidney Diseases.\* Jeff D. Williamson—*RELATED: Grant:* National Institutes of Health.\* Barry I. Freedman—*RELATED: Grant:* National Institutes of Health,\* *Comments:* The African American–Diabetes Heart Study MIND is a National Institutes of Health–funded research study (R01). Drs Maldjian, Divers, and Freedman are co-Principal Investigators on the grant. Joseph A. Maldjian—*RELATED: Grant:* National Institutes of Health,\* *Comments:* R01-funded study through the National Institute of Neurological Disorders and Stroke. \*Money paid to the institution.

## REFERENCES

- Wild S, Roglic G, Green A, et al. **Global prevalence of diabetes: estimates for the year 2000 and projections for 2030.** *Diabetes Care* 2004;27:1047–53
- Simić I, Pecin I, Tedeschi-Reiner E, et al. **Risk factors for microvascular atherosclerotic changes in patients with type 2 diabetes mellitus.** *Coll Antropol* 2013;37:783–87
- Biessels GJ. **Cerebral complications of diabetes: clinical findings and pathogenetic mechanisms.** *Neth J Med* 1999;54:35–45
- van Harten B, de Leeuw FE, Weinstein HC, et al. **Brain imaging in patients with diabetes: a systematic review.** *Diabetes Care* 2006;29:2539–48
- van Elderen SG, de Roos A, de Craen AJ, et al. **Progression of brain atrophy and cognitive decline in diabetes mellitus: a 3-year follow-up.** *Neurology* 2010;75:997–1002
- Moran C, Phan TG, Chen J, et al. **Brain atrophy in type 2 diabetes: regional distribution and influence on cognition.** *Diabetes Care* 2013;36:4036–42
- Vagelatos NT, Eslick GD. **Type 2 diabetes as a risk factor for Alzheimer's disease: the confounders, interactions, and neuropathology associated with this relationship.** *Epidemiol Rev* 2013;35:152–60
- Ryan JP, Fine DF, Rosano C. **Type 2 diabetes and cognitive impairment: contributions from neuroimaging.** *J Geriatr Psychiatry Neurol* 2014;27:47–55
- Sato N, Morishita R. **Roles of vascular and metabolic components in cognitive dysfunction of Alzheimer disease: short- and long-term modification by non-genetic risk factors.** *Front Aging Neurosci* 2013;5:64
- Peek ME, Cargill A, Huang ES. **Diabetes health disparities: a systematic review of health care interventions.** *Med Care Res Rev* 2007;64 (5 suppl):101S–56S
- Divers J, Hugenschmidt C, Sink KM, et al. **Cerebral white matter hyperintensity in African Americans and European Americans with type 2 diabetes.** *J Stroke Cerebrovasc Dis* 2013;22:e46–52
- Thabit H, Kyaw Tun T, McDermott J, et al. **Executive function and diabetes mellitus: a stone left unturned?** *Curr Diabetes Rev* 2012;8:109–15
- Qiu C, Sigurdsson S, Zhang Q, et al. **Diabetes, markers of brain pathology, and cognitive cognition: the age, gene/environment susceptibility—Reykjavik study.** *Ann Neurol* 2014;75:138–46
- Teng EL, Chui HC. **The Modified Mini-Mental State (3MS) Examination.** *J Clin Psychiatry* 1987;48:314–18
- Grace J, Nadler JD, White DA, et al. **Folstein vs modified Mini-Mental State Examination in geriatric stroke: stability, validity, and screening utility.** *Arch Neurol* 1995;52:477–84
- Nasreddine ZS, Phillips NA, Bedirian V, et al. **The Montreal Cognitive Assessment, MoCA: a brief screening tool for mild cognitive impairment.** *J Am Geriatr Soc* 2005;53:695–99
- Strauss E, Sherman S, Spreen O. *A Compendium of Neuropsychological 661 Tests: Administration, Norms, and Commentary.* 3rd ed. New York: Oxford University Press; 2006
- Duff K, Schoenberg MR, Scott JG, et al. **The relationship between executive functioning and verbal and visual learning and memory.** *Arch Clin Neuropsychol* 2005;20:111–22
- Wechsler D. *Wechsler Adult Intelligence Scale.* 3rd ed. San Antonio: Psychological Corp; 1997
- Hoyer WJ, Stawski RS, Wasylyshyn C, et al. **Adult age and digit symbol substitution performance: a meta-analysis.** *Psychol Aging* 2004;19:211–14
- Rosano C, Simonsick EM, Harris TB, et al. **Association between physical and cognitive function in healthy elderly: the health, aging and body composition study.** *Neuroepidemiology* 2005;24:8–14
- MacLeod CM. **Half a century of research on the Stroop effect: an integrative review.** *Psychol Bull* 1991;109:163–203
- Houx PJ, Jolles J, Vreeling FW. **Stroop interference: aging effects assessed with the Stroop Color-Word Test.** *Exp Aging Res* 1993;19:209–24
- Klein M, Ponds RW, Houx PJ, et al. **Effect of test duration on age-related differences in Stroop interference.** *J Clin Exp Neuropsychol* 1997;19:77–82
- Van der Elst W, Molenberghs G, Van Boxtel MP, et al. **Establishing normative data for repeated cognitive assessment: a comparison of different statistical methods.** *Behav Res Methods* 2013;45:1073–86
- Reis JP, Launer LJ, Terry JG, et al. **Subclinical atherosclerotic calcification and cognitive functioning in middle-aged adults: the CARDIA study.** *Atherosclerosis* 2013;231:72–77
- Radloff LS. **The CES-D scale: a self-report depression scale for research in the general population.** *Appl Psychol Meas* 1977;1:385–401
- Gilbar O, Ben-Zur H. **Adult Israeli community norms for the Brief Symptom Inventory (BSI).** *Int J Stress Manage* 2002;9:1–10
- Ashburner J, Friston KJ. **Voxel-based morphometry: the methods.** *Neuroimage* 2000;11:805–21
- Schmidt P, Gaser C, Arsic M, et al. **An automated tool for detection of FLAIR-hyperintense white-matter lesions in multiple sclerosis.** *Neuroimage* 2012;59:3774–83
- Maldjian JA, Whitlow CT, Saha BN, et al. **Automated white matter total lesion volume segmentation in diabetes.** *AJNR Am J Neuroradiol* 2013;34:2265–70
- Jovicich J, Czanner S, Han X, et al. **MRI-derived measurements of human subcortical, ventricular and intracranial brain volumes: reliability effects of scan sessions, acquisition sequences, data analyses, scanner upgrade, scanner vendors and field strengths.** *Neuroimage* 2009;46:177–92
- Han X, Jovicich J, Salat D, et al. **Reliability of MRI-derived measurements of human cerebral cortical thickness: the effects of field strength, scanner upgrade and manufacturer.** *Neuroimage* 2006;32:180–94
- Aggarwal NT, Wilson RS, Bienias JL, et al. **The association of magnetic resonance imaging measures with cognitive function in a biracial population sample.** *Arch Neurol* 2010;67:475–82
- Brickman AM, Schupf N, Manly JJ, et al. **Brain morphology in older African Americans, Caribbean Hispanics, and whites from northern Manhattan.** *Arch Neurol* 2008;65:1053–61
- Kumar R, Anstey KJ, Cherbuin N, et al. **Association of type 2 diabetes with depression, brain atrophy, and reduced fine motor speed in a 60- to 64-year-old community sample.** *Am J Geriatr Psychiatry* 2008;16:989–98
- Biessels GJ, Koffeman A, Scheltens P. **Diabetes and cognitive impairment: clinical diagnosis and brain imaging in patients attending a memory clinic.** *J Neurol* 2006;253:477–82
- Schmidt R, Launer LJ, Nilsson LG, et al. **Magnetic resonance imaging of the brain in diabetes: the Cardiovascular Determinants of Dementia (CASCADE) study.** *Diabetes* 2004;53:687–92
- Manschot SM, Biessels GJ, de Valk H, et al. **Metabolic and vascular determinants of impaired cognitive performance and abnormal-**

- ties on brain magnetic resonance imaging in patients with type 2 diabetes. *Diabetologia* 2007;50:2388–97
40. Kumar A, Haroon E, Darwin C, et al. **Gray matter prefrontal changes in type 2 diabetes detected using MRI.** *J Magn Reson Imaging* 2008;27:14–19
41. de Bresser J, Tichhuis AM, van den Berg E, et al. **Progression of cerebral atrophy and white matter hyperintensities in patients with type 2 diabetes.** *Diabetes Care* 2010;33:1309–14
42. Biessels GJ, Staekenborg S, Brunner E, et al. **Risk of dementia in diabetes mellitus: a systematic review.** *Lancet Neurol* 2006;5:64–74
43. Biessels GJ, Deary IJ, Ryan CM. **Cognition and diabetes: a lifespan perspective.** *Lancet Neurol* 2008;7:184–90
44. Kloppenborg RP, van den Berg E, Kappelle LJ, et al. **Diabetes and other vascular risk factors for dementia: which factor matters most? A systematic review.** *Eur J Pharmacol* 2008;585:97–108

# Repeatability of Standardized and Normalized Relative CBV in Patients with Newly Diagnosed Glioblastoma

M.A. Prah, S.M. Stufflebeam, E.S. Paulson, J. Kalpathy-Cramer, E.R. Gerstner, T.T. Batchelor, D.P. Barboriak, B.R. Rosen, and K.M. Schmainda



## ABSTRACT

**BACKGROUND AND PURPOSE:** For more widespread clinical use advanced imaging methods such as relative cerebral blood volume must be both accurate and repeatable. The aim of this study was to determine the repeatability of relative CBV measurements in newly diagnosed glioblastoma multiforme by using several of the most commonly published estimation techniques.

**MATERIALS AND METHODS:** The relative CBV estimates were calculated from dynamic susceptibility contrast MR imaging in double-baseline examinations for 33 patients with treatment-naïve and pathologically proved glioblastoma multiforme (men = 20; mean age = 55 years). Normalized and standardized relative CBV were calculated by using 6 common postprocessing methods. The repeatability of both normalized and standardized relative CBV, in both tumor and contralateral brain, was examined for each method with metrics of repeatability, including the repeatability coefficient and within-subject coefficient of variation. The minimum sample size required to detect a parameter change of 10% or 20% was also determined for both normalized relative CBV and standardized relative CBV for each estimation method.

**RESULTS:** When ordered by the repeatability coefficient, methods using postprocessing leakage correction and  $\Delta R2^*(t)$  techniques offered superior repeatability. Across processing techniques, the standardized relative CBV repeatability in normal-appearing brain was comparable with that in tumor ( $P = .31$ ), yet inferior in tumor for normalized relative CBV ( $P = .03$ ). On the basis of the within-subject coefficient of variation, tumor standardized relative CBV estimates were less variable (13%–20%) than normalized relative CBV estimates (24%–67%). The minimum number of participants needed to detect a change of 10% or 20% is 118–643 or 30–161 for normalized relative CBV and 109–215 or 28–54 for standardized relative CBV.

**CONCLUSIONS:** The  $\Delta R2^*$  estimation methods that incorporate leakage correction offer the best repeatability for relative CBV, with standardized relative CBV being less variable and requiring fewer participants to detect a change compared with normalized relative CBV.

**ABBREVIATIONS:** nRCBV = normalized relative CBV; RC = repeatability coefficient; rCBV = relative CBV; sRCBV = standardized relative CBV; wCV = within-subject coefficient of variation

Dynamic susceptibility contrast MR imaging has been increasingly used to evaluate the vascular properties of brain tumors and may be useful in other disorders of the central nervous system,

including stroke, hypoxia, stenosis, and brain trauma. DSC MR imaging is obtained by quantifying the signal-intensity change on T2\*/T2-weighted imaging following injection of contrast agent as it passes through tissue. Parameters typically derived from DSC MR imaging include cerebral blood flow, cerebral mean transit time, and relative CBV (rCBV); the latter is generally regarded as the most robust and commonly derived parameter of the 3. For patients with brain tumors, the information provided by rCBV estimates has been used to assist clinicians in the identification of brain tumor grade,<sup>1–5</sup> progression,<sup>6–8</sup> and aggressiveness or treatment response.<sup>7,9,10</sup>

Postprocessing methods used for rCBV estimation are varied,

Received November 4, 2014; accepted after revision January 23, 2015.

From the Departments of Radiology (M.A.P., K.M.S., E.S.P.) and Radiation Oncology (E.S.P.), Medical College of Wisconsin, Milwaukee, Wisconsin; Department of Radiology (S.M.S., J.K.-C., E.R.G., T.T.B., B.R.R.), Massachusetts General Hospital, Boston, Massachusetts; and Department of Radiology (D.P.B.), Duke University Medical Center, Durham, North Carolina.

This work was supported by National Institutes of Health/National Institute of Neurological Disorders and Stroke RO1 NS060918, National Institutes of Health/National Cancer Institute RO1 CA082500, National Institutes of Health/National Cancer Institute U01 CA176110 (Medical College of Wisconsin), and National Institutes of Health/National Cancer Institute U01 CA154601 (Massachusetts General Hospital).

Please address correspondence to Kathleen M. Schmainda, PhD, Department of Radiology, Medical College of Wisconsin, 8701 Watertown Plank Rd, Milwaukee, WI 53226; e-mail: kathleen@mcw.edu

Indicates open access to non-subscribers at www.ajnr.org

Indicates article with supplemental on-line appendix.

<http://dx.doi.org/10.3174/ajnr.A4374>

with no single technique implemented as the standard for use in clinical practice or research. Reports have demonstrated profound differences in derived rCBV values that depend on the choice of acquisition and postprocessing methods,<sup>11</sup> with much of this variability being attributed to the effects of contrast agent leakage due to blood-brain barrier disruption. These effects, which are especially influential when evaluating high-grade gliomas, can be minimized or corrected for by either administration of a preload dose of contrast agent to saturate T1 changes due to leakage or by a postprocessing mathematic correction or both. Without such considerations, contrast agent leakage, apparent as T1-shortening, would falsely underestimate rCBV or, if apparent as residual T2\* effects, could overestimate rCBV.<sup>3,11,12</sup>

Additionally, due to the variability of nonquantitative rCBV values within similar tissue types, scaling metrics are often applied to rCBV estimates to better assess comparisons among subjects and between examinations. Two commonly applied scaling metrics involve either normalization or standardization. Normalization involves drawing a reference ROI, typically within normal-appearing white matter, whereby all voxels are divided by the mean value of that ROI. Alternatively, standardization, which transforms rCBV maps to a standardized intensity scale, without the need to draw a reference ROI, has been shown to increase consistency in rCBV measurements across time and patients.<sup>13</sup> Although the use of scaling metrics may reduce the variability of rCBV interpretation, the variability inherent in estimation methods is not fully known.

While the accuracy of several methods used for rCBV estimation has been investigated,<sup>3,11,12,14-17</sup> the repeatability of these methods has not, including a comparison between normalized (nRCBV) and standardized (sRCBV) rCBV approaches. Although rare, studies investigating the repeatability of imaging datasets are of great importance, especially if they are to be used as reliable biomarkers of disease detection and for decision-making in clinical trials and eventually as part of patient management.<sup>18,19</sup> The aim of this study was to compare the repeatability across 6 commonly used postprocessing methods in the estimation of standardized and normalized rCBV by using double-baseline data obtained from subjects with newly diagnosed glioblastoma multiforme.

## MATERIALS AND METHODS

### Participants

Institutional review board approval was obtained to retrospectively evaluate MR imaging data from subjects for whom informed consent had been obtained for participation in a prospective National Cancer Institute–sponsored phase Ib/II clinical trial. Detailed information regarding this trial can be found on-line (ClinicalTrials.gov identifier NCT00662506) and in recently published work.<sup>20,21</sup>

In general, participants were selected for inclusion in this National Cancer Institute clinical trial if they were at least 18 years of age, had histologically confirmed glioblastoma multiforme, were scheduled to receive standard<sup>22,23</sup> postsurgical (biopsy or resection) chemoradiotherapy, had residual contrast-enhancing tumor, maintained a stable dose of steroids before their baseline and vascular MR imaging examinations, would not require concurrent treatment other than that specified by the trial, had a

Karnofsky Performance Status score of at least 60%, and had a Mini-Mental State Examination score of at least 15. In general, participants were excluded if they had uncontrolled intercurrent illness, a condition or disease contraindicated for treatment with cediranib, pregnancy, or prior anti-vascular endothelial growth factor therapy for treatment of their tumor.

The sample size used for this study was based on total enrollment in the National Cancer Institute clinical trial, and not from a predetermined power analysis. All of the subjects who participated in the National Cancer Institute clinical trial were considered for inclusion in this retrospective study, in which exclusion criteria were limited to early initiation of treatment and issues of data quality, including substantial artifacts or incomplete and missing data.

### Data Acquisition

Double-baseline MR imaging examinations were performed at Massachusetts General Hospital Cancer Center and the Dana-Farber Cancer Institute in Boston, Massachusetts. Data obtained included DSC MR imaging and pre- and post-contrast-enhanced T1-weighted imaging. All data were acquired on 3T MR imaging systems (Tim Trio; Siemens Erlangen, Germany) equipped with AutoAlign (Siemens), which aligns section positions in a standard reproducible way, and were collected by using a similar imaging protocol.<sup>24</sup>

The DSC gradient-echo echo-planar MR imaging data were collected as follows: TR = 1.45–1.50 seconds, TE = 30–32 ms, flip angle = 80° or 90°, 12 sections with section thickness = 5 mm, intersection gap = 1.5 mm, acquisition matrix = 160 × 160 or 128 × 128, and FOV = 192–768 × 192–768 mm<sup>2</sup>, using a 0.2-mmol/kg dose of gadopentetate dimeglumine contrast agent (0.1-mmol/kg preload injection and 0.1-mmol/kg at approximately 80 seconds during DSC data collection). For each patient, both baseline images were collected with the exact same parameter settings. Parameter settings varied among patients but were within the ranges listed above.

T1-weighted MR imaging data were collected as follows: TR = 0.19–0.868 seconds, TE = 12 ms, 23 sections with section thickness = 5 mm, intersection gap = 1 mm, acquisition matrix = 432–512 × 512, and FOV = 185–220.

### rCBV Estimation

The nRCBV and sRCBV estimates for 6 commonly used postprocessing methods were calculated from unmodified DSC data by using plug-ins developed at the Medical College of Wisconsin for use within Analysis of Functional NeuroImages software (<http://afni.nimh.nih.gov/afni>).<sup>24</sup> The rCBV software plug-ins incorporate data truncation, calculation of preinjection baseline signal intensity, and calculation of concentration-time curves in the estimation of rCBV for each method. Specifically, the first 5 time points were removed because transient changes in the DSC signal occur before reaching a steady-state signal. This procedure was to establish a more accurate estimation of the preinjection baseline signal intensity. A voxelwise calculation of preinjection baseline signal intensity ( $S_B$ ) was then performed according to the following equation:

$$1) \quad S_B = \frac{1}{N_b} \sum_{j=1}^{N_b} S_j,$$

**Table 1: Description of rCBV estimation methods**

Method	Description	Postprocessing Leakage Correction	Type
1	120-Point numeric integration of $\Delta R2^*(t)$ with the trapezoid rule	No	$\Delta R2^*$
2	120-Point numeric integration of $\Delta R2^*(t)$ with the trapezoid rule and correction for T1 extravasation effects	Yes	$\Delta R2^*$
3	Area under $\gamma$ -variate fit to $\Delta R2^*(t)$	Yes	$\Delta R2^*$
4	Area under $\Delta R2^*(t)$ after postbolus baseline (recirculation) correction	Yes	$\Delta R2^*$
5	Maximum signal drop of $S(t)$	No	Signal
6	Negative enhancement integral of $S(t)$	No	Signal

where  $N_b$  is the number of baseline time points following DSC signal truncation and before contrast injection and  $S_j$  is the  $j$ th image in the time-series. The concentration-time curve could then be calculated according to the following equation:

$$2) \quad \Delta R2^*(t) = -\frac{1}{TE} \ln \left[ \frac{S(t)}{S_b} \right],$$

where  $S(t)$  is the signal time course. Next a voxelwise estimation of rCBV was performed for each of the methods listed in Table 1 as detailed in Paulson and Schmainda.<sup>14</sup> Data for each estimation method were then standardized or normalized<sup>13</sup> for each visit separately, with manually drawn normal-appearing white matter reference regions or standardization files, respectively.

### Data Analysis

For each visit, the DSC and precontrast T1-weighted images were coregistered with postcontrast T1-weighted images by using a normalized mutual information cost function with 6 *df*. Enhancing tumor volume ROIs were determined for each corresponding visit by using a semiautomated, threshold-detection algorithm applied to  $\Delta T1$  maps.<sup>25</sup> Specifically, the  $\Delta T1$  maps were created from the subtraction of standardized precontrast from standardized postcontrast T1-weighted images and thresholded to exclude values below a threshold of 3000. This previously determined threshold ensures that regions containing perfused tissue are included in the final tumor ROI. This approach also ensures that regions of bright signal on precontrast T1-weighted images resulting from blood products, for example, are not included as part of the enhancing-tumor ROI.<sup>25</sup> An example of using this approach to create  $\Delta T1$  maps is shown in Fig 1. For comparison the repeatability metrics were also determined in normal-appearing contralateral brain ROIs.

### Statistical Analysis

Consistent with a previous report,<sup>18</sup> repeatability will refer to the consistency of quantitative results obtained when the same imaging test is performed at short intervals on the same subjects by using the same equipment in the same center. In this context, the repeatability coefficient (RC) with upper and lower confidence intervals ( $RC_U$ ,  $RC_L$ ), SDs, and within-subject coefficient of variation (wCV) was calculated for mean rCBV estimates within the tumor and normal brain ROIs separately.<sup>18</sup> These metrics were used as a means of comparing repeatability within and across rCBV estimation methods and not in comparison with a reference

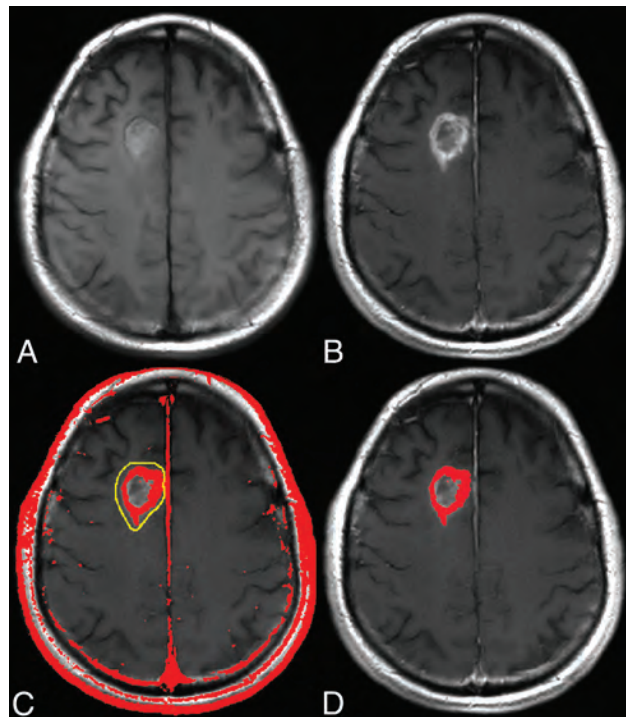


**FIG 1.**  $\Delta T1$  mask creation. Following standardization of each image, the standardized precontrast T1-weighted image (A) is subtracted from the standardized postcontrast T1-weighted image (B). The resulting  $\Delta T1$  map is thresholded, with results shown in red (C), and the abnormal region is extracted from the area identified in yellow, giving the final enhancing tumor mask (D).

standard, which would address the question of accuracy. The RC is a measure of the limits of agreement between baseline studies for a given method, wherein 95% of the test-retest measurement differences lie. Therefore, rCBV estimation methods were ordered as having greater repeatability based on a lower RC for nRCBV and sRCBV separately. Additionally, the wCV was used to compare not only the variation among rCBV estimation methods but also between standardized and normalized approaches, such that those methods showing lower variation were regarded as more consistent.

Repeatability metrics were also compared for each estimation method between normal brain and tumor ROIs by using a Wilcoxon matched pairs test with statistical significance set at  $\alpha = .05$ . All repeatability metrics were calculated as presented in Barnhart and Barboriak<sup>18</sup> and can be viewed in the On-line Appendix. All statistical tests were performed by using GraphPad Prism software (GraphPad Software, San Diego, California). Last, the minimum sample size required to detect a parameter change of 10% or 20% was calculated for each nRCBV or sRCBV estimation method with 2-tailed statistical significance set at  $\alpha = .05$  and power = 0.90. The percentage changes were based on the population mean for each estimation method and the respective scaling metric in this study.<sup>26</sup>

## RESULTS

### Participants

Forty participants were enrolled in the National Cancer Institute clinical trial between February 2009 and February 2011. Double-baseline MR imaging data were acquired within 8 days for 38

**Table 2: Metrics of rCBV estimation methods<sup>a</sup>**

Method	RC (RC <sub>L</sub> –RC <sub>U</sub> )	wCV	tSD	bSD	wSD
A) Normalized rCBV (tumor)					
2 (CTI)	1.78 (1.44–2.34)	0.31	0.96	0.71	0.64
3 (GV)	1.95 (1.57–2.57)	0.25	1.04	0.77	0.70
6 (NEI)	2.07 (1.67–2.73)	0.24	1.57	1.38	0.75
1 (UTI)	3.16 (2.55–4.16)	0.39	1.55	1.05	1.14
5 (MSD)	3.54 (2.86–4.66)	0.56	1.30	0.25	1.28
4 (PBC)	3.93 (3.17–5.18)	0.67	1.85	1.18	1.42
B) Standardized rCBV (tumor)					
2 (CTI)	3869 (3121–5093)	0.18	3142	2814	1397
4 (PBC)	4020 (3243–5292)	0.20	3045	2677	1451
3 (GV)	4214 (3399–5547)	0.17	3163	2773	1521
1 (UTI)	4261 (3437–5609)	0.19	2958	2526	1538
5 (MSD)	4591 (3703–6043)	0.13	6437	6220	1658
6 (NEI)	5250 (4235–6911)	0.16	5732	5410	1895

**Note:**— $\Delta R2^*(t)$  indicates methods for which the transverse relaxation time courses are computed from the signal time courses; UTI, integration of  $\Delta R2^*(t)$  with the trapezoid rule; CTI, integration of  $\Delta R2^*(t)$  with the trapezoid rule and correction for T1 and T2 extravasation effects; GV,  $\gamma$ -variate fit to  $\Delta R2^*(t)$ ; NEI, negative enhancement integral of S(t); MSD, maximum signal drop of S(t); PBC, postbolus baseline (recirculation) correction; RC<sub>L</sub>, lower RC confidence interval; RC<sub>U</sub>, upper RC confidence interval; tSD, total SD; bSD, between-subject SD; wSD, within-subject SD.

<sup>a</sup> Shown in A and B are the RC, upper and lower 95% CI for RC, wCV, and SDs (total, between, and within-subject) for nRCBV and sRCBV, respectively, in which methods are sorted in order of greatest repeatability, as determined by the RC for nRCBV or sRCBV.

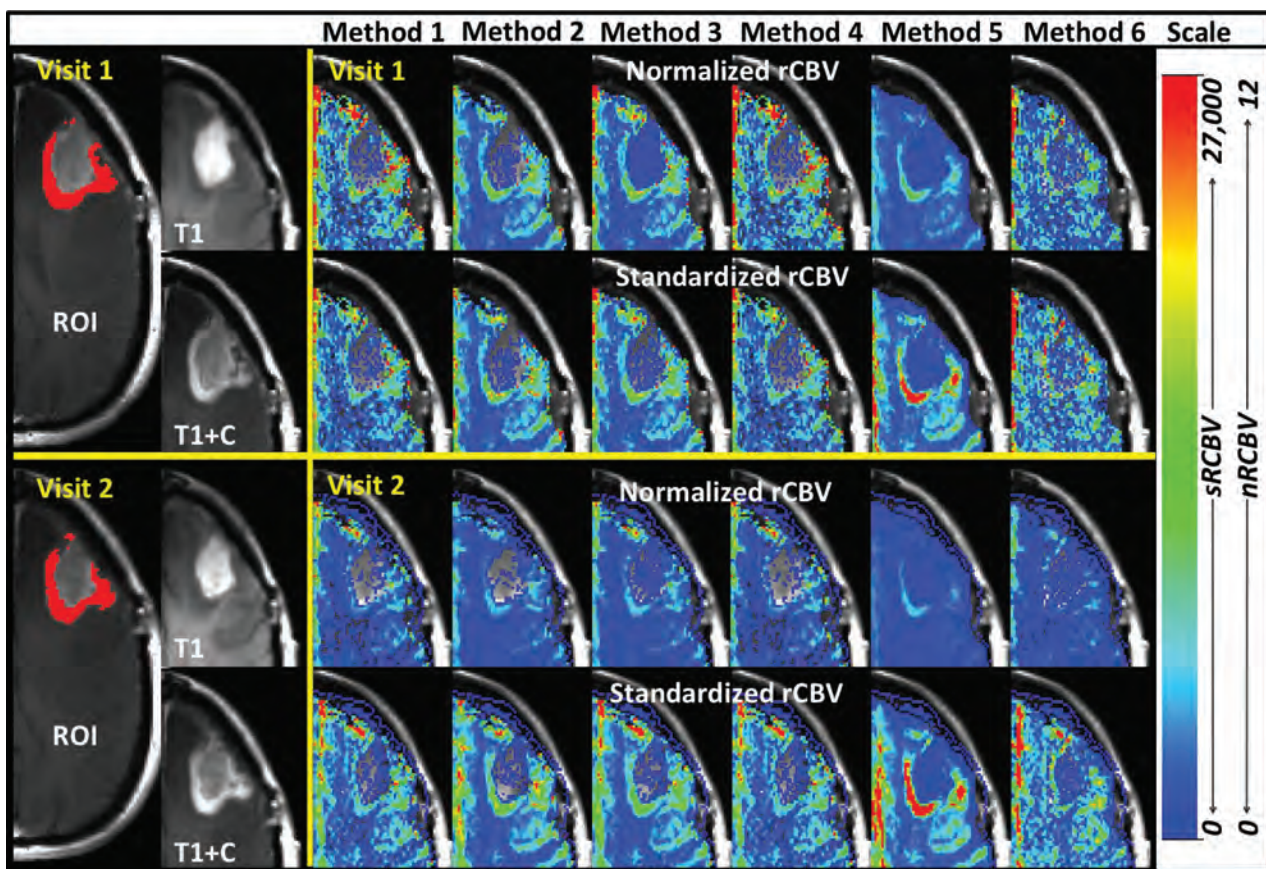


**FIG 2.** Visual comparison of nRCBV and sRCBV. Methods 1–6 (across) for visit 1 (top 2 rows) and visit 2 (bottom 2 rows) in the same subject in approximately the same section for visits 1 and 2. All data are presented with the same respective scale for nRCBV or sRCBV and are in arbitrary units.

subjects; 2 of the initial 40 subjects did not receive a second baseline examination and were therefore excluded from this analysis. Five additional subjects were excluded from analysis due to data-quality issues involving one of the baseline examinations, including the following: self-removal from the MR imaging scanner during the examination ( $n = 1$ ), poor contrast injection ( $n = 2$ ), and initiation of treatment ( $n = 2$ ). The remaining 33 subjects

were treatment-naïve, aside from maintaining a stable dose of steroids for a minimum of 5 days before initiation of the first baseline MR imaging examination and continuing through the second baseline MR imaging examination. Twenty male and 13 female subjects were included in the analyses with a mean age of  $55 \pm 10.8$  years and a mean timing between baseline examinations of  $3.6 \pm 1.4$  days.

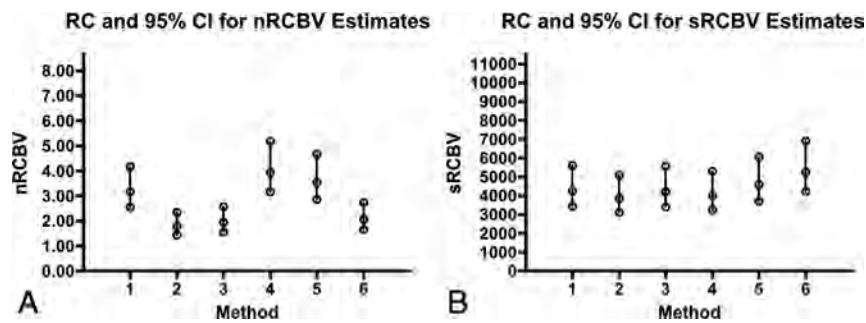


**FIG 3.** Consistency and variation in rCBV estimation. *A* and *B*, RC and 95% CI for nRCBV and sRCBV estimates, respectively. Because arbitrary units are used, values are displayed with the maximum RC as 60% of the upper limit of the y-axis. Ranges for RC are largely consistent across methods for sRCBV, but not for nRCBV.

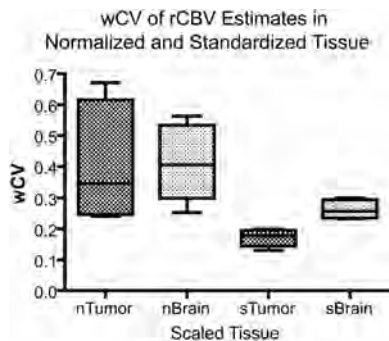


**FIG 4.** The wCV of normalized and standardized rCBV in tumor and brain tissue. The wCV is shown for nRCBV estimates in brain (nBrain) and tumor (nTumor) and for sRCBV estimates in brain (sBrain) and tumor (sTumor).

**Table 3: Sample size for rCBV estimation methods<sup>a</sup>**

Methods	Minimum Sample Size for rCBV Estimation			
	To Detect a 10% Change		To Detect a 20% Change	
	nRCBV	sRCBV	nRCBV	sRCBV
1	234	115	59	29
2	176	145	44	37
3	118	109	30	28
4	643	147	161	37
5	275	215	69	54
6	215	194	54	49

<sup>a</sup> Listed are the minimum sample sizes required to detect a parameter change of 10% or 20% in nRCBV or sRCBV.

### Statistical Measures

Repeatability metrics obtained for all rCBV analysis methods are shown in Table 2 for tumor ROIs and are sorted in order of best repeatability as determined by the RC for nRCBV and sRCBV separately. Also in Table 2 are the 95% CI ranges for RC, wCV, and SDs including total, between-subject, and within-subject SDs. While RC provides a way to assess how repeatable a given measure is (ie, nRCBV or sRCBV), the wCV is used to make comparisons across all measurement types (eg, nRCBV and sRCBV) independent of scale. Figure 2 provides a visual comparison of methods 1–6 for nRCBV and sRCBV estimates in approximately the same section from the same subject for each visit, in which all images showed the same scale for either nRCBV or sRCBV across methods and visits.

The RC shows the greatest consistency (ie, lower RC values) for leakage-corrected methods 2 and 3 for both nRCBV and sRCBV. In general, the signal-based rCBV analysis methods were among the least repeatable, particularly for method 5. Based on the 95% CIs of RC, sRCBV shows greater consistency than nRCBV between visits and across methods as shown in Fig 3. The nRCBV and sRCBV are scaled with separate arbitrary units; therefore, the overall 95% CI of RCs cannot be directly compared for the extent of

range but rather are compared for consistency within ranges for each scaling metric separately. The RC in sRCBV estimates was comparable ( $P = .31$ ) between tumor and normal brain. However, for nRCBV estimates, the repeatability in normal brain ( $P = .03$ ) was superior to that of tumor.

In general, as shown in Fig 4, wCV was higher for nRCBV in normal brain and tumor compared with sRCBV. The wCV in tumor was higher for all nRCBV methods than for any sRCBV method. As expected, due to lower mean values in normal brain, the wCV was significantly higher in normal brain compared with tumor ( $P = .03$ ) for sRCBV estimation methods. The wCV was comparable in both normal brain and tumor for nRCBV ( $P = .84$ ).

A sensitivity analysis was also performed on 14 of the subjects in whom repeat imaging was performed within a shorter, 3-day timeframe. RC had similar trends for both nRCBV and sRCBV with respect to the order of repeatability, in which method 2 had the greatest repeatability. As expected, this analysis showed improved (18.2% mean difference) RC values ( $P = .002$ ) and improved (18.5% mean difference) wCV ( $P = .003$ ) for sRCBV methods, which were statistically significant. However, there was no statistical difference detected for RC ( $P = .15$ ) or wCV ( $P = .19$ ) by excluding subjects with  $>3$  days between examinations for the nRCBV methods.

Finally, with the measurement variations in rCBV determined, a power analysis was performed to estimate the minimum number of participants needed to detect a change in rCBV of either 10% or 20%. A percentage change of 10% or 20% will be equivalent between normalized or standardized scaling metrics because both use a form of linear transformation of the data and do not alter the underlying information content.<sup>13</sup> For nRCBV, a minimum of 118–643 or 30–161 subjects is necessary to statistically power a study in which a 10% or 20% change is expected. For sRCBV, the number of participants required is fewer, with 109–215 or 28–54 subjects to detect a 10% or 20% change, respectively. These results are listed in Table 3.

### DISCUSSION

The use of rCBV to interpret treatment response has become essential for many diseases, especially for high-grade gliomas. In particular, with relatively new or even established therapies, it can be difficult to monitor with standard imaging and response crite-

ria.<sup>27-30</sup> These challenges are especially apparent in imaging of patients following chemoradiotherapy or anti-vascular endothelial growth factor therapy, in which it is difficult to distinguish pseudoprogression from true progression or pseudoresponse from true response, respectively.<sup>31</sup>

Specifically, the standard of care for patients with high-grade glioma requires the delivery of chemoradiotherapy with concomitant and adjuvant temozolomide.<sup>22,23</sup> Responses are particularly difficult to interpret within the first 3 months of treatment because standard imaging has not shown a reliable distinction between true tumor progression and pseudoprogression. Pseudoprogression presents as an early increase in enhancement on T1-weighted imaging, thought to represent an inflammatory response involving changes in the blood-brain barrier and vascular endothelium. Patients with pseudoprogression have shown longer survival rates than patients with true tumor progression.<sup>31</sup>

Additionally, anti-vascular endothelial growth factor drugs, which are now becoming the standard for treatment of patients with recurrent high-grade gliomas, decrease the permeability of the blood-brain barrier, oftentimes resulting in otherwise enhancing tumor being undetectable and difficult to interpret on contrast-enhanced T1-weighted imaging, regardless of treatment response. This normalization of the blood-brain barrier often results in improvement of symptoms and a decrease in edema, further confounding the interpretation of response clinically.<sup>31</sup> In a recent phase II clinical trial, FLAIR and postcontrast T1-weighted imaging were evaluated for their ability to predict overall survival in patients with recurrent glioblastoma multiforme treated with the anti-vascular endothelial growth factor drug bevacizumab.<sup>32</sup> It was found that an increase in enhancement was associated with poorer survival, while FLAIR progression did not reveal a significant survival disadvantage.<sup>32</sup> The results of this study are promising in predicting treatment failure for those who show progression on T1-weighted imaging, yet standard imaging has still remained ineffective in determining true responders from pseudoresponders in those who have diminished enhancement.

Among others, the treatment approaches described here have benefited from the inclusion of rCBV, in which relative values or functional changes in the direction of rCBV have been shown to be promising in predicting response to treatment, to the point at which it is now a routine clinical examination at many hospitals.<sup>3,8-10,27,33-35</sup> With the increasingly prevalent use of rCBV in the evaluation of patients with brain disease, it has become extremely important that the quality of the data being assessed be consistently produced, especially when assessing disease with time.

This study demonstrates that methods incorporating leakage correction largely have superior repeatability. Additionally, methods that use  $\Delta R2^*$  estimation perform better than those that are signal-based. Method 2, an accuracy-proved<sup>14</sup> leakage-corrected technique<sup>11</sup> that uses  $\Delta R2^*$  estimation offered the best repeatability for both normalized and standardized scaling metrics. Additionally, when methods are compared across scaling metrics, standardization decreased within-subject variations with greater consistency across techniques than did normalization. Figure 2 provides a visual contrast among methods with lower wCV and lower RC (greater repeatability) compared with those with higher

wCV and higher RC (lower repeatability) between visits. These differences in repeatability are especially evident when comparing sRCBV method 2 (best repeatability) with sRCBV method 5 (worse repeatability) between visits. Method 2 is visually consistent over visits, yet method 5 reveals an extending area of increased rCBV from visit 1 to visit 2. Less repeatable estimation methods could lead to errors in interpretation clinically because the rCBV maps in Fig 2 should appear visually the same in both visits. Clinically, using rCBV methods with greater repeatability should provide clinicians with improved confidence in interpretation by providing a reliable assessment of progression or response to treatment.

Using the rCBV estimation techniques that offer superior repeatability may help to validate its use as an imaging biomarker, both on a daily basis and in the context of planning and interpreting clinical trials in which rCBV is evaluated.<sup>18,19</sup> Furthermore, by choosing the methods with the greatest repeatability, clinical trials can be performed in a much more cost-effective and efficient manner. For example, by using the variabilities determined in this study, a power analysis was performed to estimate the number of participants required to detect a certain percent change in rCBV. The numbers required varied substantially, with the standardized leakage-corrected rCBV methods proving to be the most consistent. Consequently using sRCBV in clinical trials has the potential to improve efficiency by requiring many fewer participants to address a given hypothesis.

Although it was not addressed in this study, there is growing interest in using dynamic contrast-enhanced MR imaging for the evaluation of brain tumors. This method, which provides additional information on vascular permeability and blood volume, also has been shown to vary across analysis platforms.<sup>36</sup> As such, assessing the repeatability of DCE MR imaging among various models may also be beneficial in the future for improved consistency and widespread application.

One limitation of this study involves the subjective nature of normal-appearing white matter ROI selection used to produce nRCBV estimates. However, this inherent subjectivity is implicit to this approach and exactly what can confound nRCBV interpretation, making it less repeatable. Still, when selecting the normal-appearing white matter ROIs, care was taken to avoid including gray matter or tissue within or near abnormal regions with the goal of reducing any added variability resulting from the choice of the reference ROI.

Another limitation to this study is that data were only analyzed in high-grade gliomas. Correction techniques applied to datasets with low-grade tumors or stroke, in which blood-brain barrier distortion may not be as profound or present, may render processing methods compared here more or less repeatable in these population types. However, because tumors are assessed over time, low-grade tumors that transform to high-grade tumors would be prone to increased variability in methods that do not use some means of leakage correction.

Further limitations of this study involve the number of subjects included and the timing of repeat baseline examinations. The number of participants included was based on clinical trial enrollment requirements rather than a power analysis based on imaging parameters. In addition, in this study, repeatability was assessed in

participants with examinations that occurred up to 8 days apart. Improved accuracy in the measurement of repeatability could potentially be achieved within shorter intervals or within the same day. To further address potential limitations due to extended timing between baseline exams, the repeatability analysis was performed that included only the 14 subjects for whom repeat examinations occurred within 3 days of each other. Results of improved RC and wCV were observed in sRCBV methods as expected due to potential biologic changes during a longer timeframe. However, no improvement was made within a shorter timeframe for nRCBV methods, and this is likely due to the greater inherent variations with normalization. Even with a shorter timeframe between examinations, trends in the order of repeatability remained consistent across both nRCBV and SRCBV methods, in which method 2 displayed the greatest repeatability.

Last, only data normalized by using normal-appearing white matter reference ROIs or standardized with the method identified by Bedekar et al<sup>13</sup> were investigated. Other scaling techniques may produce differing results regarding repeatability when applied to these rCBV estimation methods. This study focused primarily on the repeatability of rCBV estimation techniques and secondarily on the use of intensity-scaling metrics applied to these techniques. Likewise, rCBV estimation techniques were not compared within nonscaled data. If different or less common scaling metrics are applied, further investigation of repeatability may be necessary, especially by using estimation methods demonstrated to be more accurate<sup>14</sup> and repeatable for both nRCBV and sRCBV (ie, leakage-corrected). However, rCBV estimation techniques tended to display a similar order of repeatability regardless of scaling metric.

## CONCLUSIONS

Characterization of the repeatability of rCBV measures is important for determining when a change in these values is an accurate representation of tumor growth or response to treatment. These results show that there is a clear difference among the repeatability of various methods for estimating rCBV. Consistent with previous reports regarding the accuracy of rCBV estimation,<sup>14</sup> the leakage-corrected estimate of rCBV demonstrates the best repeatability for both standardized and normalized values. In addition, standardization of rCBV results in decreased variability and requires fewer study participants to detect a desired change compared with normalized rCBV. Thus, we recommended leakage-corrected standardized rCBV as a best approach included in the effort to homogenize perfusion measurements across sites.

Disclosures: Steven M. Stufflebeam—RELATED: Grant: National Institutes of Health.\* Elizabeth R. Gerstner—RELATED: Grant: National Institutes of Health.\* Tracy T. Batchelor—RELATED: Grant: National Institutes of Health (National Cancer Institute);\* Comments: 2 R01 CA129371–06, 2 K24 CA125440–06; UNRELATED: Consultancy: Merck, Roche, Kirin, Novartis, Proximagen, Agenus, Spectrum, Amgen; Payment for Lectures (including service on Speakers Bureaus): Imedex, UpToDate, Educational Concepts Group, Research To Practice, Oakstone Publishing, Robert Michael Educational Institute; Travel/Accommodations/Meeting Expenses Unrelated to Activities Listed: Roche, Kirin, Novartis, Agenus; Other: Champions Biotechnology, Advance Medical. Daniel P. Barboriak—UNRELATED: Board Membership: GE Healthcare NeuroMRI Advisory Board, Comments: This board has not met for several years, and I have received no compensation for more than 36 months, but I am told that I am still a member; Grants/Grants Pending: Radiological Society of North America; Quantitative Imaging Biomarkers Alliance contract, Comments: I have received and was recently awarded a second Quantitative Imaging Biomarkers Alliance contract for research relating to dynamic contrast-enhanced MRI software; Pay-

ment for Lectures (including service on Speakers Bureaus): World Class Continuing Medical Education, Comments: I receive payment from World Class Continuing Medical Education for giving lectures at the National Diagnostic Imaging Symposium; Travel/Accommodations/Meeting Expenses Unrelated to Activities Listed: I am the imaging cochair of the ECOG-ACRIN (Eastern Cooperative Oncology Group–American College of Radiology Imaging Network) Brain Tumor Working Group and also the chair of the ACRIN Head and Neck/Brain Steering Committee, Comments: I am reimbursed for travel and expenses to the ECOG-ACRIN meetings (2 per year); Other: National Cancer Institute Brain Malignancies Steering Committee, Comments: The National Cancer Institute pays for teleconference/preparation and meeting expenses as part of my activities. Bruce Rosen—RELATED: Grant: National Institutes of Health/National Cancer Institute (5U01CA154601).\* Kathleen M. Schmainda—RELATED: Grant: National Institutes of Health\*; UNRELATED: Royalties: Medical College of Wisconsin, Comments: royalties received on Medical College of Wisconsin–owned patents of which K.M.S. is an inventor; Other: K.M.S. founded the company Imaging Biometrics LLC. \*Money paid to the institution.

## REFERENCES

- Roy B, Gupta RK, Maudsley AA, et al. **Utility of multiparametric 3-T MRI for glioma characterization.** *Neuroradiology* 2013;55:603–13
- Server A, Graff BA, Orheim TE, et al. **Measurements of diagnostic examination performance and correlation analysis using microvascular leakage, cerebral blood volume, and blood flow derived from 3T dynamic susceptibility-weighted contrast-enhanced perfusion MR imaging in glial tumor grading.** *Neuroradiology* 2011;53:435–47
- Boxerman JL, Schmainda KM, Weisskoff RM. **Relative cerebral blood volume maps corrected for contrast agent extravasation significantly correlate with glioma tumor grade, whereas uncorrected maps do not.** *AJNR Am J Neuroradiol* 2006;27:859–67
- Saito T, Yamasaki F, Kajiwara Y, et al. **Role of perfusion-weighted imaging at 3T in the histopathological differentiation between astrocytic and oligodendroglial tumors.** *Eur J Radiol* 2012;81:1863–69
- Bian W, Khayal IS, Lupo JM, et al. **Multiparametric characterization of grade 2 glioma subtypes using magnetic resonance spectroscopy, perfusion, and diffusion imaging.** *Transl Oncol* 2009;2:271–80
- Law M, Oh S, Johnson G, et al. **Perfusion magnetic resonance imaging predicts patient outcome as an adjunct to histopathology: a second reference standard in the surgical and nonsurgical treatment of low-grade gliomas.** *Neurosurgery* 2006;58:1099–107; discussion 1099–107
- Vöglein J, Tüttenberg J, Weimer M, et al. **Treatment monitoring in gliomas: comparison of dynamic susceptibility-weighted contrast-enhanced and spectroscopic MRI techniques for identifying treatment failure.** *Invest Radiol* 2011;46:390–400
- Caseiras GB, Chheang S, Babb J, et al. **Relative cerebral blood volume measurements of low-grade gliomas predict patient outcome in a multi-institution setting.** *Eur J Radiol* 2010;73:215–20
- Hu LS, Baxter LC, Smith KA, et al. **Relative cerebral blood volume values to differentiate high-grade glioma recurrence from posttreatment radiation effect: direct correlation between image-guided tissue histopathology and localized dynamic susceptibility-weighted contrast-enhanced perfusion MR imaging measurements.** *AJNR Am J Neuroradiol* 2009;30:552–58
- Mangla R, Singh G, Ziegelitz D, et al. **Changes in relative cerebral blood volume 1 month after radiation-temozolomide therapy can help predict overall survival in patients with glioblastoma.** *Radiology* 2010;256:575–84
- Boxerman JL, Prah DE, Paulson ES, et al. **The role of preload and leakage correction in gadolinium-based cerebral blood volume estimation determined by comparison with MION as a criterion standard.** *AJNR Am J Neuroradiol* 2012;33:1081–87
- Hu LS, Baxter LC, Pinnaduwa DS, et al. **Optimized preload leakage-correction methods to improve the diagnostic accuracy of dynamic susceptibility-weighted contrast-enhanced perfusion MR imaging in posttreatment gliomas.** *AJNR Am J Neuroradiol* 2010;31:40–48
- Bedekar D, Jensen T, Schmainda KM. **Standardization of relative cerebral blood volume (rCBV) image maps for ease of both inter- and inpatient comparisons.** *Magn Reson Med* 2010;64:907–13

14. Paulson ES, Schmainda KM. **Comparison of dynamic susceptibility-weighted contrast-enhanced MR methods: recommendations for measuring relative cerebral blood volume in brain tumors.** *Radiology* 2008;249:601–13
15. Essock-Burns E, Phillips JJ, Molinaro AM, et al. **Comparison of DSC-MRI post-processing techniques in predicting microvascular histopathology in patients newly diagnosed with GBM.** *J Magn Reson Imaging* 2013;38:388–400
16. Thomsen H, Steffensen E, Larsson EM. **Perfusion MRI (dynamic susceptibility contrast imaging) with different measurement approaches for the evaluation of blood flow and blood volume in human gliomas.** *Acta Radiol* 2012;53:95–101
17. Kudo K, Christensen S, Sasaki M, et al; Stroke Imaging Repository (STIR) Investigators. **Accuracy and reliability assessment of CT and MR perfusion analysis software using a digital phantom.** *Radiology* 2013;267:201–11
18. Barnhart HX, Barboriak DP. **Applications of the repeatability of quantitative imaging biomarkers: a review of statistical analysis of repeat data sets.** *Transl Oncol* 2009;2:231–35
19. Murphy PS, McCarthy TJ, Dzik-Jurasz AS. **The role of clinical imaging in oncological drug development.** *Br J Radiol* 2008;81:685–92
20. Pinho MC, Polaskova P, Kalpathy-Cramer J, et al. **Low incidence of pseudoprogression by imaging in newly diagnosed glioblastoma patients treated with cediranib in combination with chemoradiation.** *Oncologist* 2014;19:75–81
21. Batchelor TT, Gerstner ER, Emblem KE, et al. **Improved tumor oxygenation and survival in glioblastoma patients who show increased blood perfusion after cediranib and chemoradiation.** *Proc Natl Acad Sci U S A* 2013;110:19059–64
22. Stupp R, Mason WP, van den Bent MJ, et al; European Organisation for Research and Treatment of Cancer Brain Tumor and Radiotherapy Groups; National Cancer Institute of Canada Clinical Trials Group. **Radiotherapy plus concomitant and adjuvant temozolomide for glioblastoma.** *N Engl J Med* 2005;352:987–96
23. Stupp R, Hegi ME, Mason WP, et al; European Organisation for Research and Treatment of Cancer Brain Tumour and Radiation Oncology Groups; National Cancer Institute of Canada Clinical Trials Group. **Effects of radiotherapy with concomitant and adjuvant temozolomide versus radiotherapy alone on survival in glioblastoma in a randomised phase III study: 5-year analysis of the EORTC-NCIC trial.** *Lancet Oncol* 2009;10:459–66
24. Cox RW. **AFNI: software for analysis and visualization of functional magnetic resonance neuroimages.** *Comput Biomed Res* 1996;29:162–73
25. Bedekar DP, Jensen TR, Schmainda KM, et al. **Delta T1 method: an automatic post-contrast ROI selection technique for brain tumors.** *In: Proceedings of the International Society for Magnetic Resonance in Medicine*, Stockholm, Sweden. May 1–7, 2010
26. Dawson B, Trapp R. *Basic & Clinical Biostatistics*. 4th ed. New York: McGraw-Hill Companies; 2004
27. Essig M, Shiroishi MS, Nguyen TB, et al. **Perfusion MRI: the five most frequently asked technical questions.** *AJR Am J Roentgenol* 2013;200:24–34
28. Gállego Pérez-Larraya J, Lahutte M, Petrirena G, et al. **Response assessment in recurrent glioblastoma treated with irinotecan-bevacizumab: comparative analysis of the Macdonald, RECIST, RANO, and RECIST + F criteria.** *Neuro Oncol* 2012;14:667–73
29. Macdonald DR, Cascino TL, Schold SC Jr, et al. **Response criteria for phase II studies of supratentorial malignant glioma.** *J Clin Oncol* 1990;8:1277–80
30. Vogelbaum MA, Jost S, Aghi MK, et al. **Application of novel response/progression measures for surgically delivered therapies for gliomas: Response Assessment in Neuro-Oncology (RANO) Working Group.** *Neurosurgery* 2012;70:234–43; discussion 243–44
31. Hygino da Cruz LC Jr, Rodriguez I, Domingues RC, et al. **Pseudoprogression and pseudoresponse: imaging challenges in the assessment of posttreatment glioma.** *AJNR Am J Neuroradiol* 2011;32:1978–85
32. Boxerman JL, Zhang Z, Safriel Y, et al. **Early post-bevacizumab progression on contrast-enhanced MRI as a prognostic marker for overall survival in recurrent glioblastoma: results from the ACRIN 6677/RTOG 0625 Central Reader Study.** *Neuro Oncol* 2013;15:945–54
33. Schmainda KM, Prah M, Connelly J, et al. **Dynamic-susceptibility contrast agent MRI measures of relative cerebral blood volume predict response to bevacizumab in recurrent high-grade glioma.** *Neuro Oncol* 2014;16:880–88
34. Hu LS, Eschbacher JM, Dueck AC, et al. **Correlations between perfusion MR imaging cerebral blood volume, microvessel quantification, and clinical outcome using stereotactic analysis in recurrent high-grade glioma.** *AJNR Am J Neuroradiol* 2012;33:69–76
35. Hu LS, Eschbacher JM, Heiserman JE, et al. **Reevaluating the imaging definition of tumor progression: perfusion MRI quantifies recurrent glioblastoma tumor fraction, pseudoprogression, and radiation necrosis to predict survival.** *Neuro Oncol* 2012;14:919–30
36. Huang W, Li X, Chen Y, et al. **Variations of dynamic contrast-enhanced magnetic resonance imaging in evaluation of breast cancer therapy response: a multicenter data analysis challenge.** *Transl Oncol* 2014;7:153–66

# Correlation of Asymmetry Indices Measured by Arterial Spin-Labeling MR Imaging and SPECT in Patients with Crossed Cerebellar Diaschisis

K.M. Kang, C.-H. Sohn, B.S. Kim, Y.I. Kim, S.H. Choi, T.J. Yun, J.-h. Kim, S.-W. Park, G.J. Cheon, and M.H. Han



## ABSTRACT

**BACKGROUND AND PURPOSE:** Crossed cerebellar diaschisis, not only a secondary result of supratentorial infarction but also an indicator of clinical outcomes, has frequently been reported on PET and SPECT but has been rarely described with arterial spin-labeling MR imaging. The purpose of this study was to determine the ability of arterial spin-labeling MR imaging to evaluate crossed cerebellar diaschisis compared with that of SPECT. To our knowledge, this is the first study to validate arterial spin-labeling in crossed cerebellar diaschisis by using SPECT as a reference standard.

**MATERIALS AND METHODS:** This study included 16 patients in whom crossed cerebellar diaschisis was shown on SPECT and 10 control subjects in whom crossed cerebellar diaschisis was not shown on SPECT. During the qualitative analysis, asymmetric cerebellar perfusion on arterial spin-labeling was divided into 1 of the following 3 grades by 2 blinded observers: the affected cerebellum was isointense compared with the unaffected cerebellum (grade I), it was slightly hypointense (grade II), or it was markedly hypointense (grade III). In the quantitative analysis, asymmetry indices were calculated by using SPECT and arterial spin-labeling images. For statistical analysis,  $\kappa$  statistics, the interobserver correlation coefficient, the independent  $t$  test, Pearson correlation, and linear regression analysis were used.

**RESULTS:** Almost all the diagnoses of crossed cerebellar diaschisis on SPECT were noted on arterial spin-labeling in both qualitative and quantitative analyses with good interobserver agreement ( $\kappa = 0.96$ ; interobserver correlation coefficient, 0.806). The mean asymmetry index of arterial spin-labeling ( $26.06 \pm 9.00$ ) was significantly larger than that for SPECT ( $15.28 \pm 5.34$ ;  $P < .001$ ). There was a significant positive correlation between the asymmetry indices obtained for SPECT and those for arterial spin-labeling ( $r = 0.77$  [95% CI, 0.443–0.916];  $P < .001$ ). The relationship of asymmetry indices between SPECT and arterial spin-labeling ( $x, y$ ) was calculated as  $y = 6.2131 + 1.2986x$  ( $R^2 = 0.592$ ;  $P < .001$ ).

**CONCLUSIONS:** Arterial spin-labeling can be a noninvasive alternative to SPECT for evaluating crossed cerebellar diaschisis.

**ABBREVIATIONS:** AI = asymmetry index; ASL = arterial spin-labeling; CCD = crossed cerebellar diaschisis

Crossed cerebellar diaschisis (CCD) is decreased blood flow and metabolism contralateral to a damaged supratentorial area.<sup>1</sup> It is believed that the most likely mechanism of CCD is an interruption of the corticopontocerebellar fibers.<sup>1–3</sup> The deafferentation and trans-

neural metabolic depression of the affected cerebellar hemisphere are usually associated with contralateral supratentorial stroke, epilepsy, infection, or a tumor.<sup>4–8</sup> CCD is not only a secondary result of supratentorial infarction but also a prognostic indicator of neurologic improvement and clinical outcomes after infarction.<sup>9–13</sup> For example, in one study, CCD in the chronic stage was associated with neurologic improvement after infarction in the territory of the middle cerebral artery.<sup>12</sup> In another study, CCD in the early subacute stage of supratentorial infarction indicated a worse clinical outcome.<sup>10</sup> Furthermore, a PET study of acute stroke that evaluated multiple time points revealed that after reperfusion with thrombolysis, CCD recovery was observed in patients with relatively small infarcts and was strongly associated with clinical outcome measures.<sup>11</sup>

Since CCD was first described in a PET study conducted by Baron et al<sup>4</sup> in 1981, PET and SPECT have been the methods of choice in most studies for documenting changes in CBF and me-

Received December 17, 2014; accepted after revision February 20, 2015.

From the Departments of Radiology (K.M.K., C.-H.S., B.S.K., S.H.C., T.J.Y., J.-h.K., M.H.H.) and Nuclear Medicine (Y.I.K., G.J.C.), Seoul National University Hospital, Seoul, Republic of Korea; Department of Radiology (K.M.K., C.-H.S., B.S.K., S.H.C., T.J.Y., J.-h.K., S.-W.P., M.H.H.), Seoul National University College of Medicine, Seoul, Republic of Korea; Institute of Radiation Medicine (C.-H.S., S.H.C., M.H.H.), Seoul National University Medical Research Center, Seoul, Republic of Korea; and Department of Radiology (S.-W.P.), Seoul National University Boramae Hospital, Seoul, Republic of Korea.

Please address correspondence to Chul-Ho Sohn, MD, Department of Radiology, Seoul National University Hospital, 101, Daehangno, Jongno-gu, Seoul 110-744, South Korea; e-mail: neurorad63@gmail.com

Indicates article with supplemental on-line table.

<http://dx.doi.org/10.3174/ajnr.A4366>

tabolism during CCD.<sup>1,9,11,14-18</sup> Regarding perfusion MR imaging, there have been 2 studies performed by using DSC MR perfusion imaging. Yamada et al<sup>19</sup> reported that a lower regional cerebellar blood volume was observed in the affected cerebellum, and researchers in the other study<sup>20</sup> identified the frequency of CCD observed in acute stroke by using time-to-peak maps and calculated the reduction by using CBF maps. However, another study reported that DSC MR perfusion at 1.5T was not suited to show CCD after stroke because of poor accuracy compared with that of PET.<sup>21</sup>

Recently, arterial spin-labeling (ASL) was introduced as a non-invasive method for assessing cerebral hemodynamics. This method uses endogenous arterial water as a freely diffusible tracer labeled by radiofrequency pulses.<sup>22,23</sup> In contrast to DSC contrast MR perfusion imaging, PET, and SPECT, ASL imaging is a completely noninvasive method that does not require the injection of exogenous material such as gadolinium-based contrast or radioisotopes. In addition, CBF values derived by using ASL have been shown to correlate with those of SPECT in patients with Moyamoya disease<sup>24</sup> and with those of PET in patients with symptomatic ICA occlusion.<sup>25</sup>

Although the results of a recent study suggested that CCD can be detected via ASL MR imaging, this finding was not validated against a reference method.<sup>26</sup> Therefore, the purpose of our study was to investigate the value of ASL MR imaging for the evaluation of CCD compared with that of SPECT, which served as the standard of reference in patients with contralateral supratentorial lesions.

## MATERIALS AND METHODS

### Study Population

This retrospective study was approved by the Seoul National University Hospital institutional review board, and the need for informed consent was waived. From October 2011 to October 2014, among 209 SPECT examinations in patients with clinically suspected hemispheric stroke, we identified those who met the following inclusion criteria: 1) CCD on SPECT (164 cases were excluded), 2) SPECT and ASL performed within 1 day of one another (20 cases were excluded because of the lack of ASL MR perfusion imaging; 7 cases were excluded because of a long interval between SPECT and ASL), 3) no structural abnormality in the cerebellum or brain stem on MR imaging (1 patient was excluded), and 4) satisfactory image quality (1 patient was excluded). Finally, 16 patients with 16 sets of SPECT and ASL examinations were included in this study as the CCD-positive group. We also included 10 age-matched control subjects (CCD-negative group) to demonstrate the diagnostic performance of ASL. The inclusion criteria for the control group were as follows: 1) supratentorial lesion with no evidence of CCD on SPECT and 2) SPECT and ASL within 1 day of one another.

### ASL MR Technique

Each patient underwent an MR examination by a 1.5T unit (Signa HDXT; GE Medical Systems, Milwaukee, Wisconsin) with an 8-channel head coil to acquire ASL perfusion MR imaging. The imaging protocol included T1-weighted, T2-weighted, fluid-attenuated inversion recovery, and diffusion-weighted imaging

( $b = 0$  and  $1000$  s/mm<sup>2</sup>), 3D-TOF intracranial MRA, and contrast-enhanced neck MRA (On-line Table).

The ASL protocol used was a pseudocontinuous ASL, which significantly increased the flow-labeling efficacy in a single-coil setting.<sup>27,28</sup> The sequence provided by GE Healthcare performed pseudocontinuous ASL for 1.5 seconds followed by a post-spin-labeling delay of 1.5 seconds. Background suppression was performed by using saturation pulses.<sup>29</sup> Saturation was performed with crusher gradients applied inferior to the labeling plane, allowing for an increase in the sharpness of the bolus. The image acquisition consisted of a stack of interleaved FSE spiral readouts, each of which lasted 4 ms. Each spiral arm included 512 sampling points in the  $k$ -space, and a total of 8 interleaves (arms) were acquired separately. In addition, reconstruction was performed by using a Fourier transform algorithm after the  $k$ -space data were regridded into a  $64 \times 64$  matrix (TR, 1345 ms; TE, 5 ms; flip angle, 155°; sections, 32; section thickness, 5 mm; intersection gap, 0 mm; field of view,  $240 \times 240$  mm; matrix,  $256 \times 256$ ; acquired signals, 3; echo-train length, 1; voxel resolution,  $3.8 \times 3.8 \times 5.0$  mm). Image reconstruction was performed according to standard GE reconstruction by using codes written in Interactive Data Language on a virtual machine associated with the scanner. The images were filtered by using Fermi windowing for ringing artifact reduction. Grad warp was not applied.

### Brain Perfusion SPECT Acquisition and Analysis

Brain perfusion SPECT was performed by using a triple-head gamma camera (Triad XLT 9; Trionix Research Laboratory, Twinsburg, Ohio) equipped with low-energy ultra-high-resolution fan-beam collimators. Technetium Tc99m-hexamethylpropyleneamine oxime (9.25 MBq/kg) was injected intravenously for basal SPECT, and images were acquired after 5 minutes of radiotracer injection. Forty step-and-shoot images were acquired for 20–25 seconds per step, with intervals of 3°. Acetazolamide (20 mg/kg) was injected 10 minutes before the end of the basal scan, and technetium Tc-99 m-hexamethylpropyleneamine oxime (18.5 MBq/kg) was injected again at the end of the basal scan acquisition. Five minutes after technetium Tc-99 m-hexamethylpropyleneamine oxime reinjection, diamox SPECT was started without position change. All SPECT images were reconstructed on  $128 \times 128$  matrices by using a filtered back-projection method with a Metz filter. CCD was assessed on the opposite side of the cortical infarction on basal SPECT by a nuclear medicine physician. CCD was diagnosed in patients who showed significantly less uptake in the cerebellum on the contralateral side. To assess the cerebellar hemispheric asymmetry index (AI), circular ROIs, measuring 25 mm in diameter, were placed in the affected and mirrored unaffected cerebellar hemispheres. The degree of CCD was measured on a section of axial scan representing the greatest cerebellar asymmetry.<sup>26</sup> The AI was calculated between the affected cerebellar hemisphere ( $A$ ) and the unaffected cerebellar hemisphere ( $U$ ) as follows<sup>11,19,20</sup>:

$$AI = (U - A)/U \times 100\%.$$

### ASL Image Analysis

In the qualitative analysis, 2 neuroradiologists (K.M.K. and B.S.K.) who were blinded to the presence or absence of CCD

### Clinical characteristics and cerebellar AI

Patient No.	Age (y)	Sex	Cause	Supratentorial Lesion Type	Affected Side of Cerebellum	Qualitative Analysis, Grade	Quantitative Analysis, AI (%)		Interval Between SPECT and ASL, Days
							SPECT	ASL	
1	54	M	ICA occlusion	Chronic infarction	Left	III	16.96	37.85	0
2	28	M	MMD	Chronic infarction	Left	III	15.5	32.86	0
3	33	F	MMD	Previous ICH	Left	II	11.5	14.2	0
4	32	M	MMD	Chronic infarction	Right	III	14.9	20.14	0
5	71	F	ICA occlusion	Chronic infarction	Right	III	7.79	19.66	0
6	79	F	ICA occlusion	Subacute to chronic infarction	Left	III	24.13	36.31	0
7	50	F	MMD	Subacute to chronic infarction	Right	II	7.29	13.74	1
8	41	F	MMD	Previous ICH	Right	III	17.33	32.79	1
9	44	M	MMD	Chronic infarction	Left	II	17	19.91	1
10	27	M	MMD	Chronic infarction	Left	III	24.5	67.64	1
11	21	F	MMD	Chronic infarction	Left	III	15.5	20.87	1
12	43	F	MMD	Previous ICH	Left	III	22.97	39.78	1
13	66	M	ICA occlusion	Chronic infarction	Left	II	16.28	21	1
14	61	M	MMD	Previous ICH	Left	III	10.2	16.3	1
15	20	F	MMD	Chronic infarction	Left	III	10.24	28.09	1
16	56	F	MMD	Chronic infarction	Left	III	12.43	25.83	1

**Note:**—F indicates female; M, male; MMD, Moyamoya disease; ICH, intracranial hemorrhage.

and the side of the supratentorial stroke evaluated the ASL images from the CCD-positive and CCD-negative groups in random order. The observers determined the presence or absence of CCD and the side of the affected cerebellum, which showed asymmetrically decreased perfusion compared with that of the unaffected cerebellum on ASL perfusion MR imaging. For the blind study, the cerebellum was evaluated from bottom to top. The signal intensity of the affected cerebellum was divided into 1 of the 3 following grades: grade I indicates that the affected cerebellum was isointense to the unaffected cerebellum; grade II indicates that the affected cerebellum was slightly hypointense to the unaffected cerebellum; and grade III indicates that the affected cerebellum was markedly hypointense to the unaffected cerebellum. A grade of II or III was considered to be positive for the diagnosis of CCD. Two readers were trained before the study; they were shown examples of CCD and examples of what would be graded as I versus II versus III.

In the quantitative analysis of the CCD-positive group, the CBF map from ASL was used to compare the affected cerebellum with the unaffected cerebellum. The circular ROIs were drawn manually on the ASL MR images by using the same method applied for the SPECT images. All ROIs were placed to avoid the major vessels and cerebellar vermis. The degree of hypoperfusion was calculated by using the same formula as that for the SPECT AI.

To investigate correlations between cerebellar AIs and supratentorial lesion volume, we computed the volume of supratentorial lesion on FLAIR imaging by using commercial software (nordicICE, and nordicTumorEx [NordicNeuroLab, Bergen, Norway], respectively) for each section that displayed a signal-intensity abnormality by manual segmentation.

### Statistical Analysis

The interrater agreements for the presence of CCD in the qualitative analysis based on tertiary (grade I, II, and III) data were

assessed by using  $\kappa$  statistics. A  $\kappa$  value of  $<0.20$  indicated poor agreement,  $0.21$ – $0.40$  indicated fair agreement,  $0.41$ – $0.60$  indicated moderate agreement,  $0.61$ – $0.80$  indicated good agreement, and  $>0.81$  indicated excellent agreement. In addition, the diagnostic performance of each observer was assessed by using receiver operating characteristic curve analysis. The sensitivity, specificity, positive predictive value, and negative predictive value for ASL were calculated with respect to SPECT.

For the quantitative results of the CCD-positive group, the Kolmogorov-Smirnov test was used to determine whether the AI values were normally distributed. Interobserver reproducibility was assessed by the interobserver correlation coefficient.<sup>30</sup> An interobserver correlation coefficient value of  $<0.40$  indicated poor reproducibility,  $0.40$ – $0.59$  indicated fair reproducibility,  $0.60$ – $0.74$  indicated good reproducibility, and  $>0.74$  indicated excellent reproducibility.<sup>31</sup> An independent  $t$  test was used to compare significant differences between the AIs from ASL by observers 1 and 2 and between the AIs from SPECT and ASL. Linear regression and Pearson correlation coefficients were used to evaluate the correlation between the AIs from SPECT and ASL and between cerebellar AIs and supratentorial lesion volumes.<sup>27,32</sup> Significance for each test was set at a  $P$  value of  $<.05$ . Commercially available software (MedCalc for Windows, version 11.1.1.0; MedCalc Software, Mariakerke, Belgium) was used for the analysis.

### RESULTS

The clinical characteristics and results of the qualitative and quantitative analyses are summarized in the Table. The CCD-positive group consisted of 16 patients (7 men and 9 women; mean age [ $\pm$  standard deviation],  $45 \pm 18$  years; range, 20–79 years). The patients had Moyamoya disease ( $n = 12$ ) or unilateral proximal ICA occlusion ( $n = 4$ ). Each patient presented unilateral ischemic or hemorrhagic stroke on MR imaging. The ASL and SPECT examinations were performed because of subacute to chronic in-

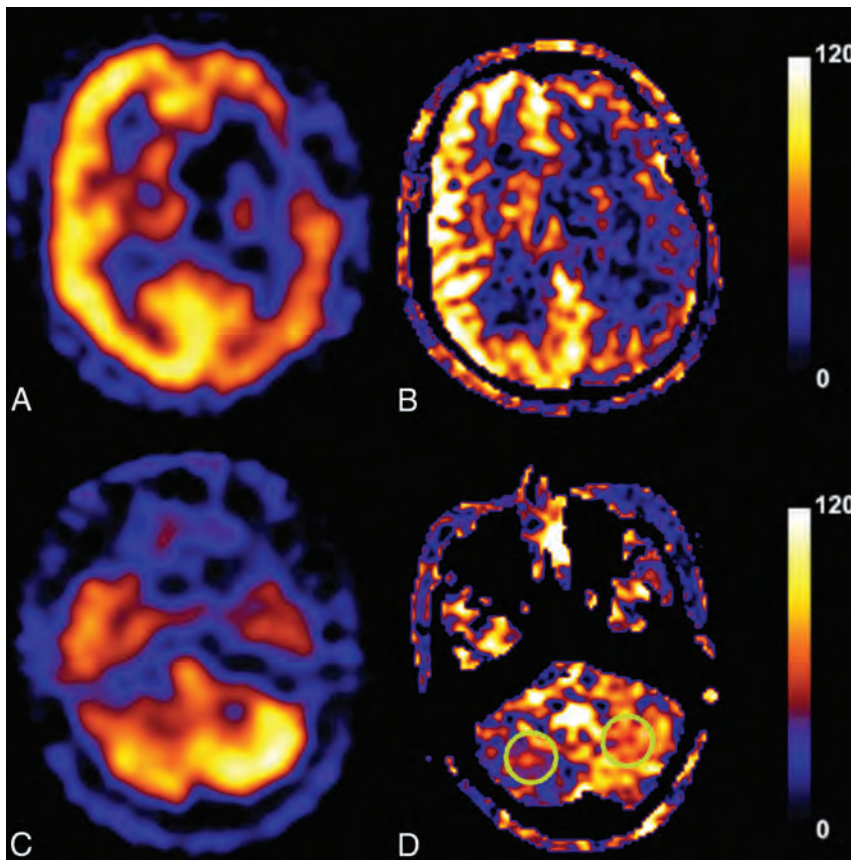


**FIG 1.** A 41-year-old female patient with previous intracranial hemorrhage caused by Moyamoya disease. The SPECT (A and C) and arterial spin-labeling (B and D) images show decreased CBF in the left cerebrum associated with right cerebellar diaschisis. The signal intensity of the affected right cerebellum was markedly hypointense to that of the unaffected left cerebellum (grade III). Two circular ROIs of 25 mm in diameter were placed in the affected and mirrored unaffected cerebellar hemispheres on a section of axial scan representing the greatest cerebellar asymmetry.

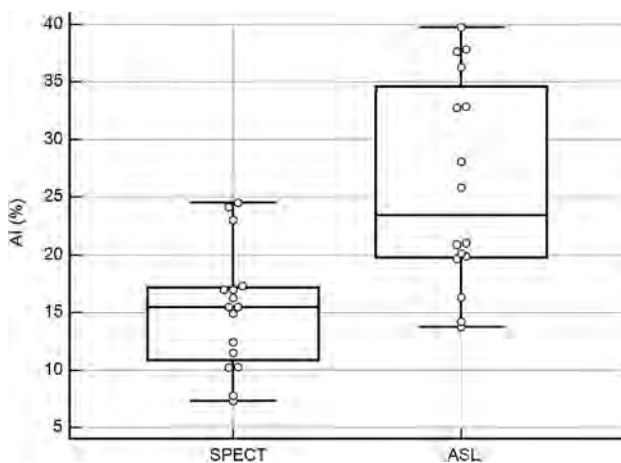


**FIG 2.** Box-and-whisker plots show the distributions, medians, and ranges of asymmetry indices (AIs) for arterial spin-labeling (ASL) and SPECT. The mean AI for ASL ( $26.06\% \pm 9.00\%$ ) was significantly different from that for SPECT ( $15.28\% \pm 5.34\%$ ;  $P < .0001$ ).

faction ( $n = 2$ ), chronic infarction ( $n = 10$ ), or previous intracranial hemorrhage ( $n = 4$ ). The CCD-negative group consisted of 10 patients (2 men and 8 women; mean age,  $46 \pm 15$  years; range, 23–70 years). Each control subject had unilateral ischemic

or hemorrhagic stroke as a result of Moyamoya disease ( $n = 8$ ) or unilateral ICA occlusion ( $n = 2$ ) without CCD on SPECT.

### Qualitative Analysis

Asymmetric cerebellar hypointensity suggestive of hypoperfusion on ASL was observed in each of the 16 patients by observer 1 and in 15 by observer 2. Therefore, the sensitivity, specificity, positive predictive value, and negative predictive value for observer 1 were all 100% for the presence of CCD. Observer 2 exhibited rates of 93.75% sensitivity (15 of 16 patients), 100% specificity (10 of 10 patients), 100% positive predictive value (15 of 15 patients), and 90.91% negative predictive value (10 of 11 patients). The laterality of the affected cerebellum on ASL was in agreement with SPECT results for all patients by observer 1 and for 15 patients by observer 2. The grades of signal intensity in the affected cerebellum classified by observers 1 and 2 were identical in all cases except for the single false-negative evaluation by observer 2. Observer 1 classified the signal intensity of the affected cerebellum as grade III in 13 cases and grade II in 3 cases; observer 2 classified the signal intensity of the affected cerebellum as grade III in 13 cases, grade II in 2 cases, and grade I in 1 case (Fig 1).

Therefore, the interrater agreement was excellent ( $\kappa = 0.961$ ).

### Quantitative Analysis

For the AIs measured by using ASL images from the CCD-positive group, the interobserver agreement was excellent (interobserver correlation coefficient between observers 1 and 2, 0.806). The mean AIs  $\pm$  standard deviations were  $24.36\% \pm 8.30\%$  for observer 1 and  $27.75 \pm 10.61$  for observer 2. There were no significant differences between the mean AIs from ASL by observers 1 and 2 ( $P = .34$ ). We used the mean values of the measurements from observers 1 and 2 to define the AIs for ASL. There was a significant difference between the mean AIs from SPECT and ASL ( $P < .001$ ). The mean AI from ASL ( $26.06\% \pm 9.00\%$ ) was significantly larger than that from SPECT ( $15.28\% \pm 5.34\%$ ) (Fig 2). There was a significant positive correlation between the AIs obtained from SPECT and ASL ( $r = 0.77$  [95% CI, 0.443–0.916];  $P < .001$ ). The regression line for this relationship ( $x =$  AI from SPECT;  $y =$  AI from ASL) was calculated as  $y = 6.2131 + 1.2986x$  ( $R^2 = 0.592$ ;  $P < .001$ ) (Fig 3).

The mean volume of supratentorial lesions was  $28.12 \pm 25.66$   $\text{cm}^3$ . Regarding the relationship of cerebellar AI and supratentorial lesion volume, there was no significant correlation between AIs from SPECT and the volumes ( $r = -0.100$  [95% CI,  $-0.568$

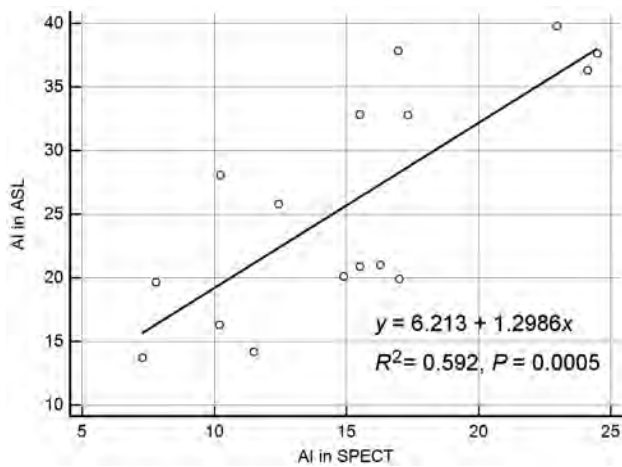


**FIG 3.** Scatter diagram of the correlations between AIs for ASL and SPECT. The AIs for SPECT and ASL exhibited a significant positive correlation ( $r = 0.77$  [95% CI, 0.443–0.916];  $P = .0005$ ).

to 0.416];  $P = .711$ ) or between AIs from ASL and the volumes ( $r = -0.036$  [95% CI,  $-0.522$  to  $0.469$ ];  $P = .896$ ). The relationships of the AIs between supratentorial lesion volume and the AI obtained from SPECT ( $x, y$ ) and between the volume and the AI obtained from ASL ( $x, y$ ) were calculated as  $y = 15.851 + -0.202x$  ( $R^2 = 0.010$ ;  $P = .711$ ) and  $y = 26.40 + -0.1012x$  ( $R^2 = 0.001$ ;  $P = .896$ ), respectively.

## DISCUSSION

CCD is a common result of cerebral stroke. Several previous studies have suggested that CCD is not only an important prognostic factor for stroke recovery but is also associated with cognitive function and the development of vascular dementia.<sup>10,13,33–35</sup> Therefore, the quantification of CCD can be used as a clinical prognostic indicator. However, few studies have reported a correlation between the clinical outcome and treatment response in patients and the quantitative value of CCD.<sup>10–13,18,20</sup> One reason is that PET and SPECT have been used as criterion standards for diagnosing and studying CCD, and the need to inject radioisotopes and the exposure to radiation have made long-term follow-up difficult. However, noninvasive ASL MR perfusion imaging has emerged as a valuable method that can be used to obtain brain-flow information noninvasively and repeatedly.<sup>36</sup> Therefore, in this study we aimed to determine the ability of ASL to assess CCD compared with the reference method, SPECT, which has been widely used to diagnose and study CCD. Almost all diagnoses of CCD on SPECT were also noted on ASL in both qualitative and quantitative analyses with good interobserver agreement. In addition, a significant positive correlation was observed between the AIs from ASL and SPECT. Although one earlier study revealed that CCD can be detected on ASL,<sup>26</sup> this study is the first to validate ASL in CCD by using SPECT as a reference standard.

In the qualitative analysis with ASL, CCD on ASL was observed in each of the 16 patients by observer 1 and in 15 of the patients by observer 2. Except for the single false-negative case by observer 2, the 2 observers agreed perfectly regarding the grade for each case. Most CCD-positive cases (13 of 16 [81%]) were classified as grade III by both observers. The false-negative case was classified as grade I by observer 2 and as grade II by observer 1. In the quanti-

tative analysis, the interobserver correlation coefficient was also excellent between the 2 observers. Our results suggest that the visualization and quantification of CCD by using ASL were reproducible across observers.

The mean AI from SPECT ( $15.28\% \pm 5.34\%$ ) in our study was similar to results ( $16.0\% \pm 7.9\%$ ) obtained in a previous study that reported a mean AI for CCD by using DSC MR imaging in patients with subacute to chronic infarction.<sup>19</sup> However, the mean AI from ASL ( $26.06\% \pm 9.00\%$ ) was significantly larger than that from SPECT ( $15.28\% \pm 5.34\%$ ), and there was a significant positive correlation between the 2 values. In addition, several previous studies reported that measured CBF values were similar between ASL and SPECT and between ASL and DSC MR imaging in patients with Moyamoya disease or carotid stenosis.<sup>24,37,38</sup> According to these results, the sensitivity of ASL might be greater than that of SPECT for assessing cerebral perfusion during follow-up in patients with CCD and correlating the findings with the clinical course. Therefore, additional study using ASL is necessary to investigate the serial changes in CCD and their clinical importance.

In our study, there were no significant correlations between the AI from SPECT and supratentorial lesion volume or between the AI from ASL and the volume. There were discordant reports relating to the severity of CCD and infarct volume.<sup>20,39,40</sup> Although CCD is reported most often in association with large cerebral hemispheric infarcts,<sup>40,41</sup> small infarcts could cause CCD.<sup>39</sup> A few previous studies reported that infarct volume contributes to the development of CCD, but the sample sizes ( $n = 20$  and  $17$ , respectively) were too small.<sup>11,20</sup> In addition, the patient populations in these previous studies were all in the acute stages of stroke. However, our population was in the subacute to chronic infarction ( $n = 2$ ), chronic infarction ( $n = 10$ ), or previous intracranial hemorrhage ( $n = 4$ ) stage. Additional larger studies using ASL may help to establish a correlation between the severity of CCD and infarct volume according to the stage of infarction.

Although ASL MR imaging has evolved methodologically and technically over the past decade, there are still several limitations and confounding factors that affect the quantification of CBF. The measured CBF is influenced by variations in labeling efficiency, arterial transit time, and blood T1.<sup>42</sup> Despite these confounding factors, ASL MR imaging is a novel and promising technique because of its completely noninvasive nature, easy acquisition, patient tolerance, relatively lower cost, and scanning time. In this study, a postlabeling delay time of 1.5 seconds was used. Although this time is appropriate for healthy subjects, it can be shorter for patients with Moyamoya disease.<sup>36</sup> We tried to overcome the potential deviations in CBF quantification in ASL by calculating an asymmetry index.

The present study has several limitations. First, this study was retrospective and vulnerable to selection and verification biases. Second, this study used SPECT as a reference standard. Generally, PET has been considered the criterion standard for CBF quantification. However, to date, several studies have used SPECT to show CBF changes in CCD.<sup>10,17,43,44</sup> In addition, some studies have shown that SPECT can be an alternative method for CBF assessment in patients with cerebrovascular diseases.<sup>45,46</sup> Finally, because ASL is technique

dependent, measurement of the AI and its correlation with SPECT can vary according to variations in the labeling delays. This factor is important to know when considering the use of this technique for longitudinal follow-up.

## CONCLUSIONS

In our study, the AIs of CCD obtained by using ASL were reproducible and significantly correlated with those obtained by using SPECT. Therefore, ASL can be a noninvasive alternative to SPECT for identifying CCD and studying the phenomenon and clinical consequences of CCD. Because ASL allows serial imaging without radiation exposure, this technique can facilitate a better understanding of the impact of CCD on disease outcome over the long term.

## REFERENCES

- Pantano P, Baron JC, Samson Y, et al. **Crossed cerebellar diaschisis. Further studies.** *Brain* 1986;109:677–94 CrossRef Medline
- Meyer JS, Obara K, Muramatsu K. **Diaschisis.** *Neurol Res* 1993;15:362–66 Medline
- Gold L, Lauritzen M. **Neuronal deactivation explains decreased cerebellar blood flow in response to focal cerebral ischemia or suppressed neocortical function.** *Proc Natl Acad Sci U S A* 2002;99:7699–704 CrossRef Medline
- Baron JC, Boussier MG, Comar D, et al. **“Crossed cerebellar diaschisis” in human supratentorial brain infarction.** *Trans Am Neurol Assoc* 1981;105:459–61 Medline
- Patronas NJ, Di Chiro G, Smith BH, et al. **Depressed cerebellar glucose metabolism in supratentorial tumors.** *Brain Res* 1984;291:93–101 CrossRef Medline
- Thajeb P, Huang KM, Shih CC. **Diaschisis in chronic viral encephalitis with Koshevnikov syndrome.** *J Neuroimaging* 1999;9:122–25 Medline
- Thajeb P, Shih BF, Wu MC. **Crossed cerebellar diaschisis in herpes simplex encephalitis.** *Eur J Radiol* 2001;38:55–58 CrossRef Medline
- Mewasingh LD, Christiaens F, Aeby A, et al. **Crossed cerebellar diaschisis secondary to refractory frontal seizures in childhood.** *Seizure* 2002;11:489–93 CrossRef Medline
- De Reuck J, Decoo D, Lemahieu I, et al. **Crossed cerebellar diaschisis after middle cerebral artery infarction.** *Clin Neurol Neurosurg* 1997;99:11–16 CrossRef Medline
- Takasawa M, Watanabe M, Yamamoto S, et al. **Prognostic value of subacute crossed cerebellar diaschisis: single-photon emission CT study in patients with middle cerebral artery territory infarct.** *AJNR Am J Neuroradiol* 2002;23:189–93 Medline
- Sobesky J, Thiel A, Ghaemi M, et al. **Crossed cerebellar diaschisis in acute human stroke: a PET study of serial changes and response to supratentorial reperfusion.** *J Cereb Blood Flow Metab* 2005;25:1685–91 CrossRef Medline
- Serrati C, Marchal G, Rioux P, et al. **Contralateral cerebellar hypometabolism: a predictor for stroke outcome?** *J Neurol Neurosurg Psychiatry* 1994;57:174–79 CrossRef Medline
- Szilágyi G, Vas A, Kerényi L, et al. **Correlation between crossed cerebellar diaschisis and clinical neurological scales.** *Acta Neurol Scand* 2012;125:373–81 CrossRef Medline
- Kim SE, Choi CW, Yoon BW, et al. **Crossed-cerebellar diaschisis in cerebral infarction: technetium-99m-HMPAO SPECT and MRI.** *J Nucl Med* 1997;38:14–19 Medline
- Kamouchi M, Fujishima M, Saku Y, et al. **Crossed cerebellar hypoperfusion in hyperacute ischemic stroke.** *J Neurol Sci* 2004;225:65–69 CrossRef Medline
- Komaba Y, Mishina M, Utsumi K, et al. **Crossed cerebellar diaschisis in patients with cortical infarction: logistic regression analysis to control for confounding effects.** *Stroke* 2004;35:472–76 CrossRef Medline
- Liu Y, Karonen JO, Nuutinen J, et al. **Crossed cerebellar diaschisis in acute ischemic stroke: a study with serial SPECT and MRI.** *J Cereb Blood Flow Metab* 2007;27:1724–32 CrossRef Medline
- Kajimoto K, Oku N, Kimura Y, et al. **Crossed cerebellar diaschisis: a positron emission tomography study with L-[methyl-11C]methionine and 2-deoxy-2-[18F]fluoro-D-glucose.** *Ann Nucl Med* 2007;21:109–13 CrossRef Medline
- Yamada H, Koshimoto Y, Sadato N, et al. **Crossed cerebellar diaschisis: assessment with dynamic susceptibility contrast MR imaging.** *Radiology* 1999;210:558–62 CrossRef Medline
- Lin DD, Kleinman JT, Wityk RJ, et al. **Crossed cerebellar diaschisis in acute stroke detected by dynamic susceptibility contrast MR perfusion imaging.** *AJNR Am J Neuroradiol* 2009;30:710–15 CrossRef Medline
- Madai VI, Altaner A, Stengl KL, et al. **Crossed cerebellar diaschisis after stroke: can perfusion-weighted MRI show functional inactivation?** *J Cereb Blood Flow Metab* 2011;31:1493–500 CrossRef Medline
- Chalela JA, Alsop DC, Gonzalez-Atavales JB, et al. **Magnetic resonance perfusion imaging in acute ischemic stroke using continuous arterial spin labeling.** *Stroke* 2000;31:680–87 CrossRef Medline
- Detre JA, Leigh JS, Williams DS, et al. **Perfusion imaging.** *Magn Reson Med* 1992;23:37–45 CrossRef Medline
- Noguchi T, Kawashima M, Irie H, et al. **Arterial spin-labeling MR imaging in Moyamoya disease compared with SPECT imaging.** *Eur J Radiol* 2011;80:e557–62 CrossRef Medline
- Bokkers RP, Bremmer JP, van Berckel BN, et al. **Arterial spin labeling perfusion MRI at multiple delay times: a correlative study with H(2)(15)O positron emission tomography in patients with symptomatic carotid artery occlusion.** *J Cereb Blood Flow Metab* 2010;30:222–29 CrossRef Medline
- Chen S, Guan M, Lian HJ, et al. **Crossed cerebellar diaschisis detected by arterial spin-labeled perfusion magnetic resonance imaging in subacute ischemic stroke.** *J Stroke Cerebrovasc Dis* 2014;23:2378–83 CrossRef Medline
- Dai W, Garcia D, de Bazelaire C, et al. **Continuous flow-driven inversion for arterial spin labeling using pulsed radio frequency and gradient fields.** *Magn Reson Med* 2008;60:1488–97 CrossRef Medline
- Garcia D, De Bazelaire C, Alsop D. **Pseudo-continuous flow driven adiabatic inversion for arterial spin labeling.** *Proc Int Soc Magn Reson Med* 2005;13:37
- Mani S, Pauly J, Conolly S, et al. **Background suppression with multiple inversion recovery nulling: applications to projective angiography.** *Magn Reson Med* 1997;37:898–905 CrossRef Medline
- Varoquaux A, Rager O, Lovblad KO, et al. **Functional imaging of head and neck squamous cell carcinoma with diffusion-weighted MRI and FDG PET/CT: quantitative analysis of ADC and SUV.** *Eur J Nucl Med Mol Imaging* 2013;40:842–52 CrossRef Medline
- Oppo K, Leen E, Angerson WJ, et al. **Doppler perfusion index: an interobserver and intraobserver reproducibility study.** *Radiology* 1998;208:453–57 CrossRef Medline
- Wong CS, Gong N, Chu YC, et al. **Correlation of measurements from diffusion weighted MR imaging and FDG PET/CT in GIST patients: ADC versus SUV.** *Eur J Radiol* 2012;81:2122–26 CrossRef Medline
- Seitz RJ, Azari NP, Knorr U, et al. **The role of diaschisis in stroke recovery.** *Stroke* 1999;30:1844–50 CrossRef Medline
- Timmann D, Daum I. **Cerebellar contributions to cognitive functions: a progress report after two decades of research.** *Cerebellum* 2007;6:159–62 CrossRef Medline
- Sui R, Zhang L. **Cerebellar dysfunction may play an important role in vascular dementia.** *Med Hypotheses* 2012;78:162–65 CrossRef Medline
- Wolf RL, Detre JA. **Clinical neuroimaging using arterial spin-la-**

- beled perfusion magnetic resonance imaging. *Neurotherapeutics* 2007;4:346–59 CrossRef Medline
37. Uchihashi Y, Hosoda K, Zimine I, et al. **Clinical application of arterial spin-labeling MR imaging in patients with carotid stenosis: quantitative comparative study with single-photon emission CT.** *AJNR Am J Neuroradiol* 2011;32:1545–51 CrossRef Medline
  38. Goetti R, O’Gorman R, Khan N, et al. **Arterial spin labelling MRI for assessment of cerebral perfusion in children with moyamoya disease: comparison with dynamic susceptibility contrast MRI.** *Neuroradiology* 2013;55:639–47 CrossRef Medline
  39. Flint AC, Naley MC, Wright CB. **Ataxic hemiparesis from strategic frontal white matter infarction with crossed cerebellar diaschisis.** *Stroke* 2006;37:e1–2 CrossRef Medline
  40. Infeld B, Davis SM, Lichtenstein M, et al. **Crossed cerebellar diaschisis and brain recovery after stroke.** *Stroke* 1995;26:90–95 CrossRef Medline
  41. Miyazawa N, Toyama K, Arbab AS, et al. **Evaluation of crossed cerebellar diaschisis in 30 patients with major cerebral artery occlusion by means of quantitative I-123 IMP SPECT.** *Ann Nucl Med* 2001;15:513–19 CrossRef Medline
  42. Wu WC, St Lawrence KS, Licht DJ, et al. **Quantification issues in arterial spin labeling perfusion magnetic resonance imaging.** *Top Magn Reson Imaging* 2010;21:65–73 CrossRef Medline
  43. Momose T, Kosaka N, Nishikawa J, et al. **Crossed cerebellar diaschisis in cerebrovascular disease detected by N-isopropyl I-123 p-iodoamphetamine (I-123 IMP) with SPECT [in Japanese].** *Kaku Igaku* 1986;23:25–34 Medline
  44. Kim J, Lee SK, Lee JD, et al. **Decreased fractional anisotropy of middle cerebellar peduncle in crossed cerebellar diaschisis: diffusion-tensor imaging-positron-emission tomography correlation study.** *AJNR Am J Neuroradiol* 2005;26:2224–28 Medline
  45. Greenberg JH, Kushner M, Rango M, et al. **Validation studies of iodine-123-iodoamphetamine as a cerebral blood flow tracer using emission tomography.** *J Nucl Med* 1990;31:1364–69 Medline
  46. Inugami A, Kanno I, Uemura K, et al. **Linearization correction of <sup>99m</sup>Tc-labeled hexamethyl-propylene amine oxime (HM-PAO) image in terms of regional CBF distribution: comparison to C15O2 inhalation steady-state method measured by positron emission tomography.** *J Cereb Blood Flow Metab* 1988;8:S52–60 CrossRef Medline

# Visualization of the Medial and Lateral Geniculate Nucleus on Phase Difference Enhanced Imaging

M. Kitajima, T. Hirai, T. Yoneda, Y. Iryo, M. Azuma, M. Tateishi, K. Morita, M. Komi, and Y. Yamashita

## ABSTRACT

**BACKGROUND AND PURPOSE:** The precise identification and measurement of the medial geniculate nucleus and lateral geniculate nucleus on MR imaging remain technically challenging because the thalamic nuclei are small structures. We compared the visualization of the medial geniculate nucleus and lateral geniculate nucleus on phase difference enhanced imaging with 3D high-resolution phase imaging, 2D-T2WI, STIR, proton attenuation-weighted imaging, and DTI acquired at 3T. We also measured the volume and height of the medial geniculate nucleus and lateral geniculate nucleus on phase difference enhanced imaging.

**MATERIALS AND METHODS:** Phase difference enhanced, 2D-T2-weighted, STIR, proton attenuation-weighted, and DTI were acquired on a 3T MR imaging unit in 10 healthy volunteers. Two neuroradiologists recorded the qualitative visualization scores of the medial geniculate nucleus and lateral geniculate nucleus, specifically the identification of their boundaries, for all images. Measurement differences were assessed with the Wilcoxon signed rank test. The volume and height of the medial geniculate nucleus and lateral geniculate nucleus were measured on phase difference enhanced imaging and compared with previously reported values.

**RESULTS:** The qualitative visualization scores of the lateral geniculate nucleus and medial geniculate nucleus were significantly higher on phase difference enhanced images than on T2-weighted, proton attenuation-weighted, STIR, or DTI ( $P < .05$ ). On phase difference enhanced imaging, the medial geniculate nucleus and lateral geniculate nucleus were bordered by low-intensity structures: the cerebral peduncle, the origin of the optic radiation, and the superior and inferior quadrigeminal brachia. The volume of the medial geniculate nucleus and lateral geniculate nucleus varied from 74.0 to 183.75 mm<sup>3</sup> (mean, 129.0 ± 34.7 mm<sup>3</sup>) and from 96.5 to 173.75 mm<sup>3</sup> (mean, 135.2 ± 28.0 mm<sup>3</sup>), respectively.

**CONCLUSIONS:** For the depiction of the medial geniculate nucleus and lateral geniculate nucleus on 3T MR imaging, phase difference enhanced imaging is superior to conventional MR imaging. The medial geniculate nucleus and lateral geniculate nucleus volumes vary among individuals.

**ABBREVIATIONS:** LGN = lateral geniculate nucleus; MGN = medial geniculate nucleus; PADRE = phase difference enhanced; PD = proton attenuation-weighted imaging

The medial geniculate nucleus (MGN) and lateral geniculate nucleus (LGN) are the specific thalamic nuclei that relay the auditory and optic pathways, respectively. The triangular LGN is located in the posterior region of the thalamus. It is bordered

anteriorly by the cerebral peduncle and the optic tract and posteriorly by the origin of the optic radiation. The oval MGN, with its long axis directed forward and laterally just medial to the LGN, is bordered anteriorly by the inferior quadrigeminal brachium and posteriorly by the superior quadrigeminal brachium. There is increasing interest in assessing the MGN and LGN in healthy subjects and in patients with ophthalmic diseases such as glaucoma.<sup>1-6</sup> However, current imaging methods for identifying the MGN and LGN vary, and imaging findings are inconsistent.

Technical advances in neuroimaging facilitate the study of subcortical structures in vivo. Phase difference enhanced (PADRE) imaging yields a high tissue contrast that delineates specific white matter tracts and intracortical structures.<sup>7-9</sup> On high-spatial-resolution 3T PADRE images, small structures, including the central tegmental tract, the medial and dorsal longitudinal fasciculus, and the stria of Gennari, which are difficult to appreciate on conven-

Received May 16, 2014; accepted after revision February 10, 2015.

From the Department of Diagnostic Radiology, Graduate School of Medical Sciences (M.K., T.H., Y.I., M.A., M.T., Y.Y.) and Department of Medical Physics in Advanced Biomedical Sciences, Faculty of Life Sciences (T.Y.), Kumamoto University, Kumamoto, Japan; and Department of Radiology (K.M., M.K.), Kumamoto University Hospital, Kumamoto, Japan.

Paper previously presented at: Annual Meeting of the American Society of Neuroradiology and the Foundation of the ASNR Symposium, May 18–23, 2013; San Diego, California.

Please address correspondence to Mika Kitajima, MD, Department of Diagnostic Radiology, Graduate School of Medical Sciences, Kumamoto University, 1-1-1, Honjo, Chuo-ku, Kumamoto-shi, Kumamoto, 860-0811, Japan; e-mail: mkitaj@kumamoto-u.ac.jp

<http://dx.doi.org/10.3174/ajnr.A4356>

tional MR images, are delineated.<sup>7,8</sup> Also, the contrast between specific white matter structure (eg, the optic radiation) is higher on PADRE than on conventional MR images.<sup>7</sup>

We compared visualization of the MGN and LGN on PADRE, 2D-T2-weighted, STIR, proton attenuation-weighted (PD), and DTI acquired at 3T. We also measured the volume and height of the MGN and LGN on PADRE images.

## MATERIALS AND METHODS

### Subjects

This study was approved by our institutional review board. Informed consent was obtained from all healthy volunteers (6 men, 4 women; age range, 28–47 years; mean,  $36.8 \pm 6.7$  years); none had a history of neurologic, psychiatric, or ophthalmologic diseases, including glaucoma.

### Imaging Protocol

All measurements were performed on a 3T MR imaging scanner (Achieva; Philips Healthcare, Best, the Netherlands). A set consisting of 3D high-resolution T1 fast-field echo images for PADRE, 2D-T2-weighted, STIR, PD, and DTI was obtained in all subjects. The images were acquired in the transverse plane parallel to the anterior/posterior commissure line. The scan parameters of each sequence were the following: 3D-T1 fast-field echo images for PADRE: TR/TE, 32/23 ms; FOV, 200 mm; matrix size,  $307 \times 384$ ; reconstructed matrix size,  $400 \times 400$ ; spatial resolution,  $0.5 \times 0.5 \times 1.0$  mm; sensitivity encoding factor, 2; flip angle,  $10^\circ$ ; 1 signal acquired; image acquisition time, 3 minutes 36 seconds. We also reconstructed PADRE images with a 3-mm thickness. For 2D-PD and T2-weighted images, the parameters were the following: TR/TE, 4000/17, 80 ms; FOV, 200 mm; matrix size,  $280 \times 400$ ; spatial resolution,  $0.4 \times 0.4$  mm; turbo factor, 9; sensitivity encoding, 1.5; refocusing angle,  $120^\circ$ ; 2 signals acquired; acquisition time, 2 minutes 16 seconds to 3 minutes 20 seconds. For STIR, the parameters were the following: TR/TE, 5000/20 ms; FOV, 200 mm; matrix size,  $224 \times 320$ ; TI, 120 ms; spatial resolution,  $0.4 \times 0.4$  mm; turbo factor, 9; sensitivity encoding factor, 2.0; refocusing angle,  $120^\circ$ ; 2 signals acquired; acquisition time, 3 minutes 10 seconds. The section thickness and gap of the 2D sequences were 3.0 and 1.0 mm, respectively. DTI was obtained with single-shot spin-echo EPI: TE, 49 ms; spatial resolution,  $0.8 \times 0.8 \times 3.0$  mm; 6 signals acquired; b-factor,  $0/700$  s/mm<sup>2</sup>; EPI factor, 49. We used a tilted  $\pi/2$  pulse and optimized outer-volume suppression. The image acquisition time was 11 minutes 15 seconds. Gray-scale fractional anisotropy maps were used for evaluation. On the fractional anisotropy map, areas with high degrees of fractional anisotropy (eg, internal capsule) are bright, and areas with low degrees of fractional anisotropy (eg, gray matter) are dark.

### Data Processing of PADRE

The PADRE technique was described in previous reports.<sup>8,9</sup> One of the major concepts responsible for the power of the PADRE technique is the “phase difference selection,” which enhances the magnetic properties of the target tissue. PADRE imaging classifies and selects various phase differences,  $\Delta\theta$ , to enhance the different tissues, and enhances all of them on the magnitude image  $|\rho|$  by

the enhancing function  $w(\Delta\theta)$ . Finally, the PADRE image  $\rho$  is reconstructed as  $\rho_{\text{PADRE}} = w(\Delta\theta) |\rho|$ .

In this study, the positive phase difference ( $\Delta\theta$ ) was selected to enhance myelin.<sup>7,8</sup>

All images were calculated off-line with in-house software.

All postprocessing of DTI and PADRE images was fully automatic without user intervention to eliminate operator bias.

### MGN and LGN Localization and Measurement

To evaluate the visibility of the boundaries of the MGN and LGN, 2 experienced neuroradiologists (T.H., Y.I. with 21 and 9 years of neuroradiology experience, respectively) independently assessed the original PADRE (1-mm thickness), reconstructed PADRE (3-mm thickness), 2D-T2-weighted, STIR, PD, and DTI by referring to the atlas of Schaltenbrand and Wahren<sup>10</sup> and Duvernoy's<sup>11</sup> atlas. They assigned MGN and LGN visualization scores to each imaging method, where 0 = no visible boundary of the nucleus, 1 = poorly visible with a fuzzy boundary, 2 = mostly visible with a slightly fuzzy boundary, and 3 = well-identified nucleus and clearly distinguishable from neighboring structures.

A third neuroradiologist (M.K. with 20 years of neuroradiology experience) subsequently measured the area of the MGN and LGN by manually outlining their boundaries on each original PADRE image section. The total volume was obtained by summing the areas of all sections. The number of sections on which the nucleus was identified was also recorded as the height of the nucleus. To assess the volume and height of the MGN and LGN, we compared our estimated volume and height based on PADRE with previously reported histologic and MR imaging measurements.<sup>5,6,12,13</sup>

### Statistical Analysis

To assess interobserver agreement for each imaging method, we calculated the percentage of agreement as the number of subjects who received identical scores from both observers divided by the number of subjects ( $n = 10$ ). Visualization scores were analyzed with the Wilcoxon signed rank test by using all 10 subjects to determine the difference between PADRE and each of the other imaging methods. A  $P$  value  $< .05$  was statistically significant. All statistical analyses were performed with MedCalc, Version 12.7.1.0 (MedCalc for Windows, Mariakerke, Belgium).

## RESULTS

Imaging was successful in all 10 subjects. In subjects with a score of  $>1$ , the triangular LGN and the ovoid MGN were slightly hyperintense on PD and STIR images (Fig 1). Although the MGNs were not identified on DTI,  $>90\%$  of the LGNs were identified. On fractional anisotropy maps, the cerebral peduncle and origin of the optic radiation exhibited bright. The LGNs were identified as triangular dark areas between the cerebral peduncle and the origin of the optic radiation (Fig 1). Although 1 LGN and 2 MGNs were not identified on reconstructed PADRE due to the failure of the unwrapping of phase information,  $>80\%$  of the MGNs and LGNs were well-identified and clearly differentiated from neighboring structures on both original and reconstructed PADRE imaging. Reference to the anatomic atlas and the textbook revealed that the LGN was hyperintense compared with

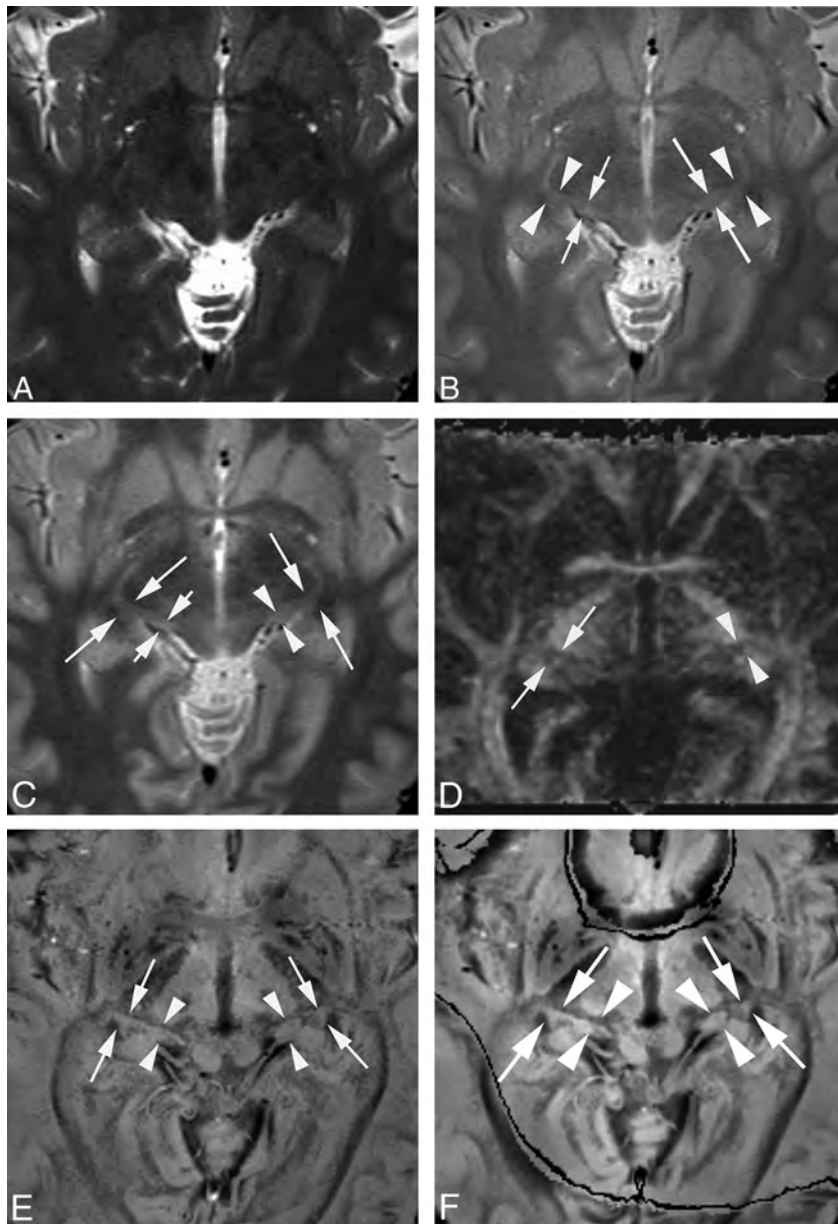


**FIG 1.** MGN and LGN in a healthy 31-year-old female volunteer. T2-weighted (A), PD (B), STIR (C), DTI (D), original PADRE (1 mm) (E), and reconstructed PADRE (3 mm) images (F). A, Neither side of the MGN or LGN is identified (visualization score = 0 by both observers). B, The right MGN is poorly visible. Its boundary is fuzzy (*short arrows*) (visualization score = 1 by both observers). The left MGN is mostly visible; its boundary is slightly fuzzy (*long arrows*) (visualization score = 2 by both observers). Both sides of the LGN are mostly visible; the boundary is slightly fuzzy (*arrowheads*) (visualization score = 2 by both observers). C, One observer assigned a visualization score of 1, the other of 2, to the right MGN (*short arrows*). The left MGN is mostly visible with a slightly fuzzy boundary (*arrowheads*) (visualization score = 2 by both observers). Both sides of the LGN are mostly visible with a slightly fuzzy border (*long arrows*) (visualization score = 2 by both observers). D, Neither side of the MGN is identified (visualization score = 0 by both observers). The right LGN is mostly visible with a slightly fuzzy border (*arrows*) (visualization score = 2 by both observers). The left LGN is poorly visible; its border is fuzzy (*arrowheads*) (visualization score = 1 by both observers). E, Both sides of the MGN (*arrowheads*) and LGN (*arrows*) are well-identified and clearly differentiated from lateral and medial neighboring structures (visualization score = 3 by both observers). F, Although the boundaries of the LGN and MGN are slightly obscure on reconstructed PADRE compared with the original PADRE, both sides of the MGN (*arrowheads*) and LGN (*arrows*) are well-identified and clearly differentiated from lateral and medial neighboring structures (visualization score = 3 by both observers).

surrounding structures, the cerebral peduncle and the origin of the optic radiation (Figs 1 and 2). The MGN was hyperintense compared with surrounding structures, the superior and infe-

rior quadrigeminal brachia, which exhibited low signal intensity (Figs 1 and 2).

Statistics of the visualization scores assigned by the 2 observers are presented in Fig 3. The average scores assigned to the LGN by the 2 observers for T2-weighted, PD, STIR, DTI, and original and reconstructed PADRE images were  $0.0 \pm 0.0$ ,  $1.33 \pm 0.57$ ,  $1.56 \pm 0.64$ ,  $1.78 \pm 0.77$ ,  $2.88 \pm 0.33$ , and  $2.82 \pm 0.51$ , respectively. The average MGN scores for T2-weighted, PD, STIR, DTI, and original and reconstructed PADRE images were  $0.10 \pm 0.30$ ,  $0.85 \pm 0.77$ ,  $1.08 \pm 0.86$ ,  $0.0 \pm 0.0$ ,  $2.98 \pm 0.16$ , and  $2.94 \pm 0.23$ , respectively. For the 20 LGN scores (10 subjects), the percentage of agreement was 100.0%, 70%, 75%, 45%, 85%, and 89.5% for T2-weighted, PD, STIR, DTI, and the original and reconstructed PADRE images, respectively. For the MGN scores, the percentage of agreement was 80%, 45%, 55%, 100%, 100%, and 88.9% for T2-weighted, PD, STIR, DTI, and original and reconstructed PADRE images, respectively. The difference in scores between original PADRE and all of the other 2D images for both the LGN and MGN was statistically significant ( $P < .01$ ). The difference in scores between reconstructed PADRE and all of the other 2D images for both the LGN and MGN was also statistically significant ( $P < .05$ ). In contrast, we found no statistically significant difference between original and reconstructed PADRE for both the LGN and MGN.

The volume of the MGN and LGN measured on original PADRE varied among individuals; for the MGN, it ranged from 74.0 to 183.75 mm<sup>3</sup> (mean, 129.0  $\pm$  34.7 mm<sup>3</sup>), and for the LGN, 96.5–173.75 mm<sup>3</sup> (mean, 135.2  $\pm$  28.0 mm<sup>3</sup>). The height of the MGN varied from 4.0 to 7.0 mm (mean, 5.7  $\pm$  0.88 mm); for the LGN, it varied from 4.0 to 7.0 mm (mean, 5.5  $\pm$  0.95 mm).

## DISCUSSION

Our results indicated that PADRE yielded a superior visibility of the MGN and LGN when directly compared with T2-weighted, DTI, PD, and STIR images.

The superior visualization on PADRE compared with T2-weighted, PD, and STIR images may be attributable to different mechanisms of signal generation (ie, the susceptibility-based

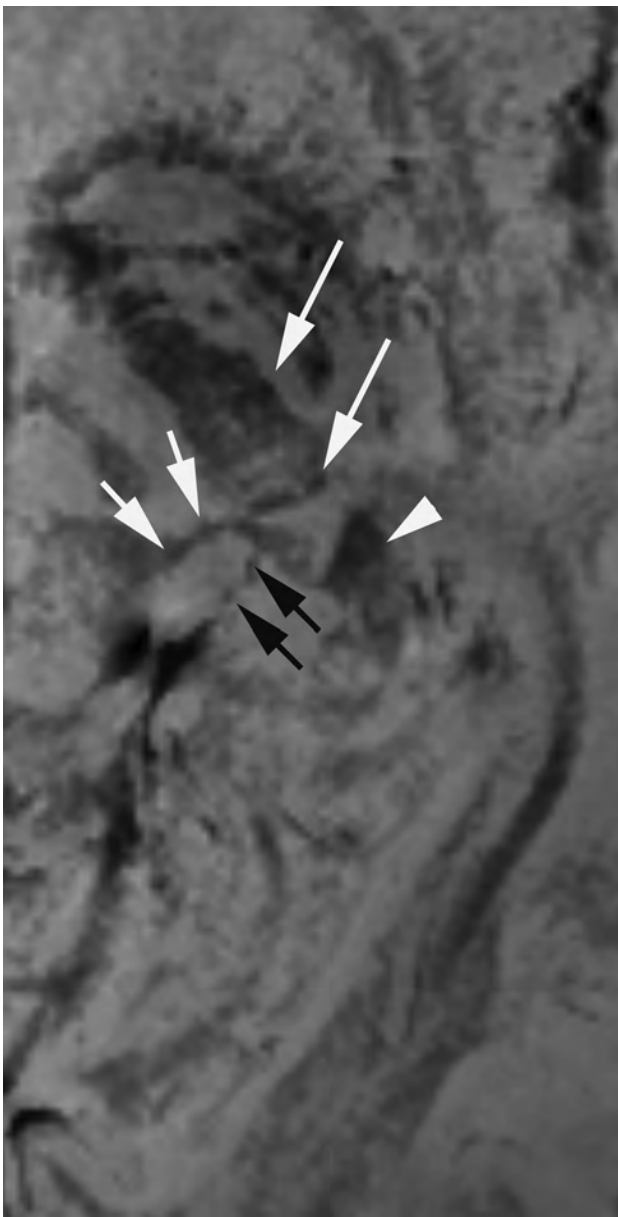


**FIG 2.** A magnified PADRE image of the left MGN and LGN in a healthy 28-year-old female volunteer. The left LGN is surrounded by the cerebral peduncle (*long arrows*) anteriorly and the origin of the optic radiation (*arrowhead*) posteriorly. The MGN is surrounded by the inferior (*arrows*) and superior quadrigeminal brachium (*black arrows*). The MGN and LGN are distinguished from surrounding structures with low signal intensity.

methods used in PADRE versus the relaxation-based techniques of T2-weighted, PD, and STIR). Phase images acquired with high magnetic fields (7T and above) yield information about biologic structures that are not usually identified by conventional MR imaging.<sup>14-16</sup> Blood deoxyhemoglobin, tissue lipid, nonheme iron content,<sup>15</sup> and water-protein exchange<sup>17</sup> have been proposed as possible origins of the MR imaging signal frequency shift responsible for the contrast on phase images. In contrast, the discrepancies between structures on relaxation-based methods originate from differences in the decay rates, which are small. Thus, high-resolution phase imaging may be able to delineate small structures that are difficult to evaluate on conventional MR images.

In addition to the comparison between original PADRE and 2D images, we also compared reconstructed PADRE and 2D sequences with nearly identical thickness. On reconstructed PADRE images, the signal-to-noise ratio becomes higher compared with original PADRE images. In contrast, the boundary between the target structures and the surrounding structures on reconstructed PADRE images becomes more obscure because of an increase in the partial volume effect. However, we found no statistically significant difference for the visualization score of LGN and MGN between original and reconstructed PADRE images.

He and Yablonskiy<sup>18</sup> reported that the optic radiation, a myelin-rich structure, exhibited a negative phase value in the left-handed system—that is, a positive phase value in the right-handed system used in our study. In our study, positive phase values appeared as dark signals. The fiber orientation of the optic radiation to the main magnetic field direction and the cerebral blood volume also affect the image contrast of the optic radiation on phase images.<sup>18</sup> Li et al<sup>19</sup> demonstrated that the structure of myelin and its orientation to the static magnetic field affect white matter fiber susceptibility, resulting in a negative susceptibility change. Ide et al<sup>7</sup> reported that the contrast between the optic radiation and the surrounding tissue on PADRE was similar to that on myelin-stained specimens. As with the optic radiation, the difference in the myelin content between the thalamic nuclei, the LGN and MGN, and their surrounding structures, specifically the cerebral peduncle, optic radiation, and the superior and inferior quadrigeminal brachia, may have affected the contrast on PADRE images. Furthermore, the fiber orientation and cerebral blood volume of those small white matter tracts also may have affected this contrast. We suggest that the high contrast between the thalamic nuclei and neighboring white matter tracts on PADRE facilitates the easy identification of the MGN and LGN.

Horton et al<sup>20</sup> provided the first PD images of the LGN; they performed postmortem studies and studies on living human subjects. They demonstrated a good correlation between MR images and anatomic sections. For the identification of the LGN, Fujita et al<sup>21</sup> documented an excellent correspondence between PD images and images obtained with functional methods by using blood oxygen level–dependent imaging. In our study, the averaged visualization scores of the LGN and MGN were higher for PD than for T2-weighted images and lower than those recorded for PADRE images. Devlin et al<sup>22</sup> reported a different approach for the identification of the MGN and LGN by using DTI. They used probabilistic tractography to automatically segment the 2 nuclei from surrounding structures on the basis of their distinctive patterns of connectivity to the rest of the brain. DTI data for probabilistic tractography were obtained by using a doubly refocused spin-echo sequence and cardiac gating with 60 diffusion-weighted images. These resulted in an acquisition time of approximately 20 minutes and a spatial resolution of  $1.875 \times 1.875 \times 2.5 \text{ mm}^3$ . They reported identifying the MGN and LGN in all of their 5 neurologically healthy volunteers. However, because probabilistic tractography requires thousands of iterations, it is computationally intensive. In contrast, PADRE images can be acquired with commonly available imaging sequences within a reasonable image acquisition time. Furthermore, PADRE provides images

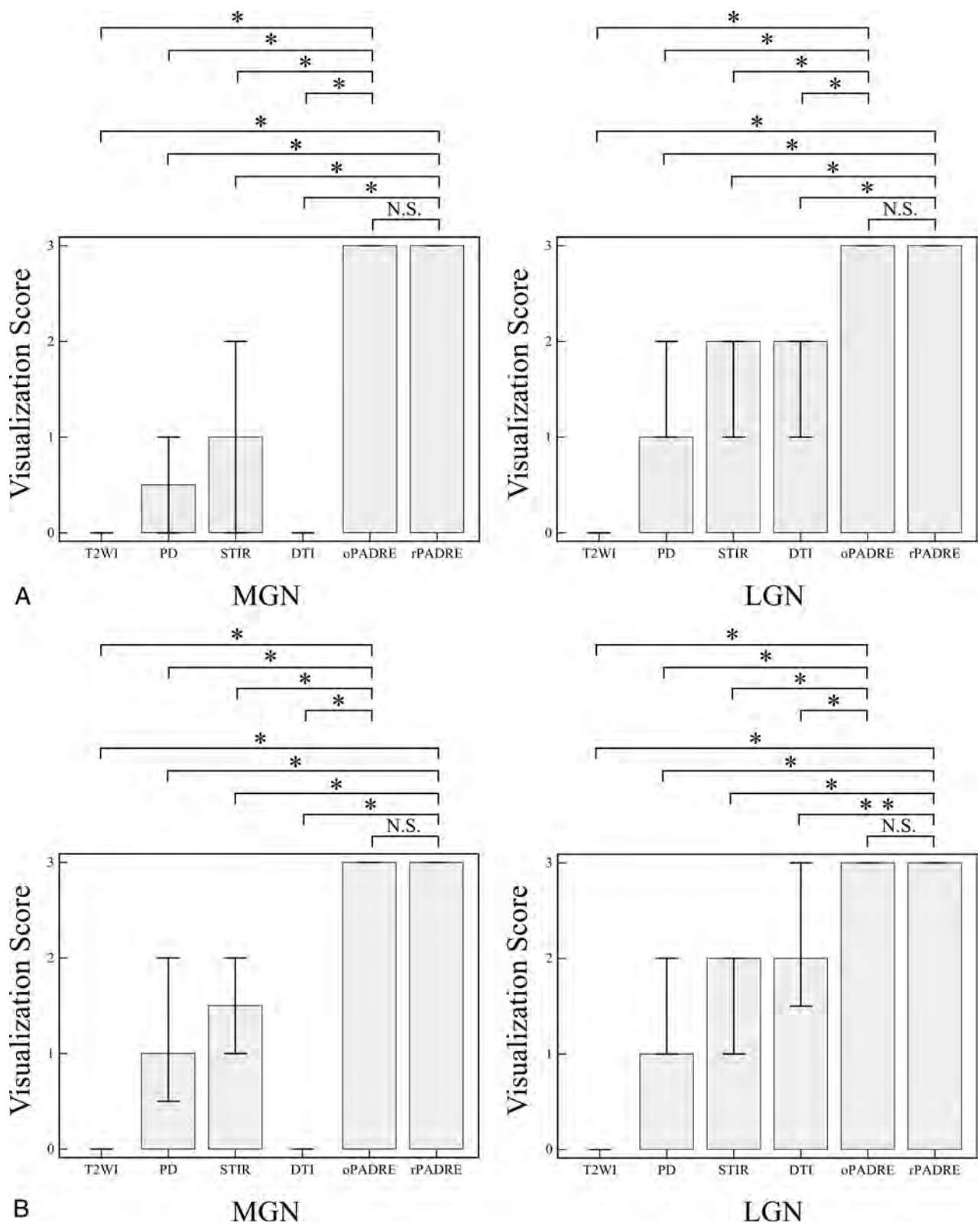


**FIG 3.** Graphs show the statistics for the visualization scores assigned by the 2 observers. The visualization scores of LGN and MGN are higher on original and reconstructed PADRE than those on other 2D sequences in observers 1 (A) and 2 (B). The height of the bar denotes the median, and error bars, the 25%–75% percentile. The asterisk indicates  $P < .01$ ; double asterisks,  $P < .05$  compared with PADRE; N.S.; not significant; oPADRE, original PADRE with 1-mm section thickness; rPADRE, reconstructed PADRE with 3-mm section thickness.

with high spatial resolution and low image distortion and is less computationally intensive than the probabilistic tractography technique.

The previously reported LGN volume measured on MR im-

ages in healthy subjects varied from 75.3 to 86.7 mm<sup>3</sup>.<sup>5,6</sup> In a histologic study,<sup>12</sup> it varied from 66 to 157 mm<sup>3</sup>; among individuals, the variation was 2- to 3-fold. In our search of the literature,

we found only 1 postmortem study on the volume of the MGN<sup>13</sup>; this nucleus was reported to be 5-mm wide, 4-mm high, and 4- to 5-mm long. Our volume measurements for LGN were larger than those reported in earlier MR imaging and histologic studies.<sup>5,6,12</sup> The height of the LGN was slightly larger than that in earlier MR imaging studies (4.7–4.8 mm), and the height of the MGN was somewhat larger than the height (4–5 mm) in the histologic investigation of Winer.<sup>13</sup>

We attribute the discrepancy between ours and earlier findings on the LGN and MGN to several factors: First, our study population was small. Second, differences in the identification techniques such as the blood oxygen level–dependent and spin-echo techniques used by others and our susceptibility-based technique affect volume measurements. Blooming artifacts may be more prominent on gradient-echo images such as PADRE than on spin-echo images. They depend on the orientation and geometry of the object and on various imaging parameters. Third, the volume of living and postmortem human brains removed from the skull and fixed with formalin may be different.

Measuring the LGN volume on MR imaging may be of clinical importance. According to earlier MR imaging studies, the volume of LGN decreases with age.<sup>6</sup> In patients with glaucoma, the LGN height and volume are diminished and the extent of atrophy of the LGN is correlated with the clinical stage.<sup>1,5</sup> We believe that the PADRE technique reinforces the clinical utility of MR imaging in the diagnosis of diseases involving the LGN and MGN. Prospective clinical studies are underway in our laboratory to confirm the utility of PADRE.

Our study has some limitations. First, all of our subjects were healthy young Japanese adults. Our findings may not be applicable to other populations or age groups. Because the volume of the LGN varies 2- to 3-fold among individuals, additional qualitative and quantitative studies of the MGN and LGN on PADRE images are required in larger independent series comprising healthy subjects and patients with diseases affecting the MGN and LGN. Second, we did not compare the visualization of the nuclei directly between the original PADRE and other 3D sequences at identical spatial resolutions. Further studies of comparison between PADRE and other 3D sequences at identical spatial resolutions are required. In addition to the direct comparison, registration of all the sequences with transparent overlay may be useful to evaluate the differences of the LGN and MGN visualization among the sequences.

## CONCLUSIONS

On PADRE images, visualization of the MGN and LGN is significantly better than that on current standard MR imaging sequences. Therefore, PADRE is useful for the localization of the MGN and LGN.

Disclosures: Tetsuya Yoneda—RELATED: Grant: Philips Healthcare.\* Comments: joint research; UNRELATED: Royalties: Philips Healthcare.\* Comments: development of SWI with phase enhancement. \*Money paid to the institution.

## REFERENCES

- Dai H, Mu KT, Qi JP, et al. **Assessment of lateral geniculate nucleus atrophy with 3T MR imaging and correlation with clinical stage of glaucoma.** *AJNR Am J Neuroradiol* 2011;32:1347–53
- O'Connor DH, Fukui MM, Pinski MA, et al. **Attention modulates responses in the human lateral geniculate nucleus.** *Nat Neurosci* 2002;5:1203–09
- Selemon LD, Begovic A. **Stereologic analysis of the lateral geniculate nucleus of the thalamus in normal and schizophrenic subjects.** *Psychiatry Res* 2007;151:1–10
- Hess RF, Thompson B, Gole G, et al. **Deficient responses from the lateral geniculate nucleus in humans with amblyopia.** *Eur J Neurosci* 2009;29:1064–70
- Gupta N, Greenberg G, de Tilly LN, et al. **Atrophy of the lateral geniculate nucleus in human glaucoma detected by magnetic resonance imaging.** *Br J Ophthalmol* 2009;93:56–60
- Li M, He HG, Shi W, et al. **Quantification of the human lateral geniculate nucleus in vivo using MR imaging based on morphometry: volume loss with age.** *AJNR Am J Neuroradiol* 2012;33:915–21
- Ide S, Kakeda S, Korogi Y, et al. **Delineation of optic radiation and stria of Gennari on high-resolution phase difference enhanced imaging.** *Acad Radiol* 2012;19:1283–89
- Kakeda S, Korogi Y, Yoneda T, et al. **A novel tract imaging technique of the brainstem using phase difference enhanced imaging: normal anatomy and initial experience in multiple system atrophy.** *Eur Radiol* 2011;21:2202–10
- Yoneda T. **Triple-layer appearance of human cerebral cortices on phase difference enhanced imaging using 3D principle of echo shifting with a train of observations (PRESTO) sequence.** In: *Proceedings of the Annual Meeting of the International Society for Magnetic Resonance in Medicine*, Honolulu, Hawaii. April 18–24, 2009
- Schaltenbrand G, Wahren W. **Microscopic series with fixed overlays for anatomic explanation.** In: Schaltenbrand G, Wahren W, eds. *Atlas for Stereotaxy of the Human Brain*. 2nd ed. Stuttgart: Thieme; 2005:51–55
- Naidich TP, Duvernoy HM, Delman BN, et al. **Internal architecture of the brain stem with key axial sections.** In: Naidich TP, Duvernoy HM, Delman BN, et al, eds. *Duvernoy's Atlas of the Human Brain Stem and Cerebellum: High-Field MRI, Surface Anatomy, Internal Structure, Vascularization and 3D Section Anatomy*. Vienna: Springer-Verlag; 2009:53–94
- Andrews TJ, Halpern SD, Purves D. **Correlated size variations in human visual cortex, lateral geniculate nucleus, and optic tract.** *J Neurosci* 1997;17:2859–68
- Winer JA. **The human medial geniculate body.** *Hear Res* 1984; 15:225–47
- Abduljalil AM, Schmalbrock P, Novak V, et al. **Enhanced gray and white matter contrast of phase susceptibility-weighted images in ultra-high-field magnetic resonance imaging.** *J Magn Reson Imaging* 2003;18:284–90
- Duyn JH, van Gelderen P, Li TQ, et al. **High-field MRI of brain cortical substructure based on signal phase.** *Proc Natl Acad Sci U S A* 2007;104:11796–801
- Marques JP, Maddage R, Mlynarik V, et al. **On the origin of the MR image phase contrast: an in vivo MR microscopy study of the rat brain at 14.1 T.** *Neuroimage* 2009;46:345–52
- Zhong K, Leupold J, von Elverfeldt D, et al. **The molecular basis for gray and white matter contrast in phase imaging.** *Neuroimage* 2008;40:1561–66
- He X, Yablonskiy DA. **Biophysical mechanisms of phase contrast in gradient echo MRI.** *Proc Natl Acad Sci U S A* 2009;106:13558–63
- Li W, Wu B, Avram AV, et al. **Magnetic susceptibility anisotropy of human brain in vivo and its molecular underpinnings.** *Neuroimage* 2012;59:2088–97
- Horton JC, Landau K, Maeder P, et al. **Magnetic resonance imaging of the human lateral geniculate body.** *Arch Neurol* 1990;47:1201–06
- Fujita N, Tanaka H, Takanashi M, et al. **Lateral geniculate nucleus: anatomic and functional identification by use of MR imaging.** *AJNR Am J Neuroradiol* 2001;22:1719–26
- Devlin JT, Sillery EL, Hall DA, et al. **Reliable identification of the auditory thalamus using multi-modal structural analyses.** *Neuroimage* 2006;30:1112–20

# Cortical Activation Through Passive-Motion Functional MRI

 A.F. Choudhri, R.M. Patel, A. Siddiqui, M.T. Whitehead, and J.W. Wheless

## ABSTRACT

**BACKGROUND AND PURPOSE:** Functional brain mapping is an important technique for neurosurgical planning, particularly for patients with tumors or epilepsy; however, mapping has traditionally involved invasive techniques. Existing noninvasive techniques require patient compliance and may not be suitable for young children. We performed a retrospective review of our experience with passive-motion functional MR imaging in anesthetized patients to determine the diagnostic yield of this technique.

**MATERIALS AND METHODS:** A retrospective review of patients undergoing passive-motion fMRI under general anesthesia at a single institution over a 2.5-year period was performed. Clinical records were evaluated to determine the indication for fMRI, the ability to detect cortical activation, and, if present, the location of cortical activation.

**RESULTS:** We identified 62 studies in 56 patients in this time period. The most common indication for fMRI was epilepsy/seizures. Passive-motion fMRI identified upper-extremity cortical activation in 105 of 119 (88%) limbs evaluated, of which 90 (86%) activations were in an orthotopic location. Lower-extremity cortical activation was identified in 86 of 118 (73%) limbs evaluated, of which 73 (85%) activations were in an orthotopic location.

**CONCLUSIONS:** Passive-motion fMRI was successful in identifying cortical activation in most of the patients. This tool can be implemented easily and can aid in surgical planning for children with tumors or candidates for epilepsy surgery, particularly those who may be too young to comply with existing noninvasive functional measures.

The criterion standard for presurgical brain mapping has typically been intraoperative cortical stimulation mapping and the Wada test.<sup>1-4</sup> Both methods are invasive procedures, and their efficacy and superiority over other mapping procedures have become less clear with advances in noninvasive brain-mapping techniques,<sup>4-12</sup> with some studies showing that these alternative methods are comparable to stand-alone and/or adjunct techniques.<sup>9-18</sup> Blood oxygen level–dependent functional MR imaging is an increasingly used imaging technique in the clinical setting. Since the early 1990s, it has been used to study brain function

in healthy individuals and particularly for surgical planning in patients with brain tumors or epilepsy.<sup>2,4,17,19-22</sup> This imaging technique maps areas of cortical activation via changes in blood flow to metabolically active brain regions during cortical activation, typically secondary to specific motor, language, and visual tasks. fMRI provides a number of benefits: it is noninvasive, it is a useful tool for presurgical evaluation for invasive procedures that involve high risk,<sup>2,4,17,19,20,23,24</sup> and it can also assess the current function of patients with brain lesions or previous brain surgery.<sup>20,25</sup> Clinically, it is performed as a task-based technique that requires the patient to cooperate and keep all other body movements to a minimum. Incomplete compliance limits the utility of this technology and introduces risk for spurious results. Compliance with the tasks and remaining still is a particular concern in young children and patients with developmental or acquired cognitive deficits.<sup>26,27</sup> Even children who can perform the task during training sessions may not be able to comply in the MR imaging scanner.<sup>27</sup>

A strategy that allows this information to be obtained from subjects who are unable to cooperate is to perform a similar fMRI task under sedation. fMRI of sedated patients performed with passive motion of the extremities has been successful in some

Received September 4, 2014; accepted after revision February 13, 2015.

From the Departments of Radiology (A.F.C., A.S., M.T.W.), Neurosurgery (A.F.C.), and Pediatrics (J.W.W.) and College of Medicine (R.M.P.), University of Tennessee Health Science Center, Memphis, Tennessee; Le Bonheur Neuroscience Institute (A.F.C., A.S., M.T.W., J.W.W.), Le Bonheur Children's Hospital, Memphis, Tennessee; and Department of Radiology (M.T.W.), Children's National Medical Center, Washington, DC.

Paper previously presented at: Annual Meeting of the American Society of Neuroradiology, April 25–30, 2015; Chicago, Illinois.

Please address correspondence to A.F. Choudhri, MD, Department of Radiology, Le Bonheur Children's Hospital, 848 Adams Ave, G216, Memphis, TN 38103; e-mail: achoudhri@uthsc.edu; @AsimChoudhriMD

<http://dx.doi.org/10.3174/ajnr.A4345>

reports.<sup>15,23,24,28,29</sup> The goal is to map the motor cortex while removing the need for task compliance and reducing or eliminating concerns for patient motion.<sup>23,24,28</sup> We performed a retrospective review of our institution's 2.5-year experience with passive-motion fMRI to assess the feasibility and reliability of this imaging technique.

## MATERIALS AND METHODS

This Health Insurance Portability and Accountability Act-compliant retrospective review was performed after institutional review board approval. We performed a retrospective chart review of all functional MR imaging scans performed at a single pediatric academic medical center over a consecutive 2.5-year period (August 2012 to December 2014), representing the first 2.5 years of a passive-motion fMRI program in which a particular acquisition technique and processing software were used.

### Functional MR Imaging

Functional MR imaging was performed on a 3T MR imaging scanner (HDxt; GE Healthcare, Milwaukee, Wisconsin) by using an 8-channel head coil. Blood oxygen level-dependent fMRI was acquired by using an echo-planar imaging sequence performed with a TR of 3000 ms. Eighty-three EPI acquisitions were performed for each functional paradigm for a scan time of 4 minutes 9 seconds. The initial 3 sets of images, acquired during the first 9 s, were discarded, and the subsequent 80 EPI acquisitions were analyzed. A block design was used for functional tasks, with 15-s alternations between the tasks and rest encompassing 5 TR intervals. For the passive-motion functional MR imaging, the neuroradiologist was in the scanner room and, during the acquisitions, performed passive motion of the hand/wrist or the foot/ankle of the patients. Passive motion was performed at a rate of approximately 1.5–2 Hz. Care was taken to isolate the induced movement only to the area of interest. During rest, the neuroradiologist maintained a stable grasp of the extremity under examination in an attempt to attenuate or eliminate somatosensory cortical activation.

All blood oxygen level-dependent functional MR images were acquired with conventional structural imaging, including a volumetric axially acquired fast-spoiled gradient-recalled sequence with 1-mm isotropic resolution and axially acquired diffusion tensor imaging with either 15 or 25 noncolinear directions of encoding.

Paradigm delivery, including timing cues for the neuroradiologist who performed passive motions, was controlled by using the Esys-fMRI system (Invivo, Pewaukee, Wisconsin). fMRI data were processed by using an FDA-approved software package (DynaSuite Neuro 3.0; Invivo) and using the clinical experience and judgment of the neuroradiologist to guide thresholding and coregistration.

All passive functional motions were performed by a fellowship-trained neuroradiologist (A.F.C., M.T.W., or A.S.). For passive motions, the examiner flexed and extended the patient's wrists and ankles. All images were processed and analyzed by 1 of 2 fellowship-trained neuroradiologists with an American Board of Radiology subspecialty certificate in neuroradiology

and with additional training and clinical experience with functional MR imaging (A.F.C. or M.T.W.). The functional maps were evaluated while overlaid on fast-spoiled gradient-recalled images.

Evaluation of the functional activation and localization for this retrospective review was performed by review of the clinical reports and images from the functional MR imaging studies. Images from all the studies were evaluated retrospectively by a neuroradiologist to confirm the presence or absence of structural abnormalities that may have been associated with absent or ectopic cortical activation.

### Sedation for fMRI

All sedation was supervised by pediatric anesthesiologists. The default sedation protocol involved general anesthesia with intravenous propofol administered at the lowest dose to keep the patient asleep after induction. Information regarding anesthesia, including the medications used for induction and maintenance, was recorded in the medical record.

### Statistical Analysis

Data were collected in a spreadsheet (Excel version 14.4.2; Microsoft, Redmond, Washington) and analyzed by using SPSS version 21 (IBM, Armonk, New York). Continuous variables were compared with a Student *t* test, and discrete variables were compared with the Fisher exact test. A *P* value of < .05 was considered significant.

## RESULTS

We identified 62 fMRI studies with passive motion performed on 56 anesthetized patients in the study time period (28 male, 28 female). The average ( $\pm$  standard deviation) age at the time of study was  $8.80 \pm 7.47$  years (range, 0.54 to 41.85 years; median, 7.6 years). No MR imaging-related complications were identified.

Of these 56 patients, 53 (95%) underwent passive-motion fMRI because of seizures, and 3 had additional indications for passive-motion fMRI being a recurrent supratentorial ependymoma without report of seizure ( $n = 1$ ), gait abnormality ( $n = 1$ ), and worsening headache ( $n = 1$ ). Of the 53 patients with seizure, 5 had tuberous sclerosis complex, 4 had a history of a tumor, 1 had hemimegalencephaly, 1 had Rasmussen encephalitis, and 1 had febrile infection-related epilepsy syndrome. Of the 4 patients with seizure and history of a tumor, 3 passive-motion fMRI scans were performed to evaluate postresection seizures. One patient had a new-onset seizure and a left medial frontal tumor, and fMRI was performed for surgical planning.

Passive motion of the upper extremities was performed in 61 (98%) of the studies. Passive motion of the lower extremities was performed in 60 (97%) of the studies; in 47 (78%) of them, the lower-extremity passive movement was performed simultaneously for each side, and in 13 (22%) of them, the lower-extremity passive motor movement was performed simultaneously.

Of the 119 iterations of upper-extremity passive motion, cortical activation was identified reliably 105 times (88%;  $P = .33$  versus upper extremity). Of these activations, 90 (86%) were in an

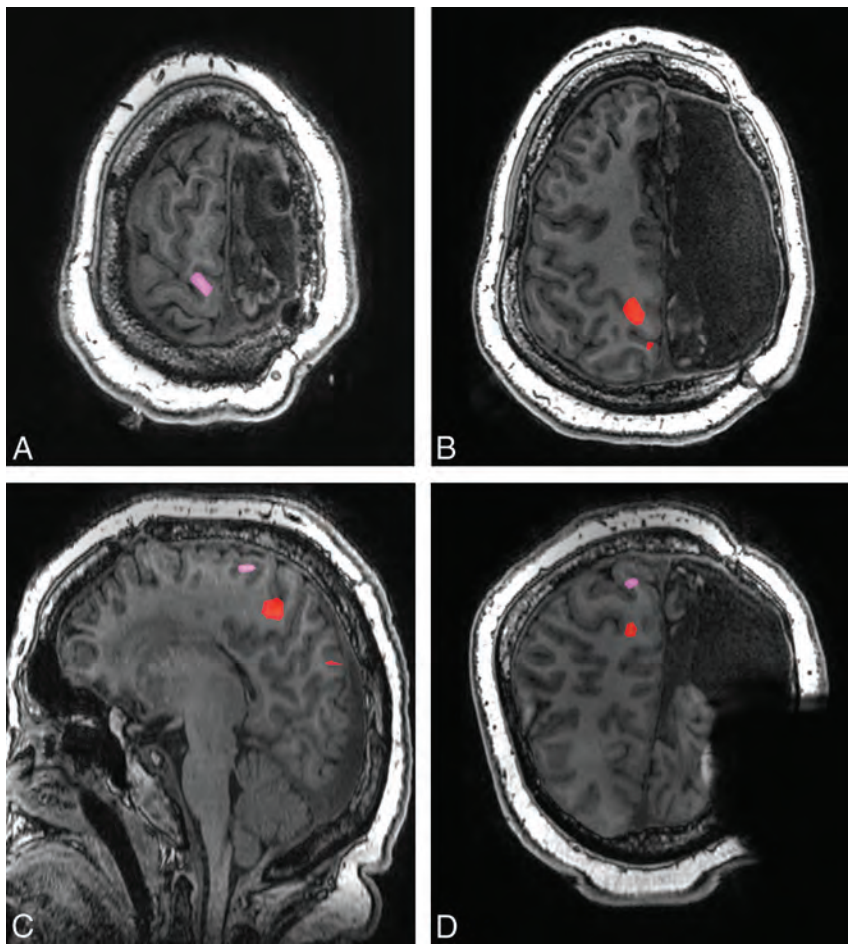


**FIG 1.** A, Axial fast-spoiled gradient-recalled image with overlay of cortical activation maps for passive movement of the left lower extremity (pink) in a 16-year-old girl with a history of left-sided functional hemispherectomy shows orthotopic cortical activation in the posterior/superior aspect of the right paracentral lobule. B, Activation maps for passive movement of the right lower extremity (red) are in a more posterior and inferior location in the right (ipsilateral) hemisphere. Parasagittal (C) and coronal-oblique (D) images show the relationship between the areas of activation for both lower extremities.

orthotopic location in the midportion of the precentral gyrus of the contralateral hemisphere. Three (2.5%) iterations were in an ectopic location in the contralateral hemisphere, and 9 (7.6%) were in an ectopic location in the ipsilateral hemisphere. Of the 119 iterations, there were no significant cortical activations in 14 (11.8%).

Of the 118 iterations of lower-extremity passive motion, cortical activation was identified 86 (73%) times. Of these, 82 (94.5%) were in an orthotopic location in the superior portion of the precentral gyrus of the contralateral hemisphere, 1 (1.2%) was in an ectopic location in the contralateral hemisphere, and 3 (3.5%) were in an ectopic location in the ipsilateral hemisphere (Fig 1). Of the 13 iterations of bilateral lower-extremity passive motion, cortical activation was identified 9 (69.2%) times in an orthotopic location in the superior portion of the precentral gyrus bilaterally. In the other 4 (30.8%) iterations, there was no significant cortical activation. Of the 105 iterations in which lower-extremity passive motion was performed separately, there were 66 (62.9%) times at which cortical activation was seen in an orthotopic location. One patient underwent passive motion for simultaneous evaluation

of both lower extremities and isolated evaluation of the right lower extremity, with concordant identification of right lower-extremity cortical activation on the 2 paradigms. There were 4 (3.8%) activations in ectopic locations. In the other 28 (23.7%) of 118 iterations in which lower-extremity passive motion was performed separately, there was no significant cortical activation. Of the 118 total iterations of lower-extremity motion, there was no significant cortical activation in 32 (27.1%).

The average age of the patients in whom no cortical activation was demonstrated in at least one upper extremity was  $6.2 \pm 2.8$  years (range, 1.94–11.27 years; median, 6.51 years [ $n = 11$ ]), and the average age was  $9.4 \pm 8.0$  years (range, 0.54–41.85 years; median, 8.11 years [ $n = 51$ ]) for patients in whom the scans revealed bilateral cortical activation ( $P = .21$ ). The average age of the patients in whom no cortical activation was demonstrated in at least one lower extremity was  $8.11 \pm 6.68$  years (range, 0.65–41.85 years; median, 6.49 years [ $n = 24$ ]), and it was  $9.2 \pm 6.7$  years (range, 0.54–30.4 years; median, 8.49 years [ $n = 38$ ]) for patients in whom there was bilateral lower-extremity cortical activation ( $P = .56$ ).

There were 4 instances in which cortical activation was identified in the left upper extremity, but there was no significant cortical activation in the right

upper extremity. In all 4 cases, there were parenchymal abnormalities in the left hemisphere in the expected location of right upper-extremity motion. These abnormalities included left-sided Rasmussen encephalitis, previous left-greater-than-right watershed ischemic injury, bilateral periventricular leukomalacia and porencephalic cysts, and tuberous sclerosis complex with left precentral gyrus dysplasia.

#### **Patients with 2 Passive-Motion fMRI Scans**

For 6 patients, passive-motion fMRI was performed on 2 separate occasions; 2 of these patients had tuberous sclerosis complex, 2 had refractory seizures, 1 had febrile infection-related epilepsy syndrome, and 1 had hemimegalencephaly and a history of functional hemispherectomy.

The scans were performed on the first patient with tuberous sclerosis complex 5 months apart, at 1.9 and 2.4 years of age. The initial study showed an orthotopic location for the right lower extremity, the left upper extremity, and the left lower extremity but did not identify right upper-extremity motor

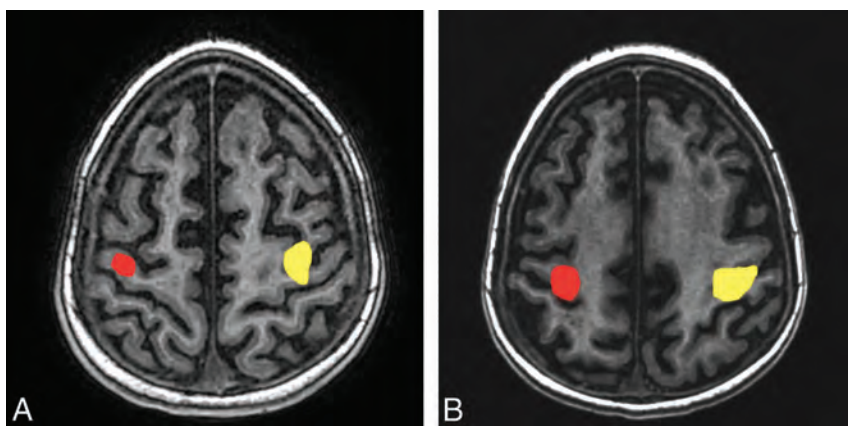


**FIG 2.** A, Axial fast-spoiled gradient-recalled image in a 1.4-year-old boy 6 weeks after initial presentation for febrile infection-related epilepsy syndrome. There was orthotopic localization of cortical activation from right (yellow) and left (red) upper-extremity passive movement. B, Axial fast-spoiled gradient-recalled image of the same patient at 1.6 years of age shows reidentification of orthotopic cortical activation from right (yellow) and left (red) upper-extremity passive movement in the setting of progressive parenchymal volume loss.

activation. The follow-up study revealed orthotopic motor cortex activation of all 4 extremities.

The scans of the second patient with tuberous sclerosis complex were performed at 0.5 and 1.5 years of age, before and after topectomy for an epileptogenic tuber. The initial and follow-up studies revealed orthotopic localization of all 4 extremities.

Two scans were performed on the patient with febrile infection-related epilepsy syndrome at 3-month intervals (at ages 1.4 and 1.6 years), during which time there was a progression of global parenchymal volume loss (Fig 2). The initial study was performed 6 weeks after the onset of symptoms. The initial and follow-up studies revealed orthotopic localization of all 4 extremities.

The patient with left-sided hemimegalencephaly had passive-motion fMRI scans at 1.7 and 3.1 years of age, and both scans showed orthotopic activation for the left upper and lower extremities and ipsilateral ectopic activation for the right upper and lower extremities.

One patient with refractory seizures had studies performed at 11.3 and 12.1 years of age. The first study showed orthotopic left lower-extremity activation and no significant activation on the other extremities. The second study showed orthotopic activation for the right and left upper and lower extremities.

The patient with refractory seizures had studies performed at 7.6 and 9.3 years of age, and both studies showed orthotopic activation for the right and left upper and lower extremities.

### Anesthesia

Of 62 scans, 57 were performed with propofol as the anesthetic agent for induction and maintenance. Propofol and sevoflurane were used in 4 scans. One scan was performed with only sevoflurane. Cortical activation was identified in 179 of 217 (82.4%) limbs evaluated in patients who received propofol anesthesia. Cortical activation was identified in 12 of 20 (60%) limbs of the patients who received either propofol and sevoflurane or sevoflurane only ( $P = .46$  versus propofol alone).

### Surgical Follow-Up

Twelve patients underwent 15 surgical procedures after the passive-motion fMRI, including 3 tumor resections, 3 tuberectomies for tuberous sclerosis complex, 3 temporal lobectomies, 3 corpus callosotomies, 2 topectomies, and 1 frontal lobectomy. Two patients had more than 1 surgery. One patient with seizures that arose from right frontal encephalomalacia underwent a topectomy. There was incomplete seizure control, and after a second passive-motion fMRI, the patient underwent a right frontal lobectomy, which resulted in the patient being seizure free at the 2-month follow-up. One patient with tuberous sclerosis complex underwent 3 separate topectomies and had an fMRI before a right angular gyrus tuber resection, which resulted in 3 months of being seizure free.

After a second passive-motion fMRI, the patient underwent a left frontopolar tuber resection, which resulted in 6 months of being seizure free. The patient subsequently underwent a left superior parietal lobule tuber resection and was seizure free for 6 months.

### DISCUSSION

Functional MR imaging has been shown to be useful in presurgical planning because of its accuracy in localizing areas of cortical activation. It has aided neurosurgical planning by identifying eloquent cortex and its relationship to lesions that require resection.<sup>2,4,17,19,20,23,24</sup> Early reports on passive-motion fMRI suggested using the known benefits of fMRI in uncooperative or very young patients.<sup>23,24</sup> Additional studies have shown the activation with passive movement to correspond to the location of volitional movement.<sup>30</sup> To our knowledge, this study involves the largest population in the existing literature on this subject. In addition, we demonstrated the ability to use passive-motion fMRI 13 times in patients younger than 2 years, the youngest of whom was 6 months of age.

One difference between passive and awake techniques is that awake patients can often trigger robust responses in not only the motor strip corresponding to upper- and lower-extremity movements but also the supplementary motor area. Similar activation in the supplementary motor area has been reported with active versus passive range-of-motion studies by using PET scans.<sup>31,32</sup> Additional studies may include facial stimulation in the passive range-of-motion paradigm. An absence of cortical activation in right upper-extremity passive motion was seen in patients with a younger mean age than those in whom cortical activation was identified, suggesting that a young age could limit the success of passive-motion mapping. However, on an individual patient basis, passive motion was successful in a patient as young as 6 months old.

The most common fMRI indication in our group was intractable epilepsy in children who were being evaluated for all treat-

ment options, including epilepsy surgery. The identification of motor cortex helps in the planning of any surgical procedure and when discussing the risks and benefits of surgery (combined with all of the other diagnostic test data, such as video-EEG, magnetoencephalography, transcranial magnetic stimulation, etc) with the parents. This information would help the clinicians and the family make the best decision about where surgery was ranked in the hierarchy of treatment options for their child.

One patient with a history of left functional hemispherectomy performed at 8 years of age for seizures related to posttraumatic encephalomalacia (Fig 1) showed evidence of remapping in the remaining hemisphere on an fMRI performed at 16 years of age. Passive motion of the right lower extremity revealed cortical activation within the right hemisphere. Similar results have been seen before. In a study in which passive-motion fMRI was performed on 8 patients who had undergone hemispherectomy, 2 patients were found to have undergone cortical remapping.<sup>33</sup> Passive movement of the hand showed cortical activation in the ipsilateral hemisphere, a location similar to that for the contralateral hand.<sup>33</sup>

Imaging of another patient with a history of febrile infection-related epilepsy syndrome (Fig 2) revealed orthotopic cortical activation of all 4 extremities 6 weeks after initial presentation. Although follow-up imaging at 1.6 years of age showed significant cerebral atrophy, there was orthotopic localization of all 4 extremities. This case provides an example of fMRI demonstrating consistently accurate results despite progressive destruction of brain parenchyma. The utility of fMRI in structurally abnormal brains has also been discussed elsewhere.<sup>20,25</sup> We did not have any patients who underwent passive-motion fMRI and later underwent awake fMRI, so we could not evaluate the concordance of the findings. There was a nonstatistical trend toward lower success in patients who did not have isolated propofol as the means of anesthesia, which corresponds with previous reports of sevoflurane being associated with lower success on passive-motion fMRI tasks.<sup>34</sup> Passive motion of the lower extremities was successful less often than that of the upper extremities; however, this difference was not statistically significant.

Limitations in this study include our inability to confirm that the cortical activation was truly related to the specific function tested. Work has been done to compare invasive procedures such as intraoperative cortical stimulation mapping and the Wada test with other noninvasive modalities, including fMRI, magnetoencephalography, and transcranial magnetic stimulation.<sup>19,35-38</sup> Other authors have used fMRI as the template to guide confirmatory intraoperative mapping<sup>2,9-11,17,39</sup>; however, this was not feasible in this retrospective study. Because fMRI postprocessing is a computationally intensive process, results on the success of a paradigm are not known until after the anesthesia-based procedure is complete, which prevents the duplication of paradigms with spurious results or without appreciable cortical activation. In addition, it is not currently possible to separate motor cortical activation from sensory activation. Although this may not be a limiting factor for orthotopic perirolandic cortical activation, in which

posterior extension is felt to be related to sensory activation, ectopic results may be more difficult to interpret. Passive facial motion and/or sensory paradigms have been measured with limited success in other studies; however, it was not evaluated in our patient population.<sup>24</sup> Manual passive motion was performed in this study, but other studies have shown a pneumatically driven device to perform more reproducible passive movements.<sup>24,40</sup>

Blood oxygen level–dependent fMRI has some benefits compared with the criterion standard, intraoperative cortical stimulation; it is noninvasive, it has superior spatial resolution, and it is not limited by the extent of craniotomy exposure.<sup>2,41</sup> Passive-motion fMRI does share one similarity with intraoperative cortical stimulation in that results may be affected by depth of sedation.<sup>17</sup> Compared with other noninvasive techniques such as electroencephalography and magnetoencephalography, blood oxygen level–dependent fMRI has a lower temporal resolution but a higher spatial resolution. Blood oxygen level–dependent fMRI depends on blood flow, and hemodynamic changes that follow neuronal activation are not identical in all patients. In addition, metabolically active brain tumors may lead to the incorrect impression of absence of cortical activation because of blood flow being redirected by the high oxygen demand of the tumor, a process known as neurovascular uncoupling.<sup>2,42,43</sup> Studies have shown, however, that blood oxygen level–dependent fMRI is still a relatively reliable tool for cortical mapping, even in patients with brain tumors.<sup>2,4,17,19-21</sup>

Our study shows that passive-motion fMRI can localize upper-extremity motor cortex reliably and in most cases can identify lower-extremity motor cortex. This technique can be applied at any institution that performs task-based fMRI. Awareness of this technique can enable functional mapping to help guide treatment planning in young children with tumors and lesion-based epilepsy. In fact, fMRI performed without adjunct intraoperative cortical stimulation in awake patients has already been shown to enable neurosurgeons to be more aggressive in resection and to shorten time in the operating room,<sup>21</sup> and no long-term neurologic deficits were observed in a study that involved 22 patients in whom fMRI was performed in adjunct with intraoperative cortical stimulation; in that study, there was an extremely high level of concordance between fMRI and intraoperative cortical stimulation mapping.<sup>44</sup>

## CONCLUSIONS

Passive-motion fMRI is an effective tool for noninvasive motor mapping in patients who are too young or otherwise unable to comply with traditional noninvasive mapping, possibly providing a safer alternative (or adjunct) to intraoperative monitoring.

## REFERENCES

1. Berger MS, Ojemann GA. **Intraoperative brain mapping techniques in neuro-oncology.** *Stereotact Funct Neurosurg* 1992;58:153–61 CrossRef Medline
2. Pillai J, Zaca D, Choudhri A. **Clinical impact of integrated physiologic brain tumor imaging.** *Technol Cancer Res Treat* 2010;9:359–80 CrossRef Medline
3. Wada J, Rasmussen T. **Intracarotid injection of sodium amytal for**

- the lateralization of cerebral speech dominance. *J Neurosurg* 2007; 106:1117–33 CrossRef Medline
4. Papanicolaou AC, Rezaie R, Narayana S, et al. Is it time to replace the Wada test and put awake craniotomy to sleep? *Epilepsia* 2014;55: 629–32 CrossRef Medline
  5. Bonelli SB, Powell RH, Yogarajah M, et al. Imaging memory in temporal lobe epilepsy: predicting the effects of temporal lobe resection. *Brain* 2010;133:1186–99 CrossRef Medline
  6. Binder JR, Swanson SJ, Hammeke TA, et al. Determination of language dominance using functional MRI: a comparison with the Wada test. *Neurology* 1996;46:978–84 CrossRef Medline
  7. Binder JR, Sabsevitz DS, Swanson SJ, et al. Use of preoperative functional MRI to predict verbal memory decline after temporal lobe epilepsy surgery. *Epilepsia* 2008;49:1377–94 CrossRef Medline
  8. Cohen-Gadol AA, Westerveld M, Alvarez-Carilles J, et al. Intracarotid amytal memory test and hippocampal magnetic resonance imaging volumetry: validity of the Wada test as an indicator of hippocampal integrity among candidates for epilepsy surgery. *J Neurosurg* 2004;101:926–31 CrossRef Medline
  9. Yetkin FZ, Hammeke TA, Swanson SJ, et al. A comparison of functional MR activation patterns during silent and audible language tasks. *AJNR Am J Neuroradiol* 1995;16:1087–92 Medline
  10. Roux FE, Boulanouar K, Ranjeva JP, et al. Cortical intraoperative stimulation in brain tumors as a tool to evaluate spatial data from motor functional MRI. *Invest Radiol* 1999;34:225–29 CrossRef Medline
  11. Roux FE, Boulanouar K, Ranjeva JP, et al. Usefulness of motor functional MRI correlated to cortical mapping in Rolandic low-grade astrocytomas. *Acta Neurochir (Wien)* 1999;141:71–79 CrossRef Medline
  12. Hirsch J, Ruge MI, Kim KH, et al. An integrated functional magnetic resonance imaging procedure for preoperative mapping of cortical areas associated with tactile, motor, language, and visual functions. *Neurosurgery* 2000;47:711–21; discussion 721–22 CrossRef Medline
  13. Binder JR, Swanson SJ, Sabsevitz DS, et al. A comparison of two fMRI methods for predicting verbal memory decline after left temporal lobectomy: language lateralization versus hippocampal activation asymmetry. *Epilepsia* 2010;51:618–26 CrossRef Medline
  14. Genetti M, Tyrand R, Grouiller F, et al. Comparison of high gamma electrocorticography and fMRI with electrocortical stimulation for localization of somatosensory and language cortex. *Clin Neurophysiol* 2015;126:121–30 CrossRef Medline
  15. Rosazza C, Aquino D, D'Incerti L, et al. Preoperative mapping of the sensorimotor cortex: comparative assessment of task-based and resting-state FMRI. *PLoS One* 2014;9:e98860 CrossRef Medline
  16. Breier JI, Simos PG, Zouridakis G, et al. Language dominance determined by magnetic source imaging: a comparison with the Wada procedure. *Neurology* 1999;53:938–45 CrossRef Medline
  17. Xie J, Chen XZ, Jiang T, et al. Preoperative blood oxygen level-dependent functional magnetic resonance imaging in patients with gliomas involving the motor cortical areas. *Chin Med J* 2008;121: 631–35 Medline
  18. Hanakawa T, Ikeda A, Sadato N, et al. Functional mapping of human medial frontal motor areas: the combined use of functional magnetic resonance imaging and cortical stimulation. *Exp Brain Res* 2001;138:403–09 CrossRef Medline
  19. Choudhri AF, Narayana S, Rezaie R, et al. Same day tri-modality functional brain mapping prior to resection of a lesion involving eloquent cortex: technical feasibility. *Neuroradiol J* 2013;26:548–54 CrossRef Medline
  20. Chaudhary K, Kumaran SS, Chandra SP, et al. Mapping of cognitive functions in chronic intractable epilepsy: role of fMRI. *Indian J Radiol Imaging* 2014;24:51–56 CrossRef Medline
  21. Petrella JR, Shah LM, Harris KM, et al. Preoperative functional MR imaging localization of language and motor areas: effect on therapeutic decision making in patients with potentially resectable brain tumors. *Radiology* 2006;240:793–802 CrossRef Medline
  22. Peck KK, Bradbury M, Petrovich N, et al. Presurgical evaluation of language using functional magnetic resonance imaging in brain tumor patients with previous surgery. *Neurosurgery* 2009;64:644–53; discussion 652–53 CrossRef Medline
  23. Li W, Wait SD, Ogg RJ, et al. Functional magnetic resonance imaging of the visual cortex performed in children under sedation to assist in presurgical planning. *J Neurosurg Pediatr* 2013;11:543–46 CrossRef Medline
  24. Ogg RJ, Laningham FH, Clarke D, et al. Passive range of motion functional magnetic resonance imaging localizing sensorimotor cortex in sedated children. *J Neurosurg Pediatr* 2009;4:317–22 CrossRef Medline
  25. Bigler ED. Magnetic resonance imaging in the evaluation of cognitive function. *Pediatr Blood Cancer* 2014;61:1724–28 CrossRef Medline
  26. Yerys BE, Jankowski KF, Shook D, et al. The fMRI success rate of children and adolescents: typical development, epilepsy, attention deficit/hyperactivity disorder, and autism spectrum disorders. *Hum Brain Mapp* 2009;30:3426–35 CrossRef Medline
  27. Rajagopal A, Byars A, Schapiro M, et al. Success rates for functional MR imaging in children. *AJNR Am J Neuroradiol* 2014;35:2319–25 CrossRef Medline
  28. Guzzetta A, Staudt M, Petacchi E, et al. Brain representation of active and passive hand movements in children. *Pediatr Res* 2007;61: 485–90 CrossRef Medline
  29. Weiller C, Jüptner M, Fellows S, et al. Brain representation of active and passive movements. *Neuroimage* 1996;4:105–10 CrossRef Medline
  30. Kocak M, Ulmer JL, Sahin Ugurel M, et al. Motor homunculus: passive mapping in healthy volunteers by using functional MR imaging—initial results. *Radiology* 2009;251:485–92 CrossRef Medline
  31. Mima T, Sadato N, Yazawa S, et al. Brain structures related to active and passive finger movements in man. *Brain* 1999;122:1989–97 CrossRef Medline
  32. Lee CC, Jack CR Jr, Riederer SJ. Mapping of the central sulcus with functional MR: active versus passive activation tasks. *AJNR Am J Neuroradiol* 1998;19:847–52 Medline
  33. Holloway V, Gadian DG, Vargha-Khadem F, et al. The reorganization of sensorimotor function in children after hemispherectomy: a functional MRI and somatosensory evoked potential study. *Brain* 2000;123:2432–44 CrossRef Medline
  34. Bernal B, Grossman S, Gonzalez R, et al. FMRI under sedation: what is the best choice in children? *J Clin Med Res* 2012;4:363–70 CrossRef Medline
  35. Picht T, Schmidt S, Brandt S, et al. Preoperative functional mapping for Rolandic brain tumor surgery: comparison of navigated transcranial magnetic stimulation to direct cortical stimulation. *Neurosurgery* 2011;69:581–88; discussion 588 CrossRef Medline
  36. Krieg SM, Sabih J, Bulbasova L, et al. Preoperative motor mapping by navigated transcranial magnetic brain stimulation improves outcome for motor eloquent lesions. *Neuro-Oncology* 2014;16: 1274–82 CrossRef Medline
  37. Krieg SM, Sollmann N, Hauck T, et al. Repeated mapping of cortical language sites by preoperative navigated transcranial magnetic stimulation compared to repeated intraoperative DCS mapping in awake craniotomy. *BMC Neurosci* 2014;15:20 CrossRef Medline
  38. Narayana S, Rezaie R, McAfee SS, et al. Assessing motor function in young children with transcranial magnetic stimulation. *Pediatr Neurol* 2015;52:94–103 CrossRef Medline
  39. Meinzer M, Lindenberg R, Darkow R, et al. Transcranial direct current stimulation and simultaneous functional magnetic resonance imaging. *J Vis Exp* 2014;(86) CrossRef Medline
  40. Shriver S, Knierim KE, O'Shea JP, et al. Pneumatically driven finger movement: a novel passive functional MR imaging technique for presurgical motor and sensory mapping. *AJNR Am J Neuroradiol* 2013;34:E5–7 CrossRef Medline

41. Krings T, Schreckenberger M, Rohde V, et al. **Functional MRI and 18F FDG-positron emission tomography for presurgical planning: comparison with electrical cortical stimulation.** *Acta Neurochir (Wien)* 2002;144:889–99; discussion 899 CrossRef Medline
42. Holodny AI, Schulder M, Liu WC, et al. **The effect of brain tumors on BOLD functional MR imaging activation in the adjacent motor cortex: implications for image-guided neurosurgery.** *AJNR Am J Neuroradiol* 2000;21:1415–22 Medline
43. Pillai JJ, Mikulis DJ. **Cerebrovascular reactivity mapping: an evolving standard for clinical functional imaging.** *AJNR Am J Neuroradiol* 2015;36:7–13 CrossRef Medline
44. Roessler K, Donat M, Lanzenberger R, et al. **Evaluation of preoperative high magnetic field motor functional MRI (3 Tesla) in glioma patients by navigated electrocortical stimulation and postoperative outcome.** *J Neurol Neurosurg Psychiatry* 2005;76:1152–57 CrossRef Medline

# Complications in Stent-Assisted Endovascular Therapy of Ruptured Intracranial Aneurysms and Relevance to Antiplatelet Administration: A Systematic Review

C.-W. Ryu, S. Park, H.S. Shin, and J.S. Koh



## ABSTRACT

**BACKGROUND AND PURPOSE:** Despite the increasing use of stent-assisted coiling for ruptured intracranial aneurysms, there is little consensus regarding the appropriate antiplatelet administration for this. The objectives of this systematic review were to provide an overview of complications and their association with the method of antiplatelet administration in stent-assisted coiling for ruptured intracranial aneurysms.

**MATERIALS AND METHODS:** A comprehensive search of the literature in the data bases was conducted to identify studies reporting complications of stent-assisted coiling for ruptured intracranial aneurysms. The pooled event rate of preprocedural thromboembolisms, hemorrhages, and mortality was estimated from the selected studies. Subgroup analyses were performed by the method of antiplatelet administration (pre-, postprocedural, and modified). Meta-analysis was conducted to compare periprocedural complications and mortality between ruptured intracranial aneurysms and unruptured intracranial aneurysms.

**RESULTS:** Of the 8476 studies identified, 33 with 1090 patients were included. The event rates of thromboembolism and intra- and postprocedural hemorrhage were 11.2% (95% CI, 9.2%–13.6%), 5.4% (95% CI, 4.1%–7.2%), and 3.6% (95% CI, 2.6%–5.1%), respectively. Subgroup analyses of thromboembolism showed a statistically significant difference between groups ( $P < .05$ ). In the preprocedural and modified antiplatelet groups, the risk for thromboembolism in stent-assisted coiling for ruptured intracranial aneurysm was not significantly different from that for unruptured intracranial aneurysm, though this risk of the postprocedural antiplatelet group was significantly higher in ruptured intracranial aneurysms than in unruptured intracranial aneurysms.

**CONCLUSIONS:** On the basis of current evidence, complications of stent-assisted coiling for ruptured intracranial aneurysm may be affected by the method of antiplatelet administration.

**ABBREVIATIONS:** RIA = ruptured intracranial aneurysm; RR = risk ratio; TEC = thromboembolic complication; UIA = unruptured intracranial aneurysm

Aneurysmal neck remodeling with stents has recently emerged as an effective treatment option. This method is beneficial for treating aneurysms with wide necks or for situations in which coils unexpectedly herniate into the parent vessel, requiring rescue with a device that can reconstrain the coil within the lesion.<sup>1</sup> Currently, various stents specialized for aneurysmal neck remodeling are used during endovascular treatment of intracranial an-

eurysms. However, physicians are often reluctant to apply stents to acutely ruptured aneurysms due to the necessity of antiplatelet medications. During implantation of stents within an intracranial artery, antiplatelet agents should be administered and maintained postoperatively to prevent in-stent thrombosis and subsequent ischemic events.<sup>2</sup> In the setting of acutely ruptured aneurysms, antiplatelet medications may lead to complications such as intraprocedural rebleeding, the need for a ventriculostomy, co-occurrence of an intraparenchymal hematoma, and a high likelihood of future invasive procedures.<sup>3-7</sup>

Despite the chance of complications, administration of antiplatelet agents is an important element of management when using an intracranial stent, regardless of the presence of an acute aneurysm rupture. The type and/or method of antiplatelet agent might affect the periprocedural complication rate of endovascular aneurysm treatment.<sup>8,9</sup> Despite many previous studies of stent-assisted aneurysm management, no published recommendations

Received December 14, 2014; accepted after revision February 11, 2015.

From the Departments of Radiology (C.-W.R., S.P.) and Neurosurgery (H.S.S., J.S.K.), Kyung Hee University Hospital at Gangdong, Kyung Hee University School of Medicine; Seoul, South Korea.

Please address correspondence to Chang-Woo Ryu, MD, Department of Radiology, Kyung Hee University Hospital at Gangdong, 892 Dongnam-ro, Gangdong-gu, Seoul, 134-727, South Korea; e-mail: md.cwryu@gmail.com



Indicates article with supplemental on-line table.

Evidence-Based Medicine Level 1.

<http://dx.doi.org/10.3174/ajnr.A4365>

or large randomized clinical trials provide a consensus as to the appropriate method of antiplatelet medication in stent-assisted endovascular treatment for ruptured intracranial aneurysms (RIAs). The medication method usually varied depending on the institution or the rationales of clinicians in most published case series. Some review articles suggested a higher risk of complications in endovascular therapy for acutely ruptured aneurysms.<sup>3,10,11</sup> However, these reviews did not analyze independent factors affecting the risk of complications in stent-assisted coiling for RIA, including the application of antiplatelet agents.

The purposes of this systematic review were to calculate the accumulated complication risk during stent-assisted coiling for RIA and to assess whether the risk of complications would be affected by the method of antiplatelet administration. This information will guide selection of safer antiplatelet administration for stent-assisted coiling of RIA.

## MATERIALS AND METHODS

### Search Strategy

We searched the PubMed, EMBASE, and Cochrane data bases from January 2000 to November 2014 to find all studies involving stent-assisted coiling for acute RIA. The following key words and alternative terms analogous to these were used for searching relevant combinations by using the Boolean operators OR and AND: “Intracranial Aneurysm,” “Subarachnoid Hemorrhage,” “Endovascular Procedures,” “Stents,” and “Embolization, Therapeutic.” In addition, the names of merchandized stent devices, such as “Neuroform,” “Enterprise,” “Leo+ stent” and “Solitaire” were used as text words to extract relevant studies. We also searched the references of all included articles for potentially relevant trials. The search was restricted to human studies in English.

Two reviewers (C.-W.R., S.P.) independently evaluated the articles in the librarian’s primary list and selected any articles that fulfilled the inclusion criteria as follows: 1) reported >5 cases of RIA treated with stent-assisted coiling; 2) were published as full articles, including clinical trials, retrospective or prospective case series, or retrospective observational studies; 3) had well-described protocols for endovascular treatment of RIA, including a precise report on each antiplatelet regimen and endovascular device; and 4) accurately described periprocedural complications, procedure-induced mortality, and/or mortality within 30 days.

When the same cases were duplicated in multiple publications, data were extracted from the publication that provided the most comprehensive information. Reports including only dissecting aneurysms and/or blood blister-like aneurysms were excluded. A PRISMA flow diagram was used to show the decision-making process regarding the studies.

### Data Extraction

Basic characteristics of articles including publication type (prospective or retrospective, registry, or randomized trials), number of subjects, and publication year were extracted from each article. We extracted data relating to characteristics of enrolling patients, such as the total number of patients with RIA and unruptured intracranial aneurysm (UIA) and the initial clinical status, which

was presented as Hunt and Hess grade or World Federation of Neurological Surgeons SAH grade.

We collected information about the method of administration and regimen of antiplatelets and administration of anticoagulation agents and procedural complications, including periprocedural thromboembolic complications (TECs), intraprocedural hemorrhage, postprocedural hemorrhage, clinical outcome, and periprocedural mortality (within 30 days or discharge).

For studies that did not provide the prevalence of complications in RIAs separately from those in UIAs, we e-mailed the author to obtain this information, which is included here as data.

### Statistical Analysis

**Pooled Event Rate of Complications.** The pooled event rate of each periprocedural complication, morbidity, and mortality was estimated with a random-effects-weighting meta-analysis. Because the definition of “morbidity” varied in each study, it was defined as mRS 3–5 or Glasgow Outcome Score 2–3 at discharge or follow-up of  $\geq 3$  months. The corresponding 95% CIs for single proportions were determined with the binomial theorem. Heterogeneity across studies in the meta-analysis was assessed by using the  $I^2$  test, in which  $>40\%$  is considered substantial heterogeneity. Sources of heterogeneity were appraised by subgroup stratification analysis based on the method of antiplatelet therapy. Between-group heterogeneity values were calculated to assess the variance of the distribution of the true effect sizes among subgroups, and a  $P$  value of  $< .05$  was considered statistically significant.

**Risk Ratio of Periprocedural Complications of Stent-Assisted Coiling in RIA Relative to UIA.** To evaluate the difference in complication rates of stent-assisted coiling between RIA and UIA, we selected studies containing data from both RIAs and UIAs from studies including previous event-rate analyses. Studies containing  $<10$  cases in each group or studies in which antiplatelets were administered after the procedure in stent-assisted coiling for UIA were excluded from the review.

Meta-analysis was conducted to compare periprocedural complications and procedure-induced mortality between RIA and UIA groups. Meta-analysis was performed by using Review Manager (Version 5.3; <http://review-manager.software.informer.com/5.3/>). Complications and mortality were reported with a risk ratio (RR) and forest plot by using Mantel Haenszel random-effects models. Heterogeneity across studies in the meta-analysis was assessed by using the  $I^2$  test. Subgroup analyses also were performed by the method of antiplatelet administration.

## RESULTS

### Study Characteristics

A total of 8476 studies were identified during the initial search. Of these, 33 studies with 1090 participants were pertinent.<sup>7,9,12-42</sup> Figure 1 is the flow diagram summarizing the literature search results. There were no randomized clinical trials in the selected studies. Three studies were prospective registry studies, and 30 were retrospective observational studies. Nineteen studies included subjects who received stent-assisted coiling for both UIA

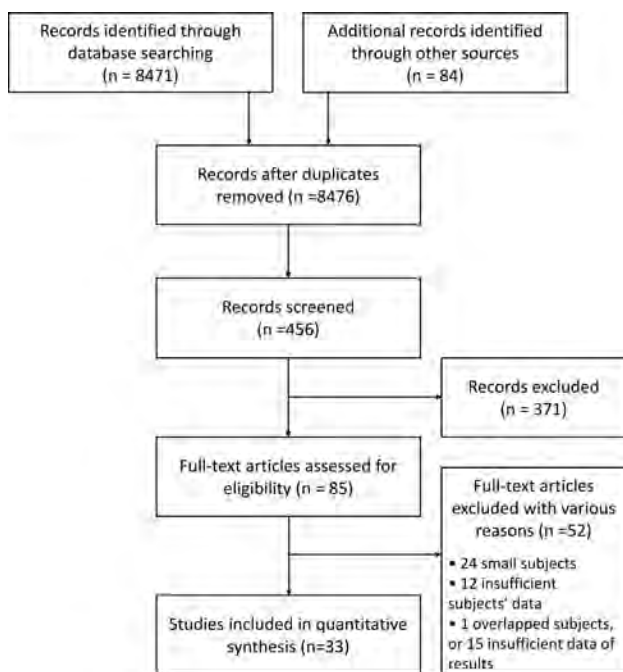


**FIG 1.** PRISMA flow diagram summarizing the search and selection of articles.

and RIA, while 14 studies included only RIA cases (On-line Table).

### Characteristics of Cohorts, Antiplatelet Method, and Endovascular Procedures

Initial clinical status could be extracted from 726 patients in 22 studies. Five hundred fifty-one patients (75.9%) had good initial clinical grades (Hunt and Hess or World Federation of Neurological Surgeons grades 1–3), and 175 patients (24.1%) had bad initial clinical grades (Hunt and Hess or World Federation of Neurological Surgeons grades 4 and 5).

In all 33 studies, antiplatelet therapy for stent-assisted coiling of RIA followed the preset protocol identified in each study. Eleven studies (331 patients) administered a loading dose of classic dual antiplatelet agents (aspirin and clopidogrel) at least 2 hours before the start of the procedure. Seventeen studies (560 patients) administered a loading dose of dual antiplatelet agents after completion of the endovascular procedure or postprocedural dual antiplatelet agents with intraprocedural administration of a kind of antiplatelet agent. The other 5 studies (199 patients) used the modified method by using intravenous administration of glycoprotein IIb/IIIa inhibitor (eptifibatid in 3 and tirofiban in 2 studies) after stent deployment. In all studies, anticoagulation treatments with heparin were maintained during the endovascular procedure, except the cases with extravasation on the intraprocedural angiogram. We classified the enrolled studies into 3 groups based on different methods of antiplatelet administration: the preprocedural, postprocedural, and modified antiplatelet administration group.

### Pooled Incidence of Periprocedural Complications

TEC and intra- and postprocedural hemorrhage rates were available in all 33 enrolled studies. Periprocedural TECs occurred in

108 patients (event rate: 11.2%; 95% CI, 9.2%–13.6%;  $I^2 = 1\%$ ). In the subgroup analysis, the event rates of TEC in preprocedural, postprocedural, and modified antiplatelet groups were 7.4% (95% CI, 5.0%–11.0%;  $I^2 = 0\%$ ), 12.3.0% (95% CI, 9.2%–16.4%;  $I^2 = 21\%$ ), and 13.9% (95% CI, 9.7%–19.5%;  $I^2 = 0\%$ ), respectively. The between-group heterogeneity was significant ( $P = .046$ ). An intraprocedural hemorrhage occurred in 46 patients (event rate: 5.4%; 95% CI, 4.1%–7.2%;  $I^2 = 0\%$ ), and event rates in the preprocedural, postprocedural, and modified antiplatelet groups were 5.3% (95% CI, 3.3%–8.5%;  $I^2 = 0\%$ ), 4.9% (95% CI, 3.3%–7.4%;  $I^2 = 0\%$ ), and 8.8% (5.2%–14.4%;  $I^2 = 29\%$ ). The overall event rate of postprocedural hemorrhage was 3.6% (95% CI, 2.6%–5.1%;  $I^2 = 0\%$ ), and subgroup event rates of preprocedural, postprocedural, and modified antiplatelet groups were 2.9% (95% CI, 1.4%–5.9%;  $I^2 = 0\%$ ), 3.9% (95% CI, 2.5%–6.3%;  $I^2 = 0\%$ ), and 3.7% (1.7%–7.9%;  $I^2 = 0\%$ ). There was no significant difference between groups in these 2 hemorrhagic complications.

Morbidity was extracted from 22 studies, and it was measured at 3–6 months in 5 studies, at discharge in 11 studies, and at an unspecified time (such as “last follow-up”) in 6 studies. Mortality was extracted from 28 studies. Pooling of morbidity and mortality yielded substantial heterogeneity ( $I^2 = 54\%$  and 56%). In the subgroup analysis, substantial heterogeneity was shown only in the preprocedural antiplatelet groups, and the event rate of morbidity in this subgroup was 9.3% (95% CI, 6.2%–13.7%;  $I^2 = 0\%$ ). Ranges of incidences of morbidity in the postprocedural and modified antiplatelet group were 3.1%–49.2% and 2.9%–20.0%. The pooling mortality rates of pre- and postprocedural antiplatelet groups were 9.8% (95% CI, 5.7%–16.4%;  $I^2 = 37\%$ ) and 13.4% (95% CI, 9.3%–19.0%;  $I^2 = 38\%$ ). The mortality range of the modified antiplatelet group was 4.3%–36.0%. Although significant between-group heterogeneity was present in both morbidity and mortality, these findings were ignored due to the heterogeneity within each subgroup.

### Risk Ratio of Periprocedural Complications of Stent-Assisted Coiling in RIA Relative to UIA

Thirteen studies were enrolled in this analysis to assess the risk ratio of periprocedural complications of stent-assisted coiling in RIA compared with UIA. There were 505 patients in the RIA group and 1790 patients in the UIA group. These studies were composed of 5 preprocedural, 5 postprocedural, and 3 modified antiplatelet groups. We did not address the meta-analysis regarding postprocedural hemorrhage and morbidity because of too many inestimable studies.

TEC occurred more frequently in patients with RIAs with stent-assisted coiling than in patients with UIAs with stent-assisted coiling (RR, 2.25; 95% CI, 1.43–3.55;  $I^2 = 33\%$ ). The risk of intraprocedural hemorrhage (RR, 5.03; 2.42–10.45;  $I^2 = 0\%$ ) and mortality (RR, 7.39; 95% CI, 3.40–16.03;  $I^2 = 39\%$ ) was also higher in the RIA than in the UIA group (Fig 2).

In the preprocedural and modified antiplatelet groups, the TEC risk in RIA was not significantly different from that in UIA (RR, 1.34; 95% CI, 0.59–3.06;  $I^2 = 0\%$ ; and RR, 1.65; 95% CI, 0.96–2.85;  $I^2 = 0\%$ ). However, TEC occurred more frequently in

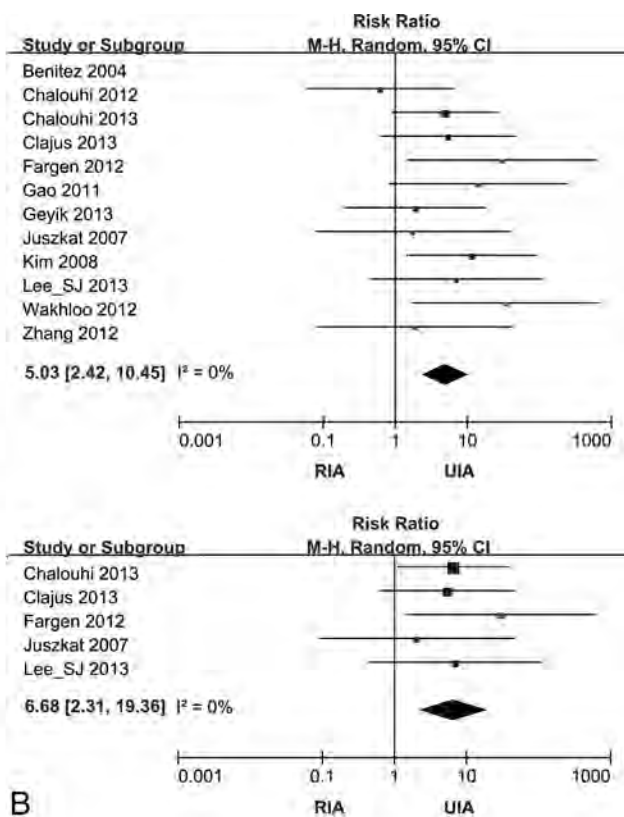
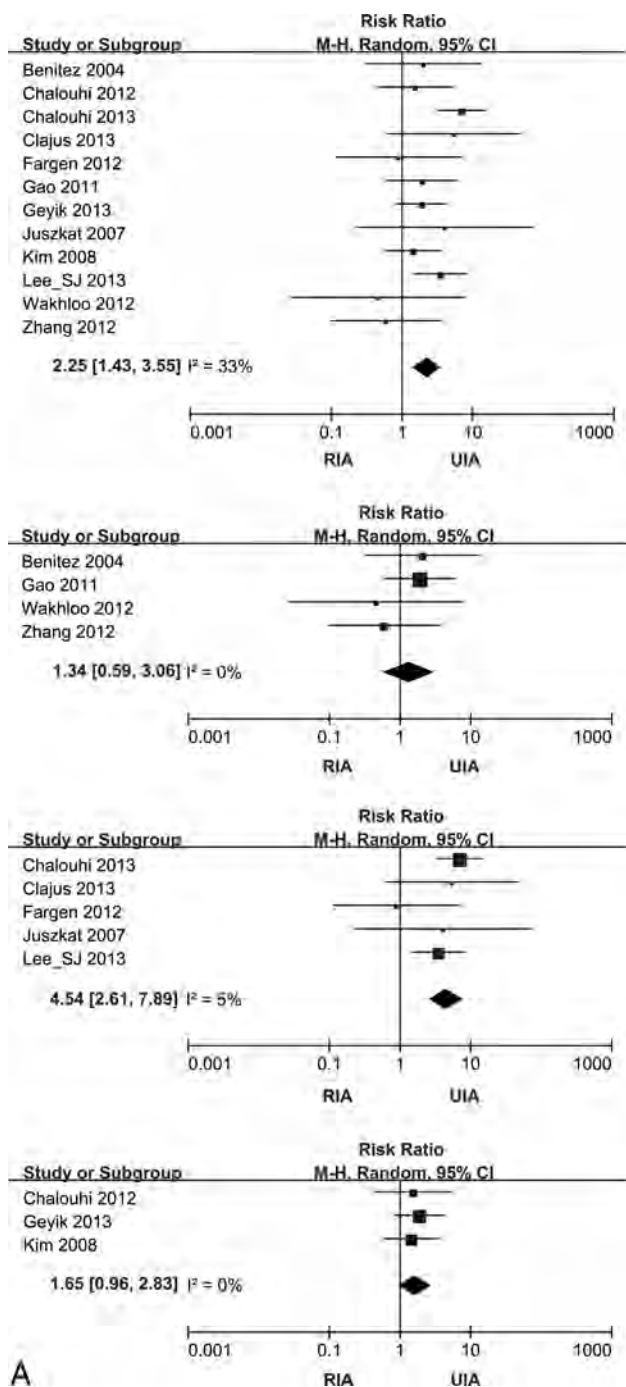


**FIG 2.** Forest plots showing the risk ratio for complications and the mortality of stent-assisted coiling comparing RIA and UIA. Effect sizes are plotted with 95% CIs. A, Forest plots for TEC. From uppermost to lowest, plots for the pooled studies and preprocedural, postprocedural, and modified antiplatelet subgroups. B, Forest plots for intraprocedural hemorrhage. The upper plot is for pooled studies, and lower one is for the postprocedural antiplatelet subgroup. C (next page), Forest plots for mortality. Starting with the uppermost, plots for the pooled studies and pre- and postprocedural antiplatelet subgroups.

RIA than in UIA in the postprocedural antiplatelet group (RR, 4.54; 95% CI, 2.61–7.89;  $I^2 = 5\%$ ) (Fig 2A). Subgroup analysis for intraprocedural hemorrhage showed that the postprocedural antiplatelet group had significantly higher rates (RR, 6.68; 95% CI, 2.31–19.36;  $I^2 = 0\%$ ) in RIA compared with UIA (Fig 2B). Subgroup analysis for intraprocedural hemorrhage of the preprocedural antiplatelet group yielded substantial heterogeneity ( $I^2 = 54\%$ ). Subgroup analysis for mortality showed that it was significant higher in RIA relative to UIA in both pre- and postprocedural antiplatelet groups (RR, 7.64; 95% CI, 1.95–29.94;  $I^2 = 28\%$ ; and RR, 13.44; 95% CI, 5.14–35.17;  $I^2 = 0\%$ ) (Fig 2C). Because results of the meta-analyses for modified-antiplatelet groups showed heterogeneity ( $I^2 = 76\%$ ) in intraprocedural hem-

orrhage and mortality, we did not present these with forest plots.

## DISCUSSION

In terms of endovascular treatment of RIA, many clinicians were concerned about the potential risk of the neck-remodeling technique, such as the complexity of the procedure, thrombotic risk, and antithrombotic drugs. Several studies such as CLARITY (Clinical and Anatomic Results in the Treatment of Ruptured Intracranial Aneurysms) reported that in treatment of ruptured aneurysms, the remodeling technique was as safe as conventional coil embolization and had higher rates of ad-

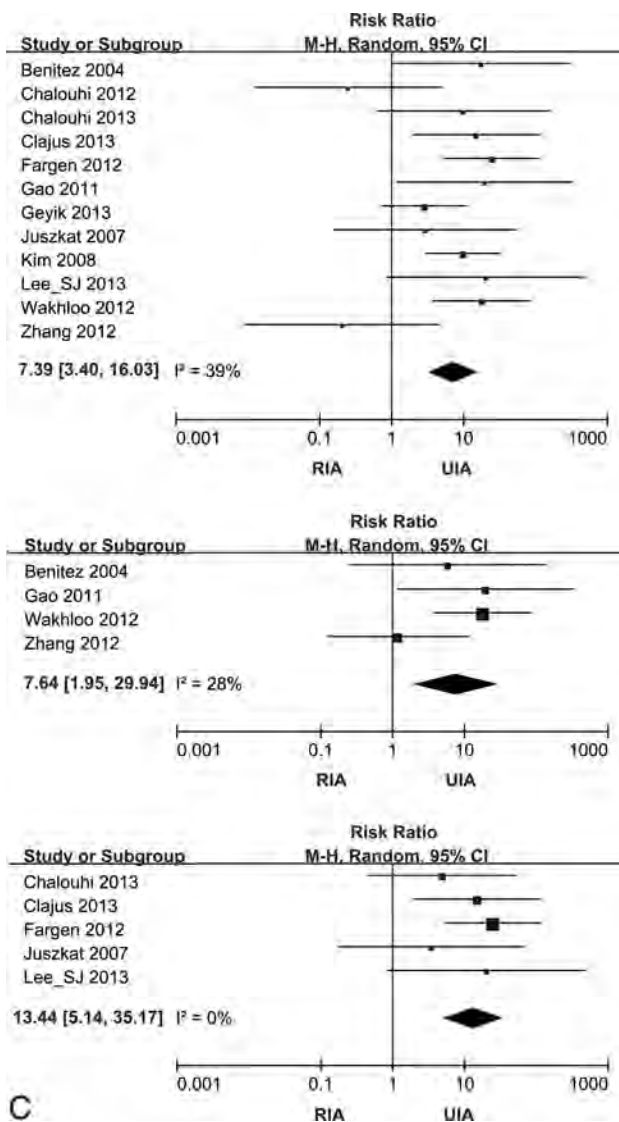


**FIG 2.** Continued

equate postoperative occlusion.<sup>43</sup> However, this assertion did not have enough evidence to end the concern about the risk of stent-assisted coiling in ruptured aneurysms. In this systematic review, the pooled incidence of TEC and periprocedural hemorrhages in stent-assisted coiling of RIA varied from 3.6% to 11.3%, which was higher than the complication rates that have been previously reported in large randomized trials of the coil embolization of RIA.<sup>44,45</sup>

Despite the present review, stent-assisted coiling for UIA is now accepted as a safe treatment option. Several studies demonstrated that the complication risk of stent-assisted coiling was not significantly higher than that in coil-alone treatment, though stented aneurysms usually have more difficult morphology than coil-alone aneurysms.<sup>46-49</sup> Most important, the stent-assisted coiling has a high rate of adequate occlusion, leading to a decrease in the recanalization rate in mid- or long-term follow-up.<sup>48,50</sup> The situation of acutely ruptured aneurysms makes it difficult to guarantee that the safety of stent-assisted coiling is the same as that for coiling alone, and research should be focused on finding more safe ways to implement stent-assisted coiling in RIA. In this re-

gard, antiplatelet medication use during endovascular RIA management is of considerable interest to clinicians because it can elevate the risk of hemorrhagic complications while preventing TEC. Nevertheless, this review showed that there was little consensus about the safe timing of antiplatelet administration that minimizes the complications in stent-assisted coiling of RIA. The methods of antiplatelet therapy varied depending on the institutions, and no high-quality evidence supports the various methods.

The result of subgroup analysis showed that the event rate of TEC varied among the different methods of antiplatelet administration. These findings support the presumption that the complications in stent-assisted RIA can be affected by the method of antiplatelet administration. That stent-assisted coiling for RIA has higher complication and mortality rates than for UIA is easily predictable. This meta-analysis also showed that the pooled risk of complication and mortality rates was significantly higher in RIA than UIA. However, in the preprocedural antiplatelet subgroup, the risk of TEC was not different between RIA and UIA. These results were contrary to the higher prevalence of RIA compared with UIA in the post-procedural antiplatelet analysis and suggested that preprocedural administration of antiplatelets might reduce the risk of TECs during stent-assisted coiling of RIA. Unfortunately, this study could not reveal which antiplatelet method could reduce the risk of hemorrhagic complications.

The present study has several limitations. First, this review was unable to include a well-designed case-control prospective study; we could not find enough studies that compared different antiplatelet therapies or complication risks between stent-assisted coiling and simple coiling for RIA to get statistically significant results. Therefore, our inferences were indirectly suggested from comparisons between the stent-assisted coiling of RIA and UIA. Second, although the severity of morbidity can vary depending on the type of complications, this analysis did not address the impact of the associated surgical procedures that complicate the risk of hemorrhage and hemorrhage-related morbidity that may result from antiplatelet use. Finally, this review also has the common limitations that threaten the validity of systematic reviews, such as publication bias and the generalization of results from different reviews. The retrospective nature of most included studies affected the availability of some variables in some studies and resulted in the absence of standardized definitions for available variables.

## CONCLUSIONS

Although various methods of antiplatelet administration have been used in published articles, there is little consensus regarding the appropriate and safe timing for the administration of antiplatelet agents. However, this study revealed that the clinical results of stent-assisted coiling for RIA would be affected by antiplatelet administration. Therefore, reliable guidelines for antiplatelet therapy in stent-assisted coiling for RIA should be determined by the results of future research. The results of this systematic review can guide future prospective case-control study design to identify more appropriate antiplatelet therapy in stent-assisted coiling of RIA.

## REFERENCES

1. Yoo E, Kim DJ, Kim DI, et al. **Bailout stent deployment during coil embolization of intracranial aneurysms.** *AJNR Am J Neuroradiol* 2009;30:1028–34
2. Hwang G, Kim JG, Song KS, et al. **Delayed ischemic stroke after stent-assisted coil placement in cerebral aneurysm: characteristics and optimal duration of preventative dual antiplatelet therapy.** *Radiology* 2014;273:194–201
3. Bodily KD, Cloft HJ, Lanzino G, et al. **Stent-assisted coiling in acutely ruptured intracranial aneurysms: a qualitative, systematic review of the literature.** *AJNR Am J Neuroradiol* 2011;32:1232–36
4. Zhang XD, Wu HT, Zhu J, et al. **Delayed intracranial hemorrhage associated with antiplatelet therapy in stent-assisted coil embolized cerebral aneurysms.** *Acta Neurochir Suppl* 2011;110(pt 2):133–39
5. Manabe H. **Ruptured cerebral aneurysms treated by stent-assisted GDC embolization—two case reports with long-term follow-up.** *Acta Neurochir Suppl* 2008;103:5–8
6. Tumialán LM, Zhang YJ, Cawley CM, et al. **Intracranial hemorrhage associated with stent-assisted coil embolization of cerebral aneurysms: a cautionary report.** *J Neurosurg* 2008;108:1122–29
7. Taylor RA, Callison RC, Martin CO, et al. **Acutely ruptured intracranial saccular aneurysms treated with stent assisted coiling: complications and outcomes in 42 consecutive patients.** *J Neurointerv Surg* 2010;2:23–30
8. Ries T, Buhk JH, Kucinski T, et al. **Intravenous administration of acetylsalicylic acid during endovascular treatment of cerebral aneurysms reduces the rate of thromboembolic events.** *Stroke* 2006;37:1816–21
9. Chalouhi N, Jabbour P, Kung D, et al. **Safety and efficacy of tirofiban in stent-assisted coil embolization of intracranial aneurysms.** *Neurosurgery* 2012;71:710–14; discussion 714
10. Ferns SP, Sprengers ME, van Rooij WJ, et al. **Coiling of intracranial aneurysms: a systematic review on initial occlusion and reopening and retreatment rates.** *Stroke* 2009;40:e523–529
11. Naggara ON, White PM, Guilbert F, et al. **Endovascular treatment of intracranial unruptured aneurysms: systematic review and meta-analysis of the literature on safety and efficacy.** *Radiology* 2010;256:887–97
12. Amenta PS, Dalyai RT, Kung D, et al. **Stent-assisted coiling of wide-necked aneurysms in the setting of acute subarachnoid hemorrhage: experience in 65 patients.** *Neurosurgery* 2012;70:1415–29; discussion 1429
13. Benitez RP, Silva MT, Klem J, et al. **Endovascular occlusion of wide-necked aneurysms with a new intracranial microstent (Neuroform) and detachable coils.** *Neurosurgery* 2004;54:1359–67; discussion 1368
14. Biondi A, Janardhan V, Katz JM, et al. **Neuroform stent-assisted coil embolization of wide-neck intracranial aneurysms: strategies in stent deployment and midterm follow-up.** *Neurosurgery* 2007;61:460–68; discussion 468–69
15. Chalouhi N, Drueding R, Starke RM, et al. **In-stent stenosis after stent-assisted coiling: incidence, predictors and clinical outcomes of 435 cases.** *Neurosurgery* 2013;72:390–96
16. Clajus C, Sychra V, Strasilla C, et al. **Stent-assisted coil embolization of intracranial aneurysms using the Solitaire AB neurovascular remodeling device: initial and midterm follow-up results.** *Neuroradiology* 2013;55:629–38
17. Fargen KM, Hoh BL, Welch BG, et al. **Long-term results of Enterprise stent-assisted coiling of cerebral aneurysms.** *Neurosurgery* 2012;71:239–44; discussion 244
18. Galal A, Bahrassa F, Dalfino JC, et al. **Stent-assisted treatment of unruptured and ruptured intracranial aneurysms: clinical and angiographic outcome.** *Br J Neurosurg* 2013;27:607–16
19. Gao X, Liang G, Li Z, et al. **Complications and adverse events associated with Neuroform stent-assisted coiling of wide-neck intracranial aneurysms.** *Neurol Res* 2011;33:841–52
20. Huang Q, Xu Y, Hong B, et al. **Stent-assisted embolization of wide-neck anterior communicating artery aneurysms: review of 21 consecutive cases.** *AJNR Am J Neuroradiol* 2009;30:1502–06
21. Jankowitz B, Thomas AJ, Vora N, et al. **Risk of hemorrhage in combined Neuroform stenting and coil embolization of acutely ruptured intracranial aneurysms.** *Interv Neuroradiol* 2008;14:385–96
22. Juszkat R, Nowak S, Smól S, et al. **Leo stent for endovascular treatment of broad-necked and fusiform intracranial aneurysms.** *Interv Neuroradiol* 2007;13:255–69
23. Katsaridis V, Papagiannaki C, Violaris C. **Embolization of acutely ruptured and unruptured wide-necked cerebral aneurysms using the Neuroform2 stent without pretreatment with antiplatelets: a single center experience.** *AJNR Am J Neuroradiol* 2006;27:1123–28
24. Kim SR, Vora N, Jovin TG, et al. **Anatomic results and complications of stent-assisted coil embolization of intracranial aneurysms.** *Interv Neuroradiol* 2008;14:267–84
25. Kim YJ. **Early experiences of Neuroform stent-assisted coiling in ruptured intracranial aneurysms.** *Interv Neuroradiol* 2007;13:31–44
26. Klisch J, Eger C, Sychra V, et al. **Stent-assisted coil embolization of posterior circulation aneurysms using Solitaire AB: preliminary experience.** *Neurosurgery* 2009;65:258–66; discussion 266
27. Lee SJ, Cho YD, Kang HS, et al. **Coil embolization using the self-expandable closed-cell stent for intracranial saccular aneurysm: a single-center experience of 289 consecutive aneurysms.** *Clin Radiol* 2013;68:256–63
28. Lodi YM, Latorre JG, El-Zammar Z, et al. **Stent assisted coiling of the ruptured wide necked intracranial aneurysm.** *J Neurointerv Surg* 2012;4:281–86
29. Piotin M, Blanc R, Spelle L, et al. **Stent-assisted coiling of intracranial aneurysms: clinical and angiographic results in 216 consecutive aneurysms.** *Stroke* 2010;41:110–15
30. Sedat J, Chau Y, Mondot L, et al. **Endovascular occlusion of intracranial wide-necked aneurysms with stenting (Neuroform) and coiling: midterm and long-term results.** *Neuroradiology* 2009;51:401–09
31. Tähtinen OI, Vanninen RL, Manninen HI, et al. **Wide-necked intracranial aneurysms: treatment with stent-assisted coil embolization during acute (<72 hours) subarachnoid hemorrhage—experience in 61 consecutive patients.** *Radiology* 2009;253:199–208
32. Wakhloo AK, Linfante I, Silva CF, et al. **Closed-cell stent for coil embolization of intracranial aneurysms: clinical and angiographic results.** *AJNR Am J Neuroradiol* 2012;33:1651–56
33. Zhang J, Lv X, Yang J, et al. **Stent-assisted coil embolization of intracranial aneurysms using Solitaire stent.** *Neurol India* 2012;60:278–82
34. Yun JH, Cho CS. **Experiences of Neuroform stent applications for ruptured anterior communicating artery aneurysms with small parent vessel.** *J Korean Neurosurg Soc* 2010;48:53–58
35. Chung J, Lim YC, Suh SH, et al. **Stent-assisted coil embolization of ruptured wide-necked aneurysms in the acute period: incidence of and risk factors for periprocedural complications.** *J Neurosurg* 2014;121:4–11
36. Geyik S, Yavuz K, Yurttutan N, et al. **Stent-assisted coiling in endovascular treatment of 500 consecutive cerebral aneurysms with long-term follow-up.** *AJNR Am J Neuroradiol* 2013;34:2157–62
37. Huang QH, Wu YF, Shen J, et al. **Endovascular treatment of acutely ruptured, wide-necked anterior communicating artery aneurysms using the Enterprise stent.** *J Clin Neurosci* 2013;20:267–71
38. Zhao R, Shen J, Huang QH, et al. **Endovascular treatment of ruptured tiny, wide-necked posterior communicating artery aneurysms using a modified stent-assisted coiling technique.** *J Clin Neurosci* 2013;20:1377–81
39. Li C, Li Y. **Stent-assisted coiling of ruptured wide-necked intracranial aneurysms.** *Interv Neuroradiol* 2013;19:283–88
40. Yang P, Liu J, Huang Q, et al. **Endovascular treatment of wide-neck middle cerebral artery aneurysms with stents: a review of 16 cases.** *AJNR Am J Neuroradiol* 2010;31:940–46
41. Chitale R, Chalouhi N, Theofanis T, et al. **Treatment of ruptured**

- intracranial aneurysms: comparison of stenting and balloon remodeling. *Neurosurgery* 2013;72:953–59
42. Lee WJ, Cho CS. Y-stenting endovascular treatment for ruptured intracranial aneurysms: a single-institution experience in Korea. *J Korean Neurosurg Soc* 2012;52:187–92
43. Pierot L, Cognard C, Anxionnat R, et al; CLARITY Investigators. Remodeling technique for endovascular treatment of ruptured intracranial aneurysms had a higher rate of adequate postoperative occlusion than did conventional coil embolization with comparable safety. *Radiology* 2011;258:546–53
44. Pierot L, Cognard C, Anxionnat R, et al; CLARITY Investigators. Ruptured intracranial aneurysms: factors affecting the rate and outcome of endovascular treatment complications in a series of 782 patients (CLARITY study). *Radiology* 2010;256:916–23
45. Molyneux AJ, Kerr RS, Yu LM, et al; International Subarachnoid Aneurysm Trial (ISAT) Collaborative Group. International Subarachnoid Aneurysm Trial (ISAT) of neurosurgical clipping versus endovascular coiling in 2143 patients with ruptured intracranial aneurysms: a randomised comparison of effects on survival, dependency, seizures, rebleeding, subgroups, and aneurysm occlusion. *Lancet* 2005;366:809–17
46. Frontera JA, Moatti J, de los Reyes KM, et al. Safety and cost of stent-assisted coiling of unruptured intracranial aneurysms compared with coiling or clipping. *J Neurointerv Surg* 2014;6:65–71
47. Hetts SW, Turk A, English JD, et al; Matrix and Platinum Science Trial Investigators. Stent-assisted coiling versus coiling alone in unruptured intracranial aneurysms in the Matrix and Platinum Science trial: safety, efficacy, and mid-term outcomes. *AJNR Am J Neuroradiol* 2014;35:698–705
48. Hong Y, Wang YJ, Deng Z, et al. Stent-assisted coiling versus coiling in treatment of intracranial aneurysm: a systematic review and meta-analysis. *PLoS One* 2014;9:e82311
49. Lopes DK, Johnson AK, Kellogg RG, et al. Long-term radiographic results of stent-assisted embolization of cerebral aneurysms. *Neurosurgery* 2014;74:286–91
50. Mine B, Aljishi A, D'Harcour JB, et al. Stent-assisted coiling of unruptured intracranial aneurysms: long-term follow-up in 164 patients with 183 aneurysms. *J Neuroradiol* 2014;41:322–28

# HydroCoils Are Associated with Lower Angiographic Recurrence Rates Than Are Bare Platinum Coils in Treatment of “Difficult-to-Treat” Aneurysms: A Post Hoc Subgroup Analysis of the HELPS Trial

W. Brinjikji, P.M. White, H. Nahser, J. Wardlaw, R. Sellar, A. Gholkar, H.J. Cloft, and D.F. Kallmes

## ABSTRACT

**BACKGROUND AND PURPOSE:** The HydroCoil Endovascular Aneurysm Occlusion and Packing Study was a randomized controlled trial that compared HydroCoils to bare platinum coils. Using data from this trial, we performed a subgroup analysis of angiographic and clinical outcomes of patients with “difficult-to-treat” aneurysms, defined as irregularly shaped and/or having a dome-to-neck ratio of  $<1.5$ .

**MATERIALS AND METHODS:** Separate subgroup analyses comparing outcomes of treatment with HydroCoils to that of bare platinum coils were performed for the following: 1) irregularly shaped aneurysms, 2) regularly shaped aneurysms, 3) aneurysms with a dome-to-neck ratio of  $<1.5$ , and 4) aneurysms with a dome-to-neck ratio of  $\geq 1.5$ . For each subgroup analysis, the following outcomes were studied at the last follow-up (3–18 months): 1) any recurrence, 2) major recurrence, 3) re-treatment, and 4) an mRS score of  $\leq 2$ . Multivariate logistic regression analysis was performed to determine if the HydroCoil was independently associated with improved outcomes in these subgroups.

**RESULTS:** Among the patients with an irregularly shaped aneurysm, the HydroCoil was associated with lower major recurrence rates than the bare platinum coils (17 of 66 [26%] vs 30 of 69 [44%], respectively;  $P = .046$ ). Among the patients with an aneurysm with a small dome-to-neck ratio, the HydroCoil was associated with lower major recurrence rates than the bare platinum coils (18 of 73 [24.7%] vs 32 of 76 [42.1%], respectively;  $P = .02$ ). No difference in major recurrence was seen between HydroCoils and bare platinum coils for regularly shaped aneurysms (42 of 152 [27.6%] vs 52 of 162 [32.1%], respectively;  $P = .39$ ) or aneurysms with a large dome-to-neck ratio (41 of 145 [28.3%] vs 50 of 155 [32.3%], respectively;  $P = .53$ ).

**CONCLUSIONS:** This unplanned post hoc subgroup analysis found that HydroCoils are associated with improved angiographic outcomes in the treatment of irregularly shaped aneurysms and aneurysms with a dome-to-neck ratio of  $<1.5$ . Because this was a post hoc analysis, these results are not reliable and absolutely should not alter clinical practice but, rather, may inform the design of future randomized controlled trials.

**ABBREVIATIONS:** D/N = dome-to-neck ratio; HELPS = HydroCoil Endovascular Aneurysm Occlusion and Packing Study

The HydroCoil Endovascular Aneurysm Occlusion and Packing Study (HELPS) was a randomized controlled trial that compared the rate of clinical and angiographic outcomes in patients treated with the HydroCoil Embolic System (MicroVention, Tustin, California) and those treated with bare platinum coils.<sup>1</sup> This study found a statistically significant lower rate of major recurrence among aneurysms treated with the HydroCoil

(a secondary trial outcome) but found no difference in the rates of trial primary composite outcome, which was a composite measure of adverse outcomes including major aneurysm recurrence at 18 months after treatment and procedure-related deaths and morbidity that resulted in the patients not having follow-up angiography.

Hydrogel coils are manufactured with an expansile hydrogel that has been shown to result in improved aneurysm filling when compared with bare platinum coils.<sup>2</sup> Experimental models have suggested that hydrogel-coated coils are more effective in filling areas of potential aneurysm growth, such as aneurysm rupture points, lobulations, and daughter sacs, and along the aneurysm neck.<sup>3–5</sup> Aneurysms with a small dome-to-neck ratio (D/N) ( $<1.5$ ) and lobulated/irregularly shaped aneurysms have been identified as difficult to coil and at high risk of recanalization after

Received November 13, 2014; accepted after revision January 30, 2015.

From the Department of Radiology (W.B., H.J.C., D.F.K.), Mayo Clinic, Rochester, Minnesota; Institute for Ageing and Health (P.M.W., A.G.), Newcastle University, Newcastle-upon-Tyne, United Kingdom; Department of Clinical Neuroscience (H.N.), University of Edinburgh, United Kingdom; and Walton Centre (J.W., R.S.), Liverpool, United Kingdom.

Please address correspondence to Waleed Brinjikji, MD, 200 1st St SW, Rochester, MN 55905; e-mail: brinjikji.waleed@mayo.edu, @wbrinjikji

<http://dx.doi.org/10.3174/ajnr.A4349>

coil embolization with bare platinum coils.<sup>6</sup> On the basis of findings from experimental models, we hypothesized that HydroCoils would result in a significantly lower rate of aneurysm recurrence than would bare platinum coils in “difficult-to-treat” aneurysms, defined as irregularly shaped aneurysms and aneurysms with a D/N of <1.5. We evaluated this hypothesis by using data from the HELPS trial and performing the following subgroup analyses: 1) analysis of angiographic and clinical outcomes in treatment groups of patients with an irregularly or regularly shaped aneurysm treated with the HydroCoil versus those treated with a bare platinum coil and 2) analysis of angiographic and clinical outcomes of patients with a small D/N (<1.5) aneurysm or large D/N ( $\geq 1.5$ ) aneurysm treated with the HydroCoil versus those treated with a bare platinum coil. Because this was not a prespecified subgroup analysis, it is important to mention that the results of this study should not be used to alter clinical management but, rather, to inform the design of future clinical trials.

## MATERIALS AND METHODS

### Patient Population

The HELPS trial enrolled patients from 24 centers in 7 countries. Enrolled were patients 1) with a previously untreated intracranial aneurysm of 2–25 mm in maximum diameter, 2) aged 18–75 years, 3) determined by a neurovascular team to benefit from coiling, 4) who were not pregnant, 5) who had anatomy such that endovascular occlusion was deemed possible, 6) who had not been previously enrolled in another trial, and 7) whom the neurointerventionist performing the surgery was content or willing to randomly assign to bare platinum or HydroCoil Embolic System coils. Patients who had more than one aneurysm that required treatment in one procedure were excluded. Details regarding informed consent, ethics approval, the coiling procedures, randomization techniques, baseline demographics, and data handling are shown elsewhere.<sup>1,7</sup>

For the purposes of this analysis, we identified the following subgroups of patients: 1) patients with an irregularly shaped aneurysm, 2) patients with a regularly shaped aneurysm, 3) patients with an aneurysm with a small D/N (<1.5), and 4) patients with an aneurysm with a large D/N ( $\geq 1.5$ ). Analysis of outcomes in these subgroups was not prespecified in the design of the HELPS trial. An aneurysm was considered irregularly shaped if it was multilobulated (ie, bilobed or multilobular). These features were recorded at the time of randomization, and trial arms were matched on them as part of the minimization algorithm (also minimized on aneurysm size, rupture status intention to use a coil assist device, and randomized in the United States versus anywhere else in the world).<sup>7</sup>

### Outcomes

For each subgroup of patients, the following baseline and procedural characteristics were obtained: sex, age, D/N, rupture status, use of assist device, aneurysm shape, and baseline World Federation of Neurosurgical Societies score. For the purposes of this subgroup analysis, we studied the following individual outcomes: 1) any recurrence, 2) major recurrence, 3) modified Rankin Scale of  $\leq 2$ , and 4) re-treatment. The presence of aneurysm recurrence

was defined as increased contrast filling of an aneurysm by using a revised 3-point Montreal scale (complete, near-complete, or incomplete occlusion). A major recurrence was defined as a recurrence sufficiently large enough to technically allow placement of further coils as defined by the core laboratory blind assessment of angiograms.<sup>8</sup> Re-treatment was classified as any further treatment of the target aneurysm. The mRS assessment was performed by a postal questionnaire completed by each patient or by his or her main caretaker and was independent of the interventional team. The outcomes listed above were studied at the last clinical or angiographic follow-up. For each subgroup, we compared the rate of these outcomes between patients randomly assigned to the HydroCoil group and those randomly assigned to the bare platinum group.

### Statistical Analysis

All means are presented with their corresponding standard deviations. Comparisons between groups of these categoric outcomes were performed by using the Fisher exact test or ANOVA. Multivariate logistic regression analyses were performed to determine if differences between the HydroCoil and control groups existed for the following outcomes: 1) any recurrence at last follow-up, 2) major recurrence at last follow-up, 3) an mRS score of  $\leq 2$  at last follow-up, and 4) re-treatment at last follow-up. Multivariate logistic regression analyses were performed to determine if coil type was independently associated with any of the outcomes listed above for each subgroup. When performing subgroup analysis according to aneurysm shape, we adjusted for aneurysm size, D/N, rupture status, and use of an assist device. When performing the subgroup analysis according to aneurysm D/N, we adjusted for aneurysm size, shape, rupture status, and use of an assist device. Statistical analysis was performed by using JMP 10.0 Pro (www.jmp.com; SAS Institute, Cary, North Carolina).

### Role of Funding Source

The study sponsor (MicroVention) had no part in trial design, data collection, analysis, or reporting, which were organized by the steering committee. The corresponding author had full access to all the data and had final responsibility for the decision to submit for publication.

## RESULTS

### Patient and Aneurysm Characteristics

Details of baseline patient characteristics for all patients and aneurysms treated in the HELPS trial were described previously.<sup>1</sup> One hundred fifty-three aneurysms (30.7%) were irregular in shape, and 346 aneurysms (69.3%) were regular in shape. When comparing patient characteristics according to aneurysm shape, there was no difference in the proportion of aneurysms in each group that had recently ruptured; 56.9% of the irregularly shaped aneurysms (87 of 153) and 51.6% of the regularly shaped aneurysms (179 of 346) had recently ruptured ( $P = .29$ ). There was a higher proportion of small aneurysms in the irregularly shaped aneurysm group (36.6% [56 of 153]) than in the regularly shaped aneurysm group (20.8% [72 of 346]) and, correspondingly, a higher proportion of large aneurysms in the regularly shaped aneurysm group (19.3% [67 of 346]) than in the irregularly shaped

aneurysm group (10.5% [16 of 153]) ( $P = .0003$ ). However, the overall mean maximum aneurysm dimension was higher in the irregularly shaped aneurysm group than in the regularly shaped aneurysm group ( $8.9 \pm 3.7$  vs  $7.5 \pm 3.2$  mm, respectively;  $P < .0001$ ). These data are summarized in Table 1.

One hundred sixty-four aneurysms had a D/N of  $<1.5$  (32.9%), and 335 aneurysms (67.1%) had a D/N of  $\geq 1.5$ . The proportions of recently ruptured aneurysms were similar in the small D/N group (51.2% [84 of 164]) and the large D/N group

(54.2% [182 of 335];  $P = .57$ ). As expected, patients in the small D/N group were more likely to have had an assist device used than those in the large D/N group (55.6% [90 of 164] vs 40.4% [133 of 335], respectively;  $P = .002$ ). The distributions of aneurysm sizes were similar between groups ( $P = .05$ ); however, the overall mean aneurysm size was lower in the small D/N group than in the large D/N group ( $7.2 \pm 3.1$  vs  $8.2 \pm 3.5$  mm, respectively;  $P = .001$ ). These data are summarized in Table 2.

**Table 1: Characteristics of patients with an irregularly or regularly shaped aneurysm**

Characteristic	Irregularly Shaped	Regularly Shaped	P
No. (%)	153 (30.7)	346 (69.3)	
Mean (SD) age, y	52.3 (11.8)	52.1 (11.6)	.86
Female, no. (%)	108 (70.6)	243 (70.0)	.92
Recently ruptured, no. (%)	87 (56.9)	179 (51.6)	.29
Assist device used, no. (%)	79 (52.3)	144 (42.4)	.05
Small D/N ratio, no. (%)	43 (28.1)	121 (34.9)	.15
Aneurysm size, no. (%)			
Small	56 (36.6)	72 (20.8)	.0003
Medium	81 (52.9)	208 (59.9)	
Large	16 (10.5)	67 (19.3)	
Mean (SD) size, mm	8.9 (3.7)	7.5 (3.2)	<.0001
WFNS score, no. (%)			
0	62 (40.5)	156 (45.0)	.38
I	73 (47.7)	161 (46.4)	
II	16 (10.5)	26 (7.5)	
III	1 (0.7)	4 (1.2)	
VI	1 (0.7)	0 (0.0)	

**Note:**—D/N indicates dome-to-neck ratio; WFNS, World Federation of Neurosurgical Societies.

**Table 2: Characteristics of patients with a small D/N aneurysm versus those with a large D/N aneurysm**

Characteristic	D/N		P
	Small	Large	
Total patients, no. (%)	164 (32.9)	335 (67.1)	
Mean (SD) age, y	52.5 (11.4)	51.9 (11.7)	.64
Female, no. (%)	118 (72.0)	233 (69.4)	.6
Recently ruptured, no. (%)	84 (51.2)	182 (54.2)	.57
Assist device used, no. (%)	90 (55.6)	133 (40.4)	.002
Irregular shape, no. (%)	121 (73.8)	226 (67.3)	.15
Aneurysm size, no. (%)			
Small	36 (22.0)	47 (14.0)	.05
Medium	93 (56.7)	196 (58.3)	
Large	35 (21.3)	93 (27.7)	
Mean (SD) size, mm	7.2 (3.1)	8.2 (3.5)	.001
WFNS, no. (%)			
0	76 (46.3)	142 (42.3)	.51
I	71 (43.3)	163 (48.5)	
II	14 (8.5)	28 (8.3)	
III	3 (1.8)	2 (0.6)	
VI	0 (0.0)	1 (0.3)	

**Table 3: Univariate outcomes according to aneurysm shape**

Outcome	Irregularly Shaped			Regularly Shaped		
	HydroCoil, n/N (%)	Bare Platinum, n/N (%)	P	HydroCoil, n/N (%)	Bare Platinum, n/N (%)	P
Good neurologic outcome	63/70 (90.0)	63/73 (86.3)	.61	141/162 (87.0)	146/164 (89.0)	.58
Any recurrence	23/66 (34.9)	41/69 (59.4)	.004	65/151 (43.0)	75/162 (46.3)	.57
Major recurrence	17/66 (25.8)	30/69 (43.5)	.046	42/152 (27.6)	52/162 (32.1)	.39
Re-treatment	2/76 (2.6)	3/77 (3.9)	.66	4/173 (2.3)	8/173 (4.6)	.26

### Univariate Outcomes According to Aneurysm Shape

For irregularly shaped aneurysms, HydroCoil treatment was associated with significantly lower rates of any angiographic recurrence than treatment with a bare platinum coil (34.9% [23 of 66] vs 59.4% [41 of 69], respectively;  $P = .004$ ) and a significantly lower rate of major recurrence (25.8% [17 of 66] vs 43.5% [30 of 69], respectively;  $P = .046$ ). There was no difference in re-treatment rates between the HydroCoil and bare platinum groups (2.6% [2 of 76] vs 3.9% [3 of 77], respectively;  $P = .66$ ). The rates of good neurologic outcome were similar in the HydroCoil and bare platinum groups (90.0% [63 of 70] vs 86.3% [63 of 73], respectively;  $P = .61$ ).

For regularly shaped aneurysms, there was no difference in the rates of any recurrence between the HydroCoil and bare platinum groups (43.0% [65 of 151] vs 46.3% [75 of 162], respectively;  $P = .57$ ) or in the rates of major recurrence (27.6% [42 of 152] vs 32.1% [52 of 162], respectively;  $P = .39$ ). There was no difference in re-treatment rates between the HydroCoil and bare platinum groups (2.3% [4 of 173] vs 4.6% [8 of 173], respectively;  $P = .26$ ). The rates of good neurologic outcome were similar in the HydroCoil and bare platinum groups (87.0% [141 of 162] vs 89.0% [146 of 164], respectively;  $P = .58$ ). These data are summarized in Table 3.

### Univariate Outcomes According to Aneurysm Dome-to-Neck Ratio

For aneurysms with a small D/N, HydroCoil treatment was associated with significantly lower rates of any angiographic recurrence than treatment with a bare platinum coil (35.6% [26 of 73] vs 55.3% [42 of 76], respectively;  $P = .02$ ) and a significantly lower rate of major recurrence (24.7% [18 of 73] vs 42.1% [32 of 76], respectively;  $P = .02$ ). There was no difference in re-treatment rates between the HydroCoil and bare platinum groups (1.2% [1 of 83] vs 3.7% [3 of 81], respectively;  $P = .36$ ). The rates of good neurologic outcome were similar in the HydroCoil and bare platinum groups (88.3% [68 of 77] vs 89.7% [70 of 78], respectively;  $P = .80$ ).

For aneurysms with a large D/N, there was no difference in the rates of any recurrence between the HydroCoil and bare platinum groups (43.1% [62 of 144] vs 47.7% [74 of 155], respectively;  $P = .49$ ) or the rates of major recurrence (28.3% [41 of 145] vs 32.3%

**Table 4: Univariate outcomes according to aneurysm D/N**

Outcome	Small D/N			Large D/N		
	HydroCoil, n/N (%)	Bare Platinum, n/N (%)	P	HydroCoil, n/N (%)	Bare Platinum, n/N (%)	P
Good neurologic outcome	68/77 (88.3)	70/78 (89.7)	.80	136/155 (87.7)	139/159 (87.4)	1.00
Any recurrence	26/73 (35.6)	42/76 (55.3)	.02	62/144 (43.1)	74/155 (47.7)	.49
Major recurrence	18/73 (24.7)	32/76 (42.1)	.02	41/145 (28.3)	50/155 (32.3)	.53
Re-treatment	1/83 (1.2)	3/81 (3.7)	.36	5/166 (3.0)	8/169 (4.7)	.57

[50 of 155], respectively;  $P = .53$ ). There was no difference in re-treatment rates between the HydroCoil and bare platinum groups (3.0% [5 of 166] vs 4.7% [8 of 169], respectively;  $P = .57$ ). The rates of good neurologic outcome were similar in the HydroCoil and bare platinum groups (87.7% [136 of 155] vs 87.4% [139 of 159], respectively;  $P = 1.00$ ). These data are summarized in Table 4.

### Multivariate Analysis

When we adjusted for aneurysm size, D/N, rupture status, and use of an assist device in the irregularly shaped aneurysm subgroup, use of the HydroCoil was associated with decreased odds of any recurrence (OR, 0.34 [95% CI, 0.19–0.89];  $P = .003$ ) and decreased odds of major recurrence (OR, 0.42 [95% CI, 0.19–0.89];  $P = .02$ ). There was no difference in the odds of good neurologic outcome (OR, 1.56 [95% CI, 0.55–4.69];  $P = .40$ ) or re-treatment (OR, 0.57 [95% CI, 0.07–3.76];  $P = .56$ ).

In the regularly shaped aneurysm subgroup, HydroCoils were not associated with any improvement in the odds of any recurrence (OR, 0.87 [95% CI, 0.54–1.39];  $P = .55$ ), major recurrence (OR, 0.79 [95% CI, 0.47–1.32];  $P = .36$ ), good neurologic outcome (OR, 0.81 [95% CI, 0.41–1.59];  $P = .54$ ), or re-treatment (OR, 0.45 [95% CI, 0.11–1.49];  $P = .19$ ) when we compared HydroCoils with bare platinum coils. These data are summarized in Table 3.

When we adjusted for aneurysm size and shape, rupture status, and use of an assist device in the small D/N aneurysm subgroup, the use of HydroCoils was associated with decreased odds of any recurrence (OR, 0.44 [95% CI, 0.22–0.87];  $P = .02$ ) and major recurrence (OR, 0.42 [95% CI, 0.19–0.89];  $P = .02$ ) in the treatment of aneurysms with a small D/N. There was no difference in good neurologic outcomes (OR, 0.81 [95% CI, 0.29–2.28];  $P = .69$ ) or re-treatment rates (OR, 0.26 [95% CI, 0.01–2.16];  $P = .22$ ).

For the large D/N aneurysm subgroup, HydroCoils were not associated with any significant improvement in the odds of any recurrence (OR, 0.78 [95% CI, 0.48–1.26];  $P = .32$ ), major recurrence (OR, 0.79 [95% CI, 0.47–1.33];  $P = .38$ ), good neurologic outcome (OR, 1.04 [95% CI, 0.53–2.06];  $P = .91$ ), or re-treatment (OR, 0.61 [95% CI, 0.18–1.87];  $P = .38$ ). These data are summarized in Table 4.

### DISCUSSION

In this unplanned post hoc subgroup analysis of patients in the HELPS trial, we found that embolization with the HydroCoil, compared with a bare platinum coil, was associated with significantly lower rates of any recurrence and major recurrence in aneurysms with a small D/N and irregularly shaped aneurysms. This improvement was seen on the univariate analysis and when we

adjusted for confounding variables such as aneurysm size, use of adjunctive devices, and aneurysm rupture status, all of which are independently associated with propensity for aneurysm recurrence. No difference was seen between HydroCoils and bare platinum coils in the treatment of aneurysms with a large D/N and regularly shaped aneurysms. These findings are important, because patients with irregularly shaped aneurysms and aneurysms with a small D/N are generally at a higher risk of recurrence; thus, identifying safe and effective endovascular treatments for such aneurysms is of utmost importance.

A number of previous studies have found that aneurysms with a small D/N and irregularly shaped aneurysms are more difficult to treat and at higher risk of recurrence after endovascular coiling with bare platinum coils than aneurysms with a large D/N and regularly shaped aneurysms, respectively.<sup>6,9-12</sup> This analysis on the HELPS control arm confirms these as risk factors for recurrence. Aneurysms with a small D/N are prone to have neck remnants after coiling, which can result in recanalization of the aneurysm, because they are exposed to high wall shear stress and blood-flow velocities.<sup>13,14</sup> Irregular aneurysm geometries also present a challenge in endovascular coiling. Aneurysms with daughter sacs or multilobular configurations are prone to higher rates of growth and rupture.<sup>15,16</sup> Because of this tendency, achieving high packing attenuations in such aneurysms may be important for sufficiently reducing intra-aneurysmal blood-flow velocity and wall shear stress to prevent further growth of such weak points within the aneurysm.<sup>17</sup>

There are a number of potential reasons why HydroCoils were independently associated with reduced recurrence rates in the treatment of wide-neck and irregularly shaped aneurysms. As mentioned previously, irregularly shaped aneurysms with multilobular configurations or daughter sacs have been shown to be more likely to grow and rupture. Because HydroCoils are designed with an expansile hydrogel that fills more of the aneurysmal lumen than platinum coils, they provide higher rates of aneurysm packing.<sup>18,19</sup> By expanding and achieving higher packing attenuations, HydroCoils may allow for increased conformation to geometric irregularities of intracranial aneurysms, such as aneurysm rupture points.<sup>3</sup> The expansile property of these coils likely explains why the recurrence rates for aneurysms with a small D/N treated with HydroCoils were lower than for those treated with bare platinum coils. Histologic studies in humans and rabbits have shown that HydroCoils are more effective at sealing the aneurysm neck.<sup>4,20</sup> Killer et al<sup>21</sup> found that HydroCoils resulted in higher rates of angiographic and histologic occlusion at both the aneurysm neck and the dome, which increased over time.

Bare platinum and modified coils have been compared in a number of studies. One meta-analysis of 82 studies found no dif-

ference in angiographic outcomes between bare platinum coils, HydroCoils, and Cerecyte coils (Codman Neurovascular, Raynham, Massachusetts).<sup>22</sup> However, no subgroup analyses were performed to examine the relative benefits of modified coils in easily identified difficult-to-treat subgroups, such as wide-neck or irregularly shaped aneurysms. Single-center studies have found that, when compared with bare platinum coils, HydroCoils are associated with decreased recurrence rates; however, none was a randomized controlled trial, and many were too small for subgroup analyses to define which patients may benefit most from HydroCoil treatment.<sup>23,24</sup> The HELPS trial found 8.6% fewer major angiographic recurrences for HydroCoil- versus bare platinum-treated aneurysms ( $P = .049$ ).<sup>1</sup> Clinical trials for other modified coils, such as the Matrix (Stryker, Kalamazoo, Michigan) and Cerecyte coils, failed to show any significant benefit for polyglycolic acid/polyglycolic/poly(lactic acid)-modified versus bare platinum coils.<sup>11,25</sup> Our data suggest that hydrogel-modified coils are more beneficial in certain subsets of patients and aneurysms; recurrence rates were reduced 17%–18% in patients with an aneurysm with a small D/N or an irregularly shaped aneurysm.

Our study had several limitations. First, because this was not a prespecified subgroup analysis for the HELPS trial, these data should not necessarily alter clinical practice but, rather, serve as a guide for the design of future trials comparing modified with bare platinum coils in reducing aneurysm recurrence rates. No follow-up data on aneurysm recurrence and re-treatment were available beyond 18 months. Given this significantly higher rate of major recurrence in the small D/N and irregularly shaped aneurysm control groups, it is conceivable that more of these patients would go on to re-treatment during the long-term follow-up period. However, this suggestion is purely speculative. The combination of low power and lack of consistent follow-up beyond 18 months may have contributed to the lack of statistical significance in aneurysm re-treatment rates between the groups, despite the higher rates of major recurrence in the control group. Another limitation is the fact that there is wide interobserver and intraobserver variability in assessments of aneurysm geometric irregularities such as dome-to-neck ratio, lobularity, and the presence of daughter sacs.<sup>26</sup> The core laboratory in this study assessed angiographic recurrence but did not assess aneurysm morphology. Last, we did not study differences in packing attenuation between groups.

## CONCLUSIONS

Our subgroup analysis of the HELPS trial found that treatment of irregularly shaped and relatively wide-neck aneurysms with HydroCoils was associated with significantly lower major and minor recurrence rates than treatment with bare platinum coils during the study period. Because this was not a prespecified analysis, these results are not reliable enough to alter clinical practice and should in no way alter the way in which these patients with an irregularly shaped aneurysm or an aneurysm with a small dome-to-neck ratio are treated. Rather, these results should guide the development and design of future randomized controlled trials on the use of modified coils in the treatment of intracranial aneurysms, because these findings suggest that inclusion of such difficult-to-treat aneurysms in future clinical trials may help to dem-

onstrate the benefits that modified coils have compared to conventional bare platinum coils.

Disclosures: Waleed Brinjikji—UNRELATED: Grants/Grants Pending: Brain Aneurysm Foundation Research Grant.\* Philip M. White—RELATED: Grant: HELPS trial (Chief Investigator, P.M.W.) was funded by MicroVention\*; Consulting Fee or Honorarium: MicroVention; Support for Travel to Meetings for the Study or Other Purposes: MicroVention, Comments: Support for travel to present HELPS results at international congresses; UNRELATED: Grants/Grants Pending: Codman\* and Covidien.\* Comments: Limited support for PISTE trial (Chief Investigator, P.M.W.) start-up phase; Payment for Lectures (including service on speakers bureaus): Codman and Covidien. Hans Nahser—RELATED: Grant: HELPS Trial.\* Comments: Sponsored by Lothian National Health service; Support for Travel to Meetings for the Study or Other Purposes: Travel for steering committee meetings in Edinburgh (HELPS Trial); UNRELATED: Consultancy: Stryker\*; Travel/Accommodations/Meeting Expenses Unrelated to Activities Listed: Stryker, Covidien, Surpass, WEB, and MicroVention, Comments: Travel and registration fees for conferences, training courses, and scientific meetings. Joanna Wardlaw—RELATED: Grant: Covidien.\* Comments: Provided funding for the trial and catheters (grant holder, P.M.W.). Anil Gholkar—UNRELATED: Consultancy: I have a consultant agreement with MicroVention, through which I organize and teach a course called Brainstorm; Payment for Lectures (including service on speakers bureaus): as stated above. David F. Kallmes—UNRELATED: Board Membership: GE Healthcare, Comments: Cost-effectiveness advisory board; Consultancy: ev3, Comments: Planning and implementing clinical trials; Grants/Grants Pending: MicroVention,\* Sequent Medical,\* Codman,\* SurModics,\* and NeuroSigma.\* Comments: Preclinical and clinical research; Royalties: UVA Patent Foundation, Comments: spinal fusion. \*Money paid to institution.

## REFERENCES

- White PM, Lewis SC, Gholkar A, et al; HELPS trial collaborators. **Hydrogel-coated coils versus bare platinum coils for the endovascular treatment of intracranial aneurysms (HELPS): a randomised controlled trial.** *Lancet* 2011;377:1655–62 CrossRef Medline
- Kallmes DF, Fujiwara NH. **New expandable hydrogel-platinum coil hybrid device for aneurysm embolization.** *AJNR Am J Neuroradiol* 2002;23:1580–88 Medline
- Watanabe K, Sugiu K, Tokunaga K, et al. **Packing efficacy of Hydro-Coil embolic system: in vitro study using ruptured aneurysm model.** *Neurosurg Rev* 2007;30:127–30; discussion 130 CrossRef Medline
- Ding YH, Dai D, Lewis DA, et al. **Angiographic and histologic analysis of experimental aneurysms embolized with platinum coils, Matrix, and HydroCoil.** *AJNR Am J Neuroradiol* 2005;26:1757–63 Medline
- Killer M, Kallmes D, Jones R, et al. **Long-term angiographic and histological results of a new hydrogel-containing filling coil in experimental rabbit aneurysms.** *Minim Invasive Neurosurg* 2010;53:97–105 CrossRef Medline
- Gonzalez N, Sedrak M, Martin N, et al. **Impact of anatomic features in the endovascular embolization of 181 anterior communicating artery aneurysms.** *Stroke* 2008;39:2776–82 CrossRef Medline
- White PM, Lewis SC, Nahser H, et al; HELPS Trial Collaboration. **HydroCoil Endovascular Aneurysm Occlusion and Packing Study (HELPS trial): procedural safety and operator-assessed efficacy results.** *AJNR Am J Neuroradiol* 2008;29:217–23 CrossRef Medline
- Raymond J, Guilbert F, Weill A, et al. **Long-term angiographic recurrences after selective endovascular treatment of aneurysms with detachable coils.** *Stroke* 2003;34:1398–403 CrossRef Medline
- Songsaeng D, Geibprasert S, ter Brugge KG, et al. **Impact of individual intracranial arterial aneurysm morphology on initial obliteration and recurrence rates of endovascular treatments: a multivariate analysis.** *J Neurosurg* 2011;114:994–1002 CrossRef Medline
- Chung EJ, Shin YS, Lee CH, et al. **Comparison of clinical and radiologic outcomes among stent-assisted, double-catheter, and balloon-assisted coil embolization of wide neck aneurysms.** *Acta Neurochir (Wien)* 2014;156:1289–95 CrossRef Medline
- Pierot L, Cognard C, Anxionnat R, et al; CLARITY Investigators. **Endovascular treatment of ruptured intracranial aneurysms: factors affecting midterm quality anatomic results: analysis in a prospec-**

- ative, multicenter series of patients (CLARITY). *AJNR Am J Neuro-radiol* 2012;33:1475–80 CrossRef Medline
12. Brinjikji W, Cloft HJ, Kallmes DF. **Difficult aneurysms for endovascular treatment: overdue or undertall?** *AJNR Am J Neuroradiol* 2009;30:1513–17 CrossRef Medline
  13. Luo B, Yang X, Wang S, et al. **High shear stress and flow velocity in partially occluded aneurysms prone to recanalization.** *Stroke* 2011; 42:745–53 CrossRef Medline
  14. Irie K, Anzai H, Kojima M, et al. **Computational fluid dynamic analysis following recurrence of cerebral aneurysm after coil embolization.** *Asian J Neurosurg* 2012;7:109–15 CrossRef Medline
  15. Morita A, Kirino T, Hashi K, et al; UCAS Japan Investigators. **The natural course of unruptured cerebral aneurysms in a Japanese cohort.** *N Engl J Med* 2012;366:2474–82 CrossRef Medline
  16. Mehan WA Jr, Romero JM, Hirsch JA, et al. **Unruptured intracranial aneurysms conservatively followed with serial CT angiography: could morphology and growth predict rupture?** *J Neurointerv Surg* 2014;6:761–66 CrossRef Medline
  17. Morales HG, Kim M, Vivas EE, et al. **How do coil configuration and packing density influence intra-aneurysmal hemodynamics?** *AJNR Am J Neuroradiol* 2011;32:1935–41 CrossRef Medline
  18. Cloft HJ, Kallmes DF. **Aneurysm packing with HydroCoil embolic system versus platinum coils: initial clinical experience.** *AJNR Am J Neuroradiol* 2004;25:60–62 Medline
  19. Gaba RC, Ansari SA, Roy SS, et al. **Embolization of intracranial aneurysms with hydrogel-coated coils versus inert platinum coils: effects on packing density, coil length and quantity, procedure performance, cost, length of hospital stay, and durability of therapy.** *Stroke* 2006;37:1443–50 CrossRef Medline
  20. Killer M, Arthur AS, Barr JD, et al. **Histomorphology of thrombus organization, neointima formation, and foreign body response in retrieved human aneurysms treated with HydroCoil devices.** *J Biomed Mater Res B Appl Biomater* 2010;94:486–92 CrossRef Medline
  21. Killer M, Hauser T, Wenger A, et al. **Comparison of experimental aneurysms embolized with second-generation embolic devices and platinum coils.** *Acta Neurochir (Wien)* 2009;151:497–505; discussion 505 CrossRef Medline
  22. Rezek I, Mousan G, Wang Z, et al. **Coil type does not affect angiographic follow-up outcomes of cerebral aneurysm coiling: a systematic review and meta-analysis.** *AJNR Am J Neuroradiol* 2013;34: 1769–73 CrossRef Medline
  23. Wei D, Wei C, Huang S, et al. **Comparison between effects of HydroCoil embolic system and ordinary coil on large- and medium-sized intracranial aneurysms.** *Pak J Med Sci* 2013;29:1334–37 Medline
  24. Lee JY, Seo JH, Lee SJ, et al. **Mid-term outcome of intracranial aneurysms treated with HydroSoft coils compared to historical controls treated with bare platinum coils: a single-center experience.** *Acta Neurochir (Wien)* 2014;156:1687–94 CrossRef Medline
  25. Molyneux AJ, Clarke A, Sneade M, et al. **Cerecyte coil trial: angiographic outcomes of a prospective randomized trial comparing endovascular coiling of cerebral aneurysms with either Cerecyte or bare platinum coils.** *Stroke* 2012;43:2544–50 CrossRef Medline
  26. Suh SH, Cloft HJ, Huston J 3rd, et al. **Interobserver variability of aneurysm morphology: discrimination of the daughter sac.** *J Neurointerv Surg* 2014 Nov. 10 [Epub ahead of print] CrossRef Medline

# Wall Mechanical Properties and Hemodynamics of Unruptured Intracranial Aneurysms

J.R. Cebral, X. Duan, B.J. Chung, C. Putman, K. Aziz, and A.M. Robertson



## ABSTRACT

**BACKGROUND AND PURPOSE:** Aneurysm progression and rupture is thought to be governed by progressive degradation and weakening of the wall in response to abnormal hemodynamics. Our goal was to investigate the relationship between the intra-aneurysmal hemodynamic conditions and wall mechanical properties in human aneurysms.

**MATERIALS AND METHODS:** A total of 8 unruptured aneurysms were analyzed. Computational fluid dynamics models were constructed from preoperative 3D rotational angiography images. The aneurysms were clipped, and the domes were resected and mechanically tested to failure with a uniaxial testing system under multiphoton microscopy. Linear regression analysis was performed to explore possible correlations between hemodynamic quantities and the failure characteristics and stiffness of the wall.

**RESULTS:** The ultimate strain was correlated negatively to aneurysm inflow rate ( $P = .021$ ), mean velocity ( $P = .025$ ), and mean wall shear stress ( $P = .039$ ). It was also correlated negatively to inflow concentration, oscillatory shear index, and measures of the complexity and instability of the flow; however, these trends did not reach statistical significance. The wall stiffness at high strains was correlated positively to inflow rate ( $P = .014$ ), mean velocity ( $P = .008$ ), inflow concentration ( $P = .04$ ), flow instability ( $P = .006$ ), flow complexity ( $P = .019$ ), wall shear stress ( $P = .002$ ), and oscillatory shear index ( $P = .004$ ).

**CONCLUSIONS:** In a study of 8 unruptured intracranial aneurysms, ultimate strain was correlated negatively with aneurysm inflow rate, mean velocity, and mean wall shear stress. Wall stiffness was correlated positively with aneurysm inflow rate, mean velocity, wall shear stress, flow complexity and stability, and oscillatory shear index. These trends and the impact of hemodynamics on wall structure and mechanical properties should be investigated further in larger studies.

**ABBREVIATIONS:** MPM = multiphoton microscope; WSS = wall shear stress

Understanding cerebral aneurysm pathogenesis is extremely important for improving aneurysm evaluation and patient management.<sup>1-3</sup> Numerous previous studies have identified many factors that potentially contribute to the development, enlargement, and rupture of intracranial aneurysms.<sup>4</sup> However, the links between these factors and the underlying mechanisms responsible for the formation, growth, and stabilization or rupture of cerebral aneurysms is still poorly understood.<sup>5,6</sup> It is generally

accepted that the evolution of cerebral aneurysms is driven by flow-induced progressive degradation of the wall.<sup>4,7,8</sup> It has been suggested that aberrant aneurysmal flow conditions cause endothelial dysfunction, which induces accumulation of cytotoxic and proinflammatory substances in the wall and thrombus formation that in turn result in the loss of mural cells and wall degeneration.<sup>9,10</sup> This conjecture is supported by histologic analysis of resected human aneurysm tissue.<sup>8</sup> Conversely, on the basis of mechanical testing of tissue samples collected after aneurysm clipping, Costalat et al<sup>11</sup> conjectured that mechanical stiffness of the aneurysm wall may be associated with rupture. Robertson et al<sup>12</sup> recently studied human aneurysm tissues by using a multiphoton microscope (MPM) and found that mechanical properties and collagen architecture can differ, even among unruptured aneurysms. However, the connections between the hemodynamic environment within the aneurysm sac and the wall structure and mechanical behavior have not been studied.

Received October 31, 2014; accepted after revision January 30, 2015.

From the Department of Bioengineering (J.R.C., B.J.C.), Volgenau School of Engineering, George Mason University, Fairfax, Virginia; Department of Mechanical Engineering and Material Science (X.D., A.R.), Swanson School of Engineering, University of Pittsburgh, Pittsburgh, Pennsylvania; Interventional Neuroradiology (C.P.), Inova Fairfax Hospital, Falls Church, Virginia; and Neurosurgery (K.A.), Allegheny General Hospital, Pittsburgh, Pennsylvania.

Please address correspondence to J.R. Cebral, PhD, Bioengineering Department, Volgenau School of Engineering, 4400 University Drive, MSN 2A1, Fairfax, VA 22030; e-mail: jcebral@gmu.edu

Indicates open access to non-subscribers at www.ajnr.org

<http://dx.doi.org/10.3174/ajnr.A4358>

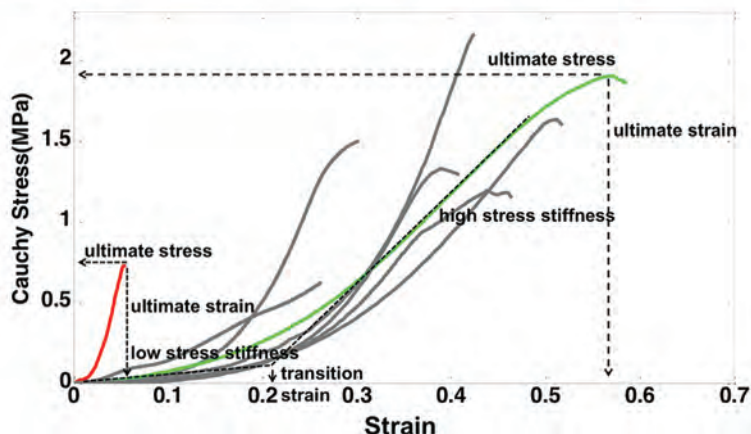


**FIG 1.** Bottom, Stress-strain relationships. Examples of an aneurysm with stiff walls and low ultimate strain and stress (CA15) and an aneurysm with softer walls and greater ultimate stress and ultimate strain (CA26) are highlighted in red and green, respectively. Top, Picture of a sample with grips before stretching (left) and after it fails (right). Note that the tear occurs near the middle of the sample, not at the grips.

The purpose of this work was to investigate possible associations between aneurysmal hemodynamics and wall mechanical properties in human intracranial aneurysms.

## MATERIALS AND METHODS

### Clinical, Imaging, and Tissue Data

We analyzed 8 sufficiently large samples (larger than  $4 \times 5$  mm) from a series of 15 harvested unruptured intracranial aneurysm domes in 46 patients who underwent elective surgical clipping and provided consent. Before intervention, each aneurysm was imaged with 3D rotational angiography. During the intervention, after placing the clip, the aneurysm dome was resected. Harvested tissue samples were placed in a prepared vial with 0.9% (weight/volume) saline solution and transported to the laboratory for analysis within 48 hours. Institutional review board approval was obtained for patient consent, handling of patient data, tissue harvesting, and analysis.

### Mechanical Testing of Wall Samples

The samples were mechanically tested to failure by using a custom-designed uniaxial loading system compatible with a multiphoton microscope that allows simultaneous testing and structural imaging of tissue samples.<sup>13</sup> In particular, because of their capacity for second harmonic generation, collagen fibers can be imaged without staining and traditional destructive techniques. Collagen fibers in the samples were imaged from the luminal (medial) and abluminal (adventitial) sides by using an FV1000 MPE multiphoton laser scanning microscope (Olympus; Tokyo, Japan) equipped with a DeepSee Mai Tai Ti-Sapphire laser (Spectra-Physics Mountain View, California) with a 1.12 numeric aperture  $\times 25$  MPE water-immersion objective at an excitation wavelength of 870 nm. The second harmonic generation signal was collected by using a 400-nm emission filter with a  $\pm 50$  spec-

tral bin. All MPM images shown are in a  $500 \times 500$ - $\mu\text{m}$  scale. For mechanical testing, rectangular strips of the aneurysm were cut in the meridional direction (samples from all aneurysms were cut to approximately the same size,  $4 \times 7$  mm), gripped by mechanical clamps, and placed in a bath of 0.9% (weight/volume) saline at room temperature in the uniaxial MPM system. Fine-grade sandpaper was adhered to the grips to avoid the need for adhesives.<sup>13</sup> Specimens were subjected to uniaxial extension at a speed of  $20 \mu\text{m/s}$ , controlled by a linear actuator (ANT-25LA; Aerotech, Pennsylvania), and force was recorded with a 5-lb load cell (MDB-5; Transducer Techniques, Rio Nedo Temecula, California). Force-versus-displacement curves were obtained after 5 cycles of preconditioning to 0.3 N and used to calculate Cauchy stress as a function of strain. Strain was defined relative to the configuration of the tissue under a load of 0.005 N. Additional details on the tissue-handling protocol, mechanical tests, and MPM imaging were published in a separate article.<sup>12</sup>

### Hemodynamics Modeling

Subject-specific computational fluid dynamics models were constructed from preoperative 3D rotational angiography images.<sup>14</sup> All aneurysms were located in the anterior circulation. All reconstructions included the internal carotid artery and were extended proximally as much as possible to minimize the effect of inlet boundary conditions on aneurysm hemodynamics. Pulsatile flow conditions were derived from phase-contrast MR measurements in healthy subjects.<sup>15</sup> Flow waveforms were scaled with the inflow vessel cross-sectional area to achieve a mean wall shear stress (WSS) of  $15 \text{ dyne/cm}^2$  according to the principle of minimum work (Murray's law).<sup>16</sup> Vessel walls were assumed rigid, and blood was assumed to be a Newtonian fluid with a density of  $1.0 \text{ g/cm}^3$  and viscosity of 0.04 poise. The 3D incompressible Navier-Stokes equations were numerically solved with finite elements on unstructured grids with a resolution of 0.2 mm and a time step of 0.01 seconds.<sup>14</sup>

### Data Analysis

A number of variables were computed from the computational fluid dynamics simulations to quantitatively characterize the aneurysm hemodynamic environment, including the aneurysm inflow rate, aneurysm mean velocity, inflow concentration index, POD entropy (a measure of stability of the intra-aneurysmal flow structure), vortex core-line length (a measure of complexity of the intra-aneurysmal flow pattern), shear concentration index (a measure of concentration of the WSS distribution), mean WSS, mean oscillatory shear index, and percent area under low wall shear stress relative to the parent vasculature. All quantities were

**Table 1: Material properties of harvested human aneurysm tissue samples**

Sample No.	Thickness (mm)	Transition Strain	Low-Strain Stiffness (MPa)	High-Strain Stiffness (MPa)	Ultimate Strain	Ultimate Stress (MPa)	Ultimate Tension (kg/s <sup>2</sup> )
CA1	0.24	0.16	0.35	12.24	0.30	1.50	285
CA11	0.21	0.11	1.66	2.93	0.26	0.63	105
CA12	0.20	0.28	0.58	14.09	0.42	2.16	320
CA15	0.13	0.02	2.35	24.41	0.05	0.73	90
CA25	0.24	0.26	0.24	6.18	0.51	1.63	280
CA26	0.45	0.22	0.90	5.43	0.57	1.90	580
CA39	0.21	0.24	0.34	6.38	0.44	1.20	183
CA46	0.30	0.24	0.22	9.11	0.38	1.34	300

**Table 2: Hemodynamic characteristics of cerebral aneurysms**

Sample No.	Q (mL/s)	ICI	VE (cm/s)	podent	corelen (cm)	SCI	WSS (dyne/cm <sup>2</sup> )	OSI	LSA (%)
CA1	1.52	2.00	9.53	0.31	2.86	4.39	19.57	0.019	49.3
CA11	0.58	0.48	6.68	0.30	1.68	11.58	11.13	0.010	79.7
CA12	0.71	0.65	10.18	0.62	2.84	6.00	25.30	0.025	75.5
CA15	3.52	2.28	23.62	1.03	5.65	3.92	42.87	0.056	59.5
CA25	0.09	0.21	0.98	0.36	0.30	21.70	1.31	0.020	97.1
CA26	0.61	0.70	7.24	0.29	2.80	10.22	14.17	0.016	69.1
CA39	0.99	0.85	8.55	0.17	3.02	4.23	14.38	0.007	40.2
CA46	2.18	1.74	14.11	0.11	1.46	2.80	23.27	0.004	62.3

**Note:**—Corelen indicates vortex core-line length; ICI, inflow concentration index; LSA, area under low wall shear stress relative to the parent vasculature; OSI, mean oscillatory shear index; podent, POD entropy; Q, aneurysm inflow rate; SCI, shear concentration index; VE, aneurysm mean velocity; WSS, mean wall shear stress.

calculated as spatial averages over the aneurysm cavity and time averages over the cardiac cycle. For precise mathematical definitions of these variables and a detailed description of the methodology used to compute them, see references 17 and 18.

The stress–strain curves for the aneurysm wall before failure are largely exponential in nature.<sup>12</sup> As such, the curves were classified into 1 of 4 regions, listed in order of increasing load (shown in Fig 1): 1) low stress region, in which the wall is highly elastic (toe region), 2) transition region, 3) high-stress region, with a nearly linear response, or 4) subfailure region, marked by a decrease in slope of the stress–strain curve and ending with failure of the tissue. The mechanical response was characterized in terms of the following parameters: 1) low-stress stiffness (slope of a linear fit for the low-stress region), 2) high-stress stiffness (slope of a linear fit for the high-stress region), 3) transition strain (strain at the intersection of the low- and high-stress-stiffness lines), 4) ultimate stress (maximum stress before failure), 5) ultimate strain (the strain corresponding to ultimate stress), and 6) ultimate tension (engineering) (the product of ultimate stress [engineering] and unloaded thickness). The ultimate tension provides a measure of the ability of the wall to withstand loading. In contrast, the ultimate stress and strain are intrinsic material properties that characterize failure behavior. Fiber orientation was quantified in projected stacks of multiphoton images following the method in reference 13.

Linear regression analysis was performed to explore possible correlations between hemodynamic variables and wall mechanical properties. All correlations were carried out by using the Python package SciPy (<http://www.scipy.org/>).

## RESULTS

Mechanical behaviors of the aneurysms are listed in Table 1 and Fig 1, and their corresponding flow characteristics are given in Table 2. The correlations for both high-stress stiffness and ultimate strain and hemodynamic variables reached statistical signif-

**Table 3: Linear regression of hemodynamic variables against wall ultimate strain and material stiffness at high stress (past the toe region)**

Wall Property and Flow Variable	Slope	R <sup>2</sup>	P Value
Ultimate strain			
Q	−0.12	0.617	.021 <sup>a</sup>
VE	−0.019	0.597	.025 <sup>a</sup>
ICI	−0.14	0.474	.059
podent	−0.36	0.423	.081
corelen	−0.067	0.412	.086
SCI	0.011	0.186	.287
WSS	−0.010	0.535	.039 <sup>a</sup>
OSI	−6.44	0.414	.085
LSA	0.24	0.069	.531
Material stiffness at high stress			
Q	5.01	0.659	.014 <sup>a</sup>
VE	1.20	0.717	.008 <sup>a</sup>
ICI	6.44	0.531	.040 <sup>a</sup>
podent	19.9	0.741	.006 <sup>a</sup>
corelen	3.48	0.629	.019 <sup>a</sup>
SCI	−0.52	0.227	.232
WSS	0.51	0.813	0.002 <sup>a</sup>
OSI	369.3	0.772	0.004 <sup>a</sup>
LSA	−0.101	0.065	0.53

**Note:**—Corelen indicates vortex core-line length; ICI, inflow concentration index; LSA, area under low wall shear stress relative to the parent vasculature; OSI, mean oscillatory shear index; podent, POD entropy; Q, aneurysm inflow rate; SCI, shear concentration index; VE, aneurysm mean velocity; WSS, mean wall shear stress.

<sup>a</sup> Statistically significant.

icance. Table 3 lists the slope of the linear regression, the correlation coefficient (R<sup>2</sup>), and the P value of the correlation between each hemodynamic variable and the measured ultimate strain and high-strain stiffness. For a P value of <.05, the slope of the corresponding linear regression is significantly different from zero with 95% confidence.

The relationships between hemodynamic quantities and ultimate strain and high-strain wall stiffness are shown in Figs 2 and 3, respectively. The lines correspond to the straight lines fitted by the linear

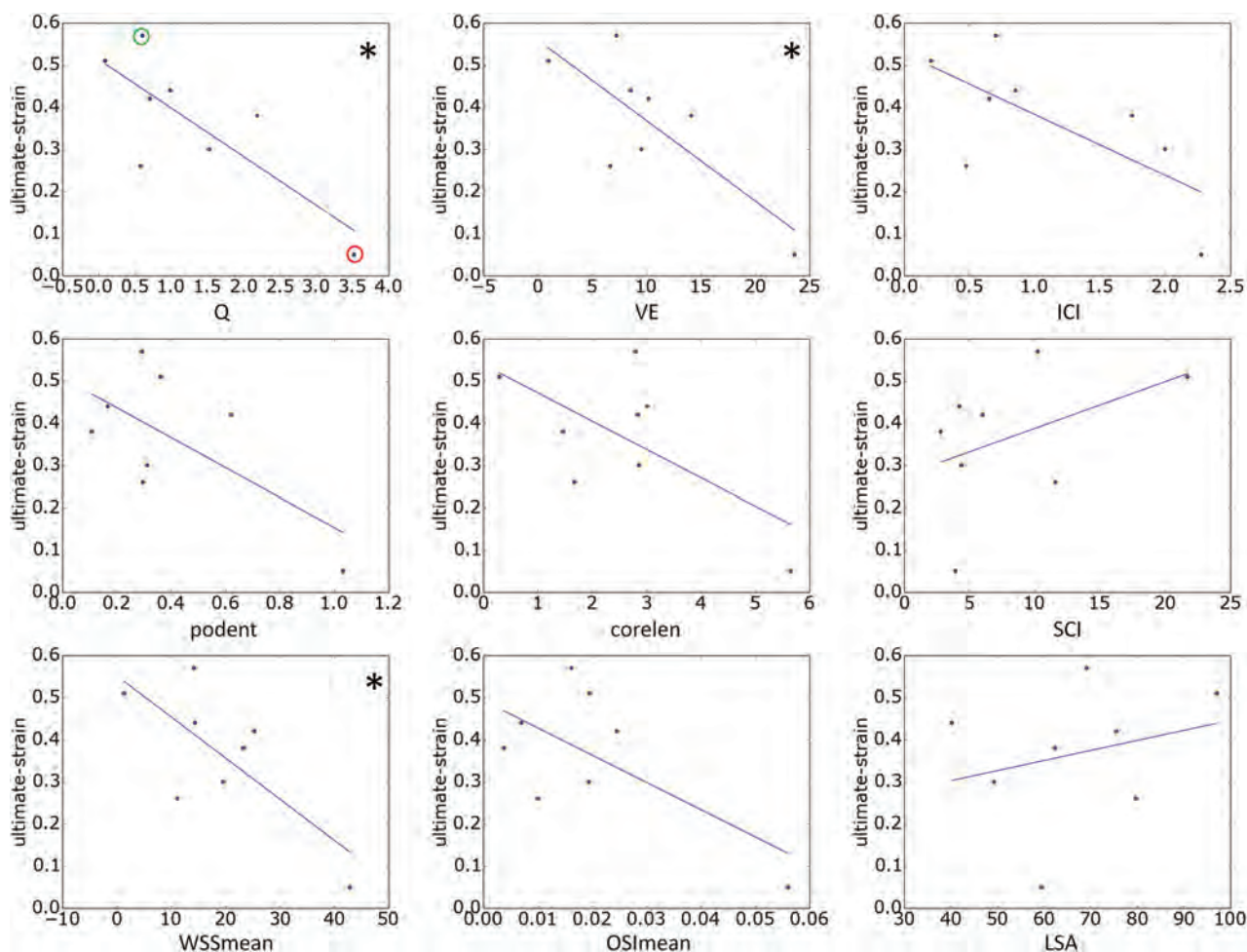


**FIG 2.** Relationships between hemodynamic variables and ultimate wall strain. Each correlation that reached statistical significance (95% confidence) is marked with an asterisk. In the top-left panel, aneurysms CA26 and CA15, exemplified in Figs 4 and 5, are marked with green and red circles, respectively. corelen indicates vortex core-line length; ICI, inflow concentration index; LSA, area under low wall shear stress relative to the parent vasculature; OSI, mean oscillatory shear index; podent, POD entropy; Q, aneurysm inflow rate; SCI, shear concentration index (a measure of concentration of the wall shear stress distribution); VE, aneurysm mean velocity; WSS, mean wall shear stress.

regression (slope and intercept provided in Table 3). Each correlation that reached statistical significance is indicated with an asterisk.

The ultimate strain was seen to decrease with increasing aneurysm inflow rate, mean velocity, inflow concentration, flow instability, flow complexity, WSS, and oscillatory shear index; whereas it decreased with increasing concentration of the WSS distribution and area under low WSS. However, only the associations with inflow rate, mean velocity, and mean WSS reached statistical significance. Ultimate stress followed the same trends but did not reach statistical significance (data not shown).

High-stress wall stiffness increased with inflow rate, mean velocity, inflow concentration, flow instability, flow complexity, WSS, and oscillatory shear index, whereas it decreased with the concentration of the WSS distribution and area under low WSS. The relations to velocity, flow instability, WSS, and oscillatory shear index reached statistical significance.

Two aneurysms (CA26 and CA15), representing distinct mechanical behaviors, are considered in greater detail in Fig 4 to illustrate these trends. In particular, with respect to failure properties, the wall of CA26 (Fig 1, green curve, and Figs 2 and 3, green circle) had the largest ultimate strain, largest ultimate tension, and nearly the

largest ultimate stress. The walls of CA15 (Fig 1, red curve, and Figs 2 and 3, red circle) had the lowest ultimate strain, lowest ultimate tension, and second lowest ultimate stress. With regard to the nature of the loading curve, CA26 had nearly the lowest stiffness in the high-stress region. In contrast, the walls of CA15 had the lowest transition strain and the largest stiffness in the high-stress region. That is, CA26 was stronger with a softer response at high stress than was CA15.

Flow visualizations of CA26 and CA15 along with MPM images of the collagen fibers of each aneurysm in their unloaded configurations are shown in Fig 4. Isovelocity surfaces (top-left frame of each panel) show a stronger inflow stream and larger intrasaccular velocity in CA15. Flow streamlines (top-center frame of each panel) also show stronger intrasaccular flow penetrating deeper into the cavity of CA15. Vortex core lines (top-right frame of each panel) indicate a more complex and unstable flow pattern within CA15. The WSS distribution (bottom-left frame of each panel) shows higher values and a more irregular WSS distribution in CA15.

The collagen fiber architectures of these 2 aneurysms are qualitatively different. On the luminal (medial) side, CA26 shows a denser distribution resulting in a smoother and more

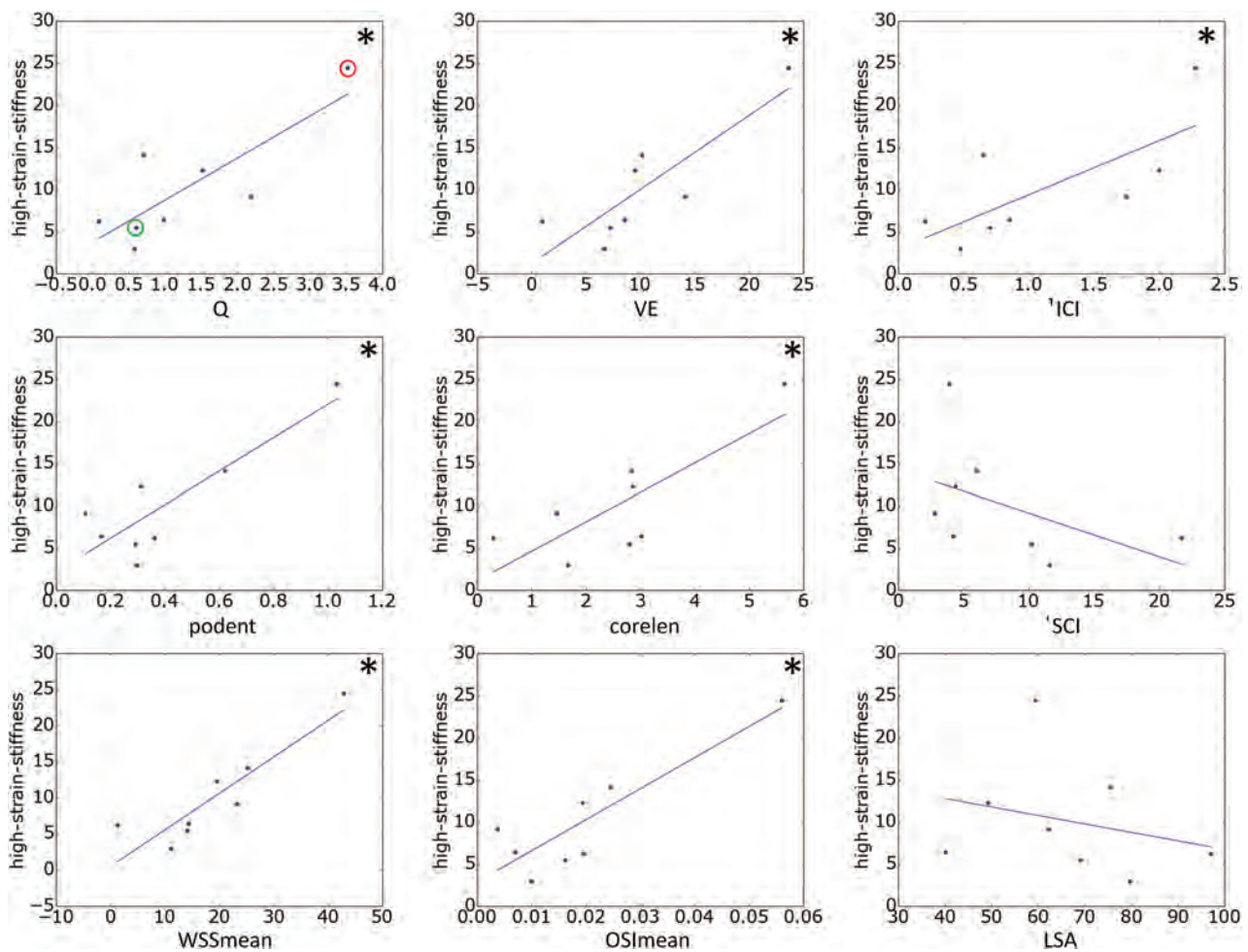


**FIG 3.** Relationships between hemodynamic variables and wall stiffness at high stress. Each correlation that reached statistical significance (95% confidence) is marked with an asterisk. In the top-left panel, aneurysms CA26 and CA15, exemplified in Figs 4 and 5, are marked with green and red circles, respectively. Corelen indicates vortex core-line length; ICI, inflow concentration index; LSA, area under low wall shear stress relative to the parent vasculature; OSImean, mean oscillatory shear index; podent, POD entropy; Q, aneurysm inflow rate; SCI, shear concentration index; VE, aneurysm mean velocity; WSSmean, mean wall shear stress.

homogeneous appearance under the MPM than CA15. On the abluminal (adventitial) side, the fibers of CA26 appear to have more than one preferred orientation direction. The fibers seem to form an interlaced mesh pattern and exhibit a larger degree of waviness. In contrast, the fibers of CA15 close to the abluminal surface appear to follow approximately a single orientation without much interlacing, whereas the fibers deeper in the wall are not unidirectional. Fibers of CA15 exhibit less waviness and, in general, are thicker. The wall thicknesses were 450  $\mu\text{m}$  in CA26 and 130  $\mu\text{m}$  in CA15.

## DISCUSSION

Although it is generally accepted that aneurysm evolution is governed by progressive degradation of the wall in response to abnormal hemodynamics,<sup>7,8</sup> the detailed mechanisms that drive the degeneration and weakening of the wall remain unknown.<sup>5</sup> Previous studies have identified possible associations between different hemodynamic factors and aneurysmal rupture.<sup>4</sup> However, it is unclear which parameters are responsible for the mechanisms controlling wall degradation and aneurysm rupture or stabilization.<sup>19</sup> Determining the influence of intra-aneurysmal hemodynamics on wall structure and strength has the potential to resolve this issue.

A previous study found that rupture site could best be explained in 8 of 9 aneurysms through an association of thinner and stiffer walls with regions of abnormally high WSS.<sup>20</sup> Results from our current study seem to support the idea that large flow activity within the aneurysm, as characterized by high velocity and inflow rates; high WSS and oscillatory shear index; and complex unstable flow structures tend to be associated with lower ultimate strains and stiffer walls. Although trends with respect to ultimate stress did not reach statistical significance, they were in agreement with the trends with respect to ultimate strain and warrant further study. In addition, the trends found in this study suggest that increasing the area exposed to low WSS increases the ultimate strain and decreases the high strain stiffness of an aneurysm wall.

In the low-stress region, collagen fibers are found to straighten and reorient as they are recruited to load bearing.<sup>12</sup> This reorientation can be seen in Fig 5, which displays MPM images of tissue from CA26 under increasing uniaxial loads and corresponding histograms of the distribution of fiber orientations calculated afterward.<sup>21</sup> In the toe region, fibers straighten as the tissue is loaded. As loading progresses through the transition region, in-

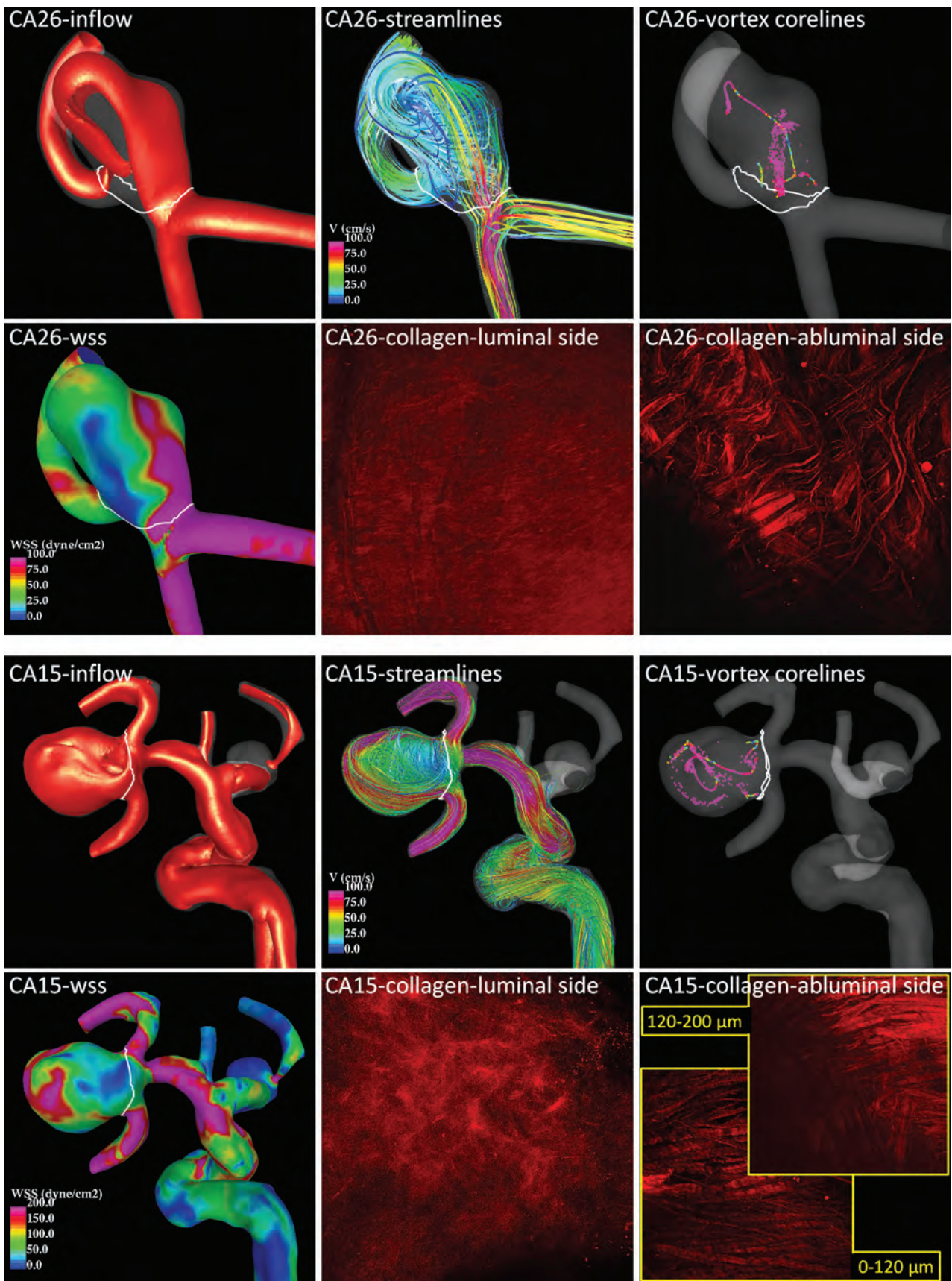


**FIG 4.** Flow and collagen fibers in 2 example aneurysms. Aneurysm CA26 (top) corresponds to the green circles in Figs 2 and 3 and the green curve in Fig 1, and aneurysm CA15 (bottom) corresponds to the red circles in Figs 2 and 3 and the red curve in Fig 1.

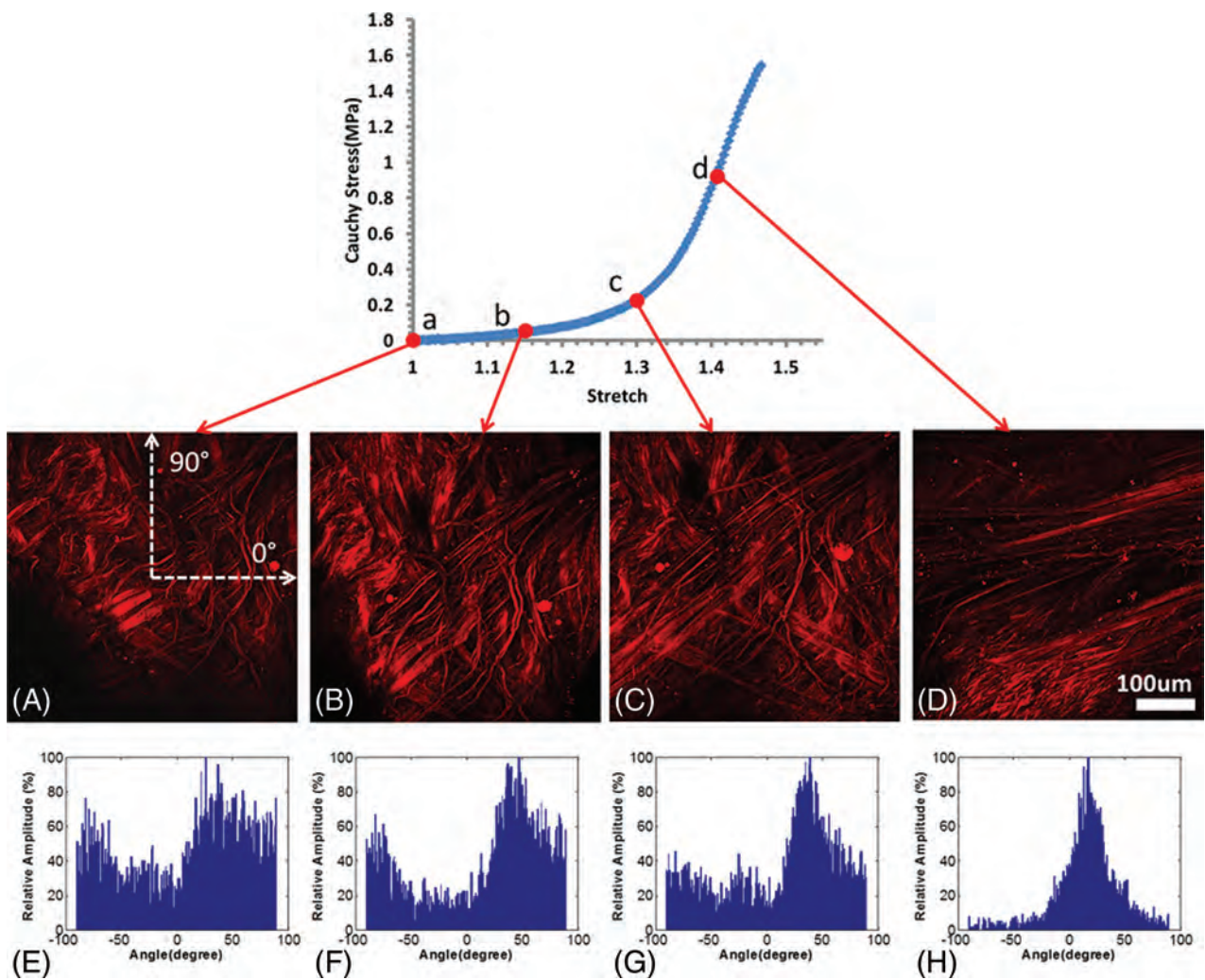


**FIG 5.** Abluminal view of collagen fiber recruitment during uniaxial loading of aneurysm sample CA26 (green in Figs 1–3) obtained by using the uniaxial MPM system. The images were obtained at stretches of 1.0 (A), 1.15 (B), 1.3 (C), and 1.4 (D) and were formed from a projection of stacks over an approximately 95- $\mu\text{m}$  depth of tissue. E–H, Histograms of fiber-orientation distribution of the MPM images at stretches of 1.0, 1.15, 1.3, and 1.4, respectively. The horizontal direction on the image is 0°, and the vertical direction is 90° (as shown in A).

creasing numbers of fibers are straightened and recruited to load bearing. Finally, in the high-stress region, small changes in stretch require large increases in load, consistent with the extensive state of recruitment of the collagen fibers. Hence, the high-strain stiffness of the tissue reflects the properties of recruited fibers. Stiffer behavior in the aneurysm wall would suggest a higher density of collagen fibers or a stiffer collagen fabric, perhaps caused by increased cross-linking. The larger waviness of collagen fibers in CA26 may explain its increased toe region relative to CA15, which showed little waviness. The magnitude of ultimate strain is influenced by a number of factors, including the size of the toe region, high-stress stiffness, and ultimate stress. CA15 failed at a lower strain relative to that of other samples, consistent with the combined effects of a smaller toe region, greater high-strain stiffness, and lower ultimate stress. The increased stiffness at high stress in this sample is consistent with a higher density of abluminal collagen fibers. In contrast, CA26 failed at a higher strain, which is consistent with its longer toe region, lower high-strain stiffness, and greater ultimate stress.

Our results suggest that the hemodynamic environment within the aneurysm sac influences the mechanical behavior of

the aneurysm wall, which in turn strongly depends on the architecture and quality of collagen fibers. The direct connection between hemodynamic conditions and collagen architecture has not yet been explored and is the focus of our ongoing research.

We assessed the connection between global hemodynamic variables and wall mechanical and failure properties. Such global hemodynamic characteristics are appealing, because they are less sensitive to local geometric features. Although this is a sound approach, local flow properties may cause focal changes to the wall in some aneurysms, which in principle can be the cause of failure. Although some of the hemodynamic parameters considered here, such as shear concentration index, reflect local features, the analysis was not performed locally. In the future, it would be valuable to find ways to directly map local mechanical properties to local hemodynamics to extend the current study.

In this study we considered unruptured aneurysms. Although in this study we focused on unruptured aneurysms, the unruptured population seems to harbor a subpopulation of aneurysms vulnerable to rupture.<sup>12</sup> Thus, studies of already ruptured aneurysms would be valuable to determine if the vulnerable subpopulation and ruptured aneurysms share the same trends identified in this study.

Among ruptured aneurysms, some are known to include a subpopulation with thin hypocellular walls devoid of endothelial cells.<sup>22</sup> Hence, this subpopulation of aneurysms may represent a later stage of aneurysm progression in which the role of hemodynamics is fundamentally different from that for the unruptured aneurysm population.

The current study suffers from some limitations. The trends reported here need to be confirmed with larger datasets. A number of idealizations, such as modeling the aneurysm wall as rigid and blood as a single-phase fluid with constant viscosity, were imposed in the hemodynamics studies. Our flow conditions were derived from healthy subjects and scaled with patient-specific inflow vessel sizes, but the effects of comorbidities such as hypertension were not considered. Although our assumptions may have been reasonable,<sup>23</sup> the effects of other comorbidities should be investigated in future studies. In addition, we considered uniaxial loading, recognizing that in vivo loading is closer to equibiaxial. This choice was motivated largely by the desire to test the tissues to failure coupled with the small size of the aneurysm samples. Nevertheless, to our knowledge, our preliminary results are the first to show the link between hemodynamics and aneurysm wall properties and suggest several provocative hypotheses about the relationship between in vivo hemodynamics, wall structure, and wall mechanical properties that need to be tested with larger series of human aneurysm tissue samples.

## CONCLUSIONS

In unruptured intracranial aneurysms, wall ultimate strain was correlated negatively with aneurysm inflow rate, mean velocity, and mean wall shear stress. Wall stiffness in the high-stress region was positively correlated with aneurysm inflow rate, mean velocity, wall shear stress, flow complexity, and in stability.

## ACKNOWLEDGMENTS

This work was supported by National Institutes of Health grant R21 NS080031.

Disclosures: Juan Cebal—RELATED: Grant: National Institutes of Health (NIH); Support for Travel to Meetings for the Study or Other Purposes: University of Pittsburgh. Comments: Paid for hotel for research visits; UNRELATED: Grants/Grants Pending: NIH\* and Philips,\* Comments: Research grants. Xinjie Duan—RELATED: Grant: NIH grant R21 NS080031.\* Christopher Putnam—UNRELATED: Consultancy: Codman Neurovascular; Payment for Lectures (including service on speakers bureaus): Codman Neurovascular, Comments: Annual fellow training program. Anne Robertson—RELATED: Grant: NIH grant IR21 NS080031-01,\* Comments: The submitted paper is based on work performed as part of this NIH R21 grant. Support for Travel to Meetings for the Study or Other Purposes: NIH grant IR21 NS080031-01, travel to the Intracranial Stent Meeting, and to the World Congress of Biomechanics. UNRELATED: Consultancy: NIH, Comments: served on a study section for the NIH; Grants/Grants Pending: NIH, Travel/Accommodations/Meeting Expenses Unrelated to Activities Listed: travel support for research visit to Oxford University and the University of Sheffield. Travel support for a presentation at Cerebrovascular Rounds, University of California at San Francisco Medical Center. Travel support to the 12th Congress of the World Federation of Interventional and Therapeutic Neuroradiology and the International Intracranial Stent Meeting. Travel support for the 51st Annual Meeting of the American Society of Neuroradiology; Other: Fees for serving on a review panel for NIH. \*Money paid to the institution.

## REFERENCES

- Francis SE, Tu J, Qian Y, et al. **A combination of genetic, molecular and haemodynamic risk factors contributes to the formation, enlargement and rupture of brain aneurysms.** *J Clin Neurosci* 2013;20:912–18 CrossRef Medline
- Lall RR, Eddleman CS, Bendok BR, et al. **Unruptured intracranial aneurysms and the assessment of rupture risk based on anatomical and morphological factors: sifting through the sands of data.** *Neurosurg Focus* 2009;26:E2 CrossRef Medline
- Weir B, Macdonald RL. **Intracranial aneurysms and hemorrhage: an overview.** In *Neurosurgery*, Wilkins RH, Rengachary SS, eds. New York: McGraw-Hill; 1996:2191–213
- Cebral JR, Raschi M. **Suggested connections between risk factors of intracranial aneurysms: a review.** *Ann Biomed Eng* 2013;41:1366–83 CrossRef Medline
- Sforza DM, Putman CM, Cebral JR. **Hemodynamics of cerebral aneurysms.** *Annu Rev Fluid Mech* 2009;41:91–107 CrossRef Medline
- Meng H, Tutino VM, Xiang J, et al. **High WSS or low WSS? Complex interactions of hemodynamics with intracranial aneurysm initiation, growth, and rupture: toward a unifying hypothesis.** *AJNR Am J Neuroradiol* 2014;35:1254–62 CrossRef Medline
- Humphrey JD, Canham PB. **Structure, mechanical properties, and mechanics of intracranial saccular aneurysms.** *J Elasticity* 2000;61:49–81 CrossRef
- Frösen J, Tulamo R, Paetau A, et al. **Saccular intracranial aneurysm: pathology and mechanisms.** *Acta Neuropathol* 2012;123:773–86 CrossRef Medline
- Ujiie H, Tachibana H, Hiramoto O, et al. **Effects of size and shape (aspect ratio) on the hemodynamics of saccular aneurysms: a possible index for surgical treatment of intracranial aneurysms.** *Neurosurgery* 1999;45:119–29; discussion 129–30 CrossRef Medline
- Frsen J. **Smooth muscle cells and the formation, degeneration, and rupture of saccular intracranial aneurysm wall—a review of current pathophysiological knowledge.** *Transl Stroke Res* 2014;5:347–56 CrossRef Medline
- Costalat V, Sanchez M, Ambard D, et al. **Biomechanical wall properties of human intracranial aneurysms resected following surgical clipping (IRRA Project).** *J Biomech* 2011;44:2685–91 CrossRef Medline
- Robertson AM, Duan X, Aziz KM, et al. **Diversity in the strength and structure of unruptured cerebral aneurysms.** *Ann Biomed Eng* 2015;43:1502–15 CrossRef Medline
- Hill MR, Duan X, Gibson GA, et al. **A theoretical and non-destructive experimental approach for direct inclusion of measured collagen orientation and recruitment into mechanical models of the artery wall.** *J Biomech* 2012;45:762–71 CrossRef Medline
- Cebral JR, Castro MA, Appanaboyina S, et al. **Efficient pipeline for image-based patient-specific analysis of cerebral aneurysm hemodynamics: technique and sensitivity.** *IEEE Trans Med Imaging* 2005;24:457–67 CrossRef Medline
- Ford MD, Alperin N, Lee SH, et al. **Characterization of volumetric flow rate waveforms in the normal internal carotid and vertebral arteries.** *Physiol Meas* 2005;26:477–88 CrossRef Medline
- Cebral JR, Castro MA, Putman CM, et al. **Flow-area relationship in internal carotid and vertebral arteries.** *Physiol Meas* 2008;29:585–94 CrossRef Medline
- Mut F, Löhner R, Chien A, et al. **Computational hemodynamics framework for the analysis of cerebral aneurysms.** *Int J Numer Method Biomed Eng* 2011;27:822–39 CrossRef Medline
- Byrne G, Mut F, Cebral J. **Quantifying the large-scale hemodynamics of intracranial aneurysms.** *AJNR Am J Neuroradiol* 2014;35:333–38 CrossRef Medline
- Kallmes DF. **Point: CFD—computational fluid dynamics or confounding factor dissemination.** *AJNR Am J Neuroradiol* 2012;33:395–96 CrossRef Medline
- Cebral JR, Vazquez M, Sforza DM, et al. **Analysis of hemodynamics and wall mechanics at sites of cerebral aneurysm rupture.** *J Neurointerv Surg* 2015;7:530–06 CrossRef Medline

21. Schriefl AJ, Reinisch AJ, Sankaran S, et al. **Quantitative assessment of collagen fibre orientations from two-dimensional images of soft biological tissues.** *J R Soc Interface* 2012;9:3081–93 CrossRef Medline
22. Frösen J, Piippo A, Paetau A, et al. **Remodeling of saccular cerebral artery aneurysm wall is associated with rupture: histological analysis of 24 unruptured and 42 ruptured cases.** *Stroke* 2004;35:2287–93 CrossRef Medline
23. Sarrami-Foroushani A, Villa-Uriol MC, Nasr Esfahany M, et al. **Modeling of the acute effects of primary hypertension and hypotension on the hemodynamics of intracranial aneurysms.** *Ann Biomed Eng* 2015;43:207–21 CrossRef Medline

# Computerized Angiographic Occlusion Rating for Ruptured Clipped Aneurysms is Superior to Subjective Occlusion Rating

A.R. Al-Schameri, G. Baltasvias, P. Winkler, M. Lunzer, M. Kral, L. Machegger, F. Weymayr, S. Emich, C. Sherif, and B. Riehling

## ABSTRACT

**BACKGROUND AND PURPOSE:** The computerized occlusion rating to estimate angiographic occlusion of embolized aneurysms is superior to the subjective occlusion rating. In this study, we compared the 2 methods in the analysis of aneurysms clipped after subarachnoid hemorrhage.

**MATERIALS AND METHODS:** The pre- and postoperative angiographic images (DSA) of 95 selected patients were analyzed and stratified in 4 grades (grade 0 for 100%, grade I for <99%–90%, grade II for <89%–70%, grade III for <70% occlusion) by using the subjective (angiographic) occlusion rating and the computerized (angiographic) occlusion rating. For the subjective occlusion rating, the occlusion rate was estimated; for the computerized occlusion rating, the “occluded” and “nonoccluded” aneurysm areas were automatically calculated in square millimeters after outlining the ideal occlusion line.

**RESULTS:** With the subjective occlusion rating, 75 (78.9%), 12 (12.6%), 7 (7.4%), and 1 (1.1%) and with the computerized occlusion rating 45 (47.4%), 24 (25.3%), 20 (21.0%), and 6 (6.3%) patients had aneurysms stratified to grades 0, I, II and III, respectively. The interobserver variation was significant with the subjective occlusion rating but not with the computerized occlusion rating. The subjective occlusion rating overestimated aneurysm occlusion in 30 (31.6%) patients. Mean values were the following: subjective occlusion rating of  $97.5 \pm 6.3\%$  and computerized occlusion rating of  $93.5 \pm 9.7\%$ ;  $P = < .001$ . No patient rebled, and 4 patients underwent retreatment during  $36 \pm 38.9$  months; the predictive value (log-rank, Kaplan-Meier) of the subjective and computerized occlusion ratings with respect to retreatment was highly significant for both methods (subjective occlusion rating:  $\chi^2$ , 29.65;  $P < .001$ ; computerized occlusion rating:  $\chi^2$ , 35.57,  $P < .001$ ).

**CONCLUSIONS:** The 2 methods showed remarkable differences in the estimation of the angiographic occlusion rates of clipped aneurysms. The clearly lower interobserver variation of the computerized versus subjective occlusion rating may indicate a superiority of the computerized occlusion rating.

**ABBREVIATIONS:** COR = computerized (angiographic) occlusion rating; SOR = subjective (angiographic) occlusion rating

Although endovascular embolization is now seen as the first-line treatment for most ruptured intracranial aneurysms, a significant percentage of patients have undergone microsurgical clipping.<sup>1</sup> The main advantage of aneurysm clipping is its potential ability to occlude aneurysms totally and permanently.<sup>2</sup> However, failures in clip placement or stability, due to misinterpreta-

tion of angiograms or surgical findings, may lead to early or late development of aneurysm remnants, possibly causing recurrent hemorrhage.<sup>3,4</sup> Aneurysm remnants are evaluated and followed up mostly by angiography. Multiple attempts have been made to categorize the great variety of different types of aneurysm remnants,<sup>2,5-8</sup> but only a few articles have been published concerning the angiographic assessment details being used to delineate and quantify aneurysm remnants after aneurysm clipping.<sup>2,4,9</sup> All authors based the angiographic assessment on the criterion standard of the subjective occlusion rating (SOR). We recently advocated the superiority of the computerized angiographic occlusion rating (COR) versus subjective occlusion estimations for ruptured embolized aneurysms, due to reduction of subjective estimation bias and interobserver variations.<sup>10</sup> In the present study, COR was retrospectively applied to a series of 95 patients who underwent aneurysm clipping after subarachnoid hemorrhage.

Received November 27, 2014; accepted after revision February 14, 2015.

From the Departments of Neurosurgery (A.R.A.-S., P.W., M.L., M.K., S.E., B.R.), Neuroradiology (L.M., F.W.), Paracelsus Private Medical University, Salzburg, Austria; Department of Neuroradiology (G.B.), University Hospitals of Zurich, Zurich, Switzerland; and Department of Neurosurgery (C.S.), Krankenhaus Rudolfstiftung, Vienna, Austria.

Please address correspondence to A.R. Al-Schameri, MD, Department of Neurosurgery, Paracelsus Private Medical University, Salzburg, Ignaz Harrer Str 79, 5020 Salzburg, Austria; e-mail: a.al-schameri@salk.at

<http://dx.doi.org/10.3174/ajnr.A4399>

**Table 1: Patient characteristics**

Characteristics	
Patients (No.)	95
Mean age (yr)	49
Male sex (No.)	31
Female sex (No.)	64
Mean time of follow-up (mo)	34, 21
Intraoperative rupture	3

**Table 2: Baseline parameters**

Grading	1	2	3	4	5
Fisher (No.)	15	37	24	19	
Hunt and Hess (No.)	53	23	14	3	2

**Table 3: Aneurysm location**

Location	No.
Anterior cerebral artery	31
Pericallosal artery	9
Internal carotid artery	9
Middle cerebral artery	38
Posterior communicating artery	4
Posterior circulation	4

## MATERIALS AND METHODS

### Patients

From a series of 671 patients treated for aneurysms at the Department of Neurosurgery, Paracelsus Private Medical University of Salzburg, from July 1998 until December 2012, 340 patients underwent clipping. Of those, 232 patients with 310 aneurysms had a subarachnoid hemorrhage. All patients were operated on by using standard microsurgical techniques; temporary clipping was applied on 12 cases. We used Aesculap® Yasargil clips (B.Braun, Tuttlingen, Germany) in all cases. From these 232 patients, 137 were excluded due to either death before follow-up angiography ( $n = 54$ ) or loss to follow-up or missing data ( $n = 83$ ). Therefore, 95 patients were included for analysis. At the time of the operation (mean, 3 days after hemorrhage; maximum/minimum, 37/0 days), 76 patients were Hunt and Hess grade 1–2, 14 patients were Hunt and Hess grade 3, and 5 were Hunt and Hess grades 4–5 (Tables 1–3). Patient data were retrospectively entered into a computerized data base.<sup>10</sup> From this data base, we extracted demographic data (name, age, sex), aneurysm location, Fisher grading, operation date, special circumstances of surgery, and follow-up data (outcome scores, angiographic results, and retreatments).

### Angiographic Image Selection

In this study, we included only patients with available pre- and postoperative and follow-up DSA examinations; each of the selected images was taken at the phase of maximum arterial perfusion. Oblique DSA projections were excluded due to inferior comparability between pre- and postoperative projections, introducing bias for later image superimposition used in COR. For SOR, 2 experienced neuroradiologists not involved in the aneurysm treatment and blinded to the patient outcome, independently evaluated the angiographic material to minimize bias caused by image selection and interpretation. For COR, 2 independent neurosurgeons not involved in the aneurysm treatment

and blinded to the patient outcome assessed the true anteroposterior and lateral views, guaranteeing ideal later image fusion. Cases of disagreement between the 2 investigators of each assessment technique were settled by consensus.

### Subjective Occlusion Rating

To estimate SOR, we had to choose noncontinuous parameters. In our previous article on coiled aneurysms,<sup>10</sup> SOR was estimated as 100%, 95%, 90%, 80%, 70%, and 60%. For clipped aneurysms, the estimation of SOR was even more difficult because the occluded aneurysm sac is invisible on postsurgical DSA. We thus defined larger intervals for low-occluded aneurysms (100%, 95%, 80%, 60%). These percentage values were used for statistical evaluations and comparisons.

After SOR was estimated by the 2 reviewers, the SOR percentage values were assigned for better comparability with the neurosurgical literature to a modified version of the classification proposed by Sindou et al<sup>2</sup> as follows: Grade 0 was added, representing 100% occlusion; grade I (range, 99.9%–90%) was assigned to SOR 95%, grade II (range, 89.9%–70%) was assigned to SOR 80%, and grade III (<70%) was assigned to 60% occlusion because we did not observe any lower SOR estimations in this series.

### Computerized Occlusion Rating

For COR, the previously published techniques by Sherif et al<sup>10</sup> had to be modified for clipped aneurysms: In coiled aneurysms, the parameters “recanalized area” and “total aneurysm area” can be easily defined on the postembolization angiograms alone because the coils are visible on the native angiograms. However, on postoperative angiograms of clipped aneurysms, the occluded aneurysm sac is always invisible. This problem was solved by superimposition of preoperative and postoperative angiograms. This was feasible because for angiography, we were always careful on precise anteroposterior and lateral projections. For superimposition, the custom-made software Control-2D (NV Tec Neurovascular Technologies, Vienna, Austria) was used. It allows DSA image superimposition with high precision, resulting in a single angiographic image disclosing the clip with or without an aneurysm remnant. After the 2 reviewers had outlined the orifice plane (“missing vessel wall” or “ideal occlusion line”) and the actual occlusion line given by the clips, the following parameters were measured automatically (Fig 1):

1) Total aneurysm area (square millimeters): Borders of the contrast-filled aneurysm and the defined orifice plane (ideal occlusion line) were outlined and the area was calculated.

2) Aneurysm nonoccluded area (square millimeters): The area filled by contrast medium outside the defined orifice plane (ideal occlusion line) was calculated as “nonoccluded area.”

3) Finally, the occluded area of the aneurysm was calculated as the difference of “total area” minus “nonoccluded area” and was given as a percentage core (to allow direct comparison with the SOR values).

### Statistics

Interobserver variability was calculated for SOR and COR by using the Wilcoxon test.

For every patient, the mean values of both observers were cal-

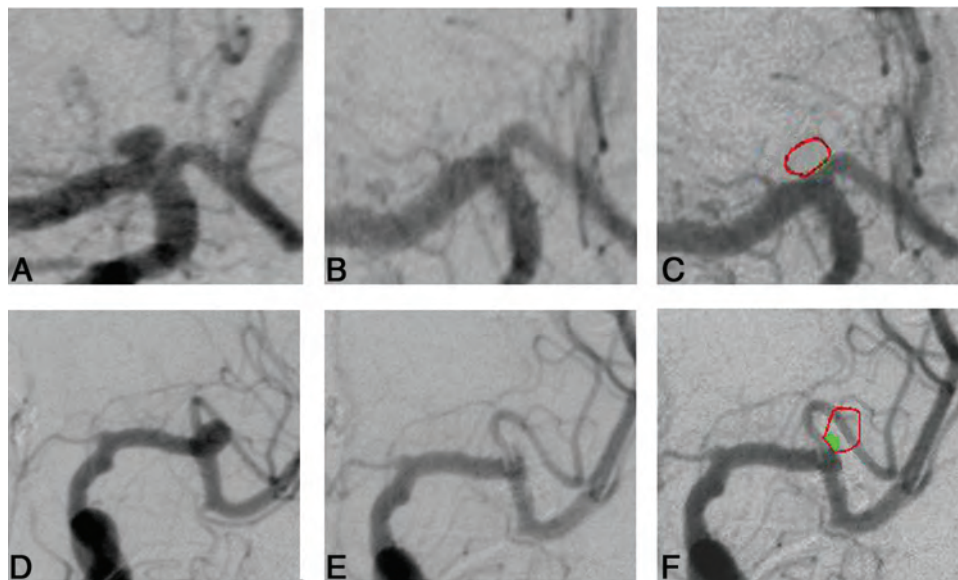


**FIG 1.** Case 1: A, disclosing ICA bifurcation aneurysm in ap projection; B, after clipping; C, superimposition of B and C; no remnant. Case 2: D, disclosing M1/M2 aneurysm in ap projection; E, after clipping; and F, shows superimposition of D and E, the outlined aneurysm (red) and the remnant (green).

**Table 4: SOR and COR results**

	0 (100%)	I (99.9%–90%)	II (89.9%–70%)	III (<70%)	
SOR pts (%)	75 (78.9%)	12.6 (12.6%)	7 (7.4%)	1 (1.1%)	95/100%
COR pts (%)	45 (47.4%)	24 (25.3%)	20 (21.0%)	6 (6.3%)	95/100%

Note:—pts indicates patients.

**Table 5: Thirty patients were stratified to a higher COR group with SOR**

Modality/Group	0	I	II	III	Total Nr.
SOR	75	12	7	1	95
COR	45	24	20	6	95
Diff. strat.	30	15	13	2	

Note:—Diff. strat. indicates patients differently stratified.

**Table 6: Stratification of the 4 retreated patients by the 2 SOR and 2 COR observers**

	SOR 1	SOR 2	COR 1	COR 2
Pt 1	0	I	II	II
Pt 2	II	III	III	III
Pt 3	I	II	III	III
Pt 4	0	0	I	I

Note:—Pt indicates patient.

culated for SOR and COR. Then COR and SOR, classified as 100%, 99.9%–90%, 89.9%–70%, and < 70%, were evaluated as predictors of outcome in univariate Kaplan-Meier analysis (log-rank test) with censoring at the time of retreatment. SOR and COR were compared by using the paired *t* test. Data are presented as mean  $\pm$  SD. A *P* value < .05 was considered significant. SAS 8.02 (SAS Institute, Cary, North Carolina) software was used for all statistical calculations.

## RESULTS

The angiographic follow-up was  $13.5 \pm 18.7$  months; the clinical follow-up was  $34.0 \pm 38.9$  months. A consensus evaluation of selected DSA projections was necessary in 5 patients (5.3%). Statistically significant interobserver variation was documented for SOR measurements (*P* = .002). For COR, the interobserver vari-

ation was not significant (*P* = 1,35).

When using the SOR method, 75 (78.9%) patients had aneurysms stratified to grade 0 (100% occlusion), compared with only 45 (47.4%) patients when using the COR technique. To grade I (99.9%–90% occlusion), 12 (12.6%) patients were stratified by using SOR technique, compared with 24 (25.3%) by using the COR method. To grade II (89.9%–70% occlusion), 7 patients (7.4%) were stratified by using SOR, but 20 (21.0%), by using COR. Finally to grade III (<70% occlusion), 1 patient (1.1%) was stratified when using SOR, but 6 patients (6.3%), when using the COR method (Table 4).

When we compared the values of SOR and COR, the SOR method overestimated the degree of aneurysm occlusion in 30 (31.6%) patients (Table 5). The mean value of SOR was  $97.5 \pm 6.3\%$ , and of COR,  $93.5 \pm 9.7\%$  (*P* = < .001). In the clinical follow-up (mean, 34 months), no patient rebled. Four patients required retreatment. Of those, 2 patients were categorized into grade 0 by using SOR; by using COR, these 2 patients were stratified to grade I. The other 2 patients were stratified by the 2 SOR observers to different grades (I, II, and III) with high interobserver variation, whereas COR classified them homogeneously to grade III (Table 6). The predictive value (log-rank, Kaplan-Meier) of SOR and COR with respect to retreatment was highly significant for both methods (SOR:  $\chi^2$ , 29.65, *P* < .0001; COR:  $\chi^2$ , 35.57, *P* < .0001).

## DISCUSSION

In the past, outcome studies after aneurysm treatment were presented even without follow-up angiography.<sup>11</sup> In the surgical arm of the Cerebral Aneurysm Rupture After Treatment study,<sup>11</sup> representing 70.6% of the total study population, aneurysm occlusion was estimated by the surgeon after clipping in those cases in which DSA was not available. Today conventional angiography

remains not only the main postoperative diagnostic tool<sup>2,3,6,8,12</sup> but also the most reliable for late follow-up. The aim of angiography after aneurysm clipping is, besides the detection of unclipped aneurysms or occluded vessels,<sup>7</sup> the verification of aneurysm remnants. This allows planning of follow-up intervals and retreatment and the prediction of rebleeding risks.<sup>2,3,5,7,11,12</sup> Because the goal of surgical aneurysm therapy is total and permanent occlusion of the aneurysm, partial occlusion has been seen as a failure due to the potential consequences of recurrent aneurysm hemorrhage.<sup>3,11</sup> Factors like the size and shape of the reperfused aneurysm, the relation of the open aneurysm part to the parent vessel, and the challenge of predicting the risk of rebleeding have been widely discussed in the literature.<sup>8,11,13,14</sup> Currently, the standard method in the assessment of the occlusion rate of a clipped aneurysm is a subjective occlusion rating based on postoperative early or late angiography. However, recently we showed that for ruptured coil-embolized cerebral aneurysms, the computerized occlusion rating is superior to the SOR by reducing subjective bias in estimating occlusion rates and by avoiding interobserver variability.<sup>10</sup> The technical differences between the occlusion of an aneurysm by coils compared with clips and the different angiographic appearance of the occluding material made it necessary to modify the initial software. Thus, the possibility of image superimposition was improved. Perfect image superimposition is mandatory for COR of clipped aneurysms because the occluded part of the aneurysm is invisible.

Because the initial occlusion rate is the most important parameter for follow-up strategies, the method of occlusion rating should be reproducible and objective. Therefore, we assessed interobserver variations of SOR and COR. The statistically significant interobserver variation for COR demonstrates that subjective bias may falsify the results of angiographic assessments and lead to incorrect follow-up or treatment decisions for patients. When further comparing SOR with COR, we found a different stratification of 31.6% of all patients to a higher occlusion rate grade. Thus, from 75 patients assigned to grade 0 by SOR, 26 were stratified to grade II; and 4, to grade III by COR (Table 5).

Neither of the 2 methods could validate the results. Both methods are (in this study) based on angiographic pictures taken in strict anteroposterior and lateral projections. With SOR, only assessments can be achieved, whereas with COR, a quantification of the “nonoccluded area” is given in square millimeters. An analysis of 3D structures must be obtained to approach a validation (see below), but because the results will still rely on angiographic pictures, true validations cannot be expected.

### **Total Aneurysm Occlusion**

Of special note, the rate of “total occlusion,” commonly seen as an important parameter expressing the quality of aneurysm surgery, was 79% by using SOR, but only 47.4% with COR. Comparing the high number of “misclippings” (21% with SOR) with literature data, one can find that of 5 publications dealing with angiographic clipping rates, 5 describe patients having both ruptured and unruptured aneurysms; there, the rates of misclipping are 4.4%–18.6%.<sup>15–18</sup> The only report analyzing only patients clipped after subarachnoid hemorrhage as in the current study is the one by Yu et al,<sup>19</sup> who, in 2007, described a series of 169 patients with rup-

tured aneurysms. The authors disclosed a misclipping rate of 16%, but there was no comparable information about preoperative clinical grading in this study, because “patients in poor conditions warranted greater delay.”<sup>19</sup> In our series, all patients had subarachnoid hemorrhage and 19 were medium or poor grade at the time of surgery (Tables 1–3). A further factor that may have influenced our misclipping rate is that in emergency cases, the operations have also been performed by neurosurgeons less experienced in aneurysm therapy. An overview of the experience level of the surgeons involved in our misclipped cases showed that more experienced surgeons had lower aneurysm remnant rates.

When we used COR, the rate of incompletely occluded aneurysms increased to 52.6%. These unusual numbers must be seen in the light of the high capacity of the COR software to detect very small areas of contrast in the field of assessment, compared with the human eye. Due to the frequent mismatch between the straight or curved clip blade and the anatomy of the neck site, the angiogram eventually shows minimal amounts of contrast material outside the “ideal occlusion line,” which was defined by the 2 investigating neurosurgeons. If the clips could not be applied parallel to the parent vessel (eg, rectangular or “palisade-like” clip application), the amount of extravasal dye may be even more. It is the responsibility of the surgeon to accept a certain mismatch or to improve his results by changing or adding clips, both steps eventually linked to an increased risk of an immediate complication, especially after previous subarachnoid hemorrhage. All these circumstances will finally influence the rate of misclipping.

### **Retreatment**

In our series, we observed no recurrent hemorrhage, but 4 patients (4.2%) underwent retreatment. When we looked at the stratification of the retreated patients, 2 patients were stratified by SOR to grade 0, but by COR, to grade I. The former indication for retreatment of these 2 patients had been made by the surgical team by using the common SOR. These 2 different SOR assessments at 2 different points in time express the influence of subjective bias with SOR. Another patient stratified to the grades I/II by the 2 SOR investigators was stratified to grades III/III by using COR. The fourth patient was stratified to II/III by SOR and to III/III by COR. Three of 4 patients stratified by SOR showed high interobserver variation. For any retreated patient, the stratification between the 2 COR observers was equal (Table 6). Again this finding shows the high impact of subjective overestimation of aneurysm occlusion by SOR. It also demonstrates that despite statistically high predictive value (log-rank, Kaplan Meier), the clinical value of SOR may be limited by incorrect overestimation of aneurysm occlusion. With the COR method however, the degree of aneurysm occlusion was in accordance with the estimated need for retreatment in all cases.

The reasons for the differences between subjective and computerized assessments of contrast-perfused areas on angiograms are the following: the higher precision of the computer to calculate gray zones in square millimeters compared with an assessment by the human eye and the lack of accuracy by using anatomic structures to compare and define percentages of occlusion.

### **Clinical Impact**

The higher potential of COR to detect small zones of dye in anatomic areas belonging to the aneurysm may stimulate discussion about the clinical significance of “total occlusion” after aneurysm clipping because none of the 20 (SOR) or 50 (COR) patients with misclipping rebled. To define the minimum COR percentage to prevent retreatment and secondary hemorrhage, larger clinical studies are warranted. Nevertheless, COR provided reproducible measurements, allowing better comparison and showing a good relation to clinical parameters. SOR, on the contrary, has significant dependency on subjective bias with high interobserver variation and often an unclear relation of the results to clinical events.

### **Limitations**

One limiting factor in the present study is its retrospective design with noncontinuous follow-up, and several patients were lost to follow-up for various reasons. Further limiting factors are the restriction to anteroposterior and lateral projections for angiography and the statistical comparison of the continuous parameter COR with the noncontinuous parameter SOR.

### **Follow-Up**

To receive more information about rebleeding and retreatment, we analyzed those patients who were excluded from the study due to leakage on follow-up angiography. From the 77 patients in this additional group, no patient had a secondary hemorrhage or a retreatment; thus the overall retreatment rate was 2.3%.

It seems realistic to assume a close relation between initial occlusion and retreatment. Because we observed enough end points to reach statistical significance despite the short follow-up, a longer follow-up could only show further end points, thus resulting in an even stronger relation. Nevertheless, our follow-up data represent a limitation in assessing potential delayed effects of incomplete, or even complete, aneurysm occlusion.

### **Angiographic Projections**

Under ideal circumstances, oblique projections allowing good visualization of the aneurysm neck are available for pre- and post-treatment angiograms. Today, using angular projections is a routine procedure in endovascular aneurysm therapy because the rotational parameters of both C-arms can be stored and reused for follow-up angiography. However, the retrospective nature of our study implied that for earlier cases of surgical therapy, oblique projections had been rarely used. If so, the repetition of an oblique projection at follow-up was either technically not possible, not seen as necessary, or performed by using nonidentical angles.

The limitations resulting from the sole use of straight projections are obvious and mainly concern the assessment of the shape and size of eventual aneurysm remnants. These limitations are equal for both methods. The primary goal of our study was to compare SOR and COR, both assessments based on the same angiographic projections and the same image content. We fully agree that oblique projections allow better assessment of aneurysm necks; the superiority of COR over SOR also improves the assessment of oblique comparative angiographic studies, as previously reported.<sup>20</sup>

In the future, COR can be used for 3D angiography of cerebral aneurysms, thus allowing not only increased precision of assessment but eventually also a volumetric quantification of aneurysm necks. A supplementary work by using 3D COR, which may elucidate this aspect, is in progress and will be reported.

### **Statistical Comparison of SOR versus COR**

Only the use of noncontinuous parameters for SOR guarantees realistic approximations of occlusion rates and comparability in an everyday clinical setting. Despite statistical imprecision, it offers a realistic basis for comparison with the continuous-parameter COR.

### **CONCLUSIONS**

The computerized angiographic occlusion rating is superior to the actual standard of subjective occlusion estimations. In addition, for clipped aneurysms, COR offers the possibility of improved quality control of the treatments by the use of the percentage of occlusion rating. It offers considerable reduction of subjective estimation bias and interobserver variations. SOR may lead to overestimations of occlusion rates, resulting in erroneous follow-up and retreatment strategies. The main factor limiting these results is the retrospective design of this study, with the consequence of reduced follow-up data and straight angiographic projections. The high sensitivity of COR in detecting minimal areas of contrast medium in the neck region should be confirmed in further studies by using 3D volumetric data.

Disclosures: Camillo Sherif—OTHER RELATIONSHIPS: shareholder of NVtec Neurovascular Technologies and CVtec Cerebrovascular Technologies.

### **REFERENCES**

1. Molyneux AJ, Kerr RS, Yu LM, et al; International Subarachnoid Aneurysm Trial (ISAT) Collaborative Group. **International subarachnoid aneurysm trial (ISAT) of neurosurgical clipping versus endovascular coiling in 2143 patients with ruptured intracranial aneurysms: a randomised comparison of effects on survival, dependency, seizures, rebleeding, subgroups, and aneurysm occlusion.** *Lancet* 2005;366:809–17
2. Sindou M, Acevedo JC, Turjman F. **Aneurysmal remnants after microsurgical clipping: classification and results from a prospective angiographic study (in a consecutive series of 305 operated intracranial aneurysms).** *Acta Neurochir (Wien)* 1998;140:1153–59
3. Wermer MJ, Rinkel GJ, Greebe P, et al. **Late recurrence of subarachnoid hemorrhage after treatment for ruptured aneurysms: patient characteristics and outcomes.** *Neurosurgery* 2005;56:197–204; discussion 197–204
4. Lee JH, Kim SJ, Cha J, et al. **Postoperative multidetector computed tomography angiography after aneurysm clipping: comparison with digital subtraction angiography.** *J Comput Assist Tomogr* 2005;29:20–25
5. el-Beltagy M, Muroi C, Roth P, et al. **Recurrent intracranial aneurysms after successful neck clipping.** *World Neurosurg* 2010;74:472–77
6. David CA, Vishteh AG, Spetzler RF, et al. **Late angiographic follow-up review of surgically treated aneurysms.** *J Neurosurg* 1999;91:396–401
7. Wermer MJ, van der Schaaf IC, Velthuis BK, et al; ASTRA Study Group. **Follow-up screening after subarachnoid haemorrhage: frequency and determinants of new aneurysms and enlargement of existing aneurysms.** *Brain* 2005;128:2421–29
8. Tsutsumi K, Ueki K, Morita A, et al. **Risk of aneurysm recurrence in**

- patients with clipped cerebral aneurysms: results of long-term follow-up angiography. *Stroke* 2001;32:1191–94
9. Elijovich L, Higashida RT, Lawton MT, et al; Cerebral Aneurysm Rerupture After Treatment (CARAT) Investigators. **Predictors and outcomes of intraprocedural rupture in patients treated for ruptured intracranial aneurysms: the CARAT study.** *Stroke* 2008;39:1501–06
  10. Sherif C, Gruber A, Schuster E, et al. **Computerized occlusion rating: a superior predictor of aneurysm rebleeding for ruptured embolized aneurysms.** *AJNR Am J Neuroradiol* 2012;33:1481–87
  11. Johnston SC, Dowd CF, Higashida RT, et al; CARAT Investigators. **Predictors of rehemorrhage after treatment of ruptured intracranial aneurysms: the Cerebral Aneurysm Rerupture After Treatment (CARAT) study.** *Stroke* 2008;39:120–25
  12. Thornton J, Bashir Q, Aletich VA, et al. **What percentage of surgically clipped intracranial aneurysms have residual necks?** *Neurosurgery* 2000;46:1294–98; discussion 1298–1300
  13. Martin NA, Bentson J, Viñuela F, et al. **Intraoperative digital subtraction angiography and the surgical treatment of intracranial aneurysms and vascular malformations.** *J Neurosurg* 1990;73:526–33
  14. Rauzzino MJ, Quinn CM, Fisher WS. **Angiography after aneurysm surgery: indications for “selective” angiography.** *Surg Neurol* 1998;49:32–40; discussion 40–41
  15. Lot G, Houdart E, Cophignon J, et al. **Combined management of intracranial aneurysms by surgical and endovascular treatment: modalities and results from a series of 395 cases.** *Acta Neurochir (Wien)* 1999;141:557–62
  16. Taha MM, Nakahara I, Higashi T, et al. **Endovascular embolization vs surgical clipping in treatment of cerebral aneurysms: morbidity and mortality with short-term outcome.** *Surg Neurol* 2006;66:277–84; discussion 284
  17. Ogilvy CS, Hoh BL, Singer RJ, et al. **Clinical and radiographic outcome in the management of posterior circulation aneurysms by use of direct surgical or endovascular techniques.** *Neurosurgery* 2002;51:14–21; discussion 21–22
  18. Murphy M, Bell D, Worth RD, et al. **Angiography postclipping and coiling of cerebral aneurysms.** *Br J Neurosurg* 2005;19:225–28
  19. Yu SC, Wong GK, Wong JK, et al. **Endovascular coiling versus neurosurgical clipping for ruptured intracranial aneurysms: significant benefits in clinical outcome and reduced consumption of hospital resources in Hong Kong Chinese patients.** *Hong Kong Med J* 2007;13:271–78
  20. Sherif C, Marbacher S, Fandino J, et al. **3D computerized occlusion rating of embolized experimental aneurysms using noninvasive 1.5T MR imaging.** *AJNR Am J Neuroradiol* 2012;33:661–66

# RNA-Sequencing Analysis of Messenger RNA/MicroRNA in a Rabbit Aneurysm Model Identifies Pathways and Genes of Interest

M. Holcomb, Y.-H. Ding, D. Dai, R.J. McDonald, J.S. McDonald, D.F. Kallmes, and R. Kadirvel



## ABSTRACT

**BACKGROUND AND PURPOSE:** Rabbit aneurysm models are used for the testing of embolization devices and elucidating the mechanisms of human intracranial aneurysm growth and healing. We used RNA-sequencing technology to identify genes relevant to induced rabbit aneurysm biology and to identify genes and pathways of potential clinical interest. This process included sequencing microRNAs, which are important regulatory noncoding RNAs.

**MATERIALS AND METHODS:** Elastase-induced saccular aneurysms were created at the origin of the right common carotid artery in 6 rabbits. Messenger RNA and microRNA were isolated from the aneurysm and from the control left common carotid artery at 12 weeks and processed by using RNA-sequencing technology. The results from RNA sequencing were analyzed by using the Ingenuity Pathway Analysis tool.

**RESULTS:** A total of 9396 genes were analyzed by using RNA sequencing, 648 (6.9%) of which were found to be significantly differentially expressed between the aneurysms and control tissues ( $P < .05$ ; false-discovery rate,  $< 0.01$ ; fold change,  $> 2$  or  $< .5$ ). Of these genes, 614 were mapped successfully, 143 were down-regulated, and 471 were up-regulated in the aneurysms as compared with controls. Using the same criteria for significance, 3 microRNAs were identified as down-regulated and 5 were identified as up-regulated. Pathway analysis associated these genes with inflammatory response, cellular migration, and coagulation, among other functions and pathologies.

**CONCLUSIONS:** RNA-sequencing analysis of rabbit aneurysms revealed differential regulation of some key pathways, including inflammation and antigen presentation. *ANKRD1* and *TACR1* were identified as genes of interest in the regulation of matrix metalloproteinases.

**ABBREVIATIONS:** IPA = Ingenuity Pathway Analysis; miRNA = microRNA

Cerebral aneurysm biology is poorly understood in general, with the mechanisms for formation, growth, healing, and rupture all in need of further elucidation. Understanding the underlying biology of aneurysms involves detailing the expression patterns of large clusters of genes and the microRNAs (miRNAs) that regulate them, alongside other biologic considerations such as hemodynamics, which involves computational modeling of the fluid dynamics of the aneurysm and surrounding vessels and has been examined in a number of recent studies.<sup>1-5</sup> miRNAs are small noncoding RNAs (~20

bp) that bind messenger RNA and mediate its degradation or repression (Fig 1). Therefore, miRNA is an important regulatory molecule, and it is known to play a role in a variety of pathologies.<sup>6-12</sup> There are only a handful of previous studies that have profiled miRNA expression in either human intracranial aneurysms or relevant animal models<sup>13-15</sup> and a small number of studies that have focused on the roles of particular miRNAs.<sup>16,17</sup> Already these studies are revealing potential biomarkers<sup>13</sup> and the importance of these regulatory molecules.

Rabbit elastase-induced experimental aneurysms have been used to study aneurysm occlusion devices and underlying aneurysm biology.<sup>2,18-22</sup> These previous studies relied on detailed information about the biologic environment of experimental rabbit aneurysms. Existing studies have used RNA microarray data to quantify gene expression.<sup>18,23-25</sup> Compared with microarrays, next-generation RNA sequencing offers increased specificity and sensitivity, broader dynamic range, and the ability to detect new transcripts and isoforms.<sup>26</sup> It also enables the detection of miRNA. In this study, we used RNA sequencing to establish dif-

Received August 21, 2014; accepted after revision January 30, 2015.

From the Neuroradiology Research Laboratory, Mayo Clinic, Rochester, Minnesota. This work was supported by research grant NS076491 from the National Institutes of Health.

Please address correspondence to Ramanathan Kadirvel, PhD, Mayo Clinic, 200 First St SW, Rochester, MN 55905; e-mail: kadir@mayo.edu

 Indicates open access to non-subscribers at [www.ajnr.org](http://www.ajnr.org)

 Indicates article with supplemental on-line table.

<http://dx.doi.org/10.3174/ajnr.A4390>

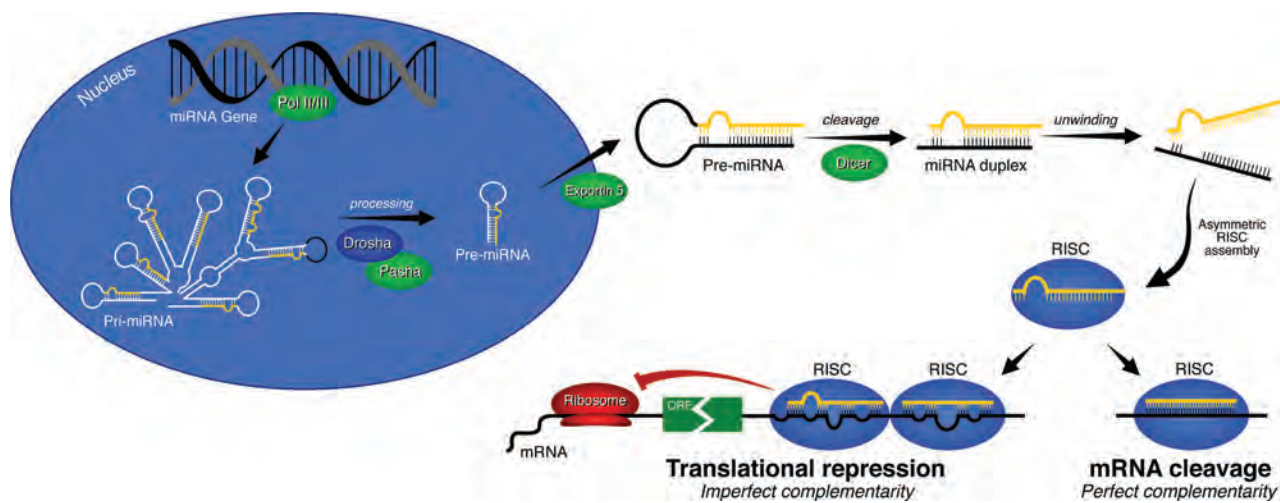


**FIG 1.** Diagram of miRNA regulation of gene expression. mRNA indicates messenger RNA; ORF, open reading frame; Pol, polymerase; Pri-miRNA, primary microRNA; RISC, RNA-induced silencing complex.

ferential expression patterns of messenger RNA and miRNA in experimental rabbit aneurysms.

## MATERIALS AND METHODS

### **Aneurysm Creation and Tissue Harvest**

The Institutional Animal Care and Use Committee approved all procedures before initiation of the study. An elastase-induced saccular aneurysm was created in each of 6 New Zealand white rabbits by using the rabbit elastase model.<sup>27</sup> Aneurysm and contralateral common carotid artery samples were harvested 12 weeks after aneurysm creation. These tissue samples were then immediately frozen in liquid nitrogen and stored at  $-70^{\circ}\text{C}$  until they were ready for messenger RNA/miRNA extraction.

### **Messenger RNA and miRNA Extraction**

RNA was isolated from the frozen tissues by using an miRNeasy mini kit (Qiagen, Valencia, California). The quantity of RNA was measured by using spectrophotometry, and the integrity of the RNA was confirmed by electrophoretic separation using the 2100 Bioanalyzer (Agilent Technologies, Palo Alto, California). The quality of the samples was determined by RNA integrity number.<sup>28</sup> An RNA integrity number of  $>6$  is considered acceptable for sequencing. One aneurysm sample that did not meet the required RNA integrity number was excluded, along with its paired control from the study, so that paired analysis could be performed on the other samples. The remaining samples ( $n = 5$  each for the controls and the aneurysms) were used for RNA-sequencing analysis.

### **RNA Sequencing**

RNA libraries were prepared according to the manufacturer's instructions for the TruSeq RNA sample prep kit version 2 (Illumina, San Diego, California). Then, the libraries were loaded onto paired-end flow cells following Illumina's standard protocol by using the Illumina cBot and cBot paired-end cluster kit (version 3). The flow cells were sequenced on an Illumina HiSeq 2000 using a TruSeq SBS sequencing kit (version 3) and HCS (version 2.0.12) data-collection software. Base calling was performed by using Illumina's RTA (version 1.17.21.3).

### **NEBNext miRNA Sequencing**

miRNA libraries were prepared according to the manufacturer's instructions for the NEBNext Multiplex small-RNA kit (New England Biolabs, Ipswich, Massachusetts). Then, the libraries were loaded onto paired-end flow cells following Illumina's standard protocol by using the Illumina cBot and cBot paired-end cluster kit (version 3). The flow cells were sequenced on an Illumina HiSeq 2000 using a TruSeq SBS sequencing kit (version 3) and HCS (version 2.0.12) data-collection software. Base calling was performed by using Illumina's RTA (version 1.17.21.3).

### **Bioinformatics Analysis**

Processing of the messenger RNA data was performed by using MAP-RSeq (version 1.2.1.3).<sup>29</sup> MAP-RSeq consists of the following steps: alignment, quality control, obtaining genomic features for each sample, and summarizing the data across samples. The pipeline provides detailed quality-control data to estimate the distance between paired-end reads, evaluates the sequencing depth for alternate splicing analysis, determines the rate of duplicate reads, and calculates the read depth across genes by using RSeQC software (version 2.3.2).<sup>30</sup> Paired-end reads were aligned by TopHat (version 2.0.6)<sup>31</sup> against the April 2009 *oryCun2* genome build by using the bowtie1<sup>32</sup> aligner option. Gene counts were generated by using HTSeq software (version 0.5.3p9),<sup>33</sup> and the gene-annotation files were obtained from Ensembl ([ftp://ftp.ensembl.org/pub/release-75/gtf/oryctolagus\\_cuniculus/Oryctolagus\\_cuniculus.OryCun2.0.75.gtf.gz](ftp://ftp.ensembl.org/pub/release-75/gtf/oryctolagus_cuniculus/Oryctolagus_cuniculus.OryCun2.0.75.gtf.gz)) and the University of California Santa Cruz (<http://hgdownload.soe.ucsc.edu/downloads.html#rabbit>). Differential expression in a sample's aneurysm tissue compared with that in the same sample's normal tissue was computed by using the edgeR algorithm (version 2.6.2)<sup>34</sup> across all samples. EdgeR (or empirical analysis of digital gene expression in R, an open-source programming environment) is a Bioconductor software package for examining differential expression of replicated count data; it calculates the log fold change, the *P* value, and the false-discovery rate between the control and experimental conditions. Human orthologs were assigned by using

ExoLocator.<sup>35</sup> The pathway analysis leveraged the Ingenuity Pathway Analysis (IPA)<sup>36</sup> software to identify pathways enriched with human ortholog targets.

### Quantitative Real-Time Polymerase Chain Reaction Analysis

First-strand complementary DNAs were synthesized from 500 ng of total RNA by using Superscript III first-strand synthesis (Invitrogen, Carlsbad, California). Real-time polymerase chain reaction assays were performed for osteopontin, von Willebrand factor, *TIMP1*, tyrosinase, and *TACR1* with an iCycler (Bio-Rad, Hercules, California).

### Statistical Analysis

The *t*-test statistics and corresponding *P* values were used as a measure of the mean change in expression between the aneurysm and control groups relative to the variability. The *t*-test-based *P* values were adjusted for multiple comparisons by using the false-discovery-rate multiple-correction approach.<sup>37</sup>

**Table 1: miRNA expression data**

Mature miRNA	Fold Change	P Value	FDR
hsa-miR-1	0.48	4.62E-05	1.01E-03
hsa-miR-9-5p	0.43	4.80E-05	1.01E-03
hsa-miR-10a-5p	2.66	8.83E-09	4.66E-07
hsa-miR-10b-5p <sup>a</sup>	2.45	3.47E-07	1.47E-05
hsa-miR-21-5p	3.51	4.43E-11	4.67E-09
hsa-miR-34a-5p	2.34	1.15E-04	2.02E-03
hsa-miR-34c-5p <sup>b</sup>	3.79	1.28E-06	4.38E-05
hsa-miR-146a-5p	3.68	1.45E-06	4.38E-05
hsa-miR-146b-5p <sup>c</sup>	3.32	9.08E-11	6.39E-09
hsa-miR-204-5p	0.48	7.32E-06	1.93E-04
hsa-miR-223-3p	3.95	6.79E-12	1.43E-09

**Note:**—FDR indicates false discovery rate.

<sup>a</sup> Grouped with miR-10a-5p by IPA for targeting purposes.

<sup>b</sup> Grouped with miR-34a-5p by IPA for targeting purposes.

<sup>c</sup> Grouped with miR-146a-5p by IPA for targeting purposes.

**Table 2: Most up-regulated canonical pathways, determined by IPA**

Canonical Biologic Pathway	No. of Genes Up-Regulated	Genes	No. of Genes Down-Regulated	Gene(s)
Dendritic cell maturation	25	<i>CD80, CD83, CD86, CDIC, COL10A1, COL1A1, COL1A2, FCGR1B, FCGR2A, HLA-A, HLA-DMA, HLA-DMB, HLA-DOB, HLA-DQA1, HLA-DRA, HLA-DRB1, HLA-DRB5, IL15, IL1B, IL1RL2, IL1RN, PIK3CG, PIK3R5, PLCB2, TREM2</i>	3	<i>CREB5, PLCB4, PLCL1</i>
Role of NFAT in regulation of the immune response	22	<i>BLNK, BTK, CD80, CD86, FCERIA, FCGR1B, FCGR2A, FOS, GNG2, HLA-DMA, HLA-DMB, HLA-DOB, HLA-DQA1, HLA-DRA, HLA-DRB1, HLA-DRB5, LCP2, LYN, PIK3CG, PIK3R5, PLCB2, SYK</i>	2	<i>PLCB4, GNAO1</i>
Antigen-presentation pathway	12	<i>CD74, HLA-A, HLA-DMA, HLA-DMB, HLA-DOB, HLA-DPA1, HLA-DPB1, HLA-DQA1, HLA-DQB2, HLA-DRA, HLA-DRB1, HLA-DRB5</i>	0	NA
Altered T-cell and B-cell signaling in rheumatoid arthritis	17	<i>CCL21, CD80, CD86, HLA-DMA, HLA-DMB, HLA-DOB, HLA-DQA1, HLA-DRA, HLA-DRB1, HLA-DRB5, IL15, IL1B, IL1RN, SPPI, TLR1, TLR8, TNFSF13B</i>	0	NA
Atherosclerosis signaling	19	<i>ALOX5, CCL2, CCR2, COL10A1, COL1A1, COL1A2, CXCR4, IL8, IL1B, IL1RN, LYZ, MSRI, PDGFB, PDGFC, PDGFD, PLA2G7, PLA2R1, SELE, VCAM1</i>	1	<i>RBP4</i>

**Note:**—NA indicates not applicable; NFAT, nuclear factor of activated T cells.

Compared with controls, genes in aneurysms with a significant difference, determined by a *P* value of  $< .05$ , a false discovery rate of  $< 0.01$ , and a fold change of  $> 2$ , were considered up-regulated, whereas those with a *P* value of  $< .05$ , a false discovery rate of  $< 0.01$ , and a fold change of  $< .5$  were considered down-regulated.

### RESULTS

Using the criteria discussed above for differential expression, 648 of 9396 (6.9%) genes were identified as being differentially expressed. Of these genes, 614 were mapped successfully; 143 were down-regulated, and 471 were up-regulated (On-line Table). The 34 unmapped genes consisted of rabbit genes for which no ortholog could be determined. Of 211 miRNAs measured, 11 (5.2%) mature miRNAs were identified as being differentially expressed by using the same criteria as were used for messenger RNA. Targeting information was available for 8 of them that target 230 genes that have been differentially expressed. Increased expression was seen in 5 of the miRNAs, and decreased expression was seen in 3 (Table 1).

### Pathways

The most up-regulated pathways are shown in Table 2 and Fig 2. The first 4 pathways, all related to immune response, have the leukocyte antigen genes (*HLA*) in common. Another pathway of interest in aneurysms is coagulation. When comparing aneurysm tissue with control tissue, IPA identified 50 up-regulated and 12 down-regulated genes related to coagulation, which includes 9 types of collagen, with 8 being up-regulated and 1 (type 28  $\alpha 1$ ) being down-regulated (0.29-fold).

### Biologic Functions of Interest

**Inflammatory Response.** The inflammatory response is projected to be a pathway of major up-regulation (*z* score, 4.387; *P* =

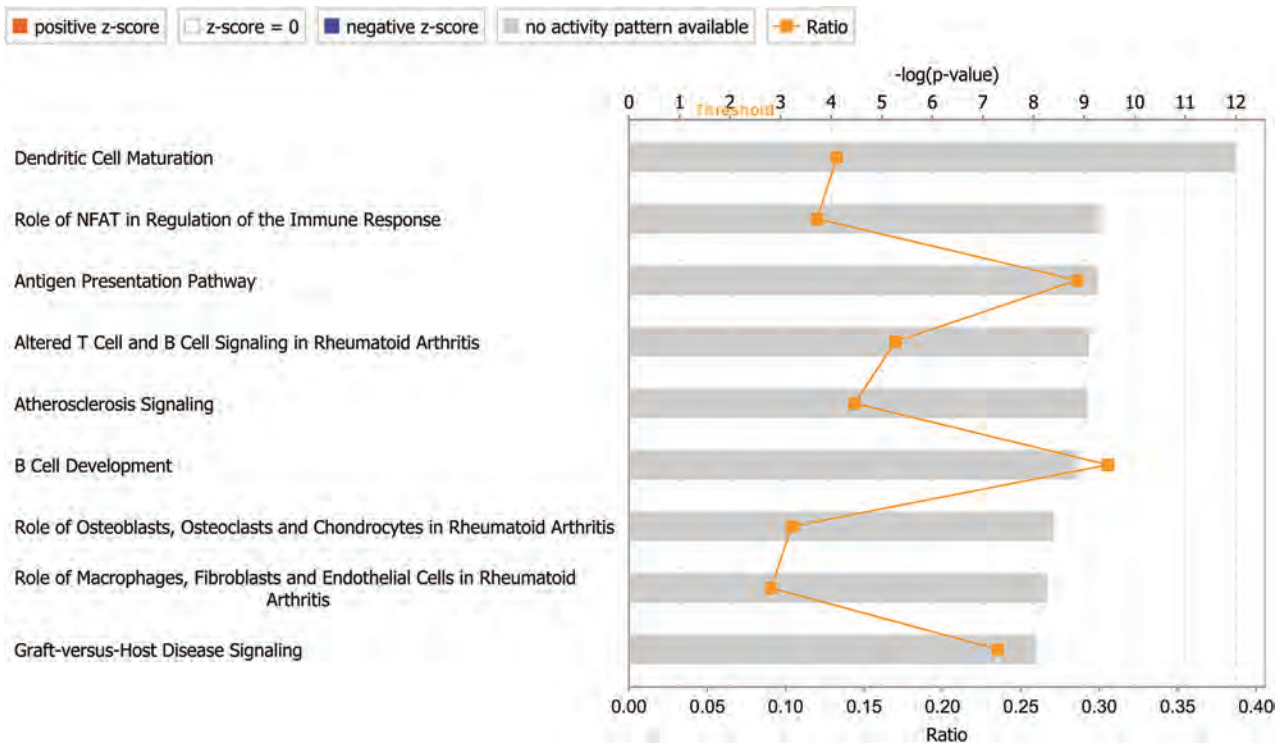


**FIG 2.** Top 10 canonical pathways identified by IPA. NFAT indicates nuclear factor of activated T cells.

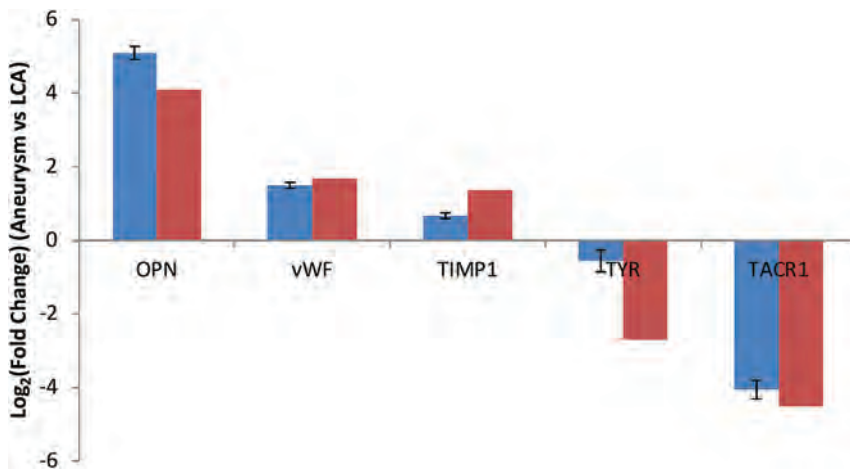


**FIG 3.** Validation of RNA-sequencing results by real-time polymerase chain reaction assays. The real-time polymerase chain reactions are indicated by blue bars, and RNA sequencing is indicated by red bars. LCA indicates left carotid artery; OPN, osteopontin; TIMP1, TIMP metalloproteinase inhibitor 1; TYR, tyrosinase; TACR1, tachykinin receptor 1; vWF, von Willebrand factor.

$1 \times 10^{-31}$ ). IPA identified 65 genes with expression directions consistent with increased activity of this pathway and 21 genes with inconsistent expression directions. CC chemokine-related molecules (ligands 2 [5.3-fold], 13 [8.7-fold], 14 [2.4-fold], 19 [7.0 fold], and 21 [8.2-fold]), and receptors type 1 [32.1-fold], 2 [13.1-fold], and 5 [24.1-fold]) were up-regulated in aneurysms compared with the control arteries. The expression of interleukins was increased over the controls (ie, 7 [3.6-fold], 8 [12.4-fold], 15 [3.9-fold], and  $1\beta$  [23.1-fold]), with interleukin 1 receptor type 1 also being up-regulated (2.1-fold). Caspase 1, involved in cleaving interleukin  $1\beta$  into its active form, also demonstrated increased expression (11.6-fold). It is worth noting that the inter-

leukin 1 receptor antagonist, an inhibitor of the interleukin 1 receptor, was also up-regulated in the aneurysms compared with the control (25.0-fold).

**Cellular Migration.** Cellular migration is up-regulated (z score, 4.587;  $P = 8 \times 10^{-43}$ ). One hundred eighteen genes with regulation directions consistent with increased migration were identified, and 61 genes with inconsistent expression directions were identified. Those involved with endothelial cell migration, which were highly expressed in aneurysms over that of the controls, included osteopontin, neuregulin 1, and fibroblast growth factor 1. Oxidized low-attenuation lipoprotein receptor 1, thrombospondin 1, and selectin E showed expression directions inconsistent with increased cellular migration in the aneurysms compared with the controls.

rysms compared with the controls.

**Validation of Microarray Data.** Verification of differential gene expression in the aneurysm and control arteries was performed for 5 selected genes. Microarray gene-expression levels were comparable with those obtained by real-time polymerase chain reactions (Fig 3).

## DISCUSSION

In our study we found differential expression in a large assortment of genes in tissue from experimental aneurysms compared with

the contralateral common carotid arteries. The differentially expressed genes included groups related to the inflammatory response, cellular migration, and coagulation, which may provide insight into the biologic environment of unruptured human intracranial saccular aneurysms.

The pathways up-regulated in aneurysms are involved primarily in the immune response. The top 4 pathways all center around the major histocompatibility complex, which is in agreement with literature on human intracranial aneurysms.<sup>38,39</sup>

Increased expression related to inflammation was noted in human intracranial aneurysms in a number of studies.<sup>38-43</sup> In particular, the up-regulation of genes related to the major histocompatibility complex,<sup>38,39</sup> the complement system,<sup>41-43</sup> interleukins,<sup>42</sup> and chemokines<sup>38,42,43</sup> has been observed. These same inflammation markers were found in our study to be up-regulated, indicating that the rabbit saccular aneurysm model maintains fidelity to the human aneurysm with respect to inflammation.

These inflammatory molecules may be up-regulated in response to a decrease in regulatory miRNA. miR-1 and miR-204-5p were both down-regulated in the tissue. miR-1 is predicted to target *CCL2* and *CXCL6* and has been observed to target *CXCR4*,<sup>44</sup> among others. miR-204-5p is predicted to target *CCR2*, *CCR5*, *CXCR4*, and *IL1B*, among others. miR-1 was reported to be down-regulated in human intracranial aneurysms and associated with an increased inflammatory response,<sup>14</sup> which is in contrast to experimentally induced rat cerebral aneurysm models, which have shown increased levels of miR-1.<sup>15</sup>

Previous studies reported down-regulation of inflammatory response genes at 2 weeks in the rabbit model.<sup>24</sup> The wider array of genes accessible via RNA sequencing in our study revealed a large number of genes with expressions consistent with increased activity of this pathway. Our results are consistent with the previous results with respect to calcium-binding glycoprotein osteonectin, which was found to be up-regulated in both studies. Although we observed a lack of histologic evidence for inflammation in the rabbit aneurysm model,<sup>45</sup> the differential expression of inflammation-related pathways noted in this study is in accordance with that in other human studies.<sup>38-43</sup>

Kriscsek et al<sup>38</sup> noted differentially regulated networks that had functions including cellular movement. In the first network they mentioned related to cellular movement, 9 of their 19 overexpressed genes were found to be overexpressed in our study as well, with none of the remaining 10 demonstrating underexpression.

*ANKRD1* was the most up-regulated gene in our dataset, which may indicate that aneurysms heal via a wound-healing pathway. A dramatic increase in the expression of this gene is associated with tissue damage, and it plays an important role in the following wound-healing process.<sup>46,47</sup> One of its modes of action is to regulate matrix metalloproteinases 13 and 10, which are involved in extracellular matrix remodeling.<sup>48</sup> *ANKRD1* has yet to receive attention in the context of aneurysm growth and healing, but its connection with matrix metalloproteinases and the wound-healing pathway, and that it was strongly up-regulated in our model, suggest that it should be a gene of interest.

*TACR1* is the most down-regulated gene in our dataset, and it also relates to matrix metalloproteinase regulation. It is associated with increased expression of matrix metalloproteinase 2,<sup>49</sup> which our

group previously reported as being differentially expressed early after aneurysm formation.<sup>45</sup> The fact that the most up-regulated and most down-regulated genes are involved in matrix metalloproteinase regulation is reflective of the fact that the role of matrix metalloproteinases in aneurysm growth, healing, and rupture is complex, being involved both for the weakening of the aneurysm wall and also the migration of endothelial cells to the neck of the aneurysm.

Our study was limited. A rabbit RNA database was used for messenger RNA expression, whereas human databases were used for miRNA because a rabbit miRNA database is not available. The RNA collected was not from a single cell type, and bias may have been introduced by the presence of cells in the aneurysm different than those in the left common carotid artery. We used IPA for pathway analysis; different software can yield different results regarding the determination of a pathway as having been up- or down-regulated. Also, “canonical” is essentially a meaningless designation, though it is the term used in the IPA software.

## CONCLUSIONS

Rabbit saccular aneurysms show differential expression in a number of pathways previously reported to play roles in aneurysm biology. This expression is dominated by antigen presentation and the inflammatory response. *TACR1* and *ANKRD1* are genes with regulatory functions over matrix metalloproteinase activity, and their roles in aneurysm biology require further elucidation.

## ACKNOWLEDGMENTS

We thank Fariborz Rakhshan Rohakhtar, Debra A. Schultz, and Christopher Kolbert (Gene Expression Core) and Jared Evans, Daniel O'Brien, and Jamie Davila (Division of Biomedical Statistics and Informatics, Mayo Clinic).

Disclosures: Jennifer S. McDonald—UNRELATED: Grants/Grants Pending: GE Healthcare.\* Comments: Investigator-initiated research grant for contrast-induced nephropathy. David F. Kallmes—UNRELATED: Board Membership: GE Healthcare, Comments: Cost-effectiveness board; Consultancy: ev3,\* Comments: Preclinical and clinical trials; Grants/Grants Pending: Microvention, ev3, Codman, Sequent, SurModics, and NeuroSigma, Comments: Preclinical research and clinical trials; Royalties: UVA Patent Foundation, Comments: Spine fusion. Ramanathan Kadirvel—RELATED: Grant: NIH (R01 NS076491).\* \*Money paid to the institution.

## REFERENCES

1. Chung B, Mut F, Kadirvel R, et al. **Hemodynamic analysis of fast and slow aneurysm occlusions by flow diversion in rabbits.** *J Neurointerv Surg* 2014 Oct 20 [Epub ahead of print] CrossRef Medline
2. Cebral JR, Raschi M, Mut F, et al. **Analysis of flow changes in side branches jailed by flow diverters in rabbit models.** *Int J Numer Method Biomed Eng* 2014;30:988–99 CrossRef Medline
3. Strother CM, Jiang J. **Intracranial aneurysms, cancer, x-rays, and computational fluid dynamics.** *AJNR Am J Neuroradiol* 2012;33:991–92 CrossRef Medline
4. Cebral JR, Mut F, Raschi M, et al. **Analysis of hemodynamics and aneurysm occlusion after flow-diverting treatment in rabbit models.** *AJNR Am J Neuroradiol* 2014;35:1567–73 CrossRef Medline
5. Karmonik C, Yen C, Gabriel E, et al. **Quantification of speed-up and accuracy of multi-CPU computational flow dynamics simulations of hemodynamics in a posterior communicating artery aneurysm of complex geometry.** *J Neurointerv Surg* 2013;5(suppl 3):iii48-55 CrossRef Medline
6. Xiao L, Wang JY. **RNA-binding proteins and microRNAs in gastrointestinal epithelial homeostasis and diseases.** *Curr Opin Pharmacol* 2014;19:46–53 CrossRef Medline

7. Zhang J, Le TD, Liu L, et al. **Inferring condition-specific miRNA activity from matched miRNA and mRNA expression data.** *Bioinformatics* 2014;30:3070–77 CrossRef Medline
8. Wu CW, Cheng YW, Hsu NY, et al. **MiRNA-221 negatively regulated downstream p27Kip1 gene expression involvement in pterygium pathogenesis.** *Mol Vis* 2014;20:1048–56 Medline
9. Naito Y, Yasuno K, Tagawa H, et al. **MicroRNA-145 is a potential prognostic factor of scirrhous type gastric cancer.** *Oncol Rep* 2014; 32:1720–26 CrossRef Medline
10. Peng SC, Liao CT, Peng CH, et al. **MicroRNAs MiR-218, MiR-125b, and Let-7g predict prognosis in patients with oral cavity squamous cell carcinoma.** *PLoS One* 2014;9:e102403 CrossRef Medline
11. Boele J, Persson H, Shin JW, et al. **PAPD5-mediated 3' adenylation and subsequent degradation of miR-21 is disrupted in proliferative disease.** *Proc Natl Acad Sci U S A* 2014;111:11467–72 CrossRef Medline
12. Li KK, Xia T, Ma FM, et al. **miR-106b is overexpressed in medulloblastomas and interacts directly with PTEN.** *Neuropathol Appl Neurobiol* 2015;41:145–64 CrossRef Medline
13. Jin H, Li C, Ge H, et al. **Circulating microRNA: a novel potential biomarker for early diagnosis of intracranial aneurysm rupture a case control study.** *J Transl Med* 2013;11:296 CrossRef Medline
14. Jiang Y, Zhang M, He H, et al. **MicroRNA/mRNA profiling and regulatory network of intracranial aneurysm.** *BMC Med Genomics* 2013;6:36 CrossRef Medline
15. Lee HJ, Yi JS, Lee HJ, et al. **Dysregulated expression profiles of MicroRNAs of experimentally induced cerebral aneurysms in rats.** *J Korean Neurosurg Soc* 2013;53:72–76 CrossRef Medline
16. Li L, Sima X, Bai P, et al. **Interactions of miR-34b/c and TP53 polymorphisms on the risk of intracranial aneurysm.** *Clin Dev Immunol* 2012;2012:567586 CrossRef Medline
17. Leeper NJ, Raiesdana A, Kojima Y, et al. **MicroRNA-26a is a novel regulator of vascular smooth muscle cell function.** *J Cell Physiol* 2011;226:1035–43 CrossRef Medline
18. Kadirvel R, Ding YH, Dai D, et al. **Differential gene expression in well-healed and poorly healed experimental aneurysms after coil treatment.** *Radiology* 2010;257:418–26 CrossRef Medline
19. Dai D, Ding YH, Danielson MA, et al. **Endovascular treatment of experimental aneurysms with use of fibroblast transfected with replication-deficient adenovirus containing bone morphogenetic protein-13 gene.** *AJNR Am J Neuroradiol* 2008;29:739–44 CrossRef Medline
20. Ding YH, Dai D, Lewis DA, et al. **Angiographic and histologic analysis of experimental aneurysms embolized with platinum coils, Matrix, and HydroCoil.** *AJNR Am J Neuroradiol* 2005;26:1757–63 Medline
21. Dai D, Yong-Hong D, Rezek I, et al. **Healing of saccular aneurysms following platinum coil embolization: lack of improved efficacy with vitamin C supplementation.** *J Neurointerv Surg* 2013;5:591–96 CrossRef Medline
22. Ding YH, Lewis DA, Kadirvel R, et al. **The Woven EndoBridge: a new aneurysm occlusion device.** *AJNR Am J Neuroradiol* 2011;32:607–11 CrossRef Medline
23. Mangrum WI, Farassati F, Kadirvel R, et al. **mRNA expression in rabbit experimental aneurysms: a study using gene chip microarrays.** *AJNR Am J Neuroradiol* 2007;28:864–69 Medline
24. Kadirvel R, Ding YH, Dai D, et al. **Gene expression profiling of experimental saccular aneurysms using deoxyribonucleic acid microarrays.** *AJNR Am J Neuroradiol* 2008;29:1566–69 CrossRef Medline
25. Kadirvel R, Ding YH, Dai D, et al. **Gene expression changes: five years after creation of elastase-induced aneurysms.** *J Vasc Interv Radiol* 2011;22:1447–51.e2 CrossRef Medline
26. Oszolak F, Milos PM. **RNA sequencing: advances, challenges and opportunities.** *Nat Rev Genet* 2011;12:87–98 CrossRef Medline
27. Altes TA, Cloft HJ, Short JG, et al. **1999 ARRS Executive Council Award. Creation of saccular aneurysms in the rabbit: a model suitable for testing endovascular devices.** *AJR Am J Roentgenol* 2000;174:349–54 CrossRef Medline
28. Schroeder A, Mueller O, Stocker S, et al. **The RIN: an RNA integrity number for assigning integrity values to RNA measurements.** *BMC Mol Biol* 2006;7:3 CrossRef Medline
29. Lanzino G, Wakhloo AK, Fessler RD, et al. **Efficacy and current limitations of intravascular stents for intracranial internal carotid, vertebral, and basilar artery aneurysms.** *J Neurosurg* 1999;91: 538–46 CrossRef Medline
30. Wang L, Wang S, Li W. **RSeQC: quality control of RNA-seq experiments.** *Bioinformatics* 2012;28:2184–85 CrossRef Medline
31. Trapnell C, Pachter L, Salzberg SL. **TopHat: discovering splice junctions with RNA-Seq.** *Bioinformatics* 2009;25:1105–11 CrossRef Medline
32. Langmead B, Trapnell C, Pop M, et al. **Ultrafast and memory-efficient alignment of short DNA sequences to the human genome.** *Genome Biol* 2009;10:R25 CrossRef Medline
33. Anders S, Pyl TP, Huber W. **HTSeq—a Python framework to work with high-throughput sequencing data.** *Bioinformatics* 2015;31: 166–69 CrossRef Medline
34. Robinson MD, McCarthy DJ, Smyth GK. **edgeR: a Bioconductor package for differential expression analysis of digital gene expression data.** *Bioinformatics* 2010;26:139–40 CrossRef Medline
35. Khoo AA, Ogrizek-Tomas M, Bulovic A, et al. **ExoLocator—an online view into genetic makeup of vertebrate proteins.** *Nucleic Acids Res* 2014;42:D879–81 CrossRef Medline
36. Piotin M, Blanc R, Spelle L, et al. **Stent-assisted coiling of intracranial aneurysms: clinical and angiographic results in 216 consecutive aneurysms.** *Stroke* 2010;41:110–15 CrossRef Medline
37. Benjamini Y, Hochberg Y. **Controlling the false discovery rate—a practical and powerful approach to multiple testing.** *J Roy Stat Soc B Met* 1995;57:289–300
38. Krischek B, Kasuya H, Tajima A, et al. **Network-based gene expression analysis of intracranial aneurysm tissue reveals role of antigen presenting cells.** *Neuroscience* 2008;154:1398–407 CrossRef Medline
39. Peters DG, Kassam AB, Feingold E, et al. **Molecular anatomy of an intracranial aneurysm: coordinated expression of genes involved in wound healing and tissue remodeling.** *Stroke* 2001;32:1036–42 CrossRef Medline
40. Chalouhi N, Ali MS, Jabbour PM, et al. **Biology of intracranial aneurysms: role of inflammation.** *J Cereb Blood Flow Metab* 2012;32: 1659–76 CrossRef Medline
41. Tulamo R, Frösen J, Junnikkala S, et al. **Complement system becomes activated by the classical pathway in intracranial aneurysm walls.** *Lab Invest* 2010;90:168–79 CrossRef Medline
42. Shi C, Awad IA, Jafari N, et al. **Genomics of human intracranial aneurysm wall.** *Stroke* 2009;40:1252–61 CrossRef Medline
43. Pera J, Korostynski M, Krzyzowski T, et al. **Gene expression profiles in human ruptured and unruptured intracranial aneurysms: what is the role of inflammation?** *Stroke* 2010;41:224–31 CrossRef Medline
44. Leone V, D'Angelo D, Rubio I, et al. **Mir-1 is a tumor suppressor in thyroid carcinogenesis targeting CCND2, CXCR4, and SDF-1 $\alpha$ .** *J Clin Endocrinol Metab* 2011;96:E1388–98 CrossRef Medline
45. Kadirvel R, Ding YH, Dai D, et al. **The influence of hemodynamic forces on biomarkers in the walls of elastase-induced aneurysms in rabbits.** *Neuroradiology* 2007;49:1041–53 CrossRef Medline
46. Samaras SE, Shi Y, Davidson JM. **CARP: fishing for novel mechanisms of neovascularization.** *J Investig Dermatol Symp Proc* 2006;11: 124–31 CrossRef Medline
47. Samaras SE, Chen B, Koch SR, et al. **26S proteasome regulation of Ankrd1/CARP in adult rat ventricular myocytes and human microvascular endothelial cells.** *Biochem Biophys Res Commun* 2012;425: 830–35 CrossRef Medline
48. Almodóvar-García K, Kwon M, Samaras SE, et al. **ANKRD1 acts as a transcriptional repressor of MMP13 via the AP-1 site.** *Mol Cell Biol* 2014;34:1500–11 CrossRef Medline
49. Mou L, Kang Y, Zhou Y, et al. **Neurokinin-1 receptor directly mediates glioma cell migration by up-regulation of matrix metalloproteinase-2 (MMP-2) and membrane type 1-matrix metalloproteinase (MT1-MMP).** *J Biol Chem* 2013;288:306–18 CrossRef Medline

# Evolution of Flow-Diverter Endothelialization and Thrombus Organization in Giant Fusiform Aneurysms after Flow Diversion: A Histopathologic Study

I. Szikora, E. Turányi, and M. Marosfoi



## ABSTRACT

**BACKGROUND AND PURPOSE:** Treatment of giant fusiform aneurysms with flow diverters has been associated with a relatively high rate of complications. Our goal was to study the evolution of flow-diverter endothelialization and thrombus organization at different time points after flow-diverter treatment in giant fusiform aneurysms to better understand reasons for flow-diverter thrombosis and delayed aneurysm ruptures.

**MATERIALS AND METHODS:** Two giant anterior and 2 posterior circulation aneurysms, all of which had partially thrombosed before treatment, were studied. An unruptured, untreated posterior circulation aneurysm was used as a control. Each specimen was removed at 7 days or at 6, 9, or 13 months after flow-diverter treatment. The 3 patients who survived longer than 7 days were followed up by angiography and MR imaging. Formaldehyde-fixed paraffin-embedded sections were stained by using H&E, Van Gieson elastic, CD34, h-Caldesmon, and Picrosirius stains and studied by light microscopy.

**RESULTS:** According to angiography, aneurysms were found to be obliterated partially at 6 and 9 months and completely at 13 months. MR imaging revealed that mass effect remained unchanged in each case. Sections of the flow diverter within the normal parent artery were covered by an endothelialized fibrous layer as early as 6 months, but there was no tissue coverage or endothelialization seen even at 13 months inside the aneurysm itself. Each treated aneurysm had a thin wall with complete lack of smooth muscle cells. No signs of thrombus organization were found at any of the time points studied.

**CONCLUSIONS:** Endothelialization of the flow diverter in giant fusiform aneurysms may not occur and thrombus organization may not be initiated inside these aneurysms for as long as 1 year, which explains delayed flow-diverter thrombosis and the possibility of delayed ruptures.

**ABBREVIATIONS:** GFA = giant fusiform aneurysm; FD = flow diverter; PED = Pipeline embolization device

**B**ecause of the limited efficacy of endovascular coil packing, intravascular flow diversion has been proposed recently for large and giant aneurysms.<sup>1-6</sup> The relative safety and high efficacy of flow diversion in saccular aneurysms presenting with mass effect have been reported.<sup>1,7,8</sup> However, a high rate of thromboem-

bolic and hemorrhagic complications has been found in giant fusiform aneurysms (GFAs), particularly in those located in the posterior fossa.<sup>9,10</sup>

Flow diversion is expected to produce aneurysm thrombosis and facilitate subsequent thrombus organization. Simultaneously, the flow diverter (FD) is supposed to become covered by an intimal layer, sealing the aneurysm cavity from the parent artery and preventing it from thromboembolic complications. Considering the poor results in giant fusiform aneurysms, it was reasonable to assume that one or both of these mechanisms did not work as expected in these lesions. The primary purpose of this study was to investigate the efficacy of these processes in GFAs. We also analyzed whether the clinical problems were related to the location (posterior circulation) or the morphology of aneurysms.

## MATERIALS AND METHODS

### Treatment and Follow-Up

A total of 5 GFAs were studied as approved by our institutional internal review board. One unruptured, nonthrombosed, and

Received July 19, 2014; accepted after revision February 4, 2015.

From the National Institute of Clinical Neurosciences (I.S., M.M.), Budapest, Hungary; and 1st Department of Pathology (E.T.), Semmelweis University Medical School, Budapest, Hungary.

This study was supported in part by grant KTIA\_NAP\_13-1-2013-0001 from the National Brain Research Program of Hungary.

Paper previously presented in part at: 12th Congress of the World Federation of Interventional and Therapeutic Neuroradiology (WFITN), November 9–13, 2013; Buenos Aires, Argentina.

Please address correspondence to I. Szikora, National Institute of Clinical Neurosciences, Amerikai ut 57, H-1145 Budapest, Hungary; e-mail: h13424szi@ella.hu

Indicates open access to non-subscribers at [www.ajnr.org](http://www.ajnr.org)

Indicates article with supplemental on-line tables.

<http://dx.doi.org/10.3174/ajnr.A4336>

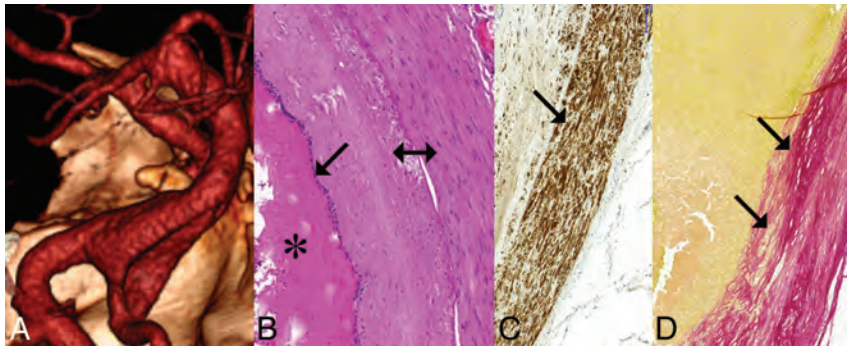


**FIG 1.** Unruptured, nonthrombosed giant fusiform aneurysm involving the vertebrobasilar junction. *A*, Volume-rendering 3D reconstruction of a CTA, demonstrating fusiform aneurysm of the vertebrobasilar junction. *B*, Histologic section of the fusiform aneurysm showing fresh clot inside the aneurysm (*star*), intact elastic lamina (*arrow*), and thick aneurysm wall (*double arrow*) (H&E staining). *C*, Section of the aneurysm wall showing a thick layer of smooth muscle cells (*arrow*) (h-Caldesmon staining). *D*, Section of the aneurysm wall showing a thick subintimal layer of connective tissue (Picrosirius staining) (*arrows*) and no connective tissue invasion into the thrombus inside the aneurysm, indicating a lack of thrombus organization.

untreated aneurysm was removed 7 days after the patient died as a result of a stroke in the brain stem. This aneurysm was used as a control. Each of the other ones was partially thrombosed, treated with an FD, and removed at 7 days or 6, 9, or 13 months after the treatment after the patients died as a result of either hemorrhagic or thromboembolic complications. Two of these aneurysms were located in the posterior and the other 2 in the anterior circulation, and all were symptomatic. Alternative surgical or endovascular treatment options, including parent artery occlusion, were discussed with each patient and excluded after multidisciplinary consultation in each case. Of the 4 patients, 3 were treated with double antiplatelets (100 mg of acetylsalicylic acid and 75 mg of clopidogrel) before and during their follow-up period; the fourth patient (patient 5) (On-line Table 1) was on dual antiplatelets for 9 months and single-antiplatelet therapy with clopidogrel afterward. Platelet functions were tested by the Platelet Function Assay (PFA 100; Siemens Medical Systems, Erlangen, Germany), adenosine diphosphate closure time (ADP-CT; Siemens), and the Innovance PY2 test (Siemens) and found to be sufficiently inhibited before the procedure. No further tests were performed during the follow-up. Four- to 5-mm-diameter telescopic Surpass FDs (Stryker Neurovascular, Kalamazoo, Michigan) were used in both posterior circulation aneurysms, and double-layer 3.5- to 4.5-mm-diameter Pipeline embolization devices (PEDs) (Covidien, Irvine, California) were applied in the anterior circulation aneurysms. All patients were scheduled for follow-up MR imaging and DSA studies at 5–6 and 12 months after the procedure. All the patients received methylprednisolone (2 × 250 mg/day) for at least 2 days before and 3–5 days after the procedure, and the dose was decreased gradually afterward (On-line Table 1).

### Histopathologic Analysis

Each aneurysm was removed during autopsy, fixed in buffered formaldehyde, sectioned, and stained with H&E and Van Gieson elastic stains. For immunohistochemistry, CD34 was used to demonstrate endothelium, h-Caldesmon to visualize smooth muscle cells, and Picrosirius to detect connective tissue. Sections were studied by light microscopy. Special attention was given to the identification of any tissue coverage on the internal surface

of the FD, to the structure of the aneurysm wall, and any signs of smooth muscle cell invasion or connective tissue formation inside the intra-aneurysmal clot, indicating thrombus organization.

## RESULTS

### Case 1: Untreated GFA of the Vertebrobasilar Junction

The cavity of this control aneurysm was filled with fresh thrombus. The aneurysm wall was well structured and had a strong muscular layer. There were no signs of inflammation within the wall or any signs of thrombus organization by immunohistochemistry within the cavity (Fig 1, On-line Table 2).

### Case 2: GFA of the Vertebrobasilar Junction 7 Days after FD Treatment

The patient died as a result of SAH related to an intraprocedural aneurysm rupture. No tissue layer was found covering the internal surface of the FD. The aneurysm cavity was filled with unorganized thrombus. The aneurysm wall was thin and fragmented with no smooth muscle cells identified in it (On-line Table 2).

### Case 3: Partially Thrombosed GFA of the MCA

This patient died as a result of a major MCA infarct that developed because of occlusion of one of the M2 branches distal to the FD 6 months after the procedure implanting the FD.

A section of the FD placed within the normal artery proximal to the aneurysm was covered by a thick tissue layer consisting of smooth muscle cells and covered by a single endothelial cell layer corresponding to intimal hyperplasia. The FD inside the aneurysm was free of any tissue coverage. The GFA was filled with unorganized clot only, despite most of the aneurysm not being filled with contrast material (as detected by angiography at 6 months). There were no signs of smooth muscle cell invasion or connective tissue formation inside the thrombus. The aneurysm wall was thick and fragmented and showed signs of chronic inflammation, including lymphocytes and macrophages (Fig 2, On-line Table 2).

### Case 4: GFA of the Vertebrobasilar Junction 9 Months after FD Treatment

This patient reportedly died as a result of a brain stem infarct, but no MR imaging was performed to confirm the diagnosis. The FD was patent, and its internal surface was covered by a thin fibrin layer only, with no smooth muscle cells or endothelial lining. The aneurysm was filled with fresh thrombus. There were no signs of clot organization. According to MR imaging and angiography, the size and filling of this aneurysm did not change at 6 months. The wall of the aneurysm was thin and fragmented (On-line Table 2).

### Case 5: GFA of the ICA 13 Months after FD Treatment

This patient died as a result of a major MCA infarct that developed after a sudden thrombosis of the FD construct, as confirmed by

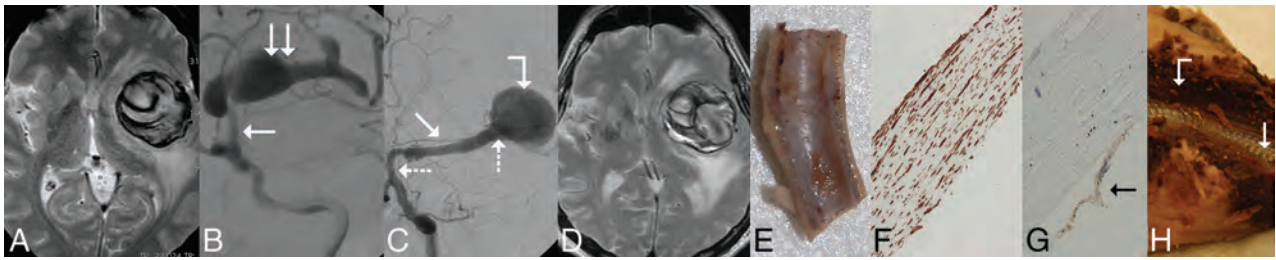


**FIG 2.** Giant, partially thrombosed, fusiform aneurysm of the left MCA treated with a construct of 2 Pipeline embolization devices; the specimen was removed 6 months after PED implantation. *A*, T2-weighted MR image before treatment, showing large mass of mixed signal intensity, associated with significant mass effect and white matter edema, consistent with a giant aneurysm. *B*, DSA of the same aneurysm. The arrow points to the proximal, normal portion of the M1 section, and the double arrow points to the fusiform aneurysm expanding into the M2 sections. *C*, Follow-up DSA 6 months later showing “angiographic reconstruction” of the distal M1 section (*arrow*), significant enlargement of the dilated proximal section of the cranial M2 branch (*bent arrow*), and lack of filling (occlusion) of this branch distal to the dilation. The PED construct can be seen between the 2 dotted arrows. *D*, Follow-up T2-weighted MR image from 6 months after treatment showing unchanged mass effect, edema, and mixed signal intensity. *E*, Longitudinal cut of the proximal landing zone. The luminal surface of the PED is covered by a smooth tissue layer. *F*, Microscopic section of the layer removed from the luminal surface of the PED showing neointimal growth consisting of smooth muscle cells (h-Caldesmon staining). *G*, The same layer is covered by a single cell layer of endothelium (*arrow*) (CD34 staining). *H*, Macroscopic cross-section of the specimen at the level of the fusiform aneurysm. The implanted PED construct (*arrow*) is uncovered and surrounded by fresh clot (*bent arrow*).

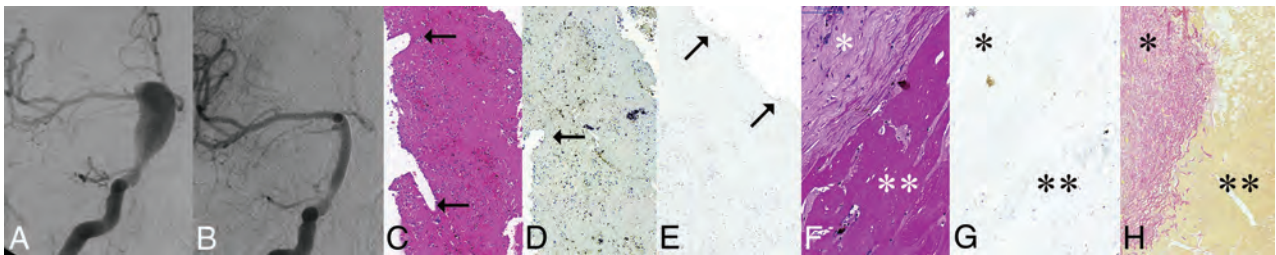


**FIG 3.** Giant, partially thrombosed fusiform aneurysm of the right ICA treated by a construct of 2 PEDs. The specimen was removed 13 months after treatment. *A*, DSA before treatment showing the circulating portion of the partially thrombosed GFA involving the supraclinoid ICA on the right. *B*, DSA 1 year after treatment showing angiographic reconstruction of the entire length of the fusiform aneurysm. *C*, Thin fibrin layer removed from the luminal surface of the PED construct by H&E staining. The arrows in *C* and *D* point to the impressions of the flow-diverter struts on the outer surface of the fibrin layer. *D*, h-Caldesmon staining fails to show smooth muscle cells inside this layer. *E*, CD34 fails to show endothelial coverage on the luminal surface (*arrows*) of the layer. *F*, Histologic section showing a thick aneurysm wall with low cell attenuation (*star*) and fresh thrombus underneath the wall (*double star*) by H&E staining. *G*, h-Caldesmon staining fails to show any smooth muscle cells within the wall (*star*) or invasion into the clot (*double star*). *H*, Picosirius staining reveals subintimal connective tissue within the thick aneurysm wall (*star*) but no invasion into the thrombus (*double star*).

DSA 1 month after the last angiography, while still on a single-antiplatelet therapy with clopidogrel.

The internal surface of the FD inside the aneurysm was covered again by a thin fibrin layer only. Despite the aneurysm not being visible by angiography, the cavity of the aneurysm was filled with fresh clot only. There were signs of chronic inflammation inside the wall, which contained no smooth muscle cells. There were no signs of smooth muscle cell invasion or any other signs of thrombus organization (Fig 3, On-line Table 2).

MR imaging showed that regardless of the angiographic occlusion of the GFA, none of the treated aneurysms changed in either size or signal intensity throughout the follow-up period up to 9 months (Fig 2). No perforator occlusions were identified in any of the follow-up angiograms.

## DISCUSSION

Fusiform aneurysms of the circle of Willis represent 3%–13% of all intracranial aneurysms, with most located in the posterior circulation.<sup>11</sup> Their etiology is unclear; both atherosclerosis and dissection have been proposed as pathogenetic factors.<sup>12</sup> Some may present with subarachnoid hemorrhage, and these are generally considered dissecting aneurysms.<sup>13</sup> Others may grow very large or

giant and become symptomatic via neural compression or ischemia. The clinical course is generally progressive and, without successful treatment, almost always devastating.

Treatment options are limited. Drake and Peerless<sup>14</sup> reported the results of 120 patients surgically treated for GFAs. Seventy-six percent of these patients with an anterior circulation GFA had a good outcome, whereas only 67% of those with a vertebrobasilar aneurysm had a good outcome. The treatment mostly included parent artery occlusion. In a more recent series, 6 of 9 symptomatic lesions resulted in poor outcomes (1 with bypass surgery, 1 with attempted clipping, and 4 with no intervention). Only those for whom parent artery occlusion was feasible fared well.<sup>15</sup>

Among the endovascular techniques, parent artery occlusion remains the best option for those with good collateral circulation.<sup>16</sup> Reconstructive endovascular techniques, including FD-supported coiling or double-FD implantation, have been successfully applied for smaller fusiform aneurysms<sup>17,18</sup> but not for giant ones.

The introduction of FDs raised enthusiasm regarding reconstructive treatment of hardly treatable intracranial aneurysms, including GFAs. Fiorella et al<sup>19–21</sup> reported 4 such patients successfully treated by FD implantation and coil packing. However, these

publications were soon followed by reports on late complications, including late thrombosis of the FD within 2 years.<sup>9</sup> Of 13 delayed ruptures after FD treatment reported by Kulcsár et al,<sup>22</sup> 4 were in patients with a GFA. In a series by Siddiqui et al,<sup>10</sup> after FD treatment for posterior circulation GFAs in 7 patients, 4 patients died and 2 had a poor outcome.

This study was undertaken to investigate potential reasons for such poor results, particularly when compared with the better outcomes achieved in patients with saccular aneurysms, even when those aneurysms were large or giant.<sup>1</sup> In general, the low efficacy of coil packing in giant aneurysms is attributed to the inability of the coils to induce permanent thrombosis and endothelial lining of the neck. In such lesions, thrombus organization and neck endothelialization were not found 2–6 months after treatment with coils.<sup>23</sup> FDs are expected to initially induce aneurysm thrombosis by intra-aneurysmal flow reduction and to seal the aneurysm cavity off from the circulation by inducing neointimal coverage of the FD surface at the neck. This seal would allow the intrasaccular thrombus to be eventually organized. In animal models, neointimal lining of the PED has been demonstrated as early as 7 days after implantation in normal arterial sections and 4–8 weeks after treatment across the neck of saccular aneurysms.<sup>24,25</sup> Studies on the endothelialization of FDs in human subjects have not been reported yet. We hypothesized that the reason for the poor results in GFAs was the lack of thrombus organization inside the aneurysm, the lack of intimal coverage of the FD, or both. Thrombus organization was expected to be visualized in the form of smooth muscle cell invasion and connective tissue formation within the clot.<sup>26</sup> Intimal growth over the luminal surface of the FD device was expected to be seen as a tissue layer consisting of smooth muscle cells covered by endothelium.

The design of the FD did not seem to make any difference. Two types were used, and each diameter was chosen to match the diameter of the normal artery proximal and distal to the fusiform dilation as closely as possible. Because of the fusiform nature of the aneurysms, all the FDs were fully opened and reached their nominal diameter inside the aneurysm. Subsequently, the device-to-vessel diameter ratio did not affect the final metal coverage, which is supposed to be approximately 30% for each device. The Surpass device had higher pore attenuation than the PED (20–32 and 15–22 pores/mm<sup>2</sup>, respectively), but that did not influence the histologic outcome up to 9 months after treatment (On-line Table 1, patient 4).

The wall of the nonthrombosed control aneurysm contained a thick layer of smooth muscle cells consistent with myointimal hyperplasia.<sup>27</sup> In contrast, the walls of all treated aneurysms were fragmented with low cell attenuation, signs of inflammation, and a lack of smooth muscle cells. Inside the GFAs, there were no signs of smooth muscle cell invasion or connective tissue formation indicating clot organization, regardless of the length of follow-up (for as long as 13 months) and regardless of occlusion or patency of the aneurysm as seen on angiography. Clinical experience and experimental evidence have shown that the loss of mural cells is associated with an inability to transform intraluminal thrombus to stable scar tissue because of the lack of smooth muscle cells inside the wall.<sup>28</sup> Subsequently, the lack of thrombus organization is likely to be related to cellular loss of the sick wall in our GFAs.

All the treated aneurysms were partially thrombosed before treatment, which is likely to be the reason for their wall degeneration. The release of thrombocyte-derived growth factors and peroxidases from the luminal thrombus, together with deoxygenation of stagnating red blood cells and a subsequent lack of oxygen, are supposed to trigger cell death and inflammation inside the wall.<sup>27</sup> FDs may significantly reduce flow velocity within the aneurysm but cannot repair the aneurysm wall and facilitate clot organization because of the pre-existing lack of necessary smooth muscle cells. In fact, the stagnation induced by the FD may trigger further release of substances, such as matrix metalloproteinases, that damage the aneurysmal wall and increase the risk of rupture.<sup>22,29</sup>

Histology showed lack of thrombus organization, which was consistent with MR imaging findings, which showed no change in signal intensity or size of the aneurysms during the follow-up period. Considering that simultaneous angiography showed partial or complete occlusion of the aneurysm and reconstruction of the parent artery, one must keep in mind that nonfilling of an aneurysm by angiography indicates only that blood is not flowing inside the aneurysm any more, but it certainly does not indicate healing of the aneurysm.

Intimal coverage is necessary for preventing FD thrombosis without aggressive antiplatelet medication. In our patients, only the section of FD implanted within the normal parent artery and circumferentially covered by normal arterial wall got covered by neointima and endothelialized as early as 6 months (patient 3). The portion of the FD inside the GFA without any contact with normal vascular wall remained uncovered, and no endothelial cells were found at any time point inside the aneurysms for as long as 13 months after treatment. This finding is similar to the lack of endothelialization seen in aortic FD grafts.<sup>30</sup> Although this is a typical characteristic of fusiform aneurysms, the same phenomenon may occur in giant aneurysms with very broad necks. Under such circumstances, any lack of sufficient platelet inhibition may result in either distal embolization or FD thrombosis.

Because histologic findings were similar in anterior and posterior fossa aneurysms, these phenomena are likely related to the fusiform morphology rather than the location of the aneurysms.

This work was limited by the small number of samples and warrants further experimental and clinical pathologic studies. High-resolution vessel wall imaging and sequential MR imaging of giant aneurysms after FD treatment may help us to understand more thoroughly the process of aneurysm thrombosis and the role of the aneurysm wall in the thrombotic process.

## CONCLUSIONS

The results of this study confirm the hypothesis that in GFAs, thrombus organization and intimal coverage of the FD may not occur for more than 1 year, which leads to a prolonged risk of aneurysm rupture and FD thrombosis. The lack of thrombus organization does not seem to be related to FD design or aneurysm location and probably results from wall degeneration of partially thrombosed GFAs. Nonfilling of the aneurysm by angiography should not be interpreted as a sign of aneurysm healing. Because of their inefficacy, FDs should be considered for this pathology only if treatment is needed and no other option is available.

## ACKNOWLEDGMENTS

The authors sincerely acknowledge the contribution of Surpass Ltd. and Ajay Kumar Wakhloo for providing material support and advising in the procedures.

Disclosures: Istvan Szikora—UNRELATED: Board Membership: Covidien Neurovascular; Consultancy: Covidien Neurovascular, Stryker Neurovascular, and Codman Neurovascular.

## REFERENCES

1. Becske T, Kallmes DF, Saatci I, et al. **Pipeline for uncoilable or failed aneurysms: results from a multicenter clinical trial.** *Radiology* 2013; 267:858–68 CrossRef Medline
2. Lylyk P, Miranda C, Ceratto R, et al. **Curative endovascular reconstruction of cerebral aneurysms with the Pipeline embolization device: the Buenos Aires experience.** *Neurosurgery* 2009;64:632–42; discussion 642–43; quiz N6 CrossRef Medline
3. Szikora I, Berentei Z, Kulcsar Z, et al. **Treatment of intracranial aneurysms by functional reconstruction of the parent artery: the Budapest experience with the Pipeline embolization device.** *AJNR Am J Neuroradiol* 2010;31:1139–47 CrossRef Medline
4. Nelson PK, Lylyk P, Szikora I, et al. **The Pipeline embolization device for the intracranial treatment of aneurysms trial.** *AJNR Am J Neuroradiol* 2011;32:34–40 CrossRef Medline
5. Saatci I, Yavuz K, Ozer C, et al. **Treatment of intracranial aneurysms using the Pipeline flow-diverter embolization device: a single-center experience with long-term follow-up results.** *AJNR Am J Neuroradiol* 2012;33:1436–46 CrossRef Medline
6. Piano M, Valvassori L, Quilici L, et al. **Midterm and long-term follow-up of cerebral aneurysms treated with flow diverter devices: a single-center experience.** *J Neurosurg* 2013;118:408–16 CrossRef Medline
7. Szikora I, Marosfoi M, Salomváry B, et al. **Resolution of mass effect and compression symptoms following endoluminal flow diversion for the treatment of intracranial aneurysms.** *AJNR Am J Neuroradiol* 2013;34:935–39 CrossRef Medline
8. Sahlein DH, Fouladvand M, Becske T, et al. **Neuro-ophthalmologic outcomes from the Pipeline for uncoilable or failed aneurysms.** *J Neurosurg* 2015. In press
9. Fiorella D, Hsu D, Woo HH, et al. **Very late thrombosis of a Pipeline embolization device construct: case report.** *Neurosurgery* 2010;67(3 suppl):onsE313-14; discussion onsE314 CrossRef Medline
10. Siddiqui AH, Abila AA, Kan P, et al. **Panacea or problem: flow diverters in the treatment of symptomatic large or giant fusiform verte-brobasilar aneurysms.** *J Neurosurg* 2012;116:1258–66 CrossRef Medline
11. Park SH, Yim MB, Lee CY, et al. **Intracranial fusiform aneurysms: it's pathogenesis, clinical characteristics and managements.** *J Korean Neurosurg Soc* 2008;44:116–23 CrossRef Medline
12. Findlay JM, Hao C, Emery D. **Non-atherosclerotic fusiform cerebral aneurysms.** *Can J Neurol Sci* 2002;29:41–48 CrossRef Medline
13. Nakayama Y, Tanaka A, Kumate S, et al. **Giant fusiform aneurysm of the basilar artery: consideration of its pathogenesis.** *Surg Neurol* 1999;51:140–45 CrossRef Medline
14. Drake CG, Peerless SJ. **Giant fusiform intracranial aneurysms: re-view of 120 patients treated surgically from 1965 to 1992.** *J Neurosurg* 1997;87:141–62 CrossRef Medline
15. Nakatomi H, Segawa H, Kurata A, et al. **Clinicopathological study of intracranial fusiform and dolichoectatic aneurysms: insight on the mechanism of growth.** *Stroke* 2000;31:896–900 CrossRef Medline
16. Gobin YP, Viñuela F, Gurian JH, et al. **Treatment of large and giant fusiform intracranial aneurysms with Guglielmi detachable coils.** *J Neurosurg* 1996;84:55–62 CrossRef Medline
17. Lubicz B, Collignon L, Lefranc F, et al. **Circumferential and fusiform intracranial aneurysms: reconstructive endovascular treatment with self-expandable stents.** *Neuroradiology* 2008;50:499–507 CrossRef Medline
18. Devulapalli KK, Chowdhry SA, Bambakidis NC, et al. **Endovascular treatment of fusiform intracranial aneurysms.** *J Neurointerv Surg* 2013;5:110–16 CrossRef Medline
19. Fiorella D, Woo HH, Albuquerque FC, et al. **Definitive reconstruction of circumferential, fusiform intracranial aneurysms with the Pipeline embolization device.** *Neurosurgery* 2008;62:1115–20; discussion 1120–21 CrossRef Medline
20. Fiorella D, Albuquerque F, Gonzalez F, et al. **Reconstruction of the right anterior circulation with the Pipeline embolization device to achieve treatment of a progressively symptomatic, large carotid aneurysm.** *J Neurointerv Surg* 2010;2:31–37 CrossRef Medline
21. Fiorella D, Kelly ME, Albuquerque FC, et al. **Curative reconstruction of a giant midbasilar trunk aneurysm with the Pipeline embolization device.** *Neurosurgery* 2009;64:212–17; discussion 217 CrossRef Medline
22. Kulcsár Z, Houdart E, Bonafé A, et al. **Intra-aneurysmal thrombosis as a possible cause of delayed aneurysm rupture after flow-diver-sion treatment.** *AJNR Am J Neuroradiol* 2011;32:20–25 CrossRef Medline
23. Molyneux AJ, Ellison DW, Morris J, et al. **Histological findings in giant aneurysms treated with Guglielmi detachable coils: report of 2 cases with autopsy correlation.** *J Neurosurg* 1995;83:129–32 CrossRef Medline
24. Kallmes DF, Ding YH, Dai D, et al. **A new endoluminal, flow-disrupting device for treatment of saccular aneurysms.** *Stroke* 2007;38:2346–52 CrossRef Medline
25. Kadirvel R, Ding YH, Dai D, et al. **Cellular mechanisms of aneurysm occlusion after treatment with a flow diverter.** *Radiology* 2014;270:394–99 CrossRef Medline
26. Szikora I, Seifert P, Hanzely Z, et al. **Histopathologic evaluation of aneurysms treated with Guglielmi detachable coils or Matrix detachable microcoils.** *AJNR Am J Neuroradiol* 2006;27:283–88 Medline
27. Frösen J, Tulamo R, Paetau A, et al. **Saccular intracranial aneurysm: pathology and mechanisms.** *Acta Neuropathol* 2012;123:773–86 CrossRef Medline
28. Marbacher S, Marjamaa J, Bradacova K, et al. **Loss of mural cells leads to wall degeneration, aneurysm growth, and eventual rupture in a rat aneurysm model.** *Stroke* 2014;45:248–54 CrossRef Medline
29. Fontaine V, Jacob MP, Houard X, et al. **Involvement of the mural thrombus as a site of protease release and activation in human aortic aneurysms.** *Am J Pathol* 2002;161:1701–10 CrossRef Medline
30. McArthur C, Teodorescu V, Eisen L, et al. **Histopathologic analysis of endovascular stent grafts from patients with aortic aneurysms: does healing occur?** *J Vasc Surg* 2001;33:733–38 CrossRef Medline

# Intrasaccular Flow Disruption in Acutely Ruptured Aneurysms: A Multicenter Retrospective Review of the Use of the WEB

T. Liebig, C. Kabbasch, C. Strasilla, A. Berlis, W. Weber, L. Pierot, T. Patankar, X. Barreau, J. Dervin, A. Kuršumović, S. Rath, B. Lubicz, and J. Klisch



## ABSTRACT

**BACKGROUND AND PURPOSE:** Use of the WEB intra-aneurysmal flow-disruption device in unruptured wide-neck bifurcation aneurysms has proven safety and efficacy. However, ruptured aneurysms are underrepresented in existing studies. This retrospective multicenter study describes the use of the WEB in patients with a ruptured intracranial aneurysm.

**MATERIALS AND METHODS:** Ten centers contributed to this study. Clinical and procedural data of 47 patients with 52 aneurysms were analyzed retrospectively together with follow-up angiographies.

**RESULTS:** There were 37 anterior and 15 posterior circulation aneurysms with a neck size of  $\geq 4$  mm in 49 of 52 (94%) aneurysms; 45 (87%) aneurysms were  $< 10$  mm, and 2 were partially thrombosed. Successful placement of the WEB was possible in every case. Adjunctive devices were used in 8 of 52 (15%) aneurysms. Thromboembolic events were observed in 4 of 52 (8%) patients. Adverse events occurred in 15 patients with 16 aneurysms, 9 of which were potentially related to the WEB procedure (3 thromboembolic events, 5 protrusions, and 1 perforations; 2 perforations were caused by the wire or catheter), but none had a clinical impact. Four patients were retreated. Short-term follow-up in 25 of 39 patients revealed complete occlusion in 15 of 25 (60%), 5 of 25 (20%) with residual neck, and 5 of 25 (20%) with residual aneurysm filling. Short- to midterm imaging in 9 of 25 patients revealed complete occlusion in 5 (55.6%), residual neck in 2 (22%), and residual aneurysm filling in 2 (22%). Of 47 patients, 23 (49%) had an mRS score of 0, 1, or 2; 13 (28%) had an mRS score of 3 or 4; and none had an mRS score of 5 at discharge.

**CONCLUSIONS:** This retrospective series showed good procedural safety, feasibility, and stability of midterm occlusion in ruptured wide-neck bifurcation aneurysms.

**ABBREVIATIONS:** CLARITY = Clinical and Anatomical Results In the Treatment of Ruptured Intracranial Aneurysms; HH = Hunt and Hess; ATENA = Analysis of Treatment by Endovascular Approach of Nonruptured Aneurysms

The prevalence of intracranial aneurysms in the general population ranges from 0.2% to 9.0%.<sup>1,2</sup> Aneurysmal subarachnoid hemorrhage occurs at an annual incidence of 7–13 per

100,000 person-years in most Western countries. It is associated with a high mortality rate of up to 50% and a high morbidity rate for patients admitted to the hospital.<sup>3,4</sup> The risk of rupture increases with aneurysm size and location.<sup>5–9</sup> The primary purpose of treating a ruptured aneurysm is to prevent recurrent hemorrhage in the acute and subacute phases.<sup>10</sup> The preferred treatment in patients with SAH, endovascular coil occlusion may be limited by aneurysm geometry, particularly in wide-neck or broad-based aneurysms that typically necessitate the use of a stent for proper reconstruction of the neck and sufficient occlusion of the aneurysm sac. This treatment usually requires the use of antiplatelet medication, which may impose an increased risk in the presence of a recently ruptured aneurysm.<sup>11</sup>

The WEB aneurysm embolization system (WEB; Sequent Medical, Aliso Viejo, California) is a self-expanding microbraid mesh implant delivered through a microcatheter and sized to fit

Received October 9, 2014; accepted after revision February 2, 2015.

From the Department of Radiology (T.L., C.K.), Universitätsklinikum Köln, Cologne, Germany; Department of Diagnostic and Interventional Radiology and Neuroradiology (C.S., J.K.), Helios General Hospital, Erfurt, Germany; Department of Diagnostic Imaging and Neuroradiology (A.B.), Klinikum Augsburg, Augsburg, Germany; Department of Neuroradiology (W.W.), Knappschafts Krankenhaus, Recklinghausen, Germany; Department of Neuroradiology (W.W.), Universitätsklinikum Knappschafts Krankenhaus Bochum, Bochum, Germany; Department of Neuroradiology (L.P.), Hôpital Maison-Blanche, Université Reims-Champagne-Ardenne, Reims, France; Leeds General Infirmary (T.P.), Leeds, United Kingdom; Department of Neuroimaging (X.B.), CHU Pellegrin, Bordeaux, France; Southern General Hospital (J.D.), Glasgow, United Kingdom; Department of Neuroradiology (A.K., S.R.), Klinikum Deggendorf, Deggendorf, Germany; and Department of Neuroradiology (B.L.), Erasme University Hospital, Brussels, Belgium.

Please address correspondence to Thomas Liebig, MD, Department of Radiology, Universitätsklinikum Köln, Kerpener Str 62, 50937 Köln, Cologne, Germany; e-mail: thomas.liebig@uk-koeln.de

Indicates open access to non-subscribers at www.ajnr.org

<http://dx.doi.org/10.3174/ajnr.A4347>

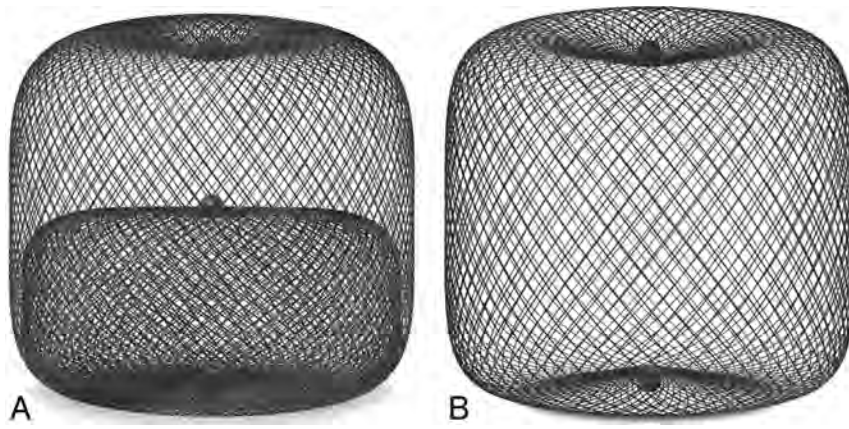


**FIG 1.** A, WEB-DL, a double-layer microbraid, used in 37 of the 52 aneurysms in this series. B, WEB-SL, a single-layer implant, used in 15 of the 52 aneurysms in this series.

and occlude an aneurysm in a single step. Two versions are available: a dual-layer type (WEB-DL), which is composed of 2 concentric cages, and a single-layer type (WEB-SL or SLS). The available sizes range from 4 to 11 mm in diameter and 3 to 9 mm in height. The mesh is designed to disrupt the flow at the neck of the aneurysm and to ultimately exclude it from the blood flow while preserving the flow in the parent artery (Fig 1). It seems to be especially suitable for broad-based bifurcation aneurysms and may eliminate the need for other reconstructive measures inside the parent artery, such as placing a stent.<sup>12</sup> Numerous publications have described the successful use of the WEB in the treatment of unruptured wide-neck bifurcation aneurysms.<sup>12-14</sup> Just recently, a single-center experience with the WEB in 6 ruptured aneurysms was reported, and the results were promising.<sup>15</sup> In this retrospective multicenter case series, we describe use of the WEB in 52 aneurysms in 47 patients who presented with subarachnoid hemorrhage secondary to a ruptured intracranial aneurysm.

## MATERIALS AND METHODS

A retrospective review of the medical records, radiographic imaging, and interventional reports was performed for 47 patients treated with a WEB device for a ruptured intracranial aneurysm at 1 of 10 European centers between May 2011 and December 2013. At each participating center, clinical and interventional treatment was provided per institutional standards of care. In each participating institution, the indication for treatment and technique (surgery or endovascular treatment) were decided on a case-by-case basis by a local multidisciplinary team that included neurosurgeons, neuroanesthesiologists, neurologists, and neuroradiologists. The selection of aneurysms treated with the WEB device was performed autonomously in each center by the interventional neuroradiologists according to aneurysm characteristics (ie, location, diameter, and neck size).

Permission from each patient to include their data was achieved in accordance to institutional ethical guidelines. Baseline patient and aneurysm characteristics, comorbidities, and SAH severity scores (Hunt and Hess [HH] or World Federation of Neurosurgical Societies classification) were compiled. Angiographic assessments were made at baseline, immediate postembolization, short-term (2–9 months [mean, 4.2 months]), and mid-term (7–25 months [mean, 12.9 months]) time points. The

immediate periprocedural hemodynamic effects and follow-up occlusion success were rated and reported by each operator as “complete,” “residual filling of the neck,” or “residual aneurysm filling,” as previously described.<sup>15</sup> Periprocedural medications, procedural complications, and clinical outcomes were compiled.

## Patient Data

Forty-seven patients harboring a total of 52 aneurysms were evaluated. SAH severity scores (HH or World Federation of Neurosurgical Societies) were available for 46 of the 47 patients. Eleven patients had an HH grade of I, 12 had an

HH grade of II, 8 had an HH grade of III, 7 had an HH grade of IV, and 5 had an HH grade of V. The median HH score was II. Three patients were rated according to the World Federation of Neurosurgical Societies system; 2 patients had a grade of I, and 1 patient had a grade of 5.

Three patients had 1 additional aneurysm, and 1 patient had 2 additional aneurysms. These aneurysms were treated during the same procedure with WEB devices. The anatomic locations of the ruptured aneurysms were distributed as follows: 18 in the MCA, 17 in the anterior communicating artery, 8 in the basilar artery, 6 in the posterior communicating artery, 1 in the ICA terminus, 1 in the PICA, and 1 in the pericallosal artery. In the 4 patients with multiple aneurysms treated (9 aneurysms total; 1 patient with 2 in the MCA and 1 in the PICA, 1 patient with 1 in the ICA terminus and posterior communicating artery, and 2 patients with 1 in the MCA and anterior communicating artery), the rupture site could not be identified with absolute certainty, and each aneurysm was treated with a WEB device. The rupture site was visible in 32 aneurysms, and in 10 it interfered with deployment of the WEB. Two of these patients were among those with periprocedural rehemorrhage, one that resulted from a microwire perforation and the other that potentially resulted from the WEB deployment itself.

Of 52 aneurysms, 10 (19.2%) were <5 mm in diameter, 35 (67.3%) were 5–10 mm in diameter, and 7 (13.5%) were >10 mm in diameter. Of the 52 aneurysms, 49 (94.2%) had a neck size of  $\geq 4$  mm (mean, 4.7 mm). Two of the large aneurysms were partially thrombosed.

## Procedural Data

Two treatments were performed as one staged procedure; one required additional coiling of a remnant during a control angiogram within 24 hours, and the other was planned as a 2-step occlusion, first of the dome, including the rupture site, followed 4 days later by stent-assisted coil occlusion with reconstruction of the neck under dual antiplatelet medication.

For 34 of the aneurysms, the index procedure was performed with the patient having been given a full bolus of IV heparin (5000 IU); 9 aneurysms were treated with a reduced bolus (2500 IU, all in the same center); and 9 were treated without heparin. Heparin was maintained at partial thromboplastin time levels of 40–50

**Table 1: Periprocedural events**

Patient No.	AN Location	Complication	Device Related	Outcome (mRS Score)	Clinical Consequence
1	MCA	TE	Yes	0 at 8 mo	None
2	MCA	TE	Yes	3 (same as before SAH)	None
3	PcomA	TE	Yes	0 at 3 mo	None
4	BA	TE	No	4 at discharge <sup>a</sup>	None
5	MCA	TE	No	3 at 2 mo	Yes
	AcomA	AN perforation	No		Yes
6	Pericallosal artery	AN perforation	Yes	0 at 1 wk	None
7	MCA	AN perforation	No	6 from initial SAH	Unknown <sup>b</sup>
8	AcomA	Induced spasm	Unknown	6 from initial SAH	Unknown <sup>b</sup>
9	MCA	Induced spasm	Unknown	Unknown	Unknown
10	PcomA	Infarction	No	2 at 6 mo	Transient
11	AcomA	WEB protrusion	Yes	0 at 6 mo	None
12	BA	WEB protrusion	Yes	0 at 8 mo	None
13	MCA	WEB protrusion	Yes	0 at 3 mo	None
14	AcomA	WEB protrusion	Yes	0 at 25 mo	None
15	rMCA, lMCA, Dissect Vert	rMCA branch partial occlusion	Yes	0 at 3 wk	None

**Note:**—AcomA indicates anterior communicating artery; AN, aneurysm; BA, basilar artery; Dissect Vert, dissecting vertebral; lMCA, left MCA; PcomA, posterior communicating artery; rMCA, right MCA; TE, thromboembolic event.

<sup>a</sup> Clinical outcome related to ventriculitis.

<sup>b</sup> Death during hospitalization secondary to the SAH, not during the procedure.

seconds for 48 hours in 5 patients from one center. Low-molecular-weight heparin was maintained in 22 patients (21 from 1 center). Only 1 patient was known to be on aspirin before the treatment. Twenty-three patients received 250–500 mg of aspirin during the intervention, usually before introduction of the WEB device. Glycoprotein IIb/IIIa inhibitors were used to counteract periprocedural thrombus formation: eptifibatid (Integrilin) in 2 cases of visible clot and abciximab (ReoPro) in 1 case of WEB protrusion. Postprocedural antiaggregation was maintained continuously in 27 patients (75–100 mg aspirin/day), and 7 of 27 received additional clopidogrel (75 mg/day) for 12 weeks. Eight patients who were kept on posttreatment antiplatelet medication were among those who had either periprocedural thrombus formation or postapplication protrusion of the WEB as the reason to keep up the medication. Another 19 patients were kept on a single antiplatelet medication without evident procedural reason (per the institutional standard of care). One patient with a periprocedural clot formation was treated with mechanical clot extraction by means of a Solitaire stent (Covidien, Irvine, California) and was administered a single 500-mg dose of aspirin, but no continuous medication was given.

Most procedures were performed with 6F access catheters/long sheaths, and 17 of 52 aneurysms were treated with intermediate catheters in addition to the dedicated microcatheters (32 VIA or VIA PLUS [Sequent Medical], 20 other catheters of  $\geq 0.027$  inches). Thirty-seven aneurysms were treated with a dual-layer device that was composed of 2 cages of 144 woven nitinol strands, and 15 aneurysms were treated with single-layer devices in which the number of nitinol strands varied from 144 to 216 (on the basis of device diameter).

## RESULTS

Eight aneurysms were treated with additional devices (4 with stent only, 1 with coils only, 1 with coils and a stent, 1 with coils and a balloon, 1 with a balloon). The reasons for adjunctive treatments were planned staged procedure (1 case), to complete neck closure or sac filling (2 cases), to treat preaneurysm stenosis (1 case), and to correct device protrusion (4 cases).

Treatment durations ranged from 15 to 193 minutes (average, 68 minutes). Treatment durations for 4 of the treatments with WEB placement in multiple aneurysms ranged from 67 to 195 minutes.

## Adverse Events

Periprocedural adverse events were reported for 15 patients during the treatment of 16 aneurysms, including 1 patient with 2 complications. Among those who underwent these procedures, 10 patients had no clinical sequelae and were discharged with an mRS score of  $< 2$  or a score equal to that before the initial SAH (Table 1).

Thirty-six aneurysms were treated without adverse events. In a maximum of 12 of 16 complicated treatments, the adverse event could possibly be attributed to the actual delivery of the WEB device. However, 3 of those were caused by the guidewire (1 perforation) or the microcatheter probing (1 perforation and 1 induced spasm).

Four events were thromboembolic in nature and required antiplatelet medication; 1 received eptifibatid, 1 received eptifibatid and additional aspirin and clopidogrel, 1 clot progressed despite 500 mg of intravenous aspirin and was removed successfully with a Solitaire stent, and in 1 case there was no information with regard to treatment. None of these patients had clinical sequelae.

Four aneurysms exhibited angiographic protrusion of the WEB that necessitated the use of a stent and, in 1 case, the additional use of IV antiplatelet drugs.

Three aneurysms were perforated during the treatment. However, only 1 case presented evidence of an additional SAH on postprocedural CT. This SAH might have occurred during the deployment of the device itself, and there was no clinical impact on the patient. The other 2 perforations were caused by a wire or a catheter.

There was no delayed bleeding in any of the patients treated with a WEB device.

**Angiographic Results.** An immediate postprocedural hemodynamic effect was achieved in 44 of 52 (84.6%) aneurysms. Twenty

**Table 2: Nonfatal complications during hospitalization**

Patient No.	AN Location	Type of Event	SAH Related	Outcome (mRS Score)
1	AcomA	Vasospasm	Yes	0 at discharge
2	MCA	Vasospasm on day 14	Yes	2 at 6 mo
3	MCA	Vasospasm on day 7	Yes	0 at discharge
4	BA	Vasospasm	Yes	4 at 12 mo
5	AcomA	Infarct on MRI	Yes	2 at 6 mo <sup>a</sup>
6	MCA	Stroke on MRI	No	0 at discharge
7	BA	Ventriculitis	Yes	4 at discharge
8	AcomA	Rehemorrhage; additional treatment with coils	No	0 at 6 mo
9	BA	New infarct on day 3 with vasospasm and stenosis visible	Yes	0 at 8 mo
10	MCA	Stroke on MRI	No	3 at discharge
11	rMCA, lMCA, Dissect Vert	Brain stem edema on day 23	No	0 at 3 wk

**Note:**—AcomA indicates anterior communicating artery; AN, aneurysm; BA, basilar artery; Dissect Vert, dissecting vertebral; lMCA, left MCA; rMCA, right MCA.

<sup>a</sup>Clinical status restored to pre-SAH value in a patient with multiple sclerosis.

(38.5%) aneurysms were completely occluded, 15 (28.8%) only showed contrast in the proximal compartment of the implant, and another 9 (17.3%) showed at least occlusion of the aneurysm dome beyond the implant. In 1 patient, a coil was also used within 24 hours to occlude an angiographic remnant outside the WEB that was not covered by the WEB itself after its initial placement. Of the 8 aneurysms that did not even partially occlude, 6 at least showed delay of the contrast washout until the venous phase, 1 even after the venous phase.

Imaging performed in 25 of 39 patients still alive at short-term follow-up (mean, 4 months [range, 2–9 months]; 21 performed with DSA, 4 performed with MRA) revealed complete occlusion of the aneurysm in 15 of 25 (60%) cases, 5 of 25 (20%) had residual filling of the neck, and 5 of 25 (20%) showed residual filling of the aneurysm. Imaging performed on 9 of 25 patients at midterm (mean, 13 months [range, 7–36 months]; all DSA) revealed complete occlusion of the aneurysm in 5 of 9 (55.6%) cases, 2 of 9 (22.2%) had residual neck, and 2 of 9 (22.2%) had residual aneurysm filling. In the midterm follow-ups, none of the implants themselves showed filling with contrast. There was no conceivable difference between the single- and dual-layer implants. Among the 20 aneurysms with immediate complete occlusion, 12 were treated with a dual-layer device, and 8 were treated with a single-layer device. None of the aneurysms that exhibited residual filling of the sac on midterm follow-up had been treated with a single-layer WEB.

Four patients required endovascular retreatment. In 1 patient, DSA was performed because of neurologic worsening on the day of the initial treatment; it was decided to treat this residual aneurysm with coils. One patient required endovascular retreatment with coils 1 month after the initial procedure. One patient had 3 aneurysms treated with a WEB device initially, and additional endovascular treatment was required because of a dissecting V4 aneurysm with coils and Y-stent placement 3 weeks later. One patient required retreatment with coils and a stent 3 months later for aneurysm regrowth caused by integration of the WEB into an intra-aneurysmal thrombus. All remnants or recurrences were treated by endovascular means without additional adverse events.

**Clinical Outcome Data.** Of 47 patients, 23 were discharged as independent survivors with an mRS score of 0, 1, or 2; 13 patients had an mRS score of 3 or 4; and none had an mRS score of 5. Eight patients died during their hospital stay, 5 as a result of the SAH and 3 for other reasons (1 from rehemorrhage 3 hours after treat-

ment, probably as a result of dissection from another aneurysm; 1 from acute respiratory distress syndrome; and 1 from vasospasm and infarction of all territories). For 3 patients, the postprocedural mRS score was not recorded.

Nineteen patients experienced a complication during their hospital stay. Of these 19 complications, 16 were related to the initial SAH (eg, vasospasm, new infarction on follow-up imaging, or ventriculitis after insertion of an extraventricular drainage). Three patients experienced postprocedural hemorrhage during their hospital stay: 1 intraparenchymal hemorrhage resulted from external ventricular drainage, 1 aneurysm was insufficiently occluded and was coiled within 24 hours after clinical worsening of the patient, which may have been caused by rehemorrhage, and 1 patient experienced rupture of an additional aneurysm 3 hours after the treatment of the index aneurysm with a WEB. This rupture was of a dissecting aneurysm that was treated with coils but had a fatal outcome. The dissecting aneurysm was identified as the source of rehemorrhage by autopsy.

Of 16 complications that were reportedly related to the intraoperative device and/or the procedure, 9 occurred in patients who were discharged with an mRS score of >2; one of these 9 patients already had a pretreatment mRS score of 3 and was discharged unchanged. Two of these 9 patients died, one of whom had a guidewire perforation during the treatment; 5 of 9 had an mRS score of 3 or 4, and no information was available for the other 2 patients.

Of the 30 patients available for midterm follow-up, 27 were independent. Of the remaining 3, two had maintained their initial status, and 1 had progressed from an mRS score of 1 at discharge to an mRS score of 4 after an episode of intraparenchymal hemorrhage after tPA administration for pulmonary artery thrombolysis (Table 2).

## DISCUSSION

Endovascular coil occlusion has been proven to increase the number of patients with good clinical outcome over that of those who undergo surgical clipping after aneurysmal subarachnoid hemorrhage.<sup>16</sup> However, it has 2 potential drawbacks. First, coil occlusion does not immediately and completely exclude the aneurysm from the bloodstream<sup>17</sup>; presumably, this is one explanation for the slightly higher rate of early rehemorrhage after coiling in the International Subarachnoid Aneurysm Trial.<sup>16</sup> Second, coiled aneurysms have a greater tendency to recur particularly if they are



**FIG 2.** Ruptured basilar tip aneurysm before (A) and immediately after (B) deployment of the WEB device. After the WEB is placed, no contrast filling can be seen inside the dome, including the bleb that is presumed to be the rupture site; furthermore, there is stasis of contrast inside the WEB beyond the venous phase, indicating sufficient hemodynamic decoupling.

large, broad-based, partially thrombosed, or ruptured. Furthermore, standard coil occlusion may be limited or unsuitable because of aneurysm geometry. Broad-based aneurysms especially may require the placement of a stent to remodel the parent artery, which by itself necessitates the use of antiplatelet medication. Thus, an endovascular treatment alternative that may be used safely for broad-based aneurysms without the need for additional implants in the bloodstream, yet offers efficacious aneurysm occlusion and prevents rehemorrhage, seems to be desirable, particularly for ruptured aneurysms. The purpose of this study was to evaluate the use of a relatively novel intra-aneurysmal microbraid implant, the WEB device, in ruptured aneurysms. In nonruptured aneurysms, the WEB has been described in a number of published series to be both safe and efficacious.<sup>12-14</sup> Because of its conceptual difference from standard coil occlusion, a potential yet unproven advantage of the WEB is faster hemodynamic separation of the aneurysm; immediate stasis is often seen after its deployment (Fig 2). The absence of overlapping radiopaque material might enable accurate positioning at the level of the neck, even in broad-based aneurysms. At the same time, stronger and larger microcatheters and the acute tip of the implant at the early stage of deployment and before unfolding may impose an increased risk for periprocedural rupture. Finally, nitinol coils have a potentially higher thrombogenicity when compared with the very inert platinum coils.<sup>18</sup> Therefore, thromboembolic events are of special concern, accepting that subarachnoid hemorrhage is known to induce a hypercoagulable state.<sup>19</sup>

Recently, a multicenter study by Papagiannaki et al<sup>20</sup> of 87 aneurysms (mostly unruptured) in 85 patients was published, and the results were favorable for the WEB when compared with those of coil occlusion in the Analysis of Treatment by Endovascular Approach of Nonruptured Aneurysms (ATENA) trial and the

Clinical and Anatomical Results in the Treatment of Ruptured Intracranial Aneurysms (CLARITY) study.<sup>21,22</sup> Although the percentage of broad-based aneurysms was much higher in the Papagiannaki et al series (85.9% vs 9.1% in CLARITY), the results for peri-interventional rupture and thromboembolic events were comparably low, and the rate of adequate occlusion was even higher with WEB than in CLARITY. Despite these observations, there is still a lack of evidence regarding the treatment results for WEB in ruptured aneurysms so far; in the Papagiannaki et al study, only 4 aneurysms (4.6%) were ruptured.

In the present series of 52 ruptured aneurysms, the technical success was 100%. However, failed attempts to place a WEB device or even the catheter and the subsequent choice of other treatment algorithms were not specifically recorded.

A limitation of this novel implant, which can be attributed to the larger microcatheter needed and greater rigidity

during the initial delivery when compared with those of coils, is the fact that in 10 of 52 aneurysms, the operator felt that the implant interfered with the rupture site during its delivery. However, only in one such case could a periprocedural rupture (seen as an increase in the extent of subarachnoid blood on postprocedural CT) potentially have been attributed to the WEB delivery and was of no clinical consequence whatsoever (patient with an mRS score of 0 on follow-up). Two other complications included microguidewire and microcatheter perforations, which occurred before each implant was advanced.

Because of the nature of subarachnoid hemorrhage, the overall clinical outcome in our series was worse than that in the Papagiannaki et al series. Eight patients died during hospitalization, and another 11 patients experienced SAH-related complications such as severe vasospasm leading to infarction or ventriculitis after external ventricular drainage. However, after the acute phase, the results were relatively good. Of the 30 patients available for midterm follow-up, 27 were independent survivors (mRS scores, 0–2). Of the remaining 3 patients, 2 have remained at their pretreatment status, and only 1 had progressed from an mRS score of 1 at discharge to an mRS score of 4 after an episode of intracranial hemorrhage after tPA administration for pulmonary artery thrombosis 7 months after the index procedure. Most important is that there was no late rerupture or late ischemia that could have been attributed to the WEB. All rehemorrhages occurred during the acute or subacute phase and could be explained by either periprocedural perforation with the wire or the catheter/WEB or incomplete occlusion of the aneurysm, leaving the potential rupture site unprotected by the implant. The midterm occlusion rates compare favorably to those of other series of ruptured aneurysms, such as CLARITY. Here, adequate occlusion was observed in 419 of 517 (81.0%) aneurysms, and an aneurysm remnant was found

in 98 of 517 (19.0%) aneurysms at midterm follow-up. In our series, only 4 aneurysms required additional treatment. One was a dissecting PICA vertebral aneurysm, initially misjudged as a PICA aneurysm and later treated with an additional stent and coils. Another procedure was staged with a WEB in the acute phase followed by surgical clipping. The remaining 2 aneurysms were a residual filling at the neck at 1 month treated with coils and regrowth of a partially thrombosed aneurysm that had been treated with 2 WEB devices, which both became integrated into the clot. The recurrence was treated with a stent and coils. Furthermore, the results of our series cannot really be compared with those of CLARITY, because 49 of the 52 ruptured aneurysms in our study had a neck size of  $\geq 4$  mm versus the only 9.1% broad-based ruptured aneurysms in CLARITY.

The 30.8% (16 of 52) rate of procedural events may seem high at first. However, the operators were asked to record all procedural events, including those without clinical sequelae, such as transient thrombus formation, aggravation of vasospasm induced by wire and catheter probing, and protrusion of the WEB. When only events that effectively resulted in clinical worsening or prolonged hospital stay were rated, this figure was reduced to 3 of 52: one aneurysm perforated with the guidewire, one thromboembolic event, and the aforementioned rehemorrhage in a case in which the presumed site of rupture was not covered with the WEB during the first treatment. One additional patient exhibited induction or aggravation of vasospasm caused by probing with the microcatheter; this patient died as a result of SAH sequelae. Thus, the overall rate of procedural complications with clinical worsening can be extrapolated to parallel that in the aforementioned series of nonruptured aneurysms treated with a WEB device (13% in the Papagiannaki et al study). The rate of intraoperative rupture (5.7% vs 1.3%) was slightly higher than that in the Papagiannaki et al study and than those of ATENA (2.6%) and CLARITY (3.7%). The small sample size in our study did not allow for a validated comparison. The same limitation exists for the rate of thromboembolic events, mainly comprising thrombus formation on the implant itself that was more or less equal to that in the Papagiannaki et al series (9.6% vs 7.6%, respectively). Morbidity and mortality rates are difficult to calculate for our group of patients with SAH, because most of the deaths and poor outcomes could be attributed to the SAH itself. There were only 3 procedural events that most likely led to clinical consequences, only one of which was related to the implant itself (thromboembolic branch occlusion). For comparison, the treatment morbidity and mortality rates were 1.3% and 0.0% in the Papagiannaki et al series, 1.7% and 1.4% in ATENA, and 3.7% and 1.5% in CLARITY, respectively.<sup>20-22</sup>

Between the 2 different types of WEB devices (single- or dual-layer), not many differences could be found. First, because of the later introduction of the WEB-SL, all treatments before June 2013 were performed with the WEB-DL. Thus, only 15 aneurysms were treated with a single-layer device. With the introduction of the single-layer WEB, the question of whether it would be similarly effective in flow disruption arose. In our series, we could not find a difference in efficacy between the 2 designs, neither with regard to the immediate angiographic result nor to long-term occlusion. The absolute numbers were actually in favor of the single-layer WEB device. Immediate complete occlusion was recorded for 12

of 37 WEB-DL and 8 of 15 WEB-SL devices. None of the aneurysms with residual filling of the sac on midterm follow-up was treated with a single-layer WEB. We interpret this trend as an indication that the flow-disrupting effect of the single-layer system most likely is at least as good as that with the dual-layer WEB; this, however, remains to be proved in a larger comparative study.

With regard to thromboembolic potential, which certainly plays an important role in the hypercoagulative state during acute SAH, our results were also in favor of the single-layer version. Only 1 thromboembolic event was recorded for the WEB-SL device, and it consisted of local clot formation that could be removed by means of stent-retriever thrombectomy; all the other thromboembolic events occurred with the WEB-DL device. Finally, protrusion of the implant seemed to be an issue that depended on aneurysm geometry, because protrusion occurred in aneurysms  $\leq 6$  mm in diameter. More important is that these aneurysms had a neck-to-height ratio of  $>1$ , meaning that these aneurysms were not only small but also shallow. With regard to protrusion, the type of implant did not seem to make a difference. Recent developments of the WEB with enhanced visibility and new angiographic visualization techniques seem to enable us to reliably detect and avoid protrusion as a potential source of adverse events in the future.<sup>23</sup> There was 1 aneurysm with partial thrombosis of the sac that had recurred at 3 months. Hope that the greater and more even surface of the WEB may sufficiently prevent migration into the clot, regularly seen with bare coils, is not warranted at the moment. Overall, the WEB provided safe aneurysm occlusion without necessitating additional stent placement in 90% of the patients. Periprocedural double-antiplatelet treatment could have been avoided in 87% of the patients and single-antiplatelet treatment in 50% of the patients in the acute phase of SAH. Although the follow-up period was shorter in our cohort, the rate of target aneurysm rerupture (1 of 52 [2%]) is comparable with that found in larger trials: 4.2% in the International Subarachnoid Aneurysm Trial for 1 year and 4.5% in a series of 44 ruptured wide-neck aneurysms treated with a stent and coils.<sup>24</sup>

## CONCLUSIONS

The WEB intra-aneurysmal flow disruptor can be used in ruptured aneurysms with safety and efficacy equal to those shown in previous experiences gathered with use of the WEB device in nonruptured aneurysms. Comparison with previous series of ruptured aneurysms was compromised by the fact that in most cases in our series, the aneurysms were broad-based. This specific geometry in combination with acute rupture renders the rate of necessary retreatments favorably in comparison with that of most series of coil occlusion. Partial thrombosis is still an unsolved issue, because the WEB may become integrated into a clot over time. The single-layer version performed as well as the dual-layer device in our series, with absolute numbers in favor of the WEB-SL, particularly with regard to thromboembolism. Protrusion of the implant is a potential problem that more likely may occur in small and shallow aneurysms, which is a limitation that will probably be overcome with an enhanced-visibility version of the braided and new angiographic imaging modalities. Overall, the WEB seems to be a very suitable treatment option for ruptured aneurysms, even if they are broad-based. Concerns that the conceptual

differences between the WEB device and coil occlusion may be associated with an increased risk of rehemorrhage are not warranted by the results of this series.

Disclosures: Thomas Liebig—UNRELATED: Consultancy: Consulting and proctoring for Sequent Medical, Acandis, MicroVention, Concentric/Stryker, and eV3. Ansgar Berlis—RELATED: Consulting Fee or Honorarium: Consultancy and proctoring agreements with Sequent Medical; UNRELATED: Payment for Lectures (including service on speakers bureaus); Penumbra and Stryker. Werner Weber—RELATED: Fees for Participation in Review Activities such as Data Monitoring Boards, Statistical Analysis, Endpoint Committees, and the Like: WEB CAST study\*; UNRELATED: Consultancy: Proctor for WEB cases in other institutions. Laurent Pierot—RELATED: Consulting Fee or Honorarium: Sequent Medical; UNRELATED: Consultancy: Codman, Covidien/eV3, MicroVention, and Stryker. Tufail Patankar—UNRELATED: Other: Proctor for WEB device. Xavier Barreau—RELATED: Fees for Participation in Review Activities such as Data Monitoring Boards, Statistical Analysis, Endpoint Committees, and the Like: Sequent Medical\*; UNRELATED: Consultancy: Sequent Medical. James Dervin—RELATED: Support for Travel to Meetings for the Study or Other Purposes: Sequent Medical. Comments: WEB training course in Magdeburg, Germany, April 2013, travel and accommodation paid by Sequent Medical; UNRELATED: Consultancy: Sela Medical. Comments: Proctor Sela Medical £1300, January 2013; Travel/Accommodations/Meeting Expenses Unrelated to Activities Listed: Covidien and Sela Medical. Comments: Travel and accommodation and registration for the following meetings from Covidien: LINC meeting, Paris, June 2013; ESMINT meeting, Nice, France, September 2014; ALICE meeting, Essen, Germany, May 2012; and Neurovascular course, Tel Aviv, December 2013. Boris Lubicz—UNRELATED: Consultancy: MicroVention and Codman. Joachim Klisch—UNRELATED: Consultancy: Sequent Medical.\* \*Money paid to the institution.

## REFERENCES

- Rinkel GJ, Djibuti M, Algra A, et al. **Prevalence and risk of rupture of intracranial aneurysms: a systematic review.** *Stroke* 1998;29:251–56
- Jeon TY, Jeon P, Kim KH. **Prevalence of unruptured intracranial aneurysm on MR angiography.** *Korean J Radiol* 2011;12:547–53
- Linn FH, Rinkel GJ, Algra A, et al. **Incidence of subarachnoid hemorrhage: role of region, year, and rate of computed tomography: a meta-analysis.** *Stroke* 1996;27:625–29
- de Rooij NK, Linn FH, van der Plas JA, et al. **Incidence of subarachnoid haemorrhage: a systematic review with emphasis on region, age, gender and time trends.** *J Neurol Neurosurg Psychiatry* 2007;78:1365–72
- Weir B, Disney L, Karrison T. **Sizes of ruptured and unruptured aneurysms in relation to their sites and the ages of patients.** *J Neurosurg* 2002;96:64–70
- International Study of Unruptured Intracranial Aneurysms Investigators. **Unruptured intracranial aneurysms—risk of rupture and risks of surgical intervention.** *N Engl J Med* 1998;339:1725–33
- Wermer MJ, van der Schaaf IC, Algra A, et al. **Risk of rupture of unruptured intracranial aneurysms in relation to patient and aneurysm characteristics: an updated meta-analysis.** *Stroke* 2007;38:1404–10
- Jeong YG, Jung YT, Kim MS, et al. **Size and location of ruptured intracranial aneurysms.** *J Korean Neurosurg Soc* 2009;45:11–15
- Asari S, Ohmoto T. **Natural history and risk factors of unruptured cerebral aneurysms.** *Clin Neurol Neurosurg* 1993;95:205–14
- Johnston SC, Dowd CF, Higashida RT, et al; CARAT Investigators. **Predictors of rehemorrhage after treatment of ruptured intracranial aneurysms: the Cerebral Aneurysm Rerupture After Treatment (CARAT) study.** *Stroke* 2008;39:120–25
- Meckel S, Singh TP, Undrén P, et al. **Endovascular treatment using predominantly stent-assisted coil embolization and antiplatelet and anticoagulation management of ruptured blood blister-like aneurysms.** *AJNR Am J Neuroradiol* 2011;32:764–71
- Lubicz B, Klisch J, Gauvrit JY, et al. **WEB-DL endovascular treatment of wide-neck bifurcation aneurysms: short- and midterm results in a European study.** *AJNR Am J Neuroradiol* 2014;35:432–38
- Pierot L, Liebig T, Sychra V, et al. **Intrasaccular flow-disruption treatment of intracranial aneurysms: preliminary results of a multicenter clinical study.** *AJNR Am J Neuroradiol* 2012;33:1232–38
- Pierot L, Klisch J, Cognard C, et al. **Endovascular WEB flow disruption in middle cerebral artery aneurysms: preliminary feasibility, clinical, and anatomical results in a multicenter study.** *Neurosurgery* 2013;73:27–34; discussion 34–35
- Caroff J, Mihalea C, Dargento F, et al. **Woven Endobridge (WEB) device for endovascular treatment of ruptured intracranial wide-neck aneurysms: a single-center experience.** *Neuroradiology* 2014;56:755–61
- Molyneux AJ, Kerr RS, Yu LM, et al; International Subarachnoid Aneurysm Trial (ISAT) Collaborative Group. **International subarachnoid aneurysm trial (ISAT) of neurosurgical clipping versus endovascular coiling in 2143 patients with ruptured intracranial aneurysms: a randomised comparison of effects on survival, dependency, seizures, rebleeding, subgroups, and aneurysm occlusion.** *Lancet* 2005;366:809–17
- Sorteberg A, Sorteberg W, Rappe A, et al. **Effect of Guglielmi detachable coils on intraaneurysmal flow: experimental study in canines.** *AJNR Am J Neuroradiol* 2002;23:288–94
- Mullan S, Raimondi AJ, Dobben G, et al. **Electrically induced thrombosis in intracranial aneurysms.** *J Neurosurg* 1965;22:539–47
- Itoyama Y, Fujioka S, Takaki S, et al. **Significance of elevated thrombin-antithrombin III complex and plasmin-alpha 2-plasmin inhibitor complex in the acute stage of nontraumatic subarachnoid hemorrhage.** *Neurosurgery* 1994;35:1055–60
- Papagiannaki C, Spelle L, Januel AC, et al. **WEB intrasaccular flow disruptor—prospective, multicenter experience in 83 patients with 85 aneurysms.** *AJNR Am J Neuroradiol* 2014;35:2106–11
- Cognard C, Pierot L, Anxionnat R, et al; Clarity Study Group. **Results of embolization used as the first treatment choice in a consecutive nonselected population of ruptured aneurysms: clinical results of the Clarity GDC study.** *Neurosurgery* 2011;69:837–41; discussion 842
- Pierot L, Spelle L, Vitry F; ATENA Investigators. **Immediate clinical outcome of patients harboring unruptured intracranial aneurysms treated by endovascular approach: results of the ATENA study.** *Stroke* 2008;39:2497–504
- Caroff J, Mihalea C, Neki H, et al. **Role of C-arm VasoCT in the use of endovascular WEB flow disruption in intracranial aneurysm treatment.** *AJNR Am J Neuroradiol* 2014;35:1353–57
- Alurkar A, Karanam LS, Nayak S, et al. **Stent-assisted coiling in ruptured wide-necked aneurysms: a single-center analysis.** *Surg Neurol Int* 2012;3:131

# Long-Term Follow-Up Results following Elective Treatment of Unruptured Intracranial Aneurysms with the Pipeline Embolization Device

A.H.Y. Chiu, A.K. Cheung, J.D. Wenderoth, L. De Villiers, H. Rice, C.C. Phatouros, T.P. Singh, T.J. Phillips, and W. McAuliffe

## ABSTRACT

**BACKGROUND AND PURPOSE:** Numerous reports of treatment of wide-neck aneurysms by flow diverters have been published; however, long-term outcomes remain uncertain. This article reports the imaging results of unruptured aneurysms treated electively with the Pipeline Embolization Device for up to 56 months and clinical results for up to 61 months.

**MATERIALS AND METHODS:** One hundred nineteen aneurysms in 98 patients from 3 centers admitted between August 2009 and June 2011 were followed at 6-month, 1-year, and 2+-year postprocedural timeframes. Analyses on the effects of incorporated vessels, previous stent placement, aneurysm size, and morphology on aneurysm occlusion were performed.

**RESULTS:** The 1- and 2+-year imaging follow-ups were performed, on average, 13 and 28 months postprocedure. At 2+-year follow-up, clinical data were 100% complete and imaging data were complete for 103/116 aneurysms (88.8%) with a 93.2% occlusion rate. From 0 to 6 months, TIA, minor stroke, and major stroke rates were 4.2%, 3.4%, and 0.8% respectively. After 6 months, 1 patient had a TIA of uncertain cause, with an overall Pipeline Embolization Device–related mortality rate of 0.8%. An incorporated vessel was significant for a delay in occlusion ( $P = .009$ ) and nonocclusion at 6 months and 1 year, with a delayed mean time of occlusion from 9.1 months (95% CI, 7.1–11.1 months) to 16.7 months (95% CI, 11.4–22.0 months). Other factors were nonsignificant.

**CONCLUSIONS:** The Pipeline Embolization Device demonstrates continued very high closure rates at 2+ years, with few delayed clinical adverse sequelae. The presence of an incorporated vessel in the wall of the aneurysm causes a delay in occlusion that approaches sidewall closure rates by 2 years.

**ABBREVIATIONS:** DAT = dual antiplatelet therapy; PED = Pipeline Embolization Device

The endovascular treatment of wide-neck aneurysms by flow-diverting devices has been previously evaluated for both small and large aneurysms. The midterm results of implantation of the Pipeline Embolization Device (PED; Covidien, Irvine, California) have been previously reported.<sup>1–6</sup> Data collection is now complete for up to 56 months with a mean of 28 months, and we report the results in patients who have previously undergone elective treatment with the PED.

## MATERIALS AND METHODS

### Patient Population

A previously published existing prospective case registry<sup>4</sup> of PED-treated elective cases (wide neck, >4 mm; unfavorable dome/neck

ratio, <1.6; fusiform anatomy, >10 mm; or previous failed therapy) at 3 centers between August 2009 and June 2011 identified 119 unruptured aneurysms in 98 patients undergoing 107 consecutive elective procedures. This includes the 57 consecutive cases originally reported. Only elective procedures were included to increase population homogeneity. Written informed consent was obtained. Perioperative management, multidisciplinary involvement, and application for use are as previously published.<sup>4</sup> Morbidity or death occurring for any reason during follow-up was noted.

### Antiplatelet and Anticoagulation Schedule

Antiplatelet and anticoagulation schedules have been published previously.<sup>4</sup> Antiplatelet protocols, use of platelet-inhibition testing, and duration of dual antiplatelet therapy (DAT) for anterior circulation aneurysms (3–6 months) varied among operators; however, all patients with posterior circulation aneurysms were prescribed 12 months of DAT routinely. Patients continued/discontinued DAT outside these timeframes at operator discretion. All continued to receive aspirin after cessation of clopidogrel, except for 3 patients: Two were continued on clopidogrel, one for an

Received October 15, 2014; accepted after revision February 2, 2015.

From the Neurological Intervention and Imaging Service (Western Australia) (A.H.Y.C., A.K.C., C.C.P., T.P.S., T.J.P., W.M.), Perth, Australia; Prince of Wales and Liverpool Hospitals (A.K.C., J.D.W.), Sydney, Australia; and Gold Coast University Hospital (L.D.V., H.R.), Gold Coast, Australia.

Please address correspondence to Albert H.Y. Chiu, MBBS (Hons.), FRANZCR, Neurological Intervention and Imaging Service (WA), Sir Charles Gairdner Hospital, 1st Floor, G Block, Hospital Ave, Nedlands, WA 6009, Australia; e-mail: albert.h.chiu@gmail.com  
<http://dx.doi.org/10.3174/ajnr.A4329>

**Table 1: Characteristics of the 7 aneurysms that failed to close during the study**

Location	Aneurysm Size (mm)	Neck Diameter (mm)	Incorporated Branch	Final Imaged Aneurysm Size (mm)	Comments
PcomA	8	5	Y	5	Patient B, previous PED (initially 15-mm aneurysm/7-mm neck)
Cavernous	18	Fusiform	N	9	
Basilar	15	6	N	10	Patient A
AcomA	13	10	N	4	Previous stent coiling
Paraclinoid	10	10	N	1	
MCA	3	2	Y	Unchanged	
PcomA	5	4	Y	Unchanged	

**Note:**—Y indicates yes; N, No; PcomA, posterior communicating artery; AcomA, anterior communicating artery.

unrelated cardiac procedure and the other for aspirin intolerance; one remained on dipyridole for aspirin allergy.

### Follow-Up Study Intervals and End Points

Clinical follow-up was recorded. Imaging follow-up was noted at approximately 6-month, 1-year, and 2+-year timeframes and was grouped as per intention-to-perform at the particular interval, but exact times varied depending on patient availability. The primary end point was defined as complete aneurysm closure, and secondary end points included in-stent stenosis, retreatment, and delayed complications, including TIA, minor stroke (mRS, 0–2), major stroke (mRS, 3–6), and SAH. Imaging was performed as a DSA or, less commonly, as MR angiography or CTA if patients were infirm or refused DSA. If delayed imaging follow-up was not performed (due to patient infirmity, refusal, or other), clinical follow-up was undertaken by outpatient clinic or telephone. Follow-up was performed earlier at the operator's discretion if there were concerns.

### Statistical Analysis

The presence of a notable artery arising from the aneurysm (ie, incorporated [yes/no], pre-existing stent [yes/no], size [dichotomized into <10/≥10 mm], and aneurysm morphology [berry/fusiform]) was analyzed with respect to occlusion rates at the 6-month, 1-year, and 2+-year timeframes by using the Fisher test (GraphPad Prism software; GraphPad Software, San Diego, California). Multiple regression was performed by using SPSS, Version 22 (IBM, Armonk, New York), and statistically significant associations were assessed for delay in occlusion by using Kaplan-Meier analysis.

For calculating aneurysm occlusion percentages, we made 2 assumptions: Aneurysms of patients missing a follow-up period but with documented occlusion before and after were assumed to have remained occluded. Second, if an aneurysm was nonoccluded at the last imaging examination, it was assumed to have remained nonoccluded regardless of additional clinical follow-up. We reviewed prior imaging in aneurysms occluded before the 6-month follow-up period for the Kaplan-Meier analysis to establish the date of occlusion.

## RESULTS

We included 119 aneurysms in 98 patients (78 female; 13–83 years of age; mean, 55.7 years) treated in 107 consecutive procedures: 43.7% (52/119) of aneurysms were ≥10 mm; of these, 7 were giant (>25 mm); 17.6% (21/119) were posterior circulation; 16.0% (19/119) were fusiform; 19.3% (23/119) had a notable in-

corporated branch; and 8.4% (10/119) had previous stent therapy.

Of the 119 aneurysms, 100% (116/116) had clinical follow-up and 88.8% (103/116) had imaging follow-up to 2+-years. Aneurysms in 11 patients (9.5%) were previously occluded and did not have imaging at the 2+-year timeframe. Two patients with 2 aneurysms refused imaging follow-up entirely and were excluded from occlusion analysis. Three deaths occurred, all between the 1- and 2+-year follow-up. Eighty-four percent (100/119) were imaged at 6 months, and 65.6% (78/119), at 1-year. Six-month follow-up ranged from 1 to 10 months (average and median, 6 months); 1-year follow-up, from 8 to 19 months (average and median, 13 ± 2.1 months); and 2+-year follow-up, from 17 to 56 months (average, 28 months; median, 26 ± 7.8 months). Average and median clinical 2+-year follow-up was 31 and 30 months, respectively (range, 17–61 months).

### Aneurysmal Occlusion

Overall aneurysmal occlusion rates increased from 81.6%, 84.1%, to 93.2% in the 6-month, 1-year, and 2+-year time periods, respectively. Twenty-one of 119 aneurysms were identified as nonoccluded at 6 months; of these, 3 closed by 1-year follow-up, and a further 11, at 2+-year follow-up.

Seven aneurysms were nonoccluded at 2+-year follow-up (Table 1). Four of these patients had stopped clopidogrel at 6 months. Three of 7 patients had an incorporated vessel (discussed below). Two of these 3 patients stopped clopidogrel at 6 months. Of the 4/7 remaining aneurysms, the first (cavernous aneurysm) was initially treated with 1 PED (5 × 20 mm) and had retreatment with a second (4.75 × 16 mm) at 12 months. Final CTA was performed 22 months post-initial PED, after which follow-up was stopped due to the patient being 80 years of age. The second case, patient A (Fig 1), had a basilar blowout aneurysm that was retreated at 20 months (discussed below). The third had a blowout aneurysm of the anterior communicating artery treated with a PED from the left A1 to the right A1/A2 junction without convincing purchase in the distal right A2. The last had a pre-existing stent (Enterprise; Codman & Shurtleff, Raynham, Massachusetts).

### Presence of Incorporated Vessel

Of the 21 nonoccluded aneurysms at 6 months, 10 had an incorporated vessel. This was statistically significant for causing delayed occlusion ( $P = .009$ ) and nonocclusion at 6 months (10/23 aneurysms with an incorporated vessel,  $P < .001$ ), and at 1 year (10/23,  $P < .001$ ), but not at 2+ years (3/23,  $P = .116$ ). Kaplan-

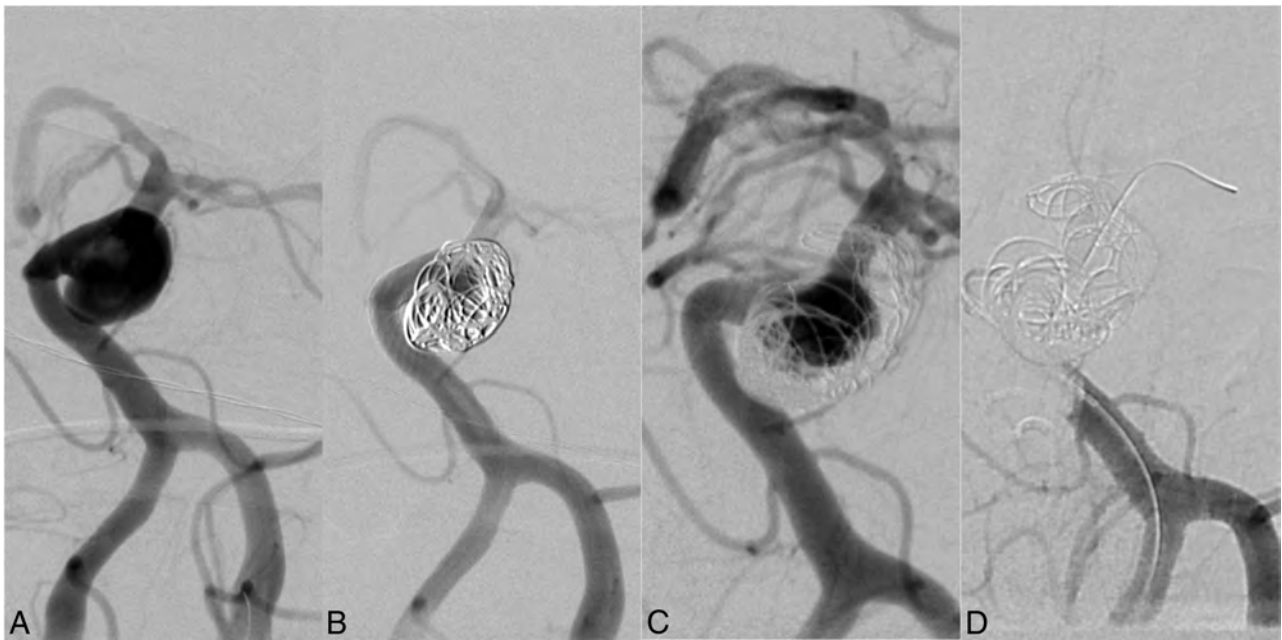


**FIG 1.** Frontal-projection DSA images of the basilar artery. Patient A is a 69-year-old man who lived in a remote location and presented with syncope and vertigo caused by mass effect from a 15-mm sidewall blowout basilar trunk aneurysm. *A*, Pretreatment DSA. *B*, This was initially treated with 2 PEDs (4 × 14 mm, 4 × 18 mm) and coils (at operator discretion) but continued to fill at 18 months, despite cessation of symptoms and clopidogrel being stopped prematurely at 6 months without issue. A third PED (4 × 20 mm) was inserted at 20 months (*C*), but the aneurysm continued to fill at 27 months on DSA (not shown). At 33 months (13 months after the last PED insertion), clopidogrel was stopped for an inguinal hernia repair in a distant peripheral hospital, resulting in PED construct thrombosis (perioperative heparin was advised), with symptoms arising 1 day after surgery, progressing to left-sided weakness, obtundation, and MR imaging evidence of multiple posterior circulation infarcts. The patient was intubated and flown to our institution, but emergency neurothrombectomy was unsuccessful (*D*) and the patient died.

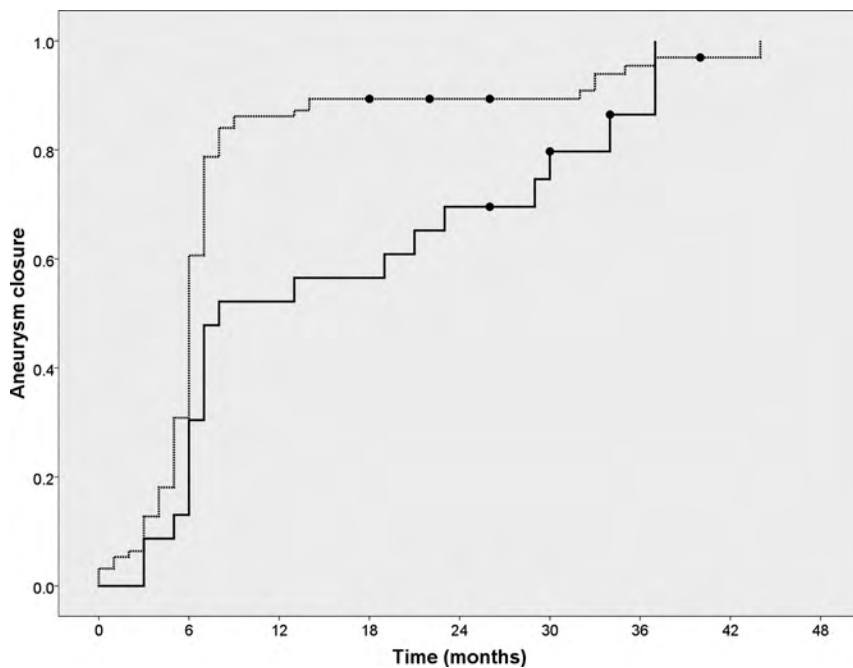


**FIG 2.** Kaplan-Meier curves of aneurysms with an incorporated vessel (*solid line*) versus no incorporated vessel (*dotted line*), demonstrating the delayed occlusion of the former group. *Shaded circles* represent censored observations (representative of nonoccluded aneurysms at the last known time of imaging).

Meier analysis suggested that the presence of an incorporated vessel results in a mean time of closure at 16.7 months (95% CI, 11.4–22.0 months) versus 9.1 months (95% CI, 7.1–11.1 months) in its absence (Fig 2). Seven of the 10 aneurysms had occluded at

final follow-up. Two of 10 remained unchanged in size compared with pretreatment; both had only 1 PED and had 26- and 30-month imaging, respectively. The third, patient B (Fig 3), had a second PED at 22 months with 40% reduction in size at 56-month follow-up.

Ten aneurysms had a previous stent, and of these, 6 demonstrated occlusion at 6 months. At 1-year follow-up, none of the remaining 4 had closed. A further 3 were occluded by 2+ years (9/10). The results trended toward significance for nonocclusion at 1 year but not at other intervals ( $P = .131$ ). No statistically significant influence on occlusion was found for size or morphology (Table 2).

#### ***In-Stent Stenosis or Vessel Occlusion***

Three cases (2.8%) of in-stent stenosis  $\geq 70\%$  were noted at 6 months. None of the patients were current smokers; all were female. The narrowing lessened with time, and the patients remained asymptomatic. In these cases, aspirin and clopidogrel were maintained. No new stenoses were identified after 6 months.

Two periprocedural PED occlusions were noted. The first patient (a 66-year-old male smoker) was treated for a 78-mm para-



**FIG 3.** A–C, Lateral DSA images of the left ICA. D, Sagittal maximum-intensity-projection reconstruction of CT angiography. Patient B is a 63-year-old man who had an asymptomatic left posterior communicating artery aneurysm, initially treated with a single PED (3.75 × 12 mm). Preinsertion (A) and immediate postinsertion images (B) of a flow diverter demonstrate the large incorporated posterior communicating artery. Twenty-two months after insertion of the initial PED, a second (3.75 × 14 mm) was inserted (not shown). C, Final available catheter angiographic imaging 9 months postinsertion of the second flow diverter. Clopidogrel was stopped 6 months postinsertion of the second PED. D, CT angiography 56 months post-initial flow diversion demonstrates persistence of the aneurysm but with a decrease in its size.

**Table 2: Summary of completeness of aneurysm follow-up and occlusion rates since initial flow-diverter therapy**

Follow-Up Period	6 Months	1 Year	2+ Years	P Value		
				6 Months	1 Year	2+ Years
No. of aneurysms with data available for analysis	114/119	107/119	103/116			
Percentage complete follow-up data	95.8	89.9	88.8			
Percentage aneurysms occluded						
Incorporated vessel	54.5	56.5	85.7	<.001	<.001	.116
No incorporated vessel	88.0	92.3	95.7			
Pre-existing stent	66.7	66.7	90	.363	.131	.484
No pre-existing stent	82.9	86.7	94.2			
<10 mm	82.5	87.3	95.3	.811	.598	.697
≥10 mm	80.4	82.4	92			
Berry	82.3	85.6	93.8	.741	.717	1
Fusiform	77.8	82.4	94.4			
Total	81.6	84.1	93.2			

clinoid aneurysm with 4 PEDs and had complications from acute stent platelet aggregation requiring abciximab. He presented 12 days postprocedure with seizures and in-stent thrombosis. Two passes with a Solitaire 4 × 15 mm device (Covidien), an 8-mg bolus of intra-arterial abciximab, and a 12-hour intravenous infusion resulted in recanalization. The patient was converted to prasugrel. This center had no P2Y12 testing. No clinical sequelae were noted, and CT at day 9 demonstrated no infarcts. The second case occurred during treatment of a pericallosal aneurysm in a 74-year-old patient, resulting in clinically silent stroke (discussed below).

Two delayed PED occlusions were detected. One, in patient C, was an asymptomatic occlusion in a 3-layer PED construct in a pericallosal fusiform aneurysm (Fig 4). The second, patient A, was in a 69-year-old man (Fig 1) who died after an elective inguinal

hernia repair from thrombosis of his 3-layer PED construct in a blowout basilar aneurysm (discussed below).

#### Retreatment

Retreatment by using the PED was required in 3/119 aneurysms in the follow-up period. The first patient, previously published,<sup>4</sup> initially had an elective flow diversion of a 16-mm superior hypophyseal aneurysm with a single PED. Thirty-four days later, on routine CTA, the PED had migrated proximally. Two PEDs were placed that day. The second, patient A (Fig 1), had a blowout basilar trunk aneurysm. This was treated with 2 telescoped PEDs and coils but continued to fill at 18 months, despite cessation of clopidogrel prematurely at 6 months. Retreatment was performed at 20 months with another PED, but the aneurysm was seen as

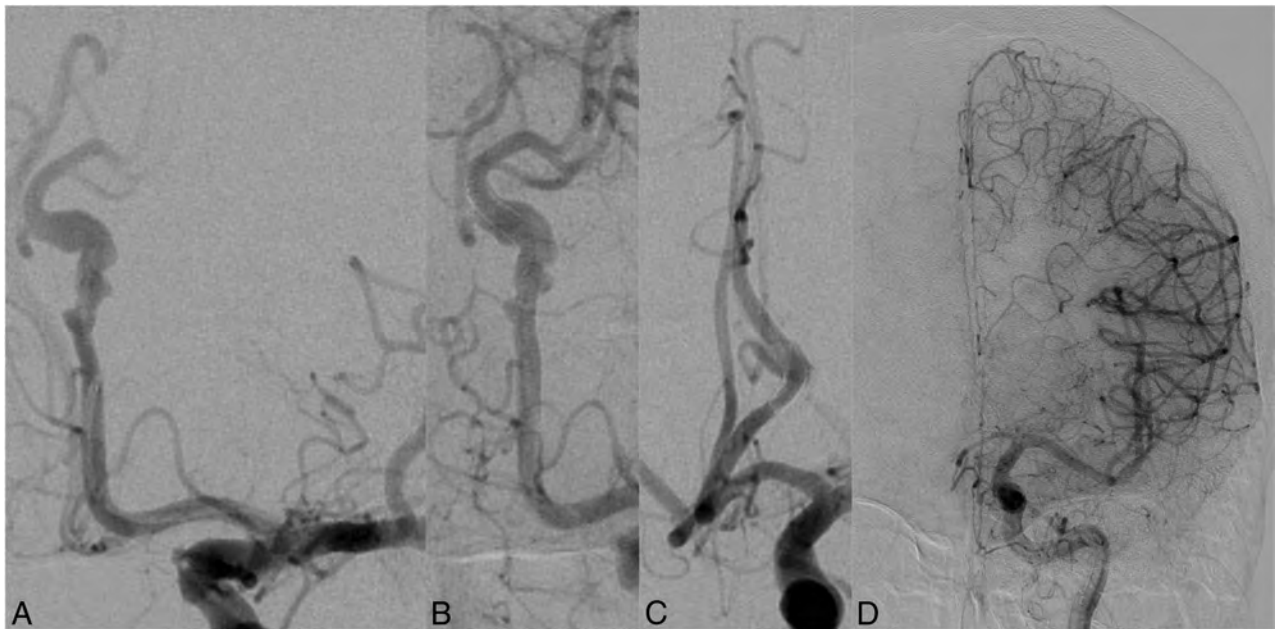


**FIG 4.** Subtracted frontal views of the left ICA DSA. Patient C is a 62-year-old nonsmoking woman who had a dysplastic 6 × 20 mm pericallosal fusiform aneurysm identified on investigation for headaches and retro-orbital pain. Pretreatment appearance (A) of a dysplastic fusiform A2 segment aneurysm and appearance immediately postdeployment (B) of 3 PEDs (2.5 × 20 mm, 2.5 × 18 mm, and 2.5 × 14 mm). Clopidogrel was stopped after 6 months, and aspirin was continued. C, At DSA 21 months post-PED deployment, the aneurysm demonstrates 90% occlusion with no in-stent stenosis, but spontaneous asymptomatic PED occlusion is found at 35 months (D). It is unknown exactly when the PED construct thrombosed (between 21 and 35 months postimplantation) because the patient was asymptomatic.

continuing to fill at 27-month DSA.<sup>7</sup> The third case was a 77-year-old patient presenting with abducens palsy from an 18-mm cavernous aneurysm. Due to nonocclusion at 11 months, a second PED was placed, but the aneurysm remained open, albeit smaller (9 mm), at 22 months. The sixth nerve palsy resolved. This case was classed as a nonocclusion because the patient declined further imaging.

#### **Transient Ischemic Attacks, Strokes, Subarachnoid Hemorrhage, and Deaths**

From 0 to 6 months, in addition to the 5 TIAs and 3 strokes (all mRS 1) in the previously reported population,<sup>4,7</sup> 2 strokes occurred, for a rate of TIA of 4.2%, minor stroke of 3.4%, and major stroke of 0.8%. The first was in a 57-year-old smoker who underwent elective flow diversion for a recurrent 5-mm right MCA aneurysm, previously coiled for acute rupture in 2009. A single 3 × 14 mm PED was placed uneventfully. The patient's clopidogrel was stopped against instructions for hematuria 11 days postprocedure, and he had an infarct on day 17, with hemiplegia and severe dysphasia (mRS 3). The second was a clinically silent stroke occurring in a 74-year-old patient with a 4-mm pericallosal aneurysm. Two PEDs were placed, and intraprocedural PED occlusion occurred; thus, 4 mg of intra-arterial abciximab was administered. Recanalization occurred within 15 minutes, and the patient remained asymptomatic. Despite this outcome, frontopolar branch and medial lenticulostriate infarcts were noted on routine 1-month CT. The patient remained neurologically intact (mRS 0). Of note, the center also did not use P2Y12 testing.

From 6-month follow-up onward, 1 case of TIA was noted, a 62-year-old smoker who experienced 3 possible TIAs on aspirin between 26 and 53 months post-PED with normal clinical examination and MR imaging findings. No action was taken.

Three deaths occurred during follow-up from all causes, for a mortality rate of 2.5%, with a PED-related mortality of 0.8%. In the first, patient A (Fig 1), the PED thrombosed, and he died at 33 months after initial insertion of 2 PEDs for his blowout basilar aneurysm (13 months after retreatment with a third PED) after stopping clopidogrel for an elective inguinal hernia repair. The second was a 58-year-old man with active non-Hodgkin lymphoma who died of unrelated causes 17 months after receiving a PED. The third was a 66-year-old patient who had undergone treatment of a 78-mm aneurysm with 4 PEDs and was placed on aspirin and prasugrel (clopidogrel resistance). The aneurysm was thrombosed at 6-month DSA, but DAT was continued for heavy smoking, and he died 12 months later from a fall-related posttraumatic right frontal hematoma.

#### **DISCUSSION**

Flow diversion has been demonstrated effective in treating aneurysms,<sup>1-6</sup> enabling repair without the need to enter the sac. These stentlike devices reduce aneurysm perfusion by directing flow through the lumen of the stent bypassing the neck, inducing aneurysm thrombosis while maintaining perfusion to side branches. Most recent articles have focused on the uncommon short- to medium-term complications of ipsilateral parenchymal hemorrhage,<sup>8-12</sup> delayed rupture<sup>1,13,14</sup> and side branch occlusion,<sup>7,15</sup> or thromboembolism<sup>2,6,12,16</sup>; there is an evolving understanding of flow-diversion complications. However, the body of knowledge relating to the long-term effects of flow diversion is still incomplete.

In our cohort, delayed aneurysmal nonocclusion is statistically associated with the presence of an incorporated vessel. The presence of flow demand is the premise by which small perforators

jailed by the PED are preserved; however, it is likely that this plays an important role in prolonging aneurysmal perfusion in these cases. Such aneurysms have been described as remodeling into an infundibulum-like structure,<sup>5</sup> and this study suggests that such a process may take longer but will eventually occur. This finding is similar to a recent study of MCA aneurysms<sup>17</sup> in which the 6-month occlusion rate was 85.7% versus 91.2% in the larger study addressing all aneurysms.<sup>5</sup> This finding is important, given that flow diverters are sometimes a preferred option in such cases; an analysis by Brinjikji et al<sup>18</sup> suggested that 22% of aneurysms may fall into this category. Most aneurysms appear to close following cessation of clopidogrel; thus, this is an important strategy to consider to promote aneurysm closure. Not all aneurysms, however, may respond because 2 of 3 patients with an incorporated vessel and nonocclusion at 2+-years had stopped clopidogrel at 6 months.

One explanation is that an incorporated branch decreases the slow, turbulent flow achieved in flow diversion of a stand-alone aneurysm; thus, the efficacy of clot formation is reduced. Only 1 of these patients had an additional PED placed to promote aneurysm closure, and perhaps additional PEDs in a delayed fashion need to be considered. This staging of treatment maximizes the temporal development of pial-pial collateralization, with the vascular territory of the incorporated branch being devolved to neighboring vessels. This result is clearly seen in flow diversion<sup>15</sup>; with a diminished requirement for high flow at the incorporated vessel, eventual aneurysm thrombosis should occur.

Our rate of severe in-stent stenosis is similar to that previously published<sup>1,4,5,19</sup>; all remained asymptomatic and the stenoses reduced with time. It would seem reasonable to continue DAT until there is an observable reduction of narrowing to at least 50%.

Two cases of delayed PED occlusion were encountered at 33 and 35 months. The first, patient A (Fig 1), occurred in a large blowout aneurysm with cessation of clopidogrel for elective surgery. Delayed thrombosis of the basilar artery in these aneurysms has been previously reported, and life-long DAT may well be required in these cases.<sup>20</sup> Intimal cover in large/giant basilar aneurysms may never occur or may be slow. The second case involved asymptomatic occlusion of an A2 vessel with 3 overlapping PEDs in a fusiform aneurysm, representing a big metal load in a small vessel. Slow asymptomatic occlusion of vessels is recognized, and the phenomenon has been reported by previous authors<sup>19,21</sup>; there may be a relation to the cessation of clopidogrel, and life-time DAT may be required in multiple overlapping PEDs in smaller vessels.

Delayed aneurysm rupture did not occur in our cohort. This phenomenon has previously been described in large or giant aneurysms.<sup>13</sup> Fifty-six percent of our cohort consisted of aneurysms of <10 mm. This supports a theory that delayed PED-related rupture is rare in smaller aneurysms.

Our occlusion rates for comparable periods are similar to those published.<sup>4-6,22-24</sup> They add to the information gleaned by O'Kelly et al,<sup>19</sup> who studied a cohort of 97 PEDs to a median follow-up 1.25 years, but from a range of 0.25–2.5 years. Saatci et al<sup>5</sup> were able to follow up a minority of cases at 18–24 months (69 aneurysms [27.5%] in 49/191 patients; 25.7%). Similarly, Szikora et al<sup>2</sup> followed a small cohort (12/19 aneurysms, 63.1%)

between 1.5 and 2 years with MRA. A third series starting with a cohort of 178 aneurysms in 143 patients and followed 58 aneurysms to 18 months.<sup>25</sup> Other larger case series followed patients to approximately an average of  $\leq 1$  year.<sup>1,3,6,19</sup> A small study of 12 patients demonstrated that all except 1 aneurysm occluded at 6-month angiography, but the authors continued to follow the cohort by CT or MR angiography to a range of 12–47 months.<sup>26</sup> Our cohort represents the largest and longest reported imaging follow-up (average duration of 28 months and a maximum follow-up of 56 months postprocedure) and clinical follow-up (average of 31 months and median of 30 months). Moreover, at 2+ years high clinical (100%) and imaging (88.8%) follow-up rates were achieved, both markedly higher compared with other published data during this time. These data give surety to the efficacy of the response to PEDs because there was no loss of patients at follow-up.

A number of limitations to our study are noted. The imaging follow-up at 2+ years is very high but, nevertheless, incomplete. Long-term 100% imaging follow-up is difficult despite a diligent approach because patients are geographically mobile and can decline follow-up. The basis of the study was taken from a registry, and the retrospective nature limited the flexibility of statistical analysis.

## CONCLUSIONS

The PED demonstrates continued favorable clinical and imaging findings up to 61 and 56 months postprocedure, respectively. From 0 to 6 months, the TIA, minor stroke, and major stroke rates were 4.2%, 3.4%, and 0.8%, respectively. The TIA rate from 6 months onward was 0.8%, with a PED-related mortality rate of 0.8%. The treatment is durable, complete, and reliable. The presence of an incorporated vessel does appear to be statistically significant in causing delayed aneurysmal occlusion, but most (85.7%) still do occlude with time. Delayed vessel thrombosis is distinctly uncommon and may be asymptomatic. Some aneurysms continue to represent a challenge, and life-long DAT may be required.

## ACKNOWLEDGMENTS

We thank Dr Ferry Dharsono (Neurological Intervention and Imaging Service of Western Australia, Perth, Australia) for assistance in data analysis, and Drs Jonathon Downer (Neurological Intervention and Imaging Service of Western Australia, Perth, Australia), Grace Aw (Prince of Wales Hospital, Sydney, Australia), and Sean Wallace (Gold Coast University Hospital, Gold Coast, Australia) for assistance in data entry.

Disclosures: Albert H.Y. Chiu—UNRELATED: *Travel/Accommodations/Meeting Expenses Unrelated to Activities Listed*: ev3/Covidien, *Comments*: ev3 supports an official interventional neuroradiologist–led morbidity and mortality meeting (Neuroexchange) for Australia and New Zealand practitioners, in which all devices from all companies are discussed freely. This meeting runs every year and is open to all practicing Australian and New Zealand interventional neuroradiologists and fellows. ev3 supplies economy return tickets and accommodations. No money is paid directly to me or my institution. I have attended this meeting since 2012. Andrew K. Cheung—UNRELATED: *Travel/Accommodations/Meeting Expenses Unrelated to Activities Listed*: Neuroexchange, *Comments*: This is the official interventional neuroradiologist–led morbidity and mortality meeting for Australasia run by members of Australia and New Zealand Society of Neuroradiology, which is supported by ev3. ev3 supplies economy return tickets and accommodations but has no control over

agenda or material reviewed. All devices available are discussed with no ev3 bias. Jason D. Wenderoth—UNRELATED: Consultancy: ev3, Covidien, Comments: procuring on Pipeline cases and consultancy fee for attendance and input at faculty meetings during development of the Pipeline Flex device; Travel/Accommodations/Meeting Expenses Unrelated to Activities Listed: ev3/Covidien, Comments: There is an annual Australia/New Zealand morbidity and mortality meeting sponsored by ev3/Covidien (Neuroexchange). All Australia and New Zealand interventional neuroradiologists are offered travel and accommodation expenses to attend this meeting. Most or all attend in this capacity on an annual basis, including myself. Henry Rice—RELATED: Support for Travel to Meetings for the Study or Other Purposes: Covidien,\* Comments: travel support to interventional neuroradiologist meetings; UNRELATED: Travel/Accommodations/Meeting Expenses Unrelated to Activities Listed: Cordis,\* Stryker,\* Covidien.\* Constantine C. Phatouros—UNRELATED: Travel/Accommodations/Meeting Expenses Unrelated to Activities Listed: Covidien, Comments: Neuroexchange Meeting: This is the official interventional neuroradiologist-led morbidity and mortality meeting for Australia and New Zealand, which is chaired by members of the Australia and New Zealand Society of Neuroradiology and financially supported by Covidien. Covidien provides return economy (coach) air travel and accommodations but does not have any direct control over the meeting agenda or material presented. Devices across the entire spectrum of interventional neuroradiology are discussed and are not limited to those of Covidien. Tejinder P. Singh—OTHER RELATIONSHIPS: ev3 sponsors a yearly Neuroexchange Meeting in Australia, where the company provides travel to and accommodations at the event. They facilitate the meeting, but no money is provided either to me or the institution. The meeting is a generic interventional neuroradiologist meeting not specific to ev3 or its products and is a forum to showcase and discuss interventional neuroradiologist techniques and complications. I have attended these meetings. Timothy J. Phillips—UNRELATED: Travel/Accommodations/Meeting Expenses Unrelated to Activities Listed: Covidien, Comments: Neuroexchange Meeting: This is the official interventional neuroradiologist-led morbidity and mortality meeting for Australia and New Zealand, which is chaired by members of the Australia and New Zealand Society of Neuroradiology and financially supported by Covidien. Covidien provides return economy (coach) air travel and accommodations but does not have any direct control over the meeting agenda or material presented. Devices across the entire spectrum of interventional neuroradiology are discussed and are not limited to those of Covidien. William McAuliffe—UNRELATED: Travel/Accommodations/Meeting Expenses Unrelated to Activities Listed: Neuroexchange Morbidity and Mortality National Australasian Interventional Neuroradiologist Meeting, Comments: This is the official interventional neuroradiologist-led morbidity and mortality meeting for Australasia run by members of Australia and New Zealand Society of Neuroradiology, which is supported by ev3. It is a serious 2-day meeting held to review complications and so forth. ev3 supplies economy return tickets and accommodations but has no control over agenda or material reviewed. All devices available are discussed with no ev3 bent. \*Money paid to the institution.

## REFERENCES

- Lylyk P, Miranda C, Ceratto R, et al. Curative endovascular reconstruction of cerebral aneurysms with the Pipeline embolization device: the Buenos Aires experience. *Neurosurgery* 2009;64:632–42; discussion 642–43; quiz N636
- Szikora I, Berentei Z, Kulcsar Z, et al. Treatment of intracranial aneurysms by functional reconstruction of the parent artery: the Budapest experience with the Pipeline embolization device. *AJNR Am J Neuroradiol* 2010;31:1139–47
- Nelson PK, Lylyk P, Szikora I, et al. The Pipeline embolization device for the intracranial treatment of aneurysms trial. *AJNR Am J Neuroradiol* 2011;32:34–40
- McAuliffe W, Wycoco V, Rice H, et al. Immediate and midterm results following treatment of unruptured intracranial aneurysms with the Pipeline embolization device. *AJNR Am J Neuroradiol* 2012;33:164–70
- Saatci I, Yavuz K, Ozer C, et al. Treatment of intracranial aneurysms using the Pipeline flow-diverter embolization device: a single-center experience with long-term follow-up results. *AJNR Am J Neuroradiol* 2012;33:1436–46
- Fischer S, Vajda Z, Aguilar Perez M, et al. Pipeline embolization device (PED) for neurovascular reconstruction: initial experience in the treatment of 101 intracranial aneurysms and dissections. *Neuroradiology* 2012;54:369–82
- Phillips TJ, Wenderoth JD, Phatouros CC, et al. Safety of the Pipeline embolization device in treatment of posterior circulation aneurysms. *AJNR Am J Neuroradiol* 2012;33:1225–31
- Velat GJ, Fargen KM, Lawson MF, et al. Delayed intraparenchymal hemorrhage following Pipeline embolization device treatment for a giant recanalized ophthalmic aneurysm. *J Neurointerv Surg* 2012;4:e24
- Cruz JP, Chow M, O'Kelly C, et al. Delayed ipsilateral parenchymal hemorrhage following flow diversion for the treatment of anterior circulation aneurysms. *AJNR Am J Neuroradiol* 2012;33:603–08
- Chiu AH, Wenderoth J. Cerebral hyperperfusion after flow diversion of large intracranial aneurysms. *J Neurointerv Surg* 2013;5:e48
- Hu YC, Deshmukh VR, Albuquerque FC, et al. Histopathological assessment of fatal ipsilateral intraparenchymal hemorrhages after the treatment of supraclinoid aneurysms with the Pipeline embolization device. *J Neurosurg* 2014;120:365–74
- Delgado Almandoz JE, Crandall BM, Scholz JM, et al. Pre-procedure P2Y12 reaction units value predicts perioperative thromboembolic and hemorrhagic complications in patients with cerebral aneurysms treated with the Pipeline embolization device. *J Neurointerv Surg* 2013;5(suppl 3):iii3–10
- Kulcsár Z, Houdart E, Bonafe A, et al. Intra-aneurysmal thrombosis as a possible cause of delayed aneurysm rupture after flow-diversion treatment. *AJNR Am J Neuroradiol* 2011;32:20–25
- Shobayashi Y, Tateshima S, Kakizaki R, et al. Intra-aneurysmal hemodynamic alterations by a self-expandable intracranial stent and flow diversion stent: high intra-aneurysmal pressure remains regardless of flow velocity reduction. *J Neurointerv Surg* 2013;5(suppl 3):iii38–42
- Puffer RC, Kallmes DF, Cloft HJ, et al. Patency of the ophthalmic artery after flow diversion treatment of paraclinoid aneurysms. *J Neurosurg* 2012;116:892–96
- Heller RS, Dandamudi V, Lanfranchi M, et al. Effect of antiplatelet therapy on thromboembolism after flow diversion with the Pipeline embolization device. *J Neurosurg* 2013;119:1603–10
- Yavuz K, Geyik S, Saatci I, et al. Endovascular treatment of middle cerebral artery aneurysms with flow modification with the use of the Pipeline embolization device. *AJNR Am J Neuroradiol* 2014;35:529–35
- Brinjiki W, Cloft HJ, Fiorella D, et al. Estimating the proportion of intracranial aneurysms likely to be amenable to treatment with the Pipeline embolization device. *J Neurointerv Surg* 2013;5:45–48
- O'Kelly CJ, Spears J, Chow M, et al. Canadian experience with the Pipeline embolization device for repair of unruptured intracranial aneurysms. *AJNR Am J Neuroradiol* 2013;34:381–87
- Klisch J, Turk A, Turner R, et al. Very late thrombosis of flow-diverting constructs after the treatment of large fusiform posterior circulation aneurysms. *AJNR Am J Neuroradiol* 2011;32:627–32
- Fiorella D, Hsu D, Woo HH, et al. Very late thrombosis of a Pipeline embolization device construct: case report. *Neurosurgery* 2010;67(3 suppl operative):onsE313–14; discussion onsE314.
- Chalouhi N, Starke RM, Yang S, et al. Extending the indications of flow diversion to small, unruptured, saccular aneurysms of the anterior circulation. *Stroke* 2014;45:54–58
- Becks T, Kallmes DF, Saatci I, et al. Pipeline for uncoilable or failed aneurysms: results from a multicenter clinical trial. *Radiology* 2013;267:858–68
- Lubicz B, Collignon L, Raphaeli G, et al. Pipeline flow-diverter stent for endovascular treatment of intracranial aneurysms: preliminary experience in 20 patients with 27 aneurysms. *World Neurosurg* 2011;76:114–19
- Yu SC, Kwok CK, Cheng PW, et al. Intracranial aneurysms: midterm outcome of Pipeline embolization device—a prospective study in 143 patients with 178 aneurysms. *Radiology* 2012;265:893–901
- Deutschmann HA, Wehrs chuetz M, Augustin M, et al. Long-term follow-up after treatment of intracranial aneurysms with the Pipeline embolization device: results from a single center. *AJNR Am J Neuroradiol* 2012;33:481–86

# pCONus Device for the Endovascular Treatment of Wide-Neck Middle Cerebral Artery Aneurysms

 B. Gory, M. Aguilar-Pérez, E. Pomero, F. Turjman, W. Weber, S. Fischer, H. Henkes, and A. Biondi



## ABSTRACT

**BACKGROUND AND PURPOSE:** Endovascular treatment of bifurcation middle cerebral artery aneurysms with a wide neck could be challenging, and many lesions are still treated by a surgical approach. The pCONus is a newly emerging device for wide-neck bifurcation intracranial aneurysms. To date, a single report on the treatment of intracranial aneurysms including all locations has been published. We report our experience with pCONus in the treatment of wide-neck MCA aneurysms.

**MATERIALS AND METHODS:** MCA aneurysms treated with pCONus in 4 European centers were retrospectively reviewed.

**RESULTS:** Forty MCA aneurysms (mean dome size, 7.7 mm; mean neck size, 5.6 mm) were treated in 40 patients (mean age, 62 years). Aneurysm coiling was performed after deployment of 1 pCONus in 95% (38/40) of cases and after deployment of 2 pCONus devices in 5% (2/40). No procedural angiographic complications were observed. Reversible neurologic complications were noted in 5% (2/40), and permanent neurologic complication, in 2.5% (1/40) at 1 month. There was no mortality. No aneurysms bled or rebled after treatment. Immediate angiographic results were complete aneurysm occlusion in 25% (10/40), neck remnant in 47.5% (19/40), and aneurysm remnant in 27.5% (11/40). Follow-up (mean, 6.8 months) was available for 33 aneurysms (82.5%). Stable or improved results were observed in all except 3 cases, including 48.5% complete occlusions (16/33), 30.3% neck remnants (10/33), and 21.2% aneurysm remnants (7/33). There was no in-stent stenosis or jailed branch occlusion. There was no angiographic recurrence of initially totally occluded aneurysms.

**CONCLUSIONS:** MCA aneurysms with a wide neck are amenable to treatment with pCONus.

Although the superiority of endovascular treatment compared with surgery appears unaffected by aneurysm location in the randomized International Subarachnoid Aneurysm Trial,<sup>1</sup> management of middle cerebral artery aneurysms remains a matter of debate. Nevertheless many institutions still use surgical clipping as the first treatment for MCA aneurysms.<sup>2,3</sup> Balloon and stent-assisted techniques have widened the indications for endovascular treatment of MCA aneurysms with a wide neck and/or unfavorable anatomy that were otherwise unsuitable for coiling.<sup>4,5</sup> However, the risk of procedure-related morbidity and mortality is

not negligible, especially with double-stent placement in Y and X configurations.<sup>4,6,7</sup> The widespread adoption of endovascular treatment for MCA aneurysms with unfavorable anatomy requires an improvement of the safety of the endovascular approach. A new device, the pCONus aneurysm implant (phenox, Bochum, Germany), has recently been developed to improve the safety of endovascular treatment of these challenging aneurysms. To date, a single published article on intracranial aneurysms treated with pCONus reported a series including some cases of MCA aneurysms.<sup>8</sup> The aim of this study was to evaluate the results in the treatment of wide-neck MCA aneurysms with the pCONus device.

## MATERIALS AND METHODS

From June 2012 to July 2014, the clinical and angiographic outcomes of 40 consecutive patients treated at 4 institutions with the pCONus device and coils for MCA aneurysms were retrospectively analyzed. "Wide neck" was defined as a neck of >4 mm. The decision to assist the aneurysm coiling with a pCONus device was made at the discretion of the operator. All patients were informed of the procedure. In each center, the procedures were performed according to the local institutional policy.

Received November 4, 2014; accepted after revision February 11, 2015.

From the Department of Interventional Neuroradiology (B.G., F.T.), Neurologic Hospital Pierre Wertheimer, Hospices Civils de Lyon, Lyon, France; Department of Neuroradiology (M.A.-P., H.H.), Klinikum Stuttgart, Stuttgart, Germany; Department of Neuroradiology (W.W., S.F.), Knappschaftskrankenhaus, Recklinghausen, Germany; and Department of Neuroradiology and Endovascular Therapy (E.P., A.B.), Jean-Minjoz Hospital, Franche-Comté University, Besançon, France.

Please address correspondence to Alessandra Biondi, MD, PhD, Department of Neuroradiology and Endovascular Therapy, Jean-Minjoz Hospital, Franche-Comté University, 3 Boulevard A. Fleming, Besançon, France; e-mail: biondi.alessandra@gmail.com

 Indicates article with supplemental on-line table.

<http://dx.doi.org/10.3174/ajnr.A4392>

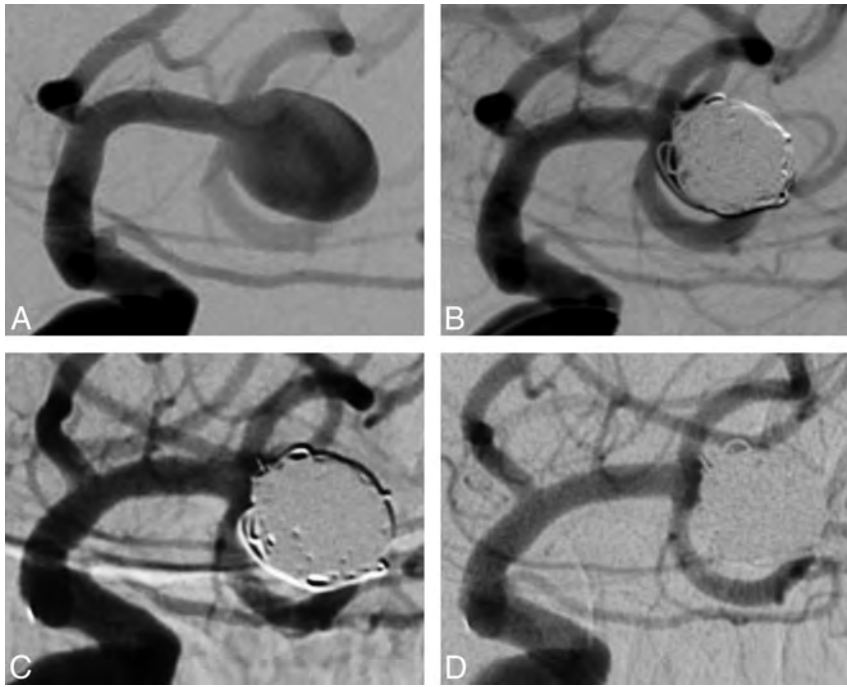


**FIG 1.** Case 1, patient 1. Left unruptured MCA aneurysm in a 76-year-old woman. *A*, Subtracted angiography of the internal carotid artery shows a wide-neck MCA aneurysm. *B*, Subtracted angiography of the internal carotid artery at the end of the procedure shows a neck remnant. *C*, Subtracted angiography of the internal carotid artery at 3 months shows complete aneurysm occlusion. *D*, Subtracted angiography of the internal carotid artery at 12 months shows persistent aneurysm occlusion.

The pCONus is a new stentlike self-expanding nitinol implant with 4 distal petals, which is fully retrievable and electrolytically detachable. The distal intra-aneurysmal inner diameter of the pCONus is additionally crossed by 6 polyamide fibers, creating a mechanical barrier between the aneurysm and the parent vessel for preventing coil protrusion into the lumen. The proximal extra-aneurysmal end of the implant and the 4 distal loops carry segmental radiopaque markers made of platinum-iridium wire. The pCONus is compatible with standard microcatheters with an inner diameter of 0.021 inches. In a suitable working projection, the distal end of the pCONus was deployed in the middle of the aneurysm sac, and the device with the microcatheter was gently pulled back; this step brings the petals more proximal to the neck of the aneurysm. Thereafter, a second microcatheter was inserted through the shaft into the aneurysm sac, and coiling was then performed.

All patients were treated under general anesthesia and full anticoagulation. In addition, double antiplatelet therapy was administered preoperatively according to the operator's protocol. A Multiplate test (Verum Diagnostica, Munich, Germany), VASP test (Lancet Laboratories, Durban, South Africa), or VerifyNow P2Y12 test (Accumetrics, San Diego, California) was systematically performed before the procedure to confirm sufficient inhibition of the platelet function. In unruptured aneurysms, a single dose of 500 mg acetylsalicylic acid and 600 mg clopidogrel was given the day before or 75 mg acetylsalicylic acid and 75 mg clopidogrel/per day were administered 5 days before the procedure. If the platelet-function inhibition was not sufficient, the patient was directly premedicated with 180 mg ticagrelor or 60 mg prasugrel. In case of SAH, patients received 600 mg clopidogrel via a gastric

tube and 500 mg acetylsalicylic acid intravenously during the procedure. Postprocedural medication included 75 mg clopidogrel for 3 months and acetylsalicylic acid (75–160 mg) orally during 12 months or for life according to each center's protocol. Postprocedural medication was the same in both the ruptured and unruptured aneurysm group.

#### **Clinical Events**

Any clinical event appearing in the postoperative course was noted. A neurologic assessment was performed before and after the treatment, at discharge, and at follow-up.

#### **Angiographic Follow-Up**

Angiographic images were acquired in anteroposterior, lateral, and working projections before and immediately after treatment. Angiographic images obtained immediately after endovascular treatment were compared with those obtained at each angiographic follow-up.

Immediate aneurysm occlusion after the procedure and at follow-up was clas-

sified by using the simplified 3-point scale (complete occlusion, neck remnant, aneurysm remnant).<sup>9</sup> In addition, the aneurysm changes were also evaluated (ie, increase or decrease in size of aneurysm neck remnants or aneurysm remnants). Two readers (B.G., A.B.) independently evaluated all the angiograms. Disagreements were solved by consensus.

The angiographic follow-up protocol consisted of a first angiographic follow-up performed from 3 to 6 months after the procedure and a second one performed at 1 year.

#### **RESULTS**

Forty MCA bifurcation aneurysms were treated with the pCONus (23 on the right side and 17 on the left). Aneurysm dome sizes ranged from 2.7 to 17.4 mm (mean, 7.7 mm), and neck sizes ranged from 2.8 to 13.8 mm (mean, 5.6 mm;  $\geq 4$  mm in 35 aneurysms). Forty patients (27 women and 13 men) ranged from 36 to 77 years of age (mean, 62 years). Ninety percent (36/40) of aneurysms were unruptured, 5% (2/40) were recanalized (all were previously treated endovascularly), and 5% (2/40) were ruptured. Thirty-eight aneurysms were treated with 1 pCONus device, and in 2 patients, the aneurysm was treated by using 2 pCONus devices. In 4 patients, the pCONus treatment was performed after failure of aneurysm endovascular treatment with the WEB aneurysm embolization system (Sequent Medical, Aliso Viejo, California). Coiling was performed with bare platinum coils in 97.5% of cases (39/40).

#### **Immediate Angiographic Results**

In all cases, the pCONus devices were successfully deployed. Anatomic outcome is detailed in the On-line Table. Immediate an-

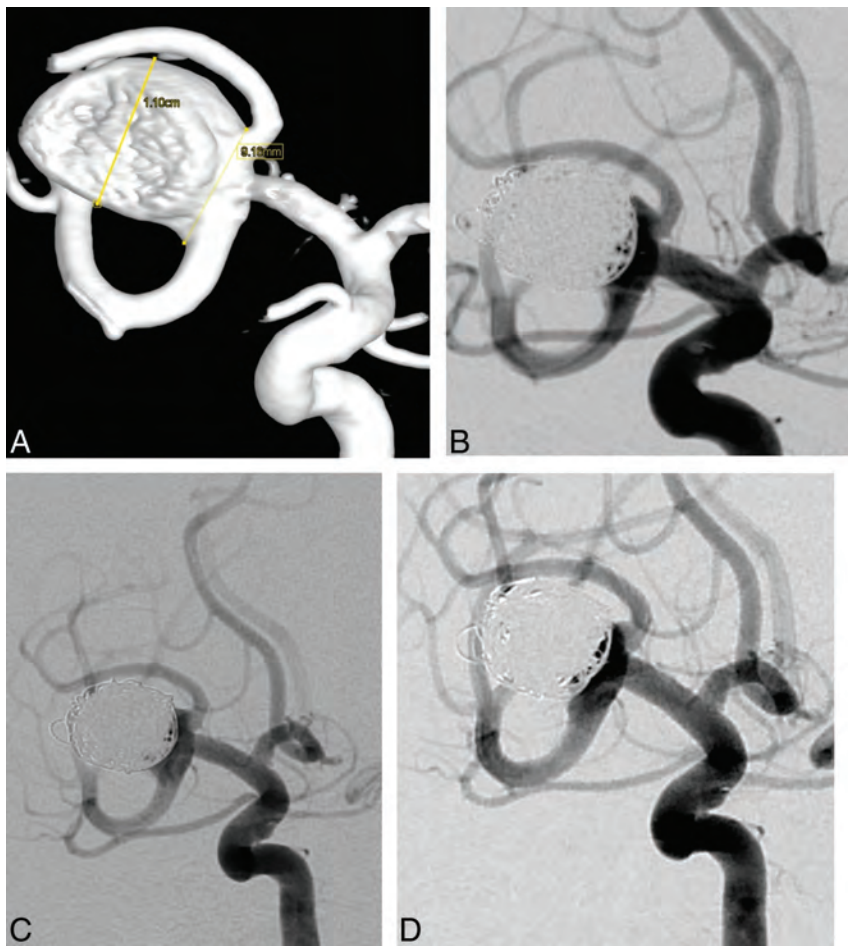


**FIG 2.** Case 2, patient 33. Right unruptured MCA aneurysm in a 50-year-old woman. **A**, 3D reconstruction after rotational angiography shows a large MCA aneurysm with a 9-mm neck. The superior branch is emerging from the neck of the aneurysm. **B**, Subtracted angiography of the internal carotid artery at the end of the procedure shows a neck remnant. Subtracted angiographies of the internal carotid artery at 6 months (**C**) and at 12 months (**D**) show a stable neck remnant.

giograms showed complete occlusion in 25% (10/40), neck remnant in 47.5% (19/40), and aneurysm remnant in 27.5% (11/40).

#### Angiographic Follow-Up

Angiographic follow-up from 3 to 12 months (mean, 6.8 months) was available in 33 aneurysms (82.5%), and 14 aneurysms (35%) had a 12-month follow-up. Angiographic follow-up showed complete occlusion in 48.5% (16/33), neck remnants in 30.3% (10/33), and aneurysm remnants in 21.2% (7/33). Adequate occlusion (total occlusion and neck remnant) was obtained in 78.8% (26/33) (On-line Table and Figs 1–3).

At follow-up, among these 33 aneurysms, aneurysm occlusion improved in 42.4% (14/33), was stable in 48.4% (16/33), and worsened in 9.2% (3/33). In 5 cases, the aneurysm remnants increased in size, requiring further endovascular procedures in 4 of them. No in-stent stenosis or jailed branch occlusion was observed. During the first year of follow-up, retreatment was performed in 17.5% of cases (7/40) due to persistent or increase in size of aneurysm remnants (6/7) or an important increase in size of the neck remnant (1/7). The size of the retreated aneurysms was

>10 mm in 57.1% (4/7). Retreated aneurysms had a neck size of  $\geq 6$  mm in 71.4% (5/7). Postoperative angiographic outcome included 1 complete occlusion, 4 neck remnants, and 2 aneurysm remnants.

#### Procedural and Clinical Complications

No angiographic thromboembolic event or intraoperative rupture was observed. Reversible neurologic complications were noted in 5% of the patients (2/40). In 1 case (patient 3), the patient sustained a reversible right hemiparesis immediately after the procedure. A thromboembolic incident with a new ischemic lesion on MR imaging was observed. The patient was asymptomatic at discharge (mRS 0). In the other case (patient 35), the patient had a transient hypostenia of her left hand immediately after the procedure. The mRS scale was 1 at discharge. A patient (patient 1) presented with a permanent neurologic complication with right hemiparesis and aphasia, due to an ischemic lesion. No specific treatment was started. The patient improved within 2 days and was discharged with NIHSS 3 and mRS 1. Consequently, permanent morbidity was 2.5% and mortality was 0% at 1 month. There were no delayed neurologic deficits or deaths at follow-up.

#### pCONus in Subarachnoid Hemorrhage

Two aneurysms (5%) were treated with pCONus in the setting of subarachnoid hemorrhage. The first was an 11.1-mm right MCA aneurysm with a 10.6-mm neck in a man 46 years of age who presented with a Fisher grade 4 SAH (patient 5). The final angiogram showed a residual aneurysm. Follow-up angiography performed 3 months and 1 year later demonstrated that the residual aneurysm was unchanged. The second case was an 11.1-mm aneurysm of the right MCA bifurcation in a 53-year-old woman with a Fisher grade 3 SAH (patient 14). The post-procedural angiogram showed a neck remnant. The follow-up angiogram at 3 months demonstrated an aneurysm remnant with worsening angiographic findings.

#### DISCUSSION

The use of pCONus in MCA bifurcation aneurysms with a wide neck allows a relatively efficient and safe endovascular treatment of the aneurysm despite the very specific population. In fact, we reported 1 permanent neurologic complication (2.5%) and no death. These findings compare favorably with the morbidity and

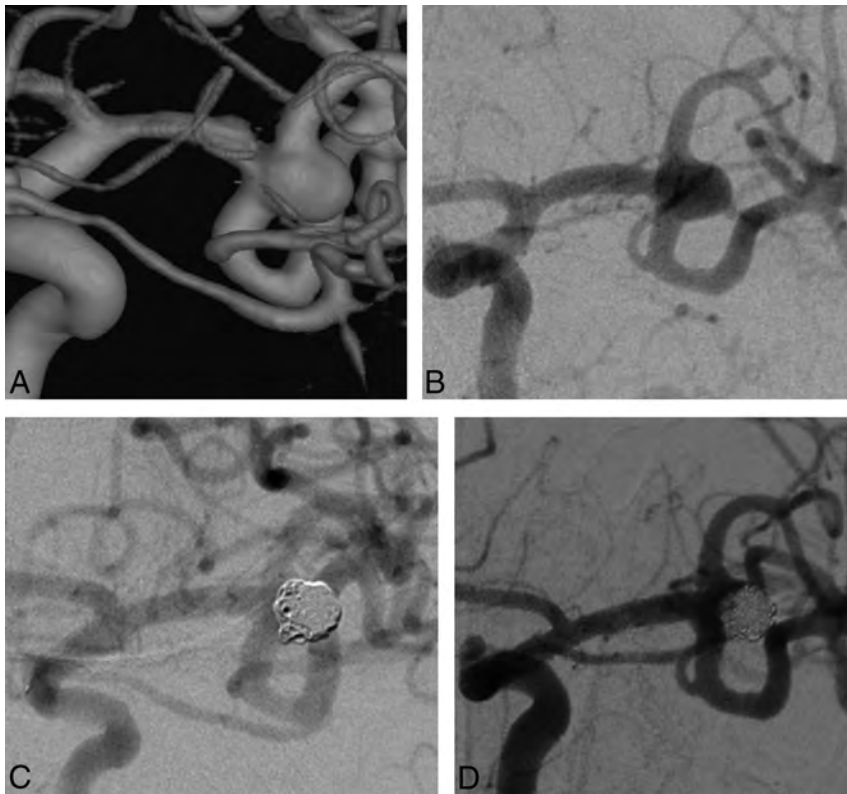


**FIG 3.** Case 3, patient 36. Left unruptured MCA aneurysm in a 41-year-old man. A, 3D reconstruction after rotational angiography and subtracted angiography (B) of the internal carotid artery shows a 4.2-mm MCA aneurysm with a 5.1-mm neck. C, Subtracted angiography of the internal carotid artery at the end of the procedure shows a neck remnant. D, Subtracted angiography of the internal carotid artery at 6 months shows a neck remnant.

mortality of endovascular treatment of MCA aneurysms reported by Brinjikji et al<sup>5</sup> (3.9% and 1.2%, respectively). In the first published series, the safety of the pCONus was also highlighted because no clinically evident complication associated with its use was observed in 28 wide-neck aneurysms, including 9 recently ruptured ones.<sup>8</sup>

An endovascular approach to MCA aneurysms often requires the use of a balloon- or stent-assisted coiling technique. In a recent prospective cohort of 131 consecutive nonselected MCA aneurysms (34.2% ruptured aneurysms), balloon assistance was required in 60.3%.<sup>4</sup> As previously reported, the balloon-assisted coiling technique does not seem to increase the complication rate compared with simple coiling in unruptured and ruptured aneurysms.<sup>4,10</sup> Similar results concerning safety have also been reported by using stent-assisted coiling of wide-neck aneurysms.<sup>11-14</sup> In a multicenter study reporting the use of the Neuroform stent (Stryker Neurovascular, Kalamazoo, Michigan),<sup>12</sup> permanent morbidity and mortality rates were 1%, respectively, at 12- to 18-month follow-up. In another article, treatment-related permanent morbidity was 1.6% and mortality was 0% by using the Solitaire AB stent (Covidien, Irvine, California).<sup>13</sup> On the contrary, other authors reported that intracranial stent placement, especially with double stents in Y and X configurations, seems to highly increase the risk of clinical complications.<sup>6,7</sup> The rate of procedure-related permanent neurologic deficits in one study was 10% in 97 patients with complex and wide-neck bifurcation aneurysms.<sup>6</sup> The odds of developing

complications were 4.8× greater when stents were used in the treatment of non-selected MCA aneurysms.<sup>4</sup> In addition, the MCA location is more likely to be associated with procedural complications in stent-assisted coiling, as recently outlined.<sup>15</sup> We encountered no case of in-stent stenosis at follow-up, a rate lower than that reported (4.2%) in a series of stent-assisted coiling of 52 unruptured MCA aneurysms with longer follow-up (mean, 14 months).<sup>16</sup> However, angiography was performed in only 58% of patients.

The University of California, San Francisco, surgery group reported a 4.6% permanent morbidity rate and a 5.3% mortality rate after surgery in 631 MCA aneurysms in 543 patients,<sup>2</sup> which seems less safe than the endovascular outcome. However, for the morbidity-mortality rate, one must consider that ruptured aneurysms were present in 51.9% in the University of California, San Francisco, series, whereas our series included only 5% ruptured lesions. In the International Subarachnoid Aneurysm Trial, patients with a ruptured MCA aneurysm treated with endovascular coiling had a significantly better

outcome at 1, 7, and 18 years compared with those treated by surgery.<sup>1,17,18</sup> Nevertheless, to date, no randomized clinical trials have addressed the question of the first treatment for wide-neck MCA aneurysms, to our knowledge. In addition, although the rate of aneurysm recurrence appears low after surgical clipping, it is difficult to compare the rate of aneurysm recurrence after endovascular treatment versus surgical clipping because only a few surgical series reported long-term angiographic follow-up.<sup>7,8</sup> In the University of California, San Francisco, surgical series, long-term follow-up with angiography was performed in only 106 of 480 patients (22%).<sup>2</sup>

Although stent placement is generally avoided in acutely ruptured aneurysms because of the requirement of dual antiplatelet medication,<sup>19</sup> 2 aneurysms of our series were ruptured. More complications were also reported in cases of ruptured MCA aneurysms managed by a surgical approach (8.5% versus 4.9%).<sup>2</sup> In the setting of acute SAH, an intrasaccular flow disrupter, such as the WEB device, could be a therapeutic solution due to the lack of antiplatelet agents. However, it may not provide the immediate protection from rebleeding offered by coiling or surgical clipping. In a recent small series of 6 patients with acute ruptured aneurysms (3 MCA and 3 anterior communicating artery aneurysms) treated with the WEB device, no rebleeding was reported.<sup>20</sup> The use of flow diverters is relatively limited in cases of bifurcation aneurysms because preservation of the bifurcation branches is unpredictable.<sup>21</sup> However, no clinical complication was recently reported after treatment of 5 large and 3 giant MCA aneurysms,<sup>22</sup>

whereas other authors reported a 16% (4/25) rate of morbidity after treatment of 25 MCA aneurysms with the Pipeline Embolization Device (Covidien).<sup>23</sup>

In the past, the TriSpan (Boston Scientific, Natick, Massachusetts) had been specifically developed for the treatment of wide-neck aneurysms. However, the TriSpan is no longer available, and few data were published. In 1 series, the authors evaluated the TriSpan neck-bridge device to assist coiling in a series of patients with wide-neck bifurcation aneurysms of the anterior circulation (6 MCA aneurysms, 6 anterior communicating artery aneurysms, 1 carotid siphon aneurysm, and 1 carotid bifurcation aneurysm).<sup>24</sup> A complication and severe procedure-related complication occurred in 6 cases (37.5%) and 1 case (6.25%), respectively. Late aneurysmal outcome, assessed by MRA or angiography at 1–39 months (mean, 12.9 months) posttreatment, was available in 8 patients and showed complete occlusion in 2 (14.3%), neck remnant in 2 (14.3%), and aneurysm remnant in 4 (28.6%) cases. A novel assisted coiling device, the PulseRider aneurysm neck reconstruction device (Pulsar Vascular, San Jose, California), intended for use in the treatment of wide-neck aneurysms arising at bifurcations, was used in 3 patients; however, the article is in press and no follow-up is available with this new device.<sup>25,26</sup>

In the present series, immediate adequate aneurysm occlusion (complete occlusion or neck remnant) was achieved in most cases (72.5%). Moreover, no case of angiographic in-stent stenosis or jailed branch occlusion was observed. Although long-term follow-up is available in only 35% of cases in our series, pCONus seems to achieve a durable treatment with a low rate of angiographic recurrence. No angiographic recurrence of initially totally occluded aneurysms was observed. In addition, the pCONus could promote progressive aneurysm thrombosis because 42.4% of aneurysms demonstrated a better angiographic result at short- or midterm follow-up. Previously published series have also reported a progressive thrombosis phenomenon after stent-assisted coiling.<sup>7,13</sup>

In a series of 33 wide-neck MCA aneurysms treated by using the WEB device, a similar adequate occlusion rate (83.3%) has been reported at follow-up.<sup>27</sup> However, in our series, the rate of neck remnants with the pCONus (30.3%) was inferior to that reported by using the WEB device (56.7%). In addition, the pCONus could be an effective treatment after WEB-placement failure. Actually, in 4 aneurysms in our series in which the WEB deployment had failed, a successful treatment with pCONus was performed in all 4 aneurysms with complete occlusion in 3. However, longer follow-up is mandatory to evaluate the efficacy of this treatment in terms of aneurysm recanalization. In our series, all patients were followed by using angiography, which remains the criterion standard. At the present, artifacts introduced by the pCONus limit the value of MR imaging as a follow-up technique, especially for the evaluation of the parent artery where the extra-aneurysmal part of the pCONus is deployed. Contrast administration could improve vessel lumen visualization.<sup>28</sup>

The present study has some limitations including the number of patients being relatively small and the long-term follow-up lacking in some cases. However, our preliminary evaluation of this new endovascular approach for the treatment of MCA aneurysms with unfavorable anatomy shows that the pCONus device can be an interesting and safe option for such complex lesions.

## CONCLUSIONS

In our selected population, pCONus stent-assisted coiling safely allows endovascular treatment of wide-neck MCA aneurysms that are usually considered surgical due to defavorable anatomy. Longer follow-up is mandatory to evaluate the efficacy of this treatment in terms of aneurysm recanalization.

Disclosures: Marta Aguilar Pérez—UNRELATED: Consultancy: phenox; Other: phenox (proctoring). Francis Turjman—UNRELATED: Consultancy: Codman,\* Covidien,\* Stryker,\* Sequent Medical\*; Grants/Grants Pending: Covidien\*; Payment for Lectures (including service on Speakers Bureaus): Codman,\* Covidien\*; Payment for Development of Educational Presentations: Codman,\* Covidien\*; Travel/Accommodations/Meeting Expenses Unrelated to Activities Listed: Covidien,\* Codman,\* Stryker.\* Werner Weber—UNRELATED: Consultancy: Proctor for the pCONus and p64 Flow Modulation Device; Payment for Lectures (including service on Speakers Bureaus): phenox (products: pCONus and flow-diverter p64 Flow Modulation Device), Comments: German Society Meeting in Cologne 2013 and 2014. Hans Henkes—RELATED: Consulting Fee or Honorarium: phenox, Comments: I have a consulting contract and a proctoring contract with phenox, which includes compensation on a fee-for-service basis; Support for Travel to Meetings for the Study or Other Purposes: phenox, Comments: Compensation for expenses related to the participation in meetings with presentation of p64 Flow Modulation Device data; Other: phenox, Comments: I am cofounder and shareholder of phenox; UNRELATED: Board Membership: phenox, Comments: Expenses related to board meetings are compensated; Grants/Grants Pending: Siemens (cooperation in relation to DynaCT),\* Covidien (stroke research support)\*; Payment for Lectures (including service on Speakers Bureaus): Covidien; Patents (planned, pending or issued): Dendron GmbH Bochum, phenox,\* Comments: participation in numerous patents filed by Dendron GmbH and phenox; Royalties: phenox; Stock/Stock Options: phenox, Comments: I am cofounder and shareholder of phenox; Travel/Accommodations/Meeting Expenses Unrelated to Activities Listed: ab medica,\* Comments: compensation for physician training courses. Alessandra Biondi—RELATED: Consulting Fee or Honorarium: phenox; UNRELATED: Travel/Accommodations/Meeting Expenses Unrelated to Activities Listed: Stryker Neurovascular, Covidien. \*Money paid to the institution.

## REFERENCES

1. Molyneux A, Kerr R, Stratton I, et al; International Subarachnoid Aneurysm Trial (ISAT) Collaborative Group. **International Subarachnoid Aneurysm Trial (ISAT) of neurosurgical clipping versus endovascular coiling in 2143 patients with ruptured intracranial aneurysms: a randomised trial.** *Lancet* 2002;360:1267–74
2. Rodríguez-Hernández A, Sughrue ME, Akhavan S, et al. **Current management of middle cerebral artery aneurysms: surgical results with a “clip first” policy.** *Neurosurgery* 2013;72:415–27
3. Pasqualin A, Meneghelli P, Cozzi F, et al. **Surgical exclusion of unruptured middle cerebral artery aneurysms: experience of 126 cases.** *Acta Neurochir Suppl* 2014;119:25–31
4. Gory B, Rouchaud A, Saleme S, et al. **Endovascular treatment of middle cerebral artery aneurysms for 120 nonselected patients: a prospective cohort study.** *AJNR Am J Neuroradiol* 2014;35:715–20
5. Brinjikji W, Lanzino G, Cloft HJ, et al. **Endovascular treatment of middle cerebral artery aneurysms: a systematic review and single-center series.** *Neurosurgery* 2011;68:397–402; discussion 402
6. Bartolini B, Blanc R, Pistocchi S, et al. **“Y” and “X” stent-assisted coiling of complex and wide-neck intracranial bifurcation aneurysms.** *AJNR Am J Neuroradiol* 2014;35:2153–58
7. Piotin M, Blanc R, Spelle L, et al. **Stent-assisted coiling of intracranial aneurysms: clinical and angiographic results in 216 consecutive aneurysms.** *Stroke* 2010;41:110–15
8. Aguilar-Pérez M, Kurre W, Fischer S, et al. **Coil occlusion of wide-neck bifurcation aneurysms assisted by a novel intra- to extra-aneurysmal neck-bridging device (pCONus): initial experience.** *AJNR Am J Neuroradiol* 2014;35:965–71
9. Raymond J, Guilbert F, Weill A, et al. **Long-term angiographic re-**

- currences after selective endovascular treatment of aneurysms with detachable coils. *Stroke* 2003;34:1398–403
10. Pierot L, Spelle L, Leclerc X, et al. Endovascular treatment of unruptured intracranial aneurysms: comparison of safety of remodeling technique and standard treatment with coils. *Radiology* 2009;251:846–55
  11. Biondi A, Janardhan V, Katz JM, et al. Neuroform stent-assisted coil embolization of wide-neck intracranial aneurysms: strategies in stent deployment and midterm follow-up. *Neurosurgery* 2007;61:460–68; discussion 468–69
  12. Gentric JC, Biondi A, Piotin M, et al; French SENAT Investigators. Safety and efficacy of Neuroform for treatment of intracranial aneurysms: a prospective, consecutive, French multicentric study. *AJNR Am J Neuroradiol* 2013;34:1203–08
  13. Gory B, Klisch J, Bonafé A, et al. Solitaire AB stent-assisted coiling of wide-necked intracranial aneurysms: short-term results from a prospective, consecutive, European multicentric study. *Neuroradiology* 2013;55:1373–78
  14. Gory B, Klisch J, Bonafé A, et al. Solitaire AB stent-assisted coiling of wide-necked intracranial aneurysms: mid-term results from the SOLARE study. *Neurosurgery* 2014;75:215–19; discussion 219
  15. Chalouhi N, Jabbour P, Singhal S, et al. Stent-assisted coiling of intracranial aneurysms: predictors of complications, recanalization, and outcome in 508 cases. *Stroke* 2013;44:1348–53
  16. Vendrell JF, Costalat V, Brunel H, et al. Stent-assisted coiling of complex middle cerebral artery aneurysms: initial and midterm results. *AJNR Am J Neuroradiol* 2011;32:259–63
  17. Molyneux AJ, Kerr RS, Yu LM, et al; International Subarachnoid Aneurysm Trial (ISAT) Collaborative Group. International Subarachnoid Aneurysm Trial (ISAT) of neurosurgical clipping versus endovascular coiling in 2143 patients with ruptured intracranial aneurysms: a randomised comparison of effects on survival, dependency, seizures, rebleeding, subgroups, and aneurysm occlusion. *Lancet* 2005;366:809–17
  18. Molyneux AJ, Birks J, Clarke A, et al. The durability of endovascular coiling versus neurosurgical clipping of ruptured cerebral aneurysms: 18 year follow-up of the UK cohort of the International Subarachnoid Aneurysm Trial (ISAT). *Lancet* 2015;385:691–97
  19. Bodily KD, Cloft HJ, Lanzino G, et al. Stent-assisted coiling in acutely ruptured intracranial aneurysms: a qualitative, systematic review of the literature. *AJNR Am J Neuroradiol* 2011;32:1232–36
  20. Caroff J, Mihalea C, Dargento F, et al. Woven Endobridge (WEB) device for endovascular treatment of ruptured intracranial wide-neck aneurysms: a single-center experience. *Neuroradiology* 2014;56:755–61
  21. Gory B, Bonafé A, Pierot L, et al. Safety and efficacy of flow-diverter stents in endovascular treatment of intracranial aneurysm: interest of the prospective DIVERSION observational study. *J Neuroradiol* 2014;41:93–96
  22. Zanaty M, Chalouhi N, Tjoumakaris SI, et al. Flow diversion for complex middle cerebral artery aneurysms. *Neuroradiology* 2014;56:381–87
  23. Yavuz K, Geyik S, Saatci I, et al. Endovascular treatment of middle cerebral artery aneurysms with flow modification with the use of the Pipeline embolization device. *AJNR Am J Neuroradiol* 2014;35:529–35
  24. De Keukeleire K, Vanlangenhove P, Defreyne L. Evaluation of a neck-bridge device to assist endovascular treatment of wide-neck aneurysms of the anterior circulation. *AJNR Am J Neuroradiol* 2008;29:73–78
  25. Spiotta AM, Chaudry MI, Turk AS, et al. Initial experience with the PulseRider for the treatment of bifurcation aneurysms: report of first three cases in the USA. *J Neurointerv Surg* 2015 Jan 5. [Epub ahead of print]
  26. Gory B, AM Spiotta, S Mangiafico, et al. PulseRider stent-assisted coiling of wide-neck bifurcation aneurysms: periprocedural results in an international series. *AJNR Am J Neuroradiol* 2015.
  27. Pierot L, Klisch J, Cognard C, et al. Endovascular WEB flow disruption in middle cerebral artery aneurysms: preliminary feasibility, clinical, and anatomical results in a multicenter study. *Neurosurgery* 2013;73:27–34; discussion 34–35
  28. Lövblad KO, Yilmaz H, Chouiter A, et al. Intracranial aneurysm stenting: follow-up with MR angiography. *J Magn Reson Imaging* 2006;24:418–22

# Artery of the Superior Orbital Fissure: An Undescribed Branch from the Pterygopalatine Segment of the Maxillary Artery to the Orbital Apex Connecting with the Anteromedial Branch of the Inferolateral Trunk

H. Kiyosue, S. Tanoue, N. Hongo, Y. Sagara, and H. Mori



## ABSTRACT

**BACKGROUND AND PURPOSE:** Some branches of the internal maxillary artery have anastomoses with the inferolateral trunk that are important as intracranial-extracranial collateral pathways and as dangerous anastomoses for transarterial embolization of these branches. We present here an undescribed branch potentially anastomosing with the anteromedial branch of the inferolateral trunk, which is provisionally named the artery of the superior orbital fissure, defined as an arterial branch from the pterygopalatine segment of the maxillary artery to the orbital apex at the superior orbital fissure.

**MATERIALS AND METHODS:** Two neuroradiologists reviewed 3D and MPR images of the external and/or common carotid artery with particular interest paid to the artery of the superior orbital fissure in 54 patients who underwent 3D angiography with a field of view covering the pterygopalatine fossa and the cavernous sinus. The underlying diseases in these patients were 17 parasellar hypervascular lesions (including 13 cavernous sinus dural arteriovenous fistulas and 4 meningiomas), 18 internal carotid artery stenoses/occlusions, and 19 other diseases.

**RESULTS:** The artery of the superior orbital fissure was identified in 20 of 54 patients; it arose at the pterygopalatine segment of the maxillary artery, either singly or from a common trunk with the artery of the foramen rotundum, and ran upward to reach the superior orbital fissure. It anastomosed with the anteromedial branch of the inferolateral trunk at the superior orbital fissure with blood flow toward the cavernous sinus ( $n = 14$ ) and/or the ophthalmic artery ( $n = 2$ ). It was more prominent in parasellar hypervascular lesions and internal carotid artery stenoses/occlusions than in other diseases.

**CONCLUSIONS:** The artery of the superior orbital fissure, a remnant of the anastomotic artery, was often identified, especially in patients with parasellar hypervascular lesions.

**ABBREVIATIONS:** ILT = inferolateral trunk; PPF = pterygopalatine fossa; SOF = superior orbital fissure

The maxillary artery is a major terminal branch of the external carotid artery, which is divided into 3 segments. The first segment originates anterosuperiorly in the deep parotid gland, and the second segment runs anteriorly to reach the pterygomaxillary fissure. It then turns medially to enter the pterygopalatine fossa (PPF) through the pterygomaxillary fissure, becoming the third segment.<sup>1</sup> The third segment, the

terminal part of the maxillary artery, runs transversely in the PPF, which is a narrow space bounded by multiple bony structures. The maxillary arterial branches from the third segment run through various fissures, canals, and foramina to supply various tissues and organs of the surrounding areas.<sup>1-7</sup> The artery of the foramen rotundum is thought to be the sole arterial branch of the third segment of the internal maxillary artery to enter the cavernous sinus through the foramen rotundum.<sup>1,5,6</sup> It can supply skull base tumors and dural arteriovenous fistulas, and it has a potential anastomosis with the anterolateral branch of the inferolateral trunk (ILT).

There are 2 communication pathways between the PPF and orbita. The uppermost part of the PPF communicates directly with the orbital apex at the superior orbital fissure (SOF), and the PPF communicates anterolaterally with the inferolateral part of the orbita through the inferior orbital fissure (Fig 1).<sup>8,9</sup> The

Received November 11, 2014; accepted after revision February 14, 2015.

From the Department of Radiology, Oita University Faculty of Medicine, Oita, Japan.

Paper previously presented at: Annual Meeting of the Radiological Society of North America, November 30–December 5, 2014; Chicago, Illinois.

Please address correspondence to Hiro Kiyosue, MD, 1-1 Idaigaoka, Hasama, Yufu City, Oita 879-5963, Japan; e-mail: hkiyosue@oita-u.ac.jp

Indicates open access to non-subscribers at [www.ajnr.org](http://www.ajnr.org)

<http://dx.doi.org/10.3174/ajnr.A4331>

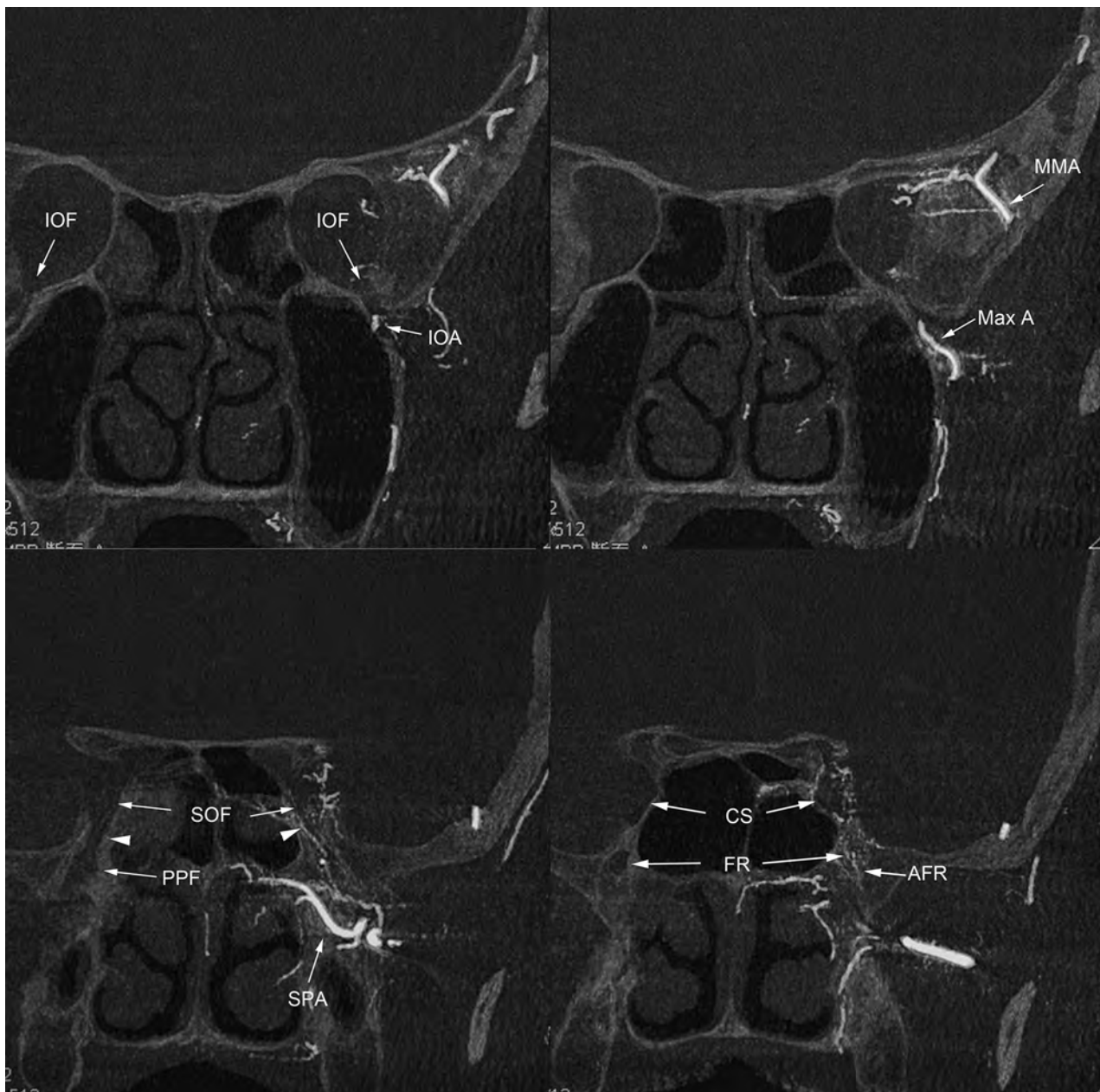


**FIG 1.** MPR images of rotational angiography in patients with left cavernous sinus dural arteriovenous fistulas. The coronal plane at the level of the inferior orbital fissure (IOF) shows the infraorbital artery (IOA) running through the inferior orbital fissure, through which the pterygopalatine fossa communicates anteriorly with the orbita. The third segment of the maxillary artery (Max A) is located in the pterygopalatine fossa. The coronal plane at the level of the medial part of the PPF shows the pterygopalatine fossa communicating superiorly with the orbital apex (*arrowheads*) at the SOF. Note a small arterial branch (artery of the SOF) running from the PPF to the SOF through this communication pathway. The PPF communicates medially with the nasal cavity via the sphenopalatine canal containing the sphenopalatine artery (SPA). The PPF communicates posteriorly with the middle cranial fossa via the foramen rotundum (FR), which contains the artery of the foramen rotundum (AFR). The superior orbital fissure continues to the cavernous sinus (CS). MMA indicates middle meningeal artery.

upward communication can be a potential pathway communicating between the PPF and the orbita as well as the middle cranial fossa. Similarly, we found an undescribed branch via the direct communicating pathway between the uppermost part of the PPF and orbital apex, which is provisionally named the artery of the SOF, which originates from the pterygopalatine segment of the maxillary artery and runs upward to reach the orbital apex at the SOF. It frequently anastomoses with the anteromedial branch of the ILT to supply parasellar hypervascular lesions through the

SOF. In this study, we investigated the presence and course of the artery of the SOF in various pathologic conditions by using 3D rotational angiography.

#### **MATERIALS AND METHODS**

We retrospectively reviewed biplane and 3D rotational angiography of the external carotid artery and/or common carotid artery performed at our institution from June 2010 to February 2014.

## Characteristics of 54 patients

Characteristic	Patient Data
Gender, <i>n</i>	
Male	30
Female	24
Age (range [average]), <i>y</i>	23–85 (67.7)
Injected arteries, <i>n</i>	
Right ECA	18
Left ECA	17
Right CCA	14
Left CCA	15
Diseases, <i>n</i>	
CSDAVF	13
Other DAVF	6
Meningioma	7
Glioma	3
Head or neck tumor	2
ICA stenosis	15
ICA occlusion	3
Other disease	5

**Note:**—CCA indicates common carotid artery; CSDAVF, cavernous sinus dural arteriovenous fistula; DAVF, dural arteriovenous fistula; ECA indicates external carotid artery.

Datasets of 3D rotational angiography of which the field of view did not cover the entire PPF, orbital apex, or cavernous sinus were excluded. Sixty-four datasets in 54 patients were selected for further evaluation. The characteristics of the 54 patients are summarized in the Table. Patient ages ranged from 23 to 85 years (mean age, 67.7 years), and there were 30 men and 24 women. Underlying diseases included 19 cases of dural arteriovenous fistula at the cavernous sinus ( $n = 13$ ), transverse-sigmoid sinus ( $n = 2$ ), or another location ( $n = 4$ ); 10 cases of brain tumor (including 7 meningiomas at the parasellar region [ $n = 4$ ] or convexity [ $n = 3$ ]); 18 cases of internal carotid artery stenosis (15 stenoses and 3 occlusions); and 7 other diseases.

Rotational angiography and biplane digital subtraction angiography of the external carotid artery and/or the common carotid artery were performed in all patients by using biplane angiography equipment (Infinix VB; Toshiba Medical, Tokyo, Japan). The rotational angle was 200°, and the rotational speed of the C-arm was 50°/s. The data were acquired in a 512 × 512 matrix by using an 8-inch field-of-view flat panel detector. A nonionic iodinated contrast material (iopamidol [Iopamiron 300; Bayer Health Care, Osaka, Japan]) was injected at a flow rate of 1.5–3.5 mL/s (14–24.5 mL of total volume) through an automatic injector, and the injection was initiated 1.0–2.0 s before the rotation. The 3D rotational angiography raw data were transferred to a workstation (Ziostation; Ziosoft, Tokyo, Japan), and 3D and MPR images consisting of sections with 0.3- to 1-mm thickness and a 0.5-mm interval were reconstructed.

All angiographic images and partial MIP and MPR images from the 3D digital angiography were reviewed by 2 experienced neuroradiologists (H.K. and S.T.) to reach consensus on the presence, origin, and course of the artery of the SOF. The artery of the SOF was defined as an arterial branch that originates from the third segment of the maxillary artery and runs superiorly in the pterygopalatine fossa to reach the orbital apex at the SOF. Selective angiography of the feeding arteries of the maxillary artery was also reviewed as a reference when available.

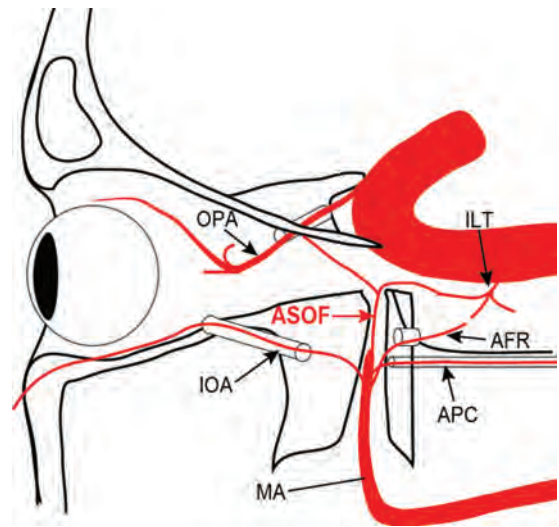


**FIG 2.** Schematic drawing of the course of the artery of the SOF from the third segment of the maxillary artery (MA). The artery of the SOF (ASOF) runs upward to reach the orbital apex and turns posteriorly to enter the cavernous sinus through the SOF. It has potential anastomosis with the anteromedial branch of the ILT and the ophthalmic artery (OPA). The artery of the foramen rotundum and the artery of the pterygoid canal (APC) run more posteriorly to enter the middle cranial fossa through the foramen rotundum and the foramen lacerum through the pterygoid canal, respectively. The infraorbital artery runs anteriorly to enter the orbital fossa through the inferior orbital fissure.

Each patient was classified into 1 of 3 groups according to the type of underlying disease: 1) parasellar hypervascular disease, including cavernous sinus dural arteriovenous fistulas and parasellar meningiomas, 2) stenosis or occlusive disease of the cervical internal carotid artery, and 3) other disease.

## RESULTS

The artery of the SOF was identified in 20 of 54 patients (20 of 64 sides). It originated upward at the pterygopalatine segment of the maxillary artery. It arose by a common trunk, with the artery of the foramen rotundum in 12 patients and independently at a more distal part of the maxillary artery in 8 patients. It ran upward in the upper part of the PPF along its posteromedial wall to reach the orbital apex at the SOF. It anastomosed with the anteromedial branch of the ILT with blood flow toward the cavernous sinus ( $n = 14$ ) and/or the ophthalmic artery ( $n = 2$ ) (Fig 2).

The artery of the SOF was seen as a feeding artery in 11 of 17 patients with parasellar hypervascular lesions (9 cavernous sinus dural arteriovenous fistulas and 2 parasellar meningiomas) (Figs 3 and 4) and as a collateral pathway communicating with the anteromedial branch of the inferolateral trunk to the internal carotid artery and/or the ophthalmic artery in 5 of 18 patients with internal carotid artery stenosis/occlusion (Fig 5). Of 19 patients with other diseases, it was observed in 4 patients, and it was very small and could not be traced beyond the SOF in any of the patients.

## DISCUSSION

In human embryos, there are several anastomotic arteries between the maxillary artery and internal carotid artery. These

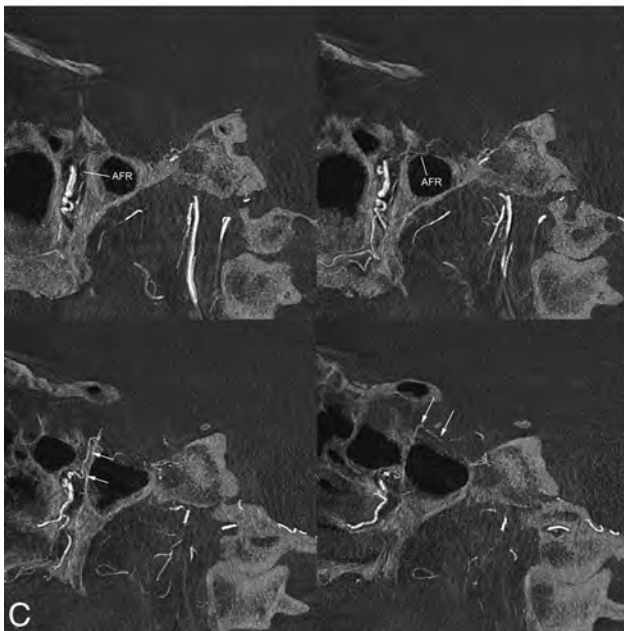
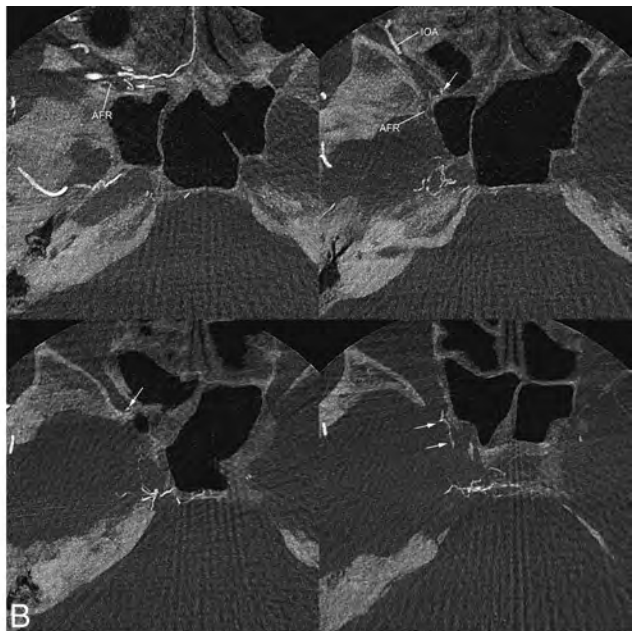


**FIG 3.** Case of left cavernous sinus dural arteriovenous fistulas supplied by the artery of superior orbital fissure. *A*, The lateral view of the right external carotid angiography shows cavernous sinus dural arteriovenous fistulas fed by multiple feeding arteries, including the artery of the foramen rotundum (arrows) and the artery of the SOF (arrowheads). The artery of the foramen rotundum (arrows) originates posterosuperiorly from the pterygopalatine segment of the maxillary artery and runs posterosuperiorly to the cavernous sinus. The artery of the SOF arises more superiorly from the maxillary artery and runs upward. *B*, Axial reformatted images of the rotational angiography of the right external carotid artery. The artery of the SOF (arrow) originates at the terminal portion of the maxillary artery just before the sphenopalatine artery. The artery of the foramen rotundum (AFR) originates at the more proximal portion of the pterygopalatine segment of the maxillary artery. The artery of the foramen rotundum runs posteriorly to enter the middle cranial fossa through the foramen rotundum. The artery of the SOF runs upward in the posteromedial portion of the pterygopalatine fossa, and then it runs posteriorly to enter the cavernous sinus through the SOF. The intracranial part of the arterial opacification represents its anastomosis with the anteromedial branch of the inferolateral trunk. Note that the inferior orbital artery (IOA) runs anteriorly to enter the orbital floor through the inferior orbital fissure. *C*, Sagittal MPR images show that the artery of the foramen rotundum runs posterosuperiorly in the pterygopalatine fossa and enters the middle cranial fossa through the foramen rotundum. The artery of the SOF (arrows) originates independently from the artery of the foramen rotundum and runs upward in the small canal to reach the orbital apex and then turns posteriorly to enter the cavernous sinus through the SOF by anastomosis with the anteromedial branch of the inferolateral trunk.

anastomotic arteries regress before birth, and remnants of these anastomotic branches of the internal carotid artery become the branches of the inferolateral trunk.<sup>10,11</sup> These anastomoses can remain as potential anastomotic pathways communicating between the maxillary artery and the inferolateral trunk, such as the cavernous sinus branch of the middle meningeal artery with the posterolateral branch, posterior branch of the accessory meningeal artery with the posterolateral branch, and the artery of the foramen rotundum with the anterolateral branch of the inferolateral trunk (Fig 6). Among these anastomotic arteries, an anastomotic branch arising from the distal portion of the maxillary artery communicates with the ophthalmic artery and an anastomotic branch of the internal carotid artery, which is a precursor of the anteromedial branch of the inferolateral trunk. The extreme variation of the remnant of anastomoses between the inferolateral trunk

and the ophthalmic artery is the so-called persistent dorsal ophthalmic artery, coined by Lasjaunias.<sup>12</sup> Similarly, the remnant of the anastomotic branch from the distal maxillary artery to the ophthalmic artery and the anteromedial branch of the inferolateral trunk would become the artery of the SOF.

In this study, the artery of the SOF anastomosing to the anteromedial branch of the ILT was frequently identified in 65% of parasellar hypervascular lesions as a feeding artery and 28% of internal carotid artery steno-occlusive lesions as a collateral pathway. It was observed in other diseases as a very tiny branch, which suggests that the artery of the SOF is difficult to identify and trace unless a pathologic condition increases its blood flow. Therefore, the artery of the SOF has not been described in anatomic studies because of its very small size. Recently, an anatomic study of the pterygopalatine fossa by Oomen et al<sup>13</sup> demonstrated a previously undescribed neural branch that communicates with the ophthal-

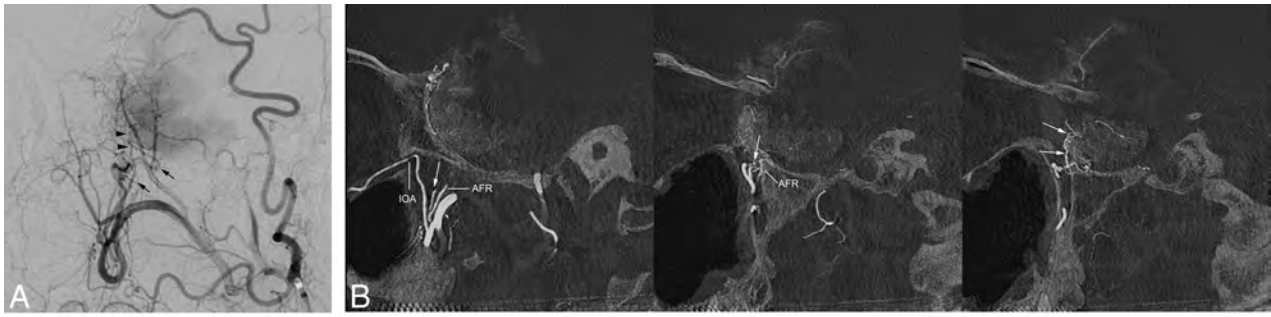


**FIG 4.** Case of parasellar meningioma supplied by the artery of the SOF. *A*, Lateral view of the right external carotid angiography in a patient with a sphenoid ridge (parasellar) meningioma showing a remarkable stain supplied by multiple feeding arteries from the maxillary arteries. *Arrows* indicate the artery of the foramen rotundum, and *arrowheads* indicate the artery of the SOF. *B*, Sagittal MPR images of rotational angiography of the right external carotid angiography show that the artery of the SOF (*arrows*) originates at the distal portion of the maxillary artery. It runs upward into the SOF and feeds the tumor. The artery of the foramen rotundum (AFR) runs posterosuperiorly through the foramen rotundum and enters the middle cranial fossa to feed the tumor. *C*, Selective angiography with contrast injection at the terminal portion of the maxillary artery clearly shows the artery of the SOF (*arrows*) supplying the tumor.

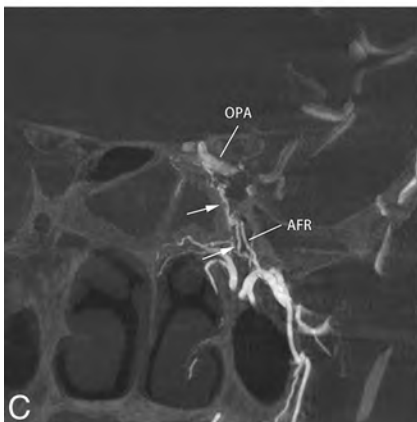
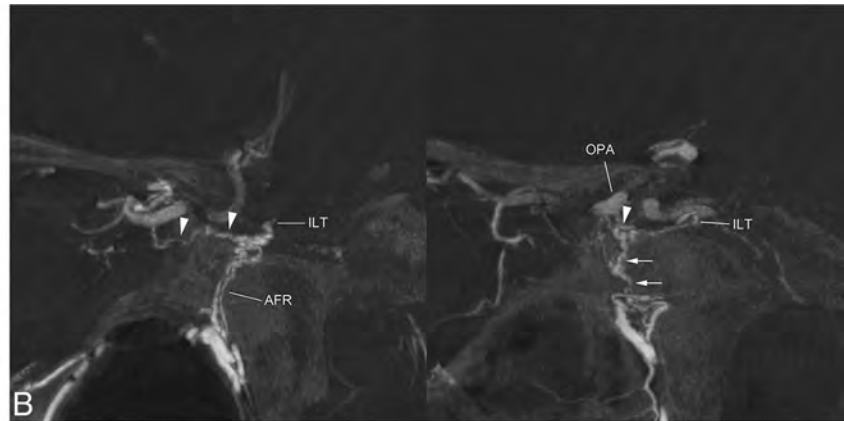
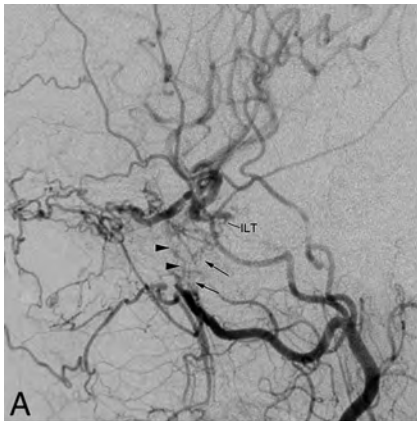
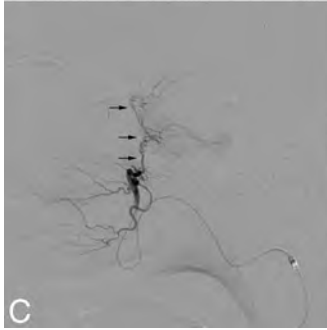


**FIG 5.** Case of left internal carotid artery occlusion with collateral from the maxillary artery to the internal carotid artery and the ophthalmic artery via the artery of the SOF. *A*, Lateral view of the left common carotid angiography in a patient with occlusion of the cervical internal carotid artery shows multiple collaterals from the external carotid artery to the ophthalmic artery and the ILT of the internal carotid artery. *Arrows* indicate the artery of the foramen rotundum communicating with the ILT. *Arrowheads* indicate the artery of the SOF communicating with the ILT and ophthalmic artery. *B*, Sagittal MPR images of rotational angiography of the left common carotid artery show the artery of the foramen rotundum running posterosuperiorly to anastomose with the ILT. The artery of the SOF (*arrows*) runs upward and connects posteriorly with the ILT and anterosuperiorly with the ophthalmic artery (OPA). *Arrowheads* indicate the anteromedial branch of the ILT. *C*, Coronal MPR image of rotational angiography of the left common carotid artery showing that the artery of the SOF (*arrows*) originates by a common trunk with the artery of the foramen rotundum (AFR). Note an anastomosis between the artery of the SOF and the ophthalmic artery at the orbital apex.

mic nerve (V1) and pterygopalatine ganglion. They reported that the nerve was identified in all 5 specimens, and it originated upward from pterygopalatine ganglion and separated into 2 rami entering the orbita anteriorly and cranial cavity posteriorly to join the ophthalmic nerve. The course of this nerve is similar to that of the artery of the SOF in our study. The branches of the maxillary artery often accompany the neural bundle, especially along with branches of the trigeminal nerve. Therefore, the presence of the

communicating neural branch between the ophthalmic nerve and the pterygopalatine ganglion supports the presence of the artery of the SOF.

In previous angiographic studies for hypervascular parasellar lesions and collateral pathways between the external carotid artery and internal carotid artery, the artery of the SOF would be ignored or confused with the artery of the foramen rotundum or other maxillary arterial branches because of the lack of recogni-

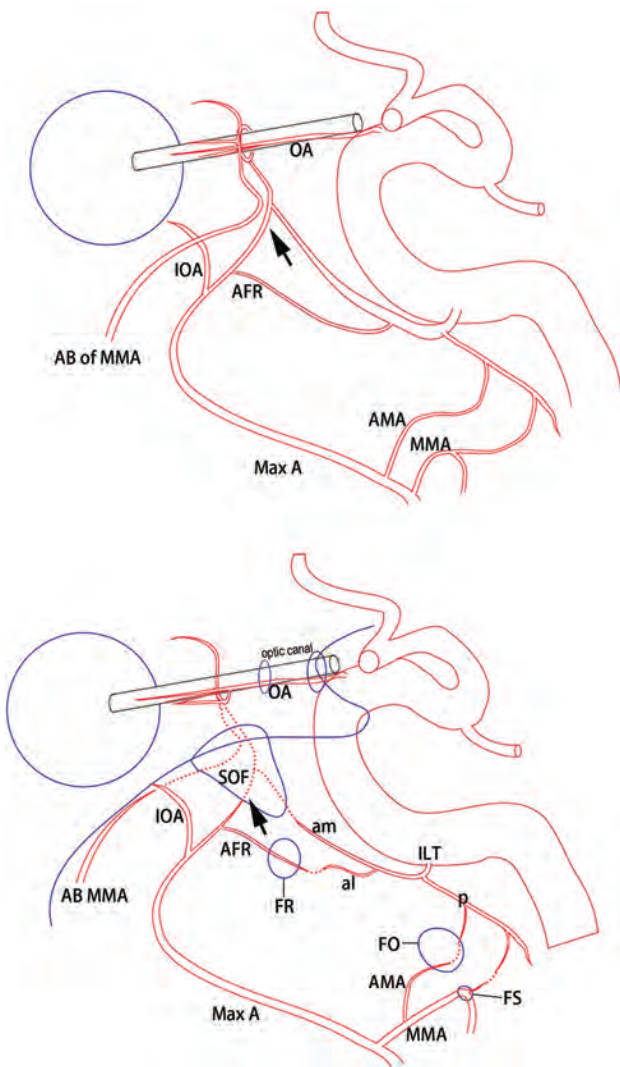


**FIG 6.** Schematic drawing of the anastomotic arteries between the maxillary artery and internal carotid artery in the fetal period (upper figure) and potential anastomosis in an adult (lower figure). The ophthalmic artery anastomoses with the anterior branch of the middle meningeal artery (AB of MMA) and an ophthalmic branch of the maxillary artery (arrow). Several branches arising from the internal carotid artery anastomose with the branches of the maxillary arteries, including the middle meningeal artery (MMA), accessory meningeal artery (AMA), artery of the foramen rotundum (ARF), and the ophthalmic branch of the maxillary artery (arrow) in the fetal period. Anastomotic branches from the internal carotid artery become branches of the ILT. There are several potential anastomoses between the maxillary artery branches and the ILT. The ophthalmic branch of the maxillary artery and its anastomoses in the fetal period becomes the artery of the superior orbital fissure.

tion and knowledge of this artery. Furthermore, it is difficult to evaluate the exact course of the small branch by conventional DSA because of overlapping vessels and a lack of information on the relationship of the branches of the maxillary artery and the complicated bony structure of the orbital apex and PPF. We used MPR and 3D images reconstructed from a rotational angiography dataset. It has been reported that CT-like reconstructions of 3D rotational angiography are superior to 2D DSA in assessing vascular structures and their relationships with bony structures.<sup>14,15</sup> After recognition of the discriminative course of the artery of the SOF via 3D rotational angiography, it can be identified easily on

the lateral view in conventional DSA. It goes straight upward to reach the level of the orbital apex, and then it turns posteriorly with an approximately 90° angle to enter the middle fossa by anastomosis with the intracranial portion of the anteromedial branch of the inferolateral trunk. It can also run anterosuperiorly in the orbital fossa to connect to the ophthalmic artery by anastomosis with the orbital portion of the anteromedial branch of the inferolateral trunk. The artery of the foramen rotundum also originates at the pterygopalatine segment of the maxillary artery, but it can be differentiated from the artery of the SOF on DSA because it runs more dorsally up to enter the middle fossa through the foramen rotundum.

Regarding the clinical importance of the artery of the SOF, it can work as a collateral pathway, communicating between the external carotid artery and the internal carotid artery and ophthalmic artery in steno-occlusive diseases of the internal carotid artery. Furthermore, it may be important to evaluate for nasopharyngeal tumors and infections, because some tumors or infectious diseases, such as adenoid cystic carcinoma, can spread along the neurovascular bundle.<sup>16</sup> Although it is well known that the foramen rotundum is an important canal through which tumors extend from the PPF into the cranial cavity, a tumor can spread from the PPF through the SOF into the cranial cavity along the artery of the SOF.

As mentioned previously, the artery of the SOF frequently works as a feeding artery for parasellar hypervascular lesions, such as meningiomas and dural arteriovenous fistulas, which are often treated by endovascular techniques. Embolization from the artery of the SOF is more dangerous than from other branches of the maxillary artery because it has a potential risk of migration of embolic materials into the internal carotid artery as well as the ophthalmic artery. Despite the apparent communication of the artery of the SOF with the ophthalmic artery, and with the anteromedial branch of the ILT (the embryonic dorsal ophthalmic artery, as termed by Lasjaunias et al), it does not seem that the artery of the SOF serves as a major pathway for collateral reconstitution of the ophthalmic artery. In fact, its existence may have been hitherto overlooked simply because it is so small. However, the possibility now exists, and extra care must be taken. Furthermore, cranial nerve injury of the ophthalmic nerve (V1), which is potentially supplied by the artery of the SOF, is another potential risk of embolization. Therefore, recognition of the artery of the SOF is important for clinical practice.

This study had some limitations. We included a relatively small number of cases, especially for normal circulation in the evaluated area. A low frequency of the presence of the artery of the SOF in patients without hypervascular parasellar lesions may be attributed to the limitations of current 3D rotational angiography resolution for depicting tiny arteries. Therefore, the exact frequency of the presence of the artery of the SOF is unclear.

## CONCLUSIONS

The artery of the SOF, an undescribed anastomotic artery between the third segment of the maxillary artery and the anteromedial branch of the ILT, was often identified, especially in patients with parasellar hypervascular lesions. A special attention

should be paid for the presence of the artery of the SOF during transarterial embolization of the branches originating from the third segment of the maxillary artery.

## REFERENCES

1. Djindjian R, Merland JJ. *Super-Selective Arteriography of the External Carotid Artery*. Berlin: Springer-Verlag; 1978:22–36
2. Daniels DL, Mark LP, Ulmer JL, et al. **Osseous anatomy of the pterygopalatine fossa**. *AJNR Am J Neuroradiol* 1998;19:1423–32 Medline
3. Osborn AG. **Radiology of the pterygoid plates and pterygopalatine fossa**. *AJR Am J Roentgenol* 1979;132:389–94 CrossRef Medline
4. Kim HS, Kim DI, Chung IH. **High-resolution CT of the pterygopalatine fossa and its communications**. *Neuroradiology* 1996;38: S120–26 CrossRef Medline
5. Lasjaunias P, Berenstein A, ter Brugge KG. *Clinical Vascular Anatomy and Variations*. Berlin: Springer-Verlag; 2001:15–87
6. Tanoue S, Kiyosue H, Mori H, et al. **Maxillary artery: functional and imaging anatomy for safe and effective transcatheter treatment**. *Radiographics* 2013;33:e209–24 CrossRef Medline
7. Daniels DL, Rauschnig W, Lovas J, et al. **Pterygopalatine fossa: computed tomographic studies**. *Radiology* 1983;149:511–16 CrossRef Medline
8. Williams PL, Gray H, Bannister LH. *Gray's Anatomy: The Anatomical Basis of Medicine and Surgery*. Edinburgh: Churchill Livingstone; 1999
9. Rusu MC, Didilescu AC, Jianu AM, et al. **3D CBCT anatomy of the pterygopalatine fossa**. *Surg Radiol Anat* 2013;35:143–59 CrossRef Medline
10. De La Torre E, Netsky MG. **Study of persistent primitive maxillary artery in human fetus: some homologies of cranial arteries in man and dog**. *Am J Anat* 1960;106:185–95 CrossRef
11. Lasjaunias P, Moret J, Mink J. **The anatomy of the inferolateral trunk (ILT) of the internal carotid artery**. *Neuroradiology* 1977;13: 215–20 CrossRef Medline
12. Willinsky R, Lasjaunias P, Berenstein A. **Intracavernous branches of the internal carotid artery (ICA): comprehensive review of their variations**. *Surg Radiol Anat* 1987;9:201–15 CrossRef Medline
13. Oomen KP, Ebbeling M, de Ru JA, et al. **A previously undescribed branch of the ganglion**. *Am J Rhinol Allergy* 2011;25:50–53 CrossRef Medline
14. Hiu T, Kitagawa N, Morikawa M, et al. **Efficacy of DynaCT digital angiography in the detection of the fistulous point of dural arteriovenous fistulas**. *AJNR Am J Neuroradiol* 2009;30:487–91 CrossRef Medline
15. Kiyosue H, Tanoue S, Okahara M, et al. **Angioarchitecture of transverse-sigmoid sinus dural arteriovenous fistulas: evaluation of shunted pouches by multiplanar reformatted images of rotational angiography**. *AJNR Am J Neuroradiol* 2013;34:1612–20 CrossRef Medline
16. Ginsberg LE, DeMonte F. **Imaging of perineural tumor spread from palatal carcinoma**. *AJNR Am J Neuroradiol* 1998;19:1417–22 Medline

# C-Arm Flat Detector CT Parenchymal Blood Volume Thresholds for Identification of Infarcted Parenchyma in the Neurointerventional Suite

M. Kamran and J.V. Byrne

## ABSTRACT

**BACKGROUND AND PURPOSE:** C-arm flat detector CT parenchymal blood volume imaging allows functional assessment of the brain parenchyma in the neurointerventional suite. This study aimed to determine the optimal C-arm flat detector CT parenchymal blood volume thresholds for demarcating irreversibly infarcted brain parenchyma by using areas of restricted diffusion on MR imaging as a surrogate marker for infarction.

**MATERIALS AND METHODS:** Twenty-six patients with delayed cerebral ischemia following aneurysmal SAH underwent research C-arm CT parenchymal blood volume scans by using a biplane angiography system and contemporaneous MR imaging. Infarct and peri-infarct tissue VOIs and their homologous VOIs in the contralateral uninvolved hemisphere were delineated on the basis of the review of DWI, PWI, and ADC images. Voxel-based receiver operating characteristic curve analysis was performed to estimate the optimal absolute and normalized parenchymal blood volume values for demarcating the infarct voxels.

**RESULTS:** For 12 patients with areas of restricted diffusion (infarct volume,  $6.38 \pm 7.09$  mL; peri-infarct tissue volume,  $22.89 \pm 21.76$  mL) based on the voxel-based receiver operating characteristic curve analysis, optimal absolute and normalized parenchymal blood volume thresholds for infarction were 2.49 mL/100 g (area under curve, 0.76; sensitivity, 0.69; specificity, 0.71) and 0.67 (area under curve, 0.77; sensitivity, 0.69; specificity, 0.72), respectively ( $P$  value  $< .01$ ). For the moderate-to-severely ischemic peri-infarct zone, mean parenchymal blood volume values of the involved hemisphere VOIs were lower compared with the uninvolved hemisphere VOIs ( $P$  value  $< .01$ ). However, for the mild-to-moderately ischemic peri-infarct zone, there was no statistically significant difference between the mean parenchymal blood volume values of the involved and uninvolved hemisphere VOIs ( $P$  value  $> .05$ ).

**CONCLUSIONS:** C-arm flat detector CT parenchymal blood volume maps in conjunction with optimal thresholds are sensitive and specific for the estimation of irreversibly infarcted parenchyma. Parenchymal blood volume maps allow reliable detection of moderate-to-severe ischemia; however, the potential for underestimation of mild-to-moderate ischemia exists.

**ABBREVIATIONS:** DCI = delayed cerebral ischemia; FDCT = flat detector CT; PBV = parenchymal blood volume; ROC = receiver operating characteristic

Flat detector equipped C-arm angiographic systems used in the neurointerventional suite are now capable of measuring parenchymal blood volume (PBV) by using a specially designed scan protocol.<sup>1</sup> Initial reports document agreement between C-arm flat detector CT (FDCT) PBV and CT perfusion–derived cerebral blood volume in both canines and humans.<sup>2,3</sup> The availability of PBV maps in the interventional suite is an important develop-

ment and has potential implications in the management of patients with ischemic cerebrovascular disease and their selection for revascularization procedures.<sup>4</sup>

Areas of reduced PBV on the initial C-arm FDCT PBV maps have been shown to correlate with the infarct volume on follow-up imaging in patients with acute middle cerebral artery occlusion.<sup>4</sup> C-arm FDCT PBV and the CTP-derived CBV are not identical. However, an equivalence between the 2 is usually inferred if a steady-state contrast concentration is achieved in the cerebral vasculature during the C-arm FDCT PBV scan; in the absence of an ideal steady-state, the PBV may have combined CBF and CBV weighting or even preferential CBF weighting.<sup>1,5</sup> For CTP, although debate exists as to which perfusion parameter best defines irreversible infarction, thresholds for various parameters corresponding to acute DWI abnormality and infarct core have been reported.<sup>6–8</sup> No such thresholds have so far been investigated for C-arm CT PBV.

Received November 18, 2014; accepted after revision February 11, 2015.

From the Nuffield Department of Surgical Sciences, University of Oxford, John Radcliffe Hospital, Headington, Oxford, United Kingdom.

M.K. is funded by the Rhodes Trust, and J.V.B. is supported by the Oxford Biomedical Research Centre.

Please address correspondence to Mudassar Kamran, MD, MSc, Nuffield Department of Surgical Sciences, University of Oxford, Room 6607, Level 6, John Radcliffe Hospital, Headington, Oxford, UK, OX3 9DU; e-mail: m.kamran@oxon.org

<http://dx.doi.org/10.3174/ajnr.A4339>

The aims of this study were: 1) to determine the optimal C-arm CT PBV thresholds for irreversibly infarcted parenchyma by using contemporaneous MR DWI in patients with delayed cerebral ischemia (DCI) following aneurysmal subarachnoid hemorrhage, and 2) to investigate whether the C-arm CT PBV values in the peri-infarct ischemic zone allow reliable demarcation of the ischemic tissue.

## MATERIALS AND METHODS

With local research ethics committee approval, a series of patients ( $n = 26$ ) with aneurysmal SAH meeting the inclusion and exclusion criteria was enrolled in this prospective study. Inclusion criteria were patients older than 18 years of age with documented aneurysmal SAH who subsequently developed symptoms and signs suggesting DCI and requiring confirmatory imaging. The diagnosis of DCI was based on clinical assessment by the multidisciplinary neuro-intensive care unit team and was defined as clinical deterioration (focal neurologic deficits or reduced level of consciousness) lasting 2 hours or longer with no evidence of re-bleed or hydrocephalus on NCCT of the head and no other medical causes such as infections or metabolic disturbances. Exclusion criteria were the following: a history of allergy to iodinated contrast medium, renal impairment, pregnancy, or contraindications to MR imaging. All recruited patients had undergone aneurysm repair by endovascular coil embolization. Written informed consents were obtained from patients or, if they were unable to complete the consent process, from a family member or a designated surrogate as defined by the research ethics committee guidelines. All recruited patients underwent an MR imaging examination concurrent with the research C-arm CT scan by using the intravenous PBV protocol. The imaging protocols and postprocessing steps for the 2 imaging studies are described in the following sections.

### C-Arm FDCT Imaging

C-arm FDCT scans were obtained on a flat panel–equipped biplane angiography system (Axiom Artis dBA; Siemens, Erlangen, Germany) in the neurointerventional suite. The imaging protocol included 2 rotational acquisitions: mask and contrast-enhanced runs. Projection data for each run were acquired by using the following parameters: 419 projection images,  $0.5^\circ$  frame angle,  $210^\circ$  angular scan range, 8-second acquisition time,  $0.36\text{-}\mu\text{Gy}$  radiation dose per frame. The contrast-enhanced dataset was acquired following manually triggered intravenous injection of radiographic contrast material, iopamidol (Niopam 370; Bracco, Milan, Italy) by using a power injector (Medrad, Indianola, Pennsylvania). The injection parameters were the following: contrast concentration, 370-mg iodine/mL; volume, 80 mL; injection rate, 4 mL/s administered through the antecubital vein; injection pressure, 300 psi; and injection duration, 20 seconds. Passage of contrast material through the cerebral vasculature was monitored on 2D fluoroscopic images (2 frames/s), and the contrast-enhanced run was triggered when maximal opacification of the superior sagittal sinus was observed, as described previously by Struffert et al.<sup>3</sup>

Postprocessing of the data to generate color-coded PBV maps was performed on a dedicated research workstation (Leonardo;

Siemens) by using prototype software. The steps involved were the following: 1) coregistration of the 2 volumes, mask and contrast-enhanced; 2) subtraction of the mask volume from the contrast-enhanced volume; 3) normalization of the subtracted data with an input function automatically estimated from the histogram analysis of vascular tree; and 4) color-coding with a standard color look-up table to generate the color-coded PBV maps for visualization and interpretation. The final PBV values were expressed in units of milliliters/1000 mL of cerebral tissue. PBV values for volume-of-interest analysis were converted to more commonly used units of milliliters/100 g by using a simple conversion factor that takes into account the cerebral tissue density (1.05 g/mL).

### MR Imaging

A standard MR image protocol comprising sagittal T1-weighted, axial T1-weighted, axial T2-weighted, diffusion-weighted, perfusion-weighted, and time-of-flight MR angiography sequences was performed on an Achieva 1.5T MR imaging unit (Philips Healthcare, Best, Netherlands). Details for the diffusion- and perfusion-weighted sequences and the parameters used for these sequences are briefly discussed below.

**DWI.** DWI parameters were the following: TR, 2897 ms; TE, 73 ms; FOV,  $174 \times 249$  mm; reconstruction matrix,  $144 \times 144$ ; sections, 25; section thickness, 5 mm; voxel size,  $1.74 \times 1.73 \times 5$  mm; b-values, 0, 1000; EPI factor, 51; scan duration, 34 seconds.

**PWI.** Perfusion data were acquired by using the dynamic susceptibility contrast technique with the following parameters: T2\*-weighted gradient-echo echo-planar sequence: TR, 2000 ms; TE, 44 ms; FOV,  $248 \times 248$  mm; reconstruction matrix,  $256 \times 256$ ; voxel size,  $0.98 \times 0.98 \times 4$  mm; sensitivity encoding factor, 2.1; bandwidth, 806 Hz/pixel; scan duration, 1 minute 46 seconds. Paramagnetic contrast material was administered intravenously with an MR imaging–compatible power injector (Medrad, Indianola, Pennsylvania) at 5 mL/s followed by a 10-mL saline flush. Fifteen sections covering the whole brain were acquired at 50 time points following the injection of 0.2 mmol/kg of gadoteridol (ProHance; Bracco).

Postprocessing of the perfusion data was performed by using commercially available software (nordicICE perfusion package; NordicNeuroLab, Bergen, Norway). After motion correction of the raw data, we created perfusion maps by using the singular value deconvolution technique. The arterial input function to deconvolve the dynamic tissue response curve was automatically determined, and singular value decomposition regularization was achieved with the truncated singular value deconvolution approach (cutoff fraction, 0.20) and iterative thresholding (target oscillation index, 0.10). Semiquantitative output perfusion maps for clinical interpretation included cerebral blood flow, cerebral blood volume, mean transit time, and time to peak.

### Postprocessing and Quantitative Image Analysis

C-arm CT PBV, PWI, apparent diffusion coefficient, and DWI were further processed by using the fMRI of the Brain Software Library tools.<sup>9</sup> The Brain Extraction Tool (<http://fsl.fmrib.ox.ac.uk/fsl/fslwiki/BET>) was used to delete the nonbrain tissues

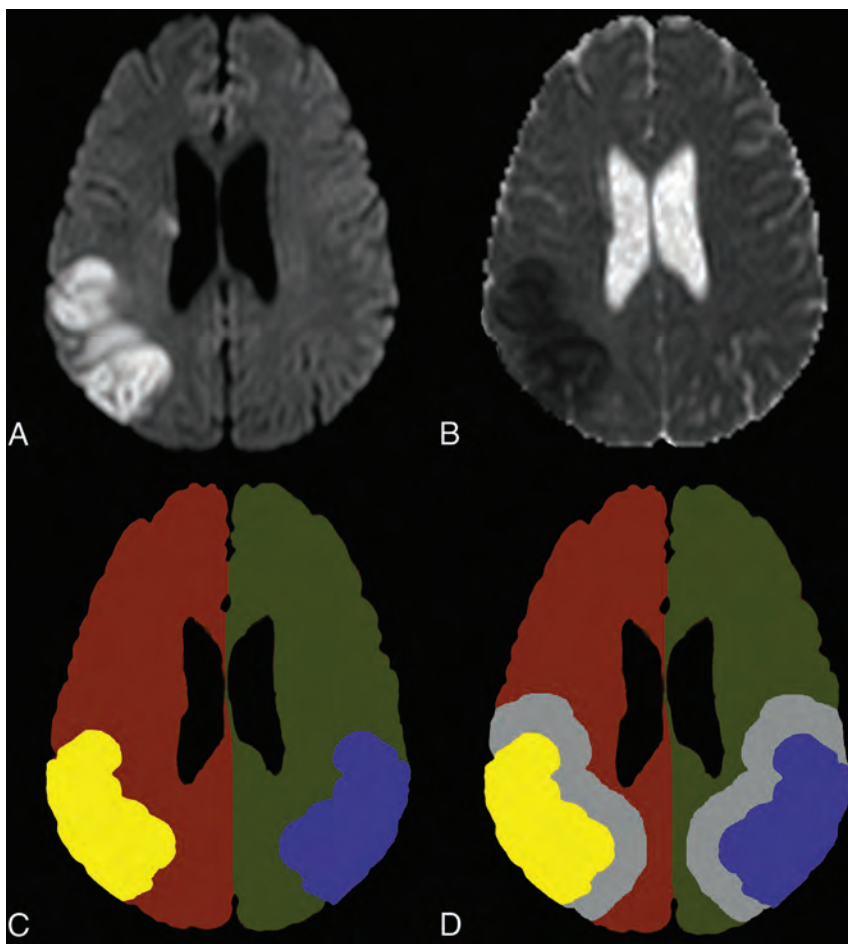


**FIG 1.** Binary masks used for VOI analysis. An area of restricted diffusion was identified on the DWI and ADC maps (A and B). Corresponding to the area of restricted diffusion (surrogate for infarcted tissue), a VOI mask (yellow) was created by a semiautomated approach, along with a mirrored VOI mask (blue) in the contralateral normal hemisphere. Surrounding the VOI mask corresponding to the area of restricted diffusion, a peri-infarct tissue VOI mask (gray) was created on the basis of the review of PWI relative CBF maps. A mirrored VOI mask for the peri-infarct tissue in the contralateral normal hemisphere was constructed by transposing the peri-infarct tissue VOI mask. Hemispheric masks for the ipsilateral (orange) and contralateral hemisphere (green) were constructed for calculation of normalized PBV values.

from the images of interest followed by linear registration of the C-arm PBV maps and the MR-PWI, PWI, and ADC images for each patient to the T1-weighted average structural template brain volume in Montreal Neurological Institute 152 space with the fMRI of the Brain (FMRIB) Linear Image Registration Tool (FLIRT; <http://www.fmrib.ox.ac.uk>).<sup>10,11</sup> Alignment of all coregistrations was visually confirmed in 3 orthogonal planes. Areas of infarction were identified on the basis of the review of DWI and ADC maps. 3D VOIs corresponding to the infarct core were defined on the DWI with a semiautomated approach by using MRicro software (<http://www.mccauslandcenter.sc.edu/mricro/mricro/mricro.html>).<sup>12</sup> In the next step, the infarct core VOIs were grown to include the peri-infarct ischemic parenchyma identified as the region of asymmetrically reduced CBF (<95% relative to the mean contralateral hemisphere CBF) surrounding the infarct core defined on the DWI. From the grown VOIs that included both the infarct core and the peri-infarct ischemic tissue, the infarct core VOIs were subtracted, thus creating the subtraction VOIs defining only the peri-infarct ischemic tissue. In the

contralateral normal hemisphere, mirrored homologous tissue VOIs were then created corresponding to the affected hemisphere infarct core and peri-infarct ischemic tissue VOIs. In a small subset of patients for whom bilateral areas of ischemia or infarction existed, substitute VOIs with comparable volume in the uninvolved adjacent parenchyma were created and used for comparison and normalization. All VOIs were subsequently transposed onto coregistered C-arm CT PBV maps. Figures 1 and 2 illustrate the VOI masks used for analysis. Mean, median, and SD of the absolute PBV values in all VOIs were measured by using FMRIB software maths (<http://fsl.fmrib.ox.ac.uk/fsl/fslwiki/Fslutils>) and FMRIB software stats utilities (<http://fsl.fmrib.ox.ac.uk/fsl/fslwiki/Fslutils>). Normalized PBV values were calculated by dividing the absolute PBV value for each VOI by the mean contralateral hemisphere PBV value obtained by using separate hemispheric masks.

### Statistical Analysis

A paired *t* test was performed to investigate whether mean PBV in the infarct tissue VOIs and the mean PBV in the contralateral uninvolved homologous tissue VOIs were statistically different and whether the mean PBV in peri-infarct ischemic parenchyma VOIs and the mean PBV in contralateral uninvolved homologous tissue VOIs were statistically different.

To test the predictive performance of C-arm CT PBV maps across various thresholds for demarcating infarcted tissue, we

performed voxel-based receiver operating characteristic (ROC) curve analysis. Sensitivity and specificity of PBV maps for demarcating the infarct voxels (DWI/ADC abnormality) from the noninfarct voxels across patients as a function of increasing PBV thresholds were computed. The accuracy of PBV maps in demarcating the infarct voxels (DWI/ADC abnormality) from the noninfarct voxels was determined from the area under curve statistic that ranges from 0.5 (no predictive value) to 1 (absolute predictive value). The ROC curve analysis was performed separately for the absolute and the normalized PBV values. The final absolute and normalized PBV thresholds for demarcating infarcted tissue were calculated as the optimal ROC curve points with equally attributed weights to sensitivity and specificity. Statistical analysis was performed by using GraphPad Prism software (GraphPad Software, San Diego, California).

## RESULTS

### Study Population Characteristics

Twenty-six patients (mean age, 55 years; 9 men, 17 women) entered the study. Patients' World Federation of Neurosurgical So-

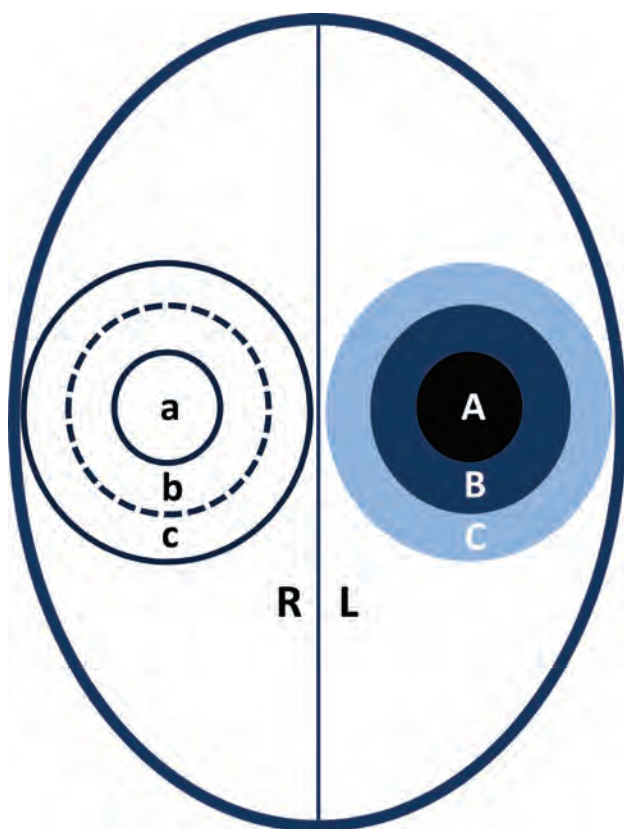


**FIG 2.** Schematic illustration of the infarct and peri-infarct VOIs. In the involved hemisphere (L), the infarct VOI (A) corresponds to the area of restricted diffusion (surrogate for infarction) on DWI and ADC images. Surrounding the infarct VOI, the peri-infarct zone (B + C) corresponds to the region of asymmetrically reduced MR imaging CBF (CBF of <95% relative to the mean contralateral hemisphere CBF). The peri-infarct zone (B + C) was further subdivided into a mild-to-moderately ischemic zone (B; CBF of 75%–95%, relative to the mean contralateral hemisphere CBF) and a moderate-to-severely ischemic zone (C; CBF of <75%–95%, relative to the mean contralateral hemisphere CBF). Contralateral homologous tissue VOIs in the uninvolved hemisphere (R) corresponding to infarct (a) and peri-infarct (b + c) zones were created by transposing the involved hemisphere VOIs across the midline.

cities grades at the time of admission to the hospital were the following: grade I in 16 (61%), grade II in 7 (27%), grade III in 2 (8%), and grade IV in 1 patient (4%). The onset of DCI after SAH varied from day 2 post-SAH to day 12 post-SAH (median, day 7 post-SAH). All patients received standard medical management according to the institutional protocol. Of the 26 patients, 8 (31%) underwent chemical angioplasty with selective intra-arterial nimodipine administration, 2 (8%) of whom received chemical angioplasty treatment twice. The mean duration between the C-arm FDCT PBV scan and the MR imaging was 124 minutes. Of the 26 patients, 12 had areas of restricted diffusion on MR imaging. On these scans, 22 VOIs each for infarcted parenchyma, peri-infarct tissue, and their contralateral homologous tissue were defined (total, 22 × 4 VOIs); The Table describes the patient characteristics and details of DWI lesions.

#### Quantitative Image Analysis

For the patients with areas of restricted diffusion on DWI, mean DWI lesion volume (infarcted parenchyma) was  $6.38 \pm 7.09$  mL

(range, 0.91–26.5 mL) and the mean peri-infarct ischemic tissue volume was  $22.89 \pm 21.76$  mL (range, 4.18–85.61 mL).

Mean PBV values in the infarct VOIs were significantly lower compared with the mean PBV values in the mirrored contralateral uninvolved homologous tissue VOIs (paired *t* test *P* value < .01), as illustrated in the box-and-whisker plot (Fig 3A). Voxel-based ROC curve analysis was performed for both absolute and normalized C-arm CT PBV volumetric parametric maps, and the resulting ROC curves are shown in Fig 4. The optimal absolute C-arm CT PBV threshold identifying the infarcted parenchyma by using DWI abnormality as a marker was 2.49 mL/100 g. The corresponding area under the curve, sensitivity, and specificity were 76.4% (95% CI, 76.1–76.7), 69.4% (95% CI, 68.9–69.8), and 70.7% (95% CI, 70.2–71.1) (*P* value < .01), respectively. The optimal normalized C-arm CT PBV threshold was 0.67. The corresponding area under the curve, sensitivity, and specificity were 76.9% (95% CI, 76.6–77.1), 69.4% (95% CI, 69.0–69.7), and 72.2% (95% CI, 71.8–72.5) (*P* value < .01), respectively.

A paired-samples *t* test conducted to compare the mean PBV values for peri-infarct ischemic tissue VOIs and the mean PBV values for corresponding mirrored VOIs in the contralateral uninvolved hemisphere showed no significant difference between the mean PBV values for the 2 groups of VOIs (*P* > .05). Given this finding, the analysis was extended by dividing each of the peri-infarct VOIs into 2 segments based on the review of MR imaging relative CBF maps: 1) moderate-to-severely ischemic peri-infarct zone with MR CBF of <75% relative to the mean contralateral hemisphere CBF, and 2) a mild-to-moderately ischemic peri-infarct zone with MR CBF of 75%–95% relative to the mean contralateral hemisphere CBF (Fig 2). VOIs and binary masks for the 2 zones were created for both the involved and the uninvolved hemisphere by following the same approach as used earlier in the analysis, followed by the application of the binary masks to the C-arm CT PBV maps. Mean PBV values for the 2 sets of VOIs corresponding to the mild-to-moderate and the moderate-to-severely ischemic peri-infarct zones were then compared with their contralateral homologous tissue VOIs by using the paired-samples *t* test. For the moderate-to-severely ischemic peri-infarct zone, the mean PBV values of the involved hemisphere VOIs were statistically significantly lower compared with the uninvolved hemisphere VOIs (Fig 3B, *P* value < .01). However, for the mild-to-moderately ischemic peri-infarct zone, there was no statistically significant difference between the mean PBV values of the involved and uninvolved hemisphere VOIs (Fig 3C, *P* value > .05).

#### DISCUSSION

This study reports optimal absolute and normalized C-arm CT PBV threshold values for demarcating irreversibly infarcted brain parenchyma in the neurointerventional suite.

In determining the PBV threshold for infarcted brain parenchyma, areas of restricted diffusion identified on the review of DWI and ADC maps were used as a marker for irreversibly infarcted tissue. Although DWI abnormality is not perfectly specific for infarct core, it is highly accurate and is an accepted standard for both clinical care and research analysis.<sup>13–15</sup> In our analysis, we used 3D VOIs, defined semiautomatically for the DWI abnormal-

### Demographic, aneurysm, and clinical characteristics of patients and the location of DWI lesions

Patient No.	Age (yr)	Sex	Aneurysm Location	Aneurysm Size (mm)	WFNS Grade	Fisher Grade	DWI Deficits	DWI Deficits Distribution
1	47	M	Anterior communicating artery	6 × 4	I	3	+	Right frontal operculum; right centrum semiovale
2	55	F	Left anterior cerebral artery	12 × 10	III	4	—	—
3	61	F	Right posterior communicating artery	8 × 5	II	3	—	—
4	49	F	Anterior communicating artery	10 × 7	I	3	—	—
5	68	F	Right posterior communicating artery	10 × 6	II	4	—	—
6	71	F	Anterior communicating artery	6 × 5	I	4	+	Right frontal and left posterior frontal lobes
7	46	M	Right middle cerebral artery	4 × 3	III	3	+	Bifrontal and posterior left parietal lobes
8	77	F	Left anterior cerebral artery	6 × 4	I	4	—	—
9	46	M	Right posterior communicating artery	4 × 4	I	4	—	—
10	50	F	Right internal carotid artery	3 × 3	I	3	+	Right frontal lobe
11	53	F	Basilar artery tip	7 × 6	II	3	+	Left frontal lobe
12	55	M	Right posterior communicating artery	5 × 3	II	4	—	—
13	55	F	Left posterior communicating artery	4 × 4	II	4	—	—
14	69	F	Left anterior cerebral artery	11 × 7	I	4	+	Bifrontal lobes
15	66	M	Anterior communicating artery	7 × 5	I	0 <sup>a</sup>	—	—
16	45	M	Anterior communicating artery	15 × 8	II	4	+	Right parietal lobe and corpus striatum
17	66	M	Right middle cerebral artery	8 × 3	IV	4	+	Right parietal lobe and Sylvian fissure
18	30	M	Anterior communicating artery	7 × 4	I	3	+	Left frontal lobe
19	39	F	Right posterior communicating artery	5 × 3.5	I	4	+	Right parietal lobe
20	50	F	Anterior communicating artery	4 × 3.5	I	4	—	—
21	69	M	Right posterior communicating artery	7 × 4	I	4	—	—
22	39	F	Right posterior communicating artery	10 × 9	I	4	+	Right frontal lobe
23	52	F	Right posterior communicating artery	5 × 5	I	4	+	—
24	54	F	Left posterior communicating artery	8 × 5	I	3	+	—
25	58	F	Right anterior cerebral artery	5 × 4	I	3	+	Right frontal lobe
26	60	F	Left pericallosal artery	12 × 8	II	4	—	—

Note:—WFNS indicates World Federation of Neurological Societies; +, present; —, absent.

<sup>a</sup> NCCT of the head was negative for SAH, which was later confirmed on lumbar puncture.

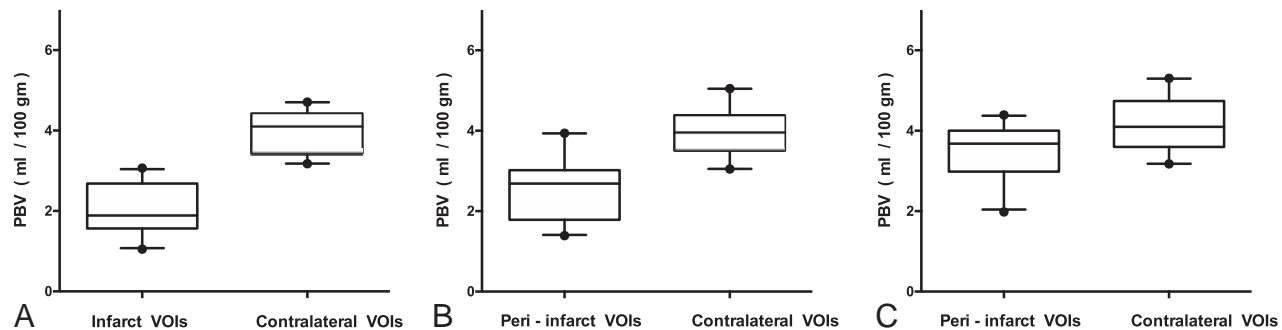


**FIG 3.** Box-and-whisker plots showing PBV (mean and SD) in the infarct VOIs—that is, areas of restricted diffusion (A), moderate-to-severely ischemic peri-infarct VOIs (relative CBF of <75%) (B), mild-to-moderately ischemic, peri-infarct VOIs (relative CBF of 75%–95%) (C), and the PBV in the corresponding mirrored contralateral homologous tissue VOIs.

ity (infarcted parenchyma), which, along with mirrored contralateral homologous tissue VOIs, were transposed onto the coregistered C-arm CT PBV maps before performing the ROC curve analysis. This objective approach toward image analysis reduces any bias that may be introduced due to subjective differences in image display, such as color look-up tables for PBV maps, window settings, and pixel conspicuity, which can be sources of error for manual segmentation.<sup>7</sup>

That any perfusion study represents a “snapshot in time” and the cerebral hemodynamics and thresholds for ischemic damage may vary with time are issues well-recognized from CTP imaging of acute brain ischemia. For acute stroke imaging, this limitation may be addressed through stratifying data by duration post-ictus.<sup>7</sup> However, unlike acute ischemic stroke, the complex pathophysiology of cerebral vasospasm and resulting hemodynamic alterations make it difficult to define a specific time-of-onset for DCI secondary to vasospasm. Moreover, the limited number of patients in our study precluded any such analysis,

which could theoretically be performed by using an arbitrary time point such as the development of neurologic deficits in patients post-SAH.

An important factor that may introduce variability in C-arm CT PBV measurements and consequently shift the optimal PBV thresholds for infarction is how well the steady-state assumption is met. For calculation of C-arm CT PBV, the intravenously administered iodinated contrast material is assumed to have reached a steady-state concentration in the cerebral vasculature (contrast concentration in arteries = contrast concentration in tissues = contrast concentration in veins), maintained for the duration of the scan.<sup>1</sup> If this assumption is fully met, the C-arm CT PBV would be equivalent to the CBV derived from dynamic perfusion imaging modalities. However, an ideal steady-state may not be achieved in practice for the clinical scans, and the contrast profile in the cerebral vasculature may show intersubject differences due to various factors such as recirculation of contrast, hemodynamic perturbation effect, and slow bolus

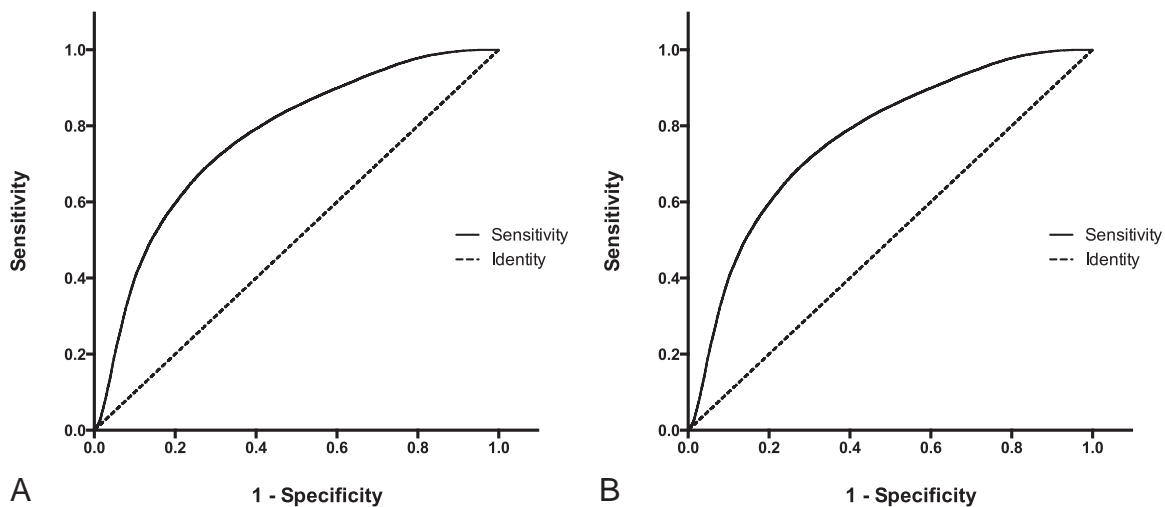


**FIG 4.** ROC curves for absolute and normalized PBV. Voxel-based ROC curves for absolute PBV (A) and normalized PBV (B), with near-identical configurations. Absolute and normalized PBV thresholds for demarcating the areas of restricted diffusion were chosen by defining the optimal point on the ROC curve with equally attributed weights to sensitivity and specificity.

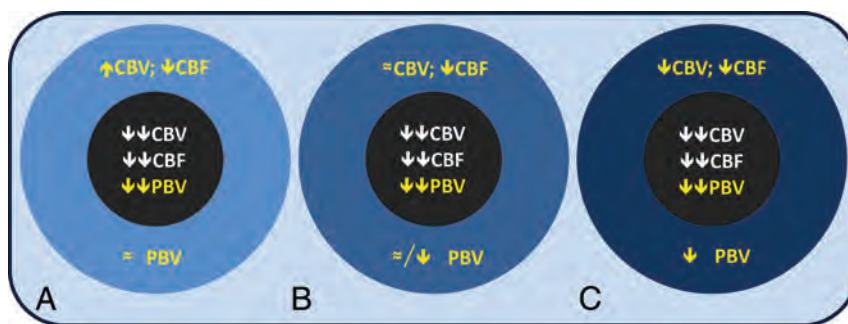


**FIG 5.** A theoretic understanding of C-arm CT PBV at various degrees of ischemia. In the infarcted tissue (black central zone in A–C), a matched decrease in CBV and CBF with consequent reduced PBV is observed, given its combined blood flow and blood volume weightings. In mild ischemia (A), CBF is reduced while there is a compensatory autoregulatory increase in CBV; consequently, PBV values may be maintained. In moderate ischemia (B), the CBF reduces further, and despite autoregulation, CBV may not increase; consequently PBV values may be in the lower part of normal range or begin to show mild reduction. In severe ischemia bordering infarction (C), both CBV and CBF would be decreased with consequent reduction in PBV.

transit in the setting of low cardiac output and multifocal vasospasm.<sup>16</sup>

Preferential contrast wash-in or washout during the acquisition of fill run data for the C-arm CT PBV study (8 seconds) may result in variable blood flow weighting to the calculated PBV. In a separate analysis for the same cohort (subject of another publication), we found that for clinical examinations, the C-arm CT PBV has  $\approx 60\%$  CBF and  $40\%$  CBV weighting, with similar supporting observations for multidetector CT.<sup>5,17</sup> Thus, differences in contrast dynamics can result in differences in blood flow and blood volume weighting to PBV, which can translate into differences in final PBV measurements. Assuming identical contrast dynamics or an ideal steady-state in all patients despite the differences in their hemodynamic physiology may overlook the blood flow weighting to C-arm CT PBV, particularly in cases in which the time-attenuation curves depart from the steady-state, thus potentially resulting in overestimation (or underestimation) of irreversibly infarcted parenchyma when using a specific threshold. This limitation can be overcome by a simple ROI-based time-attenuation-curve analysis of the raw C-arm CT projection data

for the clinical PBV scans, which can provide an estimate of how adequately the steady-state contrast concentration was achieved during a particular study.

Our results indicate that the measured PBV values in the peri-infarct ischemic tissue may or may not show reduction, depending on the severity of the ischemic insult. We found that in moderate-to-severely ischemic peri-infarct tissue (relative MR CBF,  $<75\%$ ), the PBV measurements showed statistically significant reduction compared with the contralateral uninvolved homologous tissue. However, PBV values in the mild-to-moderately ischemic peri-infarct parenchyma (relative MR CBF,  $75\%–95\%$ ) were not significantly reduced relative to

the contralateral uninvolved homologous tissue. The peri-infarct ischemic zone we identified for analysis is conceptually similar to the penumbra region seen in the setting of acute ischemic stroke. These findings are interesting and can be explained by the combined blood volume and blood flow weighting to C-arm CT PBV. CT perfusion reveals that in the setting of acute ischemic stroke, the infarcted tissue shows a matched decrease in CBV and CBF.<sup>18,19</sup> However, the ischemic tissue surrounding the infarct core has only reduced CBF, while the CBV may be maintained or elevated secondary to autoregulatory hemodynamics whereby precapillary vessels dilate in response to decreased cerebral perfusion pressure.<sup>19</sup> In the setting of severe or prolonged ischemia, the autoregulatory mechanisms fail, leading to eventual reduction in CBV. The degree to which the CBF is reduced and whether the CBV is elevated, maintained, or reduced are thus functions of the severity of the ischemic insult. In a separate analysis for the same cohort, we found that with combined blood volume and blood flow weighting (subject of another publication), C-arm CT PBV behaves as a composite parameter. Thus, in the irreversibly in-

farcted tissue, due to an underlying matched decrease in CBV and CBF, we see a definitive reduction in PBV (Fig 3A). In the perinfarct ischemic region of reduced CBF, PBV would be maintained when the ischemic insult is less severe and the autoregulatory mechanisms are intact and effective in increasing the regional CBV (Fig 3C). On the contrary, PBV measurements would be reduced if the ischemia is prolonged or worsens in severity with consequent impaired autoregulation, ineffective in increasing or maintaining the CBV (Fig 3B). Therefore, C-arm CT PBV measurements would reliably detect moderate-to-severe ischemia but can potentially underestimate mild-to-moderate ischemia.

We recognize that C-arm CT PBV imaging cannot replace DWI, which is highly accurate in the demarcation of irreversibly infarcted brain parenchyma. However, its availability in the neurointerventional suite is a unique advantage with implications for management of acute cerebrovascular ischemia. Struffert et al<sup>4</sup> proposed that PBV maps may potentially be used to guide revascularization procedures through their ability to monitor the brain viability. In this regard, a single C-arm CT study can provide both the anatomic and physiologic data for patients with acute stroke in the interventional suite without the need to transfer patients to CT or MR imaging facilities. For example, the C-arm CT soft-tissue images can reliably exclude intracranial hemorrhage, the angiographic reconstructions can help evaluate proximal vessel occlusion, and the PBV maps provide patient-specific physiologic data that can potentially be used, instead of the more generalized and nonspecific time criteria, in selecting appropriate patients for acute stroke interventions, particularly when a significant delay exists between initial imaging and patient arrival in the angiography suite.<sup>4,20</sup> Similarly, in the patients with aneurysmal SAH who develop delayed clinical deterioration, the PBV maps can be used to determine the hemodynamic significance of vessel narrowing detected on catheter angiography and to identify any ongoing ischemia or established infarcts, thus guiding the angioplasty procedures. For these applications, extended craniocaudal coverage allowing whole-brain PBV measurements would be particularly beneficial—for example, the changes related to vasospasm may be multifocal or global in nature and the acute ischemic stroke may be in a distribution located outside the traditional supratentorial coverage of CTP and may thus be better evaluated with extended craniocaudal coverage of C-arm CT PBV.

For CTP and PWI, thresholds of various perfusion parameters have been studied to demarcate the irreversibly infarcted parenchyma, and it is widely recognized that the generalizability of any specific threshold may be limited secondary to marked differences across different algorithms and postprocessing software.<sup>17,21</sup> For C-arm CT PBV measurement, currently only 1 commercially available application (syngo Neuro PBV IR; Siemens) exists. It is conceivable that in the future other similar postprocessing platforms will become available, in which case the validation of thresholds reported in this study across different platforms would be imperative.

The mean interval between the C-arm CT and MR imaging examinations in this study was 124 minutes, a duration during which the hemodynamics of the parenchymal areas included in the analysis may have altered; this change could result in an over- or underestimation of the reported thresholds. The observations

in this study should therefore be interpreted allowing for this limitation. Additionally, optimal PBV thresholds reported in this study were assessed for whole-brain tissue VOIs. However, differences between the gray and white matter exist regarding cellular composition, metabolism, the normal perfusion parameter values, and their neurochemical responses to ischemia.<sup>22-24</sup> Tissue-specific infarction thresholds may thus be more informative in predicting the tissue outcomes in the setting of cerebrovascular ischemia.<sup>25</sup> In our cohort, the limited number of patients and DWI lesions precluded such tissue-specific analysis to explore the differential variability of gray and white matter to ischemia. Future studies, including a larger number of patients with cerebral ischemia, may help in addressing this issue.

## CONCLUSIONS

This study reports the following: 1) the optimal absolute and normalized C-arm CT PBV threshold values for demarcation of the irreversibly infarcted parenchyma in the neurointerventional suite; and 2) C-arm CT PBV maps reliably detect moderate-to-severe ischemia but can potentially underestimate the mild-to-moderate ischemia with intact autoregulatory mechanisms, likely related to its combined blood flow and blood volume weighting. Optimal C-arm CT PBV thresholds for infarction have not been studied previously and are of value in providing an objective criterion for the demarcation of irreversibly infarcted parenchyma. An accurate assessment of the brain viability thus obtained has implications for the management of acute brain ischemia.

## ACKNOWLEDGMENTS

We thank Siemens for hardware and software support. We are grateful to the members and staff of the neuroradiology department, John Radcliffe Hospital, Oxford, where all the imaging data were acquired for this study.

Disclosures: Mudassar Kamran—RELATED: Grant: Siemens,\* Comments: a research grant was made to the University of Oxford. In addition, Siemens provided the hardware and software support for the research scans. James V. Byrne—RELATED: Grant: Siemens,\* Comments: a small one-off grant to support work indirectly related to the project reported in this article; OTHER RELATIONSHIPS: historical scientific advisory board member for Siemens, for which travel expenses and so forth were paid. \*Money paid to the institution.

## REFERENCES

1. Zellerhoff M, Deuerling-Zheng Y, Strother CM, et al. Measurement of cerebral blood volume using angiographic C-arm systems. *Proc SPIE* 2009;7262:72620H; doi:10.1117/12.812097
2. Ahmed AS, Zellerhoff M, Strother CM, et al. C-arm CT measurement of cerebral blood volume: an experimental study in canines. *AJNR Am J Neuroradiol* 2009;30:917–22
3. Struffert T, Deuerling-Zheng Y, Kloska S, et al. Cerebral blood volume imaging by flat detector computed tomography in comparison to conventional multislice perfusion CT. *Eur Radiol* 2011;21:882–89
4. Struffert T, Deuerling-Zheng Y, Engelhorn T, et al. Feasibility of cerebral blood volume mapping by flat panel detector CT in the angiography suite: first experience in patients with acute middle cerebral artery occlusions. *AJNR Am J Neuroradiol* 2012;33:618–25
5. Sharma M, Fox AJ, Symons S, et al. CT angiographic source images: flow- or volume-weighted? *AJNR Am J Neuroradiol* 2011;32:359–64
6. Christensen S, Mouridsen K, Wu O, et al. Comparison of 10 perfusion MRI parameters in 97 sub-6-hour stroke patients using voxel-based receiver operating characteristics analysis. *Stroke* 2009;40:2055–61

7. Kamalian S, Kamalian S, Maas MB, et al. **CT cerebral blood flow maps optimally correlate with admission diffusion-weighted imaging in acute stroke but thresholds vary by postprocessing platform.** *Stroke* 2011;42:1923–28
8. Kamalian S, Kamalian S, Konstas AA, et al. **CT perfusion mean transit time maps optimally distinguish benign oligemia from true “at-risk” ischemic penumbra, but thresholds vary by postprocessing technique.** *AJNR Am J Neuroradiol* 2012;33:545–49
9. Jenkinson M, Beckmann CF, Behrens TEJ, et al. **FSL.** *Neuroimage* 2012;62:782–90
10. Smith SM. **Fast robust automated brain extraction.** *Hum Brain Mapp* 2002;17:143–55
11. Jenkinson M, Bannister P, Brady M, et al. **Improved optimization for the robust and accurate linear registration and motion correction of brain images.** *Neuroimage* 2002;17:825–41
12. Rorden C, Brett M. **Stereotaxic display of brain lesions.** *Behav Neurol* 2000;12:191–200
13. Schellinger PD, Bryan RN, Caplan LR, et al. **Evidence-based guideline: the role of diffusion and perfusion MRI for the diagnosis of acute ischemic stroke—report of the Therapeutics and Technology Assessment Subcommittee of the American Academy of Neurology.** *Neurology* 2010;75:177–85
14. Wintermark M, Albers GW, Alexandrov AV, et al. **Acute stroke imaging research roadmap.** *AJNR Am J Neuroradiol* 2008;29:e23–30
15. Wintermark M, Albers GW, Broderick JP, et al. **Acute stroke imaging research roadmap II.** *Stroke* 2013;44:2628–39
16. Bae KT. **Intravenous contrast medium administration and scan timing at CT: considerations and approaches.** *Radiology* 2010;256:32–61
17. Konstas AA, Goldmakher GV, Lee T-Y, et al. **Theoretic basis and technical implementations of CT perfusion in acute ischemic stroke. Part 2. Technical implementations.** *AJNR Am J Neuroradiol* 2009;30:885–92
18. Murphy BD, Fox AJ, Lee DH, et al. **Identification of penumbra and infarct in acute ischemic stroke using computed tomography perfusion-derived blood flow and blood volume measurements.** *Stroke* 2006;37:1771–77
19. Powers WJ, Grubb RL, Raichle ME. **Physiological responses to focal cerebral ischemia in humans.** *Ann Neurol* 1984;16:546–52
20. Maulaz A, Piechowski-Józwiak B, Michel P, et al. **Selecting patients for early stroke treatment with penumbra images.** *Cerebrovasc Dis* 2005;20(suppl 2):19–24
21. Kudo K, Sasaki M, Yamada K, et al. **Differences in CT perfusion maps generated by different commercial software: quantitative analysis by using identical source data of acute stroke patients.** *Radiology* 2010;254:200–09
22. Dohmen C, Kumura E, Rosner G, et al. **Adenosine in relation to calcium homeostasis: comparison between gray and white matter ischemia.** *J Cereb Blood Flow Metab* 2001;21:503–10
23. Helenius J, Perkiö J, Soinne L, et al. **Cerebral hemodynamics in a healthy population measured by dynamic susceptibility contrast MR imaging.** *Acta Radiol* 2003;44:538–46
24. Stys PK, Ransom BR, Waxman SG, et al. **Role of extracellular calcium in anoxic injury of mammalian central white matter.** *Proc Natl Acad Sci U S A* 1990;87:4212–16
25. Arakawa S, Wright PM, Koga M, et al. **Ischemic thresholds for gray and white matter: a diffusion and perfusion magnetic resonance study.** *Stroke* 2006;37:1211–16

# Histologic Analysis of Retrieved Clots in Acute Ischemic Stroke: Correlation with Stroke Etiology and Gradient-Echo MRI

S.K. Kim,  W. Yoon, T.S. Kim, H.S. Kim, T.W. Heo, and M.S. Park

## ABSTRACT

**BACKGROUND AND PURPOSE:** It is unclear whether clot composition analysis is helpful to predict a stroke mechanism in acute large vessel occlusion. In addition, the relationship between early vessel signs on imaging studies and clot compositions has been poorly understood. The purpose of this study was to elucidate the relationship between clot composition and stroke etiology following mechanical thrombectomy and to investigate the effect of varied clot compositions on gradient-echo MR imaging of clots.

**MATERIALS AND METHODS:** Histopathologic analysis of retrieved clots from 37 patients with acute MCA occlusion was performed. Patients underwent gradient-echo imaging before endovascular therapy. Retrieved clots underwent semiquantitative proportion analysis to quantify red blood cells, fibrin, platelets, and white blood cells by area. Correlations between clot compositions and stroke subtypes and susceptibility vessel signs on gradient-echo imaging were assessed.

**RESULTS:** Stroke etiology was classified as cardioembolism in 22 patients (59.4%), large-artery atherosclerosis in 8 (21.6%), and undetermined in 7 (18.9%). The clots from cardioembolism had a significantly higher proportion of red blood cells (37.8% versus 16.9%,  $P = .031$ ) and a lower proportion of fibrin (32.3% versus 48.5%,  $P = .044$ ) compared with those from large-artery atherosclerosis. The proportion of red blood cells was significantly higher in clots with a susceptibility vessel sign than in those without it (48.0% versus 1.9%,  $P < .001$ ), whereas the proportions of fibrin (26.4% versus 57.0%,  $P < .001$ ) and platelets (22.6% versus 36.9%,  $P = .011$ ) were significantly higher in clots without a susceptibility vessel sign than those with it.

**CONCLUSIONS:** The histologic composition of clots retrieved from cerebral arteries in patients with acute stroke differs between those with cardioembolism and large-artery atherosclerosis. In addition, a susceptibility vessel sign on gradient-echo imaging is strongly associated with a high proportion of red blood cells and a low proportion of fibrin and platelets in retrieved clots.

**ABBREVIATIONS:** GRE = gradient-echo; RBC = red blood cell; WBC = white blood cell

Endovascular therapy is increasingly used for treating acute ischemic stroke due to intracranial large-vessel occlusion. Among various endovascular therapies, mechanical thrombectomy is now accepted as the first-line endovascular therapy for acute large-vessel occlusion. Recent studies have shown that thrombectomies with a retrievable stent or flexible aspiration catheter were associated with high-recanalization and low-complication rates.<sup>1-5</sup> One of the striking features of mechanical

thrombectomy is that it enables physicians to perform histopathologic examination of clots retrieved from human intracranial arteries. Recent studies suggested that histologic examination of retrieved clots can offer new insights into the pathogenesis of acute stroke due to intracranial large-vessel occlusion.<sup>6-9</sup> However, it is currently unclear whether clot-composition analysis is helpful to predict a stroke mechanism in acute large-vessel occlusion. Only a few studies have been conducted on this topic, and prior studies have yielded only vague and contradictory results.<sup>8-10</sup>

In addition, histopathologic analysis of retrieved clots allows understanding of the pathologic basis of early vessel signs on imaging studies in patients with acute ischemic stroke. Several studies have shown that the hyperattenuated vessel sign on CT and the susceptibility vessel sign on gradient-echo (GRE) MR imaging were more often associated with erythrocyte-rich thrombi (red thrombi) than fibrin-rich thrombi (white thrombi).<sup>8,10,11</sup> Platelets play an important role in the pathogenesis of white thrombi

Received December 19, 2014; accepted after revision February 6, 2015.

From the Departments of Radiology (S.K.K., W.Y., T.W.H.), Neurosurgery (T.S.K.), Forensic Medicine (H.S.K.), and Neurology (M.S.P.), Chonnam National University Medical School, Chonnam National University Hospital, Gwangju, Republic of Korea.

Please address correspondence to Woong Yoon, MD, Department of Radiology, Chonnam National University Hospital, 671 Jebong-Ro, Dong-Gu, Gwangju, 501-757, Republic of Korea; e-mail: radyoon@jnu.ac.kr

<http://dx.doi.org/10.3174/ajnr.A4402>

associated with atherosclerotic plaque rupture.<sup>12</sup> However, the relationship between early vessel signs on imaging studies and the proportion of platelets within the retrieved clots has been poorly understood. Thus, we performed histopathologic analysis on retrieved clots from patients with acute MCA occlusion to further elucidate the relationship between clot composition and stroke etiology and to investigate the effect of platelet levels on GRE MR imaging of clots.

## **MATERIALS AND METHODS**

### **Patients**

From January 2011 to October 2012, 56 consecutive patients presenting with acute stroke due to MCA occlusions were treated with mechanical thrombectomy, including stent-based thrombectomy and manual aspiration thrombectomy at a tertiary university hospital. Patients underwent a nonenhanced CT scan and multimodal MR imaging before endovascular thrombectomy procedures. Of these patients, those who had GRE images of insufficient quality for reliable evaluation ( $n = 7$ ) or did not have thrombus material suitable for histopathologic analyses ( $n = 12$ ) were excluded. This step left 37 patients in this study. We prospectively collected the following clinical and radiologic data of these 37 patients: demographic features, cerebrovascular risk factors, NIHSS scores on admission and at discharge, use of IV thrombolysis, time to endovascular treatment, procedure time, time to reperfusion, revascularization status, clinical outcomes, and stroke subtypes.

Subtypes of ischemic stroke were determined at the time of discharge by stroke neurologists according to the classification of the Trial of Org 10172 in Acute Stroke Treatment.<sup>13</sup> Large-artery atherosclerosis was defined as “catheter angiographic” findings showing  $>50\%$  stenosis or occlusion of the ipsilateral extracranial or intracranial carotid artery proximal to the occlusion site without evidence of potential sources of cardioembolism in other diagnostic studies. Moderate or severe ( $>50\%$ ) underlying intracranial atherosclerotic stenosis was also regarded as large-artery atherosclerosis. Cardioembolism was defined as having at least 1 of the following predisposing factors: atrial fibrillation or flutter, left atrial thrombus, a prosthetic valve, severe mitral stenosis, a patent foramen ovale, concomitant acute myocardial infarction, congestive heart failure, infective endocarditis, and sick sinus syndrome, in the absence of moderate or severe ( $>50\%$ ) ipsilateral arterial stenosis on imaging studies. The institutional ethics committee approved this study. For each patient, written informed consent for endovascular therapy and histopathologic analysis of retrieved thrombi was obtained from a family member.

### **Endovascular Treatment**

On admission, a stroke neurologist performed a neurologic assessment based on the NIHSS. The inclusion criteria for endovascular thrombectomy were as follows: presentation within 6 hours of stroke onset; baseline NIHSS score of  $\geq 4$ ; no intracranial hemorrhage detected on cranial CT or MR imaging; a target mismatch pattern on multimodal MR imaging based on visual estimation (time-to-peak map of perfusion imaging showing a lesion volume  $\geq 30\%$  larger than that detected with diffusion imaging); and infarct volume on diffusion imaging or nonenhanced CT of less than one-third of the MCA territory.

Cerebral angiography and endovascular therapy were performed with the patient under conscious sedation. In cases of agitation, an intravenous bolus of midazolam was given and repeated if necessary. Stent-based thrombectomy with a Solitaire stent (Covidien, Irvine, California) was performed as the first-line endovascular treatment. When stent-based thrombectomy was unsuccessful, additional mechanical approaches were performed, including manual aspiration thrombectomy with a Penumbra reperfusion catheter (Penumbra, Alameda, California). The details of the techniques used for stent-based thrombectomy and manual aspiration thrombectomy were previously described.<sup>5,14</sup> Revascularization status was assessed on the final angiogram and was classified according to the modified TICI scale,<sup>15</sup> and successful revascularization was defined as a modified TICI grade of 2b or 3. Clinical outcome was assessed by a stroke neurologist by using the mRS during an outpatient visit 3 months after treatment. If patients were unable to attend the outpatient clinic, outcomes were obtained via telephone interview. A good clinical outcome was defined as an mRS score of  $\leq 2$ .

### **MR Imaging Analysis**

MR imaging examinations were performed by using a 1.5T unit (Signa HDxt; GE Healthcare, Milwaukee, Wisconsin). Before the endovascular procedure, patients underwent MR imaging including DWI, GRE, FLAIR, 3D TOF MRA, and perfusion imaging. GRE sequence parameters included a TR of 750–800 ms, TE of 14 ms, flip angle of 20°, section thickness of 4 mm, intersection gap of 0 mm, and FOV of 230 × 230 mm. All GRE images were retrospectively reviewed by 2 neuroradiologists (with 2 and 4 years of experience, respectively) who were blinded to the findings of conventional angiography. Conclusions were reached by consensus regarding the presence or absence of the susceptibility vessel sign on GRE imaging. A positive susceptibility vessel sign was defined as a hypointense signal change on GRE imaging within the occluded MCA, in which the diameter of the hypointense signals exceeded that of the contralateral MCA.<sup>16,17</sup> A negative susceptibility vessel sign was defined as an absence of a positive susceptibility vessel sign in the occluded MCA.

### **Histopathologic Analysis**

Retrieved clot material was fixed in 10% neutralized buffered formalin immediately after retrieval. Formalin-fixed, paraffin-embedded tissue was cut at 4- $\mu\text{m}$  thickness. All clots were stained with hematoxylin-eosin. Then, deparaffinized sections were immunohistochemically stained with antibodies for platelet glycoprotein IIIa, CD61 (LifeSpan Biosciences, Seattle, Washington). Immunostains were performed by the routine avidin-biotin complex method. Immunoreactivity was visualized with a diaminobenzidine (DAB; Dako, Glostrup, Denmark) solution and then counterstained with hematoxylin.

Stained slides were scanned at  $\times 200$  magnification by using a Scanscope XT digital scanner (Aperio, Vista, California). ImageJ software (National Institutes of Health, Bethesda, Maryland) was used for semiquantitative analysis of the percentage of red blood cells (RBCs), fibrin, platelets, and white blood cells (WBCs) by area. Histopathologic analysis was performed by an experienced

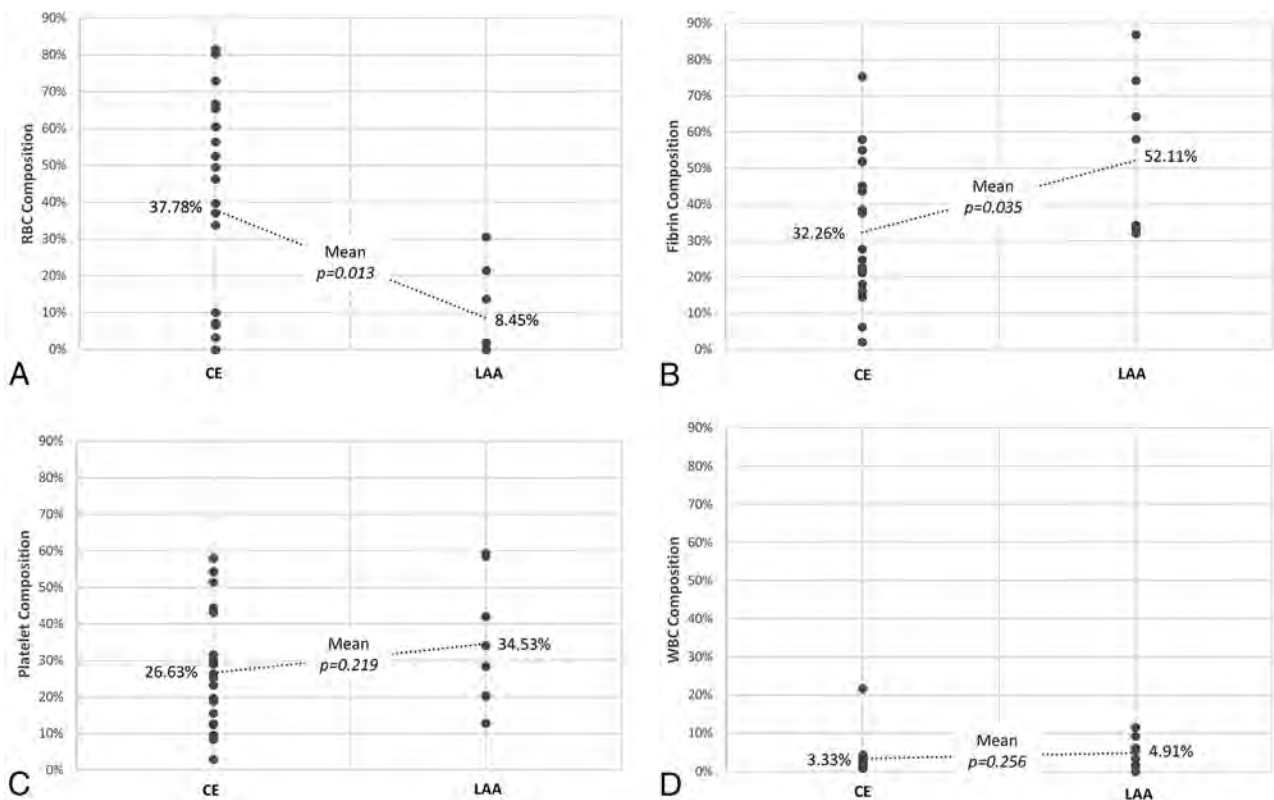


**FIG 1.** Differences in the mean percentages of clot compositions between cardioembolism (CE) and large-artery atherosclerosis (LAA). Red blood cell (A), fibrin (B), platelet (C), and white blood cell (D) composition.

pathologist without knowledge of the patient characteristics and imaging findings.

### Statistical Analysis

Continuous data are presented as means or medians with SDs, and categorical data are presented as frequencies and percentages. Percentages of each specific clot component were regarded as continuous variables. First, the percentages of each clot component were compared between patients with cardioembolism and those with large-artery atherosclerosis. Then, the percentages of RBCs, fibrin, platelets, and WBCs were compared between patients with a positive susceptibility vessel sign on GRE imaging and those with a negative susceptibility vessel sign. The  $\chi^2$  or Fisher exact test was used for categorical variables, and the Mann-Whitney *U* or Kruskal-Wallis test was used for continuous variables. All statistical analyses were performed with SPSS software (Version 21.0; IBM, Armonk, New York).  $P < .05$  indicated a statistically significant difference.

### RESULTS

During the study period, 37 eligible patients (20 men and 17 women; mean age, 69 years; age range, 40–91 years) were identified. In our study group, 68% (25/37) of patients had hypertension, 51% (19/37) had atrial fibrillation, 32% (12/37) had dyslipidemia, 24% (9/37) had a history of ischemic stroke, 16% (6/37) had a smoking history, 11% (4/37) had diabetes mellitus, 8% (3/37) had a history of coronary artery disease, and 5% (2/37) had congestive heart failure.

The median NIHSS score on admission was 15, with scores

ranging from 5 to 19. The median time from symptom onset to endovascular therapy was 240 minutes (range, 60–360 minutes), the median procedure time was 30 minutes (range, 10–90 minutes), and the median time to reperfusion was 257 minutes (range, 93–420 minutes). IV rtPA was administered in 23 patients (62%) before mechanical thrombectomy. Of 37 patients, 5 had a tandem occlusion at the proximal cervical portion of the ICA and received carotid artery stent placement before the intracranial revascularization procedure. Successful reperfusion (modified TICI 2b or 3) was achieved in 83.7% (31/37) of patients, and complete reperfusion (modified TICI grade 3) occurred in 70.2% (26/37) of patients. No patient had symptomatic hemorrhage during the hospital stay. At discharge, the NIHSS score improved (decrease of  $\geq 4$  points) in 28 patients (75.6%). The median NIHSS score at discharge was 5. At the 3-month follow-up, 16 patients (43.2%) showed a good clinical outcome (mRS 0–2). Mortality was 14% (5/37) at 3 months.

On histopathologic examination, the mean percentage of components across all retrieved clots was  $29.3 \pm 29.33\%$  RBCs,  $38.8 \pm 22.64\%$  fibrin,  $28.4 \pm 14.89\%$  platelets, and  $3.5 \pm 3.90\%$  WBCs. Cholesterol crystals or calcified material was not identified in extracted clots in this study.

The subtypes of stroke were classified as cardioembolism in 22 (59.4%), large-artery atherosclerosis in 8 (21.6%), and undetermined in 7 (18.9%). The percentages of RBC and fibrin composition differed significantly between patients with cardioembolism and those with large-artery atherosclerosis (Fig 1). The clots in patients with a cardioembolism had a higher proportion of

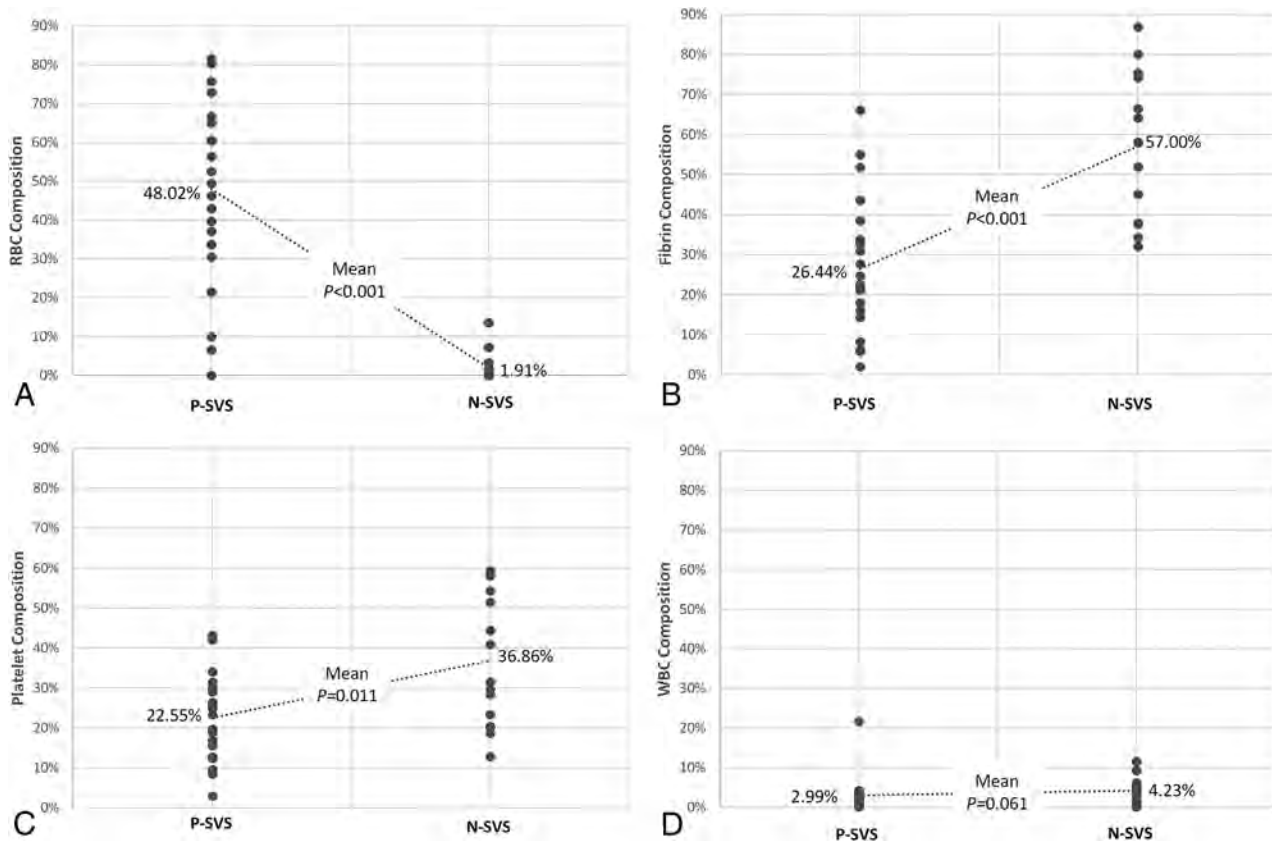


**FIG 2.** Differences in the mean percentages of clot compositions relative to a positive susceptibility vessel sign (P-SVS) and a negative susceptibility vessel sign (N-SVS). Red blood cell (A), fibrin (B), platelet (C), and white blood cell (D) composition.

RBCs (37.8% versus 8.5%,  $P = .013$ ) and a lower proportion of fibrin (32.3% versus 52.1%,  $P = .035$ ) than in those with large-artery atherosclerosis. There were no significant differences in the proportion of platelets (26.6% versus 34.5%) and WBCs (3.3% versus 4.9%) between patients with a cardioembolism and those with large-artery atherosclerosis. There were no correlations between the proportion of clot components and initial stroke severity or subsequent revascularization status or clinical outcome. The mean percentage of clot components in patients with undetermined etiology was  $26.6 \pm 33.81\%$  RBCs,  $44.3 \pm 29.59\%$  fibrin,  $26.7 \pm 7.99\%$  platelets, and  $2.4\% \pm 2.07\%$  WBCs. There were no significant differences in the proportion of clot components between patients with an undetermined etiology and those with a cardioembolism or large-artery atherosclerosis.

At GRE imaging, a positive susceptibility vessel sign was identified in 22 (59.4%) of 37 patients. The relationships between clot component proportion and susceptibility vessel sign on GRE imaging are shown in Fig 2. The mean percentage of RBC composition was higher in clots with a positive susceptibility vessel sign (48.0% versus 1.9%,  $P < .001$ ) (Fig 3), whereas the percentages of fibrin composition (26.4% versus 57.0%,  $P < .001$ ) and platelets (22.6% versus 36.9%,  $P = .011$ ) were significantly higher in clots with a negative susceptibility vessel sign (Fig 4). The percentage of WBC composition was consistently low in all clots and was not statistically different between clots with a positive susceptibility vessel sign and those with a negative susceptibility vessel sign (3.0% versus 4.2%).

## DISCUSSION

This study demonstrated that histologic compositions of clots from patients with acute stroke differ between 2 major subtypes of ischemic stroke, namely, large-artery atherosclerosis and cardioembolism. To date, very few studies investigating a possible relationship between the histology of retrieved clots and stroke mechanisms have been reported.<sup>8-10</sup> Moreover, the results of previous studies have been inconsistent and confusing. Liebeskind et al<sup>10</sup> performed histopathologic analysis of retrieved clots in 50 patients with acute ischemic stroke who had undergone endovascular thrombectomy. They briefly stated that clot composition was unrelated to the final determination of stroke etiology; however, they did not provide detailed data on this issue. More recently, Niesten et al<sup>8</sup> investigated 22 thrombi retrieved after mechanical thrombectomy in patients with acute stroke. In contrast to our study, they reported that clots originating from large-artery atherosclerosis had the highest percentage of RBCs compared with other stroke subtypes, while there were no significant differences in the proportion of fibrin and platelets between different stroke subtypes. In their study, the patient population included a small number of patients with large-artery atherosclerosis ( $n = 8$ ) and cardioembolism ( $n = 6$ ), which was the major limitation. The most recent study by Boeckh-Behrens et al<sup>9</sup> investigated the histopathology of retrieved clots from 34 patients with acute anterior circulation stroke. They reported that there was a significantly higher proportion of WBCs in the thrombi of patients with cardioembolism compared with those with other stroke subtypes. In

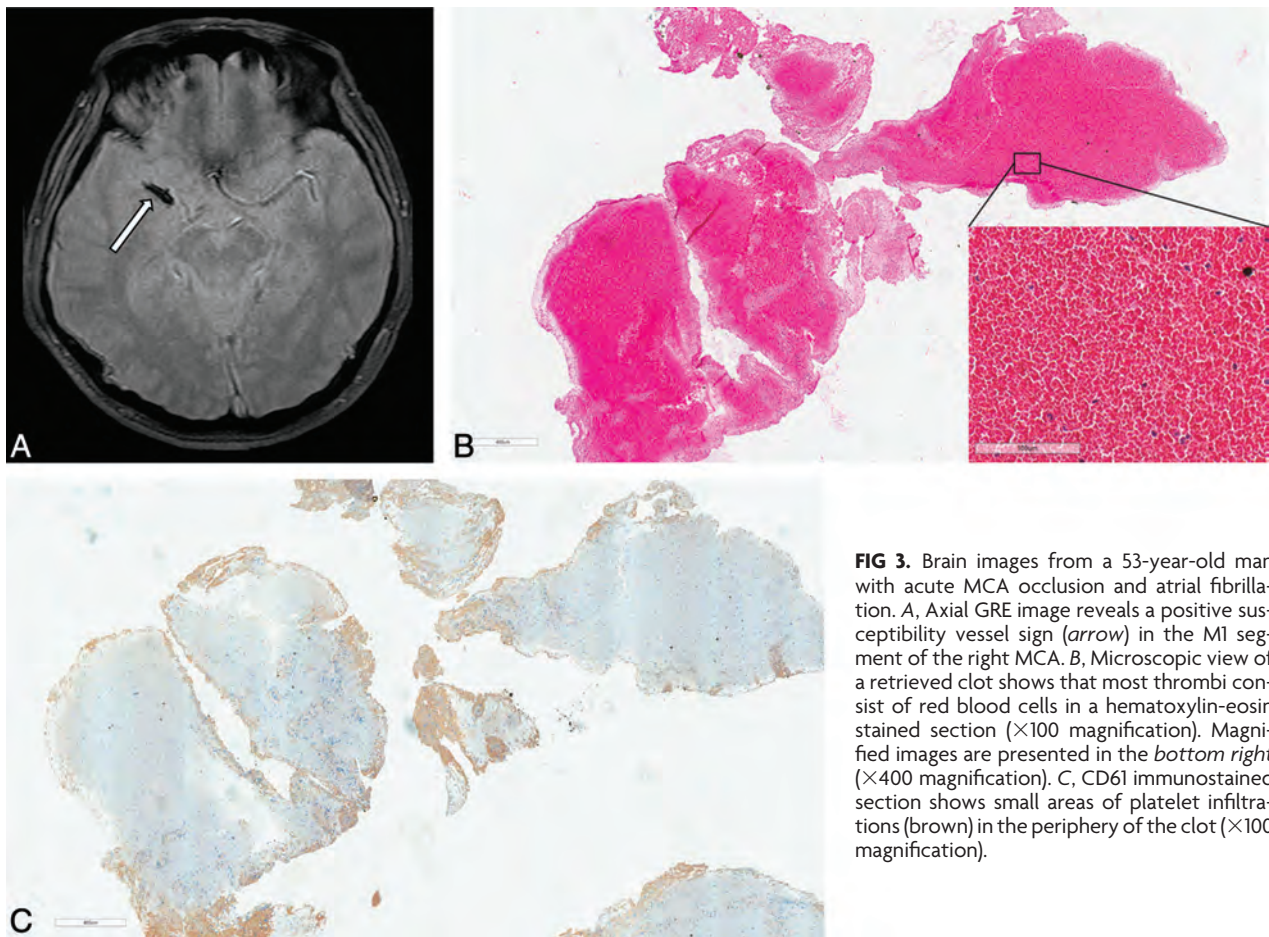


**FIG 3.** Brain images from a 53-year-old man with acute MCA occlusion and atrial fibrillation. A, Axial GRE image reveals a positive susceptibility vessel sign (*arrow*) in the M1 segment of the right MCA. B, Microscopic view of a retrieved clot shows that most thrombi consist of red blood cells in a hematoxylin-eosin stained section ( $\times 100$  magnification). Magnified images are presented in the *bottom right* ( $\times 400$  magnification). C, CD61 immunostained section shows small areas of platelet infiltrations (brown) in the periphery of the clot ( $\times 100$  magnification).

their study, the quantitative composition of all thrombi consisted of 60% fibrin, 32% RBC, and 8% WBC, and the patient population included 16 patients with cardioembolism and only 3 with large-artery atherosclerosis. They did not provide detailed data regarding proportions of RBCs and fibrin between different stroke subtypes.

In contrast to those previous studies, our study supports the traditional concept that cardioembolic thrombi forming in regions of stasis or slow flow are mainly composed of entrapped RBCs, and thrombi occurring in the context of atherosclerotic large arteries are mainly composed of fibrin and platelets,<sup>12,18</sup> in the setting of acute ischemic stroke. In our study, we found that the proportion of RBC composition in retrieved clots was higher in patients with cardioembolism compared with those with large-artery atherosclerosis, whereas the proportion of fibrin composition was higher in patients with large-artery atherosclerosis compared with those with cardioembolism. There were no differences in proportions of platelets and WBCs between large-artery atherosclerosis and cardioembolism in our study. In the coronary circulation, most of the thrombi detected at atherosclerotic plaque rupture sites consisted of a mixture of fibrin and platelets, and fibrin was more abundant.<sup>19</sup> The results from our study are exactly in accordance with those in a previous postmortem study by Sato et al,<sup>18</sup> which examined the cerebral arteries and thrombi of 17 patients who had died of cardioembolic ( $n = 11$ ) and large-artery atherosclerotic ( $n = 6$ ) strokes within 30 days of stroke onset. They found that the ratio and total area of RBCs in thrombi

were significantly larger in cardioembolic than in large-artery atherosclerotic stroke and that the ratio of the area of fibrin was 3-fold larger in large-artery atherosclerotic than in cardioembolic stroke.

Our study also confirmed the relationship between clot composition and early vessel signs on MR imaging. Paramagnetic intracellular deoxyhemoglobin in acute clots leads to a nonuniform magnetic field and resultant rapid dephasing of spins, which causes marked signal loss on GRE imaging—that is, a susceptibility vessel sign.<sup>16,20</sup> Only 1 previous study investigated the relationship between retrieved clot composition and susceptibility vessel signs on GRE imaging. Liebeskind et al<sup>10</sup> correlated susceptibility vessel signs on GRE imaging and the composition of retrieved clots in 32 patients with acute MCA stroke. In their study, a susceptibility vessel sign on GRE imaging occurred in 56% (17/32) of patients. They found that a susceptibility vessel sign was more common in RBC-dominant clots and mixed clots compared with fibrin-dominant clots and the mean percentage of RBCs was greater in clots with a susceptibility vessel sign than in those without a susceptibility vessel sign. These results are in line with those in the present study. In our study, a susceptibility vessel sign occurred in 59% (22/37) of patients. The mean percentage of RBC component was significantly higher in clots with a positive susceptibility vessel sign than in those with a negative susceptibility vessel sign, whereas the percentage of fibrin component was significantly higher in clots with a negative susceptibility vessel sign than in those with a positive susceptibility vessel sign. Moreover,

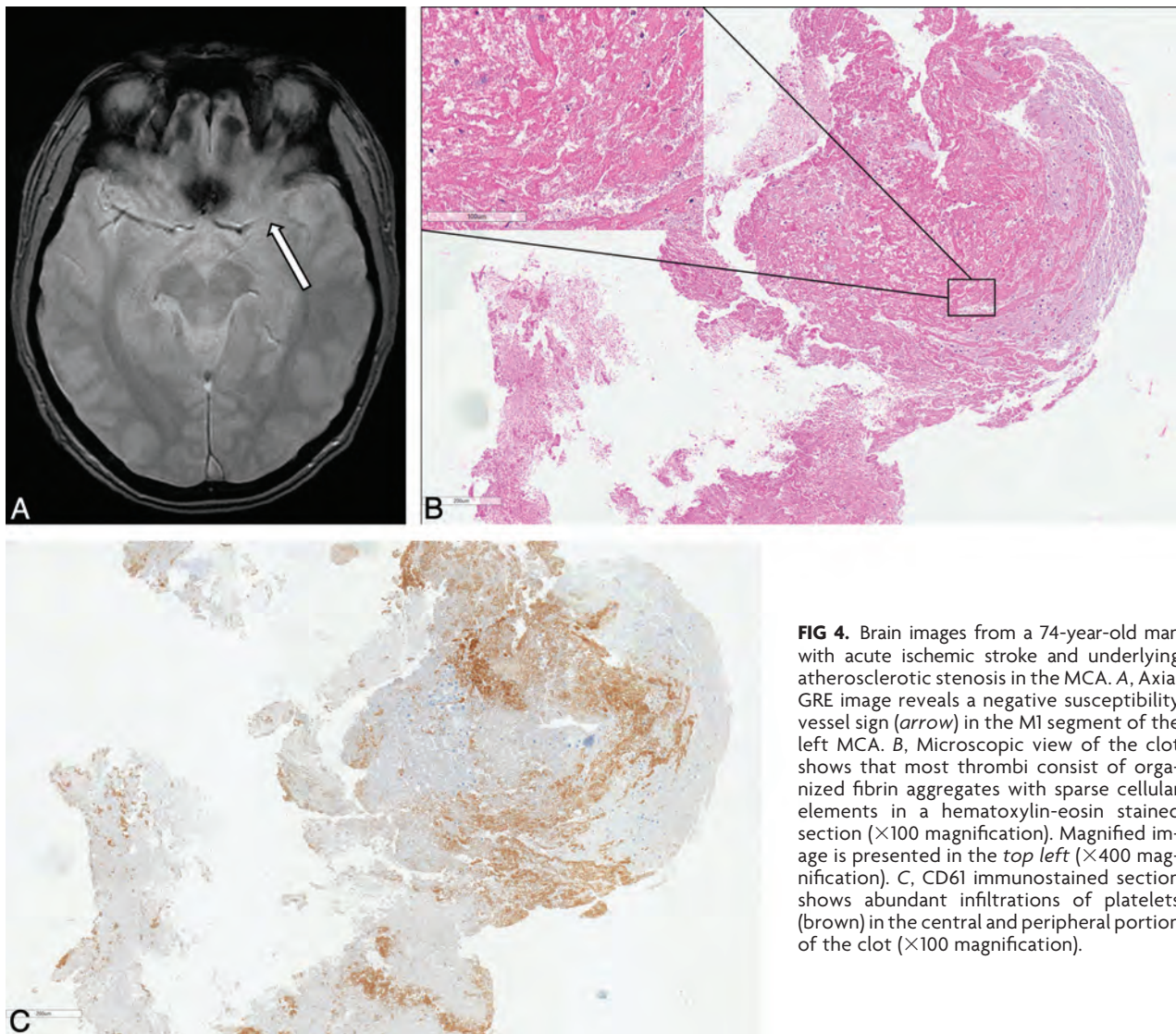


**FIG 4.** Brain images from a 74-year-old man with acute ischemic stroke and underlying atherosclerotic stenosis in the MCA. *A*, Axial GRE image reveals a negative susceptibility vessel sign (*arrow*) in the M1 segment of the left MCA. *B*, Microscopic view of the clot shows that most thrombi consist of organized fibrin aggregates with sparse cellular elements in a hematoxylin-eosin stained section ( $\times 100$  magnification). Magnified image is presented in the *top left* ( $\times 400$  magnification). *C*, CD61 immunostained section shows abundant infiltrations of platelets (brown) in the central and peripheral portion of the clot ( $\times 100$  magnification).

we found that the proportion of platelets was significantly different between clots with and without a susceptibility vessel sign on GRE imaging. In our study, the proportion of platelets was significantly higher in clots with a negative susceptibility vessel sign than in those with a positive susceptibility vessel sign; this finding has not been reported previously.

Platelets were not investigated in the study of Liebeskind et al.<sup>10</sup> Only 1 study investigated the platelet component in retrieved clots with an immunohistochemical study. Niesten et al<sup>8</sup> performed CD31 immunostaining to investigate platelet composition in retrieved clots, in addition to hematoxylin-eosin staining, and correlated clot compositions with attenuation on noncontrast CT. They found a nonsignificant, weak negative correlation between CT attenuation and the proportion of platelets.

Our study has several limitations. The size of the study population was too small to draw a strong conclusion. The number of patients with large-artery atherosclerosis was relatively small compared with those with cardioembolism. During the study period, many cases were excluded because of a lack of retrieved thrombi or insufficient thrombi or incomplete imaging. In addition, successful reperfusion occurred in 84% of

patients in the present study. Thus, we could not evaluate whole clots occluding the MCA in 16% of cases. Finally, clot composition might be affected by medical treatment in patients before the stroke onset and intravenous rtPA given before mechanical thrombectomy.<sup>10</sup>

## CONCLUSIONS

This study suggests that the histologic composition of clots retrieved from cerebral arteries in patients with acute stroke is different between stroke subtypes. We found that the proportion of RBC composition in retrieved clots is higher in patients with cardioembolism compared with those with large-artery atherosclerosis, whereas the proportion of fibrin composition is higher in patients with large-artery atherosclerosis compared with those with cardioembolism. In addition, a susceptibility vessel sign on GRE MR imaging is strongly associated with a high proportion of RBCs and a low proportion of fibrin and platelets in retrieved clots. These findings would be helpful for clinicians in predicting clot composition and stroke etiology with GRE imaging before endovascular therapy in patients with acute ischemic stroke.

## REFERENCES

1. Saver JL, Jahan R, Levy EI, et al; SWIFT Trialists. **Solitaire flow restoration device versus the Merci retriever in patients with acute ischaemic stroke (SWIFT): a randomised, parallel-group, non-inferiority trial.** *Lancet* 2012;380:1241–49
2. Nogueira RG, Lutsep HL, Gupta R, et al; TREVO 2 Trialists. **Trevo versus Merci retrievers for thrombectomy revascularisation of large vessel occlusions in acute ischaemic stroke (TREVO 2): a randomised trial.** *Lancet* 2012;380:1231–40
3. Pereira VM, Gralla J, Davalos A, et al. **Prospective, multicenter, single-arm study of mechanical thrombectomy using Solitaire Flow Restoration in acute ischemic stroke.** *Stroke* 2013;44:2802–07
4. Turk AS, Frei D, Fiorella D, et al. **ADAPT FAST study: a direct aspiration first pass technique for acute stroke thrombectomy.** *J Neurointerv Surg* 2014;6:260–64
5. Kim SK, Yoon W, Moon SM, et al. **Outcomes of manual aspiration thrombectomy for acute ischemic stroke refractory to stent-based thrombectomy.** *J Neurointerv Surg* 2015;7:473–77
6. Marder VJ, Chute DJ, Starkman S, et al. **Analysis of thrombi retrieved from cerebral arteries of patients with acute ischemic stroke.** *Stroke* 2006;37:2086–93
7. Mehta BP, Nogueira RG. **Should clot composition affect choice of endovascular therapy?** *Neurology* 2012;79(suppl 1):S63–67
8. Niesten JM, van der Schaaf IC, van Dam L, et al. **Histopathologic composition of cerebral thrombi of acute stroke patients is correlated with stroke subtype and thrombus attenuation.** *PLoS One* 2014;9:e88882
9. Boeckh-Behrens T, Schubert M, Förschler A, et al. **The impact of histological clot composition in embolic stroke.** *Clin Neuroradiol* 2014 Sep 27. [Epub ahead of print]
10. Liebeskind DS, Sanossian N, Yong WH, et al. **CT and MRI early vessel signs reflect clot composition in acute stroke.** *Stroke* 2011;42:1237–43
11. Simons N, Mitchell P, Dowling R, et al. **Thrombus composition in acute ischemic stroke: a histopathological study of thrombus extracted by endovascular retrieval.** *J Neuroradiol* 2015;42:86–92
12. Viereck J, Ruberg FL, Qiao Y, et al. **MRI of atherothrombosis associated with plaque rupture.** *Arterioscler Thromb Vasc Biol* 2005;25:240–45
13. Adams HP Jr, Bendixen BH, Kappelle LJ, et al; TOAST Investigators. **Classification of subtype of acute ischemic stroke: definitions for use in a multicenter clinical trial.** *Stroke* 1993;24:35–41
14. Yoon W, Jung MY, Jung SH, et al. **Subarachnoid hemorrhage in a multimodal approach heavily weighted toward mechanical thrombectomy with Solitaire stent in acute stroke.** *Stroke* 2013;44:414–19
15. Zaidat OO, Yoo AJ, Khatri P, et al; Cerebral Angiographic Revascularization Grading (CARG) Collaborators, STIR Revascularization working group, STIR Thrombolysis in Cerebral Infarction (TICI) Task Force. **Recommendations on angiographic revascularization grading standards for acute ischemic stroke: a consensus statement.** *Stroke* 2013;44:2650–63
16. Rovira A, Orellana P, Alvarez-Sabin J, et al. **Hyperacute ischemic stroke: middle cerebral artery susceptibility sign at echo-planar gradient-echo MR imaging.** *Radiology* 2004;232:466–73
17. Cho KH, Kim JS, Kwon SU, et al. **Significance of susceptibility vessel sign on T2\*-weighted gradient echo imaging for identification of stroke subtypes.** *Stroke* 2005;36:2379–83
18. Sato Y, Ishibashi-Ueda H, Iwakiri T, et al. **Thrombus components in cardioembolic and atherothrombotic strokes.** *Thromb Res* 2012;130:278–80
19. Sato Y, Hatakeyama K, Yamashita A, et al. **Proportion of fibrin and platelets differs in thrombi on ruptured and eroded coronary atherosclerotic plaques in humans.** *Heart* 2005;91:526–30
20. Patel MR, Edelman RR, Warach S. **Detection of hyperacute primary intraparenchymal hemorrhage by magnetic resonance imaging.** *Stroke* 1996;27:2321–24

# The Preventive Effect of Endovascular Treatment for Recurrent Hemorrhage in Patients with Spinal Cord Arteriovenous Malformations

Y. Niimi, H. Matsukawa,  N. Uchiyama, and A. Berenstein

## ABSTRACT

**BACKGROUND AND PURPOSE:** Spinal cord AVMs represent rare and insufficiently studied pathologic entities. Embolization is thought to play an important role in the management of spinal cord AVMs. Factors for recurrent hemorrhage and the impact of endovascular treatment on prevention of recurrent hemorrhage remain to be confirmed. We aimed to assess recurrent hemorrhagic incidence of spinal cord AVMs and its prevention by endovascular treatment.

**MATERIALS AND METHODS:** We reviewed 80 patients with spinal cord AVMs by spinal cord angiography who had hemorrhage before the first endovascular treatment at New York University Medical Center, Beth Israel Medical Center, or Roosevelt Hospital in New York. We compared the baseline and radiologic characteristics of patients with and without recurrent hemorrhage by the log-rank test and the Cox proportional hazards model.

**RESULTS:** We observed recurrent hemorrhage in 35 (44%) patients (1/41 patients with endovascular treatment and 34/39 patients without endovascular treatment). The median length of total follow-up was 659 days (interquartile range, 129–2640 days), and the median length from first-to-recurrent hemorrhage was 369 days (interquartile range, 30–1596 days). The log-rank test revealed that endovascular treatment and venous thrombosis reduced recurrent hemorrhage, and associated aneurysm was related to recurrent hemorrhage. Even in multivariate analysis, the endovascular treatment reduced (hazard ratio, 0.027;  $P < .0001$ ) and associated aneurysm increased (hazard ratio, 3.4;  $P = .044$ ) the risk of recurrent hemorrhage.

**CONCLUSIONS:** Endovascular embolization is the first choice of treatment for spinal cord AVMs and is effective in preventing recurrent hemorrhage.

**ABBREVIATIONS:** ASA = anterior spinal artery; NBCA = *n*-butyl 2-cyanoacrylate; SCAVM = spinal cord AVM

Spinal cord AVMs (SCAVMs) represent rare and insufficiently studied pathologic entities characterized by considerable variation.<sup>1</sup> Insufficient study of this disease is associated with the rarity and complexity of its diagnosis.<sup>2,3</sup> Spinal cord arteriovenous fistula is a direct communication between arteries and veins, while spinal cord arteriovenous malformation in its narrow denotation has a nidus, an abnormal vascular network interposed between arteries and veins. On some occasions, both AVF and AVM constitute a shunt, which is also called AVM in its broader

meaning.<sup>4</sup> Spinal cord AVFs and AVMs manifest with sudden or gradual deterioration of sensorimotor function in the extremities and/or of micturition, defecation, or sexual function due mainly to venous hypertension/ischemia and, in some cases, arterial steal, hemorrhage, or mass effect.<sup>4</sup>

There has been advancement in endovascular treatment of SCAVM, including monitoring systems. Treatment of an SCAVM aims to decrease the risk of hemorrhage and arrest the progression of neurologic deterioration.<sup>5</sup> Embolization is thought to play an important role in the management of SCAVMs, both as a primary treatment and as an adjunct to surgical excision. However, complete cure of SCAVMs by endovascular embolization is exceptional except for spinal cord AVFs, and endovascular treatment often results in partial obliteration of the lesion by target embolization. Target embolization aims at occluding dangerous structures causing hemorrhage or neurologic symptoms, such as aneurysms, high-flow fistulas, and nerve root lesions for radicular pain. To date, various studies investigated the factors related to

Received July 31, 2014; accepted after revision February 4, 2015.

From the Departments of Neuroendovascular Therapy (Y.N.) and Neurosurgery (H.M.), St. Luke's International Hospital, Tokyo, Japan; Department of Neurosurgery (N.U.), Kanazawa University, Kanazawa, Japan; and Center for Endovascular Surgery (A.B.), Roosevelt Hospital, New York, New York.

Please address correspondence to Yasunari Niimi, MD, Department of Neuroendovascular Therapy, St. Luke's International Hospital, 9-1 Akashi-cho, Chuo-ku, Tokyo 104-8560, Japan; e-mail address: yasanm@luke.ac.jp

<http://dx.doi.org/10.3174/ajnr.A4396>

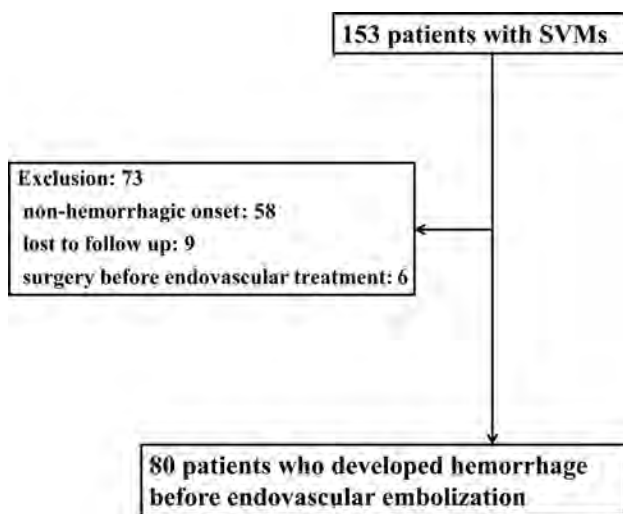


**FIG 1.** Exclusion criteria of the present study. SVM indicates spinal vascular malformation.

initial hemorrhage.<sup>6-10</sup> However, factors for recurrent hemorrhage and the impact of endovascular treatment on prevention of recurrent hemorrhage remain to be confirmed. The purpose of this study was to assess the recurrent hemorrhagic incidence of SCAVMs and its prevention by endovascular treatment.

## MATERIALS AND METHODS

The study is reported on the basis of criteria from the Strengthening the Reporting of Observational Study in Epidemiology statement.<sup>11</sup>

### Study Participants

We retrospectively reviewed 153 patients diagnosed with SCAVM by spinal cord angiography at centers where the senior author worked (New York University Medical Center, Beth Israel Medical Center, or Roosevelt Hospital in New York) between April 1980 and October 2010. Exclusion criteria are shown in Fig 1. After exclusions, we analyzed 80 patients with SCAVMs who had hemorrhage before the first endovascular treatment.

### Clinical Characteristics

We collected the following data: age, sex, the presence of SCAVM-related syndrome, endovascular treatment after the first hemorrhage or radiation therapy, and radiologic characteristics. We defined pediatrics as younger than 18 years of age.

Radiologic characteristics included hemorrhage type, detailed diagnosis, lesion level, the presence of an associated aneurysm, venous thrombosis, venous stricture, venous ectasia, and venous hypertension.

### Improvement of Angiographic and Embolization Techniques

There has been improvement in angiographic and embolization techniques during the 30 years of the study and continuous improvement in knowledge of disease, angiographic imaging quality, endovascular equipment including microcatheters, microguidewires, embolic agents, and monitoring systems. We started by using guidewire-assisted and flow-guided microcatheters in the

late 1980s. As a monitoring system, somatosensory evoked potentials introduced in the mid-1980s, and transcranial motor evoked potentials, in the mid-1990s as well as the provocative testing method.<sup>12</sup> We switched from isobutyl cyanoacrylate to *n*-butyl 2-cyanoacrylate (NBCA) as a liquid embolic agent in the late 1980s. Detachable coils became available for certain diseases in the early 1990s. All these improvements enhanced the safety and adequacy of endovascular occlusion of SCAVMs. However, our conceptual approach for endovascular treatment of an SCAVM (ie, partial targeted embolization) is, in principle, unchanged during the 30 years of the study because we still have difficulty in completely obliterating an SCAVM by embolization itself. Therefore, we decided to analyze all cases of SCAVMs during 30 years.

### Current Angiographic/Embolization Protocol

All angiographic procedures were performed with the patients under general anesthesia with neuroleptic agents and neurophysiologic monitoring, including somatosensory evoked potentials and transcranial motor evoked potentials. Superselective catheterization of the appropriate feeding pedicles was performed by using a microcatheter before embolization to analyze the vascular anatomy of the lesion. Pharmacologic provocative testing was performed with superselective injection of amobarbital sodium and lidocaine when indicated. The details of the indication, technique, and results of neurophysiologic monitoring and provocative testing for SCAVMs have been described previously.<sup>12</sup> After hemorrhage with neurologic deficits, patients were treated conservatively until their neurologic deficits became stabilized, and we then performed endovascular treatment if indicated. We perform targeted partial embolization for nidus-type SCAVMs to close aneurysms and fistulas to prevent hemorrhage and improve spinal cord hemodynamics to treat symptomatic myelopathy/venous hypertension. Complete angiographic cure is not the goal with most intradural lesions with the exception of AVFs. *n*-butyl 2-cyanoacrylate was the main embolic agent for both intra- and extradural lesions. Particulate embolization was used when NBCA embolization was not feasible on the basis of the flow dynamics of the lesion. Coils were used for embolization of aneurysms, high-flow fistulas, and protection of the normal vascular territories when embolizations were performed from proximal positions (nonintranidal). Ethylene-vinyl alcohol copolymer (Onyx; Covidien, Irvine, California) was not used for intradural lesions. The embolization procedure was repeated in a staged fashion if considered preferable.

### Outcome

The treatment results were confirmed by angiography after embolization. MR imaging was also performed if indicated. Clinical follow-up was performed in a multidisciplinary clinic attended by both interventional neuroradiologists and neurosurgeons. In case of any clinical suspicion of recurrence or progression of the disease, MR imaging or angiography or both were repeated at that time. Repeat embolization was performed on the basis of the angiographic findings. Annual follow-up MR imaging was performed if the patient was neurologically stable. If there was any change in the appearance, spinal angiography was performed with the intent to treat.

**Table 1: Duration between initial and recurrent hemorrhage in patients with SCAVMs**

Duration	No. (n = 35)	Percentage
<7 Days	6	18
8–31 Days	5	14
1–6 Months	2	5.7
6 Months to 1 year	4	11
1–2 Years	2	5.7
2–3 Years	3	8.6
>3 Years	13	37

The end points were survival without recurrent hemorrhage from SCAVMs.

### Statistical Analysis

Statistical analysis was performed by using SPSS for Mac (Version 21.0; IBM, Armonk, New York). Variables are expressed as mean  $\pm$  SD, median (interquartile range: 25th–75th percentile), or number of patients (percentage) as appropriate. The normality of the data was evaluated by using the Shapiro-Wilk test. We performed receiver operating characteristics curve analysis for age and the binary end point of recurrent hemorrhage, and we selected the age cutoff point that optimized sensitivity and specificity.

We compared the baseline and radiologic characteristics of patients with and without recurrent hemorrhage by the log-rank test and performed multivariate analysis by the Cox proportional hazards model by using variables that were marginally or significantly associated with progression on the log-rank test ( $P < .20$ ). The probability of freedom from recurrent hemorrhage was estimated by using the Kaplan-Meier method; comparisons of the survival curves by the number of factors were performed by using the log-rank test. Differences were considered significant at  $P < .05$  for a 95% CI.

### RESULTS

Forty-four patients (55%) presented with subarachnoid hemorrhage and 36 (45%) presented with hematomyelia. Types of initial hemorrhage were not related to recurrent hemorrhage ( $P = .54$ ). We observed recurrent hemorrhage in 35 (44%) patients, including 1 of 41 patients treated by embolization and 34 of 39 patients not treated by embolization. The median length of total follow-up was 659 days (interquartile range, 129–2640 days), and the median length from the first-to-recurrent hemorrhage was 369 days (interquartile range, 30–1596 days). We found that 31% of patients rebled within 1 month of the first hemorrhage and 40% of them rebled in  $>3$  years (Table 1). Associated diseases were noted in several patients: spinal arteriovenous metamerism syndrome in 10 patients (13%) with recurrent hemorrhage and in 9 (20%) without recurrent hemorrhage; Klippel-Trenaunay-Weber syndrome in 1 (2.9%) with recurrent hemorrhage, not seen in those without recurrent hemorrhage; and Osler-Weber-Rendu disease in 1 (2.9%) with recurrent hemorrhage, not seen in those without recurrent hemorrhage. No significant difference was found among these associated diseases and recurrent hemorrhage ( $P = .94$ ). Radiation therapy was performed in 3 patients (8.6%) with recurrent hemorrhage and was not performed in patients without recurrent hemorrhage ( $P = .42$ ). Clinical and radiologic charac-

teristics of 80 patients with and without recurrent hemorrhage are shown in Table 2. The log-rank test revealed that endovascular treatment (Fig 2) and venous thrombosis significantly and marginally reduced recurrent hemorrhage, respectively, and an associated aneurysm was significantly related to recurrent hemorrhage. Even in multivariate analysis, the endovascular treatment reduced and associated aneurysm increased the risk of recurrent hemorrhage (Table 3).

### Illustrative Case

This male patient initially presented with a spinal subarachnoid hemorrhage at 11 years of age. A diagnosis of an SCAVM was made by MR imaging and spinal angiography at that time, but no treatment was performed. He then experienced 3 spinal subarachnoid hemorrhages in a month, documented by spinal tap at 14 years of age. He was then referred to us for endovascular treatment. On admission, he was neurologically intact. Angiographic study demonstrated a nidus-type SCAVM at the T2 spinal level supplied mainly by the anterior spinal artery (ASA) with multiple intranidal aneurysms (Fig 3A). Superselective angiography from a feeder coming off the ASA failed to demonstrate the aneurysms (Fig 3B, -C). Superselective angiography from the ASA near the feeder origin demonstrated an intranidal aneurysm supplied by a branch of the ASA different from the feeder that was previously catheterized (Fig 3D). Because of the inability to superselectively catheterize the feeder supplying the aneurysm, embolization from the ASA near the origin of the feeder was performed by using NBCA (Fig 3E). Control angiography after the embolization showed decreased size of the AVM without opacification of the aneurysms. The ASA was disconnected for a short segment, but the distal segment was opacified through the collateral. The remaining nidus was also opacified by the ASA and the posterior spinal artery opacified from the left T10 and the left T8 intercostal artery, respectively (not shown). The patient remained neurologically intact and had no further hemorrhage during the follow-up for 6 years after the embolization.

### DISCUSSION

The results of the present study showed that the endovascular treatment reduced and associated aneurysm increased the risk of recurrent hemorrhage in patients with hemorrhagic SCAVM.

### Hemorrhage

The congenital nature of SCAVMs in their form at presentation is also debatable,<sup>13</sup> because their appearance after hemorrhage may reflect the result of decompensation of the vasculature lesion and the surrounding spinal cord, which occurred after birth. It has previously been reported that once a patient hemorrhages, the incidence of recurrent hemorrhage is very high.<sup>14</sup> The overall annual hemorrhage rate was 4%, increasing to 10% for spinal glomus (type 2) SCAVMs with previous hemorrhage,<sup>8</sup> and lesions with initial hemorrhage also had a greater annual rate of recurrent hemorrhage (5.6%) compared with nonhemorrhagic lesions (0.4%) in spinal cord AVE.<sup>15</sup> Our series showed an higher incidence of hemorrhage: 58% as the initial symptom and 66% before treatment. In the literature, initial hemorrhage was encountered in 70% of pediatric and 27%–45% of adult patients with

**Table 2: Univariate freedom from recurrent hemorrhage of SCAVMs<sup>a</sup>**

Variables	Total (n = 80)	Recurrent Hemorrhage		Unadjusted P Value
		(+) (n = 35)	(-) (n = 45)	
Baseline characteristics				
Median age (yr) (IQR)	20 (10–32)	18 (8–25)	21 (15–38)	
Pediatric	30 (38)	16 (46)	14 (31)	.87
Male	31 (39)	12 (34)	19 (42)	.73
Endovascular embolization <sup>b</sup>	41 (51)	1 (2.9)	40 (89)	<.0001
Radiologic characteristics				
Subclassification				.51
SCAVM	63 (79)	31 (89)	32 (71)	
SCAVF, single hole	7 (8.8)	1 (2.9)	6 (13)	
SCAVF, multiple holes	10 (13)	4 (11)	6 (13)	
SCAVM level				.92
Cranial-cervical	2 (2.5)	1 (2.9)	1 (2.2)	
Cervical	33 (41)	16 (46)	17 (39)	
Cervical-thoracic	1 (1.3)	0	1 (2.2)	
Thoracic	31 (39)	13 (37)	18 (40)	
Thoracic-lumbar	9 (11)	4 (11)	5 (11)	
Lumbar	4 (5.0)	1 (2.9)	3 (6.7)	
Associated aneurysm <sup>b</sup>	56 (70)	31 (89)	25 (56)	.049
Venous thrombosis <sup>b</sup>	7 (8.8)	1 (2.9)	6 (13)	.19
Venous stricture	2 (2.5)	0	2 (4.4)	.21
Venous ectasia	16 (20)	7 (20)	9 (20)	.24
Venous hypertension	16 (20)	7 (20)	9 (20)	.66

Note:—SCAVF indicates spinal cord AVF; IQR, interquartile range 25th–75th percentile.

<sup>a</sup> Data are expressed as number of lesions (%), unless otherwise indicated.

<sup>b</sup> Variables related to the recurrent hemorrhage by log-rank test ( $P < .20$ ).

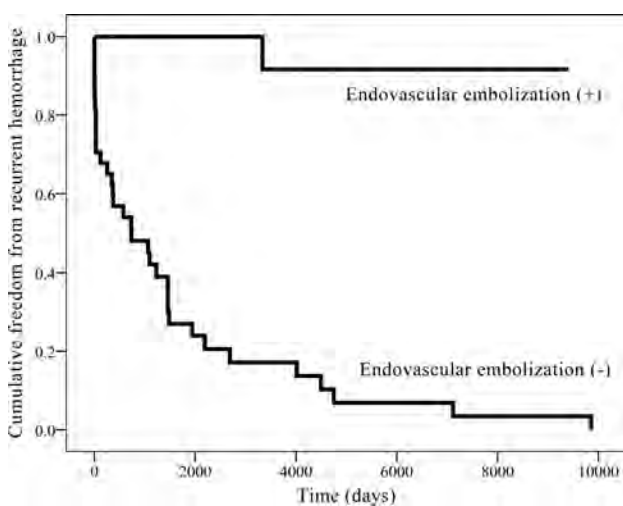


**FIG 2.** Kaplan-Meier plot of cumulative freedom from the progression by endovascular embolization.

**Table 3: Multivariate analyses using the Cox proportional hazards model for recurrent hemorrhage from SCAVMs**

Variable	Adjusted		Multivariable Adjusted P Value
	HR	95% CI	
Endovascular treatment <sup>a</sup>	0.027	0.0040–0.19	<.0001
Associated aneurysm <sup>a</sup>	3.4	1.2–11	.044
Venous thrombosis	0.61	0.082–4.5	.63

Note:—HR indicates hazard ratio.

<sup>a</sup> Variables related to recurrent hemorrhage.

SCAVMs, 20%–37% of pediatric and adult patients with AVF, and 50% of pediatric and adult patients with glomus-type AVMs.<sup>6,8,9,15,16</sup> In the present study, initial hemorrhage was seen in 52% of all patients, 51% of pediatric patients, and 53% of

adults, and this finding supported the results of the previous studies. Previous study also showed that early (within the 12 months after the first hemorrhage) recurrent hemorrhage was seen in 4.8% of pediatric patients and in 3.6% of adults, and late (>1 year after the first hemorrhage) recurrent hemorrhage was seen in 4.8% of pediatric patients and 14% of adults with SCAVM.<sup>6</sup> However, early recurrent hemorrhage was seen in 20% of pediatric patients and in 20% of adults, and late recurrent hemorrhage was seen in 33% of pediatric patients and in 18% of adults in the present study. This result indicated that the rate of recurrent hemorrhage from SCAVMs in both pediatric patients and adults was higher than previously expected.

Recurrent hemorrhages after endovascular embolization were seen in 4%, and all of these were cervical SCAVMs in the previous study.<sup>17</sup> We observed that only 1 of 41 patients (2.4%) had recurrent hemorrhage among those who un-

derwent endovascular treatment, as opposed to 34 of 39 patients (87.2%) without endovascular treatment. Many of those who had rehemorrhage without endovascular treatment were treated by endovascular embolization without further hemorrhage in our series (data not shown). The low incidence of hemorrhage after partial embolization of SCAVMs has also been reported by other authors.<sup>5</sup>

Associated aneurysms of the feeding arteries and nidus are common in SCAVMs.<sup>7</sup> Spinal cord artery and intranidal aneurysms are associated with a high risk for hemorrhage in SCAVMs.<sup>7</sup> Some studies have shown that SCAVM-related arterial aneurysms (distinct from false aneurysms) were associated with initial hemorrhage,<sup>6,8,14,18</sup> though one group of authors showed that arterial aneurysms (distinct from false aneurysms) were not related to hemorrhagic presentation.<sup>16</sup> It was also reported that recurrent hemorrhages were mostly due to reupture of an associated false aneurysm in SCAVMs.<sup>6</sup> The results of the present study showed that associated aneurysms were seen in 89% of patients with recurrent hemorrhage and in 56% of those without recurrent hemorrhage and supported the relationship between associated aneurysms and recurrent hemorrhage in patients with an SCAVM.

Although venous architectural factors (either venous ectasias or venous stricture) were most often associated with initial hemorrhage,<sup>16</sup> they were not related to recurrent hemorrhage in the present study.

### Endovascular Treatment

Embolization of an SCAVM is performed once the endovascular “dissection” of the SCAVM with microcatheter angiography and provocative testing is complete. Analysis of vascular anatomy is most important for safe embolization, but electrophysiologic

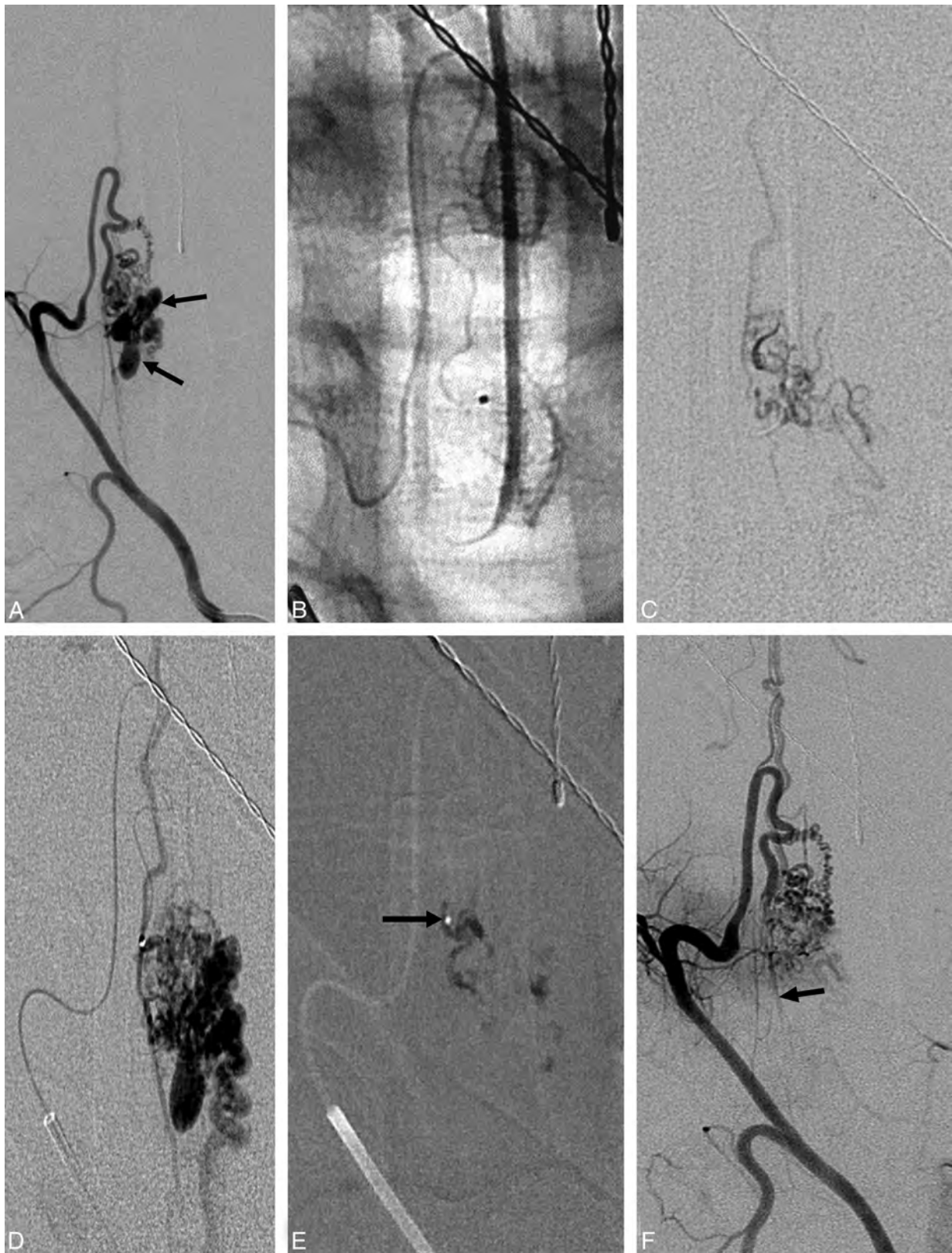


**FIG 3.** A, Posteroanterior view of the right T2 intercostal artery angiogram showing a nidus-type SCAVM supplied by the anterior spinal artery with multiple intranidal aneurysms (*arrows*). B, Nonsubtracted image of the microcatheter inserted into a feeder to the SCAVM. C, Superselective angiogram from the microcatheter inserted into the same feeder as B. No aneurysms are visualized. D, Superselective angiogram from a microcatheter placed in the ASA at the origin of the feeder to the SCAVM. Intranidal aneurysms and the distal anterior spinal artery are visualized. Embolization was performed from this catheter position using NBCA. E, Cast of NBCA. A small amount of NBCA is in the ASA axis near the catheter tip (*arrow*). F, Posteroanterior view of the right T2 intercostal artery after embolization. There is decreased visualization of the nidus without opacification of the intranidal aneurysms. The distal ASA is seen through the collateral (*arrow*).

monitoring with provocative testing provides additional safety, especially when vascular anatomy is modified by previous hemorrhage or treatment.<sup>12</sup> We prefer to use a flow-guided microcatheter for embolization because it is smaller in caliber and less traumatic to the blood vessel compared with a guidewire-assisted microcatheter. We prefer to use NBCA as an embolic agent because of its penetration small vessels and long-lasting occlusion effect. We try to reach the target as close as possible, but if not possible, we modify our technique to accomplish occlusion of the target as demonstrated in the illustrative case. We avoid embolization from a microcatheter wedged in a feeding artery because of the high risk of penetration of the embolic material into the normal territory or draining veins. The details of embolization techniques have been described elsewhere.<sup>12,14</sup> We proved that targeted embolization is beneficial to prevent recurrent hemorrhage even if it is partial treatment. We believe that endovascular embolization is the treatment of choice for most SCAVMs. The only exception is slow-flow, perimedullary AVFs located at the conus or filum terminale. It is important to obtain periodic clinical and radiologic follow-up and early endovascular intervention before significant deterioration occurs to obtain the best possible prognosis for SCAVMs.

### Limitations

First, our study had a retrospective design with inherent limitations leading to potential ascertainment bias. Second, the number of patients was small, spread across many years, during which technical advancements were observed, though this may be unavoidable given that SCAVM is a rare disease. Third is the possibility of random error; overall, 13 univariate comparisons have been performed. Given the  $\alpha$  level of .10, the high number of statistical tests makes it likely that 2 of the associations found may actually be the result of chance. Therefore, the interpretation of the results of univariate analysis was performed carefully, and the conclusion was performed by the multivariate analysis. As noted above, the results of the present study should be further clarified using an independent cohort would be difficult to perform given the rarity of SCAVMs.

### CONCLUSIONS

The low rate of recurrent hemorrhage after endovascular treatment, compared with the high incidence of recurrent hemorrhage in conservative management, proves that endovascular treatment is effective to prevent hemorrhage.

### REFERENCES

1. Veznedaroglu E, Nelson PK, Jabbour PM, et al. **Endovascular treatment of spinal cord arteriovenous malformations.** *Neurosurgery* 2006;59(5 suppl 3):S202–09; discussion S3–13 Medline
2. Kim LJ, Spetzler RF. **Classification and surgical management of spinal arteriovenous lesions: arteriovenous fistulae and arteriovenous malformations.** *Neurosurgery* 2006;59:S195–201; discussion S3–13 CrossRef Medline
3. Zozulya YP, Slin'ko EI, Al-Qashqish II. **Spinal arteriovenous malformations: new classification and surgical treatment.** *Neurosurg Focus* 2006;20:E7 Medline
4. Inagawa S, Yamashita S, Hiramatsu H, et al. **Clinical results after the multidisciplinary treatment of spinal arteriovenous fistulas.** *Jpn J Radiol* 2013;31:455–64 CrossRef Medline
5. Biondi A, Merland JJ, Reizine D, et al. **Embolization with particles in thoracic intramedullary arteriovenous malformations: long-term angiographic and clinical results.** *Radiology* 1990;177:651–58 CrossRef Medline
6. Rodesch G, Hurth M, Alvarez H, et al. **Angio-architecture of spinal cord arteriovenous shunts at presentation: clinical correlations in adults and children.** *Acta Neurochir (Wien)* 2004;146:217–26; discussion 226–27 CrossRef Medline
7. Biondi A, Merland JJ, Hodes JE, et al. **Aneurysms of spinal arteries associated with intramedullary arteriovenous malformations, II: results of AVM endovascular treatment and hemodynamic considerations.** *AJNR Am J Neuroradiol* 1992;13:923–31 Medline
8. Gross BA, Du R. **Spinal glomus (type II) arteriovenous malformations: a pooled analysis of hemorrhage risk and results of intervention.** *Neurosurgery* 2013;72:25–32; discussion 32 CrossRef Medline
9. Mourier KL, Gobin YP, George B, et al. **Intradural perimedullary arteriovenous fistulae: results of surgical and endovascular treatment in a series of 35 cases.** *Neurosurgery* 1993;32:885–91; discussion 891 Medline
10. Rosenblum B, Oldfield EH, Doppman JL, et al. **Spinal arteriovenous malformations: a comparison of dural arteriovenous fistulas and intradural AVM's in 81 patients.** *J Neurosurg* 1987;67:795–802 CrossRef Medline
11. von Elm E, Altman DG, Egger M, et al; STROBE Initiative. **The Strengthening the Reporting of Observational Studies in Epidemiology (STROBE) statement: guidelines for reporting observational studies.** *Lancet* 2007;370:1453–57 CrossRef Medline
12. Niimi Y, Sala F, Deletis V, et al. **Neurophysiologic monitoring and pharmacologic provocative testing for embolization of spinal cord arteriovenous malformations.** *AJNR Am J Neuroradiol* 2004;25:1131–38 Medline
13. Lasjaunias P. **A revised concept of the congenital nature of cerebral arteriovenous malformations.** *Interv Neuroradiol* 1997;3:275–81 CrossRef Medline
14. Berenstein A, Lasjaunias P, TerBrugge K. **Spinal arteriovenous malformations.** In: *Surgical Neuroangiography.* Berlin Heidelberg: Springer-Verlag; 2004:737–847
15. Gross BA, Du R. **Spinal pial (type IV) arteriovenous fistulae: a systematic pooled analysis of demographics, hemorrhage risk, and treatment results.** *Neurosurgery* 2013;73:141–51; discussion 151 CrossRef Medline
16. Rodesch G, Hurth M, Alvarez H, et al. **Spinal cord intradural arteriovenous fistulae: anatomic, clinical, and therapeutic considerations in a series of 32 consecutive patients seen between 1981 and 2000 with emphasis on endovascular therapy.** *Neurosurgery* 2005;57:973–83; discussion 973–83 CrossRef Medline
17. Rodesch G, Hurth M, Alvarez H, et al. **Embolization of spinal cord arteriovenous shunts: morphological and clinical follow-up and results—review of 69 consecutive cases.** *Neurosurgery* 2003;53:40–49; discussion 49–50 CrossRef Medline
18. Konan AV, Raymond J, Roy D. **Transarterial embolization of aneurysms associated with spinal cord arteriovenous malformations: report of four cases.** *J Neurosurg* 1999;90(1 suppl):148–54 CrossRef Medline

# Characterization of Craniocervical Artery Dissection by Simultaneous MR Noncontrast Angiography and Intraplaque Hemorrhage Imaging at 3T

Q. Li, J. Wang, H. Chen, X. Gong, N. Ma, K. Gao, L. He, M. Guan, Z. Chen, R. Li, D. Mi, C. Yuan, X. Zhao, and X.H. Zhao



## ABSTRACT

**BACKGROUND AND PURPOSE:** Craniocervical artery dissection is the most common cause of ischemic stroke identified in young adults. For the diagnosis of craniocervical artery dissection, multisequence MR imaging is recommended but is time-consuming. Recently, investigators proposed a simultaneous noncontrast angiography and intraplaque hemorrhage imaging technique allowing simultaneous noncontrast MRA and vessel wall imaging in a single scan. This study sought to investigate the feasibility of 3D simultaneous noncontrast angiography and intraplaque hemorrhage MR imaging in the characterization of craniocervical artery dissection.

**MATERIALS AND METHODS:** Twenty-four symptomatic patients (mean age,  $45.0 \pm 16.1$  years; 21 men) with suspected craniocervical artery dissection were recruited. The 3D simultaneous noncontrast angiography and intraplaque hemorrhage 3D TOF MRA and black-blood imaging sequences were performed on a 3T MR imaging scanner. The agreement between simultaneous noncontrast angiography and intraplaque hemorrhage imaging and multisequence MR imaging in evaluating arterial dissection was determined.

**RESULTS:** Dissection was found to involve 1 artery in 22 patients and 2 arteries in 2 patients. The intramural hematoma and luminal occlusion were detected in 19 (79.2%) and 11 (45.8%) patients, respectively. In measuring stenosis, the Cohen  $\kappa$  value between 3D TOF MRA and simultaneous noncontrast angiography and intraplaque hemorrhage imaging was 0.82 ( $P < .001$ ). All intramural hematomas on multisequence imaging were successfully identified by simultaneous noncontrast angiography and intraplaque hemorrhage imaging.

**CONCLUSIONS:** 3D simultaneous noncontrast angiography and intraplaque hemorrhage imaging showed excellent agreement with multisequence MR imaging in evaluating luminal stenosis and intramural hematoma in patients with craniocervical artery dissection. The simultaneous noncontrast angiography and intraplaque hemorrhage imaging saved nearly 50% of scanning time compared with multisequence MR imaging. Our findings suggest that 3D simultaneous noncontrast angiography and intraplaque hemorrhage imaging might be an alternative, time-efficient diagnostic tool for craniocervical artery dissection.

**ABBREVIATIONS:** CCAD = craniocervical artery dissection; IMH = intramural hematoma; MERGE = Multi-Echo Recombined Gradient Echo; SNAP = simultaneous noncontrast angiography and intraplaque hemorrhage

Craniocervical artery dissection (CCAD) is the most common cause of stroke identified in young and middle-aged adults.<sup>1,2</sup> Pathophysiologically, arterial dissections occur when a tear develops

in  $\geq 1$  layer of the vessel wall, allowing blood to enter the wall and split the layers; this condition is characterized by a cavity or intramural hematoma (IMH).<sup>3</sup> The increased volume of the IMH may narrow or occlude the lumen, and it can also damage the intima and trigger thrombosis. Because this arterial disorder is strongly associated with acute ischemic events,<sup>4,5</sup> it is clinically preferable to diagnose CCAD at the early stages so that clinicians can properly treat and prevent potential neurologic complications.<sup>6</sup>

Received October 30, 2014; accepted after revision February 13, 2015.

From the Departments of Neurology (Q.L., X.G., D.M., X.Z.) and Interventional Neuroradiology (N.M., K.G.), Beijing Tiantan Hospital, Capital Medical University, Beijing, China; Department of Neurology (Q.L.), People's Hospital of Xinjiang Uygur Autonomous Region, Urumqi, China; Clinical Sites Research Program (J.W.), Philips Research North America, Briarcliff Manor, New York; Department of Biomedical Engineering (H.C., L.H., Z.C., R.L., C.Y., X.H.Z.), Center for Biomedical Imaging Research, Tsinghua University School of Medicine, Beijing, China; Department of Radiology (M.G.), Yangzhou First People's Hospital, Yangzhou, China; and Department of Radiology (C.Y.), University of Washington, Seattle, Washington.

This study was supported in part by a grant from the National Natural Science Foundation of China (81271536), a grant from the Beijing Municipal Science and Technology Commission (D111107003111007), and Philips Healthcare.

Drs Xi Hai Zhao and Xingquan Zhao are co-corresponding authors who contributed equally to this study.

Paper previously presented in part at: Annual International Workshop on Magnetic Resonance Angiography, August 20–23, 2013; New York, New York.

Please address correspondence to Xi Hai Zhao, MD, PhD, Center for Biomedical Imaging Research, Tsinghua University School of Medicine, Haidian District, 100084, Beijing, China; e-mail: xihai.zhao@tsinghua.edu.cn; and Xingquan Zhao, MD, PhD, Department of Neurology, Beijing Tiantan Hospital, Capital Medical University, No. 6 Tiantanxili, Dongcheng District, 100050, Beijing, China; e-mail: zxq@vip.163.com

Indicates open access to non-subscribers at [www.ajnr.org](http://www.ajnr.org)

<http://dx.doi.org/10.3174/ajnr.A4348>

Angiographic imaging modalities, such as CTA, MRA, and DSA, have been widely used for the diagnosis of CCAD in clinical settings.<sup>7-9</sup> These approaches can only provide the information of luminal narrowing or occlusion but are unable to directly delineate IMH, which is a key sign of CCAD. Some investigators believe that cranio-cervical arteries with occlusion but without evidence of IMH cannot be diagnosed as dissection unless the dissected wall is completely recanalized.<sup>10</sup> MR vessel wall imaging has been increasingly used for the diagnosis of CCAD due to its capability of directly visualizing IMH in the vessel wall.<sup>11-13</sup> Recently, a multisequence MR imaging protocol, which includes both MRA and MR vessel wall imaging sequences, was recommended for the diagnosis of CCAD.<sup>10</sup> However, this protocol needs independent acquisition of 2 different time-consuming MR imaging sequences.

Most recently, a simultaneous noncontrast angiography and intraplaque hemorrhage (SNAP) MR imaging technique has been proposed for the evaluation of vulnerable carotid atherosclerotic plaques.<sup>14</sup> The major advantage of the 3D SNAP imaging sequence is acquiring noncontrast MRA and vessel wall images simultaneously in a single scan. The vessel wall images derived from the 3D SNAP sequence carry heavy T1-weighting, which is very sensitive to intraplaque hemorrhage or IMH. The other advantages of SNAP imaging include fast scanning, large longitudinal coverage (up to 250 mm), and isotropic high resolution (0.8 mm<sup>3</sup>). Those advantages make SNAP an ideal candidate for quick and reliable identification of dissection, particularly for tortuous cranio-cervical arteries with longer lesions.

We hypothesized that the 3D SNAP MR imaging technique is capable of characterizing CCAD by providing both luminal and vessel wall information simultaneously. In this study, we sought to evaluate the feasibility of 3D SNAP MR imaging in the diagnosis of CCAD.

## MATERIALS AND METHODS

### Participants

Patients with recent ischemic cerebrovascular symptoms (within 2 weeks) and with suspected cranio-cervical artery dissection were prospectively and consecutively recruited in this study. The inclusion criteria were the following: 1) recent ischemic symptoms and/or neck pain and/or headache; 2) MR angiography revealing stenosis with a string sign or total occlusion or a double lumen or luminal dilation (pseudoaneurysm).<sup>15</sup> The exclusion criteria were as follows: 1) subjects with evidence of cardiogenic ischemic stroke, 2) subjects with evidence of cerebrovascular atherosclerotic disease according to traditional imaging examinations, and 3) subjects with contraindications to MR imaging. The clinical characteristics, including age, sex, hypertension, diabetes, smoking, and hyperlipidemia, were collected. The study protocol was approved by the local institutional review board before the initiation of this study, and written consent forms were obtained from all subjects.

### MR Imaging

All subjects underwent MR imaging on a 3T Achieva TX scanner (Philips Healthcare, Best, the Netherlands) with a custom-designed 36-channel neurovascular coil.<sup>16</sup> The multisequence MR imaging, including 3D TOF MRA and 3D Multi-Echo Recombined Gradient Echo (MERGE; GE Healthcare, Milwaukee, Wis-

consin), was performed with the following parameters: 3D TOF MRA, turbo field echo; TR/TE, 25/3.5 ms; flip angle, 20°; FOV, 180 × 180 × 84 mm<sup>3</sup> for intracranial arteries and 130 × 168 × 140 mm<sup>3</sup> for carotid arteries; voxel size, 0.3 × 0.3 × 0.7 mm<sup>3</sup> for intracranial arteries and 0.6 × 0.6 × 0.9 mm<sup>3</sup> for carotid arteries; total scanning time, 9 minutes; 3D MERGE, turbo field echo; TR/TE, 9.2/4.3 ms; flip angle, 6°; FOV, 250 × 160 × 40 mm<sup>3</sup>; scanning time, 4 minutes 6 seconds. In this study, the presence of IMH was determined by 3D MERGE images when lesions appeared hyperintense because the imaging sequence MERGE has T1 contrast-weighting and has the potential to identify intraplaque hemorrhage.<sup>17</sup> In contrast, the 3D SNAP imaging sequence was acquired with the following parameters: 3D SNAP, turbo field echo sequence; TR/TE, 10/4.8 ms; flip angle, 11°/5°; FOV, 250 × 160 × 32 mm<sup>3</sup>; voxel size, 0.8 × 0.8 × 0.8 mm<sup>3</sup>; scanning time, 6 minutes 45 seconds. The 3D SNAP and MERGE images were acquired in the coronal direction, and 3D TOF MRA images were acquired in the axial direction. Both extracranial carotid arteries and intracranial arteries were covered on MR imaging.

### Image Interpretation

The 3D TOF MRA, MERGE, and SNAP images were reconstructed by using maximum intensity projection, minimum intensity projection, and MPR at the workstation Extended MR Workspace (Version 2.0.3.3; Philips Healthcare). A color-coded algorithm was used to create 3D maximum intensity projection images from SNAP images for joint display of luminal changes and the components with hyperintense signal in the vessel wall.<sup>14</sup> Blinded to clinical information and SNAP images, 2 reviewers evaluated with consensus the degree of luminal stenosis on 3D TOF MRA images and the presence or absence of IMH, which is defined as hyperintense signal in the vessel wall on 3D MERGE images. The diagnosis of IMH was made when the signal intensity of the vessel wall was 2 times as high as the reference tissue of muscle. The other 2 reviewers measured the luminal stenosis on noncontrast MRA derived from SNAP images and identified the presence or absence of IMH on vessel wall images from SNAP imaging blinded to clinical information and 3D TOF MRA and MERGE image findings. Luminal stenosis was measured by using the NASCET method.<sup>18</sup> All observers were neuroradiologists and had >3 years' experience in cerebrovascular imaging. The luminal stenosis was divided into the following categories: mild stenosis (<50%), moderate stenosis (50%–70%), severe stenosis (70%–99%), and occlusion (100%). The presence or absence of pseudoaneurysm, double lumen and intimal flaps, and lesion length was also assessed.

### Statistical Analysis

The continuous variables were described as mean ± SD, and categorical ones were presented as absolute frequencies or percentages. The Cohen  $\kappa$  was used for evaluating the agreement between 3D TOF MRA and SNAP imaging in measuring luminal stenosis. The agreement between 3D SNAP and 3D MERGE in the identification of IMH, pseudoaneurysm, intimal flaps, and double lumen was also determined. A *P* value of <.05 was statistically significant. All statistical analyses were conducted in SPSS 19.0 (IBM, Armonk, New York).

## RESULTS

In total, 24 patients (mean age, 45.0 ± 16.1 years; 21 men) were recruited for this study between June 2012 and September 2014. Of the 24 patients, 4 (16.7%) presented with headache, 3 (12.5%) presented with neck pain, 20 (83.3%) had ischemic stroke, and 4 (16.7%) had TIA. All patients denied blunt traumatic injury to the head and neck. The clinical characteristics are summarized in Table 1.

### Characteristics on Multisequence 3D MR Imaging

The characteristics of each subject on multisequence MR images are shown in Table 2. Twenty-two patients developed dissection in 1 artery, and 2 patients had dissection in 2 arteries. The dissection involvement in different vascular beds was as follows: 3

(12.5%) in the common carotid artery, 8 (33.3%) in the C1 segment of the internal carotid arteries, 3 (12.5%) in the middle cerebral artery, 6 (25%) in the basilar artery, and 6 (25%) in the vertebral artery. IMHs were detected in 19 (79.2%) patients. In arteries with dissection, we found no luminal changes (stenosis or dilation) in 3 (12.5%) patients, mild stenosis in 2 (8.3%) patients, moderate stenosis in 3 (12.5%) patients, severe stenosis in 3 (12.5%) patients, and occlusion in 11 (45.8%) patients. The pattern of pseudoaneurysm and intimal flaps and double lumen was observed in 2 (8.3%) and 3 (16.7%) patients, respectively.

### Agreement between 3D SNAP and Multisequence 3D MR Imaging

In measuring luminal stenosis of diseased arteries, the Cohen  $\kappa$  value between 3D TOF MRA and SNAP imaging was 0.82 ( $P < .001$ ). Figure 1 demonstrates mild stenosis in the basilar artery on the MRA image derived from SNAP imaging (Fig 1A), corresponding to the TOF MRA image (Fig 1B), while the hyperintense signal on the SNAP vessel wall image (Fig 1C) indicates IMH. One patient with mild stenosis on 3D TOF MRA was classified as having moderate stenosis by SNAP imaging, and 2 patients with severe stenosis on 3D TOF MRA were diagnosed as having occlusion. All IMHs on multisequence imaging were successfully identified by SNAP imaging. IMH appeared hyperintense on the 3D SNAP image, corresponding to the 3D MERGE images (Fig 2). In addition, the characteristics of pseudoaneurysm, intimal flaps, and double lumen on multisequence imaging were also accurately determined by SNAP imaging (Fig 3). Figure 4 is an example of the excellent joint visualization of luminal changes and IMH in the vessel wall on SNAP images after color-coded reconstruction.

**Table 1: Clinical characteristics of study population**

Characteristics	Mean or No. (%)	Range (if Applicable)
Age (yr)	45.0 ± 16.1	14–70
Male sex	21 (87.5)	
Weight (kg)	75.1 ± 8.5	60–90
Height (cm)	171.2 ± 5.5	160–183
Smoking	10 (41.7)	
Hypertension	13 (54.2)	
Diabetes	6 (25)	
High-density lipoprotein (mmol/L)	1.0 ± 0.2	0.5–1.8
Low-density lipoprotein (mmol/L)	2.3 ± 0.8	1.0–5.7
Total cholesterol (mmol/L)	4.0 ± 1.1	2.2–7.8
Triglycerides (mmol/L)	1.5 ± 0.7	0.6–3.0
Headache	4 (16.7)	
Neck pain	3 (12.5)	
Ischemic stroke	20 (83.3)	
Transient ischemic attack	4 (16.7)	

**Table 2: Characteristics of 24 patients with CCAD on multisequence MR imaging**

Patient No.	Sex/Age (yr)	Location	Length (mm)	Category of Stenosis <sup>a</sup>	Presence or Absence		
					IMH	Pseudo-aneurysm	Intimal Flaps and Double Lumen
1	M/65	BA	16.7	Moderate	+	–	–
2	M/24	MCA	8.1	Occlusion	+	–	–
3	M/14	MCA	6.0	Mild	+	–	–
4	M/53	ICA (C1)	35.8	No stenosis	–	+	+
5	M/20	BA	12.7	No stenosis	–	–	+
6	M/40	ICA (C1)	70.2	Occlusion	+	–	–
7	M/62	BA and VA	44.1	Occlusion	+	–	–
8	M/59	BA	22.2	No stenosis	–	+	–
9	M/36	MCA	10.7	No stenosis	–	–	+
10	F/18	CCA	23.3	Occlusion	+	–	–
11	M/34	VA	10.1	Moderate	–	–	–
12	F/38	ICA (C1)	42.4	Severe	+	–	–
13	F/66	CCA	44.8	No stenosis	+	–	–
14	M/43	VA	7.5	Occlusion	+	–	–
15	M/62	ICA (C1)	40	Severe	+	–	–
16	M/68	CCA	37.1	Occlusion	+	–	–
17	M/42	VA	24.8	Occlusion	+	–	–
18	M/35	ICA (C1)	63.4	Occlusion	+	–	–
19	M/51	BA and VA	50.8	Mild	+	–	–
20	M/69	ICA (C1)	57	Occlusion	+	–	–
21	M/56	ICA (C1)	66.4	Severe	+	–	–
22	M/40	ICA (C1)	13.6	Occlusion	+	–	–
23	M/41	VA	42.7	Occlusion	+	–	–
24	M/43	BA	11.6	Moderate	+	–	+

**Note:**—BA indicates basilar artery; VA, vertebral artery; CCA, common carotid artery; +, positive; –, negative.

<sup>a</sup> Mild stenosis, 1%–49%; moderate stenosis, 50%–69%; severe stenosis, 70%–99%; occlusion, 100%.

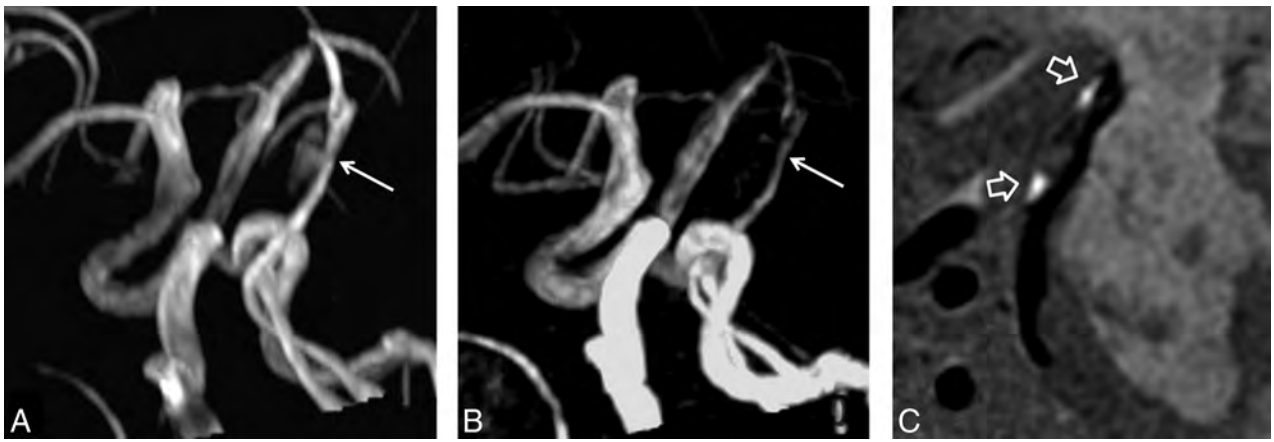


**FIG 1.** Excellent agreement between SNAP imaging and TOF MRA in measuring stenosis. Mild stenosis in the basilar artery is determined by MRA images derived from SNAP imaging (A), which corresponds to the TOF MRA image (B). The hyperintense signal on the SNAP vessel wall image (C) indicates intramural hematoma.

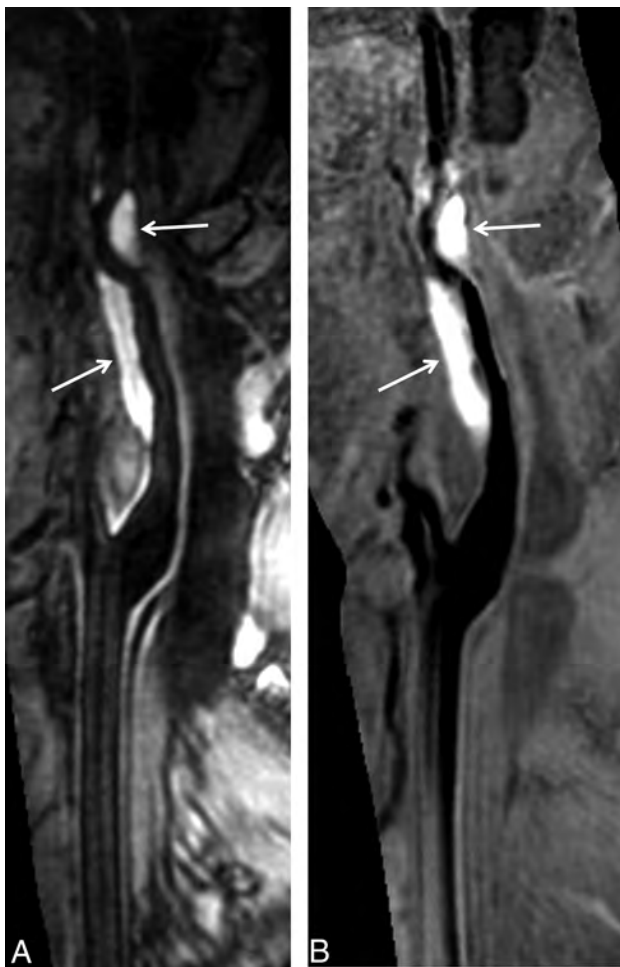


**FIG 2.** SNAP imaging depicts intramural hematoma. The intramural hematoma in the internal carotid artery appears hyperintense on both 3D MERGE (A, white arrows) and SNAP images (B, white arrows).

## DISCUSSION

This study investigated the feasibility of 3D SNAP imaging in characterizing CCAD. We found that 3D SNAP imaging showed excellent agreement with multisequence 3D MR imaging in

measuring luminal stenosis and identification of IMH. In addition, 20.8% (5/24) of patients developed no or mild stenosis and 79.2% (19/24) of patients had IMH, indicating the importance of delineating wall changes by vessel wall imaging in the diagnosis of dissection. Because SNAP imaging provides non-contrast MRA and vessel wall images simultaneously with large longitudinal coverage and much shorter scanning time, it might be an alternative, time-efficient diagnostic tool for characterization of CCAD compared with multisequence 3D MR imaging.

We found that noncontrast MRA images derived from SNAP imaging showed excellent agreement with 3D TOF MRA in evaluating the luminal stenosis in patients with craniocervical artery dissection. Our findings are consistent with those in previous studies. Wang et al<sup>14</sup> demonstrated that there was significant correlation between SNAP imaging and TOF MRA in the quantification of the lumen area of carotid arteries (intraclass correlation coefficient = 0.96; 95% CI, 0.94–0.97). Previous study<sup>14</sup> has also shown that the SNAP image will generate a smaller lumen size compared with TOF MRA when the lumen area is <20 mm<sup>2</sup>, indicating that it may overestimate the degree of stenosis at the arterial segment with a naturally small lumen size or severe luminal narrowing. Similarly, the luminal stenosis measured by SNAP images was overestimated compared with 3D TOF MRA in 3 arteries. In addition, the SNAP technique does not require contrast injection, so it can be used in patients with poor intravenous access or contraindications to gadolinium contrast administration (eg, pregnancy or renal failure). Our results indicate that noncontrast MRA derived from SNAP imaging might be an alternative approach for assessing the luminal changes in arterial dissection.

All the IMHs of this study population were successfully detected by 3D SNAP imaging. The IMH exhibited hyperintense signals on SNAP images, indicating the component with a short T1. It has been shown that the SNAP imaging sequence increased the contrast between hemorrhage and the vessel wall by another 35%, which allows more detection of carotid intraplaque hemorrhage compared with the widely used 3D magnetization prepared rapid acquisition of gradient echo sequence.<sup>14</sup> In previous studies,

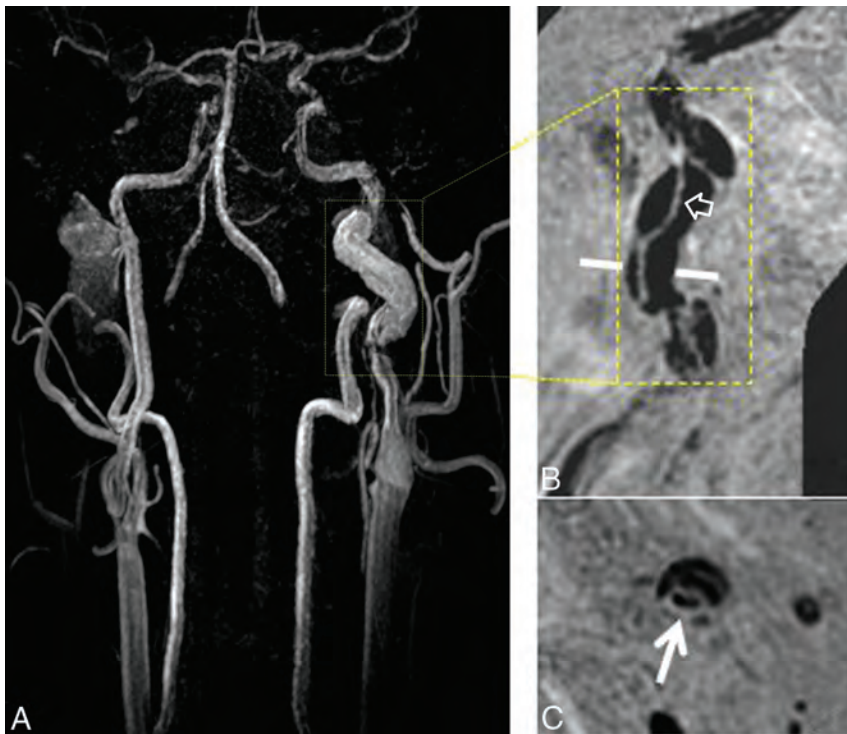


**FIG 3.** SNAP imaging delineates the intimal flaps. The SNAP MRA image (A) shows a dilated lumen (pseudoaneurysm) in the internal carotid artery. The intimal flaps (*hollow arrow*) and double lumen (*white arrow*) are noted on vessel wall images derived from SNAP imaging in the coronal (B) and axial (C) views after MPR reconstruction. The white line on the coronal view indicates the location of the axial view acquisition.

the IMH was evaluated by 2D T1-weighted MR imaging with fat saturation.<sup>11-13</sup> However, acquisition of 2D T1-weighted images is time-consuming and has limited longitudinal coverage. Recently, the 3D black-blood T1-weighted imaging technique has been used to detect IMH in patients with arterial dissection.<sup>19-21</sup> Taking advantage of large coverage, black-blood effect, and high spatial resolution, 3D black-blood imaging sequences seem to be a substitute for 2D imaging techniques. Similar to the 3D T1-weighted imaging sequences, 3D SNAP imaging techniques enable fast and high-resolution imaging with large longitudinal coverage of up to 250 mm. Benefiting from the large coverage of SNAP imaging, the extent of IMHs, particularly those involving multiple vascular beds, can be delineated.

In the present study, a substantial number of patients only had intimal flaps and double lumen without evidence of luminal stenosis and IMH. The intimal flaps and double lumen were

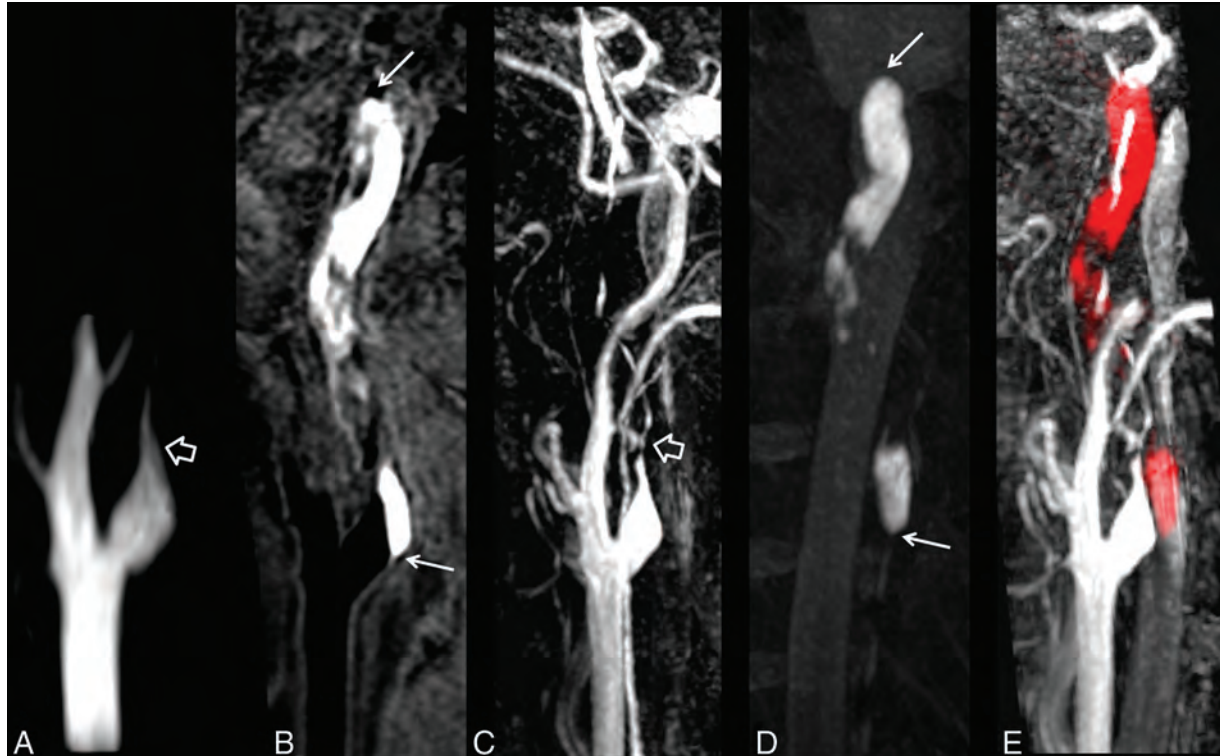


**FIG 4.** The luminal narrowing and intramural hematoma are jointly visualized in a single SNAP image. Total occlusion in the internal carotid artery is demonstrated by TOF MRA (A, *hollow arrow*) and SNAP MRA (C, *hollow arrow*). A vessel wall image (B) derived from SNAP imaging shows a hyperintense lesion in the vessel wall (*white arrows*), indicating intramural hematoma. The intramural hematoma is well-depicted by maximum intensity projection of SNAP images (D). The MRA and vessel wall images derived from SNAP imaging are naturally registered to jointly visualize luminal narrowing and intramural hematoma in red (E) after color-coded processing.

successfully depicted on the vessel wall images derived from SNAP imaging in this study. Similar to luminal narrowing and IMH, these characteristics are important evidence for the diagnosis of dissection. It has been shown that these patterns exist when patients developed complete recanalization after dissection, but they were only seen in approximately 10% of cases.<sup>22</sup> Our findings suggest that SNAP imaging might be a useful tool for comprehensive evaluation of CCAD.

For the diagnosis of arterial dissection, SNAP imaging seems to be a time-efficient approach that saves nearly 50% of scanning time compared with the recommended multisequence imaging protocol with 2 separate sequences (MRA and MR vessel wall imaging). This difference is because the 3D SNAP imaging can provide noncontrast MRA and vessel wall images simultaneously in a single scan in a much shorter scanning time. On the other hand, the MRA and vessel wall images generated from SNAP imaging are intrinsically registered by avoiding the misregistration between images acquired from 2 independent sequences. SNAP imaging enables joint visualization of the lumen and arterial wall changes at a single image. The assessment of the location of the relationship between the lumen and vessel wall in arteries with dissection might be useful for treatment planning of revascularization. Although SNAP imaging is capable of identifying CCAD comprehensively, multisequence MR imaging techniques might be needed in some complicated cases.

In this study, a custom-designed 36-channel coil was used to acquire intracranial and extracranial vessel wall images simultaneously. Compared with a commercialized neurovascular coil, this coil allows large-coverage MR imaging with a sufficient signal-to-noise ratio due to the dedicated coil elements for extracranial carotid arteries. The design of this 36-channel coil might be desirable for assessment of the arterial dissection, particularly for lesions involving a large extent of vessel wall or multiple vessels (carotid arteries and vertebral arteries) simultaneously.

Our study has several limitations. First, the sample size of this study was small, and all patients were suspected of having dissection. Future studies with a large sample size and a broad spectrum of disease should be conducted. Second, to determine the feasibility of SNAP imaging in the detection of IMH, the 3D MERGE imaging sequence was considered as a reference technique. This may decrease the specificity of identifying IMH because 3D MERGE introduces both T1- and T2-contrast-weighting during imaging. Finally, the signal pattern of IMH on SNAP imaging was obtained at only 1 time point. Previous studies reported that the signal of IMH will change with time on MR vessel wall imaging.<sup>13,22</sup> To evaluate the usefulness of SNAP imaging in the characterization of CCAD, further prospective studies with larger sample sizes are warranted.

## CONCLUSIONS

We found 3D SNAP imaging to have excellent agreement with multisequence MR imaging in the assessment of luminal stenosis and intramural hematoma in patients with CCAD. Our findings

suggest that benefiting from fast imaging with large longitudinal coverage, 3D SNAP imaging might be an alternative, time-efficient diagnostic tool for CCAD compared with multisequence MR imaging.

Disclosures: Jinnan Wang—UNRELATED: Employment: Philips Research North America, Comments: full-time employee; Huijun Chen—RELATED: Grant: National Natural Science Foundation of China (research grants); UNRELATED: Philips Healthcare (research grants). \* Chun Yuan—RELATED: Grant: Philips Healthcare, \* National Institutes of Health, \* UNRELATED: Consultancy: Philips Healthcare, Comments: I am a member of the Radiology Medical Advisory Network of Philips Healthcare; Patents (planned, pending or issued): A patent was filed for the imaging technique used in this study. \* \*Money paid to the institution.

## REFERENCES

1. Leys D, Bandu L, Hénon H, et al. **Clinical outcome in 287 consecutive young adults (15 to 45 years) with ischemic stroke.** *Neurology* 2002;59:26–33
2. Ducrocq X, Lacour JC, Debouverie M, et al. **Cerebral ischemic accidents in young subjects: a prospective study of 296 patients aged 16 to 45 years.** *Rev Neurol* 1999;155:575–82
3. Schievink WI. **Spontaneous dissection of the carotid and vertebral arteries.** *N Engl J Med* 2001;344:898–906
4. Benninger DH, Georgiadis D, Kremer C, et al. **Mechanism of ischemic infarct in spontaneous carotid dissection.** *Stroke* 2004;35:482–85
5. Dziewas R, Konrad C, Dräger B, et al. **Cervical artery dissection—clinical features, risk factors, therapy and outcome in 126 patients.** *J Neurol* 2003;250:1179–84
6. Biousse V, D'Anglejan-Chatillon J, Touboul PJ, et al. **Time course of symptoms in extracranial carotid artery dissections: a series of 80 patients.** *Stroke* 1995;26:235–39
7. Sturzenegger M, Mattle HP, Rivoir A, et al. **Ultrasound findings in carotid artery dissection: analysis of 43 patients.** *Neurology* 1995;45:691–98
8. Leclerc X, Godefroy O, Salhi A, et al. **Helical CT for the diagnosis of extracranial internal carotid artery dissection.** *Stroke* 1996;27:461–66
9. Lévy C, Laissy JP, Raveau V, et al. **Carotid and vertebral artery dissections: three-dimensional time-of-flight MR angiography and MR imaging versus conventional angiography.** *Radiology* 1994;190:97–103
10. Debette S, Leys D. **Cervical-artery dissections: predisposing factors, diagnosis, and outcome.** *Lancet Neurol* 2009;8:668–78
11. Ozdoba C, Sturzenegger M, Schroth G. **Internal carotid artery dissection: MR imaging features and clinical-radiologic correlation.** *Radiology* 1996;199:191–98
12. Rodallec MH, Marteau V, Gerber S, et al. **Cranio-cervical arterial dissection: spectrum of imaging findings and differential diagnosis.** *Radiographics* 2008;28:1711–28
13. Goldberg HI, Grossman RI, Gomori JM, et al. **Cervical internal carotid artery dissecting hemorrhage: diagnosis using MR.** *Radiology* 1986;158:157–61
14. Wang J, Börner P, Zhao H, et al. **Simultaneous noncontrast angiography and intraplaque hemorrhage (SNAP) imaging for carotid atherosclerotic disease evaluation.** *Magn Reson Med* 2013;69:337–45
15. Patel RR, Adam R, Maldjian C, et al. **Cervical carotid artery dissection: current review of diagnosis and treatment.** *Cardiol Rev* 2012;20:145–52
16. Wang X, Li R, Hayes C, et al. **A new designed 36-channel neurovascular coil at 3T.** In: *Proceedings of the Annual Meeting of the International Society of Magnetic Resonance in Medicine*, Melbourne, Australia. May 5–11, 2012;21:2787

17. Balu N, Yarnykh VL, Chu B, et al. **Carotid plaque assessment using fast 3D isotropic resolution black-blood MRI.** *Magn Reson Med* 2011;65:627–37
18. North American Symptomatic Carotid Endarterectomy Trial Collaborators. **Beneficial effect of carotid endarterectomy in symptomatic patients with high-grade carotid stenosis.** *N Engl J Med* 1991;325:445–53
19. Cuvinciuc V, Viallon M, Momjian-Mayor I, et al. **3D fat-saturated T1 SPACE sequence for the diagnosis of cervical artery dissection.** *Neuroradiology* 2013;55:595–602
20. Edjlali M, Roca P, Rabrait C, et al. **3D fast spin-echo T1 black-blood imaging for the diagnosis of cervical artery dissection.** *AJNR Am J Neuroradiol* 2013;34:E103–06
21. Takano K, Yamashita S, Takemoto K, et al. **MRI of intracranial vertebral artery dissection: evaluation of intramural haematoma using a black blood, variable-flip-angle 3D turbo spin-echo sequence.** *Neuroradiology* 2013;55:845–51
22. Flis CM, Jager HR, Sidhu PS. **Carotid and vertebral artery dissections: clinical aspects, imaging features and endovascular treatment.** *Eur Radiol* 2007;17:820–34

# Accuracy of Preoperative Imaging in Detecting Nodal Extracapsular Spread in Oral Cavity Squamous Cell Carcinoma

A.H. Aiken, S. Poliashenko, J.J. Beitler, A.Y. Chen, K.L. Bagnon, A.S. Corey, K.R. Magliocca, and  P.A. Hudgins



## ABSTRACT

**BACKGROUND AND PURPOSE:** The increasing impact of diagnosing extracapsular spread by using imaging, especially in patients with oropharyngeal squamous cell carcinoma, highlights the need to rigorously evaluate the diagnostic accuracy of imaging. Previous analysis suggested 62.5%–80.9% sensitivity and 60%–72.7% specificity. Our goals were to evaluate the accuracy of imaging in diagnosing extracapsular spread in a cohort of patients with oral cavity squamous cell carcinoma (pathologic confirmation of extracapsular spread routinely available), as a proxy for oropharyngeal squamous cell carcinoma, and to independently assess the reliability of imaging features (radiographic lymph node necrosis, irregular borders/stranding, gross invasion, and/or node size) in predicting pathologically proven extracapsular spread.

**MATERIALS AND METHODS:** One hundred eleven consecutive patients with untreated oral cavity squamous cell carcinoma and available preoperative imaging and subsequent lymph node dissection were studied. Two neuroradiologists blinded to pathologically proven extracapsular spread status and previous radiology reports independently reviewed all images to evaluate the largest suspicious lymph node along the expected drainage pathway. Radiologic results were correlated with pathologic results from the neck dissections.

**RESULTS:** Of 111 patients, 29 had radiographically determined extracapsular spread. Pathologic examination revealed that 28 of 111 (25%) had pathologically proven extracapsular spread. Imaging sensitivity and specificity for extracapsular spread were 68% and 88%, respectively. Radiographs were positive for lymph node necrosis in 84% of the patients in the pathology-proven extracapsular spread group and negative in only 7% of those in the pathologically proven extracapsular spread–negative group. On logistic regression analysis, necrosis ( $P = .001$ ), irregular borders ( $P = .055$ ), and gross invasion ( $P = .068$ ) were independently correlated with pathologically proven extracapsular spread.

**CONCLUSIONS:** Although the specificity of cross-sectional imaging for extracapsular spread was high, the sensitivity was low. Combined logistic regression analysis found that the presence of necrosis was the best radiologic predictor of pathologically proven extracapsular spread, and irregular borders and gross invasion were nearly independently significant.

**ABBREVIATIONS:** ECS = extracapsular spread; OCSCC = oral cavity squamous cell carcinoma; OPSCC = oropharyngeal squamous cell carcinoma; pECS = pathologically proven extracapsular spread

The presence of pathologically proven extracapsular spread (pECS) in squamous cell carcinoma of the head and neck portends a poor prognosis with decreased 5-year overall survival rates and increased rates of locoregional recurrences and distant

metastases.<sup>1,2</sup> In a large 10-year multicohort study, Shaw et al<sup>3</sup> found that extracapsular spread (ECS) in patients with oral cavity squamous cell carcinoma (OCSCC) doubled the local recurrence rate, doubled the distant metastasis rate, and tripled the incidence of regional recurrence. However, recent literature has debated whether ECS affects disease-specific survival in patients with p16-positive or p16-negative oropharyngeal squamous cell carcinoma (OPSCC).<sup>4</sup> Radiographically determined ECS has been shown to be an independent prognosticator for poor distant control and survival,<sup>5</sup> but although CT and MR imaging may suggest the radiologically visible presence of macroscopic ECS, the criterion standard for diagnosing ECS in patients with head and neck cancer has been pathologic evaluation of a neck-dissection specimen. Distinct from OCSCC, oropharyngeal cancers (eg, OPSCC)

Received March 3, 2014; accepted after revision March 3, 2015.

From the Departments of Radiology and Imaging Sciences (J.J.B., A.H.A., A.S.C., K.L.B., P.A.H.), Otolaryngology Head and Neck Surgery (A.Y.C., J.J.B.), Radiation Oncology (J.J.B.), Hematology and Medical Oncology, and Pathology (K.R.M.), Emory University School of Medicine (S.P.), Atlanta, Georgia.

Paper previously presented at: Annual Meeting of the American Society of Neuro-radiology, May 18, 2013, 2013; San Diego, California.

Please address correspondence to A.H. Aiken, MD, Emory University Hospital, 1364 Clifton Rd NE, Atlanta GA 30322; e-mail: ashley.aiken@emoryhealthcare.org

<http://dx.doi.org/10.3174/ajnr.A4372>

are routinely and successfully treated with radiation therapy alone for early disease and chemoradiation for more advanced disease.<sup>6</sup> Technical advances have resulted in a renewed interest in transoral robotic surgery for the treatment of early disease.<sup>7</sup> Some patients with surgically treated early OPSCC are spared the need for adjuvant radiation. Conversely, because a combination of European Organisation for Research and Treatment of Cancer and Radiation Therapy Oncology Group studies showed survival advantages when chemotherapy was added to routine postoperative radiation in patients who had either unsatisfactory margins or ECS,<sup>8</sup> many clinicians would not offer surgery for patients with oropharyngeal cancer if they knew preoperatively that pECS was present. Therefore, to spare the patients trimodality treatment, especially in the human papillomavirus era, patients with oropharyngeal cancer with ECS on pretherapy imaging are generally treated with concurrent chemoradiation, and surgery is reserved for possible salvage. In light of these considerations, radiographically determined ECS is crucial for the upfront management of OPSCC.

The crucial role of preoperative imaging in this particular scenario prompted our investigation of the accuracy of imaging for diagnosing ECS. Although our clinical question arose from patients with OPSCC, we used patients with OCSCC in this study as a proxy cohort, because elective neck dissection provides a pECS status for nearly all patients.

The sensitivity and specificity for radiographically determined ECS have been reported to range from 62.5% to 80.9% and from 60% to 93%, respectively.<sup>9–14</sup> A small study in 17 patients by Zoumalan et al<sup>15</sup> found that lymph node necrosis was a good predictor of ECS. Classical imaging features of ECS include spiculated or irregular node borders, loss of the adjacent fat or muscle planes, and frank infiltration into structures adjacent to the lymph node.<sup>16</sup> Our study objectives were to evaluate the accuracy of cross-sectional contrast-enhanced CT imaging for diagnosing ECS in patients with OCSCC (as a proxy for those with OPSCC) and to independently assess the reliability of imaging features (radiographically determined lymph node necrosis, irregular borders/stranding, gross invasion, and/or node size) for predicting pECS.

## MATERIALS AND METHODS

### Inclusion Criteria

After institutional review board approval for this retrospective review, the imaging data warehouse at our institution was queried for previously untreated patients with International Classification of Diseases, Ninth Revision, codes for OCSCC subsites between 2007 and 2012. This search yielded 229 patients. Subsites of OCSCC included in the study were the oral tongue, retromolar trigone, buccal mucosa, and gingival regions. Inclusion criteria were having had 1) a neck dissection at our institution, 2) preoperative contrast-enhanced CT, and 3) pathologic review specifically for ECS.

From the 229 patients identified in this search, 165 who underwent subsequent neck dissection at our institution were included. Fifty-four patients were excluded because preoperative images were not available ( $n = 43$ ), they underwent only MR imaging ( $n = 8$ ), or their CT was performed without contrast

( $n = 3$ ). Therefore, 111 patients with preoperative CT imaging and who had a neck dissection at our institution and pathologic evaluation for ECS were included in this study.

### Pathology Review

The diagnosis of squamous cell carcinoma, pathologically determined lymph node stage, lymph node size, and presence of ECS were recorded from original pathology reports in the electronic medical record. The histologic criterion for extracapsular spread in a metastatic lymph node was defined as carcinoma invading beyond the nodal capsule. The measured extent of carcinoma beyond the lymph node capsule (micro-ECS vs macro-ECS) was not a routine practice during this timeframe. This cohort included a mixture of radiographically determined positive and negative necks and pathologically determined positive and negative necks. All neck dissections for OCSCC in the study time range that met inclusion criteria were included.

### Imaging Methods

Patients underwent imaging on one of several commercially available CT systems with multidetector capability ranging from 8 to 64 channels. Onsite imaging CT studies were performed on a LightSpeed VCT 64-section, Discovery HD 750, Discovery 16-section, or BrightSpeed 16-section scanner (all from GE Healthcare, Milwaukee, Wisconsin) or Somatom Definition 64-slice and Somatom Emotion 16-slice CT scanners (Siemens, Erlangen, Germany). Our split-bolus technique used a total of 110 mL of intravenous iopamidol (Isovue-370; Bracco, Princeton, New Jersey); 55 mL was injected first at a rate of 2.5 mL/s, followed by a 40-second delay, and then another 55 mL was added at the same rate, with a total scan delay of 90 seconds, including a precontrast and postcontrast saline bolus. We acquired contiguous axial images from the skull base through the mediastinum with the following settings: section thickness, 1.25 mm; pitch, 0.984:1; gantry rotation time, 0.7 second; FOV, 25 cm; 120 kVP; and Smart mA with a noise index of 13.78. Reformatted images with 2.5-mm section thicknesses in the axial planes and 3-mm sagittal and coronal reformations were sent to a PACS.

### Image Review

Two Certificate of Added Qualification–certified neuroradiologists with a focus on head and neck imaging (A.H.A. and P.A.H., who have 8 and 29 years of experience, respectively) reviewed all 111 cases. The reviewers were blinded to the original reports, final pathology, and the other reviewer's conclusions. For each case, they recorded a dichotomous interpretation for the following features of the largest suspicious ipsilateral node along the expected drainage pathway: 1) mild perinodal stranding or irregular node borders, 2) necrosis, 3) gross invasion, and 4) overall impression of macroscopic ECS. Evidence of ECS was defined as irregular node borders, fat stranding, and/or invasion of adjacent structures (Fig 1). When there was disagreement between the 2 reviewers, a consensus read without knowledge of pECS status was performed.

In addition to the blinded review, each of the 111 cases was interpreted initially by 1 of 4 Certificate of Added Qualification–certified and dedicated head and neck radiologists in our practice



**FIG 1.** A, A right level IIA lymph node (arrow) in a patient with OCSCC. This rounded low-attenuation node has irregular borders and fat stranding. Imaging prospectively diagnosed ECS, which was confirmed with pathologic examination (true-positive result). B, A right level IIA lymph node (arrow) in a patient with OCSCC. This small 1-cm lymph node shows subtle fat stranding. Imaging prospectively diagnosed ECS, which was confirmed with pathologic examination (true-positive result). C, A right level IIA lymph node (arrows) in a patient with OCSCC. This large necrotic node demonstrates invasion of the adjacent sternocleidomastoid muscle. Imaging prospectively diagnosed ECS, which was confirmed with pathologic examination (true-positive result).

(each with 6, 8, 15, or 29 years' experience). Initial reports included the radiologic staging of lymph nodes, presence of radiographically determined ECS, size of the nodal disease, and lymph node necrosis. Node size was measured in the longest axis in the axial plane and categorized into one of the following groups: 0–1, 1–2, 2–3, or >3 cm.

### Statistical Analysis

A multivariate logistic regression analysis was performed, and the sensitivity, specificity, accuracy, positive predictive value, and negative predictive value were calculated. A Cohen weighted  $k$  statistic was calculated to evaluate interobserver agreement. Observer agreement was categorized as poor (<0.20), fair (0.20–0.39), moderate (0.40–0.59), good (0.60–0.79), or excellent ( $\geq 0.80$ ).

### RESULTS

Our population included 111 patients with OCSCC who underwent primary resection and neck dissection at our institution within a 5-year period.

Interobserver analysis revealed almost perfect interobserver agreement between the readers for overall impression of ECS ( $\kappa = 0.86$ ;  $P < .001$ ) and for stranding/irregular borders around a lymph node ( $\kappa = 0.835$ ;  $P < .001$ ). Radiographically determined ECS was noted in 29 of the 111 cases, and 19 of those 29 were true-positive results. There were 9 false-negative results. Pathologically proven ECS was confirmed in 28 of 111 cases. The readers had only 6 of 111 discrepancies for ECS, with each reader's conclusion being validated pathologically in 3 of 6 cases. Therefore, the readers had the same overall sensitivity and specificity results. For the review, the imaging diagnosis of ECS had a sensitivity of 68%, a specificity of 88%, a positive predictive value of 66%, and a negative predictive value of 89%.

Radiographically determined lymph node necrosis was present in 27 of 111 patients, and 21 of these 27 lymph nodes were truly positive for ECS. Radiographically determined lymph node necrosis, therefore, had a sensitivity of 66% and a specificity of

93% for predicting pECS. Radiographically determined lymph node necrosis was present in 84% of nodes with pathology-proven ECS but only 7% of nodes without ECS (6 of 86). There was a strong association between radiologically determined lymph node necrosis and pECS ( $P < .001$ ) according to the Fisher exact test.

Radiographic evidence of gross invasion of surrounding structures, such as the sternocleidomastoid muscle, was noted in 8 of 111 cases, and pECS was present in all 8 of these cases (specificity, 100%). As expected, the sensitivity of gross invasion was low (34%).

Radiographically determined perinodal stranding had a sensitivity of 63% and a specificity of 89% for predicting ECS, very similar to the overall imaging sensitivity and specificity rates; stranding usually prompts a positive overall impression for radiographically determined ECS.

A logistic regression analysis was performed for each of the reviewers to determine which radiologic factors were most predictive of ECS (Table). Imaging necrosis had the highest classification accuracy (ie, it was the most predictive of pECS [ $P = .001$  for the combined analysis]). Stranding ( $P = .055$ ) and gross invasion ( $P = .068$ ) were also marginally significant. Therefore, all 3 factors were nearly independently significant.

From the original reports, radiographically determined ECS was reported in only 17 cases (compared with 29 cases in the blind review). The original reports' diagnosis of ECS had a sensitivity of 46%, a specificity of 95%, a positive predictive value of 76%, and a negative predictive value of 84%. The interobserver variability between the original report and the blinded review showed good or substantial agreement ( $\kappa = 0.676$ ;  $P < .001$ ).

Two-sample  $t$  tests were performed to compare lymph node size between the pathologically positive and negative ECS groups. Continuous variables for those in the ranges of 0–1, 1–2, 2–3, and >3 cm were evaluated. For all of the groups, the  $P$  value was .20, suggesting that we could not find a significant association between size and ECS, primarily because 100% (4 of 4) of the small-

### Logistic Regression Analysis for individual readers and combined analysis

Reader No. and Parameter	Estimate	Standard Error	z Value	Pr(> z )
1 (A.H.A.)				
(Intercept)	-2.045	0.344	-5.948	<.001
Stranding	1.072	0.741	1.447	.148
Necrosis	1.714	0.78	2.198	.028
Gross invasion	1.553	1.208	1.285	.199
2 (P.A.H.)				
(Intercept)	-2.229	0.370	-6.016	<.001
Stranding	0.875	0.764	1.145	.252
Necrosis	1.902	0.702	2.710	.007
Gross invasion	1.306	0.975	1.339	.180
1 and 2 (A.H.A. and P.A.H. [combined analysis])				
(Intercept)	-2.129	0.251	-8.493	0
Stranding	1.006	0.525	1.917	.055
Necrosis	1.78	0.515	3.457	.001
Gross invasion	1.358	0.744	1.824	.068

Note:—Pr(>|z|) indicates a P value from a z score.

est group of lymph nodes (<1 cm) had ECS. It should be noted that these were false-negative radiographic results. However, the results of an evaluation of the remaining individual groups suggested a trend. The rates of pathologically proven ECS among the other groups was 60% in the 1- to 2-cm group, 83% in the 2- to 3-cm group, and 100% in the >3-cm group.

### DISCUSSION

It became clear during our multidisciplinary tumor boards that our clinicians were increasingly relying on the imaging diagnosis of ECS to make major treatment decisions in patients with OPSCC. Escalating therapy to a multimodal approach involves significant morbidity and thus must be appropriately justified. Specifically, our clinicians were deciding against transoral robotic surgery in patients with preoperative radiographic evidence of ECS to avoid trimodality therapy for the patients. Because our institution did not have an adequate sample size to test the accuracy of imaging in diagnosing ECS in patients with OPSCC, we chose to evaluate its accuracy in a well-defined cohort of patients with OCSCC. Our primary objective was to determine the accuracy of imaging in diagnosing ECS so that our tumor board could best plan the treatment of patients with OPSCC, assuming that it is reasonable to extrapolate results based on OCSCC and apply them to OPSCC.

If treatment decisions are going to potentially be based on imaging detection of ECS, then the accuracy and limitations of imaging results must be taken into account. When we reviewed the literature, we found wide variation in the accuracy of imaging, mixed cohorts, and conflicting data. Furthermore, at least for oropharyngeal cancer, the biology has changed; most of our oropharyngeal cancers are related to human papillomavirus rather than to smoking or drinking alcohol.<sup>17</sup> The cystic appearance of many human papillomavirus 16 positive oropharyngeal node metastases may complicate the radiologic evaluation of necrosis. Another important consideration is whether to err on the side of being overly sensitive or of being overly specific.<sup>18</sup>

Recently, Prabhu et al<sup>19</sup> examined 432 patients undergoing neck dissections for head and neck cancer. The sensitivity and specificity for radiographically determined ECS were reported to be 43% and 97.7%, respectively. The sensitivity was lower and specificity much higher than previously reported. One possibility for the lower sensi-

tivity of radiographically determined ECS in their study may have been the criteria for radiographically positive and negative ECS. When ECS status was not mentioned in the initial radiology report, it was recorded as radiographically negative for ECS. The preoperative images were not blindly reviewed, because the authors' purpose was to assess the predictive value of the original diagnostic interpretation. Because many of the study patients had OCSCC and the radiographic diagnosis of ECS would have been less critical and had little impact on the decision for neck dissection, it may not have always been reported initially by the neuroradiologist, falsely depressing sensitivity. Our study addressed this potential pitfall with a

blinded review for all cases, in addition to the initial report, to validate these preliminary results.

In a second recent study, Chai et al<sup>20</sup> concluded that "radiologic findings suggestive of ECS should not be relied on for treatment planning in squamous cell carcinoma of the head and neck." Chai et al<sup>20</sup> used a 5-point scale for the evaluation of radiographically determined ECS, included a wider range of primary tumors, and had 2 different observers with specificities of 54% and 84%, respectively. Our study aimed to limit a few of these variables by restricting the cohort to a single primary tumor for which surgical resection of the primary and cervical lymphatics is the standard initial treatment and by reporting "yes or no" for radiographically determined ECS on the basis of specific imaging features.

Our study not only tested the accuracy of the imaging diagnosis of ECS and interobserver agreement between 2 reviewers (A.H.A. and P.A.H.) but also examined the interobserver agreement between the original report and the subsequent blinded review looking specifically for ECS. It was not surprising that the reviewers detected a few more cases of ECS at the expense of more false-positive results. In other words, reviewers became more sensitive (67% compared with 46% in the original report) but slightly less specific (88% compared with 95% in the original report). Overall, both the review and the original report had high specificities for ruling in macroscopic ECS. Interobserver agreement between an original report and a subsequent blinded review has not been evaluated often, but it has important implications for practical use. We have shown that in a closed head and neck radiology group with a focus on staging head and neck cancers, interobserver agreement and specificity for ECS are strong. Our clinicians prefer a high specificity before recommending chemoradiation over transoral robotic surgery.

A very careful search for ill-defined node borders is key for identifying subtle ECS on imaging. We found that imaging specificity is high when fat stranding and ill-defined borders are identified. In these cases, the clinicians can rely on radiographically determined ECS to make treatment decisions (Fig 1A). When these specific imaging signs are absent, however, pECS is still present in nearly 50% of the cases, and therefore imaging cannot be used to exclude ECS (Fig 2).



**FIG 2.** A left 1-cm level IB lymph node (arrow) with abnormal FDG uptake and rounded morphology. Although it was interpreted from contrast-enhanced CT as a metastatic node, it was thought to be negative for ECS. This was a false-negative result, because ECS was found in the final pathologic examination.

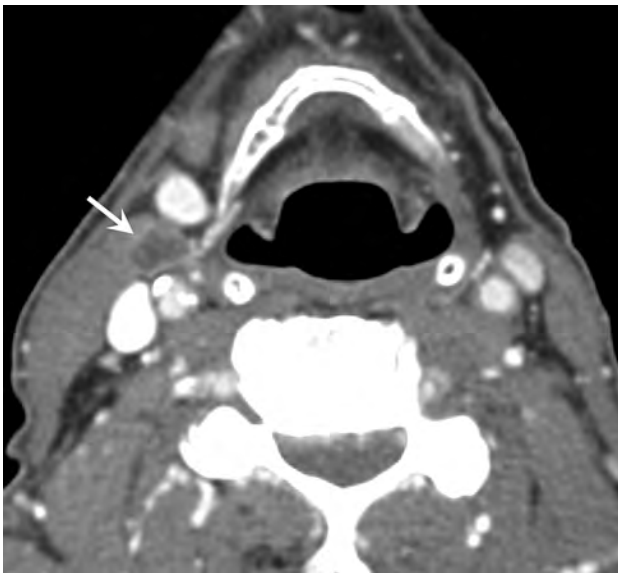


**FIG 3.** A right 1.2-cm level IIA lymph node (arrow) in a patient with OCSCC. Necrosis was reported and ECS was diagnosed from imaging. This was a true-positive result that was confirmed with pathologic examination.

Lymph node necrosis was the most important radiologic factor associated with radiographically determined ECS even when there was no irregularity of borders or stranding (Fig 3). One study reported a strong correlation between ECS and necrosis with 95% sensitivity and 85% specificity.<sup>15</sup> A recent study by Joo et al,<sup>21</sup> which involved PET/CT for the identification of ECS, showed that fluorodeoxyglucose uptake could elevate sensitivity and specificity for the detection of ECS above those of contrast-

enhanced CT or MR imaging alone. The study showed that maximum standardized uptake values were significantly correlated with ECS (standardized uptake value detection cutoff, 2.25 on receiver operating characteristic curve demonstration; sensitivity and specificity, 85% and 88%, respectively).

Limitations of this study include its retrospective nature. We used this cohort of patients with OCSCC to examine radiographic accuracy for diagnosing ECS and to extrapolate the diagnostic test characteristics to make treatment decisions for patients with OPSCC. The pathologic pattern of ECS may differ between these subsites, and therefore results of the imaging accuracy evaluation may have been affected. Second, our finding that lymph node necrosis was significantly correlated with ECS may be less reliable in a population of patients with oropharyngeal cancer because of the distinct pattern of cystic nodes in this population. Finally, the importance of both microscopic and macroscopic pECS was first appreciated in the era when oropharyngeal cancers were largely caused by tobacco and alcohol abuse, and as the virally induced oropharyngeal cancers are better understood, the prognostic effects of ECS may not be confirmed.<sup>4</sup> At this time, however, pretreatment imaging profoundly influences the management of patients with oropharyngeal cancer, and accuracy remains of paramount importance.

## CONCLUSIONS

Recent management trends for OPSCC rely on pretreatment imaging diagnosis of ECS. We used a cohort of patients with OCSCC with pathologically proven or excluded ECS to conclude that though contrast-enhanced CT has high specificity for the detection of ECS, its sensitivity for the detection of ECS remains low. Lymph node necrosis seen on contrast-enhanced CT was significantly correlated with pECS and was the most accurate radiologic criterion of those investigated. Stranding and gross invasion were marginally significant as independent factors correlated with pECS.

Disclosures: Jonathan Beitler—RELATED: Grant: Georgia Cancer Coalition Distinguished Scholar\*; UNRELATED: Employment: Connecticut National Guard; Payment for Lectures (including service on speakers bureaus): ASTRO, Head and Neck Cancer Symposium; Payment for Development of Educational Presentations: Oakstone Medical Publishing (Practical Reviews in Cancer Management). Amanda Corey—UNRELATED: Payment for Lectures (including service on speakers bureaus): Osler Institute, Comments: Did an ear, nose, and throat review course lecture to ear, nose, and throat specialists preparing for board examinations. Patricia Hudgins—UNRELATED: Royalties: Amirsys, Comments: Medical education company. \*Money paid to the institution.

## REFERENCES

1. Kokemueller H, Rana M, Rublack J, et al. **The Hannover experience: surgical treatment of tongue cancer—a clinical retrospective evaluation over a 30 years period.** *Head Neck Oncol* 2011;3:27 CrossRef Medline
2. Jan JC, Hsu WH, Liu SA, et al. **Prognostic factors in patients with buccal squamous cell carcinoma: 10-year experience.** *J Oral Maxillofac Surg* 2011;69:396–404 CrossRef Medline
3. Shaw RJ, Lowe D, Woolgar JA, et al. **Extracapsular spread in oral squamous cell carcinoma.** *Head Neck* 2010;32:714–22 CrossRef Medline
4. Maxwell JH, Ferris RL, Gooding W, et al. **Extracapsular spread in head and neck carcinoma: impact of site and human papillomavirus status.** *Cancer* 2013;119:3302–8 CrossRef Medline
5. Kann BH, Buckstein M, Carpenter TJ, et al. **Radiographic extracapsular**

- extension and treatment outcomes in locally advanced oropharyngeal carcinoma. *Head Neck* 2014;36:1689–94 CrossRef Medline
6. O'Sullivan B, Huang SH, Siu LL, et al. **Deintensification candidate subgroups in human papillomavirus-related oropharyngeal cancer according to minimal risk of distant metastasis.** *J Clin Oncol* 2013; 31:543–50 CrossRef Medline
  7. Adelstein DJ, Ridge JA, Brizel DM, et al. **Transoral resection of pharyngeal cancer: summary of a National Cancer Institute Head and Neck Cancer Steering Committee Clinical Trials Planning Meeting, November 6–7, 2011, Arlington, Virginia.** *Head Neck* 2012;34:1681–703 CrossRef Medline
  8. Bernier J, Cooper JS, Pajak TF, et al. **Defining risk levels in locally advanced head and neck cancers: a comparative analysis of concurrent postoperative radiation plus chemotherapy trials of the EORTC (#22931) and RTOG (# 9501).** *Head Neck* 2005;27:843–50 CrossRef Medline
  9. Steinkamp HJ, Beck A, Werk M, et al. **Extracapsular spread of cervical lymph node metastases: diagnostic value of magnetic resonance imaging** [in German]. *Rofo* 2002;174:50–55 CrossRef Medline
  10. Steinkamp HJ, van der Hoeck E, Böck JC, et al. **The extracapsular spread of cervical lymph node metastases: the diagnostic value of computed tomography** [in German]. *Rofo* 1999;170:457–62 CrossRef Medline
  11. Carvalho P, Baldwin D, Carter R, et al. **Accuracy of CT in detecting squamous carcinoma metastases in cervical lymph nodes.** *Clin Radiol* 1991;44:79–81 CrossRef Medline
  12. Yousem DM, Som PM, Hackney DB, et al. **Central nodal necrosis and extracapsular neoplastic spread in cervical lymph nodes: MR imaging versus CT.** *Radiology* 1992;182:753–59 CrossRef Medline
  13. King AD, Tse GM, Yuen EH, et al. **Comparison of CT and MR imaging for the detection of extranodal neoplastic spread in metastatic neck nodes.** *Eur J Radiol* 2004;52:264–70 CrossRef Medline
  14. Souter MA, Allison RS, Clarkson JH, et al. **Sensitivity and specificity of computed tomography for detection of extranodal spread from metastatic head and neck squamous cell carcinoma.** *J Laryngol Otol* 2009;123:778–82 CrossRef Medline
  15. Zoumalan RA, Kleinberger AJ, Morris LG, et al. **Lymph node central necrosis on computed tomography as predictor of extracapsular spread in metastatic head and neck squamous cell carcinoma: pilot study.** *J Laryngol Otol* 2010;124:1284–88 CrossRef Medline
  16. Saindane AM. **Pitfalls in the staging of cervical lymph node metastasis.** *Neuroimaging Clin N Am* 2013;23:147–66 CrossRef Medline
  17. Ang KK, Harris J, Wheeler R, et al. **Human papillomavirus and survival of patients with oropharyngeal cancer.** *N Engl J Med* 2010;363:24–35 CrossRef Medline
  18. Yokota T, Onitsuka T, Kusafuka K, et al. **Is postoperative adjuvant chemoradiotherapy necessary for high-risk oropharyngeal squamous cell carcinoma?** *Int J Clin Oncol* 2014;19:38–44 CrossRef Medline
  19. Prabhu RS, Magliocca KR, Hanasoge S, et al. **Accuracy of computed tomography for predicting pathologic nodal extracapsular extension in patients with head-and-neck cancer undergoing initial surgical resection.** *Int J Radiat Oncol Biol Phys* 2014;88:122–29 CrossRef Medline
  20. Chai RL, Rath TJ, Johnson JT, et al. **Accuracy of computed tomography in the prediction of extracapsular spread of lymph node metastases in squamous cell carcinoma of the head and neck.** *JAMA Otolaryngol Head Neck Surg* 2013;139:1187–94 CrossRef Medline
  21. Joo YH, Yoo IR, Cho KJ, et al. **Extracapsular spread and FDG PET/CT correlations in oral squamous cell carcinoma.** *Int J Oral Maxillofac Surg* 2013;42:158–63 CrossRef Medline

# Increased Prevalence of Developmental Venous Anomalies in Children with Intracranial Neoplasms

B.V. Jones, L. Linscott, G. Koberlein, T.R. Hummel, and J.L. Leach

## ABSTRACT

**BACKGROUND AND PURPOSE:** Developmental venous anomalies are considered variants of venous development that, in and of themselves, are of little clinical import. A possible association between intrinsic brain tumors and developmental venous anomalies has been suggested, but a rigorous investigation has not been performed. The aim of this study was to assess any association between developmental venous anomalies and intrinsic brain neoplasms.

**MATERIALS AND METHODS:** A radiology report text search of terms used to describe developmental venous anomalies was performed on a study population of 580 patients with primary intracranial neoplasms and on a control population of 580 patients without neoplasms from the same time period. All positive results were reviewed to confirm that the report was describing a developmental venous anomaly, and the imaging examination was reviewed to confirm the diagnosis.

**RESULTS:** Fifty-nine of the 580 subjects with brain tumors (10.17%) had a developmental venous anomaly identified by report and confirmed on review of the imaging. Thirty-one of the 580 controls (5.34%) had a developmental venous anomaly identified by report and confirmed on review of the imaging ( $P = .003$ ). No statistically significant difference was noted in the prevalence of developmental venous anomalies among tumor types. No developmental venous anomaly drained the vascular territory of the tumor, and there was no correlation between the location of the developmental venous anomaly and the location of the neoplasm.

**CONCLUSIONS:** The prevalence of developmental venous anomalies in this pediatric population with intracranial primary neoplasms is significantly greater than in those without neoplasms, suggesting an association that may be related to shared causative factors or susceptibilities to the development of these 2 separate entities.

**ABBREVIATION:** DVA = developmental venous anomaly

Developmental venous anomalies (DVAs) are vascular lesions that consist of a group of venous channels that drain into a common collecting vein, which, in turn, traverses the brain parenchyma to drain to either the superficial or deep venous systems. They are the most common cerebral vascular malformation, frequently identified on routine MR imaging of the brain with contrast. Postmortem studies 3 decades ago suggested a prevalence of 2.7%<sup>1</sup>; however, with the use of modern imaging techniques, the prevalence is estimated to be much higher (6.4%).<sup>2</sup> DVAs are typically considered variants of venous devel-

opment that, in and of themselves, are of little clinical import. However, a small percentage of DVAs have been associated with such findings as cavernous malformations,<sup>3,4</sup> thrombosis with subsequent venous infarction,<sup>5,6</sup> lobar atrophy,<sup>7</sup> T2 and FLAIR signal-intensity abnormalities,<sup>8,9</sup> perfusion abnormalities,<sup>10,11</sup> and SWI hypointensities.<sup>12</sup>

In our daily pediatric neuroradiology practice, we had noticed a high prevalence of presumed incidental DVAs in our oncology patient population. A possible association between intrinsic brain tumors and DVAs had been suggested before by Pryor et al,<sup>13</sup> but a rigorous investigation has not been performed. This study tested the null hypothesis that there is no association between DVAs and intrinsic brain neoplasms.

## MATERIALS AND METHODS

This retrospective study was approved by our institutional review board. The study population was derived from a data base of patients referred to the neuro-oncology service at our institution

Received January 30, 2015; accepted after revision February 5.

From the Department of Radiology (B.V.J., L.L., G.K., J.L.L.) and Division of Pediatric Oncology (T.R.H.), Cincinnati Children's Hospital Medical Center, University of Cincinnati College of Medicine, Cincinnati, Ohio.

Please address correspondence to Blaise V. Jones, MD, Cincinnati Children's Hospital Medical Center, 3333 Burnet Ave, ML 5031, Cincinnati, OH 45229; e-mail: blaise.jones@cchmc.org; @CincyKidsRad

<http://dx.doi.org/10.3174/ajnr.A4352>

**Table 1: Study and control population characteristics<sup>a</sup>**

	Mean Age (Range)	Sex		Field Strength		Scan Type	
		Male	Female	1.5T	3T	Planar	Volumetric
Neoplasm	9.1 yr (1 day to 35 yr)	306	274	504	76	470	110
Controls	10.2 yr (1 day to 31 yr)	274	306	486	94	473	107

<sup>a</sup> The neoplasm group was slightly younger than the control group ( $P = .001$  by 2-tailed  $t$  test). No significant differences were identified in sex ( $P = .07$ ), field strength ( $P = .16$ ), or scan type ( $P = .89$ ) between the 2 groups.

**Table 2: Prevalence of DVAs in study and control populations<sup>a</sup>**

	Total	DVA+ (%)	95% CI	Z Score	P Value
Neoplasm	580	59 (10.17)	7.97–12.90	3.07	.003
Controls	580	31 (5.34)	3.79–7.48		

**Note:**—DVA+ indicates the number of subjects in group who had a confirmed DVA.  
<sup>a</sup> The neoplasm group had a >10% prevalence of DVAs, compared with just over 5% for the control group. The latter is similar to recently published prevalence data.

from 1990 through 2011, a total of 719 cases. Cases were excluded from consideration if the diagnosis of neoplasm was not confirmed by either biopsy or documented progression; if the neoplasm was not intra-axial in origin; or if there was a vascular malformation (arteriovenous malformation, arteriovenous fistula, facial venous malformation), venous thrombosis, syndrome associated with vascular anomalies, major structural abnormalities limiting evaluation of the brain parenchyma, or no reviewable imaging. Metastatic neoplasms to the brain were also excluded. This process left a study population of 580 patients with primary intracranial neoplasms. A radiology report text search was then performed with the software program Softek Illuminate (Softek Solutions, Prairie Village, Kansas), by using the search terms “venous,” “DVA,” and “angioma.” Positive results were reviewed to identify reports describing a DVA, and the imaging for each identified case was reviewed to confirm the diagnosis, document adequate diagnostic quality, and determine the location of the DVA. The MR imaging field strength (1.5 or 3T), whether postcontrast imaging was performed with a planar or volumetric technique, the year of the earliest available examination demonstrating the DVA, and patient age and sex were documented in all cases.

A control population of 580 studies was then derived from the radiology data base of all brain MR imaging examinations performed with intravenous contrast during the same study period. The number of control cases per year was matched to those of the study population, and the same text search was performed. Cases were excluded from consideration if there was a diagnosis of intracranial neoplasm or potential neoplasm (including nonspecific signal abnormalities) requiring follow-up. As with the tumor group, cases were also excluded if there was a vascular malformation (arteriovenous malformation, arteriovenous fistula, facial venous malformation), venous thrombosis, a syndrome associated with vascular anomalies, or major structural abnormalities limiting the evaluation of the brain parenchyma. The same text search was performed on this control population, positive results were reviewed to confirm that the report was describing a DVA, and the imaging examination was reviewed to confirm the diagnosis and document adequate diagnostic quality, with the same documentation of field strength, postcontrast technique, and subject demographics performed.

As a means of identifying false-negative rates of DVA iden-

tification, ~10% of the reported negative cases from each group (55 from the study population and 55 from the control population) were randomly selected and analyzed for the presence of DVAs.

### Statistical Analysis

Statistical analysis of frequency data was performed by using the  $\chi^2$  test (continuity-corrected), confidence intervals of proportions (continuity-corrected), and z-ratio of independent proportions (VassarStats: Website for Statistical Computation; vassarstats.net). Continuous variables (age) were assessed with a 2-tailed  $t$  test (vassarstats.net).  $P < .05$  was significant.

### RESULTS

Our selection process resulted in 2 groups of subjects with MR imaging of the brain (1 without and 1 with brain tumors), evaluated during the same time period, by the same group of radiologists, using similar imaging techniques. Exclusion criteria were identical in each group, with the exception of the presence of intracranial neoplasm in the tumor cohort. Demographics and MR imaging study type distribution for the study and control groups are provided in Table 1. The tumor group was slightly younger than the control group (mean, 9.0 years versus 10.1 years;  $P = .002$ , 2-tailed  $t$  test). No significant differences were noted in sex ( $P = .07$ ), field strength ( $P = .16$ ), or scan type ( $P = .89$ ) between groups.

Fifty-nine of the 580 subjects with brain tumors (10.17%) had a DVA identified by report and confirmed on review of the imaging. Thirty-one of the 580 controls (5.34%) had a DVA identified by report and confirmed on review of the imaging (Table 2,  $P = .003$ ). Forty-two of the positive cases in the study population had glial tumors (71%); 5 had glioneuronal tumors; 9, embryonal; 2 ependymal; and 1, germ cell (Fig 1). This prevalence was similar to the distribution of tumor types in the study population overall, with the result that there was no statistically significant difference in the prevalence of DVAs among tumor types. Thirty-eight subjects had DVAs in the frontal lobes, 11 in the parietal lobes, and 4 in the temporal lobes, with 4 in the posterior fossa, 2 in the occipital lobes, and 1 in the basal ganglia. Four subjects had more than 1 DVA. None of the DVAs drained the vascular territory of the tumor, and there was no correlation between the location of the DVA and the location of the neoplasm in terms of lobe, side of the brain, or supratentorial-versus-infratentorial compartments.

The DVA was visible on the oldest imaging study available for review in all cases. In 51 of the 59 DVA-positive cases, the original study diagnosing a neoplasm was available for review, and in all of these, the DVA was visible. In the remaining 8 cases, the oldest imaging study available for review was not the original diagnostic examination that identified the neoplasm. In 4 of these 8 cases, the report of the original examination was available, and it documented the presence of the DVA. Of the remaining 4 cases, in one, the oldest available study was performed 5 months after diagnosis, with no intervening treatment. In another, the oldest available study was performed 2 years after surgical resection of the neoplasm, without intervening adjuvant therapy. In the 2 remaining

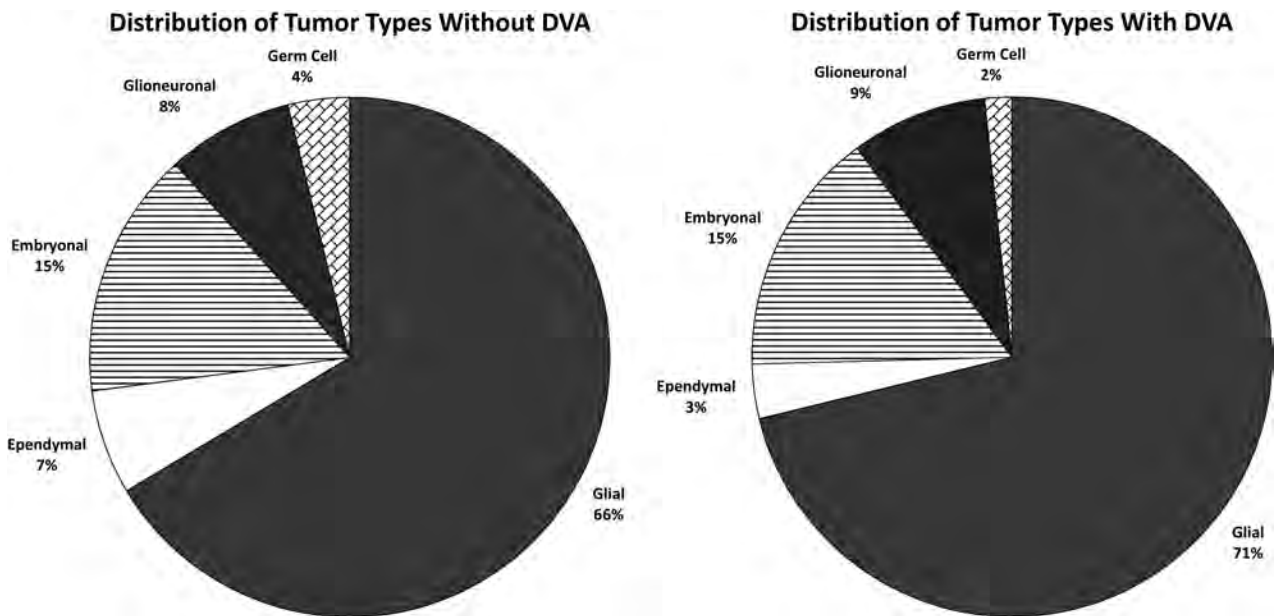


**FIG 1.** Pie charts show the distribution of tumor types among the study population in those without DVAs (*left*) and those with DVAs (*right*). Both groups are dominated by glial tumors, without a statistically significant difference between the 2.

cases, the oldest examinations available for review were performed >4 years after diagnosis and treatment of the neoplasm, and there was intervening treatment with both chemotherapy and radiation therapy.

Of the 55 cases with negative findings randomly selected from the study population, one (1.8%) showed a DVA on review. Similarly, one of the cases randomly selected from the control population demonstrated a DVA on review. Extrapolating this false-negative rate to the entire population would suggest a prevalence of approximately 12% in children with neoplasms and 7% in those without.

## DISCUSSION

DVAs are encountered with frequency in daily neuroradiology practice and are generally considered to be essentially benign variants of venous development. Several theories have been proposed to explain their etiology, the most broadly accepted of which is that they represent a response of the developing brain to a regional compromise of the normal venous drainage caused by stenosis, thrombosis, or maldevelopment.<sup>14</sup> Others have suggested that abnormalities of fetal angiogenesis and regression may lead to their development.<sup>15</sup> There is consensus that they arise in utero, though there have been reports documenting postnatal evolution.<sup>16</sup>

It has long been recognized that a substantial number of DVAs are associated with cavernous malformations, and it is theorized that both lesions represent differing responses to a compromise of regional venous drainage.<sup>17-20</sup> However, DVAs are also seen with a high prevalence in patients with lymphatic or venolymphatic malformations of the head and neck,<sup>21,22</sup> and they have an increased incidence in a variety of genetically driven syndromes such as the blue rubber bleb nevus syndrome.<sup>23</sup> These associations suggest that DVA development is not solely a reaction to focal abnormalities of venous drainage but may also be a consequence of widespread perturbations of vascular development. Re-

cent reports have identified associated parenchymal signal abnormalities in 11.6% of children and young adults<sup>9</sup> and in 12.5% of older adults<sup>8</sup> with DVAs, suggesting that the altered drainage they provide may have consequences on the surrounding brain. All of these associations lend credence to concerns that DVAs may have a deleterious impact on the surrounding brain or may be a harbinger of more widespread abnormalities. Our findings indicate that DVAs may be more prevalent in pediatric patients with intracranial neoplasms than in controls.

Because DVAs are lesions that primarily impact the brain parenchyma, we limited our study population to those patients with intra-axial tumors. The distribution of tumor types in our study population parallels the known relative prevalence of these lesions in the pediatric population, and the prevalence of DVAs within our study subjects generally follows the distribution of tumor types. We found no statistically significant association of DVA prevalence with tumor type, and the distribution of DVA location within the brain was consistent with that in prior reports.<sup>24</sup>

The reason that DVAs may be more prevalent in children with primary intracranial neoplasms is not known. The fact that in none of our cases did the DVA drain the territory of the neoplasm essentially eliminates any direct causative link. However, if DVAs are exclusively the result of focal compromise of venous development, the same abnormality that led to the venous compromise may have caused a concomitant insult elsewhere in the brain that increases the risk of developing a neoplasm. Alternatively, if they are a consequence of a more widespread alteration of vascular development, as suggested by their association with venolymphatic malformations and neurocutaneous syndromes, it is conceivable that they may be associated with an increased vulnerability to neoplastic differentiation in the brain tissue.

It is reasonable to question whether the DVAs in this population could be a consequence of treatment for neoplasms, much as cavernous malformations are associated with prior radiation

therapy.<sup>25</sup> However, in all except 2 of our cases, there was the clearly documented presence of the DVA before any chemotherapy or radiation treatment. There was no instance of a DVA becoming evident with time; they could be identified on the oldest available study for review in all cases. Furthermore, growth in response to therapy contradicts the generally accepted developmental nature of DVAs and would suggest that the DVAs identified in this analysis are substantially different from those recognized in the general population. The standard distribution and characteristic appearance of the DVAs in our study population would argue against this hypothesis. The possibility that the development of a DVA is somehow caused by the presence of a neoplasm elsewhere in the brain cannot be excluded, but the possible causal link is not apparent.

This study is weakened by its retrospective nature and dependence on reporting. It is not a study of lesion prevalence but rather one of lesion-identification prevalence, raising the question of bias in the interpretation of studies in controls compared with subjects. However, the prevalence of DVAs identified in our control population was similar to that demonstrated in the most recent imaging-based studies, suggesting a similar degree of sensitivity of detection. Furthermore, a 10% sampling of cases with negative findings from each group demonstrated no difference between detection rates. The same group of fellowship-trained neuroradiologists generated the reports in each group during their daily clinical practice; because they were working under the general assumption that DVAs are incidental variants with no relation to neoplasms, it is unlikely that they would have been sensitized to their presence in oncologic patients relative to controls. We found no significant differences in examination techniques that would favor the detection of DVA in one group or the other. The fact that most of the subjects had multiple examinations undoubtedly increased the chance of lesion detection, but nearly all DVAs were recognized on the initial studies performed, minimizing the impact of multiple studies.

## CONCLUSIONS

We found that the prevalence of DVAs in children with primary intracranial neoplasms is significantly greater than in those without neoplasm, suggesting an association that may be related to shared causative factors or susceptibilities to development of these 2 separate entities. A prospective study could more clearly delineate the association between these processes and provide greater insight into the potential causative factors. New knowledge gained about either entity should be considered in the study of the other, and one should recognize that there may be more commonality among these lesions than previously appreciated.

## REFERENCES

- Sarwar M, McCormick WF. **Intracerebral venous angioma: case report and review.** *Arch Neurol* 1978;35:323–25
- Gökçe E, Acu B, Beyhan M, et al. **Magnetic resonance imaging findings of developmental venous anomalies.** *Clin Neuroradiol* 2014;24:135–43
- Abe T, Singer RJ, Marks MP, et al. **Coexistence of occult vascular malformations and developmental venous anomalies in the central nervous system: MR evaluation.** *AJNR Am J Neuroradiol* 1998;19:51–57
- Beall DP, Bell JP, Webb JR, et al. **Developmental venous anomalies and cavernous angiomas: a review of the concurrence, imaging, and treatment of these vascular malformations.** *J Okla State Med Assoc* 2005;98:535–38
- Kiroglu Y, Oran I, Dalbasti T, et al. **Thrombosis of a drainage vein in developmental venous anomaly (DVA) leading venous infarction: a case report and review of the literature.** *J Neuroimaging* 2011;21:197–201
- Teo M, St George J, Jenkins S, et al. **Developmental venous anomalies—two cases with venous thrombosis.** *Br J Neurosurg* 2012;26:886–87
- San Millán Ruiz D, Delavelle J, Yilmaz H, et al. **Parenchymal abnormalities associated with developmental venous anomalies.** *Neuroradiology* 2007;49:987–95
- Santucci GM, Leach JL, Ying J, et al. **Brain parenchymal signal abnormalities associated with developmental venous anomalies: detailed MR imaging assessment.** *AJNR Am J Neuroradiol* 2008;29:1317–23
- Linscott LL, Leach JL, Zhang B, et al. **Brain parenchymal signal abnormalities associated with developmental venous anomalies in children and young adults.** *AJNR Am J Neuroradiol* 2014;35:1600–07
- Iv M, Fischbein NJ, Zaharchuk G. **Association of developmental venous anomalies with perfusion abnormalities on arterial spin labeling and bolus perfusion-weighted imaging.** *J Neuroimaging* 2015;25:243–50
- Sharma A, Zipfel GJ, Hildebolt C, et al. **Hemodynamic effects of developmental venous anomalies with and without cavernous malformations.** *AJNR Am J Neuroradiol* 2013;34:1746–51
- Takasugi M, Fujii S, Shinohara Y, et al. **Parenchymal hypointense foci associated with developmental venous anomalies: evaluation by phase-sensitive MR imaging at 3T.** *AJNR Am J Neuroradiol* 2013;34:1940–44
- Pryor J, Setton A, Berenstein A. **Venous anomalies and associated lesions.** *Neurosurg Clin N Am* 1999;10:519–25
- Saito Y, Kobayashi N. **Cerebral venous angiomas: clinical evaluation and possible etiology.** *Radiology* 1981;139:87–94
- Wilson CB. **Cryptic vascular malformations.** *Clin Neurosurg* 1992;38:49–84
- Leach JL, Howard T, Abruzzo T, et al. **Postnatal evolution of developmental venous anomaly.** *J Pediatr Neuroradiol* 2012;1:305–11
- Campeau NG, Lane JI. **De novo development of a lesion with the appearance of a cavernous malformation adjacent to an existing developmental venous anomaly.** *AJNR Am J Neuroradiol* 2005;26:156–59
- Maeder P, Gudinchet F, Meuli R, et al. **Development of a cavernous malformation of the brain.** *AJNR Am J Neuroradiol* 1998;19:1141–43
- Dillon WP. **Cryptic vascular malformations: controversies in terminology, diagnosis, pathophysiology, and treatment.** *AJNR Am J Neuroradiol* 1997;18:1839–46
- Cakirer S. **De novo formation of a cavernous malformation of the brain in the presence of a developmental venous anomaly.** *Clin Radiol* 2003;58:251–56
- Boukoba M, Enjolras O, Guichard JP, et al. **Cerebral developmental venous anomalies associated with head and neck venous malformations.** *AJNR Am J Neuroradiol* 1996;17:987–94
- Bisdorff A, Mulliken JB, Carrico J, et al. **Intracranial vascular anomalies in patients with periorbital lymphatic and lymphaticovenous malformations.** *AJNR Am J Neuroradiol* 2007;28:335–41
- Gabikian P, Clatterbuck RE, Gailloud P, et al. **Developmental venous anomalies and sinus pericranii in the blue rubber-bleb nevus syndrome: case report.** *J Neurosurg* 2003;99:409–11
- Lee C, Pennington MA, Kenney CM 3rd. **MR evaluation of developmental venous anomalies: medullary venous anatomy of venous angiomas.** *AJNR Am J Neuroradiol* 1996;17:61–70
- Nimjee SM, Powers CJ, Bulsara KR. **Review of the literature on de novo formation of cavernous malformations of the central nervous system after radiation therapy.** *Neurosurg Focus* 2006;21:e4

# Choroid Plexus Neoplasms: Toward a Distinction between Carcinoma and Papilloma Using Arterial Spin-Labeling

V. Dangouloff-Ros, D. Grevent, M. Pagès, T. Blauwblomme, R. Calmon, C. Elie, S. Puget, C. Sainte-Rose, F. Brunelle, P. Varlet, and N. Bodaert



## ABSTRACT

**SUMMARY:** Pediatric choroid plexus papillomas and carcinomas are highly vascularized neoplasms, which are difficult to distinguish with conventional imaging. We aimed to analyze the diagnostic accuracy of PWI, by using both pseudocontinuous arterial spin-labeling and DSC-PWI. We reviewed the PWI of 13 children with choroid plexus neoplasms (7 papillomas and 6 carcinomas). We quantified CBF, relative CBF, and relative CBV in each lesion and compared papillomas and carcinomas. Relative CBF values by using arterial spin-labeling were significantly higher for carcinomas ( $P = .028$ ). The median value of relative CBF was 1.7 (range, 1.4–1.9) for carcinomas and 0.4 (range, 0.3–0.6) for papillomas. The CBF median value was 115 mL/min/100 g (range, 90–140 mL/min/100 g) for carcinomas and 41 mL/min/100 g (range, 10–73 mL/min/100 g) for papillomas ( $P = .056$ ). Measures with DSC-PWI were more variable and not significantly different ( $P = .393$ ). Arterial spin-labeling is a promising technique to differentiate choroid plexus carcinomas and papillomas.

**ABBREVIATIONS:** ASL = arterial spin-labeling; rCBF = relative CBF; rCBV = relative CBV

Choroid plexus neoplasms are rare intraventricular tumors, which account for approximately 2% of pediatric brain tumors<sup>1,2</sup> but are comparatively more common in neonates (5%–20% of perinatal brain tumors<sup>3</sup>). Benign papillomas are reported to account for approximately 80% of neoplasms, and carcinomas, 20%.<sup>4</sup>

Pathologic examination of papillomas reveals a papillary architecture composed of delicate fibrovascular connective tissue fronds covered by a single layer of uniform epithelial cells. In carcinomas, it reveals the blurring of the papillary pattern, with poorly structured sheets of tumor cells and necrotic areas.<sup>4</sup> These different patterns are responsible for a very dissimilar vascular organization.

Conventional imaging alone does not allow differentiating

these 2 entities, and a pathologic examination is always needed.<sup>5</sup> A preoperative diagnosis could be very useful, even if surgery is performed for all cases. Differentiation of the 2 tumors on imaging could change management. In fact, it may allow the surgeon to adapt his or her surgical strategy (possible preoperative embolization for example) because carcinomas are more invasive and tend to be more hemorrhagic.

Therefore, advanced MR imaging techniques such as perfusion-weighted imaging could provide additional information on tumor vascularization that may help in the differential diagnosis. Two previous studies<sup>6,7</sup> reported various results for DSC-PWI of papillomas, and there is no report for carcinomas. One recent study<sup>8</sup> reported arterial spin-labeling (ASL) PWI of pediatric brain tumors, including 1 carcinoma and 4 choroid plexus papillomas, with higher relative tumor blood flow for the carcinoma.

The objective of our study was to analyze the perfusion pattern of pediatric choroid plexus papilloma and carcinoma with perfusion weighted-imaging, by using ASL or DSC-PWI.

## MATERIALS AND METHODS

### Patients

We performed a retrospective analysis of the prospective data base for brain tumors of our pediatric neurosurgery department (Hôpital Necker–Enfants Malades, Paris) from January 2011 (when we began to use ASL for pediatric brain tumors) to September 2014, looking for all choroid plexus lesions.

Inclusion criteria were the following: available MR imaging with PWI (ASL or DSC) in our radiology department; no prior

Received December 8, 2014; accepted after revision January 14, 2015.

From the Departments of Pediatric Radiology (V.D.-R., D.G., R.C., F.B., N.B.) and Pediatric Neurosurgery (T.B., S.P., C.S.-R.) and Clinical Research Unit (C.E.), Hôpital Necker–Enfants Malades, Assistance-Publique Hôpitaux de Paris, Paris, France; University René Descartes (D.G., M.P., T.B., R.C., S.P., C.S.-R., F.B., P.V., N.B.), Pôle de recherche et d'enseignement supérieur Sorbonne Paris Cité, Paris, France; U1000 (V.D.-R., D.G., R.C., F.B., N.B.) and U781 (N.B.), Institut national de la santé et de la recherche médicale, Paris, France; Inserm UMR1163 - Institut Imagine (D.G., R.C., F.B., N.B.), Université Paris Descartes-Sorbonne Paris Cité, Paris, France; and Department of Neuropathology (M.P., P.V.), Centre Hospitalier Sainte Anne, Paris, France.

Paper previously presented at: Journées Française de Radiologie, October 16–20, 2014; Paris, France.

Please address correspondence to Volodia Dangouloff-Ros, MD, Assistance-Publique Hôpitaux de Paris, Hôpital Necker–Enfants Malades, Department of Pediatric Radiology, 149 rue de Sèvres, 75015 Paris, France; e-mail: vdangouloffros@yahoo.fr; @Volodia\_DR



Indicates article with supplemental on-line tables.



Indicates article with supplemental on-line photo.

<http://dx.doi.org/10.3174/ajnr.A4332>

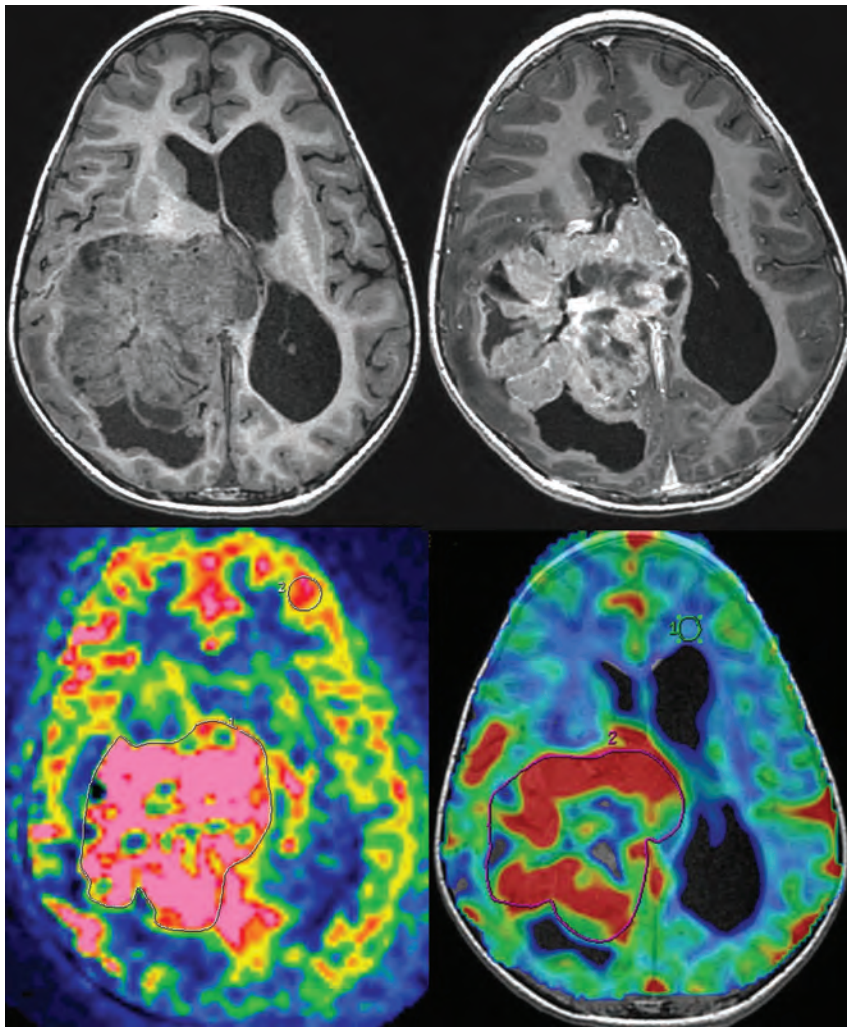


**FIG 1.** Measurement of ASL and DSC-PWI of a choroid plexus carcinoma (patient 8). *Top left:* 3D T1-weighted MR imaging. *Top right:* 3D T1-weighted MR imaging with gadolinium injection. *Bottom left:* arterial spin-labeling. ROIs are drawn around the whole tumor and in the contralateral gray matter. *Bottom right:* dynamic susceptibility contrast perfusion-weighted imaging. ROIs are drawn around the whole tumor and in the contralateral white matter.

surgical resection, biopsy, or treatment of the tumor; and a histologic diagnosis of choroid plexus papilloma or carcinoma.

### Imaging Methods

MR imaging was performed on a Signa HDxt 1.5T system (GE Healthcare, Milwaukee, Wisconsin) by using a 12-channel Head-Neck-Spine coil (GE Healthcare). The MR imaging investigation included standard sequences for tumoral diseases (3D T1-weighted images, 3D T1WI with gadolinium injection, 3D T2-weighted images, diffusion-weighted images), noncontrast perfusion imaging with 3D pseudocontinuous arterial spin-labeling MR imaging, and dynamic susceptibility contrast perfusion-weighted MR imaging.

Acquisition parameters for the ASL sequence were the following: 80 axial partitions; FOV,  $240 \times 240 \times 4$  mm<sup>3</sup>; acquisition matrix, 8 spiral arms in each 3D partition, 512 points per arm; TE, 10.5 ms; TR, 4428 ms; postlabeling delay, 1025 ms; flip angle, 155°; acquisition time, 4 minutes 17 seconds.

Acquisition parameters for the DSC sequence were the following: 18 axial partitions repeated 75 times; FOV,  $240 \times 240 \times$

5 mm<sup>3</sup>; gradient echo: TE, 60 ms; TR, 2000 ms; flip angle, 90°; acquisition time, 2 minutes 30 seconds.

### Imaging Analysis

Using an Advantage Workstation (Version 4.2; GE Healthcare), we automatically realigned the 3D T1 (with and without gadolinium) and ASL or DSC sequences and fused them in a volume viewer. The color scale of cerebral blood flow or cerebral blood volume maps was set to rainbow.

ROIs were drawn around each tumor to obtain mean CBF (for ASL and DSC-PWI) and mean CBV (for DSC-PWI) (Figs 1 and 2). ROIs were also placed in the most perfused areas of the lesions, selected visually on CBF and CBV maps, to obtain maximal CBF and maximal CBV.

To correct for age-dependent and patient-dependent variations of mean cerebral perfusion, CBF was normalized to an ROI in the contralateral normal-appearing cortical gray matter to produce the relative CBF (rCBF). Gray matter was chosen as a reference, as in the study of Yeom et al,<sup>8</sup> because it has a higher signal-to-noise ratio. CBV was normalized to an ROI in the normal-appearing contralateral white matter to produce the relative CBV (rCBV). White matter was chosen here, as usually found in the literature, because of its better reproducibility.<sup>9</sup>

ROIs were placed independently by a senior neuroradiologist (D.G., with 10 years of experience), blinded to clinical and pathologic data, and a radiology resident (V.D.-R., with 3 years of experience). We analyzed the mean value for each variable and the concordance between the 2 observers.

### Histopathologic Analysis

Tumor samples were analyzed by using hematoxylin-eosin staining and an immunohistochemistry panel. The tumors were classified according to the WHO Classification of Tumors of the Central Nervous System (2007).<sup>4</sup>

There were 5- $\mu$ m tissue sections of formalin-fixed, paraffin-embedded tissue used for immunostaining with a monoclonal mouse antihuman CD34 antibody (IM 1185, IOPath; Beckman Coulter, Marseille, France). The reaction was carried out in an automated immunohistochemistry instrument (Discovery XT; Ventana Medical Systems, Basel, Switzerland).

Quantitative and qualitative analysis of microvessels was performed in all cases by light microscopy. Microvascular architecture (arborescent or not) and the presence of endothelial capillary prolif-

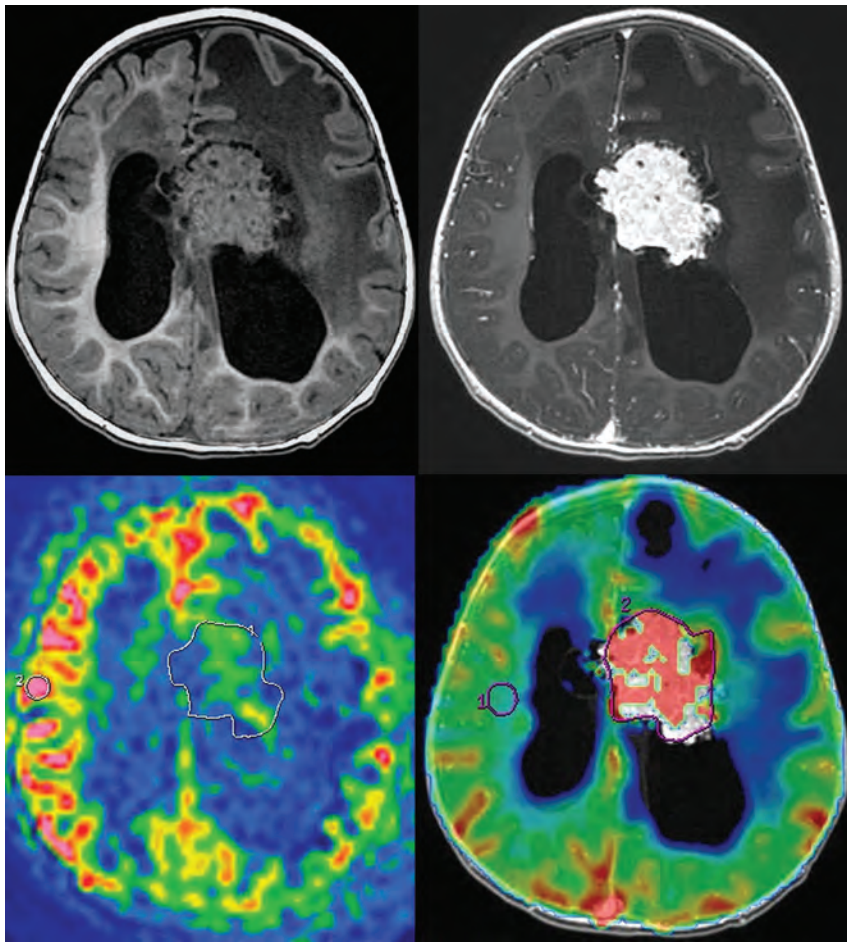


**FIG 2.** Measurement of ASL and DSC-PWI of a choroid plexus papilloma (patient 1). *Top left:* 3D T1-weighted MR imaging. *Top right:* 3D T1-weighted MR imaging with gadolinium injection. *Bottom left:* arterial spin-labeling. ROIs are drawn around the whole tumor and in the contralateral gray matter. *Bottom right:* dynamic susceptibility contrast perfusion-weighted imaging. ROIs are drawn around the whole tumor and in the contralateral white matter.

eration and parietal vascular necrosis were noted. A quantitative analysis was performed on 3 fields ( $0.5 \text{ mm}^2$  per field) selected in the most vascularized tumor areas on each specimen. Any CD34-positive endothelial cells clearly separated from tumoral cells were considered as a countable microvessel. The results are described as a mean of CD34-positive microvessels per  $0.5 \text{ mm}^2$ .

### Statistical Analysis

We performed a statistical analysis by using R statistical computing software (<http://www.r-project.org>) and GraphPad Prism software (GraphPad Software, San Diego, California).

We compared the distribution of perfusion values between papillomas and carcinomas by using a nonparametric Mann-Whitney test with an a priori significance level of  $P = .05$ . Papillomas and atypical papillomas were grouped in the statistical analysis because they showed similar vascularization patterns on histopathology and imaging. We estimated the reproducibility of the values between the 2 readers by using Bland-Altman plots.

## RESULTS

### Patients

Thirty-eight patients underwent a resection of choroid plexus lesions (29 papillomas, 6 carcinomas, 2 cysts, 1 neurocytoma), and

2 patients were followed for choroid plexus hyperplasia. Twenty-five patients had no PWI before surgery, mainly because the imaging was performed at another institution.

We included 13 patients with the following conditions: 6 carcinomas (1 had MR imaging with ASL and DSC-PWI, 1 with only ASL, and 4 with only DSC-PWI; see an example in Fig 1) and 7 papillomas (3 had MR imaging with ASL and DSC-PWI, 4 with only ASL; see an example in Fig 2). The median age of the 13 patients included was 1 year 6 months (range, 7 months to 16 years). There were 5 girls and 8 boys.

### Histopathologic Analysis

Four lesions were classified as choroid plexus papillomas (cases 1–4); 3, as atypical papillomas (cases 5, 6, and 7); and 6, as carcinomas (cases 8–13). Two examples are shown in Fig 3. Quantitative and qualitative analyses of microvessels are listed in Fig 4 and On-line Tables 1 and 2.

Papillomas showed delicate arborescent microvascular architecture within the fibroconnective tissue. Conversely, carcinomas showed a disorganization of microvascular architecture with dilated vessels and budding.

Five carcinoma specimens displayed a vascular necrosis, but only 2 cases of papilloma showed it. Most interesting,

the 2 cases of papilloma showing focal vascular necrosis also revealed less well-organized microvascular architecture than other papilloma specimens and had been classified as atypical papillomas.

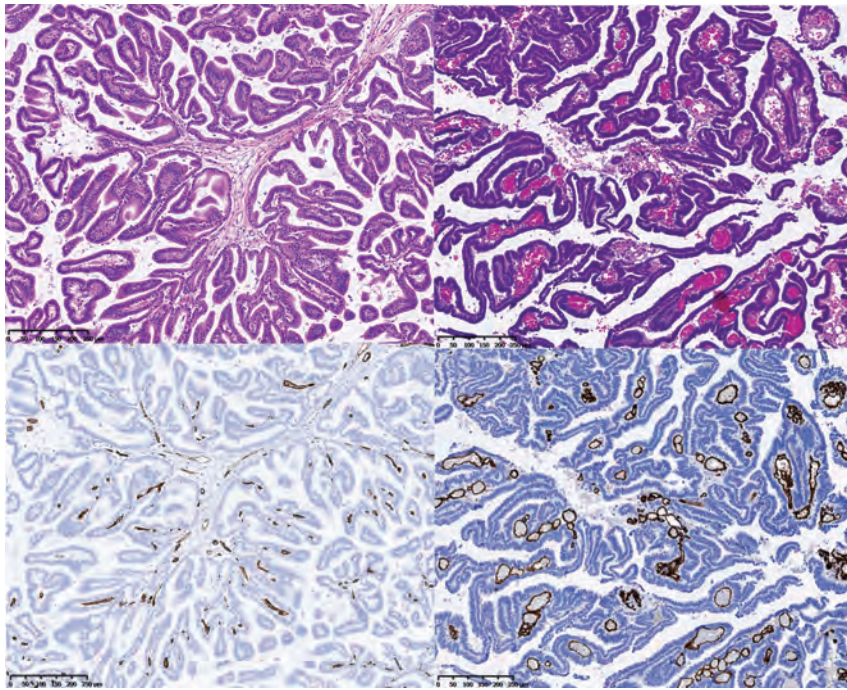
Moreover, no papilloma showed endothelial capillary proliferation, whereas 4 cases of carcinomas showed endothelial capillary proliferation.

Four carcinoma samples had a mean microvessel count of  $>60$  per  $0.5 \text{ mm}^2$ , whereas only 1 papilloma specimen had a count that exceeded 60 microvessels per  $0.5 \text{ mm}^2$  (probable overestimation due to a crushing artifacts). The median of the total microvessel count per  $0.5 \text{ mm}^2$  excluding this specimen was 47 (range, 22–54) in papillomas and 75 (range, 25–114) in carcinomas. However, we found no statistical difference ( $P = .16$ ), even excluding this specimen.

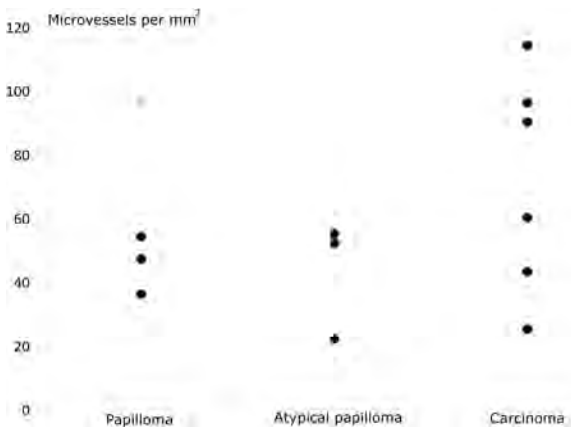
### Comparison Using ASL-PWI

Figure 5, On-line Fig 1, and On-line Tables 1 and 2 summarize the ASL results of 9 patients.

The values obtained for carcinomas were always higher than those of papillomas for all the variables. rCBF values were significantly higher for carcinomas than for papillomas ( $P = .028$ ). The



**FIG 3.** Histopathology. Hematoxylin-eosin staining (*top*) and CD34 immunostaining (*bottom*) of 1 representative patient with papilloma (case 3, on the *left*) and 1 representative patient with carcinoma (case 8, on the *right*), showing the differences in the microvascular architecture. (Magnification  $\times 250$ .)



**FIG 4.** Number of microvessels per square millimeter for papillomas, atypical papillomas, and carcinomas. The *gray point* in the papillomas corresponds to patient 4, in whom microvessels are probably overestimated due to crushing artifacts.

median value of rCBF was 1.7 (range, 1.4–1.9) for carcinomas and 0.4 (range, 0.3–0.6) for papillomas. CBF, maximal CBF, and maximal rCBF values were not strictly significantly different between carcinomas and papillomas, but there were strong tendencies ( $P = .056$ ). The CBF median value was 115 mL/min/100 g (range, 90–140 mL/min/100 g) for carcinomas and 41 mL/min/100 g (range, 10–73 mL/min/100 g) for papillomas. The maximal rCBF median value was 3.4 (range, 2.7–4.1) for carcinomas and 1.1 (range, 0.5–1.1) for papillomas (On-line Fig 1).

#### Comparison Using DSC-PWI

Figure 6 and On-line Tables 1 and 2 summarize the DSC-PWI results of 8 patients.

Once again, carcinomas tended to have higher perfusion values for all variables, but the values overlapped, with 2 papillomas having a higher perfusion than 2 carcinomas. For example, the median rCBV value was 3.6 (range, 1.7–5.8) for carcinomas and 2.5 (range, 1.3–3.2) for papillomas. The median rCBF (compared with gray matter) value was 1.0 (range, 0.9–1.5) for carcinomas and 0.7 (range, 0.4–1.1) for papillomas.

No variable showed any statistical difference ( $P = .393$  to  $P = .786$ ; On-line Tables 1 and 2).

#### Concordance between Observers

Bland-Altman plots are shown in Fig 7.

Concordance was better for each ASL variable than for DSC-PWI. For rCBF by using ASL, the analysis revealed a mean difference between the 2 readers of 0.027, with limits of agreement of  $-0.099$  at the lower limit and 0.15 at the upper limit ( $-18\%$  and  $24\%$  of difference, respectively); by using DSC-PWI, the mean difference was 0.077, with limits of agreement of  $-0.77$  at the lower

limit and 0.92 at the upper limit ( $-101\%$  and  $93\%$ , respectively).

#### DISCUSSION

In this study, we report 13 pediatric cases of choroid plexus tumors explored with perfusion MR imaging by using ASL or DSC-PWI.

ASL-MR imaging is very relevant in a pediatric population because it takes only 5 minutes and does not require intravenous injection.

We measured a higher rCBF with ASL in carcinomas, therefore allowing differentiation between choroid plexus carcinomas and papillomas. ASL rCBF values were very reproducible between the 2 observers. We could find a statistical difference, despite the small number of patients, supporting a strong difference between those neoplasms. The results are similar to those of the previous study by using ASL in pediatric brain tumors, by using a 3T MR imaging magnet,<sup>8</sup> which had only 4 papillomas and 1 carcinoma. Indeed, studying in the report only maximal rCBF, Yeom et al<sup>8</sup> found a median value of 1.13 for papillomas ( $n = 3$ ) versus 0.95 in our study ( $n = 4$ ) and 1.34 for atypical papillomas ( $n = 1$ ) versus 1.1 ( $n = 3$ ) in our study. They found a higher maximal rCBF at 7.96 ( $n = 1$ ) versus 3.4 ( $n = 2$ ) for carcinomas. Nevertheless, the ranking was always the same, and the values never overlapped between the 2 studies.

DSC-PWI rCBV values were higher for carcinomas, but tendencies were weak and so was the concordance between the 2 observers. This lack of concordance and the smaller predictive value of DSC-PWI may be explained by the use of gradient-echo EPI for DSC-PWI, which is very sensitive to susceptibility artifacts that may be caused by bleeding in those tumors. Furthermore, the low injection flow in young children (which is variable among patients, from 0.5 to 1.5 mL/s) may explain problems in modeling the arterial input function. To our knowledge, no report has been pub-

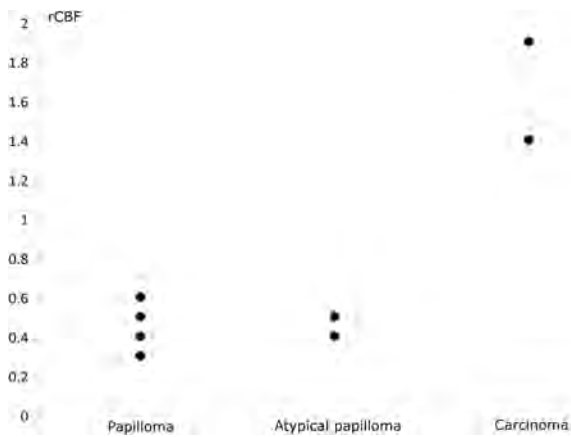


**FIG 5.** Relative cerebral blood flow of papillomas, atypical papillomas, and carcinomas by using ASL. rCBF is normalized to the contralateral gray matter. Two atypical papillomas had the same value and share the same point (0.4).

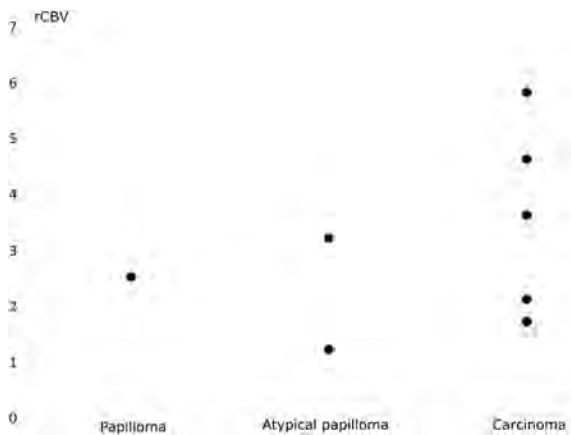


**FIG 6.** Relative cerebral blood volume of papillomas, atypical papillomas, and carcinomas by using DSC-PWI. rCBV is normalized to the contralateral white matter.

lished concerning the use of DSC-PWI for choroids plexus carcinomas, and only a few,<sup>6,7</sup> concerning papillomas.

Histopathologic substrates may explain differences between papillomas and carcinomas in rCBV measured with ASL. Indeed, carcinomas tend to have a higher number of microvessels and a very dissimilar organization, with frequent endothelial capillary proliferation and vascular necrosis. To our knowledge, this is the first study with vessel quantification in choroid plexus tumors, and the previous qualitative studies only reported architectural features.

There are 2 major limits to our study. First, the small number of patients seems to be unavoidable because this tumor is rare and because ASL only became available in our department in 2011. Second, some patients lacked perfusion-weighted sequences because of the retrospective design of our study.

## CONCLUSIONS

ASL perfusion MR imaging can discriminate preoperatively between choroid plexus carcinomas and papillomas; this finding helps the surgeon to adapt his or her operative strategy (possible

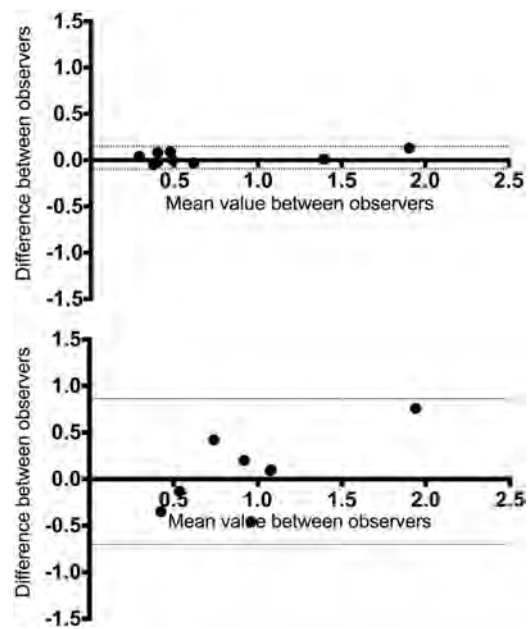


**FIG 7.** Bland-Altman plots comparing the 2 observers. Difference versus average of rCBF by using ASL (top) and DSC-PWI (bottom). Solid lines and adjacent numbers indicate the difference between observers and mean values between observers, while dashed lines indicate the limits of agreement.

preoperative embolization). This sequence could also be of great interest in the follow-up of patients to detect tumor recurrence.

Disclosures: Pascale Varlet—UNRELATED: Board Membership: Hoffman-LaRoche\*; Consultancy: Boehringer Ingelheim\*; Grants/Grants Pending: La Ligue contre le cancer, l'Institut national du cancer. \*Money paid to the institution.

## REFERENCES

- Rickert CH, Paulus W. **Epidemiology of central nervous system tumors in childhood and adolescence based on the new WHO classification.** *Childs Nerv Syst* 2001;17:503–11
- Kaderali Z, Lamberti-Pasculli M, Rutka JT. **The changing epidemiology of paediatric brain tumours: a review from the Hospital for Sick Children.** *Childs Nerv Syst* 2009;25:787–93
- Severino M, Schwartz ES, Thurnher MM, et al. **Congenital tumors of the central nervous system.** *Neuroradiology* 2010;52:531–48
- Paulus W, Brandner S. **Choroid plexus tumours.** In: Louis DN, Cavenee WK, Ohgaki H, et al. *World Health Organization Classification of Tumours of the Central Nervous System.* Lyon: IARC; 2007:82–85
- Smith AB, Smirniotopoulos JG, Horkanyne-Szakaly I. **From the radiologic pathology archives: intraventricular neoplasms: radiologic-pathologic correlation.** *Radiographics* 2013;33:21–43
- Holveck A, Grand S, Boini S, et al. **Dynamic susceptibility contrast-enhanced MRI evaluation of cerebral intraventricular tumors: preliminary results.** *J Neuroradiol* 2010;37:269–75
- Zimny A, Sasiadek M. **Contribution of perfusion-weighted magnetic resonance imaging in the differentiation of meningiomas and other extra-axial tumors: case reports and literature review.** *J Neurooncol* 2011;103:777–83
- Yeom KW, Mitchell LA, Lober RM, et al. **Arterial spin-labeled perfusion of pediatric brain tumors.** *AJNR Am J Neuroradiol* 2014; 35:395–401
- Cha S, Knopp EA, Johnson G, et al. **Intracranial mass lesions: dynamic contrast-enhanced susceptibility-weighted echo-planar perfusion MR imaging.** *Radiology* 2002;22:11–29

# Celebrating 35 Years of the AJNR

September 1980 edition

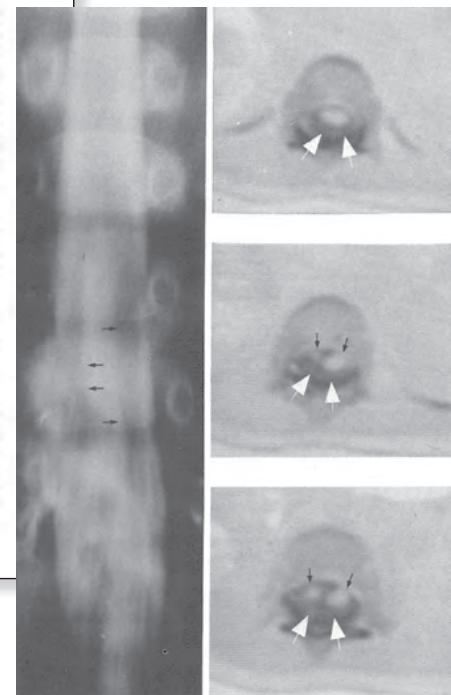
## Diastematomyelia in Children: Metrizamide and CT Myelography

Giuseppe Scotti<sup>1</sup>  
Mark A. Misgravi<sup>2</sup>  
Derek C. Harwood-Nash<sup>3</sup>  
Charles R. Fitz<sup>4</sup>  
Sylvester H. Chuang<sup>5</sup>

Diastematomyelia is an uncommon dysraphic lesion of the spine which has been diagnosed more frequently since the advent of newer diagnostic methods. A series of 21 cases was examined using metrizamide myelography and computed tomographic metrizamide myelography (CTMM) over a 2-year period. These examinations, in addition to plain radiographs of the spine, have demonstrated certain features of diastematomyelia hitherto unreported. A bony or cartilaginous spur was an uncommon finding, occurring in only six cases. Also, the split spinal cord was found within an enlarged dorsal sac in 13 cases. Coexistent tethering of the spinal cord, even in the absence of a spur, was present in 16 of the 21 cases. CTMM proved superior to metrizamide myelography in demonstrating the spinal cord anomalies; plain films and CT are complementary in defining the bony anomalies. The radiographic investigative protocol of diastematomyelia includes plain anteroposterior and lateral spine films, metrizamide myelography, and CTMM. Conventional tomography and plain CT are unnecessary; improved density resolution and availability of computed radiographic anteroposterior and lateral scout views will further reduce the need for plain films and tetraethyl injection of contrast medium.

Computed tomography (CT), metrizamide myelography (MM), and computed tomographic metrizamide myelography (CTMM) have, in recent years, added a new dimension to the diagnosis of dysraphic lesions of the spine [1-3]. An uncommon condition in this group of anomalies is diastematomyelia, which is anatomically characterized by a longitudinal splitting of the spinal cord at one or more vertebral levels, usually in the lower thoracic and upper lumbar areas, sometimes associated with a bony, cartilaginous, or fibrous spur lying within the spinal canal and protruding through the dorsal sac into the spinal cord. This is distinct from split-spina which is a true duplication of the spinal cord with two distinct dorsal sacs and two pairs of anterior and posterior nerve roots, and which is very rarely diagnosed during life.

It is known to be associated with the following embryologic defects: fused vertebral bodies, and increased proliferation in part or in whole on contralateral and several fractions of embryogenesis [4-6]. These malformations of the neural tube from early weeks of gestation, resulting in the neural tube [4, 5] and (2) a split neural tube [6]. According to the literature, such congenital malformations may lead to such congenital malformations, butterfly vertebrae, basal cysts, and intraspinal bony



## Intravenous Angiography Using Digital Video Subtraction: Intravenous Cervicocerebrovascular Angiography

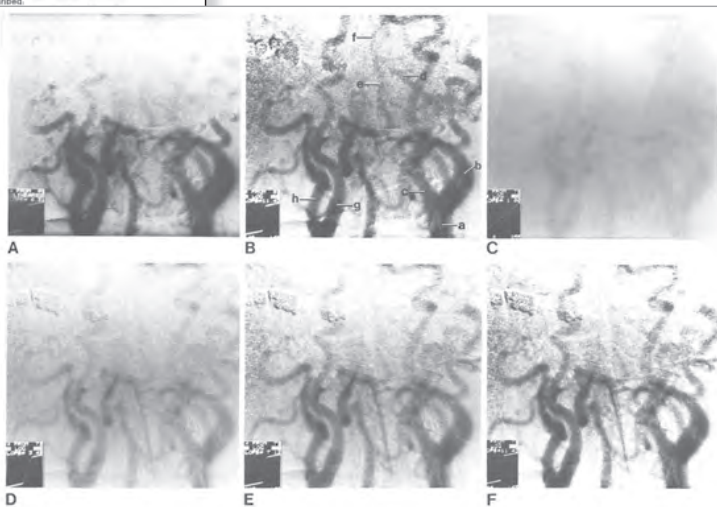
Peter C. Christenson<sup>1</sup>  
Theron W. Ouhl<sup>2</sup>  
H. Donald Fisher III<sup>3</sup>  
Mervyl M. Froar<sup>4</sup>  
Sari Nusselman<sup>5</sup>  
Hani Roshing<sup>6</sup>

The clinical application of intravenous angiography to study the cervicocerebrovascular system using the digital video subtraction system described in a companion article is reported. About 0.75 ml/kg of a standard 76% iodine contrast solution is injected into an antecubital vein using a power injector. Then 15-20 exposures of the head and neck region at a 1/300 sec rate are made on the image intensifier. The images are recorded by a high performance video system and the output signal is digitized for subsequent computer manipulation. The subtraction images of these vessels produced by the computer show the vessels clearly, even though they contain very low concentrations of contrast media. Standard exposure factors of 75-90 kVp, 8-10 msec at 300-1,000 mA are used. Clinically pertinent features of the data alteration and flow through the system and the step-by-step computer procedures used to acquire and analyze the various forms of subtracted images are discussed.

Five experimental and clinical cases demonstrate applications of intravenous cervicocerebrovascular disease: (1) evaluating the effects of an atherosclerosis; (2) providing a screening angiographic technique for detecting aneurysms and/or positive nonvascular studies; (3) significant generalized vascular disease; either pre- or postoperative; (4) providing a screening angiographic technique for detecting aneurysms and/or positive nonvascular studies; (5) patients in whom standard angiography has higher risk; (6) asymptomatic patients who are medicated at higher risk. Numerous examples of the various types of images (1) linear subtraction; (2) logarithmic subtraction; (3) edge enhancement (map steps); (4) the usefulness of a series of images; (5) the importance of multiple projections with this technique.

Intravenous angiography has added to the armamentarium for evaluation of atherosclerotic disease [1-3]. Satisfactory intravenous angiographic techniques for visualizing and screening the entire cervicocerebrovascular system. Although selective transcatheter techniques play a major role in the detailed radiographic diagnosis of intracranial lesions, it is not appropriately used as a screening technique in whom either a screening examination is either contraindicated or unachievable.

With the system described in our companion article, clinically diagnostic images of the cervical arteries are acquired. We can use these images to make a conservative versus nonoperative care in about 60% of most angiograms, transiently positive findings were angiography.



Received April 17, 1980; accepted May 13, 1980.  
Presented in part at the annual meeting of the American Society of Neuroradiology, Toronto, Canada, May 1979.  
This work was supported by National Health, Education, and Human Resources Grant NS21,474 (P.C.C.).  
\*Aspirin, Disulfiram, and other drugs; University of Alabama, Tuscaloosa, AL 35424. Address reprint requests to P. C. Christenson.  
The article appears in December/October 1980 AJNR 31:1791-1796, September/October 1980 31:1791-1796, and 1980 AJNR 31:1791-1796.  
© American Neuroradiology Society



10<sup>th</sup> Annual Meeting of the  
American Society of  
**FUNCTIONAL NEURORADIOLOGY**

February 29 - March 2, 2016

in co-sponsorship with the

American Society of  
**PEDIATRIC NEURORADIOLOGY**

February 28 - 29, 2016

**Renaissance Austin Hotel**  
Austin, Texas

**Optional BOLD Functional MRI Hands On Workshop**  
**Saturday, February 27, 2016**

Separate Registration Required  
Registration is Limited to 20 Attendees Per Session.

For More Information, visit [www.asfnr.org](http://www.asfnr.org)

## Target® Detachable Coil

See package insert for complete indications, contraindications, warnings and instructions for use.

### INTENDED USE / INDICATIONS FOR USE

Target Detachable Coils are intended to endovascularly obstruct or occlude blood flow in vascular abnormalities of the neurovascular and peripheral vessels.

Target Detachable Coils are indicated for endovascular embolization of:

- Intracranial aneurysms
- Other neurovascular abnormalities such as arteriovenous malformations and arteriovenous fistulae
- Arterial and venous embolizations in the peripheral vasculature

### CONTRAINDICATIONS

None known.

### POTENTIAL ADVERSE EVENTS

Potential complications include, but are not limited to: allergic reaction, aneurysm perforation and rupture, arrhythmia, death, edema, embolus, headache, hemorrhage, infection, ischemia, neurological/intracranial sequelae, post-embolization syndrome (fever, increased white blood cell count, discomfort), TIA/stroke, vasospasm, vessel occlusion or closure, vessel perforation, dissection, trauma or damage, vessel rupture, vessel thrombosis. Other procedural complications including but not limited to: anesthetic and contrast media risks, hypotension, hypertension, access site complications.

### WARNINGS

- Contents supplied STERILE using an ethylene oxide (EO) process. Do not use if sterile barrier is damaged. If damage is found, call your Stryker Neurovascular representative.
- For single use only. Do not reuse, reprocess or resterilize. Reuse, reprocessing or resterilization may compromise the structural integrity of the device and/or lead to device failure which, in turn, may result in patient injury, illness or death. Reuse, reprocessing or resterilization may also create a risk of contamination of the device and/or cause patient infection or cross-infection, including, but not limited to, the transmission of infectious disease(s) from one patient to another. Contamination of the device may lead to injury, illness or death of the patient.
- After use, dispose of product and packaging in accordance with hospital, administrative and/or local government policy.
- **This device should only be used by physicians who have received appropriate training in interventional neuroradiology or interventional radiology and preclinical training on the use of this device as established by Stryker Neurovascular.**
- Patients with hypersensitivity to 316LVM stainless steel may suffer an allergic reaction to this implant.
- MR temperature testing was not conducted in peripheral vasculature, arteriovenous malformations or fistulae models.
- The safety and performance characteristics of the Target Detachable Coil System (Target Detachable Coils, InZone Detachment Systems,

delivery systems and accessories) have not been demonstrated with other manufacturer's devices (whether coils, coil delivery devices, coil detachment systems, catheters, guidewires, and/or other accessories). Due to the potential incompatibility of non Stryker Neurovascular devices with the Target Detachable Coil System, the use of other manufacturer's device(s) with the Target Detachable Coil System is not recommended.

- To reduce risk of coil migration, the diameter of the first and second coil should never be less than the width of the ostium.
- In order to achieve optimal performance of the Target Detachable Coil System and to reduce the risk of thromboembolic complications, it is critical that a continuous infusion of appropriate flush solution be maintained between a) the femoral sheath and guiding catheter, b) the 2-tip microcatheter and guiding catheters, and c) the 2-tip microcatheter and Stryker Neurovascular guidewire and delivery wire. Continuous flush also reduces the potential for thrombus formation on, and crystallization of infusate around, the detachment zone of the Target Detachable Coil.
- Do not use the product after the "Use By" date specified on the package.
- Reuse of the flush port/dispenser coil or use with any coil other than the original coil may result in contamination of, or damage to, the coil.
- Utilization of damaged coils may affect coil delivery to, and stability inside, the vessel or aneurysm, possibly resulting in coil migration and/or stretching.
- The fluoro-saver marker is designed for use with a Rotating Hemostatic Valve (RHV). If used without an RHV, the distal end of the coil may be beyond the alignment marker when the fluoro-saver marker reaches the microcatheter hub.
- If the fluoro-saver marker is not visible, do not advance the coil without fluoroscopy.
- Do not rotate delivery wire during or after delivery of the coil. Rotating the Target Detachable Coil delivery wire may result in a stretched coil or premature detachment of the coil from the delivery wire, which could result in coil migration.
- Verify there is no coil loop protrusion into the parent vessel after coil placement and prior to coil detachment. Coil loop protrusion after coil placement may result in thromboembolic events if the coil is detached.
- Verify there is no movement of the coil after coil placement and prior to coil detachment. Movement of the coil after coil placement may indicate that the coil could migrate once it is detached.
- Failure to properly close the RHV compression fitting over the delivery wire before attaching the InZone® Detachment System could result in coil movement, aneurysm rupture or vessel perforation.
- Verify repeatedly that the distal shaft of the catheter is not under stress before detaching the Target Detachable Coil. Axial compression or tension forces could be stored in the 2-tip microcatheter causing the tip to move during coil delivery. Microcatheter tip movement could cause the aneurysm or vessel to rupture.
- Advancing the delivery wire beyond the microcatheter tip once the coil has been detached involves risk of aneurysm or vessel perforation.
- The long term effect of this product on extravascular tissues has not been established so care should be taken to retain this device in the intravascular space.

Copyright © 2014 Stryker  
NV00006677.AA

## Trevo® XP ProVue Retrievers

See package insert for complete indications, complications, warnings, and instructions for use.

### INDICATIONS FOR USE

The Trevo Retriever is intended to restore blood flow in the neurovasculature by removing thrombus in patients experiencing ischemic stroke within 8 hours of symptom onset. Patients who are ineligible for intravenous tissue plasminogen activator (IV t-PA) or who fail IV t-PA therapy are candidates for treatment.

### COMPLICATIONS

Procedures requiring percutaneous catheter introduction should not be attempted by physicians unfamiliar with possible complications which may occur during or after the procedure. Possible complications include, but are not limited to, the following: air embolism; hematoma or hemorrhage at puncture site; infection; distal embolization; pain/headache; vessel spasm, thrombosis, dissection, or perforation; embolic; acute occlusion; ischemia; intracranial hemorrhage; false aneurysm formation; neurological deficits including stroke, and death.

### COMPATIBILITY

3x20 mm retrievers are compatible with Trevo® Pro 14 Microcatheters (REF 90231) and Trevo® Pro 18 Microcatheters (REF 90238). 4x20 mm retrievers are compatible with Trevo® Pro 18 Microcatheters (REF 90238). Compatibility of the Retriever with other microcatheters has not been established. Performance of the Retriever device may be impacted if a different microcatheter is used. The Merci® Balloon Guide Catheters are recommended for use during thrombus removal procedures. Retrievers are compatible with the Abbott Vascular DOC® Guide Wire Extension (REF 22260).

### WARNINGS

- Contents supplied STERILE, using an ethylene oxide (EO) process. Nonpyrogenic.
- To reduce risk of vessel damage, adhere to the following recommendations:
  - Take care to appropriately size Retriever to vessel diameter at

Copyright © 2014 Stryker  
NV00009028.AA

Damaged delivery wires may cause detachment failures, vessel injury or unpredictable distal tip response during coil deployment. If a delivery wire is damaged at any point during the procedure, do not attempt to straighten or otherwise repair it. Do not proceed with deployment or detachment. Remove the entire coil and replace with undamaged product.

- After use, dispose of product and packaging in accordance with hospital, administrative and/or local government policy.

### CAUTIONS / PRECAUTIONS

- Federal Law (USA) restricts this device to sale by or on the order of a physician.
- Besides the number of InZone Detachment System units needed to complete the case, there must be an extra InZone Detachment System unit as back up.
- Removing the delivery wire without grasping the introducer sheath and delivery wire together may result in the detachable coil sliding out of the introducer sheath.
- Failure to remove the introducer sheath after inserting the delivery wire into the RHV of the microcatheter will interrupt normal infusion of flush solution and allow back flow of blood into the microcatheter.
- Some low level overhead light near or adjacent to the patient is required to visualize the fluoro-saver marker; monitor light alone will not allow sufficient visualization of the fluoro-saver marker.
- Advance and retract the Target Detachable Coil carefully and smoothly without excessive force. If unusual friction is noticed, slowly withdraw the Target Detachable Coil and examine for damage. If damage is present, remove and use a new Target Detachable Coil. If friction or resistance is still noted, carefully remove the Target Detachable Coil and microcatheter and examine the microcatheter for damage.
- If it is necessary to reposition the Target Detachable Coil, verify under fluoroscopy that the coil moves with a one-to-one motion. If the coil does not move with a one-to-one motion or movement is difficult, the coil may have stretched and could possibly migrate or break. Gently remove both the coil and microcatheter and replace with new devices.
- Increased detachment times may occur when:
  - Other embolic agents are present.
  - Delivery wire and microcatheter markers are not properly aligned.
  - Thrombus is present on the coil detachment zone.
- Do not use detachment systems other than the InZone Detachment System.
- Increased detachment times may occur when delivery wire and microcatheter markers are not properly aligned.
- Do not use detachment systems other than the InZone Detachment System.



**Stryker Neurovascular**  
47900 Bayside Parkway  
Fremont, CA 94538-6515

[stryker.com/neurovascular](http://stryker.com/neurovascular)

Date of Release: FEB/2014

EX\_EN\_US

### PRECAUTIONS

- Prescription only – device restricted to use by or on order of a physician.
- Store in cool, dry, dark place.
- Do not use open or damaged packages.
- Use by "Use By" date.
- Exposure to temperatures above 54°C (130°F) may damage device and accessories. Do not autoclave.
- Do not expose Retriever to solvents.
- Use Retriever in conjunction with fluoroscopic visualization and proper anti-coagulation agents.
- To prevent thrombus formation and contrast media crystal formation, maintain a constant infusion of appropriate flush solution between guide catheter and Microcatheter and between Microcatheter and Retriever or guidewire.
- Do not attach a torque device to the shaped proximal end of DOC® Compatible Retriever. Damage may occur, preventing ability to attach DOC® Guide Wire Extension.



**Concentric Medical**  
301 East Evelyn  
Mountain View, CA 94041

EC REP

EMERGO Europe  
Molenstraat 15  
2513 BH, The Hague  
The Netherlands

CE 0459

**Stryker Neurovascular**  
47900 Bayside Parkway  
Fremont, CA 94538-6515

[stryker.com/neurovascular](http://stryker.com/neurovascular)  
[stryker.com/emea/neurovascular](http://stryker.com/emea/neurovascular)

Date of Release: JUN/2014

EX\_EN\_GL



## Target<sup>®</sup> DETACHABLE COILS



### Smooth and Stable

Whether you are framing, filling or finishing, Target Detachable Coils deliver consistently smooth deployment and exceptional microcatheter stability. Focused on design, Target Coils feature a host of advantages to ensure the high-powered performance you demand.

For more information, please visit [www.strykerneurovascular.com/Target](http://www.strykerneurovascular.com/Target) or contact your local Stryker Neurovascular sales representative.

**stryker<sup>®</sup>**  
Neurovascular